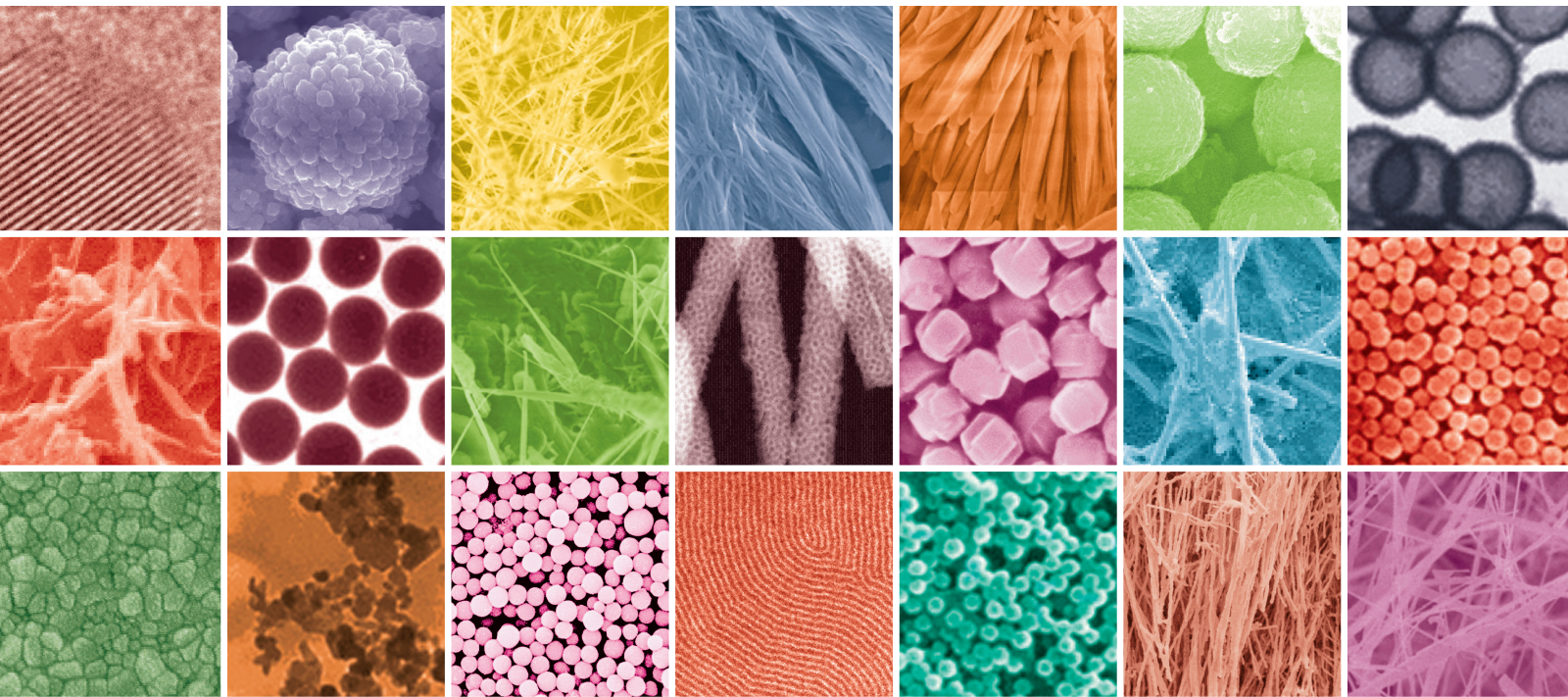


Development and Fabrication of Advanced Materials for Energy and Environment Applications 2014

Guest Editors: Ming-Guo Ma, Wen Zeng, Jie-Fang Zhu, Shao-Wen Cao,
and Zhong-Chang Wang





**Development and Fabrication of
Advanced Materials for Energy and
Environment Applications 2014**

**Development and Fabrication of
Advanced Materials for Energy and
Environment Applications 2014**

Guest Editors: Ming-Guo Ma, Wen Zeng, Jie-Fang Zhu,
Shao-Wen Cao, and Zhong-Chang Wang



Copyright © 2014 Hindawi Publishing Corporation. All rights reserved.

This is a special issue published in "Journal of Nanomaterials." All articles are open access articles distributed under the Creative Commons Attribution License, which permits unrestricted use, distribution, and reproduction in any medium, provided the original work is properly cited.

Editorial Board

Katerina E. Aifantis, USA
Nageh K. Allam, USA
Margarida Amaral, Portugal
Xuedong Bai, China
Lavinia Balan, France
Enrico Bergamaschi, Italy
Theodorian Borca-Tasciuc, USA
C. Jeffrey Brinker, USA
Christian Brosseau, France
Xuebo Cao, China
Shafiq Chowdhury, USA
Kwang-Leong Choy, UK
Cui ChunXiang, China
Miguel A. Correa-Duarte, Spain
Shadi A. Dayeh, USA
Ali Eftekhari, USA
Claude Estourns, France
Alan Fuchs, USA
Lian Gao, China
Russell E. Gorga, USA
Hongchen Chen Gu, China
Mustafa O. Guler, Turkey
John Z. Guo, USA
Smrati Gupta, Germany
Michael Harris, USA
Zhongkui Hong, China
Michael Z. Hu, USA
David Hui, USA
Y.-K. Jeong, Republic of Korea
Sheng-Rui Jian, Taiwan
Wanqin Jin, China
Rakesh K. Joshi, UK
Zhenhui Kang, China
Fathallah Karimzadeh, Iran
Alireza Khataee, Iran

Do Kyung Kim, Korea
Alan K. T. Lau, Hong Kong
Burtrand Lee, USA
Jun Li, Singapore
Benxia Li, China
Xing-Jie Liang, China
Shijun Liao, China
Gong-Ru Lin, Taiwan
Tianxi Liu, China
Jun Liu, USA
Songwei Lu, USA
Daniel Lu, China
Jue Lu, USA
Ed Ma, USA
Gaurav Mago, USA
Santanu K. Maiti, India
Sanjay R. Mathur, Germany
Vikas Mittal, UAE
Weihai Ni, China
Sherine Obare, USA
Atsuto Okamoto, Japan
Abdelwahab Omri, Canada
Edward A. Payzant, USA
Kui-Qing Peng, China
Anukorn Phuruangrat, Thailand
Mahendra Rai, India
Suprakas Sinha Ray, South Africa
Ugur Serincan, Turkey
Huaiyu Shao, Japan
Donglu Shi, USA
Vladimir Sivakov, Germany
Marinella Striccoli, Italy
Bohua Sun, South Africa
Saikat Talapatra, USA
Nairong Tao, China

Titipun Thongtem, Thailand
Somchai Thongtem, Thailand
Alexander Tolmachev, Ukraine
Valeri P. Tolstoy, Russia
Tsung-Yen Tsai, Taiwan
Takuya Tsuzuki, Australia
Raquel Verdejo, Spain
Mat U. Wahit, Malaysia
Zhenbo Wang, China
Ruiping Wang, Canada
Shiren Wang, USA
Cheng Wang, China
Yong Wang, USA
Jinquan Wei, China
Ching-Ping Wong, Hong Kong
Xingcai Wu, China
Guodong Xia, Hong Kong
Ping Xiao, UK
Zhi Li Xiao, USA
Yangchuan Xing, USA
Shuangxi Xing, China
Nanping Xu, China
Doron Yadlovker, Israel
Yingkui Yang, China
Khaled Youssef, USA
Kui Yu, Canada
William W. Yu, USA
Haibo Zeng, China
Tianyou Zhai, China
Bin Zhang, China
Renyun Zhang, Sweden
Yanbao Zhao, China
Lianxi Zheng, Singapore
Chunyi Zhi, Hong Kong

Contents

Development and Fabrication of Advanced Materials for Energy and Environment Applications 2014, Ming-Guo Ma, Wen Zeng, Jie-Fang Zhu, Shao-Wen Cao, and Zhong-Chang Wang
Volume 2014, Article ID 643579, 2 pages

Simple, Fast, and Cost-Effective Fabrication of Wafer-Scale Nanohole Arrays on Silicon for Antireflection, Di Di, Xuezhong Wu, Peitao Dong, Chaoguang Wang, Jian Chen, Haoxu Wang, Junfeng Wang, and Shengyi Li
Volume 2014, Article ID 439212, 6 pages

Hydrothermal Synthesis and Hydrogen Sensing Properties of Nanostructured SnO₂ with Different Morphologies, Weigen Chen, Hongli Gan, Wei Zhang, and Zeyu Mao
Volume 2014, Article ID 291273, 7 pages

Facile Hydrothermal Synthesis and Basic Gas-Sensing Properties of Two Three-Dimensional Nanostructures of SnO₂, Lingna Xu, Weigen Chen, Caisheng Wang, Tuoyu Gao, and Qu Zhou
Volume 2014, Article ID 954734, 6 pages

The Removal of Uranium onto Nanoscale Zero-Valent Iron Particles in Anoxic Batch Systems, Richard A. Crane and Thomas B. Scott
Volume 2014, Article ID 956360, 9 pages

Selective Synthesis of Manganese/Silicon Complexes in Supercritical Water, Jiancheng Wang, Zhaoliang Peng, Bing Wang, Lina Han, Liping Chang, Weiren Bao, and Gang Feng
Volume 2014, Article ID 713685, 8 pages

Physical, Mineralogical, and Micromorphological Properties of Expansive Soil Treated at Different Temperature, Jian Li, Xiyong Wu, and Long Hou
Volume 2014, Article ID 848740, 7 pages

Catalytic Hydrolysis of Ammonia Borane by Cobalt Nickel Nanoparticles Supported on Reduced Graphene Oxide for Hydrogen Generation, Yuwen Yang, Fei Zhang, Hualan Wang, Qilu Yao, Xiangshu Chen, and Zhang-Hui Lu
Volume 2014, Article ID 294350, 9 pages

Nanocatalysts for Hydrogen Generation from Ammonia Borane and Hydrazine Borane, Zhang-Hui Lu, Qilu Yao, Zhujun Zhang, Yuwen Yang, and Xiangshu Chen
Volume 2014, Article ID 729029, 11 pages

Formulation of Synthesized Zinc Oxide Nanopowder into Hybrid Beads for Dye Separation, H. Shokry Hassan, M. F. Elkady, A. H. El-Shazly, and Hisham S. Bamufleh
Volume 2014, Article ID 967492, 14 pages

Development and Evaluation of Solbrax-Water Nanoemulsions for Removal of Oil from Sand, Priscila F. Oliveira, Thiago M. Oliveira, Luciana S. Spinelli, and Claudia R. E. Mansur
Volume 2014, Article ID 723789, 8 pages

Preparation of Polyvinyl Alcohol/Xylan Blending Films with 1,2,3,4-Butane Tetracarboxylic Acid as a New Plasticizer, Cun-dian Gao, Jun-li Ren, Shuai-yang Wang, Run-cang Sun, and Li-hong Zhao
Volume 2014, Article ID 764031, 8 pages

Synthesis and Characterization of Different Crystalline Calcium Silicate Hydrate: Application for the Removal of Aflatoxin B1 from Aqueous Solution, Lu Zeng, Ligang Yang, Shuping Wang, and Kai Yang
Volume 2014, Article ID 431925, 10 pages

In Situ Formation of Carbon Nanomaterials on Bulk Metallic Materials, J. Y. Xu, X. C. Lei, R. Yang, and Z. Z. Fan
Volume 2014, Article ID 690630, 9 pages

Influence of Sn Doping on Phase Transformation and Crystallite Growth of TiO₂ Nanocrystals, Guozhu Fu, Yanqiu Yang, Gang Wei, Xin Shu, Ning Qiao, and Li Deng
Volume 2014, Article ID 835450, 5 pages

A First Principle Comparative Study on Chemisorption of H₂ on C₆₀, C₈₀, and Sc₃N@C₈₀ in Gas Phase and Chemisorption of H₂ on Solid Phase C₆₀, Hongtao Wang, Lijuan Chen, Yongkang Lv, Jianwen Liu, and Gang Feng
Volume 2014, Article ID 676908, 7 pages

The Synthesis of a Novel Cellulose Physical Gel, Jiufang Duan, Xiaojian Zhang, Jianxin Jiang, Chunrui Han, Jun Yang, Liujun Liu, Hongyun Lan, and Daozhan Huang
Volume 2014, Article ID 312696, 7 pages

Effects of Emulsifiers on Preparing Spherical Urea-Formaldehyde Paraffin Capsules Modified by β -Cyclodextrin for Energy Storage, Xin Yu, Zhanhua Huang, and Kaixuan Yu
Volume 2014, Article ID 236016, 7 pages

Organic/Inorganic Superabsorbent Hydrogels Based on Xylan and Montmorillonite, Shuang Zhang, Ying Guan, Gen-Que Fu, Bo-Yang Chen, Feng Peng, Chun-Li Yao, and Run-Cang Sun
Volume 2014, Article ID 675035, 11 pages

Catalytic Properties of Pd Modified Cu/SAPO-34 for NO_x Removal from Diesel Engine, J. C. Wang, H. Qiao, L. N. Han, Y. Q. Zuo, L. P. Chang, W. R. Bao, and G. Feng
Volume 2013, Article ID 625739, 9 pages

Editorial

Development and Fabrication of Advanced Materials for Energy and Environment Applications 2014

Ming-Guo Ma,¹ Wen Zeng,² Jie-Fang Zhu,³ Shao-Wen Cao,⁴ and Zhong-Chang Wang⁵

¹ Beijing Key Laboratory of Lignocellulosic Chemistry, College of Materials Science and Technology, Beijing Forestry University, Beijing 100083, China

² College of Materials Science and Engineering, Chongqing University, Chongqing 400040, China

³ Department of Materials Chemistry, The Ångström Laboratory, Uppsala University, 75121 Uppsala, Sweden

⁴ School of Materials Science and Engineering, Nanyang Technological University, Singapore 639798

⁵ WPI Research Center, Advanced Institute for Materials Research, Tohoku University, Sendai 980-8577, Japan

Correspondence should be addressed to Ming-Guo Ma; mg_ma@bjfu.edu.cn

Received 5 June 2014; Accepted 5 June 2014; Published 19 June 2014

Copyright © 2014 Ming-Guo Ma et al. This is an open access article distributed under the Creative Commons Attribution License, which permits unrestricted use, distribution, and reproduction in any medium, provided the original work is properly cited.

Recently, environmental and energy problems have been receiving more and more attention. It is reported that advanced materials are promising applications in environmental and energy fields. Therefore, this special issue focused on the development and fabrication of advanced materials for energy and environment applications. It is expected that this special issue would provide a communication platform on the recent development of these fields.

The *Call for Papers* of the special issue was posted online on November 10, 2013, and closed for submission on February 21, 2014. We received 24 papers for submission in less than four months. Finally, 19 papers were selected for publication.

J. C. Wang et al. applied the hydrothermal method for the synthesis of the Cu/SAPO-34 catalysts with different Cu contents, which was modified by impregnating Pd. It was found that the Cu/SAPO-34 catalysts with Cu/Si ratios of 0.05, 0.1, and 0.2 had better de-NO_x activity than other catalysts, by the selective catalytic reduction by C₃H₆ and NH₃. Experimental results indicated that the maximum conversion of NO with Pd could reach 90%.

L. Zeng et al. reported the synthesis and characterization of calcium silicate hydrates by hydrothermal method, which was used to adsorb carcinogenic aflatoxin B1. It was shown that the adsorption followed the pseudo-second-order kinetic model and the data of equilibrium

adsorption were fitted to Langmuir and Freundlich equations.

The mechanism especially for H₂ molecules adsorption on solid C₆₀ under high pressure was proposed by H. Wang et al. via a first principle comparative study. They demonstrated that the initial H₂ adsorption on two adjacent C₆₀ gave a much lower barrier 1.36 eV in comparison with the barrier of adsorption on a single C₆₀ (about 3.0 eV).

S. Zhang et al. prepared the organic/inorganic superabsorbent hydrogels based on xylan and inorganic clay montmorillonite via grafting copolymerization of acrylic acid and 2-acrylamido-2-methylpropanesulfonic acid with *N,N*-methylenebisacrylamide as a cross-linking agent and potassium persulfate as an initiator. Experimental results indicated that the hydrogels exhibited the high compressive modulus about 35–55 KPa. The maximum equilibrium swelling ratios of hydrogels in distilled water and 0.9 wt% sodium chloride solutions were up to 1423 g g⁻¹ and 69 g g⁻¹, respectively. The effect of various cationic salt solutions (LiCl, CaCl₂, and FeCl₃) on the swelling has the following order: Li⁺ > Ca²⁺ > Fe³⁺.

X. Yu et al. prepared urea-formaldehyde paraffin capsules modified by β -cyclodextrin with excellent energy storage capacity using different emulsifiers. It was reported that OP-10 for use with PCMs as emulsifier had a better emulsifying

capacity, thermal stability, and mechanical stirring stability than SDBS for use with PCMs as emulsifier.

J. Wang et al. synthesized Mn/Si complexes in supercritical water using a tube reactor by a series of manganese salts ($\text{Mn}(\text{NO}_3)_2$, MnCl_2 , MnSO_4 , and $\text{Mn}(\text{Ac})_2$) and silicon materials (silica sand, silica sol, and tetraethyl orthosilicate). It was found that MnO_2 , Mn_2O_3 , and Mn_2SiO_4 could be obtained in supercritical water at 673 K in 5 min and the hydroxyl groups on the surface of SiO_2 from different silicon sources enhanced the reactivity of SiO_2 . H. S. Hassan et al. prepared zinc oxide with 94.9% dye removal ability within 1 h by sol-gel technique, which was a promising adsorbent material for dye decolorization from the polluted water.

As promising hydrogen storage materials, ammonia borane (NH_3BH_3) and hydrazine borane ($\text{N}_2\text{H}_4\text{BH}_3$) have hydrogen content as high as 19.6 wt% and 15.4 wt%. Z.-H. Lu et al. survey the research progresses in nanocatalysts for hydrogen generation from the hydrolysis or methanolysis of NH_3BH_3 and $\text{N}_2\text{H}_4\text{BH}_3$. Moreover, they synthesized well dispersed magnetically recyclable bimetallic CoNi nanoparticles supported on the reduced graphene oxide by one-step in situ coreduction of aqueous solution of cobalt(II) chloride, nickel(II) chloride, and graphite oxide with ammonia borane as the reducing agent under ambient condition. It was found that the CoNi/reduced graphene oxide nanoparticles exhibited excellent catalytic activity with a total turnover frequency value of $19.54 \text{ mol H}_2 \text{ mol catalyst}^{-1} \text{ min}^{-1}$ and a low activation energy value of $39.89 \text{ kJ mol}^{-1}$ at room temperature.

C.-d. Gao et al. prepared miscible, biodegradable poly(vinyl alcohol)/xylan blending films in the range of the PVA/xylan weight ratio from 1:2 to 3:1 by casting method using 1,2,3,4-butane tetracarboxylic acid as a new plasticizer. It was shown that blending films were biodegraded almost by 41% with an addition of 10% 1,2,3,4-butane tetracarboxylic acid in blending films within 30 days in soil.

As mentioned in the above results, this issue provides the recent development of advanced materials for energy and environment applications. More importantly, we hope that more attention should be paid to the research of these fields and rapid progress will be achieved in the near future.

Ming-Guo Ma
Wen Zeng
Jie-Fang Zhu
Shao-Wen Cao
Zhong-Chang Wang

Research Article

Simple, Fast, and Cost-Effective Fabrication of Wafer-Scale Nanohole Arrays on Silicon for Antireflection

Di Di,¹ Xuezhong Wu,¹ Peitao Dong,^{1,2} Chaoguang Wang,¹ Jian Chen,¹
Haoxu Wang,¹ Junfeng Wang,¹ and Shengyi Li¹

¹ College of Mechatronics and Automation, National University of Defense Technology, Changsha 410073, China

² State Key Laboratory of Transducer Technology, Chinese Academy of Sciences, Shanghai 200050, China

Correspondence should be addressed to Peitao Dong; ptdong@nudt.edu.cn

Received 12 February 2014; Accepted 21 April 2014; Published 15 June 2014

Academic Editor: Jie-Fang Zhu

Copyright © 2014 Di Di et al. This is an open access article distributed under the Creative Commons Attribution License, which permits unrestricted use, distribution, and reproduction in any medium, provided the original work is properly cited.

A simple, fast, and cost-effective method was developed in this paper for the high-throughput fabrication of nanohole arrays on silicon (Si), which is utilized for antireflection. Wafer-scale polystyrene (PS) monolayer colloidal crystal was developed as templates by spin-coating method. Metallic shadow mask was prepared by lifting off the oxygen etched PS beads from the deposited chromium film. Nanohole arrays were fabricated by Si dry etching. A series of nanohole arrays were fabricated with the similar diameter but with different depth. It is found that the maximum depth of the Si-hole was determined by the diameter of the Cr-mask. The antireflection ability of these Si-hole arrays was investigated. The results show that the reflection decreases with the depth of the Si-hole. The deepest Si-hole arrays show the best antireflection ability (reflection < 9%) at long wavelengths (>600 nm), which was about 28 percent of the nonpatterned silicon wafer's reflection. The proposed method has the potential for high-throughput fabrication of patterned Si wafer, and the low reflectivity allows the application of these wafers in crystalline silicon solar cells.

1. Introduction

Solar cell is an important development direction for clean and renewable energy [1]. Crystal silicon solar cells dominated a significant position in the commercial solar cell market [2]. However, high reflectivity of silicon wafer on visible light (more than 30%) has greatly hindered the light conversion efficiency [2, 3]. Recently, various antireflection methods have been developed to reduce the reflection loss of solar cells, such as antireflection multilayer films and patterned coatings [4].

Constructing periodic patterns directly on silicon substrates is attractive for solar cells due to its strong enhanced light trapping and potential low cost [4]. For example, vertically aligned nanowire, nanorod, nanocone, or nanohole arrays have been studied to improve light absorption for solar cells [4–9]. Theoretical research suggests that nanohole architectures display strong optical absorption ability because of the effective optical coupling between the array and the incident sunlight as well as the large density of waveguide

modes [4]. Nanohole arrays also exhibit better mechanical robustness, compared with multilayer antireflection films and free-standing nanowire structures.

As mentioned above, nanohole arrays have great potential for efficient solar photovoltaics. A simple, controllable, cost-effective, and high-throughput fabrication method was of primary importance for practical commercial application. Deep ultraviolet lithography and electron beam lithography have been used to fabricate the nanopatterns on silicon wafer surface [4, 10]. However, the high cost and low-throughput hindered its wide application. Laser holographic lithography has also been used to fabricate silicon nanoholes [11–13]. It was considered a potentially high throughput process for periodic nanostructures fabrication. However, it is limited by the light wavelength in fabrication and the huge cost. Nanosphere lithography has been widely used in the fabrication of periodic nanopatterns for its low cost and good controllability [14–19]. Manufacturing efficiency may be the biggest problem commonly encountered [2, 3, 9].

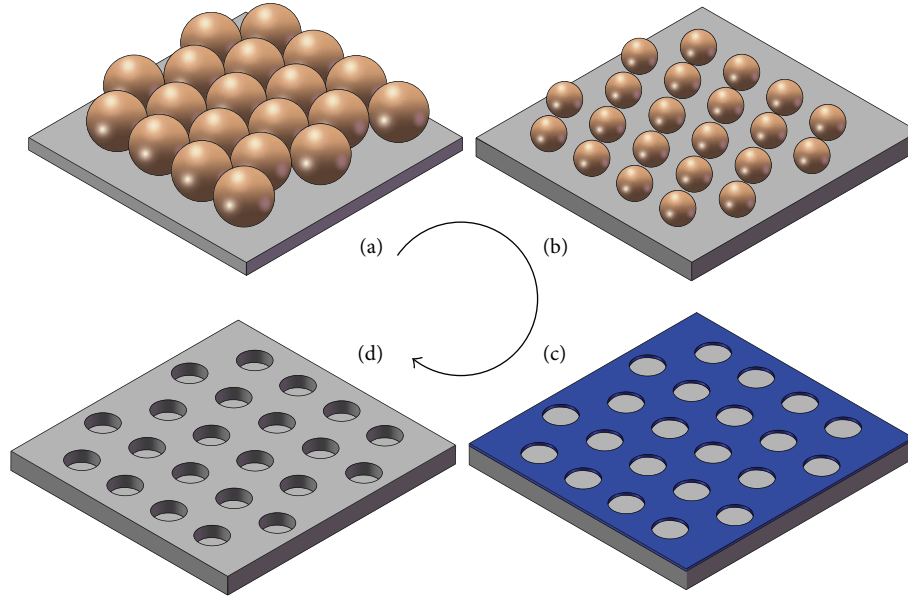


FIGURE 1: Schematic of nanohole array fabrication procedures: (a) PS monolayer colloidal crystal prepared by spin-coating; (b) PS beads size reduction by oxygen etching; (c) Si-hole preparation by lifting off the etched PS bead from the Cr-layer; (d) Si-hole array fabrication by silicon dry etching.

Herein, we demonstrated a simple, fast, and cost-effective strategy for high-throughput fabrication of antireflective nanohole arrays on silicon. Spin-coating method was employed to fabricate wafer-scale crystal templates. And some other standard microfabrication methods, such as O_2 reaction ion etching, metal film deposition, and silicon dry etching, were in turn implemented to fabricate silicon nanoholes arrays. A series of Si-hole arrays were successfully fabricated in a controlled manner. And their antireflection ability was further investigated.

2. Experimental

2.1. Materials and Instruments. PS beads with a mean diameter of 310 nm were purchased from Sigma-Aldrich (Germany). $\langle 100 \rangle$ silicon wafers ($500 \mu\text{m}$ thickness, n type, from Tianjin Semiconductor Technology Research Institute) were used as substrates. Other chemicals were purchased from Sinopharm (Shanghai), including concentrated sulfuric acid (H_2SO_4 , 98%), hydrogen peroxide (H_2O_2 , 30%), ethanol (EtOH), and acetone. Cr etchants and deionized water (DI) were prepared in laboratory. All chemicals were used as received.

A spin-coater (EASYLINE-S-200TT, Solar-semi, Germany) was employed to prepare well-organized crystal domain. An inductively coupled plasma reactive ion etching system (ICP-2B, Chuangweina, Beijing) was utilized to etch the PS beads and Si substrate. An e-beam evaporator (ZZS500, Nanguang, Chengdu) was used for Cr-layer deposition. Optical microscopy, scanning electron microscopy (SEM, S-4800, Hitachi), and atomic force microscopy (AFM, dimension Icon, Bruker Nano Surfaces Division) were used to analyze the nanoscale morphologies. UV-VIS spectrophotometer (Hitachi U-4100) was used here for reflectivity measurements.

2.2. Fabrication Procedures. The schematic of nanohole array fabrication procedures was illustrated in Figure 1.

PS beads were first dispersed in a mixed solution of H_2O and EtOH ($v:v = 1:1$). The silicon wafers were cleaned in the “Piranha” solution ($v:v = 3:1$ mixture of H_2SO_4 and H_2O_2) for one hour to improve their hydrophilicity. The cleaned wafer was stored in ethanol and dried with a stream of nitrogen gas before use. A drop ($1200 \mu\text{L}$) of PS dispersions was spread onto silicon wafer, and the solution was allowed to uniformly cover the wafer surface for 30 s before spin-coating process started. The rotation speed was 2000 rpm and spinning time was 120 s. PS monolayer colloidal crystal was developed on the 3-inch silicon wafer and used as starting templates (Figure 1(a)).

The PS monolayer colloidal crystal was then etched in the oxygen plasma to reduce size, operating at $4.6 e^{-1}$ Pa (chamber pressure), 32 sccm (flow rate), and 28 W (RF power) (Figure 1(b)). Subsequently, a 200 \AA thick Cr film was deposited in an e-beam evaporator with the evaporation rate of $2\sim 5 \text{ \AA/s}$. The etched PS beads were then lifted off from the Cr-layer, leaving behind the Cr-hole mask (Figure 1(c)). Silicon substrate dry etching process was employed to fabricate the Si-hole arrays. A mixture of SF_6 gas and Ar_2 gas was used as etching gas with the operating parameter characters of 0.1 Pa (chamber pressure), 46 sccm (flow rate), and 45 W (RF power). Cr nanohole mask was then removed by the Cr etchant as shown in Figure 1(d). Finally, silicon substrate was ultrasonically cleaned in deionized water for several minutes.

3. Results and Discussions

3.1. Wafer-Scale Fabrication. Photovoltaic production calls for simple, fast, and cost-effective fabrication process. Also, the process should be compatible with current techniques.

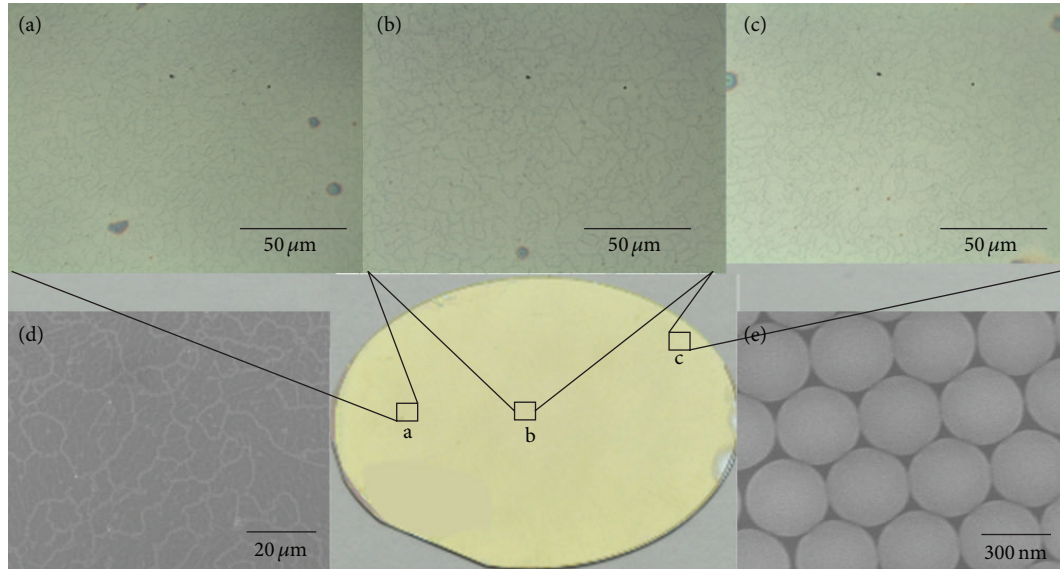


FIGURE 2: Optical microscopy photographs and SEM images of spin-coated PS monolayer. These points were randomly selected and kept a great distance away from each other.

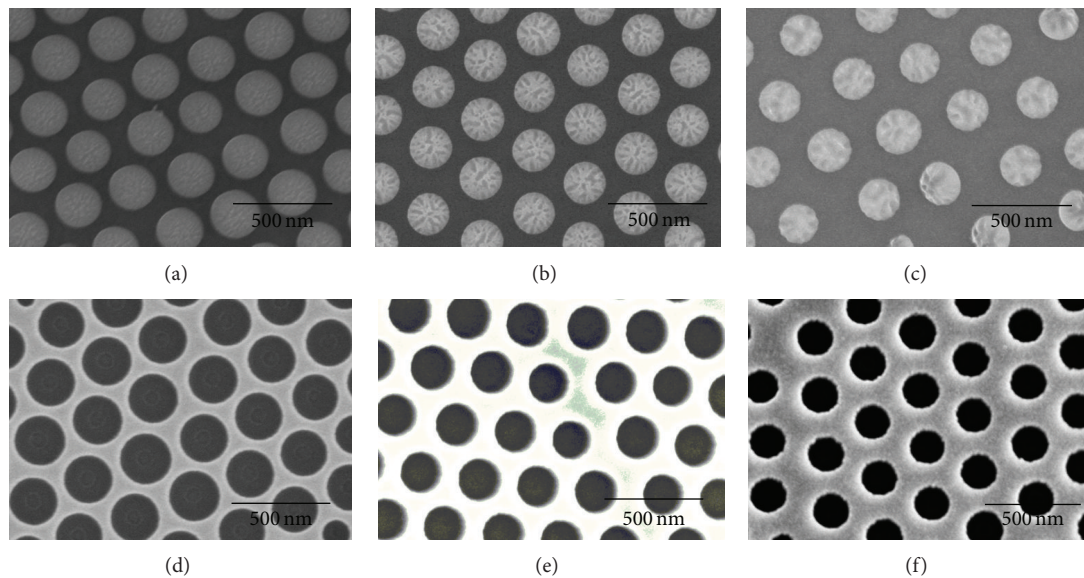


FIGURE 3: SEM images of size reduced PS NCP beads and the Cr nanoholes. ((a)–(c)) SEM images of PS beads with average diameters of 235 nm, 215 nm, and 185 nm, respectively; ((e)–(f)) SEM images of Cr nanoholes with average diameters of 244 nm, 219 nm, and 191 nm, respectively.

The nowadays widely used methods are either time-assuming or of low-throughput. Herein, spin-coating technique was utilized to prepare wafer-scale crystal domain. Spin-coating is a facile, cost-effective, and laborsaving technique, which is compatible with mature IC technique [20, 21].

Figure 2 shows a digital camera photograph of a 3-inch silicon wafer, on which PS beads formed a uniform monolayer by spin-coating technique. Nearly the whole wafer presents yellow color when illuminated with white light. As the color of PS film changed obviously with the layer and the orientation of colloidal crystal, the homogeneity color of the wafer demonstrates the uniformity of the PS

film [21]. The uniformity of PS film was further validated by the microscope images as shown in Figures 2(a), 2(b), and 2(c). The microscopy photographs were obtained at randomly selected areas that are far away from each other. It is monotonous yellowish green in the microscopy images. The arrays of close-packed PS beads were filled in the field of vision. The dark dots among the PS monolayer are a result of the incomplete dispersion of the PS sol., which can be avoided by complete dispersion.

Figures 2(d) and 2(e) show the low and high magnified SEM images of the PS monolayer colloidal crystal. The PS monolayer is constituted with regions of hexagonally

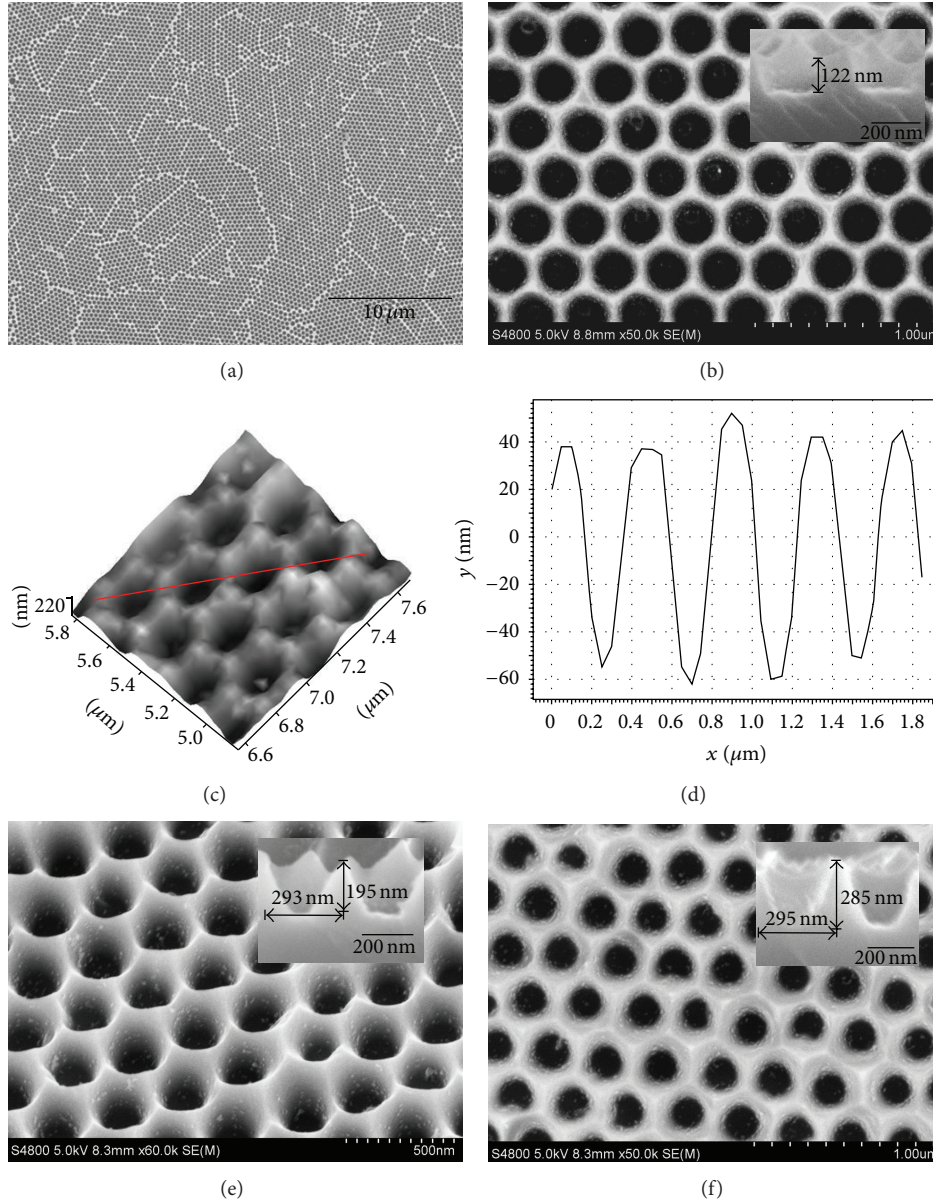


FIGURE 4: SEM and AFM images of Si-hole arrays. ((a)-(b)) The high and low magnification SEM images of Si-hole arrays after 3 min etching; (c) the 3D AFM images 3 min etched Si-hole arrays; (d) height profile of the red line marked in (c); ((e)-(f)) SEM images of Si-hole arrays after 5 min and 7 min etching, respectively.

close-packed (HCP) PS beads. Thus, the colloid film was long-range ordered. It has been demonstrated that there is no difference in photovoltaics for long-range ordered arrays and strict-ordered arrays [22]. The area of the HCP regions was on the order of several $1000 \mu\text{m}^2$.

3.2. Etching Mask Preparation. To control the diameter of Cr-mask, the PS beads were etched in O_2 plasma. The oxygen etching parameters, such as etching power and etching time, were optimized to control the diameter of the PS beads. Figures 3(a), 3(b), and 3(c) show the SEM images of etched PS beads. The etched PS beads were nonclosed, packed, and round in shape seen from the top view. The beads' diameters were reduced to 235 nm, 215 nm, and 185 nm after

240 s, 260 s, and 300 s oxygen etching, respectively. These nonclosed packed PS beads arrays were covered by Cr-layer and then lifted off by adhesive tape leaving behind the Cr-hole arrays as shown in Figures 3(d), 3(e), and 3(f). The Cr-hole arrays served as etching mask in silicon nanohole fabrication. The diameters of Cr-hole are 244 nm, 219 nm, and 191 nm, respectively. They are a little larger than corresponding colloidal templates, which is a result of the lateral growth of the deposited metal [23].

3.3. Vertical Etching and Lateral Erosion. To investigate the relationship between the antireflection ability and the depth of the Si-hole, the diameters of Si-holes were controlled to about 300 nm, which is much close to the period of

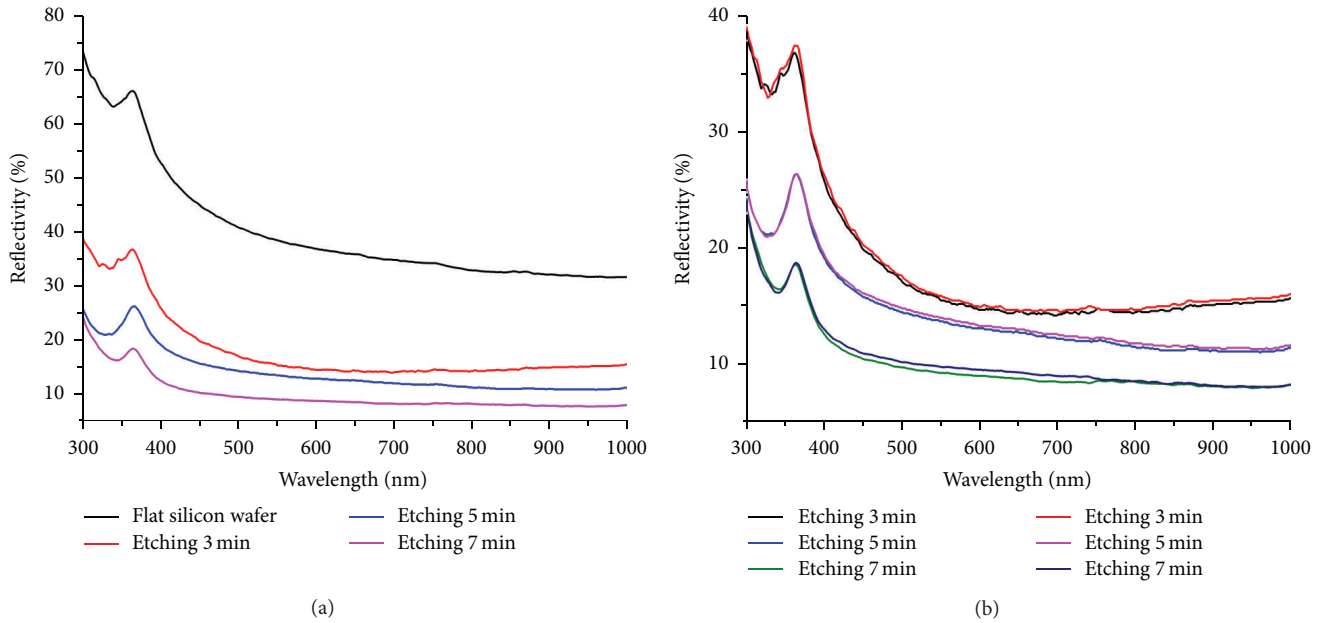


FIGURE 5: (a) Specular reflectance curves of flat silicon wafer and Si-hole arrays that etched for 3 min, 5 min, and 7 min; (b) homogeneity of the Si-hole arrays substrate.

the Si-hole array (diameter of unetched PS sphere, about 310 nm). The morphologies of these Si-hole arrays were characterized by SEM and AFM imaging as shown in Figure 4. Figure 4(a) shows the low-magnified SEM image of the Si-hole arrays etched for 3 min. These arrays are long-range ordered following the orientation of spin-coated PS beads. Figure 4(b) shows the high-magnified SEM image of Si-hole arrays. And the inset shows the cross-section view of a Si-hole. Figure 4(c) shows the 3D AFM image after etching for 3 min. And Figure 4(d) shows the height profile of the red line marked in Figure 4(c). These AFM images confirmed the morphology of the Si-hole characterized by SEM. Figures 4(e) and 4(f) show the SEM images of Si-hole arrays that etched for 5 min and 7 min, respectively. The insets show the corresponding cross-sections.

Judging from the insets of Figures 4(b), 4(e), and 4(f), the depths of the Si-holes after 3 min, 5 min, and 7 min etching processes were about 122 nm, 195 nm, and 285 nm, respectively. All the diameters of the Si-holes are about 300 nm. There is lateral erosion in the Si etching process considering that the corresponding diameters of Cr-masks were 244 nm, 219 nm, and 191 nm, respectively. Seen from the insets of Figures 4(e) and 4(f), the sidewalls of the Si-holes were nearly triangle. Thus, the Si-hole would not be deepened by extending the etching time due to the lateral erosion. The Si-hole can be deepened if smaller Cr-mask was utilized. Thus, the maximum depth of Si-hole was depending on the diameter of Cr-mask.

3.4. Antireflection Characterization. The patterned Si wafers were utilized for antireflection. These arrays were fabricated with similar diameters but with different depth. The specular reflectance curves of the substrates were shown in Figure 5(a).

The incident light was perpendicular to the substrate surface, and the reflectivity was measured between wavelengths 300 nm and 1000 nm. The black line represents the reflection curve obtained from a flat Si wafer. The flat Si wafer exhibits high reflectivity (>32%) in both visible and near infrared wavelengths range. All patterned substrates perform much better than the flat silicon substrate. The reflectivity decreased with the depth of the Si-hole arrays. The Si-hole arrays that etched for 7 min exhibit the best antireflection ability (<9%), which is about 28 percent of the nonpatterned silicon wafer's reflection.

To investigate the homogeneity of proposed Si-hole arrays, redundancy reflection spectra were measured for each substrate. The redundancy spots were selected far away from the originally measured one on each wafer. These curves were shown in Figure 5(b). The curves coincide to each other well for corresponding etching time, which demonstrated the homogeneity of the patterned antireflection wafer.

The proposed Si-hole based antireflection substrate performs better than the reported colloid-based antireflection coatings [2, 24]. Moreover, the advantages of the proposed method are the cost-effectiveness, high-throughput, and controllability. And the antireflection performance of proposed structure can be further improved in future research by optimizing the fabrication parameters.

4. Conclusions

In summary, a simple, fast, and cost-effective method is developed based on nanosphere lithography in this paper for high-throughput fabrication of wafer-scale nanohole arrays on silicon. These patterned structures perform well in antireflection and have the potential in photovoltaic manufacture.

The spin-coating technique was introduced herein to confirm the simple, fast, and wafer-scale fabrication. And the fabrication procedure was of high-throughput and cost-effective. It is found that the reflectivity of the substrate decreases with the depth of the Si-hole. And the maximum depth of Si-hole is dependent on the diameter of Cr-mask. The Si-hole substrate with 285 nm depth shows the best antireflection ability (<9%), which is about 28 percent of the nonpatterned silicon wafer's reflection. The fabricated structures are able to reduce reflectivity at the visible and near infrared wavelengths range. The proposed strategy is attractive for the antireflective substrate fabrication, which have a great potential to improve the solar cell conversion efficiency.

Conflict of Interests

The authors declare that there is no conflict of interests regarding the publication of this paper.

Acknowledgments

The authors would like to thank the financial support provided by National Natural Science Foundation of China (91023028) and the Foundation of State Key Laboratory of Transducer Technology (SKT1201).

References

- [1] Y. Tian, C. Hu, Y. Xiong et al., "ZnO pyramidal arrays: novel functionality in antireflection," *Journal of Physical Chemistry C*, vol. 114, no. 22, pp. 10265–10269, 2010.
- [2] C.-H. Sun, W.-L. Min, N. C. Linn, P. Jiang, and B. Jiang, "Templated fabrication of large area subwavelength antireflection gratings on silicon," *Applied Physics Letters*, vol. 91, no. 23, Article ID 231105, 2007.
- [3] C.-H. Sun, W.-L. Min, N. C. Linn, P. Jiang, and B. Jiang, "Large-scale assembly of periodic nanostructures with metastable square lattices," *Journal of Vacuum Science and Technology B: Microelectronics and Nanometer Structures*, vol. 27, no. 3, pp. 1043–1047, 2009.
- [4] K.-Q. Peng, X. Wang, L. Li, X.-L. Wu, and S.-T. Lee, "High-performance silicon nanohole solar cells," *Journal of the American Chemical Society*, vol. 132, no. 20, pp. 6872–6873, 2010.
- [5] Y. Lu and A. Lal, "High-efficiency ordered silicon nano-conical-frustum array solar cells by self-powered parallel electron lithography," *Nano Letters*, vol. 10, no. 11, pp. 4651–4656, 2010.
- [6] Z. Yu, H. Gao, W. Wu, H. Ge, and S. Y. Chou, "Fabrication of large area subwavelength antireflection structures on Si using trilayer resist nanoimprint lithography and liftoff," *Journal of Vacuum Science and Technology B: Microelectronics and Nanometer Structures*, vol. 21, no. 6, pp. 2874–2877, 2003.
- [7] N. D. Lam, Y. Kim, K. Kim, and J. Lee, "Influences of InGaP conical frustum nanostructures on the characteristics of GaAs solar cells," *Journal of Nanomaterials*, vol. 2013, Article ID 785359, 6 pages, 2013.
- [8] E. C. Garnett, M. L. Brongersma, Y. Cui, and M. D. McGehee, "Nanowire solar cells," *Annual Review of Materials Research*, vol. 41, pp. 269–295, 2011.
- [9] C.-M. Hsu, S. T. Connor, M. X. Tang, and Y. Cui, "Wafer-scale silicon nanopillars and nanocones by Langmuir-Blodgett assembly and etching," *Applied Physics Letters*, vol. 93, no. 13, Article ID 133109, 2008.
- [10] N. A. Yahaya, N. Yamada, Y. Kotaki, and T. Nakayama, "Characterization of light absorption in thin-film silicon with periodic nanohole arrays," *Optics Express*, vol. 21, no. 5, pp. 5924–5930, 2013.
- [11] D. Valerie, X. Meng, O. El Daif et al., "Micrometer-thin crystalline-silicon solar cells integrating numerically optimized 2-D photonic crystals," *IEEE Journal of Photovoltaics*, vol. 4, no. 1, pp. 215–223, 2014.
- [12] X. Meng, V. Depauw, G. Gomard et al., "Design, fabrication and optical characterization of photonic crystal assisted thin film monocrystalline-silicon solar cells," *Optics Express*, vol. 20, supplement 4, pp. A465–A475, 2012.
- [13] X. Meng, G. Gomard, O. El Daif et al., "Absorbing photonic crystals for silicon thin-film solar cells: design, fabrication and experimental investigation," *Solar Energy Materials and Solar Cells*, vol. 95, supplement 1, pp. S32–S38, 2011.
- [14] S.-M. Yang, S. G. Jang, D.-G. Choi, S. Kim, and H. K. Yu, "Nanomachining by colloidal lithography," *Small*, vol. 2, no. 4, pp. 458–475, 2006.
- [15] C. Qian, C. Ni, W. Yu et al., "Highly-ordered, 3D petal-like array for surface-enhanced raman scattering," *Small*, vol. 7, no. 13, pp. 1801–1806, 2011.
- [16] S. Zhu and W. Zhou, "Topical review: design, fabrication, and applications of hybrid nanostructured array," *Journal of Nanomaterials*, vol. 2012, Article ID 206069, 3 pages, 2012.
- [17] C. Cong, W. C. Junus, Z. Shen, and T. Yu, "New colloidal lithographic nanopatterns fabricated by combining pre-heating and reactive ion etching," *Nanoscale Research Letters*, vol. 4, no. 11, pp. 1324–1328, 2009.
- [18] H. Qi, O. J. Glembocki, and S. M. Prokes, "Plasmonic properties of vertically aligned nanowire arrays," *Journal of Nanomaterials*, vol. 2012, Article ID 843402, 7 pages, 2012.
- [19] C. Wang, X. Wu, P. Dong et al., "Diversification of nanostructure morphology by modifying angle-resolved heterogeneous shadow mask," *Journal of Nanoscience and Nanotechnology*, vol. 13, no. 12, pp. 8259–8265, 2013.
- [20] M. Giuliani, W. González-Viñas, K. M. Poduska, and A. Yethiraj, "Dynamics of crystal structure formation in spin-coated colloidal films," *Journal of Physical Chemistry Letters*, vol. 1, no. 9, pp. 1481–1486, 2010.
- [21] J. Chen, P. Dong, D. Di et al., "Controllable fabrication of 2D colloidal-crystal films with polystyrene nanospheres of various diameters by spin-coating," *Applied Surface Science*, vol. 270, pp. 6–15, 2013.
- [22] A. R. Madaria, M. Yao, C. Chi et al., "Toward optimized light utilization in nanowire arrays using scalable nanosphere lithography and selected area growth," *Nano Letters*, vol. 12, no. 6, pp. 2839–2845, 2012.
- [23] S. Ye, A. L. Routzahn, and R. L. Carroll, "Fabrication of 3D metal dot arrays by geometrically structured dynamic shadowing lithography," *Langmuir*, vol. 27, no. 22, pp. 13806–13812, 2011.
- [24] N. A. Yahaya, N. Yamada, and T. Nakayama, "Light trapping potential of hexagonal array silicon nanohole structure for solar cell application," *Advanced Materials Research*, vol. 512–515, pp. 90–96, 2012.

Research Article

Hydrothermal Synthesis and Hydrogen Sensing Properties of Nanostructured SnO₂ with Different Morphologies

Weigen Chen,¹ Hongli Gan,¹ Wei Zhang,² and Zeyu Mao¹

¹ State Key Laboratory of Power Transmission Equipment & System Security and New Technology, Chongqing University, Chongqing 400030, China

² Key Laboratory of Multi-Scale Manufacturing Technology, Chongqing Institute of Green and Intelligent Technology, Chinese Academy of Sciences, Chongqing 400714, China

Correspondence should be addressed to Hongli Gan; hongligan@foxmail.com and Wei Zhang; zhangwei@cigit.ac.cn

Received 20 February 2014; Revised 1 May 2014; Accepted 15 May 2014; Published 15 June 2014

Academic Editor: Wen Zeng

Copyright © 2014 Weigen Chen et al. This is an open access article distributed under the Creative Commons Attribution License, which permits unrestricted use, distribution, and reproduction in any medium, provided the original work is properly cited.

In this work, nanoscale SnO₂ with various geometrical morphologies, including pine needle-like, sphere-like, sheet-like, grape-like nanostructures, was prepared via a facile hydrothermal process. Microstructures and morphologies of all the as-synthesized products were characterized by X-ray diffraction (XRD) and field emission scanning electron microscopy (FESEM). Meanwhile, the specific surface areas of the as-prepared SnO₂ nanostructures were determined by Brunauer-Emmett-Teller (BET) analysis. Gas sensors were fabricated and their gas sensing properties towards hydrogen were systematically investigated. The results indicate pine needle-like SnO₂ structure exhibits exclusive better gas sensing performances to hydrogen than the other morphologies, which can be attributed to its novel shape with a large specific surface area. Such an unexpected morphology is a promising candidate for the use of SnO₂ as a gas sensing material in future hydrogen sensor applications.

1. Introduction

As important fundamental materials, metal oxides such as ZnO [1, 2], CuO [3], WO₃ [4, 5], and SnO₂ [6–8] have attracted a remarkable interest due to their unique physico-chemical properties. Among them, the n-type large gap semiconductor SnO₂ has been extensively applied in the field of catalysts [9], Li-ion batteries [10], solar cells [11], and gas sensors [12–14]. It is well known that factors such as morphology, crystal structure, and grain size, as well as synthesis method can dramatically affect the gas sensing properties of SnO₂-based sensor [15–19]. Among these factors, the fabrication of well-defined morphology is of great interest and significance to enhance the sensing characteristics of SnO₂ gas sensors for the past few years. Various SnO₂ nanoarchitectures with special morphologies including nanorods [20], nanoflowers [21], nanosheets [22], nanocubes [23], and nanowires [24] have been successfully synthesized via different methods. Indeed, these structures have showed good sensitivity and selectivity to inflammable or toxic gases, such as C₂H₅OH, CO, H₂S, or NO₂. However, up to now, little attention has

been paid to the effect of different SnO₂ morphologies on the H₂ gas sensing performances. To date, a variety of methods have been employed to prepare nanocrystalline SnO₂, for instance, sol-gel process [25], chemical vapor deposition [26], coaxial electrospinning [27], and hydrothermal reaction [28]. Compared to other techniques, hydrothermal approach is often adopted for its obvious advantages of simplicity, mild fabrication condition, high purity of product, and low cost [28–30].

In this work, several types of SnO₂ nanomaterials with different morphologies were successfully prepared through an environmentally friendly hydrothermal route. Furthermore, sensing properties of the sensors based on the samples, such as sensitivity, optimum operating temperature, response and recovery times as well as the long-term stability, were systematically tested and compared with each other. The pine needle-like SnO₂ displays better sensitivity, lower working temperature, and more rapid response-recovery time to H₂ than that of the other samples, which implies that the gas sensing properties of SnO₂ sensors can be highly enhanced by preparing SnO₂ with desired morphology.

2. Experimental

2.1. Materials Synthesis. All the reagents purchased from Chongqing Chuandong Chemical Reagent Co., Ltd. were of analytical grade and used as received without any further purification.

Pine needle-like, sphere-like, sheet-like, and grape-like SnO_2 were realized by the hydrothermal synthesis route [28–30].

(a) Pine needle-like SnO_2 structures were prepared as follows: in a typical experiment, 0.05 g $\text{Na}_2\text{SnO}_3 \cdot 3\text{H}_2\text{O}$ and 0.02 g NaOH were dissolved into 40 mL deionized water with vigorous stirring for 10 min, and then 0.03 g HMT was added. After the complete dissolution, the precursor was transferred to a Teflon-lined stainless steel autoclave of 50 mL volume and kept at 180 °C for 24 h.

(b) Synthesis of SnO_2 nanospheres: 4.0 mmol $\text{SnCl}_2 \cdot 2\text{H}_2\text{O}$ and 10 mmol $\text{Na}_3\text{C}_6\text{H}_5\text{O}_7 \cdot 2\text{H}_2\text{O}$ were mixed together in 20 mL distilled water and stirred for 5 min. 0.02 mmol NaOH was then added to the above solution with continuous stirring to form a homogeneous solution, which was finally transferred to a 25 mL Teflon-lined stainless steel autoclave and heated at 180 °C for 12 h.

(c) SnO_2 nanosheets were synthesized as the following process, in which, 0.09 g $\text{SnCl}_2 \cdot 2\text{H}_2\text{O}$, 0.15 g $\text{Na}_3\text{C}_6\text{H}_5\text{O}_7 \cdot 2\text{H}_2\text{O}$, and 0.05 g NaOH were added into 40 mL basic mixture of ethanol and water (1:1, v/v) with intense magnetic stirring over 30 min. The reaction mixture was transferred into a 50 mL Teflon-lined stainless steel autoclave at 180 °C in 12 h.

(d) The fabrication of grape-like SnO_2 structures is as follows. In a typical procedure, 0.4 g $\text{SnCl}_4 \cdot 5\text{H}_2\text{O}$ was added into NaOH solution (0.5 g, 20 mL). After stirring for 5 min, 30 mmol HMT was added into above solution under vigorous stirring. Then, 20 mL of absolute ethanol was dropwise added to obtain a white translucent suspended solution. Transfer the well-mixed solution into a 50 mL stainless steel autoclave at 180 °C for 24 h.

All the above heating autoclaves were cooled to room temperature naturally. The obtained precipitates were retrieved by centrifugation, and then washed several times with distilled water and anhydrous ethanol to remove any possible residues. Finally, all the samples were dried in air at 60 °C for about 12 h for further characterizations.

2.2. Fabrication of Gas Sensor. The detailed fabrication of a side-heated gas sensor was as follows: first, each of the above as-synthesized samples was mixed with diethanolamine and ethanol to form a homogeneous paste and then coated onto an alumina tube on which a pair of Au electrodes was previously printed; later, a Ni-Cr heating wire was inserted into the tube for adjusting the operating temperature of the sensor. Finally, all the as-prepared sensors were aged at 300 °C for 120 h to enhance their stability and repeatability. The schematic diagram of the gas sensor is shown in Figure 1.

2.3. Characterization and Measurement of Gas Sensing Properties. The crystalline structures of the prepared samples were

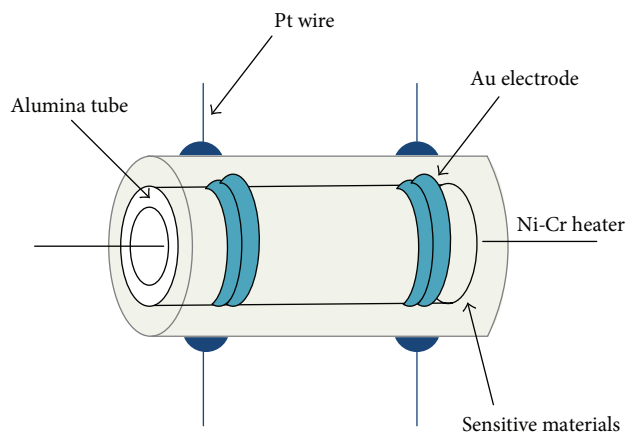


FIGURE 1: The schematic diagram of the gas sensor.

identified by X-ray diffraction (XRD) with a Rigaku D/Max-1200X diffractometer employing $\text{Cu K}\alpha$ radiation (40 kV, 200 mA and $\lambda = 1.5418 \text{ \AA}$). The general morphologies and microstructures were characterized by a Nova 400 Nano field emission scanning electron microscopy (FESEM, FEI, Hillsboro, OR, USA) operated at 5 kV. Meanwhile, the specific surface areas of the products were estimated using the single point Brunauer-Emmett-Teller (BET) method by the 3H-2000 nitrogen adsorption apparatus.

Gas sensing properties were measured by the chemical gas sensor-8 temperature pressure (CGS-8TP) intelligent gas sensing analysis system (Beijing Elite Tech Co., Ltd). It is convenient to gain parameters for sensor resistance, sensitivity, environmental temperature, and operating temperature, as well as relative humidity from the analysis system. All the sensors needed to be preheated at different operating temperatures for about 30 min. When the sensor resistance value kept steady, a certain concentration of target gas was then injected into the test chamber through a microinjector. The tested gas and air were mixed together using two fans of the analysis system. After the resistance of the sensor attained a new stable value, the test chamber was opened to recover the sensor. The whole experiment process was carried out at constant environment temperature and relative humidity. Repeat all the measurements a few times to ensure the reproducibility of the gas sensing response.

The gas response in this paper was defined as the ratio of sensor resistance in dry air to that in tested gases [31]. The response and recovery times were expressed as the time taken by the sensor to achieve 90% of the total resistance change in the case of adsorption and desorption, respectively [32, 33].

3. Results and Discussion

3.1. Structural and Morphological Characteristics. Figure 2 presents the XRD patterns from the final SnO_2 products. All diffraction peaks are well in accordance with the tetragonal rutile SnO_2 structure (JCPDS file number 41-1445); no other crystal phases and any characteristic peaks from the impurities are observed, confirming that all the samples are of high

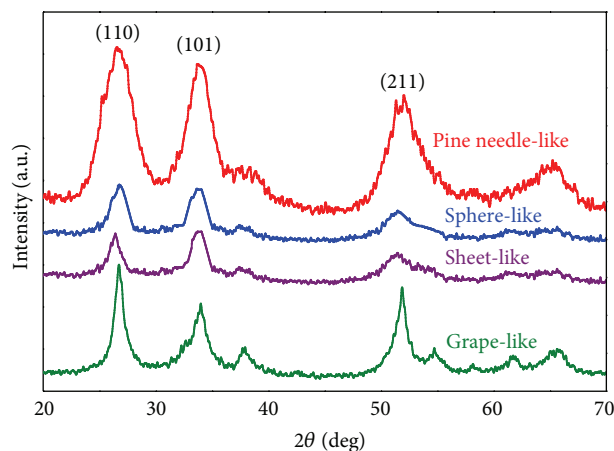


FIGURE 2: XRD patterns of all the SnO₂ samples.

purity and crystallinity. In addition, pine needle-like SnO₂ has broader peaks in comparison with other samples, which demonstrates that the pine needle-like sample has smaller crystal size. BET analysis results indicate that the surface area of pine needle-like, sphere-like, sheet-like, and grape-like was about 30.4 m² g⁻¹, 21.3 m² g⁻¹, 20.8 m² g⁻¹, and 18.2 m² g⁻¹, respectively. Clearly, pine needle-like SnO₂ possesses much higher specific surface area as compared to other samples. Generally, larger surface area means more active sites and diffusion pathways for gas exchange, which may lead to a larger response.

To gain insight into the detailed morphology of SnO₂ products, typical FESEM images of all the samples can be observed in Figure 3. From Figure 3(a), numerous SnO₂ nanoparticles with smooth surface are clearly observed. They are uniformly distributed and have a nearly spherical morphology with average diameter of 350 nm. As seen in Figure 3(b), the sample contains a large scale of pine needle-like leaves which are well arranged and rather uniform in shape and size. These thin leaves are about 400–500 nm in length and 50–80 nm in width. No other morphologies could be detected, suggesting a high yield of these nanostructures. To the best of our knowledge, such unique shape has not been reported so far, and it may have an obvious influence on promoting gas sensing performances of SnO₂. Figure 3(c) exhibits SnO₂ with grape-like structures assembled from dozen of rugged spheres. Figure 3(d) presents a panoramic image of the SnO₂ sample that consisted of randomly arranged nanosheets and some unshaped nanosheets which are growing.

3.2. H₂ Sensing Properties. Operating temperature is an important fundamental characteristic of gas sensors for its significant impact on sensor response. Figure 4 describes the response curves of these sensors to 200 ppm of H₂ as a function of temperature from 220 to 480°C with an interval of 20°C. Apparently, the responses of the sensors increase with a raise of temperature and reach the maximum and then decrease with further increase of working temperature.

Usually, operating temperature of the oxide semiconductor sensor depends on two parameters: electron density of the sensor and reaction rate coefficient between H₂ molecules and adsorbed oxygen species [34]. On one hand, they both increase as the temperature rises. On the other hand, gas response is proportional to reaction rate coefficient but inversely proportional to electron density. Therefore, there should be an optimal temperature to balance the two parameters for achieving the maximum sensor response. In contrast, SnO₂ sensors using samples of pine needle-like, sphere-like, and sheet-like are more sensitive to H₂ than that of grape-like at the same temperature. The highest gas response for pine needle-like, sphere-like, sheet-like, and grape-like SnO₂ was about 20.5, 18, 17, and 14 at temperature of 360°C, 380°C, 380°C, and 400°C, respectively. Herein, the optimal operating temperatures were determined to further examine the characteristics of the sensors. Furthermore, the higher response of pine needle-like SnO₂ probably results from its very fine grain size and large specific surface area.

Figure 5 shows the correlation between the response of SnO₂ sensors and H₂ gas concentrations, where the sensors worked at their own optimum operating temperature as mentioned above. From the curves, it is evident that the response of the sensors increases nonlinearly with no sign of saturation when H₂ concentration ranges from 100 to 1000 ppm. This usually is explained through the gas-diffusion theory by which the oxide based sensor response can be written as $S = aC^b + 1$ [34, 35]. In the formula, a is a controllable constant, b is a charge parameter which reflects oxygen ion species on the surface of SnO₂ sensors, and C is the concentration of the tested gas. Normally, b has value of 1 for O⁻ and 0.5 for O²⁻. Besides, it is necessary to know that the growth trends are gradually slowed down with a further rise of gas concentrations. The corresponding data is not presented. This phenomenon might be owing to both the change of stoichiometry about the elementary reactions and the competitions of gas molecules for reaction sites as gas concentrations increase progressively [36, 37]. Specifically, the SnO₂ sensor with pine needle-like structure shows relatively higher sensitivity to H₂ than that of other sensors.

The response and recovery characteristics were studied with the sensors being orderly exposed to 200 ppm of H₂ gas at their own optimum operating temperature, and the curves are depicted in Figure 6. The response and recovery times for the pine needle-like, sphere-like, sheet-like, and grape-like SnO₂ were estimated to be 19–22 s, 22–26 s, 24–27 s, and 25–29 s, respectively. Interestingly, it seems that voltages of all the samples increase dramatically when H₂ is in but go back to their original states when the gas is out. Comparing with the other three SnO₂ nanostructures, it could be noted that the pine needle-like SnO₂ has the shortest response and recovery times, reflecting its excellent sensing performance once again.

Figure 7 displays the long-term stability of the sensors to 200 ppm of H₂ at their own optimum operating temperature with relative humidity of 35%. It could be known that gas response changed slightly after a month, suggesting that all the sensors have good stability and repeatability.

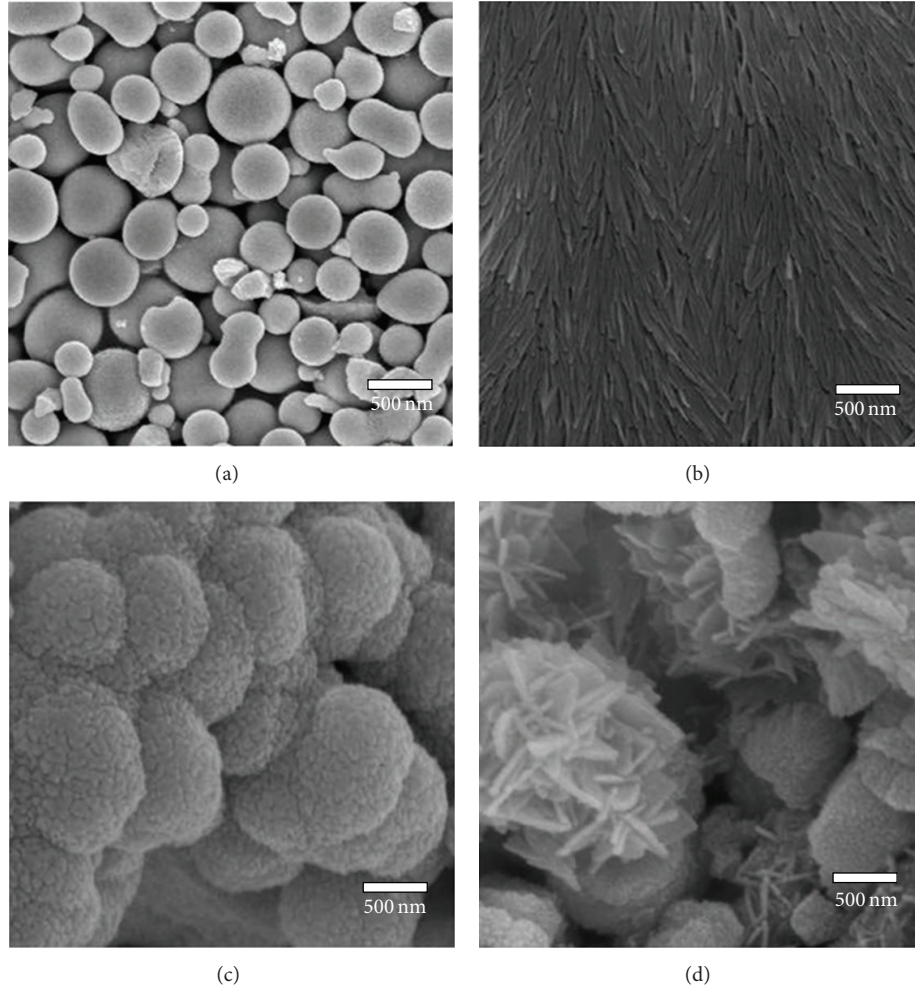
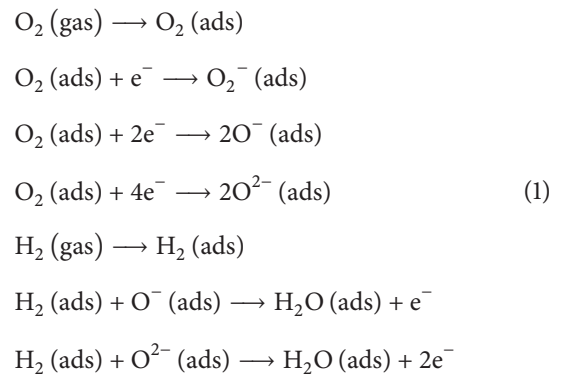


FIGURE 3: FESEM images of (a) sphere-like, (b) pine needle-like, (c) grape-like, and (d) sheet-like SnO_2 .

On the basis of above discussions, one can draw a conclusion that pine needle-like SnO_2 exhibits the most superior sensing properties to H_2 among the four samples.

3.3. Gas Sensing Mechanism. It is believed that the gas sensing mechanism of SnO_2 sensors follows the surface charge model. When sensors contact with different gases, the resistance would have a change. Both the species and amount of oxygen ions play crucial roles in the variation of resistance. When the sensors are exposed to air, oxygen molecules adsorbed on the surface of SnO_2 nanostructures would be ionized to O^{2-} , O^- , or O_2^- by capturing free electrons from the conduction band of SnO_2 , which causes a depletion layer and consequently increases the resistance of the sensors. As a reducing gas such as H_2 is introduced, chemical reactions between the H_2 molecules and the ionized oxygen are active. This process releases the trapped electrons back to the SnO_2 surface and thus leads to an increase in the carrier concentration and carrier mobility of SnO_2 . The gas sensing reaction process on the SnO_2 surface is seen in Figure 8.

The possible reactions involved in the above process are expressed as follows [38, 39]:



In this experiment, the different sensing properties of the four SnO_2 samples toward H_2 can be ascribed to the different morphologies and nanostructures. Moreover, the higher sensitivity of pine needle-like SnO_2 is mainly based on its special structure with a large surface area which can

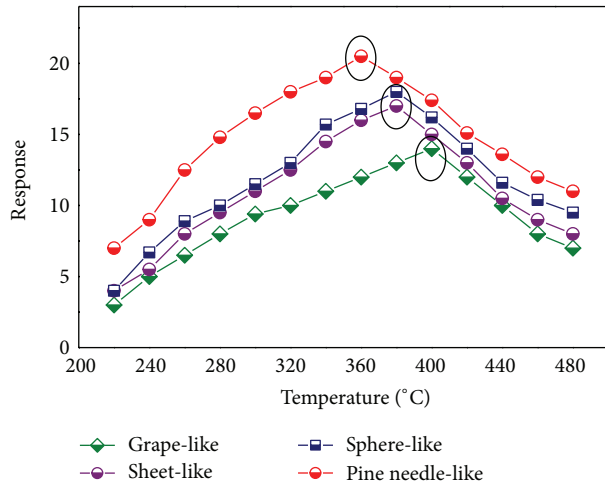


FIGURE 4: Response of the sensors to 200 ppm of H_2 with different operating temperature (room temperature at $25^\circ C$ and relative humidity as 35%).

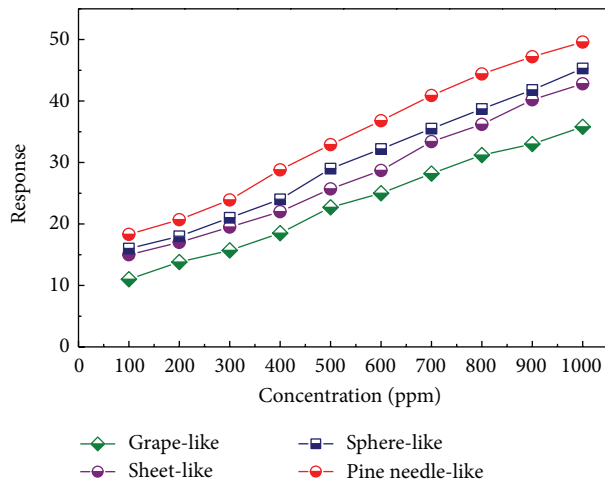


FIGURE 5: Response of the sensors as a function of H_2 gas concentrations (room temperature at $25^\circ C$ and relative humidity as 35%).

provide more active sites and quick passages for gas exchange and thus enhance the interaction between SnO_2 surface and H_2 molecules.

4. Conclusions

In summary, SnO_2 nanostructures with various morphologies including pine needle-like, sphere-like, sheet-like, and grape-like were realized by hydrothermal preparation. Additionally, both their microstructures and gas sensing properties to H_2 were tested. As compared to other three sensors, pine needle-like SnO_2 sensor exhibits more excellent performances in terms of higher response, faster response-recovery time, and lower working temperature. The good sensing properties may be attributed to the novel pine needle-like structure which has a large specific surface area with massive gas-diffusion channels. The obtained results indicate

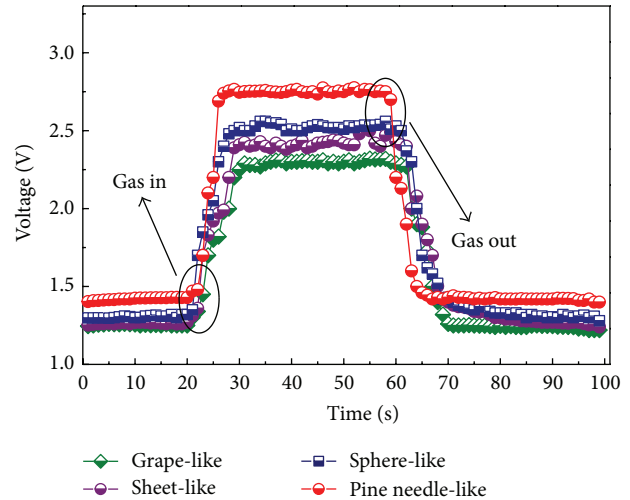


FIGURE 6: Response-recovery curves of the sensors to 200 ppm of H_2 (room temperature at $25^\circ C$ and relative humidity as 35%).

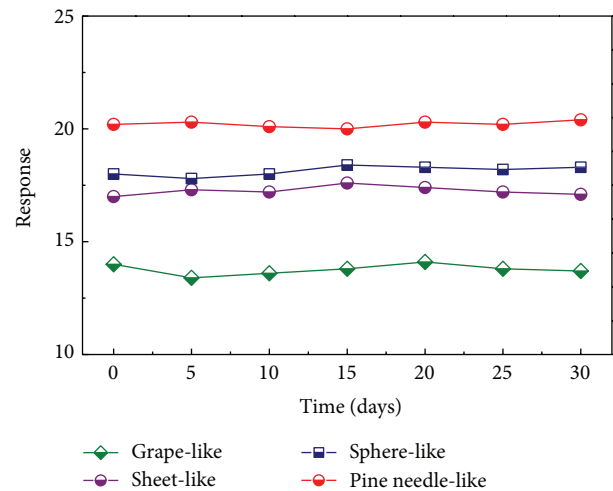


FIGURE 7: The long-term response value of the sensors to 200 ppm of H_2 (room temperature at $25^\circ C$ and relative humidity as 35%).

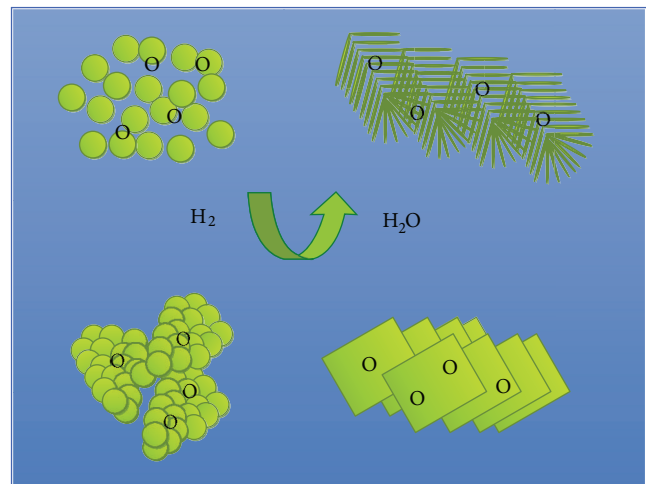


FIGURE 8: Schematic of the H_2 sensing reaction process.

that the gas sensing properties of SnO₂ sensing materials can be significantly improved by tailoring their surface structures and shapes. These findings offer new opportunities for designing and developing high-performance H₂ gas sensors.

Conflict of Interests

The authors declare that there is no conflict of interests regarding the publication of this paper.

Acknowledgments

The authors appreciate the financial support of the National Natural Science Foundation of China (nos. 51277185 and 51202302), and National Special Fund for Major Research Instrumentation Development (no. 2012YQ16000705).

References

- [1] P. Rai, Y.-S. Kim, H.-M. Song, M.-K. Song, and Y.-T. Yu, "The role of gold catalyst on the sensing behavior of ZnO nanorods for CO and NO₂ gases," *Sensors and Actuators B: Chemical*, vol. 165, no. 1, pp. 133–142, 2012.
- [2] L. Zhang, J. Zhao, J. Zheng, L. Li, and Z. Zhu, "Hydrothermal synthesis of hierarchical nanoparticle-decorated ZnO microdisks and the structure-enhanced acetylene sensing properties at high temperatures," *Sensors and Actuators B: Chemical*, vol. 158, no. 1, pp. 144–150, 2011.
- [3] D. Gopalakrishna, K. Vijayalakshmi, and C. Ravidhas, "Effect of annealing on the properties of nanostructured CuO thin films for enhanced ethanol sensitivity," *Ceramics International*, vol. 39, no. 7, pp. 7685–7691, 2013.
- [4] J.-Y. Leng, X.-J. Xu, N. Lv, H.-T. Fan, and T. Zhang, "Synthesis and gas-sensing characteristics of WO₃ nanofibers via electrospinning," *Journal of Colloid and Interface Science*, vol. 356, no. 1, pp. 54–57, 2011.
- [5] X. Liu, J. Zhang, T. Yang, X. Guo, S. Wu, and S. Wang, "Synthesis of Pt nanoparticles functionalized WO₃ nanorods and their gas sensing properties," *Sensors and Actuators B: Chemical*, vol. 156, no. 2, pp. 918–923, 2011.
- [6] Y. J. Chen, X. Y. Xue, Y. G. Wang, and T. H. Wang, "Synthesis and ethanol sensing characteristics of single crystalline SnO₂ nanorods," *Applied Physics Letters*, vol. 87, Article ID 233503, 2005.
- [7] M. Wu, W. Zeng, Q. He, and J. Zhang, "Hydrothermal synthesis of SnO₂ nanocorals, nanofragments and nanogras and their formaldehyde gas-sensing properties," *Materials Science in Semiconductor Processing*, vol. 16, no. 6, pp. 1495–1501, 2013.
- [8] J. Liu, X.-C. Tang, Y.-H. Xiao, H. Jia, M.-L. Gong, and F.-Q. Huang, "Porous sheet-like and sphere-like nano-architectures of SnO₂ nanoparticles via a solvent-thermal approach and their gas-sensing performances," *Materials Science and Engineering B: Solid-State Materials for Advanced Technology*, vol. 178, no. 18, pp. 1165–1168, 2013.
- [9] I. T. Weber, A. Valentini, L. F. D. Probst, E. Longo, and E. R. Leite, "Catalytic activity of nanometric pure and rare earth-doped SnO₂ samples," *Materials Letters*, vol. 62, no. 10–11, pp. 1677–1680, 2008.
- [10] X. W. Lou, Y. Wang, C. Yuan, J. Y. Lee, and L. A. Archer, "Template-free synthesis of SnO₂ hollow nanostructures with high lithium storage capacity," *Advanced Materials*, vol. 18, no. 17, pp. 2325–2329, 2006.
- [11] Y. Fukai, Y. Kondo, S. Mori, and E. Suzuki, "Highly efficient dye-sensitized SnO₂ solar cells having sufficient electron diffusion length," *Electrochemistry Communications*, vol. 9, no. 7, pp. 1439–1443, 2007.
- [12] W. G. Chen, Q. Z. Li, H. L. Gan et al., "Study of CuO-SnO₂ heterojunction nanostructures for enhanced CO gas sensing properties," *Advances in Applied Ceramics*, vol. 113, no. 3, pp. 139–146, 2014.
- [13] M. A. Andio, P. N. Browning, P. A. Morris, and S. A. Akbar, "Comparison of gas sensor performance of SnO₂ nanostructures on microhotplate platforms," *Sensors and Actuators B: Chemical*, vol. 165, no. 1, pp. 13–18, 2012.
- [14] Q. Yu, K. Wang, C. Luan, Y. Geng, G. Lian, and D. Cui, "A dual-functional highly responsive gas sensor fabricated from SnO₂ porous nanosolid," *Sensors and Actuators B: Chemical*, vol. 159, no. 1, pp. 271–276, 2011.
- [15] G. Zhang and M. Liu, "Effect of particle size and dopant on properties of SnO₂-based gas sensors," *Sensors and Actuators B: Chemical*, vol. 69, no. 1, pp. 144–152, 2000.
- [16] R. K. Mishra and P. P. Sahay, "Synthesis, characterization and alcohol sensing property of Zn-doped SnO₂ nanoparticles," *Ceramics International*, vol. 38, no. 3, pp. 2295–2304, 2012.
- [17] S. Dai and Z. Yao, "Synthesis of flower-like SnO₂ single crystals and its enhanced photocatalytic activity," *Applied Surface Science*, vol. 258, no. 15, pp. 5703–5706, 2012.
- [18] N. Talebian and F. Jafarinezhad, "Morphology-controlled synthesis of SnO₂ nanostructures using hydrothermal method and their photocatalytic applications," *Ceramics International*, vol. 39, no. 7, pp. 8311–8317, 2013.
- [19] L. Fei, Y. Xu, Z. Chen et al., "Preparation of porous SnO₂ helical nanotubes and SnO₂ sheets," *Materials Chemistry and Physics*, vol. 140, no. 1, pp. 249–254, 2013.
- [20] S. Supothina, R. Rattanakam, S. Vichaphund, and P. Thavorniti, "Effect of synthesis condition on morphology and yield of hydrothermally grown SnO₂ nanorod clusters," *Journal of the European Ceramic Society*, vol. 31, no. 14, pp. 2453–2458, 2011.
- [21] J. Huang, K. Yu, C. Gu et al., "Preparation of porous flower-shaped SnO₂ nanostructures and their gas-sensing property," *Sensors and Actuators B: Chemical*, vol. 147, no. 2, pp. 467–474, 2010.
- [22] P. Sun, Y. Cao, J. Liu, Y. Sun, J. Ma, and G. Lu, "Dispersive SnO₂ nanosheets: hydrothermal synthesis and gas-sensing properties," *Sensors and Actuators B: Chemical*, vol. 156, no. 2, pp. 779–783, 2011.
- [23] L. Yu, M. Zhang, Y. J. Chen et al., "Assembling SnO₂ nanocubes to nanospheres for high-sensitivity sensors," *Solid State Sciences*, vol. 14, no. 4, pp. 522–527, 2012.
- [24] G. D. Zhang and N. Liu, "A novel method for massive synthesis of SnO₂ nanowires," *Bulletin of Materials Science*, vol. 36, no. 6, pp. 953–960, 2013.
- [25] M. A. Dal Santos, A. C. Antunes, C. Ribeiro et al., "Electric and morphologic properties of SnO₂ films prepared by modified sol-gel process," *Materials Letters*, vol. 57, no. 28, pp. 4378–4381, 2003.
- [26] J. B. Zhang, X. N. Li, S. L. Bai, R. X. Luo, A. F. Chen, and Y. Lin, "High-yield synthesis of SnO₂ nanobelts by water-assisted chemical vapor deposition for sensor applications," *Materials Research Bulletin*, vol. 47, no. 11, pp. 3277–3282, 2012.

- [27] Y. Zhang, J. Li, G. An, and X. He, "Highly porous SnO₂ fibers by electrospinning and oxygen plasma etching and its ethanol-sensing properties," *Sensors and Actuators B: Chemical*, vol. 144, no. 1, pp. 43–48, 2010.
- [28] W. G. Chen, Q. Zhou, and S. D. Peng, "Hydrothermal synthesis of Pt-, Fe-, and Zn-doped SnO₂ nanospheres and carbon monoxide sensing properties," *Advances in Materials Science and Engineering*, vol. 2013, Article ID 578460, 8 pages, 2013.
- [29] Y. L. Wang, M. Guo, M. Zhang, and X. D. Wang, "Facile synthesis of SnO₂ nanoglass array films by hydrothermal method," *Thin Solid Films*, vol. 518, no. 18, pp. 5098–5103, 2010.
- [30] B. Mehrabi Matin, Y. Mortazavi, A. A. Khodadadi, A. Abbasi, and A. Anaraki Firooz, "Alkaline- and template-free hydrothermal synthesis of stable SnO₂ nanoparticles and nanorods for CO and ethanol gas sensing," *Sensors and Actuators B: Chemical*, vol. 151, no. 1, pp. 140–145, 2010.
- [31] W. G. Chen, Q. Zhou, L. N. Xu et al., "Improved methane sensing properties of Co-doped SnO₂ electrospun nanofibers," *Journal of Nanomaterials*, vol. 2013, Article ID 173232, 9 pages, 2013.
- [32] Y. Gui, F. Dong, Y. Zhang, and J. Tian, "Preparation and gas sensitivity of WO₃ hollow microspheres and SnO₂ doped heterojunction sensors," *Materials Science in Semiconductor Processing*, vol. 16, no. 6, pp. 1531–1537, 2013.
- [33] Q. Zhou, W. Chen, L. Xu, and S. Peng, "Hydrothermal synthesis of various hierarchical ZnO nanostructures and their methane sensing properties," *Sensors*, vol. 13, no. 5, pp. 6171–6182, 2013.
- [34] N. Hongsith, E. Wongrat, T. Kerdcharoen, and S. Choopun, "Sensor response formula for sensor based on ZnO nanostructures," *Sensors and Actuators B: Chemical*, vol. 144, no. 1, pp. 67–72, 2010.
- [35] Q. Wan, Q. H. Li, Y. J. Chen et al., "Fabrication and ethanol sensing characteristics of ZnO nanowire gas sensors," *Applied Physics Letters*, vol. 84, no. 18, pp. 3654–3656, 2004.
- [36] M. Chen, Z. Wang, D. Han, F. Gu, and G. Guo, "High-sensitivity NO₂ gas sensors based on flower-like and tube-like ZnO nanomaterials," *Sensors and Actuators B: Chemical*, vol. 157, no. 2, pp. 565–574, 2011.
- [37] M.-W. Ahn, K.-S. Park, J.-H. Heo, D.-W. Kim, K. J. Choi, and J.-G. Park, "On-chip fabrication of ZnO-nanowire gas sensor with high gas sensitivity," *Sensors and Actuators B: Chemical*, vol. 138, no. 1, pp. 168–173, 2009.
- [38] S. Mishra, C. Ghanshyam, R. A. M. Nathai, S. Singh, R. P. Bajpai, and R. K. Bedi, "Alcohol sensing of tin oxide thin film prepared by sol-gel process," *Bulletin of Materials Science*, vol. 25, no. 3, pp. 231–234, 2002.
- [39] M. Hübner, R. G. Pavelko, N. Barsan, and U. Weimar, "Influence of oxygen backgrounds on hydrogen sensing with SnO₂ nanomaterials," *Sensors and Actuators B: Chemical*, vol. 154, no. 2, pp. 264–269, 2011.

Research Article

Facile Hydrothermal Synthesis and Basic Gas-Sensing Properties of Two Three-Dimensional Nanostructures of SnO₂

Lingna Xu,¹ Weigen Chen,^{1,2} Caisheng Wang,² Tuoyu Gao,¹ and Qu Zhou^{1,3}

¹ State Key Laboratory of Power Transmission Equipment & System Security and New Technology, College of Electrical Engineering, Chongqing University, Chongqing 400030, China

² Department of Electrical and Computer Engineering, Wayne State University, Detroit, MI 48202, USA

³ College of Engineering and Technology, Southwest University, Chongqing 400715, China

Correspondence should be addressed to Lingna Xu; lingnaxu@cqu.edu.cn

Received 21 February 2014; Revised 8 May 2014; Accepted 15 May 2014; Published 2 June 2014

Academic Editor: Wen Zeng

Copyright © 2014 Lingna Xu et al. This is an open access article distributed under the Creative Commons Attribution License, which permits unrestricted use, distribution, and reproduction in any medium, provided the original work is properly cited.

The hierarchical SnO₂ sphere-like architecture, consisting of numerous thin nanosheets, was successfully synthesized via a facile hydrothermal method. The structures and morphologies of this hierarchical architecture were characterized in detail by means of powder X-ray diffraction (XRD), field-emission scanning electron microscopy (FE-SEM), and Brunauer-Emmett-Teller (BET). Further comparative experiments of gas-sensing performances of the as-prepared SnO₂ were investigated towards ethanol. It shows this three-dimensional, sheet-spheres, SnO₂ as a potential gas-sensing material for a broad range of future sensor applications, like sensitive response to other gases such as hydrogen, carbonic oxide, and methane.

1. Introduction

In the nanoscale, tremendous efforts have been paid to develop methods to adjust the microstructures of materials and thus tuning their functionalities [1–4]. Tin oxide (SnO₂), as an *n*-type semiconductor with a wide band gap ($E_g = 3.6$ eV, at 300 K), has been the attractive material in various fields, such as gas sensors [5], catalysts [6], Li-ion batteries [7, 8], and electrode materials [9]. It has received considerable attention in both fundamental studies and practical applications due to unique properties such as photocatalysis and gas-sensing [10, 11]. As we know, many fundamental physical and chemical properties of semiconductor materials rely not only on the composition but also on the structure, phase, shape, and size; synthesis of nanomaterials with a tunable shape or morphology has been the subject of intensive research [12–14]. Recently, numerous studies have demonstrated that materials with large surface area, efficient catalytic activity, and structural stability, such as three-dimensional (3D) structures (e.g., spheres-like [15], aloe-like [16], and flowers-like [17]), exhibit enhanced gas-sensing performance. There are various preparation methods, such

as thermal evaporation technique [18], sol-gel method [19], and hydrothermal route [20] which have been developed for 3D hierarchical architectures. Li et al. discuss porous SnO₂ spheres which are synthesized through a solvothermal method [15]; Wang et al. use a sol-gel template synthetic technique to make SnO₂ tubes [21]; Qi et al. study SnO₂ fibers which are synthesized via a simple electrospinning method [22]. Among them, the hydrothermal method has been proved to be effective for preparation hierarchical SnO₂ architectures [23]. Although the various nanostructure spheres of SnO₂ have been synthesized, it still remains a huge challenge to shape-controlled routes with well-defined morphology and uniform size.

In this paper, we detailed a controllable synthesis of SnO₂ sphere-like nanostructure through the straightforward hydrothermal process via the HMT (Hexamethylenetetramine) assisted. Both of these two SnO₂ spheres samples exhibit the obvious high gas-sensing activities to ethanol during the experiments such as response and recovery time test, optimum operating temperature test, and different gas concentration test. Based on comparative studies, the possible formation mechanism was discussed basically.

The gas-sensing properties of SnO₂ sheet-spheres are found better than pointed columnar-spheres ones because of the higher voltage during the response-recovery time, lower working temperature, and more sensitive response in the same concentration to ethanol. The results not only provide a cheap and effective way to control the morphology and synthesize high performance three-dimensional sensing SnO₂ to ethanol but also lay the foundation for the gas-sensitive reaction to the other gases (hydrogen, carbonic oxide, methane, etc.) for the future research.

2. Experimental

During the experiment, all chemicals are analytical-grade reagents from Chongqing Chuandong Chemical Reagent Co., Ltd., and used without any further purification.

Both of the SnO₂ with nanostructures were compounded via the stable and controllable hydrothermal process.

2.1. Synthesis of SnO₂ Sheet-Spheres. In a typical hydrothermal process, 0.53 g NaSnO₃·3H₂O (2 mmol) and 0.20 g NaOH (5 mmol) were dissolved into 75 mL deionized water. Then with magnetic continuously stirring, we got cleared solution. Next, 0.3 g HMT was dissolved into this cleared solution and stirred for next 30 minutes to get the reaction solution. Afterwards, the solution was transferred into a Teflon-lined stainless steel autoclave and maintained at 180°C for 24 h. Finally, the product was collected by centrifugation, washed with deionized water and ethanol for six times, respectively, and finally dried at 60°C for 24 h to get the powder.

2.2. Synthesis of SnO₂ Pointed Columnar-Spheres. Typically, 0.26 g SnCl₄·5H₂O, 0.32 g NaOH and 0.10 g Na₂SO₄ were dissolved into a 10 mL deionized water to stir for 5 minutes. Then 12 mL ethanol was dissolved into it to get white transparent suspension solution. After that, the evenly stirring mixtures were transferred into a Teflon-lined stainless steel autoclave and then heated in an oven at 180°C for 24 h. After cooling down to room temperature naturally, the product was collected by centrifugation and washed six times with deionized water and absolute ethanol, subsequently. Finally, a white precipitate was harvested by glass culture dish and dried at 60°C overnight to get the solid powder.

2.3. Fabrication of Gas Sensor. The gas sensors were fabricated by dispersing the powders with ethanol to form pastes. The pastes were subsequently coated onto a ceramic tube to form a thin layer of sensing film (thickness about 10–20 μm), positioned with a pair of Au electrodes at each end point. A Ni-Cr heating wire was inserted into the alumina tube to control the operating temperature by tuning the heating voltage. Figures 1(a) and 1(b) show a photograph of the sensor on the socket and a schematic image of the as-fabricated sensor, respectively. All the as-prepared sensors were finally aged at 240°C for 72 h to improve their stability and repeatability. The gas sensing properties of the samples were conducted using the Chemical Gas Sensor-8 (CGS-8) gas sensitivity

instrument and analysis system (Beijing Elite Tech Co., Ltd.) that is a static test system with a heated area to place volatile liquid in the chamber. All the sensors were put into the test chamber and preheated at different operating temperature to keep steady. Then saturated target vapor was added which was the volatilization of the ethanol after heating. When the gas evenly filled the chamber, the system attained a new stable value. After that, the test chamber was opened to recover the sensor and repeated all the measurements several times to make sure the reproducibility of the gas-sensing response. The sensors are operated using a circuit voltage (V_c), which was applied to allow for a measurement of the output voltage (V_{out}) across. When air and ppm-level target gases flowed through the test chamber, the corresponding resistances of the sensor in air (R_a) and in the presence of the target gas in air (R_t) were measured by monitoring the V_{out} . Gas-sensing studies are carried out under laboratory condition with room temperature as 27°C and relative humidity as 40%. Gas response in this paper is defined as $S = R_a/R_t$, in which R_a and R_t are the resistance of the sensor in air and in ethanol gas, respectively. And the response and recovery time are counted as the time taken by the sensor to achieve 90% of the total resistance change in the case of adsorption and desorption, respectively.

3. Result and Discussion

3.1. Structure Characterization. The phase purity of the prepared samples was characterized by X-ray diffraction (XRD, scanning rate: 0.02° s⁻¹ in the 2-theta range of 10–90°). All the diffraction peaks of the sample in Figure 2 were well indexed to the SnO₂ with the rutile structure (space group: P4₂, JCPDS card number 41-1445) and no obvious characteristic peaks from other impurities were detected, indicating the high purity and crystallinity of the final products. It is easy to see that both two samples have similar XRD patterns such as location, intensity, and breadth, suggesting that the samples exhibit almost the same crystal size. Meanwhile, the structure of the solid powder was investigated using a Nova 400 Nano field emission scanning electronic microscopy (FE-SEM).

Figure 3(a) displays the low-magnification SEM images of the sheet-spheres samples. It shows that the SnO₂ sheet-spheres products exhibit a unique hierarchical sheet architecture, and these spheres dispersed in the samples with a diameter about 700 nm. An enlarged SEM image of an individual sphere-like architecture is shown in Figure 3(b), which apparently shows that the unique hierarchical sphere-like architecture is regularly composed of numerous well-ordered thin nanosheets. Figures 3(c) and 3(d) show the SnO₂ pointed columnar-spheres in 1 μm and 500 nm, respectively, and the diameter of it is larger than the sheet-sphere-like one.

Based on the experimental observations and analysis, we propose a plausible growth mechanism for the morphologies evolution of the SnO₂, as shown in Figure 4. The SnO₂ nanocrystal was formed from the hydrolysis of Sn²⁺ ions. To eliminate the surface energy, the SnO₂ colloids were next aggregated to form nanosheets and finally formed hierarchical sphere-like architectures. In our study, the HMT plays a key role in the formation and the space distribution of

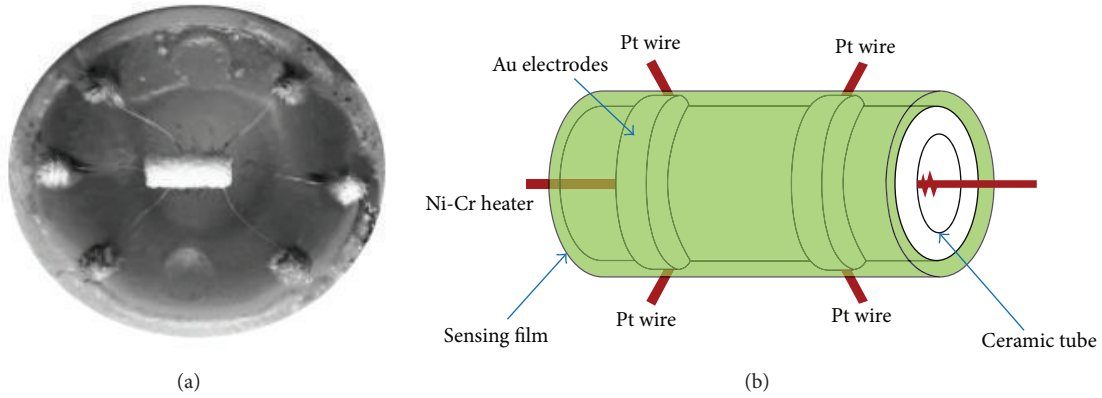


FIGURE 1: (a) Fabricated sensor and (b) schematic diagram of indirect-heating sensor.

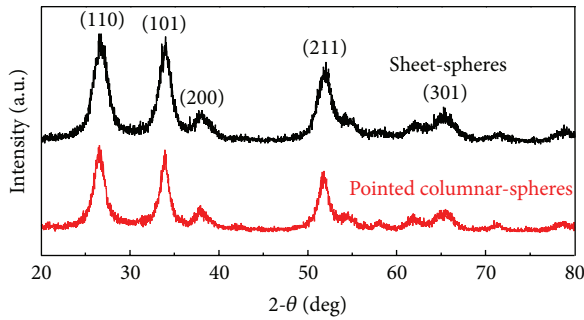


FIGURE 2: XRD patterns of the samples.

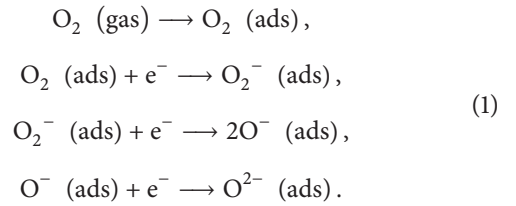
TABLE 1: BET surface area and pore structure parameters.

Sample	S_{BET} (m^2/g)	V_p (cm^3/g)	d_p (nm)
Sheet-spheres	22.3	0.04	23.8
Pointed columnar-spheres	17.8	0.02	23.9

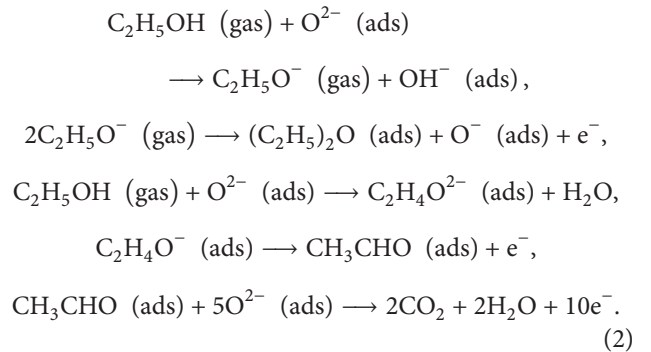
the precursor. A large number of Sn^{2+} ions accumulated on the long chains of HMT in the solution and decreased the concentration of free Sn^{2+} ion; thus, HMT provided many nucleation sites; with reaction time passing by, numerous tiny SnO_2 crystals nucleated on HMT chains and grew further, which resulted in the formation of SnO_2 nanosheets.

The main factors that affect the sensing mechanism qualitatively are the specific surface area and pore structure of the materials, which can be measured using the BET method [24]. As shown in Table 1, the obtained specific surface areas for the sheet-spheres and pointed columnar-spheres are $22.3 \text{ m}^2/\text{g}$ and $17.8 \text{ m}^2/\text{g}$. What counts is that the larger specific surface area may facilitate the interaction between the material surface and the gas molecule, which triggers even more substantial output in electric signal. This, together with the scale of surface pores, suggests that the sheet-spheres of SnO_2 may exhibit a better sensing behavior.

3.2. Gas Sensing Mechanism. It is well known that the SnO_2 belongs to an *n*-type semiconductor and its sensing character is governed by the change of surface resistance; the species and amount of chemisorbed oxygen on surface are critical for the variation in resistance. As the sensor was first aged in air, oxygen can be absorbed on its surface and can act as a trap for the conduction band electrons of SnO_2 due to their strong electronegativity, which would be ionized to O^{2-} , O^- , or O_2^- by capturing free electrons from the conduction band of SnO_2 . The entire adsorption and reaction process can be expressed as follows [25–29]:



The absorbed oxygen could cause a depletion layer and band bending on the surface, which consequently increases the energy barrier, namely, the resistance of the sensing material SnO_2 . As the $\text{C}_2\text{H}_5\text{OH}$ is introduced, chemical reactions take place between the $\text{C}_2\text{H}_5\text{OH}$ and the ionized oxygen O_2^- , which gives out electrons back to the SnO_2 surface. The possible reactions are summarized by the following equations:



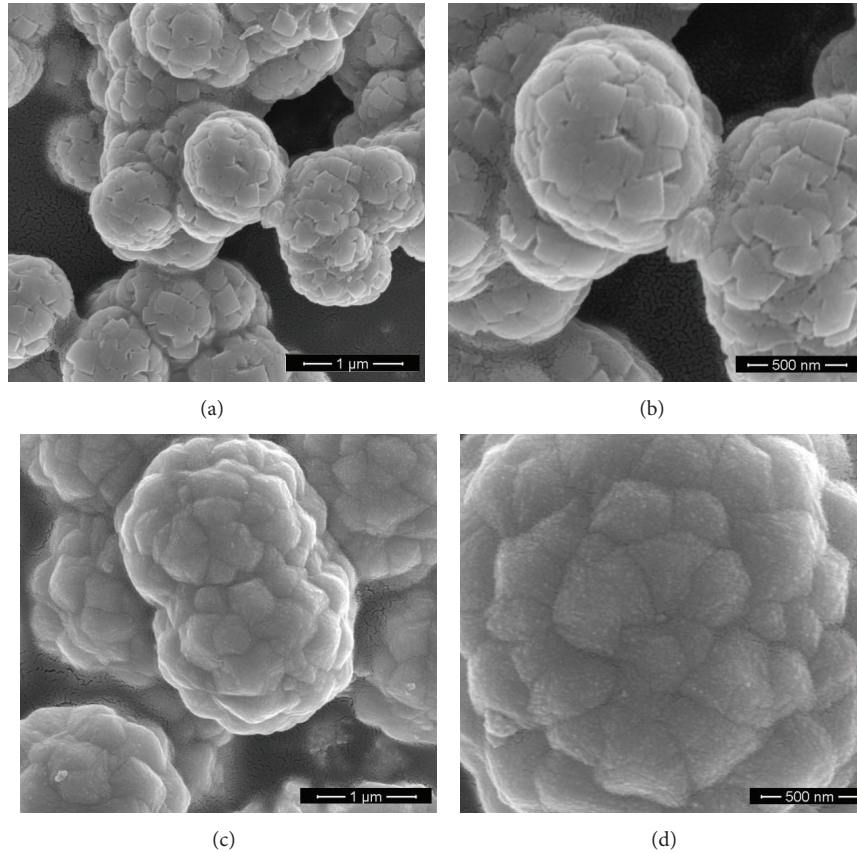


FIGURE 3: SEM images of the sheet-spheres and pointed columnar-spheres: (a) 1 μm , (b) 500 nm, (c) 1 μm , and (d) 500 nm.

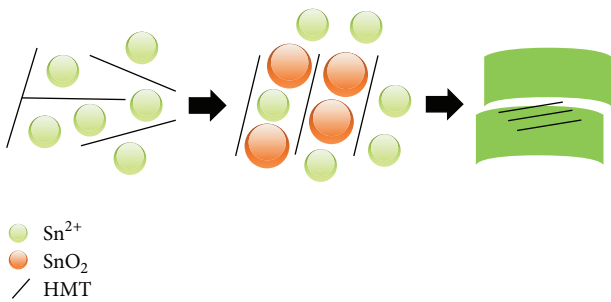


FIGURE 4: Schematic illustration of the evolution processes of the SnO₂ sheet-spheres.

In general, there are two types of reactions occurring simultaneously on the oxide surface: ① the target gas molecules react with the preabsorbed oxygen, and ② the target gas molecules react directly with the surface atoms of oxide. Whatever the reaction type, the electrons that are produced from these reactions would decrease the resistance significantly, which results in drastic increase of output voltage, as generally observed at the working stage of a sensor in Figure 5. It presents a representative response-recovery characteristic for the sensor operated at 340°C under ethanol gas concentration of 100 ppm. The response and recovery times are two key quantities for a sensor, which are defined as the time needed

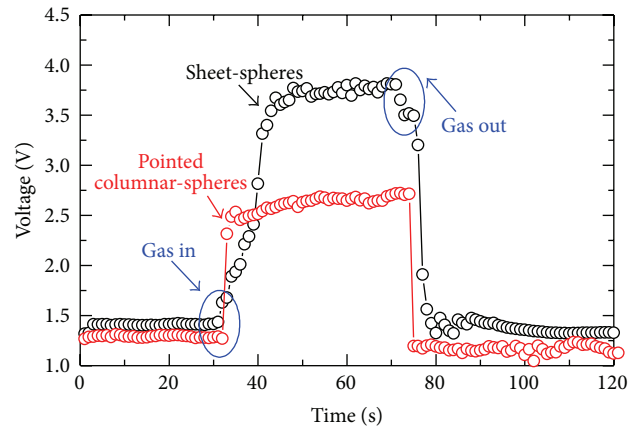


FIGURE 5: Response-recovery characteristics of the sensors at 340°C under 100 ppm ethanol.

to reach 90% response or recovery when gas is in or out. Under the definition described above, the response and recovery times for the sheet-spheres and pointed columnar-spheres are evaluated to be about 21–23 s and 19–21 s, which meet the basic demands for an industrial application. As seen in Figure 5, voltages of both two kinds of samples increase when gas is in but return to their original state when gas is out. The major difference among the sensors is that the voltage

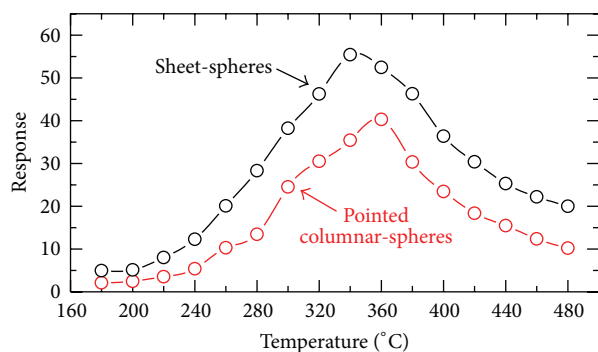


FIGURE 6: Gas response of the sensors to different operating temperature under 250 ppm ethanol.

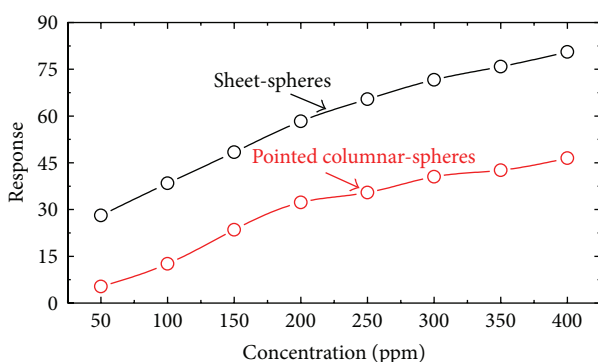


FIGURE 7: Gas response of the sensors to different gas concentration ranking from 50 to 400 ppm.

for the sheet-spheres is substantially larger than that for the pointed columnar-spheres sensor at working stage, verifying its better sensing performances.

To investigate how the various morphologies of SnO_2 impact their gas sensing properties, we further make a systematic comparison of the gas sensing performance of these two 3-dimensional SnO_2 nanostructure materials.

Obviously, the response of the sensors increases with a raise of temperature till reaching the maximum value and then decreases with any further increase of temperature. The gas response to 250 ppm ethanol was firstly investigated at different operating temperatures and the result is shown in Figure 6. One can see that sheet-spheres SnO_2 exhibit exclusive better sensing performances to ethanol than that of pointed columnar-spheres. The highest gas response to the ethanol is estimated to be 55 for SnO_2 sheet-spheres, obviously higher than 40 for pointed columnar-nanospheres case. Moreover, we further determine the optimum working temperature of sheet-spheres sensor to be about 340°C , lower than that of the pointed columnar-spheres sensor with value of 360°C .

To further investigate how the gas concentration affects the gas response, we present in Figure 7 the gas response to ethanol with operating temperature of 340°C . Independent of the sensor types, the gas response increases dramatically with no sign of saturation, as the concentration ranges from

50 to 400 ppm. We find again that in the two of the samples, the sheet-spheres show higher response in the measured concentrations, although it is well known that the response may be affected by the concentration of examined gas. Further, we notice that, independent of the samples, the response increases in a nonlinear manner with the rise of gas concentration, which can be explained from the gas-diffusion theory [30].

According to the measurement above, we thus conclude that the 3-dimensional SnO_2 for sheet-spheres exhibit distinctive better sensing properties than that of the pointed columnar-spheres.

4. Conclusions

In summary, we have prepared nanostructure SnO_2 sheet-spheres and pointed columnar-spheres through the effective hydrothermal method and investigated their structures and gas sensing properties. In particular, we compared systematically the ethanol sensing properties between these two 3D SnO_2 . The results show that SnO_2 sheet-spheres exhibit higher gas response to ethanol as well as lower working temperature as compared to that of pointed columnar-spheres. These results indicate that the gas-sensing properties of SnO_2 materials can be enhanced by controlling their shapes and surface structures. Also these samples lay the foundation for the gas-sensitive reaction to other gases (hydrogen, carbonic oxide, methane, etc.) for the future research.

Conflict of Interests

The authors declare that there is no conflict of interests regarding the publication of this paper.

Acknowledgments

The authors appreciate the financial supports of the National Natural Science Fund of China (nos. 51277185 and 51202302) and the National Special Fund for Major Research Instrumentation Development (no. 2012YQ16000705).

References

- [1] C. B. Murray, D. J. Norris, and M. G. Bawendi, "Synthesis and characterization of nearly monodisperse CdE (E = sulfur, selenium, tellurium) semiconductor nanocrystallites," *Journal of the American Chemical Society*, vol. 115, no. 19, pp. 8706–8715, 1993.
- [2] X. Wang, J. Zhuang, Q. Peng, and Y. Li, "A general strategy for nanocrystal synthesis," *Nature*, vol. 437, no. 7055, pp. 121–124, 2005.
- [3] J. Hu, L.-S. Li, W. Yang, L. Manna, L.-W. Wang, and A. P. Alivisatos, "Linearly polarized emission from colloidal semiconductor quantum rods," *Science*, vol. 292, no. 5524, pp. 2060–2063, 2001.
- [4] A. P. Alivisatos, "Semiconductor clusters, nanocrystals, and quantum dots," *Science*, vol. 271, no. 5251, pp. 933–937, 1996.

- [5] W. Zeng, B. Miao, Q. Zhou, and L. Lin, "Hydrothermal synthesis and gas sensing properties of variety low dimensional nanostructures of SnO₂," *Physica E*, vol. 47, pp. 116–121, 2013.
- [6] K.-I. Shimizu, M. Katagiri, S. Satokawa, and A. Satsuma, "Sintering-resistant and self-regenerative properties of Ag/SnO₂ catalyst for soot oxidation," *Applied Catalysis B: Environmental*, vol. 108-109, pp. 39–46, 2011.
- [7] Y. Idota, T. Kubota, A. Matsufuji, Y. Maekawa, and T. Miyasaka, "Tin-based amorphous oxide: a high-capacity lithium-ion-storage material," *Science*, vol. 276, no. 5317, pp. 1395–1397, 1997.
- [8] M.-S. Park, G.-X. Wang, Y.-M. Kang, D. Wexler, S.-X. Dou, and H.-K. Liu, "Preparation and electrochemical properties of SnO₂ nanowires for application in lithium-ion batteries," *Angewandte Chemie—International Edition*, vol. 46, no. 5, pp. 750–753, 2007.
- [9] Z. Wen, F. Zheng, and K. Liu, "Synthesis of porous SnO₂ nanospheres and their application for lithium-ion battery," *Materials Letters*, vol. 68, pp. 469–471, 2012.
- [10] N. D. Khoang, D. D. Trung, N. van Duy, N. D. Hoa, and N. van Hieu, "Design of SnO₂/ZnO hierarchical nanostructures for enhanced ethanol gas-sensing performance," *Sensors and Actuators B: Chemical*, vol. 174, pp. 594–601, 2012.
- [11] H. Li, F. Meng, J. Liu et al., "Synthesis and gas sensing properties of hierarchical meso-macroporous SnO₂ for detection of indoor air pollutants," *Sensors and Actuators B: Chemical*, vol. 166-167, pp. 519–525, 2012.
- [12] J. Y. Park, S.-W. Choi, and S. S. Kim, "Junction-tuned SnO₂ nanowires and their sensing properties," *Journal of Physical Chemistry C*, vol. 115, no. 26, pp. 12774–12781, 2011.
- [13] Q. Zhou, W. Chen, L. Xu, and S. Peng, "Hydrothermal synthesis of various hierarchical ZnO nanostructures and their methane sensing properties," *Sensors*, vol. 13, no. 5, pp. 6171–6182, 2013.
- [14] L. Shi and H. Lin, "Preparation of band gap tunable SnO₂ nanotubes and their ethanol sensing properties," *Langmuir*, vol. 27, no. 7, pp. 3977–3981, 2011.
- [15] Z. Li, Q. Zhao, W. Fan, and J. Zhan, "Porous SnO₂ nanospheres as sensitive gas sensors for volatile organic compounds detection," *Nanoscale*, vol. 3, no. 4, pp. 1646–1652, 2011.
- [16] L. Mei, J. Deng, X. Yin et al., "Ultrasensitive ethanol sensor based on 3D aloe-like SnO₂," *Sensors and Actuators B: Chemical*, vol. 166-167, pp. 7–11, 2012.
- [17] H. Wang, Q. Liang, W. Wang, Y. An, J. Li, and L. Guo, "Preparation of flower-like SnO₂ nanostructures and their applications in gas-sensing and lithium storage," *Crystal Growth and Design*, vol. 11, no. 7, pp. 2942–2947, 2011.
- [18] Z. R. Dai, Z. W. Pan, and Z. L. Wang, "Growth and structure evolution of novel tin oxide diskettes," *Journal of the American Chemical Society*, vol. 124, no. 29, pp. 8673–8680, 2002.
- [19] Q. Dong, H. Su, J. Xu, and D. Zhang, "Influence of hierarchical nanostructures on the gas sensing properties of SnO₂ biomorphic films," *Sensors and Actuators B: Chemical*, vol. 123, no. 1, pp. 420–428, 2007.
- [20] M. Wu, W. Zeng, and Y. Li, "Hydrothermal synthesis of novel SnO₂ nanoflowers and their gas-sensing properties," *Materials Letters*, vol. 104, pp. 34–36, 2013.
- [21] G. X. Wang, J. S. Park, M. S. Park, and X. L. Gou, "Synthesis and high gas sensitivity of tin oxide nanotubes," *Sensors and Actuators B: Chemical*, vol. 131, no. 1, pp. 313–317, 2008.
- [22] Q. Qi, T. Zhang, L. Liu, X. Zheng, and G. Lu, "Improved NH₃, C₂H₅OH, and CH₃COCH₃ sensing properties of SnO₂ nanofibers by adding block copolymer P123," *Sensors and Actuators B: Chemical*, vol. 141, no. 1, pp. 174–178, 2009.
- [23] H. Zhang, Q. He, X. Zhu, D. Pan, X. Deng, and Z. Jiao, "Surfactant-free solution phase synthesis of monodispersed SnO₂ hierarchical nanostructures and gas sensing properties," *CrystEngComm*, vol. 14, no. 9, pp. 3169–3176, 2012.
- [24] W. Zeng, T. Liu, and Z. Wang, "Impact of Nb doping on gas-sensing performance of TiO₂ thick-film sensors," *Sensors and Actuators B: Chemical*, vol. 166-167, pp. 141–149, 2012.
- [25] W. G. Chen, Q. Zhou, and L. N. Xu, "Improved methane sensing properties of Co-doped SnO₂ electrospun nanofibers," *Journal of Nanomaterials*, vol. 2013, Article ID 173232, 9 pages, 2013.
- [26] Z. Weng and L. Tian-mo, "Gas-sensing properties of SnO₂-TiO₂-based sensor for volatile organic compound gas and its sensing mechanism," *Physica B: Condensed Matter*, vol. 405, no. 5, pp. 1345–1348, 2010.
- [27] N. Bârsan, M. Hübner, and U. Weimar, "Conduction mechanisms in SnO₂ based polycrystalline thick film gas sensors exposed to CO and H₂ in different oxygen backgrounds," *Sensors and Actuators B: Chemical*, vol. 157, no. 2, pp. 510–517, 2011.
- [28] M. Hübner, R. G. Pavelko, and N. Bârsan, "Influence of oxygen backgrounds on hydrogen sensing with SnO₂ nanomaterials," *Sensors and Actuators B: Chemical*, vol. 154, no. 2, pp. 264–269, 2011.
- [29] W. G. Chen, Q. Zhou, and S. D. Peng, "Hydrothermal synthesis of Pt-, Fe-, and Zn-doped SnO₂ nanospheres and carbon monoxide sensing properties," *Advances in Materials Science and Engineering*, vol. 2013, Article ID 578460, 8 pages, 2013.
- [30] G. Sakai, N. Matsunaga, K. Shimano, and N. Yamazoe, "Theory of gas-diffusion controlled sensitivity for thin film semiconductor gas sensor," *Sensors and Actuators B: Chemical*, vol. 80, no. 2, pp. 125–131, 2001.

Research Article

The Removal of Uranium onto Nanoscale Zero-Valent Iron Particles in Anoxic Batch Systems

Richard A. Crane and Thomas B. Scott

Interface Analysis Centre, University of Bristol, UK

Correspondence should be addressed to Richard A. Crane; richardandrewcrane@gmail.com

Received 14 January 2014; Revised 14 February 2014; Accepted 14 February 2014; Published 25 May 2014

Academic Editor: Jie-Fang Zhu

Copyright © 2014 R. A. Crane and T. B. Scott. This is an open access article distributed under the Creative Commons Attribution License, which permits unrestricted use, distribution, and reproduction in any medium, provided the original work is properly cited.

The removal of uranium (U) onto nanoscale zero-valent iron particles has been studied for uranium-bearing mine water and synthetic uranyl solutions in the presence and absence of dissolved oxygen. The work has been conducted in order to investigate the differential nanoparticle corrosion behaviour and associated mechanisms of U removal behaviour in conditions representative of near-surface and deep groundwater systems. Batch systems were analysed over a 28-day reaction period during which the liquid and nanoparticulate solids were periodically analysed to determine chemical evolution of the solutions and particulates. Analysis of aqueous samples using inductively coupled plasma mass spectrometry recorded near-total U removal after 1 hour of reaction in all systems studied. However, in the latter stages of the reaction (after 48 hours), significant rerelease of uranium was recorded for the mine water batch system with dissolved O₂ present. In contrast, less than 2% uranium rerelease was recorded for the anoxic batch system. Concurrent analysis of extracted nanoparticle solids using X-ray diffraction recorded significantly slower corrosion of the nanoparticles in the anoxic batch system, with residual metallic iron maintained until after 28 days of reaction compared to only 7 days of reaction in systems with dissolved O₂ present. Results provide clear evidence that the corrosion lifespan and associated U⁶⁺ removal efficacy of nanoscale zero-valent iron replace enhanced in the absence of dissolved oxygen.

1. Introduction

To date, a key environmental legacy of mankind's military and civil nuclear activities has been the release of uranium (U) into the natural environment. U can exist in five oxidation states: +2, +3, +4, +5, and +6. However, in the natural environment, the +4 and +6 valence states dominate. U⁴⁺ commonly exists in chemically reducing environments and typically forms chemical species of relatively low solubility [1]. In contrast, U⁶⁺ is predominant in oxidising environments and typically forms compounds of relatively high solubility [2]. Reduction of U⁶⁺ to U⁴⁺ has therefore been proposed as a suitable approach to U remediation.

In recent years, a wide range of electron donors have been demonstrated to chemically reduce U⁶⁺ including reduced iron, including magnetite, [3] ferrous hydroxides, [4] Fe²⁺ sorbed on hematite surfaces [5], and zero-valent iron [6]; microorganisms, including dissimilatory metal-reducing bacteria [7] and sulphate reducing bacteria [8];

organic compounds, including acetate [9] and lactate [10]; and dissolved and solid sulphide species [11–16]. In contaminated sites the presence of competitive electron acceptors, toxic heavy metals, and/or unfavourable pH/Eh conditions can significantly limit the suitability of many biotic methods for uranium remediation [17, 18]. As a consequence, much focus has been applied in recent years on the use of chemical reducing agents, namely, zero-valent iron [19–28]. Recent work, investigating the removal of uranium in waste effluents [19] and mine water [22], has determined that the key role complexing agents, commonly found in natural waters, such as carbonate, phosphate, and sulphate, play on the long term removal of uranium onto nanoscale zero-valent iron. Results have provided clear evidence that such complexing agents (namely, carbonate) significantly enhance the relative stability of U⁶⁺, promoting U desorption from particle surfaces following an initial period of removal onto nanoscale zero-valent iron. The mechanism has been attributed to incomplete chemical reduction of surface-precipitated U⁶⁺,

allowing U rerelease during subsequent nanoparticle corrosion and the reformation of highly stable aqueous U-complexes. There accordingly exists a fundamental need to understand the reversible nature of U removal in complex and/or natural waters using iron-based materials, specifically the link between nanoparticle corrosion and U desorption. The current work has therefore been established to contrast the sorption-desorption behaviour of U onto nanoscale zero-valent iron in natural waters containing dissolved oxygen (and dissolved oxygen recharge), that is, the vadose zone, with waters where dissolved oxygen is only available in trace levels, that is, the phreatic zone.

2. Materials and Methods

2.1. Experimental Procedure. Four 500 mL Schott Duran jars were each filled with 400 mL of the U-bearing mine water. Further four jars were filled with 400 mL of uranyl solution at 0.5 ppm U, with the solution pH adjusted to 9.52 using 0.01 M NaOH. The addition of NaOH was performed slowly, dropwise, to avoid the formation of hydroxocarbonyl complexes. Two of the mine water solutions and two of the uranyl solutions were then purged with oxygen-free $N_{2(g)}$ (>99.998%) at 1 L m^{-1} for 30 minutes to reduce the content of $O_{2(g)}$ to <0.1 ppm and left in a Saffron Scientific glovebox for 7 days to equilibrate. The glovebox atmosphere consisted of N_2/H_2 (95:5) and a Coy Laboratory “Stak-Pak” palladium catalyst was used to catalyse the removal of $O_{2(g)}$, via reaction with $H_{2(g)}$, producing $H_2O_{(l)}$. The two remaining mine water solutions were stored on the benchtop. To two of the mine water solutions (one oxic and one anoxic) and two of the uranyl solutions (one oxic and one anoxic), 0.2 g (0.5 g L^{-1}) of nano- Fe^0 was added. The two remaining mine water solutions (oxic and anoxic) and the two uranyl solutions (oxic and anoxic) were run as nanoparticle-free control systems. In each case, the nano- Fe^0 was suspended in 2 mL of ethanol and dispersed by sonification for 30 seconds. During the experiment, the glovebox containing the anoxic batch systems was purged with N_2/H_2 (95:5) gas at 0.5 bar for 5 minutes every 24 hours.

2.2. Sampling Methods. Each system was sampled at 0 h, 1 h, 2 h, 4 h, 24 h, 48 h, 7 d, 14 d, and 28 d. Prior to sampling, the jars were gently agitated to ensure homogeneity and pH and Eh measurements were taken using a Hanna Instruments meter (model HI 8424) with a combination gel electrode pH probe and a platinum ORP electrode, respectively. Dissolved oxygen (DO) measurements were taken using a Jenway 970 DO_2 meter. Aliquots of 10 mL were taken from each jar and centrifuged using a Hamilton Bell Vanguard V6500 desktop centrifuge at 6500 rpm for 30 seconds to separate the liquid and solid phases. The liquid was decanted, filtered through a $0.22\text{ }\mu\text{m}$ cellulose acetate filter, and then prepared for inductively coupled plasma atomic emission spectrometry (ICP-AES) and inductively coupled plasma mass spectrometry (ICP-MS). The solid was prepared for X-ray diffraction (XRD) and X-ray photoelectron spectroscopy (XPS) by sequential rinsing in 3 mL each of Milli-Q water,

ethanol, and then acetone, with the resultant suspension pipetted onto a glass optical microscope slide and aluminium stub, respectively.

2.3. Nanoparticle Synthesis. Iron nanoparticles were synthesised following the method first described by Wang and Zhang [29] using sodium borohydride to reduce ferrous iron to a metallic state. 1.35 g of $FeCl_3 \cdot 6H_2O$ was dissolved in 50 mL of Milli-Q water ($>18.2\text{ M}\Omega\text{ cm}$) and then a 4 M NaOH solution was used to adjust the solution pH to 6.8. The addition of NaOH was performed slowly, dropwise, to avoid the formation of hydroxocarbonyl complexes. The salts were reduced to metallic nanoparticles by the addition of 2.0 g of $NaBH_4$. The nanoparticle product was then isolated through centrifugation and sequentially washed with water, ethanol, and acetone (20 mL of each). The nanoparticles were dried in a desiccator under low vacuum (approx. 10^{-2} mbar) for 48 hours and then stored in the oxygen-free nitrogen environment of a Saffron Scientific glovebox until required.

2.4. ICP-AES Preparation. The liquid samples were prepared for ICP-AES analysis by a 10-time dilution in 1% nitric acid (analytical quality concentrated HNO_3 in Milli-Q water). Blanks and standards for analysis were also prepared in 1% nitric acid, with Fe standards of 0.1, 0.25, 0.5, 1, 2.5, 5, and 10 ppm. A Jobin Yvon Ultima ICP-AES (sequential spectrometer) fitted with a cyclone spray chamber and a Burgener Teflon Mira Mist Nebulizer was used. The Fe concentration was measured using the emission line at 259.94 nm.

2.5. ICP-MS Preparation. Samples were prepared for ICP-MS analysis by a 10-time dilution in 1% nitric acid (analytical quality concentrated HNO_3 in Milli-Q water). Blanks and uranium standards at 0.1, 0.5, 1, 5, and 10 ppb were also prepared in 1% nitric acid (analytical quality concentrated HNO_3 in Milli-Q water). An internal Bi standard of 10 ppb was added to blanks, standards, and samples. The ICP-MS instrument used was Thermo Elemental PQ3.

2.6. XPS. Solid samples were analysed at $<5 \times 10^{-8}\text{ mbar}$ in a Thermo Fisher Scientific Escascope equipped with a dual anode X-ray source ($Al_{K\alpha}$ 1486.6 eV and $Mg_{K\alpha}$ 1253.6 eV). $Al_{K\alpha}$ radiation was used at 400 W (15 kV, 23 mA). High resolution scans were acquired using a 30 eV pass energy and 200 ms dwell times. Following the acquisition of “wide” spectra over a wide binding energy range, the regions containing the C and U peaks were scanned at a higher energy resolution. Data analysis was carried out using Pisce software (Dayta Systems Ltd.) with binding energy values of the recorded lines referenced to the adventitious hydrocarbon C1s peak at 284.8 eV.

2.7. XRD. A Phillips Xpert Pro diffractometer with a $Cu_{K\alpha}$ radiation source ($\lambda = 1.5406\text{ \AA}$) was used for XRD analysis (generator voltage of 40 keV; tube current of 30 mA). XRD spectra were acquired between 2θ angles of $0-90^\circ$, with a step size of 0.02° and a 2 s dwell time.

TABLE 1: Bulk and surface properties of the nano-Fe⁰ used in the current work.

Parameter	Nano-Fe ⁰	
Particle size distribution (%)	0–50 nm	85
	50–100 nm	8
	>100 nm	7
Crystallinity	Amorphous (α-Fe)	
Oxide thickness (nm)	3–4	
Surface area (m ² g ⁻¹)	14.8	
Surface composition (%)	Fe	30.5
	O	32.1
	C	14.5
	B	22.9
Surface stoichiometry	(Fe ⁰ /Fe ²⁺ + Fe ³⁺)	0.02
	Fe ²⁺ /Fe ³⁺	0.38

Note: a significant proportion of the carbon detected is likely to be adventitious carbon.

3. Results

3.1. Preliminary Characterisation of the Nanoparticles. Preliminary characterisation of the nano-Fe⁰ was performed using Brunauer, Emmett, and Teller (BET) surface area analysis, transmission electron microscopy (TEM), XRD, and XPS. BET analysis determined that the starting surface area of the nano-Fe⁰ was 14.8 m² g⁻¹. TEM analysis determined that the nano-Fe⁰ were roughly spherical, with an approximate size range of 20–100 nm and an average diameter of 34 nm. The density contrast between the Fe⁰ core and oxide shell in the nano-Fe⁰ was identified; however, the material was recorded as relatively amorphous with no clear grain structure. Individual particles were recorded as aggregated into chains and rings, attributed to the magnetic properties of the Fe⁰ cores. XRD analysis recorded a broad diffraction peak at 44.9° 2θ and other low intensity peaks at 65° and 82° 2θ, implying the presence of amorphous Fe⁰. XPS analysis confirmed the presence of a mixed valent (Fe²⁺/Fe³⁺) oxide at the surface of the material. The results are summarised in Table 1.

3.2. Preliminary Characterisation of the U-Bearing Mine Water. Prior to nanoparticle addition, the U-bearing mine water was characterised using ICP-AES (Fe, Mg, Cu, and Mo), ICP-MS (U), volumetric titration (HCO₃⁻, NO₃⁻, and PO₄³⁻), and gravimetry (SO₄²⁻) with supplementary Eh, pH, and DO measurements. The analysis indicated that HCO₃⁻, well documented to form uranyl complexes of high thermodynamic stability [30], was the most common ligand species present, with a concentration of approximately 974 ppm (Table 2).

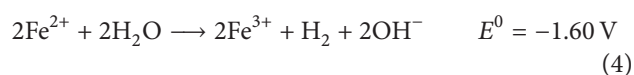
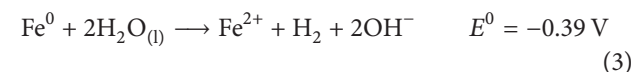
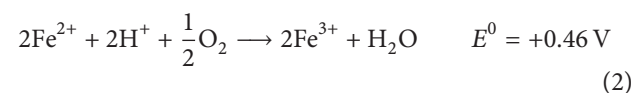
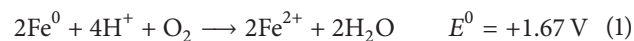
3.3. The Effect of Inert Gas Sparging. Following N₂ gas sparging a decrease in solution Eh, from 65 mV to -49 mV, was recorded concurrent with a significant decrease in DO, from 8.93 ppm to 0.09 ppm, and ascribed to the expulsion

TABLE 2: Concentrations of notable chemical species present in the mine water, analysed by ICP-MS (U), ICP-AES (Fe, Mg, Cu, and Mo), volumetric titration (HCO₃⁻, NO₃⁻, and PO₄³⁻), and gravimetry (SO₄²⁻) along with the recorded Eh, pH, and DO.

Chemical species	Concentration (ppm)
Cations	
Cu	0.044
Fe	0.021
Mg	12.11
Mo	0.21
U	1.41
Anions	
HCO ₃ ⁻	974.42
NO ₃ ⁻	18.53
PO ₄ ³⁻	0.15
SO ₄ ²⁻	0.51
Solution conditions	
DO (ppm)	8.84
Eh (mV)	65
pH	9.29

of DO from the mine water. An increase in solution pH, from 9.29 to 9.52, was also recorded. This is a common phenomenon reported for carbonate-rich solutions during inert gas sparging and attributed to the expulsion of dissolved CO₂, resulting in the hydrolysis of HCO₃⁻ (in the form of NaHCO₃) and the formation of OH⁻ [31–33].

3.4. Changes in DO/Eh/pH. Following the addition of the nanoparticles a shift to chemically reducing Eh and near-zero DO was recorded within 15 minutes of reaction for all batch systems (Figure 1). An accompanying increase in system pH was also recorded in all systems (Figure 1). For the oxic batch systems, in the early stages of reaction (<15 minutes), the predominant mechanism of nano-Fe⁰ corrosion is considered to have been through reaction with H⁺ via the consumption of DO (see (1) and (2)). For the anoxic batch systems (and the oxic batch systems following total DO consumption) the absence of DO dictates that corrosion could only proceed through the direct reaction (hydrolysis) with water (see (3) and (4)). The slower pH/Eh change recorded for the anoxic batch systems in the current work is therefore ascribed to the slower reaction kinetics of nano-Fe⁰ in the absence of DO:



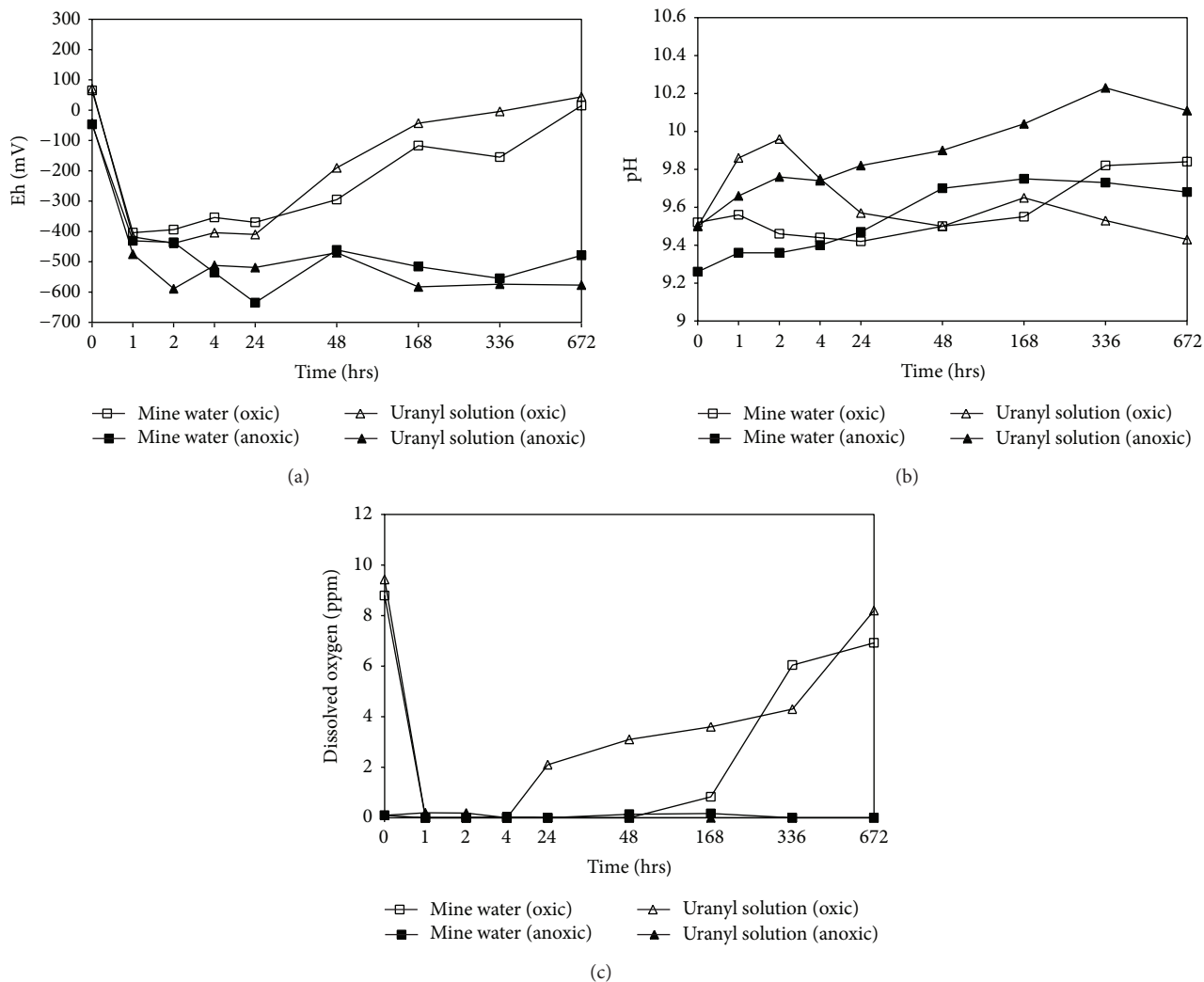


FIGURE 1: (a) Eh (mV) as a function of reaction time (0–672 hrs). The control (nanoparticle-free) solutions (not shown) recorded a variation of <10 mV in all systems; (b) pH as a function of reaction time (0–672 hrs). The control (nanoparticle-free) solution (not shown) recorded a variation of <0.2 pH units in all systems; (c) dissolved oxygen (ppm) as a function of reaction time (0–672 hrs). The control (nanoparticle-free) solution (not shown) recorded a variation of <0.05 ppm units in all systems.

In addition, fast pH/Eh changes were recorded for the uranyl solutions compared to the mine water batch systems. This is attributed to the lack of major ions in the former systems to buffer the aforementioned geochemical perturbation imbued by nanoparticle corrosion.

After 4 hours of reaction, a recovery in DO and Eh was recorded for the oxic batch systems only. In contrast, Eh and DO were maintained as less than -430 mV and <0.2 ppm O_2 , respectively, for the entire 28-day reaction period for both anoxic batch systems. Near-zero DO (<0.1 ppm) was recorded for the anoxic (nanoparticle-free) batch system for the entire 28-day reaction period. This provides clear evidence of minimal oxygen ingress into the anoxic batch systems.

3.5. Changes in Aqueous U and Fe Concentration. Analysis of liquid samples using ICP-MS recorded rapid and near-total U removal in all systems treated using nano- Fe^0 (Figure 2) with removal of $>99\%$ $U_{(aq)}$ recorded after 1 hour in all systems

and maintained until 48 hours of reaction. Onwards from 48 hours a gradual increase in $U_{(aq)}$ concentration was recorded for the oxic mine water batch system (Figure 2). In contrast, no appreciable U rerelease was recorded for the anoxic mine water and the uranyl batch systems in both oxic and anoxic conditions. This is attributed to the presence of complexing agents (namely, carbonate) in the mine water, allowing the reformation of dissolved U-complexes concurrent with nanoparticle corrosion during the ingress of atmospheric gases into the batch systems as previously observed [22]. As reported by Crane et al., [22] it is likely that chemical reduction of aqueous U^{6+} to solid U^{4+} (as UO_2) occurred for all batch treatment systems during the initial stage of U sorption onto the nano- Fe^0 . However, for the mine water solutions containing dissolved oxygen, oxidation back to aqueous U^{6+} is likely to have occurred due to a combination of (i) the increased availability of dissolved oxygen and (ii)

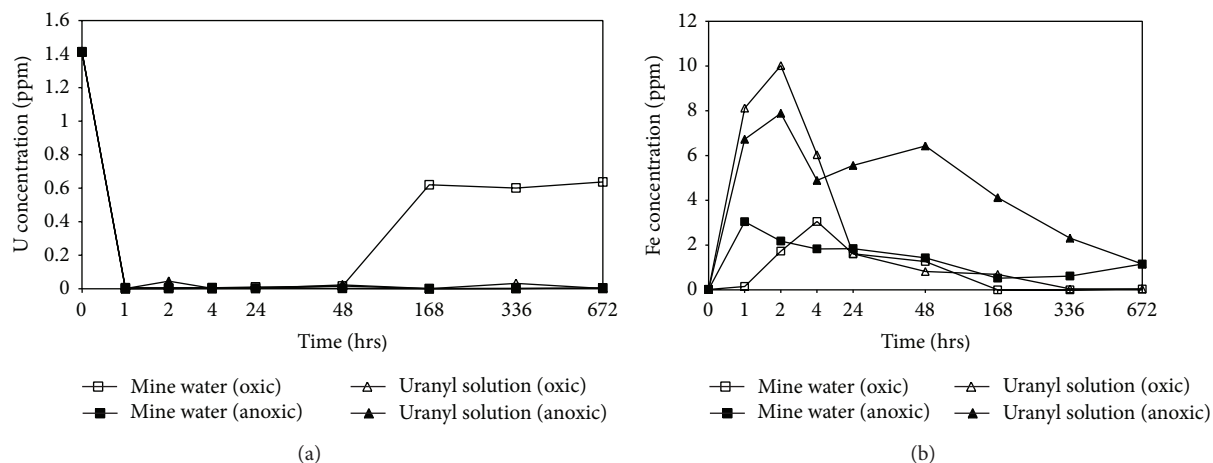


FIGURE 2: (a) Aqueous uranium concentration (ppm) as a function of reaction time (0–672 hrs). The control (nanoparticle-free) solutions (not shown) recorded a variation of <0.01 ppm from the starting concentration in all systems; (b) aqueous iron concentration (ppm) as a function of reaction time (0–672 hrs). The control (nanoparticle-free) solutions (not shown) recorded a variation of <0.02 ppm from the starting concentration in all systems.

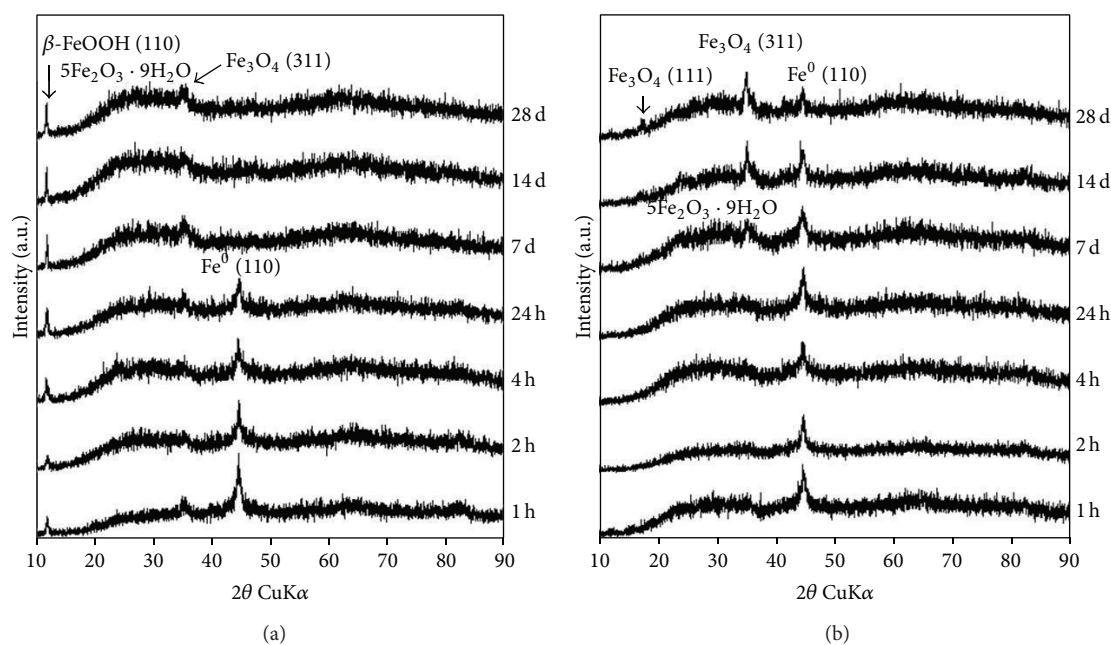


FIGURE 3: X-ray diffraction (XRD) spectra (for the range of 10 – 90° 2θ) recorded for the oxic (a) and anoxic (b) mine water batch systems after reaction times of 1 h, 2 h, 4 h, 24 h, 7 d, 14 d, and 28 d.

the enhanced solubility of U in the presence of complexing agents, such as carbonate.

Analysis of liquid samples using ICP-AES recorded an increase in $\text{Fe}_{(\text{aq})}$ following the addition of the nanoparticles, with maximum $\text{Fe}_{(\text{aq})}$ concentrations recorded in all systems within the first 48 hours of reaction and attributed to the rapid corrosion of nanoparticulate surfaces. The greatest $\text{Fe}_{(\text{aq})}$ concentrations were recorded for the uranyl solutions and ascribed to the lower ionic concentration compared to the mine water.

3.6. Analysis of Reacted Nanoparticulate Solids

3.6.1. X-Ray Diffraction. XRD was used to determine the bulk crystallinity and composition of nano- Fe^0 solids extracted from both oxic and anoxic batch systems at periodic intervals during the experiment (Figure 3). A transition from Fe^0 , with peaks centred at 44.6 , 65.6 , and 82.6° 2θ (lattice reflections: $\text{Fe}(110)$, $\text{Fe}(200)$, and $\text{Fe}(211)$, resp.), to a mixture of akaganéite (β - FeOOH), ferrihydrite ($5\text{Fe}_2\text{O}_3 \cdot 9\text{H}_2\text{O}$), and magnetite (Fe_3O_4) was recorded for both oxic and anoxic batch systems. Total Fe^0 conversion was, however, not recorded for

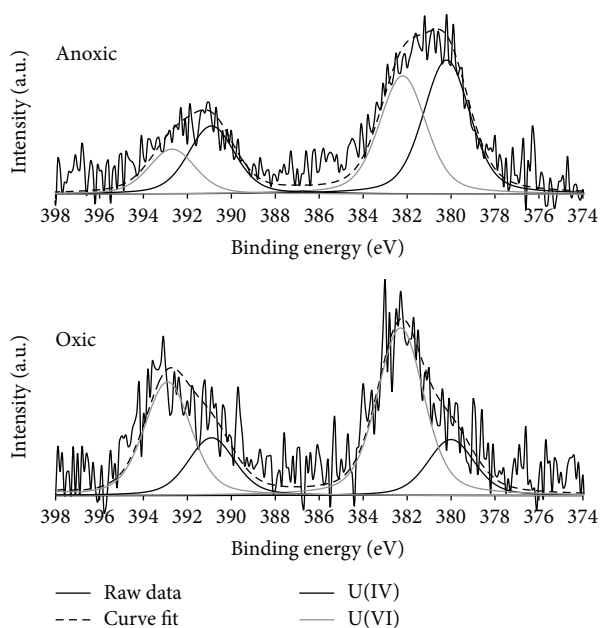


FIGURE 4: Curve fitted XPS U 4f photoelectron peaks acquired after 24 hours of reaction for mine water batch systems treated with nano- Fe^0 .

the anoxic system with residual Fe^0 present after 28 days of reaction compared to full conversion exhibited by the oxic batch system after 7 days of reaction. This is ascribed to the slower corrosion of nano- Fe^0 in the absence of DO as discussed above.

The formation of ferrihydrite and magnetite was not unexpected, given that both species are common Fe^0 corrosion products in near-neutral to alkaline solutions [34–38]. The presence of chloride ions (which are necessary for akaganéite formation) was likely to have been provided by the dissolution of FeCl_2 , present in the nano- Fe^0 due to incomplete conversion of FeCl_2 to Fe^0 during the nano- Fe^0 synthesis. In the latter stages of the reaction (>7 days) the akaganéite peak was recorded to shift by approximately $-0.5^\circ 2\theta$, suggesting an increase in the lattice parameter of the material. This was attributed to cationic substitution of a larger ion, such as Ca^{2+} (0.212 nm compared to 0.166 nm), into the lattice structure [39].

3.6.2. X-Ray Photoelectron Spectroscopy. X-ray photoelectron spectroscopy (XPS) was used to determine the surface chemistry of extracted particulates including any sorbed species extracted from the oxic and anoxic batch systems at regular intervals throughout the experiment (Figure 4). Curve fitting of recorded $\text{Fe } 2p_{3/2}$ photoelectron peaks (not shown) determined a decrease in the $\text{Fe}^{2+}/\text{Fe}^{3+}$ ratio throughout the reaction period, ascribed to the oxidation of the nanoparticle surfaces. This occurred most rapidly during the initial stages of the reaction, with oxic and anoxic systems recording a shift in $\text{Fe}^{2+}/\text{Fe}^{3+}$ ratio to 0.23 and 0.32, respectively, after 1 hour of

reaction. The higher proportion of Fe^{3+} in the oxic system is attributed to a greater concentration of DO at the start of the reaction. Following this initial and rapid oxidation phase, a more gradual decrease in the $\text{Fe}^{2+}/\text{Fe}^{3+}$ ratio was recorded in all oxic systems to minima of 0.11 after 28 days of reaction. In contrast, no appreciable change was recorded for all anoxic systems, indicating that minimal nano- Fe^0 oxidation had occurred.

XPS data recorded from the samples of extracted particulates failed to record detectable peaks in the U 4f binding energy region of the recorded photoelectron spectra in all the reacted samples, even during the initial period of maximum U removal. This was not unexpected, given the small amount of U in each system ($1413 \mu\text{L}^{-1}$) relative to the large surface area presented by the nanoparticles ($14.8 \text{ m}^2 \text{ g}^{-1}$). U 4f photoelectron peaks were detected for both oxic and anoxic mine water samples after 4 hours of reaction. Curve fitting, following the method of Scott et al., determined that U present was in a partially reduced state for both systems with a $\text{U}^{4+}/\text{U}^{6+}$ ratio of 0.34 and 1.13 recorded for the oxic and anoxic system, respectively. Greater proportion of U^{4+} relative to U^{6+} recorded for the anoxic batch system is attributed to enhanced chemical reduction of U in low oxygen conditions. This is likely to be due to the significantly lower (and sustained) Eh conditions imbued by the nano- Fe^0 in the low oxygen environment, where Fe^0 is maintained throughout the 28-day reaction period (see Section 3.6.1). In contrast Fe^0 was recorded to be oxidised to (oxy)hydroxide species more rapidly in the batch systems containing dissolved oxygen, which would have resulted in lower chemical reduction of U^{6+} to U^{4+} .

4. Discussion

Nano- Fe^0 have been tested in the current work for the removal of U from mine water batch systems in both dissolved oxygen containing (starting DO ~ 9.5 ppm and batch systems handled and stored in the open laboratory) and anoxic (starting DO < 0.1 ppm and batch systems handled and stored in a nitrogen-filled glovebox) batch systems. Nano- Fe^0 were documented as highly effective for the rapid removal of U despite the high concentration of complexing agents present in the mine water, namely, bicarbonate at 974 ppm, with near-total U removal recorded after 1 hour of reaction for all systems studied. Limited long term U removal, however, was recorded for the batch systems with DO present, with significant U rerelease recorded within 7 days of nano- Fe^0 application. In contrast, no appreciable U rerelease was recorded for the anoxic mine water batch system. XRD analysis of nano- Fe^0 extracted from both oxic and anoxic systems determined that whilst total conversion of nano- Fe^0 to (oxy)hydroxide corrosion products had occurred in the oxic systems, Fe^0 was maintained in the anoxic systems. Concurrent XPS analysis determined that sorbed U was present in a partially reduced state in both oxic and anoxic systems; however, greater chemical reduction

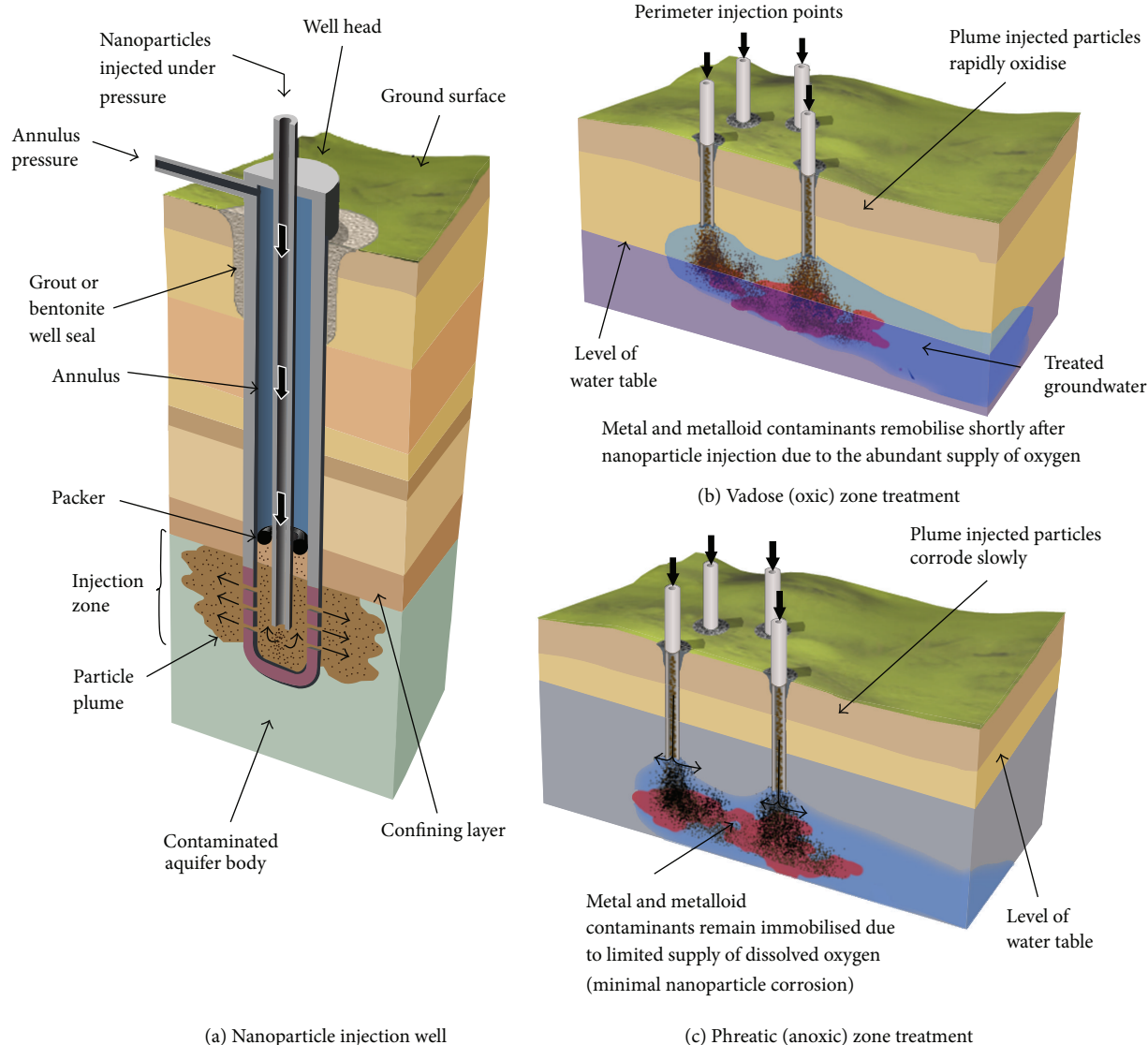


FIGURE 5: Schematic diagram of the following: (a) a typical nanoparticle injection well: the technology is very similar to that used for injection of CO_2 into subterranean storage reservoirs; (b) *in situ* vadose (oxic) zone treatment of metal and metalloid aqueous contaminant species using nanoscale zero-valent iron particles: contaminants remobilise shortly after nanoparticle injection due to the abundant supply of dissolved oxygen; and (c) *in situ* phreatic (anoxic) zone treatment of metal and metalloid aqueous contaminant species using nanoscale zero-valent iron particles: contaminants remain immobilised due to the limited supply of dissolved oxygen.

was recorded for the anoxic systems. The mechanism of U rerelease in the oxic systems is therefore attributed to the incomplete chemical reduction of surface-precipitated U (from soluble U^{6+} to insoluble U^{4+}) within the mine water samples, allowing the rerelease of U^{6+} during the ingress of DO back into batch systems, and the reformation of highly stable (nominally carbonate) aqueous U-complexes. This was not recorded for the anoxic systems because the absence of DO allowed Fe^0 to be maintained (and associated strongly chemically reducing conditions) throughout the 28-day reaction period. Figure 5 displays a schematic diagram of this hypothesis applied for the *in situ* treatment of metal and metalloid aqueous contaminant species using nanoscale zero-valent iron particles.

5. Conclusions

The rerelease of metal and metalloid contaminant species following a period of “apparent remediation” is a key engineering challenge which may limit the development of nano- Fe^0 as a new technology for mine water treatment. The current work has provided clear evidence that nano- Fe^0 is only appropriate for the *in situ* treatment of U in surface and/or vadose zone waters if extremely robust secondary method(s) are applied to prevent DO ingress into the contaminant treatment zone. Example materials include impermeable geomembranes and bentonite. For the *in situ* treatment of anoxic mine water, it is shown that U removal can be maintained on a long term or even quasi-permanent basis

if there is sufficiently low DO flux to maintain the strongly chemically reducing groundwater conditions imbued by the nano-Fe⁰.

Further work is required to examine the reversible nature of metal and metalloid remediation in complex and/or natural waters using nano-Fe⁰. This will provide validation of the technology for sites where assurance of medium to long term immobilisation of contaminants is required.

Conflict of Interests

The authors declare that there is no conflict of interests regarding the publication of this paper.

Acknowledgments

The authors would like to thank the National Company Uranium (Romania) for providing mine water samples for the current work. They would also like to thank scientists from the National Institute for Metals and Radioactive Resources, Bucharest, Romania, for help with arranging delivery of the mine water samples to the University of Bristol. The work was funded by the Engineering and Physical Sciences Research Council.

References

- [1] D. Langmuir, "Uranium solution-mineral equilibria at low temperatures with applications to sedimentary ore deposits," *Geochimica et Cosmochimica Acta*, vol. 42, no. 6, pp. 547–569, 1978.
- [2] R. Guillaumont, T. Fanghanel, J. Fuger et al., *Update on the Chemical Thermodynamics of Uranium, Neptunium, and Plutonium*, Elsevier, Amsterdam, The Netherlands, 2nd edition, 2003.
- [3] T. B. Scott, G. C. Allen, P. J. Heard, and M. G. Randell, "Reduction of U(VI) to U(IV) on the surface of magnetite," *Geochimica et Cosmochimica Acta*, vol. 69, no. 24, pp. 5639–5646, 2005.
- [4] E. J. O'Loughlin, S. D. Kelly, R. E. Cook, R. Csencsits, and K. M. Kemner, "Reduction of uranium(VI) by mixed iron(II)/iron(III) hydroxide (green rust): formation of UO₂ nanoparticles," *Environmental Science and Technology*, vol. 37, no. 4, pp. 721–727, 2003.
- [5] E. Liger, L. Charlet, and P. Van Cappellen, "Surface catalysis of uranium(VI) reduction by iron(II)," *Geochimica et Cosmochimica Acta*, vol. 63, no. 19–20, pp. 2939–2955, 1999.
- [6] B. Gu, L. Liang, M. J. Dickey, X. Yin, and S. Dai, "Reductive precipitation of uranium(VI) by zero-valent iron," *Environmental Science and Technology*, vol. 32, no. 21, pp. 3366–3373, 1998.
- [7] D. R. Lovley, "Dissimilatory metal reduction," *Annual Review of Microbiology*, vol. 47, pp. 263–290, 1993.
- [8] D. R. Lovley, E. E. Roden, E. J. P. Phillips, and J. C. Woodward, "Enzymatic iron and uranium reduction by sulfate-reducing bacteria," *Marine Geology*, vol. 113, no. 1–2, pp. 41–53, 1993.
- [9] D. R. Lovley, E. J. P. Phillips, Y. A. Gorby, and E. R. Landa, "Microbial reduction of uranium," *Nature*, vol. 350, no. 6317, pp. 413–416, 1991.
- [10] D. R. Lovley and E. J. P. Phillips, "Bioremediation of uranium contamination with enzymatic uranium reduction," *Environmental Science and Technology*, vol. 26, no. 11, pp. 2228–2234, 1992.
- [11] A. Kochenov, K. Korolev, V. Dubinchuk, and Y. Medvedev, "Experimental data on the conditions of precipitation of uranium from aqueous solutions," *Geochemistry International*, vol. 14, pp. 82–87, 1987.
- [12] P. Wersin, M. F. Hochella Jr., P. Persson, G. Redden, J. O. Leckie, and D. W. Harris, "Interaction between aqueous uranium (VI) and sulfide minerals: spectroscopic evidence for sorption and reduction," *Geochimica et Cosmochimica Acta*, vol. 58, no. 13, pp. 2829–2843, 1994.
- [13] L. N. Moyes, R. H. Parkman, J. M. Charnock et al., "Uranium uptake from aqueous solution by interaction with goethite, lepidocrocite, muscovite, and Mackinawite: an x-ray absorption spectroscopy study," *Environmental Science and Technology*, vol. 34, no. 6, pp. 1062–1068, 2000.
- [14] C. E. Barnes and J. K. Cochran, "Uranium geochemistry in estuarine sediments: controls on removal and release processes," *Geochimica et Cosmochimica Acta*, vol. 57, no. 3, pp. 555–569, 1993.
- [15] P. Wersin, M. F. Hochella Jr., P. Persson, G. Redden, J. O. Leckie, and D. W. Harris, "Interaction between aqueous uranium (VI) and sulfide minerals: spectroscopic evidence for sorption and reduction," *Geochimica et Cosmochimica Acta*, vol. 58, no. 13, pp. 2829–2843, 1994.
- [16] F. R. Livens, M. J. Jones, A. J. Hynes et al., "X-ray absorption spectroscopy studies of reactions of technetium, uranium and neptunium with mackinawite," *Journal of Environmental Radioactivity*, vol. 74, no. 1–3, pp. 211–219, 2004.
- [17] S. C. Brooks, J. K. Fredrickson, S. L. Carroll et al., "Inhibition of bacterial U(VI) reduction by calcium," *Environmental Science and Technology*, vol. 37, no. 9, pp. 1850–1858, 2003.
- [18] B. Wielinga, B. Bostick, C. M. Hansel, R. F. Rosenzweig, and S. Fendorf, "Inhibition of bacterially promoted uranium reduction: ferric (Hydr)oxides as competitive electron acceptors," *Environmental Science and Technology*, vol. 34, no. 11, pp. 2190–2195, 2000.
- [19] M. Dickinson and T. B. Scott, "The application of zero-valent iron nanoparticles for the remediation of a uranium-contaminated waste effluent," *Journal of Hazardous Materials*, vol. 178, no. 1–3, pp. 171–179, 2010.
- [20] O. Riba, T. B. Scott, K. Vala Ragnarsdottir, and G. C. Allen, "Reaction mechanism of uranyl in the presence of zero-valent iron nanoparticles," *Geochimica et Cosmochimica Acta*, vol. 72, no. 16, pp. 4047–4057, 2008.
- [21] T. B. Scott, G. C. Allen, P. J. Heard, A. C. Lewis, and D. F. Lee, "The extraction of uranium from groundwaters on iron surfaces," *Proceedings of the Royal Society A: Mathematical, Physical and Engineering Sciences*, vol. 461, no. 2057, pp. 1247–1259, 2005.
- [22] R. A. Crane, M. Dickinson, I. C. Popescu, and T. B. Scott, "Magnetite and zero-valent iron nanoparticles for the remediation of uranium contaminated environmental water," *Water Research*, vol. 45, no. 9, pp. 2931–2942, 2011.
- [23] T. B. Scott, I. C. Popescu, R. A. Crane, and C. Noubactep, "Nanoscale metallic iron for the treatment of solutions containing multiple inorganic contaminants," *Journal of Hazardous Materials*, vol. 186, no. 1, pp. 280–287, 2011.
- [24] S. Yan, B. Hua, Z. Bao, J. Yang, C. Liu, and B. Deng, "Uranium(VI) removal by nanoscale zerovalent iron in anoxic batch

- systems," *Environmental Science and Technology*, vol. 44, no. 20, pp. 7783–7789, 2010.
- [25] S. Klimkova, M. Cernik, L. Lacinova, J. Filip, D. Jancik, and R. Zboril, "Zero-valent iron nanoparticles in treatment of acid mine water from in situ uranium leaching," *Chemosphere*, vol. 82, no. 8, pp. 1178–1184, 2011.
- [26] R. A. Crane and T. B. Scott, "Nanoscale zero-valent iron: future prospects for an emerging water treatment technology," *Journal of Hazardous Materials*, vol. 211–212, pp. 112–125, 2012.
- [27] R. A. Crane and T. B. Scott, "The effect of vacuum annealing of magnetite and zero-valent iron nanoparticles on the removal of aqueous uranium," *Journal of Nanotechnology*, vol. 2013, Article ID 173625, 11 pages, 2013.
- [28] C. Noubactep, S. Caré, and R. Crane, "Nanoscale metallic iron for environmental remediation: prospects and limitations," *Water, Air, and Soil Pollution*, vol. 223, no. 3, pp. 1363–1382, 2012.
- [29] C. Wang and W. Zhang, "Synthesizing nanoscale iron particles for rapid and complete dechlorination of TCE and PCBs," *Environmental Science & Technology*, vol. 31, pp. 2154–2156, 1997.
- [30] K. Ragnarsdottir and L. Charlet, "Uranium behaviour in natural environments. Environmental mineralogy—microbial interactions, anthropogenic influences, contaminated land and waste management," *Mineralogical Society Series*, vol. 9, pp. 245–289, 2000.
- [31] H. Kurokawa and M. Senna, "Morphology control of goethite acicular particles during aging by nitrogen bubbling and subsequent reactive aeration," *Journal of Materials Science*, vol. 43, no. 14, pp. 4737–4741, 2008.
- [32] L. Maya, "Hydrolysis and carbonate complexation of dioxouranium(VI) in the neutral-pH range at 25°C," *Inorganic Chemistry*, vol. 21, no. 7, pp. 2895–2898, 1982.
- [33] D. Harris, *Quantitative Chemical Analysis*, W. H. Freeman, New York, NY, USA, 6th edition, 2003.
- [34] S. Das, M. J. Hendry, and J. Essilfie-Dughan, "Transformation of two-line ferrihydrite to goethite and hematite as a function of pH and temperature," *Environmental Science and Technology*, vol. 45, no. 1, pp. 268–275, 2011.
- [35] L. E. Davidson, S. Shaw, and L. G. Benning, "The kinetics and mechanisms of schwertmannite transformation to goethite and hematite under alkaline conditions," *American Mineralogist*, vol. 93, no. 8–9, pp. 1326–1337, 2008.
- [36] R. Cornell and U. Schwertmann, *The Iron Oxides: Structure, Properties, Reactions, Occurrences and Uses*, Wiley-VCH, 2003.
- [37] T. Missana, M. García-Gutiérrez, and V. Fernández, "Uranium (VI) sorption on colloidal magnetite under anoxic environment: experimental study and surface complexation modelling," *Geochimica et Cosmochimica Acta*, vol. 67, no. 14, pp. 2543–2550, 2003.
- [38] S. Mann, N. H. C. Sparks, S. B. Couling, M. C. Lacombe, and R. B. Frankel, "Crystallochemical characterization of magnetic spinels prepared from aqueous solution," *Journal of the Chemical Society, Faraday Transactions 1: Physical Chemistry in Condensed Phases*, vol. 85, no. 9, pp. 3033–3044, 1989.
- [39] E. Murad, "Mossbauer and X-ray data on β -FeOOH (aka-gańite)," *Clay Minerals*, vol. 14, pp. 273–283, 1979.

Research Article

Selective Synthesis of Manganese/Silicon Complexes in Supercritical Water

Jiancheng Wang,¹ Zhaoliang Peng,¹ Bing Wang,¹ Lina Han,^{1,2} Liping Chang,¹ Weiren Bao,¹ and Gang Feng³

¹ State Key Laboratory Breeding Base of Coal Science and Technology Co-founded by Shanxi Province and the Ministry of Science and Technology, Taiyuan University of Technology, Taiyuan 030024, China

² College of Materials Science and Engineering, Taiyuan University of Technology, Taiyuan 030024, China

³ Shanghai Research Institute of Petrochemical Technology, SINOPEC, Shanghai 201208, China

Correspondence should be addressed to Weiren Bao; baoweiren@tyut.edu.cn and Gang Feng; fengg.sshy@sinopec.com

Received 9 February 2014; Accepted 14 March 2014; Published 4 May 2014

Academic Editor: Wen Zeng

Copyright © 2014 Jiancheng Wang et al. This is an open access article distributed under the Creative Commons Attribution License, which permits unrestricted use, distribution, and reproduction in any medium, provided the original work is properly cited.

A series of manganese salts ($\text{Mn}(\text{NO}_3)_2$, MnCl_2 , MnSO_4 , and $\text{Mn}(\text{Ac})_2$) and silicon materials (silica sand, silica sol, and tetraethyl orthosilicate) were used to synthesize Mn/Si complexes in supercritical water using a tube reactor. X-ray diffraction (XRD), X-ray photoelectron spectrometer (XPS), transmission electron microscopy (TEM), and scanning electron microscopy (SEM) were employed to characterize the structure and morphology of the solid products. It was found that MnO_2 , Mn_2O_3 , and Mn_2SiO_4 could be obtained in supercritical water at 673 K in 5 minutes. The roles of both anions of manganese salts and silicon species in the formation of manganese silicon complexes were discussed. The inorganic manganese salt with the oxyacid radical could be easily decomposed to produce $\text{MnO}_2/\text{SiO}_2$ and $\text{Mn}_2\text{O}_3/\text{SiO}_2$. It is interesting to find that $\text{Mn}(\text{Ac})_2$ can react with various types of silicon to produce Mn_2SiO_4 . The hydroxyl groups of the SiO_2 surface from different silicon sources enhance the reactivity of SiO_2 .

1. Introduction

Recently, the growth of manganese silicate (Mn_2SiO_4) and manganese dioxide (MnO_2) barrier layers on the SiO_2 surface through the deposition of metal Mn and Mn/Cu alloys after high temperature annealing has attracted considerable investigations [1, 2]. These self-forming diffusion barrier layers can effectively prevent the diffusion of Cu, O, and H_2O and have been proposed as a scalable alternative to Ta/TaN barrier layers in the future [3, 4]. However, the synthesis method employed was limited to high temperature annealing and the unreacted metallic Mn still remained after the formation of barrier layer, which would diffuse to the surface of the deposited Cu interconnect. Moreover, the uncertainty of chemical composition of products undermined the potential application of this barrier layer [5, 6]. Furthermore, the low-valence manganese oxides, supported and unsupported, have attracted great attentions as catalytically active components in a variety of catalytic reactions, for example, the selective

catalytic reduction of NO with NH_3 [7, 8], the oxidation of alcohol [9, 10], and the removal of hydrogen sulfide [11]. Various active manganese oxides and dispersion of particles can be obtained using different precursors and preparation methods, which seriously influence the activity of the catalysts in catalytic reactions or other utilizations.

Supercritical water (SCW, above 647 K and 22.1 MPa) can provide an excellent reaction environment for hydrothermal synthesis. The physical and chemical properties of water, such as viscosity, diffusion coefficient, dielectric constant, and ionic product, vary dramatically around the critical point depending on the state variables (pressure, temperature, and density) [12–14]. These properties make fast reaction rate and crystal nucleation rate which leads to high degree of crystallinity, small grain size, and narrow size distribution of the produce materials [15]. The size and morphology of the produced particles can be controlled by the pressure and temperature during preparation [16]. In addition, there is no liquid-gas interface and surface tension in

the supercritical state, and a homogenous reducing or oxidizing atmosphere can be obtained by introducing oxygen, hydrogen, or other gases [17, 18]. The supercritical hydrothermal synthesis method can also synthesize many materials that conventional hydrothermal synthesis method or solid-phase synthesis cannot synthesize. Thus, these specific properties of supercritical water have contributed to its widespread applications in materials synthesis [19–22], catalysis [23–25], and semiconductor [26, 27].

Our recent work found that the precursor of Mn plays a crucial role during the supercritical water impregnation, and Mn_3O_4 and Mn_2SiO_4 can be obtained from $\text{Mn}(\text{NO}_3)_2$ and $\text{Mn}(\text{Ac})_2 \cdot 4\text{H}_2\text{O}$ reacting with Si species containing in coal-derived active carbon, respectively [28].

In this work, we proposed a supercritical water synthesis method for the production of Mn_2SiO_4 and SiO_2 supported manganese oxide. A series of manganese salts ($\text{Mn}(\text{NO}_3)_2$, MnCl_2 , MnSO_4 , and $\text{Mn}(\text{Ac})_2$) and silicon materials (silica sand, silica sol, and tetraethyl orthosilicate) were used as raw materials. Three kinds of products (MnO_2 , Mn_2O_3 , and Mn_2SiO_4) can be selectively produced by choosing different raw materials. The roles of both anions of manganese salts and silicon sources in the formation of the products under supercritical water conditions were discussed primarily.

2. Experimental

2.1. Materials. Manganese nitrate (50% $\text{Mn}(\text{NO}_3)_2$ in water), manganese chloride (MnCl_2), manganese sulfate monohydrate ($\text{MnSO}_4 \cdot \text{H}_2\text{O}$), manganese acetate tetrahydrate ($\text{MnC}_4\text{H}_6\text{O}_4 \cdot 4\text{H}_2\text{O}$), and tetraethyl orthosilicate ($\text{C}_8\text{H}_{20}\text{O}_4\text{Si}$) were obtained from Aladdin Chemistry Co. (Shanghai, China). JN-30 silica sol, N-butanol ($\text{C}_4\text{H}_{10}\text{O}$), hydrofluoric acid, and silica sand were obtained from Fengchuan Chemistry Co. (Tianjin, China). Distilled and deionized (DDI) water was produced in our lab. The purities of all chemicals except manganese nitrate are above 98%.

2.2. Apparatus. The sample synthesis was conducted using a 16.7 mL stainless steel tube reactor. Figure 1 shows the schematic diagram of the tube reactor system. It was heated by a molten salt bath, and the temperature of salt bath was measured by a K-type thermocouple. The molten salt bath is made of 45 wt% KNO_3 and 55 wt% NaNO_3 . It helps to keep the temperature of the reaction system constant and translate heat fast and uniformly. The reactor can be driven to swing up and down by a motor at a speed of $120 \text{ cycles} \cdot \text{min}^{-1}$ over a range from 613 K to 773 K with $\pm 1 \text{ K}$ error in our synthesis experiments. The pressure was calculated according to the temperature and the content of water in the reactor.

2.3. Synthesis

2.3.1. Reaction of Manganese Salt and Silica Sand. Four metal manganese salts ($\text{Mn}(\text{NO}_3)_2$, MnCl_2 , MnSO_4 , and $\text{Mn}(\text{Ac})_2$) were dissolved in water and the salt solutions were prepared with a concentration of 1 M. Each solution was then fed into the reactor followed by an addition of silica sand. The mole

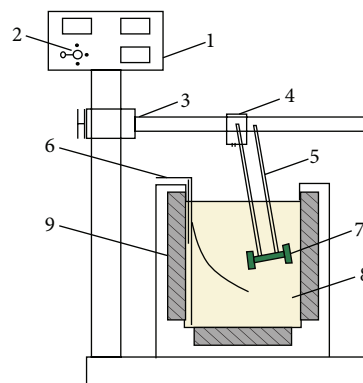


FIGURE 1: Schematic diagram of experimental apparatus. (1) temperature-controlling instrument, (2) speed controller, (3) cantilever, (4) motor, (5) crank, (6) thermocouples, (7) tube reactor, (8) KNO_3 - NaNO_3 salt, and (9) heater.

ratio of Mn : Si was kept to 1 : 1. The reactor was immersed into the salt bath when the desired reaction temperature was reached. After the reaction, the reactor was rapidly quenched and cooled to room temperature in a water bath. Every reaction was conducted at the temperature of 673 K with a resident time of 5 minutes. The content of water was 6.0 mL and the corresponding pressure was about as 30 MPa. The products were filtered, washed with distilled water, and dried at 343 K for 12 hours. The solid powders were obtained and characterized.

2.3.2. Reaction of Manganese Salt and Silica Sol. Each manganese salt solution with a concentration of 1 M was added dropwise into the silica gel under magnetic stirring for 10 minutes. The temperature, contents of water, resistant time, and other step were the same as those in Section 2.3.1.

2.3.3. Reaction of Manganese Salt and Tetraethyl Orthosilicate. 10.42 g tetraethyl orthosilicate was mixed with 11.12 g n-butanol under magnetic stirring, in which n-butanol was used to facilitate the followed hydrolysis and condensation reaction. Then as catalyst, a mixture of 9 g water and 0.25 g HF was added dropwise into the mixture. After 25 minutes, the aqueous manganese salt solution with a concentration of 1 M was added and then the mixture was fed into the reactor under the same conditions as those in Section 2.3.1.

2.4. Characterization. The structure of each sample was measured by X-ray diffraction (XRD) using a D/Max-2500 V/PC Rigaku X-ray diffractometer (Japan) with a Cu K α radiation source ($\lambda = 0.1543 \text{ nm}$) at room temperature in the range of $2\theta = 5\text{--}80^\circ$. The system was operated at 100 mA and 40 kV.

The morphology of each sample was studied using a JEOL JSM-7001F scanning electron microscope (SEM).

X-ray photoelectron spectroscopy (XPS) was conducted to determine the surface concentration and binding energy of Mn $2p_{3/2}$, using a Kratos AXIS Ultra DLD spectrometer (Shimadzu, Japan) equipped with a monochromated Al

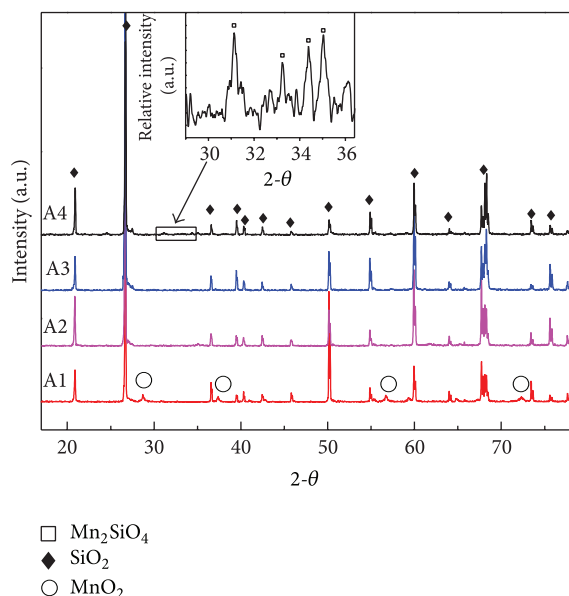


FIGURE 2: XRD patterns of samples prepared by manganese salt and silica sand (A1, A2, A3, and A4 represent the solid products from reaction of $\text{Mn}(\text{NO}_3)_2$, MnCl_2 , MnSO_4 , and $\text{Mn}(\text{Ac})_2$ with silica sand, resp.).

$K\alpha$ source ($h\nu = 1486.6$ eV, 75 W). The spectrometer was calibrated using the photoemission lines of Au ($\text{Au } 4f_{7/2} = 83.95$ eV), Ag ($\text{Ag } 3d_{5/2} = 368.2$ eV), and Cu ($\text{Cu } 2p_{3/2} = 932.62$ eV). No smoothing routine of data was applied to analyze the results.

The crystalline phases of samples were measured by transmission electron microscopy (TEM) at room temperature with a JEM-2010 microscope operating at 200 kV.

3. Results and Discussion

3.1. XRD Characterization. XRD patterns of the samples synthesized by different manganese salts and silica sand in supercritical water are shown in Figure 2. The diffraction peaks of SiO_2 crystal and MnO_2 crystal can be identified in the XRD patterns of the sample (A1) prepared by $\text{Mn}(\text{NO}_3)_2$ and silica sand. Moreover, the intensity of SiO_2 diffraction peak is much higher than that of MnO_2 . This means that the crystal form or the degree of crystallinity of SiO_2 is far better than that of MnO_2 in A1. However, all the diffraction peaks of samples (A2 and A3) synthesized by the two kinds of manganese salts (MnCl_2 and MnSO_4) reacted with silica sand clearly show the appearance of SiO_2 only. The characteristic peaks of samples (A4) obtained by the reaction of $\text{Mn}(\text{Ac})_2$ and silica sand indicate Mn_2SiO_4 and SiO_2 crystal although the peak intensity of Mn_2SiO_4 (the inset in Figure 2) is very low. Based on above results, it can be concluded that $\text{Mn}(\text{NO}_3)_2$ and $\text{Mn}(\text{Ac})_2$ can react with silica sand in supercritical water at 673 K for 5 minutes and the main products are MnO_2 and Mn_2SiO_4 , respectively.

XRD patterns of the samples prepared by different manganese salts and silica sol in supercritical water are given

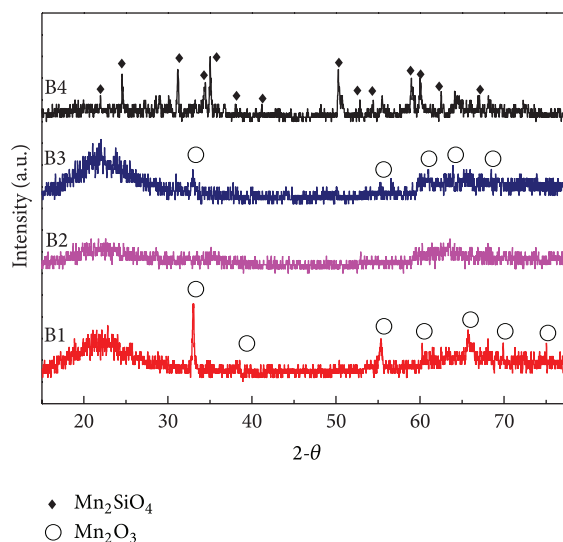


FIGURE 3: XRD patterns of samples prepared by manganese salt and silica sol. (B1, B2, B3, and B4 represent the solid products from reaction of $\text{Mn}(\text{NO}_3)_2$, MnCl_2 , MnSO_4 , and $\text{Mn}(\text{Ac})_2$ with silica sol, resp.).

in Figure 3. The diffraction peaks of Mn_2O_3 crystal can be found in the XRD patterns of the samples B1 and B3. This means that both $\text{Mn}(\text{NO}_3)_2$ and MnSO_4 can react with silica sol to produce Mn_2O_3 at 673 K for 5 minutes. The broad peak at about 22° can be attributed to the amorphous SiO_2 hydrolyzed by the silica sol. There is no diffraction peak except the characteristic peak of the amorphous SiO_2 in the XRD pattern of the sample B2. It indicates that MnCl_2 cannot react with silica sol and only amorphous SiO_2 can be obtained from this reaction. It is noted that the good crystalline for Mn_2SiO_4 in sample B4 was obtained from the reaction between $\text{Mn}(\text{Ac})_2$ and silica sol. Note that the SiO_2 characteristic peaks in B4 cannot be resolved. The reason may be that they are marked by the peaks of the crystalline Mn_2SiO_4 . It can be concluded that $\text{Mn}(\text{NO}_3)_2$, MnSO_4 , and $\text{Mn}(\text{Ac})_2$ can react with silica sol in supercritical water at 673 K for 5 minutes and the main products are Mn_2O_3 and Mn_2SiO_4 .

Figure 4 shows the XRD patterns of samples prepared by different manganese salts and tetraethyl orthosilicate in supercritical water. It is found that the crystalline Mn_2SiO_4 was produced by the reaction of $\text{Mn}(\text{Ac})_2$ and tetraethyl orthosilicate (C1). Both $\text{Mn}(\text{NO}_3)_2$ and MnSO_4 can react with tetraethyl orthosilicate to generate Mn_2O_3 in supercritical water. It should be noted that no characteristic peaks of SiO_2 , crystalline or amorphous, can be observed in the XRD pattern of C1. It also can be found that MnCl_2 could not react with tetraethyl orthosilicate in the cases of silicon sand and silica sol. Tetraethyl orthosilicate can also produce the amorphous SiO_2 in supercritical water.

Based on the XRD analyses, it can be concluded that $\text{Mn}(\text{Ac})_2$ is the best manganese precursor among the four manganese salts to synthesize Mn_2SiO_4 in supercritical water. Both $\text{Mn}(\text{NO}_3)_2$ and MnSO_4 can produce Mn_2O_3 or MnO_2

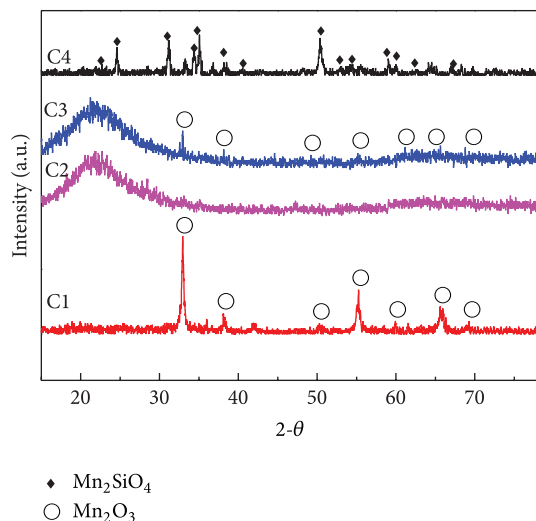


FIGURE 4: XRD patterns of samples prepared by manganese salt and tetraethyl orthosilicate. (C1, C2, C3, and C4 represent the solid products from reaction of $\text{Mn}(\text{NO}_3)_2$, MnCl_2 , MnSO_4 , and $\text{Mn}(\text{Ac})_2$ with tetraethyl orthosilicate, resp.).

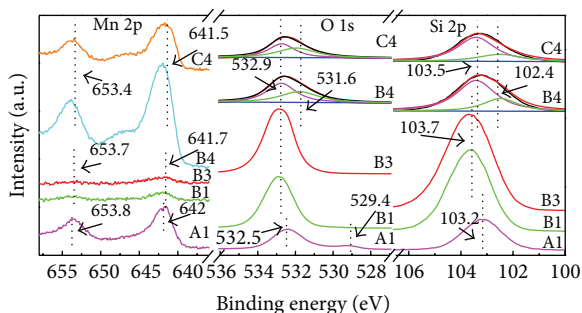


FIGURE 5: Mn 2p, O 1s, and Si 2p XPS spectra of samples prepared by reaction between different aqueous manganese salt (A1: $\text{Mn}(\text{NO}_3)_2$ with silica sand, B1: $\text{Mn}(\text{NO}_3)_2$ with silica sol, B3: MnSO_4 with silica sol, B4: $\text{Mn}(\text{Ac})_2$ with silica sol, and C4: $\text{Mn}(\text{Ac})_2$ with tetraethyl orthosilicate, resp.).

while MnCl_2 could not react with any of the three kinds of silicon materials.

On the aspect of silicon source, tetraethyl orthosilicate and silica sol have similar activity and both can react with $\text{Mn}(\text{Ac})_2$ to produce Mn_2SiO_4 . Silica sand has the least reactive among the three kinds of silicon sources and only $\text{Mn}(\text{Ac})_2$ can react with it to generate small amount of Mn_2SiO_4 in supercritical water. That is due to the high stability of the SiO_2 crystal which is the main component of silica sand. The diffraction peaks from SiO_2 of B4 and C4 in Figures 3 and 4 may be covered by that of Mn_2SiO_4 .

3.2. XPS Characterization. The chemical states of the surface species of the representative products were investigated using XPS and the results are presented in Figure 5. And the surface atomic concentrations of samples characterized by XPS results are shown in Table 1. The amounts of Mn on the surface of sample A1 are 6.11%, while those of samples B1 and

TABLE 1: Surface atomic concentration (%) of samples characterized by XPS.

Sample	Mn 2p	O 1s	Si 2p	N 1s	C 1s
A1	6.11	69.62	23.21	1.06	—
B1	0.70	69.66	29.35	0.35	—
B3	0.39	65.82	27.46	0.26	6.07
B4	7.38	51.30	15.57	—	25.75
C4	2.99	36.46	4.99	—	55.56

Note: A1, B1, B3, B4, and C4 are the samples from reaction of $\text{Mn}(\text{NO}_3)_2$ with silica sand, $\text{Mn}(\text{NO}_3)_2$ with silica sol, MnSO_4 with silica sol, $\text{Mn}(\text{Ac})_2$ with silica sol, and $\text{Mn}(\text{Ac})_2$ with tetraethyl orthosilicate, respectively.

B3 are only 0.70% and 0.39%, respectively. As for the Mn 2p spectra, different products exhibit different binding energies (BE) of Mn $2p_{3/2}$ and Mn $2p_{1/2}$ levels. The binding energies of the Mn $2p_{3/2}$ and Mn $2p_{1/2}$ in the sample A1 are 642.0 eV and 653.8 eV, which is attributed to MnO_2 [28–30]. Similarly, the BE of the Mn $2p_{3/2}$ and Mn $2p_{1/2}$ in the samples B1 and B3 are 641.7 eV and 653.7 eV which can be assigned to Mn_2O_3 [28, 29]. This also agrees well with the XRD results. Compared with the Mn 2p spectra of A1, the peak intensities belonging to B1 and B3 are very weak; this is because the surface atomic concentration of samples B1 and B3 is very low. In addition, the BE of the Mn $2p_{3/2}$ and Mn $2p_{1/2}$ in the sample B4 and C4 are in the range of 641.7–642.2 eV and 653.4–653.7 eV, respectively. These may be attributed to $\text{Mn}_2\text{SiO}_4/\text{MnSiO}_3$, MnO , and/or their mixtures [31]. The peak intensity of B4 is the highest among the five lines, which is in agreement with the surface atomic concentration. The surface atomic concentration of Mn in sample B4 is the highest (7.38%, Table 1).

As for the O 1s region, the BE of O 1s in the sample A1 are 532.5 eV and 529.4 eV, which are attributed to SiO_2 and MnO_2 , respectively [30, 32]. The BE of O 1s in samples B1 and B3 are 532.9 eV, which can be assigned to SiO_2 [32]. However, the O 1s peak assigned to Mn_2O_3 in samples B1 and B3 is not resolved; it is possibly because the XPS signal of Mn_2O_3 in samples B1 and B3 is too weak comparing to SiO_2 . The BE of O 1s in samples B4 and C4 appearing at the positions of 533.9 eV and 531.6 eV can be attributed to SiO_2 and $\text{Mn}_2\text{SiO}_4/\text{MnSiO}_3$, MnO , and/or their mixtures [31], respectively.

As for the Si 2p spectra, the Si 2p peak in sample A1 at 103.2 eV is attributed to SiO_2 [32] but is attributed to SiO_2 in samples B1 and B3 appearing at the position of 103.7 eV, which shifted slightly higher. The Si 2p peaks in the samples B4 and C4 at 103.5 eV and 102.4 eV are attributed to SiO_2 and Mn_2SiO_4 [31], respectively. Combined with the XRD results, Mn2p XPS spectra, and O1s XPS spectra, the products synthesized by $\text{Mn}(\text{Ac})_2$ and silica sol or tetraethyl orthosilicate contain Mn_2SiO_4 and SiO_2 .

3.3. TEM Characterization. Figure 6 shows the representative TEM images of all samples. It was revealed that fine particles with high level of dispersion were formed on the bulk products in A1 and the morphology of bulk products was single sphere. Based on the XRD analyses, the fine particles were MnO_2 , and the bulk products were SiO_2 . TEM

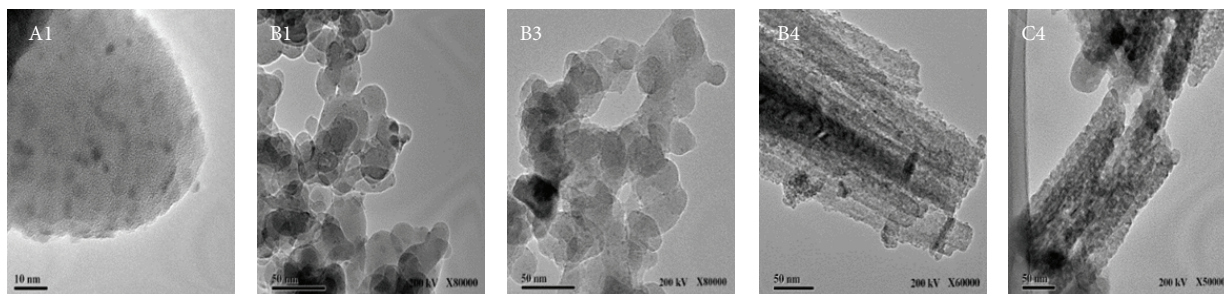


FIGURE 6: High resolution TEM images of samples prepared by reaction between different aqueous manganese salt (A1: $\text{Mn}(\text{NO}_3)_2$ with silica sand, B1: $\text{Mn}(\text{NO}_3)_2$ with silica sol, B3: MnSO_4 with silica sol, B4: $\text{Mn}(\text{Ac})_2$ with silica sol, and C4: $\text{Mn}(\text{Ac})_2$ with tetraethyl orthosilicate).

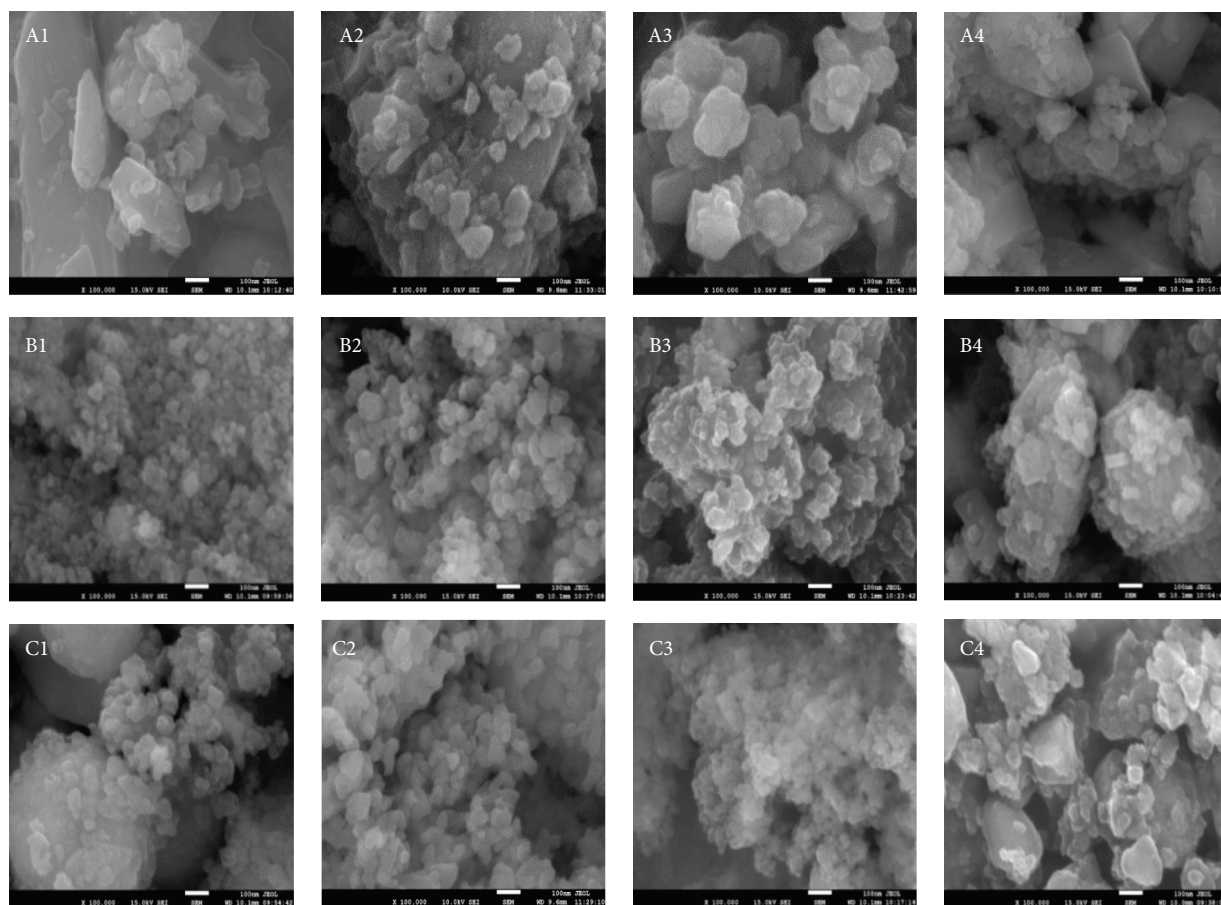


FIGURE 7: SEM images of samples prepared by reaction between various sources of silica (A: silica sand, B: silica sol, C: tetraethyl orthosilicate) and different aqueous manganese salt (1: $\text{Mn}(\text{NO}_3)_2$, 2: MnCl_2 , 3: MnSO_4 , and 4: $\text{Mn}(\text{Ac})_2$).

images of B1 and B3 samples were similar: highly dispersed fine particles were formed on top of the bulk products, and the bulk products were uniform spheres with a diameter of approximate 20 nm. These spheres were bonded together and formed some irregular rings with a diameter of about 40 nm. Based on the XRD analyses, the fine particles should be Mn_2O_3 , and the bulk products should be SiO_2 . TEM images of samples B4 and C4 were similar: stick-like products were obtained with a length of about 200 nm. The chemical

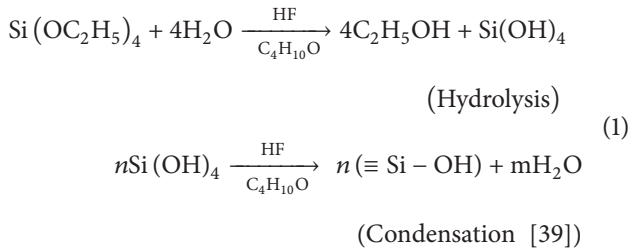
composition of products may be Mn_2SiO_4 or a mixture of Mn_2SiO_4 and SiO_2 .

3.4. SEM Characterization. SEM micrographs of the solid products were shown in Figure 7. The products obtained by different manganese salts reacting with silica sand are some fine particles and irregular flaky polyhedron. While the products generated by reactions between different salts ($\text{Mn}(\text{NO}_3)_2$, MnSO_4 , and MnCl_2) and silica sol or tetraethyl

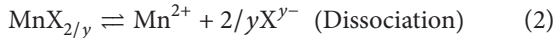
orthosilicate are regular spheres and fine particles, the products formed by $\text{Mn}(\text{Ac})_2$ and silica sol or tetraethyl orthosilicate are slightly different, agglomerated to be unregular ellipsoid and flaky polyhedron.

3.5. Reaction Mechanism. The main products synthesized from four kinds of manganese salts and three kinds of silicon sources under supercritical water conditions are one or several of the followings: SiO_2 , MnO_2 , Mn_2O_3 , and Mn_2SiO_4 . And the reaction mechanism will be discussed in this section.

The SiO_2 gel micronucleus can be formed by the hydrolysis and condensation reaction of tetraethyl orthosilicate. This is a fast and environmentally friendly process, and the reaction equation can be expressed as follows:



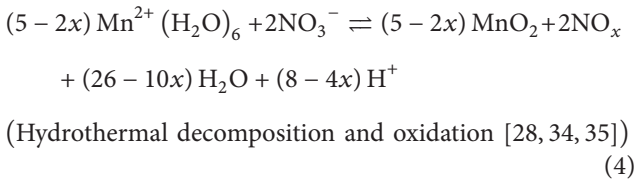
All the manganese salts can hydrolyze first in the water:



(X is NO_3^- , SO_4^{2-} , Cl^- , and Ac^- , and $y = 1, 2$)



The reaction equilibrium biases in favor of the left under atmospheric conditions. However, under the supercritical condition, the reaction equilibrium biases in favor of the right [33, 34] and the radical ion under acidic conditions such as NO_3^- will be decomposed. Chlistunoff et al. [35, 36] investigated the decomposition of aqueous HNO_3 solution in supercritical water and reported that NO_2 or HNO_2 and O_2 can be formed at 673 K. If a reducing agent was added, NO and N_2O can be generated. The reaction equation of hydrothermal decomposition and oxidation can [27, 33, 34] be expressed as follows:

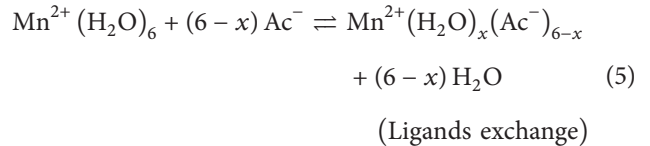


The $\text{Mn}(\text{NO}_3)_2$ can be transformed to MnO_2 or Mn_2O_3 in supercritical water, but only Mn_2O_3 can be produced from MnSO_4 in supercritical water. This may be attributed to the oxidative capacity of the acid ion in the supercritical water and the effect of hydroxyl ligands generated by the silicon sources. The supercritical water is an oxidative reaction environment due to the dissolved O_2 and the NO_3^- has strong oxidative capacity in the supercritical water [37]. Therefore, the Mn^{2+} species in the $\text{Mn}(\text{NO}_3)_2$ supercritical

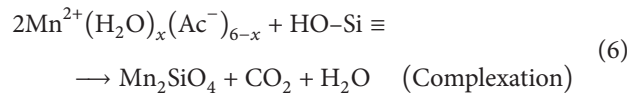
water solution can be oxidized into MnO_2 , and the SiO_2 crystal (silica sand) existing in the supercritical water almost does not affect the reaction. The SO_4^{2-} with weaker oxidative capacity is hard to be decomposed compared with NO_3^- under acidic conditions, so the oxidized Mn species cannot be produced.

The silica sands are crystal particles and the silica sol or tetraethyl orthosilicate has irregular and porous structure. There is almost no hydroxyl groups on the surface of silica sand, but plenty on the surface of the silica hydrolyzed from silica sol or tetraethyl orthosilicate [38]. Hair [39–41] has investigated the hydroxyl groups on silica surface using infrared (IR) gravimetric adsorption at various temperatures. Their results indicated that the maximum water sorption will occur at 673 K where both rehydration of the surface and sorption can occur simultaneously. The hydroxyl groups on the surface of SiO_2 can act as ligands. It is easy to combine with Mn^{2+} to form complex which enhances its reactivity. The reaction of MnSO_4 with silica sol or tetraethyl orthosilicate can produce Mn_2O_3 , but the $\text{Mn}(\text{NO}_3)_2$ with silica sol or tetraethyl orthosilicate will form Mn_2O_3 while reacting with silica sand and will form MnO_2 . This may be because the surface hydroxyl ligands suppress the oxidation of Mn^{2+} . Cl^- has not oxidative capacity and cannot be decomposed, so there was hardly manganese oxides produced in the supercritical water by reaction of MnCl_2 with any silicon sources.

The products prepared by $\text{Mn}(\text{Ac})_2$ are obviously different from the other three Mn salts. The reason may be that the Ac^- is a good candidate which is easy to be combined with Mn^{2+} via a ligand exchange reaction to form $\text{Mn}^{2+}(\text{H}_2\text{O})_x(\text{Ac}^-)_{6-x}$ instead of the hydrolysis of $\text{Mn}^{2+}(\text{H}_2\text{O})_6$ to form Mn oxides according to



The H_2O and Ac^- ligands are further exchanged with surface hydroxyl ligands of SiO_2 forming Mn_2SiO_4 and the reaction can be expressed as follows [27, 42]:



By these ligands exchanging reactions, the Mn_2SiO_4 loaded on the surface of SiO_2 was generated. Due to the different morphology and chemical composition of SiO_2 , the amount of resulting Mn_2SiO_4 varied: the silica sol and tetraethyl orthosilicate produced more Mn_2SiO_4 for more surface hydroxyl ligands and amorphous surface which is easy to interact with the reactants, while the silica sand has fewer hydroxyl ligands and regular crystal structure which leads to poor reactivity.

4. Conclusions

Reactions of various manganese salts ($\text{Mn}(\text{NO}_3)_2$, MnCl_2 , MnSO_4 , and $\text{Mn}(\text{Ac})_2$) and various silicon sources (silica sand, silica sol, and tetraethyl orthosilicate) have been investigated in supercritical water using a tube reactor. It is found that the anion of manganese salt has a significant effect on the composition of products. The inorganic manganese salt with the oxyacid radical, which is easy to be decomposed, can produce $\text{MnO}_2/\text{SiO}_2$ and $\text{Mn}_2\text{O}_3/\text{SiO}_2$. The organic manganese salt with ligands like $\text{Mn}(\text{Ac})_2$ can react with various types of silicon to generate Mn_2SiO_4 . The hydroxyl groups on the surface of SiO_2 from different silicon sources enhance the reactivity of SiO_2 . Depending on the applications, the selective materials can be fast synthesized in supercritical water by choosing different Mn salt precursor and different types of silicon sources.

Conflict of Interests

The authors declare that there is no conflict of interests regarding the publication of this paper.

Acknowledgments

The financial support from the National Natural Science Foundation of China (20976117) and China Postdoctoral Science Foundation (CPSF, 20110491630) is gratefully acknowledged.

References

- [1] P. Casey, J. Bogan, J. G. Lozano, P. D. Nellist, and G. Hughes, "Chemical and structural investigation of the role of both Mn and Mn oxide in the formation of manganese silicate barrier layers on SiO_2 ," *Journal of Applied Physics*, vol. 110, no. 5, Article ID 054507, 2011.
- [2] V. K. Dixit, K. Neishi, N. Akao, and J. Koike, "Structural and electronic properties of a Mn oxide diffusion barrier layer formed by chemical vapor deposition," *IEEE Transactions on Device and Materials Reliability*, vol. 11, no. 2, pp. 295–302, 2011.
- [3] Y. Otsuka, J. Koike, H. Sako et al., "Graded composition and valence states in self-forming barrier layers at Cu-Mn/ SiO_2 interface," *Applied Physics Letters*, vol. 96, no. 1, Article ID 012101, 2010.
- [4] P. Casey, J. Bogan, B. Brennan, and G. Hughes, "Synchrotron radiation photoemission study of in situ manganese silicate formation on SiO_2 for barrier layer applications," *Applied Physics Letters*, vol. 98, no. 11, Article ID 113508, 2011.
- [5] J. Iijima, Y. Fujii, K. Neishi, and J. Koike, "Resistivity reduction by external oxidation of Cu-Mn alloy films for semiconductor interconnect application," *Journal of Vacuum Science and Technology B: Microelectronics and Nanometer Structures*, vol. 27, no. 4, pp. 1963–1968, 2009.
- [6] J. M. Ablett, J. C. Woicik, Z. Tökei, S. List, and E. Dimasi, "Phase identification of self-forming Cu-Mn based diffusion barriers on p-SiOC:H and SiO_2 dielectrics using x-ray absorption fine structure," *Applied Physics Letters*, vol. 94, no. 4, Article ID 042112, 2009.
- [7] S. M. Soltani, S. Hosseini, and M. R. Malekbala, "A review on monolithic honeycomb structures and fabrication techniques," *Applied Scientific Research*, vol. 9, no. 4, pp. 1–12, 2013.
- [8] E. García-Bordejé, M. J. Lázaro, R. Moliner, J. F. Galindo, J. Sotres, and A. M. Baró, "Structure of vanadium oxide supported on mesoporous carbon-coated monoliths and relationship with its catalytic performance in the SCR of NO at low temperatures," *Journal of Catalysis*, vol. 223, no. 2, pp. 395–403, 2004.
- [9] V. R. Choudhary, P. A. Chaudhari, and V. S. Narkhede, "Solvent-free liquid phase oxidation of benzyl alcohol to benzaldehyde by molecular oxygen using non-noble transition metal containing hydrotalcite-like solid catalysts," *Catalysis Communications*, vol. 4, no. 4, pp. 171–175, 2003.
- [10] Y. Su, L. C. Wang, Y. M. Liu, Y. Cao, H. Y. He, and K. N. Fan, "Microwave-accelerated solvent-free aerobic oxidation of benzyl alcohol over efficient and reusable manganese oxides," *Catalysis Communications*, vol. 8, no. 12, pp. 2181–2185, 2007.
- [11] J. P. Wakker, A. W. Gerritsen, and J. A. Moulijn, "High temperature H_2S and COS removal with MnO and FeO on $\gamma\text{-Al}_2\text{O}_3$ acceptors," *Industrial and Engineering Chemistry Research*, vol. 32, no. 1, pp. 139–149, 1993.
- [12] J. Fages, C. Aymonier, F. Cansell, and J. Mercadier, "New trends in supercritical fluids: energy; materials; processing. A special issue—9th international symposium on supercritical fluids, May 18–20, 2009, Arcachon, France," *Journal of Supercritical Fluids*, vol. 53, no. 1–3, p. 1, 2010.
- [13] C. Slostowski, S. Marre, O. Babot, T. Toupance, and C. Aymonier, "Near- and supercritical alcohols as solvents and surface modifiers for the continuous synthesis of cerium oxide nanoparticles," *Langmuir*, vol. 28, no. 48, pp. 16656–16663, 2012.
- [14] T. Glasnov, "Highlights from the flow chemistry literature 2011 (part 3)," *Journal of Flow Chemistry*, vol. 2, no. 1, pp. 28–36, 2012.
- [15] A. Loppinet-Serani, C. Aymonier, and F. Cansell, "Supercritical water for environmental technologies," *Journal of Chemical Technology and Biotechnology*, vol. 85, no. 5, pp. 583–589, 2010.
- [16] H. Hayashi and Y. Hakuta, "Hydrothermal synthesis of metal oxide nanoparticles in supercritical water," *Materials*, vol. 3, no. 7, pp. 3794–3817, 2010.
- [17] F. Cansell, C. Aymonier, and A. Loppinet-Serani, "Review on materials science and supercritical fluids," *Current Opinion in Solid State and Materials Science*, vol. 7, no. 4-5, pp. 331–340, 2003.
- [18] A. G. Kalinichev, Y. E. Gorbaty, and A. V. Okhulkov, "Structure and hydrogen bonding of liquid water at high hydrostatic pressures: Monte Carlo NPT-ensemble simulations up to 10 kbar," *Journal of Molecular Liquids*, vol. 82, no. 1-2, pp. 57–72, 1999.
- [19] J. W. Lee, J. H. Lee, T. T. Viet, J. Y. Lee, J. S. Kim, and C. H. Lee, "Synthesis of $\text{LiNi}_{1/3}\text{Co}_{1/3}\text{Mn}_{1/3}\text{O}_2$ cathode materials by using a supercritical water method in a batch reactor," *Electrochimica Acta*, vol. 55, no. 8, pp. 3015–3021, 2010.
- [20] Y. H. Shin, S. M. Koo, D. S. Kim et al., "Continuous hydrothermal synthesis of HT- LiCoO_2 in supercritical water," *Journal of Supercritical Fluids*, vol. 50, no. 3, pp. 250–256, 2009.
- [21] K. Kanamura, A. Goto, R. Y. Ho et al., "Preparation and electrochemical characterization of LiCoO_2 particles prepared by supercritical water synthesis," *Electrochemical and Solid-State Letters*, vol. 3, no. 6, pp. 256–258, 2000.
- [22] S. A. Hong, S. J. Kim, J. Kim, K. Y. Chung, B. W. Cho, and J. W. Kang, "Small capacity decay of lithium iron phosphate (LiFePO_4) synthesized continuously in supercritical water:

- comparison with solid-state method," *Journal of Supercritical Fluids*, vol. 55, no. 3, pp. 1027–1037, 2011.
- [23] C. Xu and A. S. Teja, "Supercritical water synthesis and deposition of iron oxide (α -Fe₂O₃) nanoparticles in activated carbon," *Journal of Supercritical Fluids*, vol. 39, no. 1, pp. 135–141, 2006.
- [24] J. R. Kim, W. Myeong, and S. K. Ihm, "Characteristics of CeO₂-ZrO₂ mixed oxide prepared by continuous hydrothermal synthesis in supercritical water as support of Rh catalyst for catalytic reduction of NO by CO," *Journal of Catalysis*, vol. 263, no. 1, pp. 123–133, 2009.
- [25] H. Hayashi, Y. Hakuta, and Y. Kurata, "Hydrothermal synthesis of potassium niobate photocatalysts under subcritical and supercritical water conditions," *Journal of Materials Chemistry*, vol. 14, no. 13, pp. 2046–2051, 2004.
- [26] J. D. Holmes, D. M. Lyons, and K. J. Ziegler, "Supercritical fluid synthesis of metal and semiconductor nanomaterials," *Chemistry*, vol. 9, no. 10, pp. 2144–2150, 2003.
- [27] K. J. Ziegler, R. C. Doty, K. P. Johnston, and B. A. Korgel, "Synthesis of organic monolayer-stabilized copper nanocrystals in supercritical water," *Journal of the American Chemical Society*, vol. 123, no. 32, pp. 7797–7803, 2001.
- [28] J. C. Wang, B. Qiu, L. N. Han et al., "Effect of precursor and preparation method on manganese based activated carbon sorbents for removing H₂S from hot coal gas," *Journal of Hazardous Materials*, vol. 213–214, pp. 184–192, 2012.
- [29] M. Toupin, T. Brousse, and D. Bélanger, "Charge storage mechanism of MnO₂ electrode used in aqueous electrochemical capacitor," *Chemistry of Materials*, vol. 16, no. 16, pp. 3184–3190, 2004.
- [30] X. Vanden Eynde, J. P. Servais, and M. Lamberigts, "Investigation into the surface selective oxidation of dual-phase steels by XPS, SAM and SIMS," *Surface and Interface Analysis*, vol. 35, no. 12, pp. 1004–1014, 2003.
- [31] S. Swaminathan and M. Spiegel, "Thermodynamic and kinetic aspects on the selective surface oxidation of binary, ternary and quaternary model alloys," *Applied Surface Science*, vol. 253, no. 10, pp. 4607–4619, 2007.
- [32] V. P. Zakaznova-Herzog, H. W. Nesbitt, G. M. Bancroft, and J. S. Tse, "Characterization of leached layers on olivine and pyroxenes using high-resolution XPS and density functional calculations," *Geochimica et Cosmochimica Acta*, vol. 72, no. 1, pp. 69–86, 2008.
- [33] T. Adschiri, Y. Hakuta, and K. Arai, "Hydrothermal synthesis of metal oxide fine particles at supercritical conditions," *Industrial and Engineering Chemistry Research*, vol. 39, no. 12, pp. 4901–4907, 2000.
- [34] T. Adschiri, K. Kanazawa, and K. Arai, "Rapid and continuous hydrothermal crystallization of metal oxide particles in supercritical water," *Journal of American Ceramic Society*, vol. 75, no. 4, pp. 1019–1022, 1992.
- [35] J. Chlistunoff, K. J. Ziegler, L. Lasdon, and K. P. Johnston, "Nitric/nitrous acid equilibria in supercritical water," *Journal of Physical Chemistry A*, vol. 103, no. 11, pp. 1678–1688, 1999.
- [36] C. Ratcliffe and D. Irish, "Vibrational spectral studies of solutions at elevated temperatures and pressures. VII. Raman spectra and dissociation of nitric acid," *Canadian Journal of Chemistry*, vol. 63, no. 12, pp. 3521–3525, 1985.
- [37] C. Aymonier, P. Beslin, C. Jolival, and F. Cansell, "Hydrothermal oxidation of a nitrogen-containing compound: the fenuron," *Journal of Supercritical Fluids*, vol. 17, no. 1, pp. 45–54, 2000.
- [38] L. L. Hench and J. K. West, "The Sol-Gel process," *Chemical Reviews*, vol. 90, no. 1, pp. 33–72, 1990.
- [39] M. L. Hair, "Hydroxyl groups on silica surface," *Journal of Non-Crystalline Solids*, vol. 19, pp. 299–309, 1975.
- [40] P. Van Der Voort, I. Gillis-D'Hamers, and E. F. Vansant, "Estimation of the distribution of surface hydroxyl groups on silica gel, using chemical modification with trichlorosilane," *Journal of the Chemical Society, Faraday Transactions*, vol. 86, no. 22, pp. 3751–3755, 1990.
- [41] G. M. S. El Shafei and M. M. Mokhtar, "Interaction between molybdena and silica: FT-IR/PA studies of surface hydroxyl groups and pore structure assessment," *Colloids and Surfaces A: Physicochemical and Engineering Aspects*, vol. 94, no. 2-3, pp. 267–277, 1995.
- [42] P. Kanninen, C. Johans, J. Merta, and K. Kontturi, "Influence of ligand structure on the stability and oxidation of copper nanoparticles," *Journal of Colloid and Interface Science*, vol. 318, no. 1, pp. 88–95, 2008.

Research Article

Physical, Mineralogical, and Micromorphological Properties of Expansive Soil Treated at Different Temperature

Jian Li,¹ Xiyong Wu,¹ and Long Hou²

¹ Department of Geosciences and Environmental Engineering, Southwest Jiaotong University, Chengdu, Sichuan 610031, China

² Wanzhou District Commission of Urban-Rural Development, Wanzhou, Chongqing 404000, China

Correspondence should be addressed to Jian Li; jlicivil@gmail.com

Received 11 February 2014; Accepted 6 April 2014; Published 28 April 2014

Academic Editor: Wen Zeng

Copyright © 2014 Jian Li et al. This is an open access article distributed under the Creative Commons Attribution License, which permits unrestricted use, distribution, and reproduction in any medium, provided the original work is properly cited.

Different characterizations were carried out on unheated expansive soil and samples heated at different temperature. The samples are taken from the western outskirts of Nanning of Guangxi Province, China. In the present paper, the mineral and chemical composition and several essential physical parameters of unheated expansive soil are indicated by XRD and EDX analysis. Moreover, the structural transition and change of mechanical properties of samples heated in the range of room temperature to 140°C are proved by TG-DTA and SEM observation. The mean particle diameter, density, hydraulic behaviors, and bond strength also have been investigated. The results indicate that, along with the loss of free water, physical absorbed water, and chemically bound water, the microstructure experiences some obvious change. In addition, the particle size and density both will increase rapidly before 100°C and undertake a slow growth or decline when higher than 100°C. The hydraulic behaviors and strength performance of unheated samples and the one heated at 100°C are given out as well. All these researches play fundamental role in the pollution prevention, modification, and engineering application of expansive soil.

1. Introduction

Expansive soils are soils that expand when water is added and shrink when it dries out. This continuous change in soil volume can cause homes and roads built on this soil to move unevenly and crack [1–3]. The special engineering properties of this soil are determined by the mineral phase and the chemical composition [4]. Therefore, researches on them are not only necessary for exploring the engineering properties of expansive soils and discussing the expansion mechanism but also indispensable as to the improvement and reinforcement of expansive soils and the discussion of new soil research techniques and methods [5, 6]. During the application of expansive soils in the construction and employment of embankment, the peculiarity is influenced by both the nature of the denudation and deliquescence of expansive soils [7–9].

The variation of temperature has a critical influence on the engineering properties of soils [10–12]. The relevant researches were as early as the 20th century AD, which were

mainly focused on the soil evaporation and the invasion of precipitation [2, 13]. On the other hand, more recent studies are primarily on how temperature affects the transformation and the further strength character of soil [14–16]. De Bruyn et al. have analyzed the results of triaxial test carried out at different temperature (50°C, 80°C, and 110°C) and different confining pressure (2.1, 3.1, and 4.1 MPa), given the conclusion that the shear strength will increase with the rise of temperature [17, 18]. However, researches on the influences of temperature on the change of physical and chemical properties including microstructure and hydraulic behaviors have been rarely reported before.

In this research, the expansive soil samples collected from the western outskirts of Hanzhong of Shanxi Province were characterized to analyse the chemical and mineral components. In addition, researches on the influence of temperature on the microstructure and physiochemical properties were also carried out. It is critically important to carry out this research project for the further pollution prevention, modification, and engineering application of expansive soil.

TABLE 1: The mineral components and content of expansive soil (unit: %).

Components	Montmorillonite	Illite	Kaolin	Quartz	Feldspar
Content	13	39	31	9	8

2. Materials and Experimental Procedure

2.1. Materials. Expansive soils samples were collected 1.3~1.5 m below earth surface from the western outskirts of Hanzhong of Shanxi Province, China. Approximately 3~5 Kg of soils samples was collected from six different sites. Samples were separated into several portions. Powder batches of about 500 g were kept or dried for 6 h at 20, 40, 60, 80, 90, 100, 120, and 140°C. Then the samples were removed from the furnace and cooled to room temperature in air. A powder batch of about 500 g was treated by air drying for the purpose of comparison experiment and TG-DT analysis.

2.2. Experimental Methods. X-ray diffraction (XRD) analysis was carried out on a Rigaku (Japan) D/MAX 2500C diffractometer using $\text{CuK}\alpha$ radiation, voltage 40 kV, and current 200 mA, equipped with a graphite monochromator in the diffracted beam. Crystalline phases were identified using the database of the International Center for Diffraction Data-JCPDS for inorganic substances. [JCPDS, International Centre for Diffraction Data, 1601 Park Line, Swarthmore, PA, 1987.]

Thermal analysis was performed on a Netzsch (Germany) STA 449 simultaneous analyzer. Thermogravimetric (TG) and differential thermal (DT) analysis were performed in the range of 20–140°C (stripping gas: dry N_2 , helium flow = 100 mL/min, and heating rate: 5°C/min). Measurements were carried out in 0.3 cm³ volume alumina crucibles using α -alumina as reference, analyzing \approx 100 mg of dry sample.

The volume frequency of particle diameter is characterized by a Winner2008A (Chinese) laser particle size analyzer, whose measuring range is 0.01–2000 μm . The density measurements were performed with a helium pycnometer (Micromeritics, Model 1305, USA). And the strength performance of expansive soil heated at different temperature is tested on a Trautwein DigiShearTM (Chinese) multifunctional direct shear test systems with the following testing condition: the shear rate is 0.03 mm/minute and the maximum shear displacement is 6.5 mm.

SEM observation EDX analysis was performed on TESCAN VEGA II scanning electron microscope for the characterization of the micromorphology of expansive soil treated at different temperature.

3. Components and Properties in Room Temperature

3.1. Chemical and Mineral Components. The mineral component of expansive soil consists of clay mineral and detrital mineral. The ingredients of the clay mineral are mainly quartz, mica, feldspar, and a few of the calcites and gypsums, which are the major part of coarse grain [7]. Generally, due

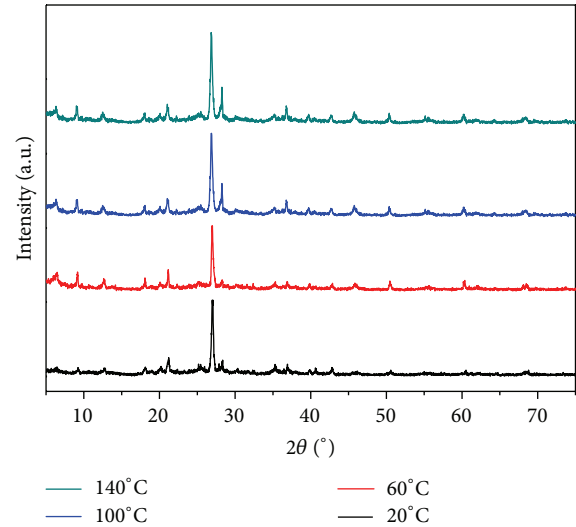


FIGURE 1: XRD patterns of untreated expansive soils (20°C) and samples heated at 60°C, 100°C, and 140°C.

to the low content in expansive soil, the coarse grain has low effect on the swell-shrink property. On the contrary, the engineering properties of expansive soil are principally determined by the clay mineral, the fine grain, and especially the mineral like smectites.

The X-ray diffraction patterns of expansive soil samples are shown in Figure 1, which reflects that the main clay minerals are illite, montmorillonite, kaolinite, quartz, potash feldspar, and plagioclase according to the JCPDS cards. Moreover, the diffraction peaks have not waved and the intensity also has not changed with the variation of temperature (20, 60, 100, and 140°C), which indicates that the main mineral component has not changed. The mineral composition and the component can be given through the quantitative calculation of the intensity of the diffraction peak and full width at half maximum, which are shown in Table 1. It indicates that expansive soils from Hanzhong are mainly composed of illite and kaolin, which separately take 39% and 31% part of the total air drying sample, while the percentages of quartz and feldspar are lower than 10%. It should be mentioned that the clay mineral component is not exactly close to the soil from other sites, which is because of the different depositional environment of mother rock and rate of decay during the soil-forming process.

In this project, EDX analysis was also employed to study the stability of expansive soil and the chemical composition and component which are shown in Table 2. From this table, it can be illustrated that, even though the result would vary with the EDX detection sites and the main components are SiO_2 , Al_2O_3 , and Fe_2O_3 , which three components accounting

TABLE 2: The mineral components and content of expansive soil (unit: %).

Components	Na ₂ O	MgO	Al ₂ O ₃	SiO ₂	K ₂ O	Fe ₂ O ₃	SiO ₂ /Al ₂ O ₃
Content	3.2	6.7	19.5	47.3	8.4	12.8	2.1

TABLE 3: The physical parameters of expansive soil.

Index	Specific weight $\gamma/\text{kN}\cdot\text{m}^{-3}$	Liquid limit $\omega_L/\%$	Plastic limit $\omega_p/\%$	Plasticity index I_p	Free swell ratio $\delta_{ef}/\%$
Soil	19.7	37.9	17.3	20.6	54

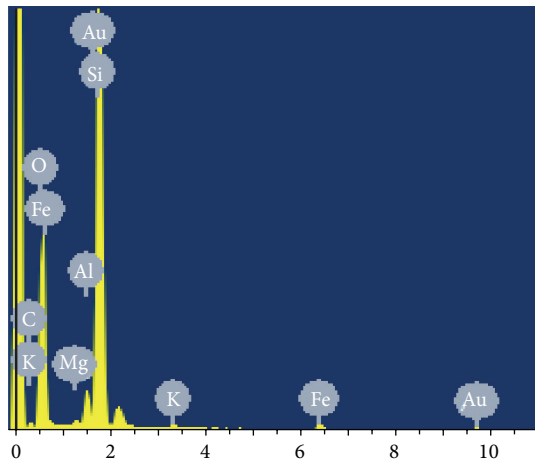


FIGURE 2: The result of expansive soil sample with EDX.

for around 80% of expansive soil. As a consequence, the enrichment of quartz mineral in course mineral and the enrichment of aluminum silicate clay minerals in fine mineral can be concluded.

Among the chemical compositions of colloidal particle of expansive soil, the molecular ratio of silicon aluminum is 3.94, which indicates that the major mineral composition is illite, corresponding to the identification result. The high components of vivacious alkali metals and alkaline-earth metals such as K, Na, Ca, and Mg demonstrate the low degree of the weathering leaching and chemical weathering and that this soil can be further weathered when the climate, aqueous medium, and oxidoreduction environment are different. Consequently, the engineering properties would be worse for the hydrophilic enhancement. The EDX pattern is shown in Figure 2 where the existence of Au element is due to the spraying for SEM observation.

3.2. Physical Property. The sample soils belong to the mound hilly mudstone swell-shrinking soil area, the bed rock of which is lacustrine deposition mud and silty mud and the surface of which is soil from intense weathering and shows the structure of stratiform and color of greyish-green [19]. What is more, this soil is interbedded by silty mudstone and mudstone siltstone. That is the reason why strong expansive soils from Hanzhong are famous. The physical parameters

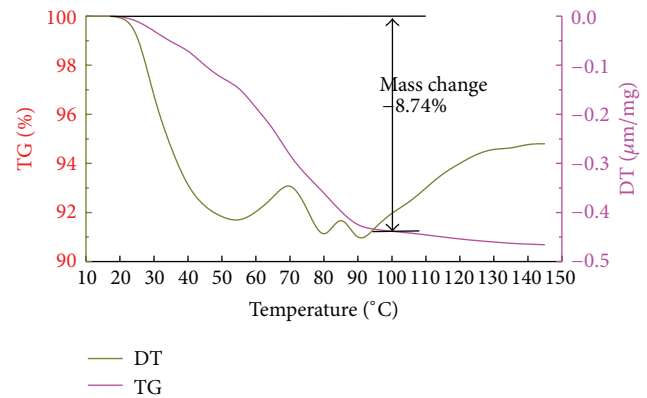


FIGURE 3: Thermogravimetric (TG) and differential thermal (DT) analysis diagram of heated expansive soil.

including specific weight, liquid limit, and plastic limit of expansive soil are given in Table 3.

Table 3 shows that the specific weight is $19.7 \text{ } \gamma/\text{kN}\cdot\text{m}^{-3}$, which is similar to that of soil from the north of Hubei, China [7], while the liquid limit and plastic limit are separately 37.9% and 17.3%, in which the two can be used to identify the status of the soil and be further helpful for the application of expansive soil. In addition, the plasticity index is 20.6, which means that the expansive soil can have a high hydrophilic. Except for the parameters on the plasticity given before, another one is free swell ratio as large as 54%, which can directly reflect the high expansibility of expansive soil.

4. The Influence of Temperature

4.1. TG-DT Analysis. The TG-DTA diagram (Figure 3) shows a continuous weight loss distributed in the range of 20–140°C. The figure shows two main portions of mass loss as the rise of temperature. The first one is during the heating temperature interval of 20–100°C when the free water and some physically absorbed water are off. Before the heating temperature is up to 100°C, the sample loses 8.74% of its total weight. The proportion of physically absorbed water is small. Combined with Table 3 of physical properties, it can be known that the lost water is mainly from the free water. Therefore, the moisture content of expansive soil is around 8%, which is lower than the liquid limit and the airing treated expansive soil is in the semisolid state.

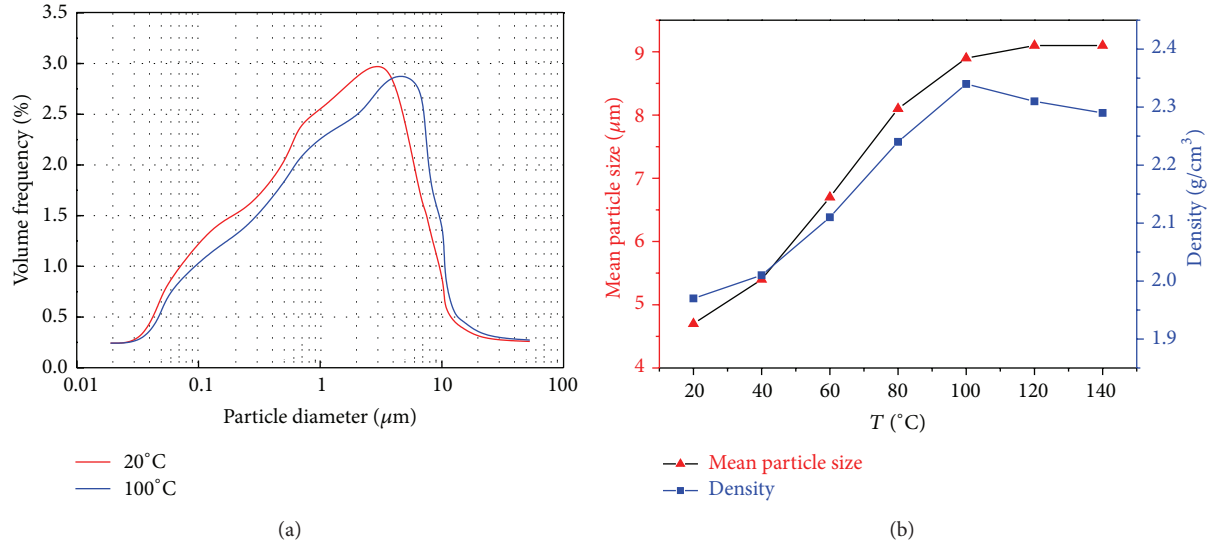


FIGURE 4: (a) Particle size distribution of expansive soil at room temperature (20°C) and heated at 100°C. (b) Mean particle size and density at different heated temperature.

Then the mass of the sample undertakes a slight decline in the range of 100~140°C with a mass change of 1.18%. This portion of mass decrement is due to the drain of part of physically absorbed water and chemically bound water. For the existence of $\text{Al}(\text{OH})_3$ and carbonate terrane in the clay mineral of expansive soil, the lost chemically bound water is mainly from the release of H_2O and CO_2 separately from the decomposition of $\text{Al}(\text{OH})_3$ and carbonate terrane. The comparison of the different parts of loss illustrates that the loss of expansive soil during the heat treatment is occurring mainly before 100°C as a consequence of the elimination of free water and physical absorbed water.

4.2. Particle Size and Density. The physical properties such as particle size, density, and strength change with the increase of the heated temperature of expansive soil. These properties of expansive soil can significantly influence the occurring possibility of landslide and the settlement of the foundation [20]. The particles size distribution of the unheated expansive soil (20°C) and expansive soil heated at 100°C is shown in Figure 4(a). It can be seen that the unheated expansive soil particles are mostly in the range of 0.096–13.5 μm with a mean value of 4.67 μm . Compared with the unheated expansive soil, the heat treated one has a relatively large particle diameter. The particle diameter of expansive soil heated at 100°C is between 0.052 μm and 11.7 μm with an average value of 8.81 μm . It is believed that the rise of particle size is due to the dehydration consolidation during the evaporation process.

With the change of heated temperature from 20°C to 140°C, which can indicate from Figure 4(b) that the average particle diameter of expansive soil rise from 4.67 μm at 20°C to 9.03 μm at 140°C, the temperature from 20°C to 100°C saw the rapid increase of mean particle size from 4.67 μm to 8.81 μm , followed by a slow rise to 9.03 μm at 140°C.

With a similar increase tendency of mean particle size, the density of expansive soil also sharply grows from 1.94 g/cm^3 to 2.28 g/cm^3 . As the temperature is increasing from 20°C to 100°C, the density of expansive soil experiences a rapid increase to the value of 2.35. And then the density declines slightly from 2.35 g/cm^3 at 100°C to 2.28 g/cm^3 at 140°C. As well as the particle size, the density also rises up because of the dehydration consolidation. As to the large growth rate before 100°C, it comes from the high water content and fast free water loss during the heat treatment. While the loss of physically absorbed water and chemically bonded water will exert a weak influence on both the density and the particle size. But the decomposition of $\text{Al}(\text{OH})_3$ and carbonate terrane can lead to the creak and transformation of some clay mineral particle, which will further make the density at a low value.

4.3. SEM Characterization. The microstructure and the morphology play important role in the status of expansive soil and influence the expanding and shrinking behavior of expansive soil [21]. For the purpose of further comprehending the phase change progress of expansive soil during heat treatment, untreated expansive soil and samples heated at 60°C, 100°C, and 140°C are dispersed in anhydrous alcohol and grinded by ultrasonic vibration for the same time (4 h). Then the samples were observed by scanning electron microscope to obtain the micromorphology maps of these samples. The SEM images of unheated expansive soil and heat treated one are shown in Figure 5.

From Figure 5(a) it can be known that the microscopic structure of untreated expansive soil is relatively loose, with high porosity and small particle size. On the contrary, the diagrams of expansive soil heated at a series of temperatures (Figures 5(b)–5(d)) indicate that the heat treatment can improve the value of particle diameter and make the particles

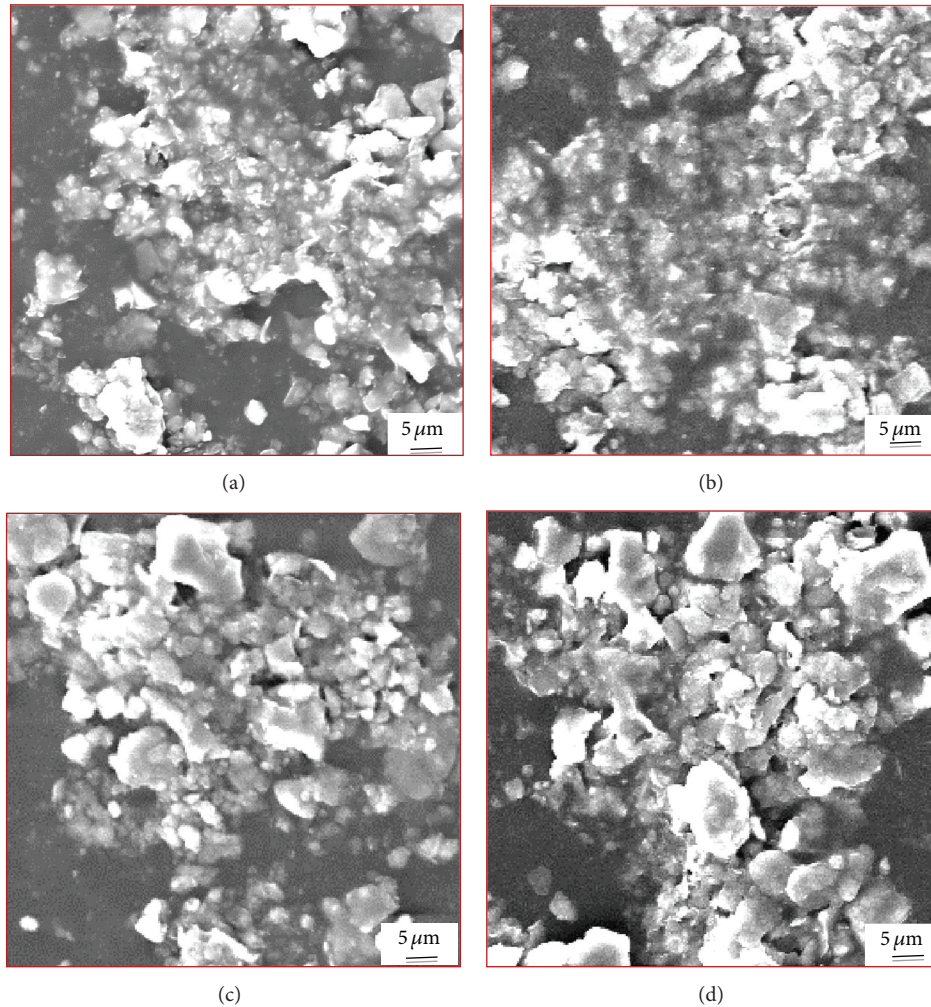


FIGURE 5: The SEM images of expansive soil (a) at room temperature (20°C) and heated at (b) 60°C, (c) 100°C, and (d) 140°C.

easy to gather together. The increasing tendency of particle size is consistent with the values measured by laser particle size analyzer as shown in Figure 4(b).

Different microstructures result from different physical and chemical progresses. With the influence of heating at 60 and 100°C, expansive soil lose the majority of its free water and part of physically absorbed water. So Figures 5(b)–5(c) present small particles and a high porosity, corresponding to a low density as shown in Figure 4(b). When heated at 140°C, with the decomposition of phases like carbonate terrane, expansive soil has lost almost all the physically absorbed water and part of the chemically bound water. So it can have larger particle and higher porosity (also higher density) than when heated at 60°C (Figure 5(d)).

4.4. Hydraulic Behaviors and Shearing Resistance. As one type of unsaturated soil, the existence of gaseous phase, water, and soil skeleton in expansive soil is the main reason leading to the complex properties. Thus, the research on the existing form of gas phase and water phase and the migration law of gas

and water under stress is indispensable to know its physical properties [20, 22, 23]. And the hydraulic behaviors and strength performance play fundamental role in the pollution prevention, modification, and engineering application of expansive soil. Therefore, these relevant researches have been carried out and the test results are shown in Figure 6.

Both unheated expansive soil (20°C) and samples heated at 100°C for 6 h belong to alkaline engineering materials. The hydraulic behaviors of expansive soil would critically influence the spread of harmful substances in underground water and further lead to serious pollution of the surrounding soil, air, and groundwater. Therefore, a deep recognition of the hydrodynamic characteristics of expansive soil is necessary for the pollution prevention of underground water. The measured hydraulic characteristics can be illustrated by soil-water characteristic curve (SWCC) and hydraulic conductivity characteristics curve (HCF), which are shown in Figure 6(a).

The SWCC curves indicate that, with the same change of water content, the change of matrix suction of unheated

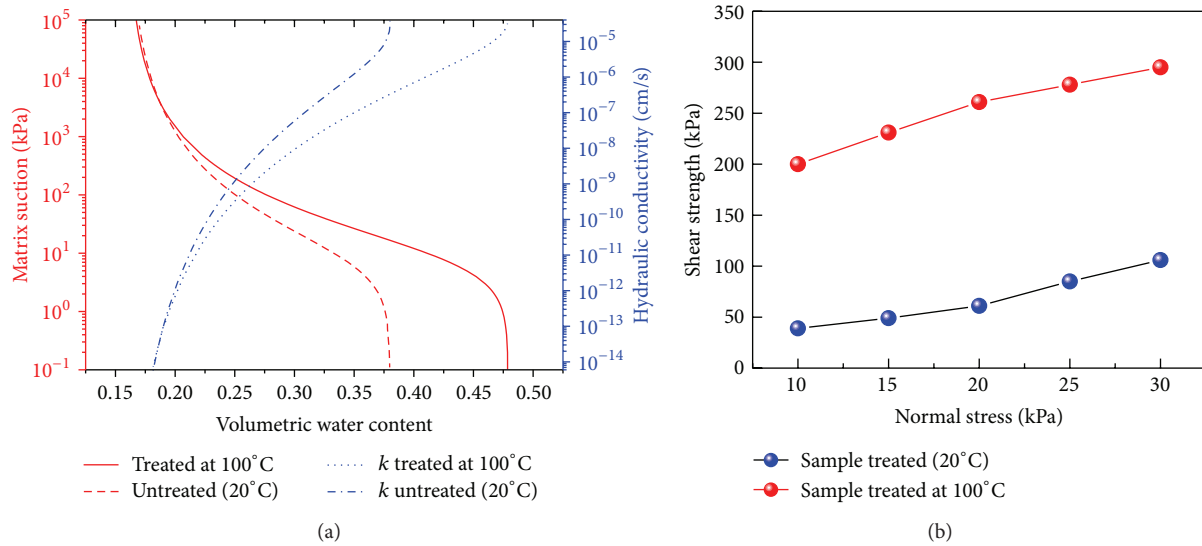


FIGURE 6: (a) The hydraulic characteristics of unheated (20°C) and heated (100°C) expansive soil. (b) Bond strength as the functions of heated temperature.

expansive soil (matrix suction value is a function of several factors like free water, electric combination water, cement force, and electrochemical power) is greater than that of expansive soil heated at 100°C. This means that the water sensitivity of unheated expansive soil is greater than heated ones. As a consequence, under the same natural conditions, the stability of expansive soil after heat treatment is lower than that of unheated expansive soil. On the other hand, with the same water content, the hydraulic conductivity of the heated sample is better. It indicates that the liquid pollutants in expansive soil under high temperature are easier to filtrate and diffuse into the underground water and the surrounding environment.

The measurement shows that the strength of heated expansive soil is far higher than that of unheated soil. Then the direct shear tests were carried out for the purpose of further understanding the strength performance of the expansive soil under different temperature conditions. The testing results are shown in Figure 6(b).

The curves in Figure 6(b) indicate that, under the same experimental conditions, expansive soil heated at 100°C for 6 h has significantly high intensity. This is the same with the conclusion obtained in the sites. The bond strength of the two samples can be calculated through extending the strength envelope curve towards the left to the longitudinal axis of the coordinate system. The bond strength of heated expansive soil, 178 kPa, is significantly greater than that of unheated samples which is 26.3 kPa. In addition, it can be known that the angles of internal friction of the two materials are almost the same from the fact that two shear strength envelope curves are roughly parallel. These phenomena illustrate that the main reason why the strength of heated expansive soil is substantially higher is that it comes from the increase of bond strength.

5. Conclusion

In this project, the mineral and chemical composition and several essential physical parameters of unheated expansive soil samples taken from the western outskirts of Hanzhong of Shanxi Province, China, are tested and given out. Moreover, along with the change of temperature from 20°C to 140°C, free water, physical absorbed water, and chemically bound water are lost in sequence. The mean particle diameter undertakes a sharp increase and the SEM shows that the microstructure becomes larger and more porous due to the decomposition of phases like carbonate terrane. The hydraulic behaviors and strength performance of unheated samples and the one heated at 100°C are also given out to demonstrate the mechanical properties during the engineering application. All these researches play fundamental role in the pollution prevention, modification, and engineering application of expansive soil.

Conflict of Interests

The authors declare that there is no conflict of interests regarding the publication of this paper.

Acknowledgment

The authors wish to thank Yuchao Xia for providing thoughtful and critical comments on the paper. The funding for this research is provided by the National Natural Science Foundation of China (Grant no. 41172261) which is greatly appreciated.

References

- [1] J. K. Mitchell, *Fundamentals of Soil Behavior*, John Wiley & Sons, New York, NY, USA, 1993.

- [2] J. R. Philip and D. A. de Vries, "Moisture movement in porous materials under temperature gradients," *Transactions, American Geophysical Union*, vol. 38, no. 2, pp. 222–232, 1957.
- [3] A. E. Dief and W. F. Blumel, "Expansive soils under cyclic drying and wetting," *Geotechnical Testing Journal*, vol. 14, no. 1, pp. 96–102, 1991.
- [4] H.-Z. Yu, X.-Q. Li, and J.-W. Yao, "Experimental study and analysis of expansive soil improved with chemical medicine," *Rock and Soil Mechanics*, vol. 27, no. 11, pp. 1941–1944, 2006.
- [5] N. R. Morgenstern and J. S. Tchalenko, "Microscopic structure in kaolin subjected to direct shear," *Geotechnique*, vol. 17, no. 4, pp. 309–328, 1967.
- [6] Q. Yang, H. Zhang, and M. Luan, "Testing study on shear strength of unsaturated expansive soils," *Chinese Journal of Rock Mechanics and Engineering*, vol. 23, no. 3, pp. 420–425, 2004.
- [7] S.-B. Dai, J. Huang, and L. Xia, "Analysis of mineral composition and chemical components of expansive soil in North Hubei," *Rock and Soil Mechanics*, vol. 26, supplement 1, pp. 296–299, 2005.
- [8] A. A. Al-Rawas, A. W. Hago, and H. Al-Sarmi, "Effect of lime, cement and Sarooj (artificial pozzolan) on the swelling potential of an expansive soil from Oman," *Building and Environment*, vol. 40, no. 5, pp. 681–687, 2005.
- [9] B. R. Phani Kumar and R. S. Sharma, "Effect of fly ash on engineering properties of expansive soils," *Journal of Geotechnical and Geoenvironmental Engineering*, vol. 130, no. 7, pp. 764–767, 2004.
- [10] Y. Xie, Z.-H. Chen, and G. Li, "Research of thermal effects on shear strength and deformation characteristics of unsaturated bentonite soils," *Chinese Journal of Geotechnical Engineering*, vol. 27, no. 9, pp. 1082–1085, 2005.
- [11] A. A. Basma, A. S. Al-Homoud, A. I. Husein Malkawi, and M. A. Al-Bashabsheh, "Swelling-shrinkage behavior of natural expansive clays," *Applied Clay Science*, vol. 11, no. 2–4, pp. 211–227, 1996.
- [12] Z.-H. Chen, Y. Xie, S.-G. Sun, X.-W. Fang, and G. Li, "Temperature controlled triaxial apparatus for soils and its application," *Chinese Journal of Geotechnical Engineering*, vol. 27, no. 8, pp. 928–933, 2005.
- [13] S. M. Rao and P. Shivananda, "Role of curing temperature in progress of lime-soil reactions," *Geotechnical and Geological Engineering*, vol. 23, no. 1, pp. 79–85, 2005.
- [14] K. Harishkumar and K. Muthukkumaran, "Study on swelling soil behaviour and its improvements," *International Journal of Earth Sciences and Engineering*, vol. 4, no. 6, pp. 19–25, 2011.
- [15] X.-W. Li, L.-W. Kong, A.-G. Guo, and Y. Zhang, "Strength characteristics of expansive soil considering effect of hydrous state," *Rock and Soil Mechanics*, vol. 29, no. 12, pp. 3193–3198, 2008.
- [16] Y. Xie, Z.-H. Chen, and G. Li, "Thermo-nonlinear model for unsaturated expansive soils," *Rock and Soil Mechanics*, vol. 28, no. 9, pp. 1937–1942, 2007.
- [17] D. de Bruyn and J.-F. Thimus, "The influence of temperature on mechanical characteristics of boom clay: the results of an initial laboratory programme," *Engineering Geology*, vol. 41, no. 1–4, pp. 117–126, 1996.
- [18] H. Xiao, K. Teng, H. Xu et al., "Experimental study on deformation of nanning expansive soil consolidation and creep coupling," *Journal of Hunan University of Technology*, vol. 23, no. 5, pp. 1–6, 2009.
- [19] X.-D. Ou, H. Wu, and D. Zhou, "Comparative study on thermodynamics characteristics of red clay and expansive soils in Guangxi," *Rock and Soil Mechanics*, vol. 26, no. 7, pp. 1068–1072, 2005.
- [20] C. Bao, "Behavior of unsaturated soil and stability of expansive soil slope," *Chinese Journal of Geotechnical Engineering*, vol. 26, no. 1, pp. 1–15, 2004.
- [21] T. Mao and L. Xia, "Experimental research on microstructure of expansive soil in north of Hubei province," *Journal of Huazhong University of Science and Technology Urban Science*, vol. 27, no. 2, pp. 48–52, 2010.
- [22] A. T. Corey, "Measurement of water and air permeability in unsaturated soil," *Proceedings of the Soil Science Society of America*, no. 21, pp. 7–10, 1957.
- [23] L. Zhan, *Field and Laboratory Study of an Unsaturated Expansive Soil Associated with Rain-Induced Slope Instability*, The Hong Kong University of Science and Technology (HKUST), Hong Kong, 2003.

Research Article

Catalytic Hydrolysis of Ammonia Borane by Cobalt Nickel Nanoparticles Supported on Reduced Graphene Oxide for Hydrogen Generation

Yuwen Yang,¹ Fei Zhang,¹ Hualan Wang,² Qilu Yao,¹ Xiangshu Chen,¹ and Zhang-Hui Lu¹

¹ College of Chemistry and Chemical Engineering, Jiangxi Normal University, Nanchang 330022, China

² Department of Information, Yunnan Institute of Technology and Information, Kunming 650224, China

Correspondence should be addressed to Xiangshu Chen; xiangshuchenjx@126.com and Zhang-Hui Lu; luzh@jxnu.edu.cn

Received 19 February 2014; Accepted 11 March 2014; Published 14 April 2014

Academic Editor: Ming-Guo Ma

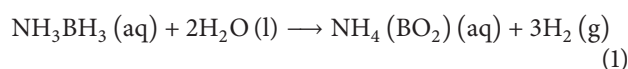
Copyright © 2014 Yuwen Yang et al. This is an open access article distributed under the Creative Commons Attribution License, which permits unrestricted use, distribution, and reproduction in any medium, provided the original work is properly cited.

Well dispersed magnetically recyclable bimetallic CoNi nanoparticles (NPs) supported on the reduced graphene oxide (RGO) were synthesized by one-step in situ coreduction of aqueous solution of cobalt(II) chloride, nickel (II) chloride, and graphite oxide (GO) with ammonia borane (AB) as the reducing agent under ambient condition. The CoNi/RGO NPs exhibits excellent catalytic activity with a total turnover frequency (TOF) value of 19.54 mol H₂ mol catalyst⁻¹ min⁻¹ and a low activation energy value of 39.89 kJ mol⁻¹ at room temperature. Additionally, the RGO supported CoNi NPs exhibit much higher catalytic activity than the monometallic and RGO-free CoNi counterparts. Moreover, the as-prepared catalysts exert satisfying durable stability and magnetically recyclability for the hydrolytic dehydrogenation of AB, which make the practical reusing application of the catalysts more convenient. The usage of the low-cost, easy-getting catalyst to realize the production of hydrogen under mild condition gives more confidence for the application of ammonia borane as a hydrogen storage material. Hence, this general method indicates that AB can be used as both a potential hydrogen storage material and an efficient reducing agent, and can be easily extended to facile preparation of other RGO-based metallic systems.

1. Introduction

Hydrogen, as a globally accepted clean and environmentally friendly fuel, has attracted widespread research concerns and interests [1]. However, for the widespread use of hydrogen as an energy carrier to achieve sustainable mobility, developing a compact, safe, and affordable means of storing hydrogen remains a major obstacle [2]. Chemical hydrogen storage is thought to be one of the most promising approaches to meet this challenge, because of its considerably high gravimetric and volumetric hydrogen density [3–6]. In recent years, ammonia borane (AB) was discovered as an efficient and safe storage medium for H₂ due to the high capacity (19.6 wt.% and 0.145 kg H₂/L) and stability in ambient atmosphere [7–11]. In the presence of a suitable catalyst, three moles of hydrogen can be released from one mole of AB at room

temperature. The hydrolysis of AB can be represented as follows [12–14]:



So, the discovery of suitable catalysts becomes the main issue of the practical application of AB as an on-board hydrogen medium. With the trend of nanocatalysts applied in the hydrolysis of AB system, transition metal nanoparticles (NPs) catalysts are considered to be a promising option because of their novel structure, electronic properties, and magnetic performances [15–18]. So far, not only nonnoble metal NPs [12, 19–24] and noble metal NPs [13, 20, 25–29], but also their composites [14, 30–38] have been tested for hydrolytic dehydrogenation of AB; among them platinum [20, 25, 26] shows the highest activity. However, concerning

the element abundance and related economic issues, it is clearly a desired goal to prepare low-cost catalysts with high catalytic activity for the terminal practical application of this reaction system in the fuel cell. The catalytic performance of the metal NPs is highly dependent on the dispersion of the active metals. Thus, the aggregation of metal NPs during the catalytic process due to the high surface energies and magnetic properties is the main impediment to restraint their development [36]. To solve this problem, various surfactants and substrates are successfully utilized to obtain catalysts with preferable dispersity [12–14]. Graphene, a single layer of sp^2 carbon lattices, could be an ideal substrate for growing and anchoring metal NPs with good dispersion due to its high specific surface area and large density of free electrons [37–39].

In this work, we have discovered that the CoNi/RGO exhibits excellent catalytic activity in hydrolysis of AB for hydrogen generation. Separation of this catalyst from reactant liquid is quite simple by using a magnet, as CoNi/RGO has an excellent magnetic property. This mild and rapid strategy provides great potential for application of ammonia borane as an on-board hydrogen medium.

2. Experimental

2.1. Graphite Oxide (GO) Preparation. GO was made by a modified Hummers method [40, 41]. Briefly, natural graphite powder (325 mesh) was placed into an 80°C solution of concentrated H_2SO_4 (30 mL), $K_2S_2O_8$ (2.5 g), and P_2O_5 (2.5 g). The mixture was carefully diluted with distilled water and filtered using a 0.2 micron Nylon Millipore filter to remove the residual acid. The product was dried at 80°C under ambient condition overnight. The preoxidized graphite was put into cold concentrated H_2SO_4 , then $KMnO_4$ was added gradually under stirring, and the temperature of the mixture was kept below 20°C for 2.5 h. The mixture was stirred at 35°C for 4 h. Afterwards, 250 mL of deionized water was added and the suspension was stirred at 100°C for another 2 h. Subsequently, additional 300 mL of deionized water was added. Shortly after that, 7 mL of 30% H_2O_2 was added to the mixture to terminate the reaction. The suspension was then repeatedly centrifuged and washed first with 5% HCl solution and then with water. Exfoliation of graphite oxide to GO was achieved by ultrasonication of the dispersion for 30 min [42].

2.2. In Situ Synthesis of RGO Supported CoNi NPs (Co/Ni = 0.5/0.5) and Their Catalytic Activities toward the Hydrolysis of AB (Catalysts/AB = 0.05). 8 mL aqueous solution containing $CoCl_2$ (6.01 mg), $NiCl_2$ (6.60 mg), and GO solution (1.77 g containing 0.68‰ GO) was kept in a 25 mL two-necked round-bottom flask. One neck was connected to a gas burette and the other was connected to a pressure-equalization funnel to introduce AB in 2 mL of aqueous solution containing 34.3 mg AB (1 mmol). The reactions were started when the aqueous AB solution was added to the flask with vigorous stirring. The evolution of gas was monitored using the gas burette. After the hydrogen generation reaction was completed, 34.3 mg AB (1 mmol) was added to the flask

and the evolution of gas was monitored. A water bath was used to control the temperature of the reaction solution.

For comparison, RGO supported CoNi NPs with different Co/Ni ratio, GO reduced by AB, RGO-free CoNi reduced by AB, and CoNi/RGO reduced by $NaBH_4$ were synthesized using the same method.

2.3. Different Supported Carbon Materials. Sets of experiments with different supported carbon materials (such as activated charcoal and graphite powder) were performed at room temperature. All the experiments were performed in the same way as described in Section 2.2.

2.4. Kinetic Studies of Hydrolytic Dehydrogenation of AB Catalyzed by CoNi/RGO NPs. Temperature was varied at 25°C, 30°C, 35°C, and 40°C, while the ratio of the concentration of CoNi (0.05 mmol) and AB (1 mmol) was kept constant at 0.05 to obtain the activation energy (E_a).

2.5. Stability Test. For stability test, catalytic reactions were repeated 5 times by adding other equivalents of AB (1 mmol) into the mixture after the previous cycle. The molar ratio of catalyst/AB was kept at 0.05.

2.6. Catalyst Characterization. Transmission electron microscope (TEM), energy-dispersive X-ray spectroscopy (EDS), and selected area electron diffraction (SAED) were observed using FEI Tecnai G20 U-Twin TEM instrument operating at 200 kV. Powder X-ray diffraction (XRD) studies were performed on a Rigaku RINT-22005 X-ray diffractometer with a $Cu_{K\alpha}$ source (40 kV, 20 mA). X-ray photoelectron spectroscopy (XPS) measurement was performed with a Thermo ESCALAB 250XI multifunctional imaging electron spectrometer. FTIR spectra were collected at room temperature by using a Thermo Nicolet 870 instrument using KBr discs in the 500–4000 cm^{-1} region. Raman spectrometer was carried out using a confocal Raman microscope (LabRAM HR).

3. Results and Discussion

3.1. Synthesis and Characterization. Chemical reduction methods are widely employed for the synthesis of NPs in solution phase in the presence of surfactant [43], whose presence on the surface diminishes the activity to some extent by blocking some of the active sites when NPs are employed as a catalyst [44]. Surfactant-free NPs are difficult to synthesize because growth of in situ generated nuclei cannot be halted. Herein, RGO supported CoNi NPs were successfully synthesized without using any external surfactant. We employed AB itself (much milder than $NaBH_4$) as the reducing agent in our reactions.

When AB was added to the precursor solution containing $CoCl_2$ and $NiCl_2$ at room temperature, reaction started after an induction period of 55 min, while with the precursor solution with graphene oxide (GO), the induction period time decreased to 3.5 min, as shown in Figure S1 (see Figure S1 in Supplementary Materials available online

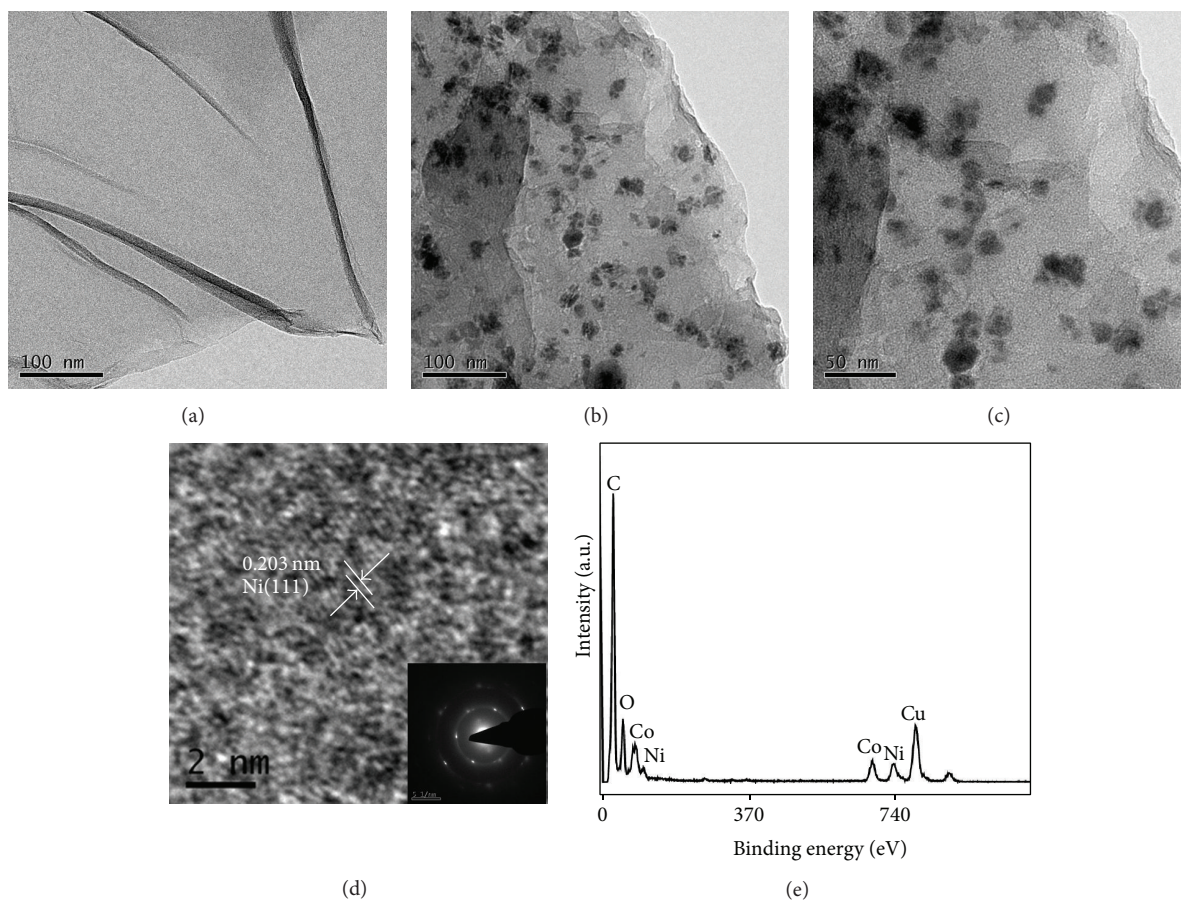


FIGURE 1: (a) TEM images of GO sheets and (b) and (c) TEM images of CoNi/RGO, (d) HRTEM image of CoNi/RGO, (d inset) SEAD pattern, and (e) EDS spectrum of CoNi/RGO.

at <http://dx.doi.org/10.1155/2014/294350/>). The decrease of induction period may result from the cooperative effect between RGO and metal NPs, which is mainly caused by the charge transfer across the graphene-metal interface due to the graphene-metal spacing and Fermi level difference. Just before the onset of H_2 evolution, a black colored material was formed. The black powder was RGO supported CoNi NPs (CoNi/RGO).

The microstructures of the CoNi/RGO were characterized by transmission electron microscopy (TEM), high-resolution TEM (HRTEM), energy-dispersive X-ray spectrometer (EDS), and selective area electron diffraction (SAED) (Figure 1). The GO sheets shown in Figure 1(a) are transparent and corrugated together. As shown in Figures 1(b) and 1(c), the NPs were well dispersed on RGO, which helps to prevent the agglomeration. A close examination of the catalysts by HRTEM (Figure 1(d)) indicates that the d-spacing of the particle lattice is ~ 0.203 nm, which is consistent with the (111) plane of cubic Ni (JCPDS number 04-0850). The EDS spectrum of the specimen shows the presence of Co and Ni (Figure 1(e)), which was taken from the specially marked area in the TEM image), with the atomic ratio for Co: Ni being detected to be 0.02:0.02, which is in good agreement with the appointed atomic ratio (1:1). Therefore, the Co NPs may be in amorphous phase.

Figure 2S shows the power XRD pattern of the Co/RGO and Ni/RGO. The diffraction peak attributed to Ni (111) is observed. However, no diffraction peak of Co exists, which may be caused by the amorphous phase of Co. Therefore, the peak at around 44.10° in the power XRD pattern of the as-prepared CoNi/RGO (Figure 2) corresponds to the Ni (111). Furthermore, the most intense peak at around 11.5° that corresponds to the (001) reflection of GO disappeared and a new peak at around 25.1° is observed in the as-synthesized RGO supported CoNi NPs, indicating that GO is successfully reduced to RGO.

CoNi/RGO was further characterized by X-ray photoelectron spectroscopy (XPS) to investigate the surface nature of the CoNi NPs and RGO (Figure 3). Compared with the peaks of GO (Figure 3(a)), the intensities of oxygen containing functional groups (such as $-C-O$, $-C=O$, and $-COO$) in Co/RGO (Figure 3(b)) decrease significantly, which also reveal the reduction of GO to RGO. Figure 3(c) shows the peaks of Co 2p. There are three peaks whose peak tops are 778.6, 781.7, and 786.0 eV, which stand for zero valent Co and oxidized Co [45]. Figure 3(d) shows the peaks of Ni 2p. There are two peaks at 853.2 and 870.0 eV which are attributed to zero valent Ni, while the other two peaks at 856.6 eV and 874.0 eV stand for oxidized Ni [46]. The formation of the

TABLE 1: Catalytic activity of different catalysts used for the hydrolytic dehydrogenation of AB.

Catalyst	TOF (mol H ₂ ·mol catalyst ⁻¹ ·min ⁻¹)	E _a (kJ mol ⁻¹)	Reference
Ru/γ-Al ₂ O ₃	23.05	67	[27]
CoNi/RGO	19.54	39.89	This work
Ag@CoNi/graphene	15.89	47	[35]
Au@Co	13.64	—	[40]
Co _{0.32} Pt _{0.68} /C	10.99	41.5	[31]
Ag@Co/graphene	10.24	20.03	[32]
PSMA-Ni	10.1	38.12	[21]
Cu@Co/graphene	8.36	51.3	[22]
Ag@Ni/graphene	7.7	49.56	[32]
Co _{0.75} B _{0.25}	7.24	40.85	[23]
RGO/Pd	6.25	51 ± 1	[28]
Ag/C/Ni	5.32	38.91	[33]
RuCo/γ-Al ₂ O ₃	3.64	47	[34]
Ni/γ-Al ₂ O ₃	2.45	—	[20]
Co/γ-Al ₂ O ₃	2.27	62	[20]

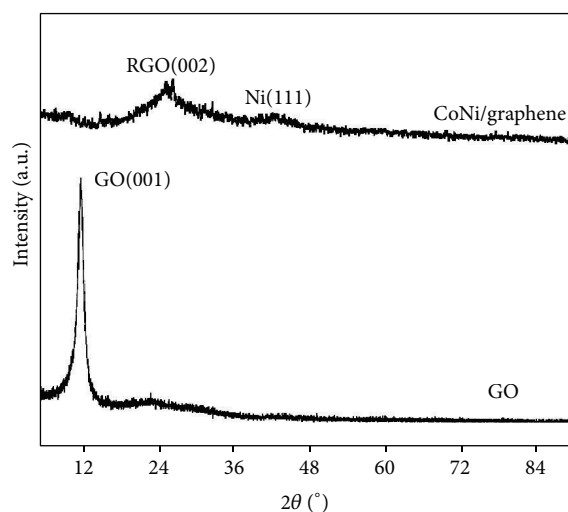


FIGURE 2: XRD patterns of GO and CoNi/RGO.

oxidized Co and oxidized Ni most likely occurs during the sample preparation process for XPS measurements.

Two peaks centered at 1316 and 1577 cm⁻¹ appear in the Raman spectra of the GO and RGO supported CoNi NPs (Figure 4(a)), corresponding to the *D* and *G* bands of the carbon products, respectively. The intensity ratio of the *D* to *G* band (*I_D*/*I_G*) is generally accepted to reflect the degree of graphitization of carbonaceous materials and defect density. After loading of the CoNi NPs, the *I_D*/*I_G* of GO is increased from 1.14 to 1.61. The relative changes in the *D* to *G* peak intensity ratio confirm the reduction of GO during the in situ fabrication. Figure 4(b) displays the FTIR spectra of GO and CoNi/RGO NPs. After the formation of RGO supported CoNi NPs, the disappearance of C=O peak at 1716 cm⁻¹, C–OH peak at 1399 cm⁻¹, and C–O peak at 1064 cm⁻¹ of GO further indicates that the GO was reduced to RGO during the process.

3.2. Catalytic Activities for Hydrolysis of AB. Figure 5(a) shows the composition effect of RGO supported Co_{1-x}Ni_x on AB hydrolysis ($x = \text{Co}:\text{Co} + \text{Ni}$), with the molar ratio for catalysts to AB being 0.05. Obviously, by changing the molar ratio, the NPs demonstrate different catalytic activities. As a result, Co_{0.5}Ni_{0.5}/RGO displays the best catalytic performance in the hydrolysis of AB, generating a stoichiometric amount of hydrogen (H₂/AB = 3.0) in the shortest time (3.07 min) with a turnover frequency (TOF) value of 19.54 mol H₂ mol catalyst⁻¹ min⁻¹, which is higher than the most reported nonnoble metal-based NPs and even many noble metal-based NPs, as shown in Table 1, while CoNi/RGO show better activity than pure Co NPs or pure Ni NPs supported on RGO, indicating the positive effect of metal interaction in the bimetallic CoNi NPs on hydrogen generation from hydrolysis of AB. As shown in Figure S3, compared with the NPs reduced by NaBH₄, the as-synthesized NPs generated by AB exhibit higher catalytic activities, which confirms that it is possible to achieve much more control over the nucleation and growth process of the RGO by choosing weaker reducing agents.

Figure 5(b) presents the plots of the volume of hydrogen generated from the AB solution versus the reaction time at room temperature in the presence of pure Co_{0.5}Ni_{0.5}NPs, GO, and the Co_{0.5}Ni_{0.5}/RGO catalysts. No hydrogen generation was observed for GO, suggesting that GO has no catalytic activity for the hydrolysis of AB. The hydrogen productivity from AB catalyzed by pure Co_{0.5}Ni_{0.5}NPs is around 49.3% in 79.7 min. However, the activity of Co-Ni/RGO is much higher than that of pure Co-Ni NPs without RGO. The enhanced catalytic activity for AB hydrolysis reaction should result from the cooperative effect between RGO and Co-Ni NPs. Furthermore, to study the effects of the supported carbon materials on the catalytic performances of the as-synthesized bimetallic NPs, Co_{0.5}Ni_{0.5}/graphite powder and Co_{0.5}Ni_{0.5}/activated charcoal are prepared and their catalytic activities toward hydrolysis of AB are studied. As

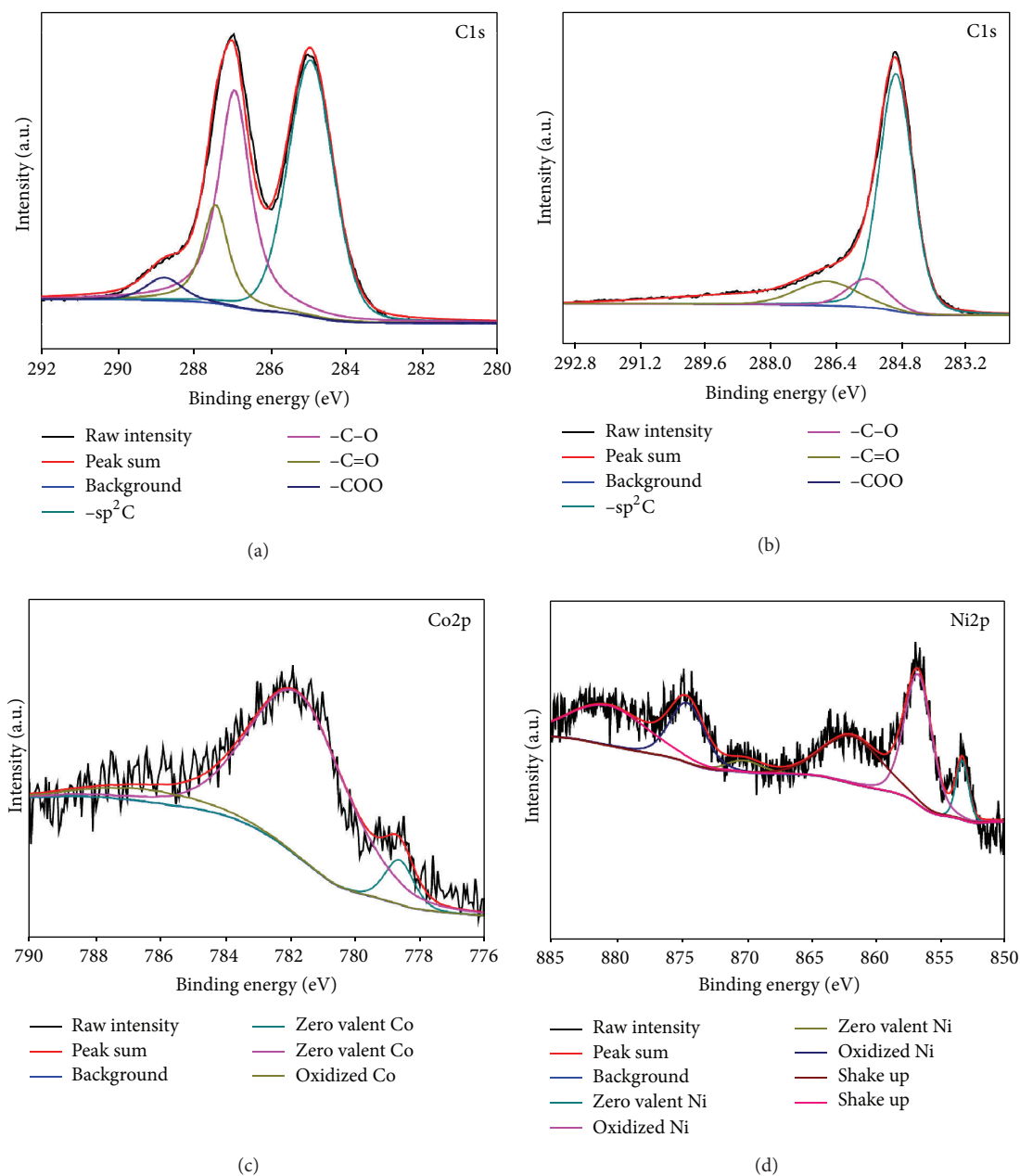


FIGURE 3: XPS of spectra of ((a) and (b)) C1s of GO and CoNi/RGO, (c) Co2p of CoNi/RGO, and (d) Ni2p of CoNi/RGO.

shown in Figure S4, their catalytic activities are inferior to that of Co_{0.5}Ni_{0.5}/RGO NPs, highlighting the dominant factor of RGO in facilitating hydrolysis of AB in our system.

In order to get the activation energy (E_a) of the AB hydrolysis catalyzed by CoNi/RGO NPs, the hydrolytic reactions at different temperatures in the range of 298–313 K were carried out. The values of the rate constant k at different temperatures were calculated from the slope of the linear part of each plot from Figure 6(a). The Arrhenius plot of $\ln k$ versus $1/T$ for the catalyst is plotted in Figure 6(b), from which the apparent activation energy was determined to be approximately 39.89 kJ/mol, being lower than most of the

reported E_a values (Table 1), indicating the superior catalytic performance of the as-synthesized CoNi/RGO catalysts.

3.3. Reusability and Recycle Ability. The reusability of the catalysts is crucial in the practical application. The recyclability of CoNi/RGO catalysts up to the fifth run for hydrolysis of AB is shown in Figure 7. The as-synthesized CoNi/RGO catalysts retain 68% of their initial activities in the hydrolysis of AB in the fifth run, indicating their superior recycle stabilities. The observed activity loss is likely to result from the precipitation of metabolates to the catalyst surface [19]. Moreover, the in situ synthesized CoNi/RGO

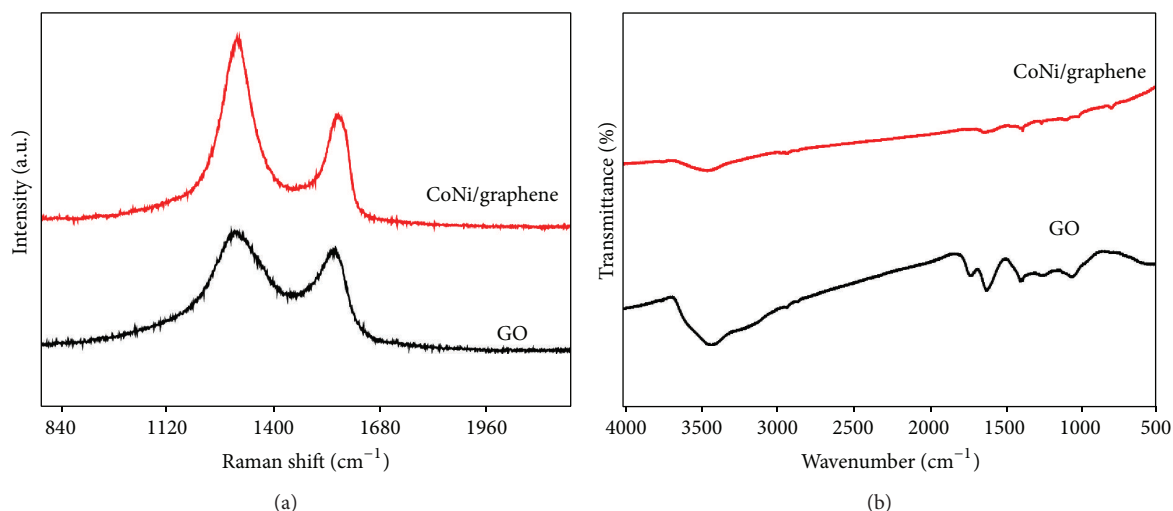


FIGURE 4: (a) Raman spectra and (b) FTIR spectra of the GO and CoNi/RGO.

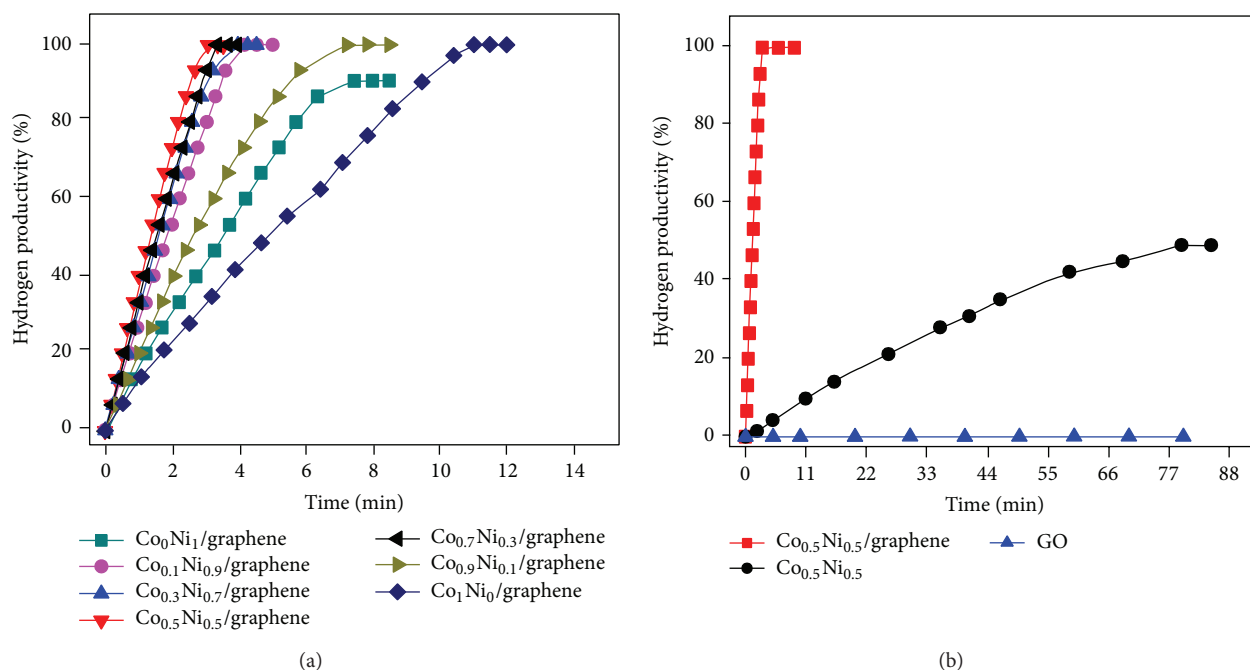


FIGURE 5: Hydrogen generation from hydrolysis of ammonia borane (0.10 M, 10 mL) over (a) the CoNi/RGO catalysts at ambient condition. CoNi/AB = 0.05 (molar ratio) and (b) the $\text{Co}_{0.5}\text{Ni}_{0.5}/\text{RGO}$, $\text{Co}_{0.5}\text{Ni}_{0.5}$, and GO.

are magnetic and thus can be separated from the reaction solution by an external magnet (Figure 7 inset), which makes the practical recycling application of nanocatalysts more convenient.

4. Conclusion

In summary, we have developed a facial in situ one-step method for the synthesis of magnetic RGO supported bimetallic CoNi NPs using AB as a reductant. The CoNi/RGO exhibit superior catalytic activity, with a turnover frequency (TOF) value of $19.54 \text{ H}_2 \text{ mol catalyst}^{-1} \text{ min}^{-1}$ and an

activation energy (E_a) value of $39.89 \text{ kJ mol}^{-1}$. The RGO supported CoNi NPs exhibit much higher catalytic activity than the graphite powder and activated charcoal supported or monometallic and RGO-free CoNi counterparts. Compared with catalysts reduced by NaBH_4 , the CoNi/RGO catalysts generated by the milder reducing agent AB exhibit higher catalytic activities. Moreover, the CoNi/RGO catalysts show good durable stability and magnetic recyclability for the hydrolytic dehydrogenation of AB, which makes the practical recycling application of the catalyst more convenient. This simple synthetic method can be extended to other RGO-based bimetallic systems for more application.

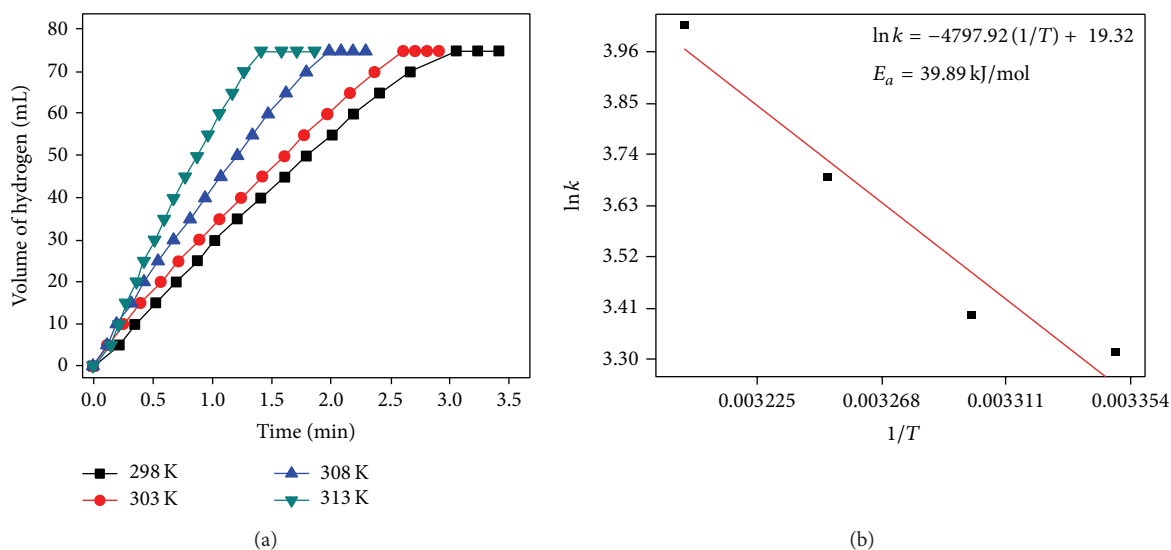


FIGURE 6: (a) Plots of volume of hydrogen generated versus time for $\text{Co}_{0.5}\text{Ni}_{0.5}/\text{RGO}$ catalyzed hydrolysis of AB at four different temperatures in the range of 298–313 K, $\text{CoNi}/\text{AB} = 0.05$ and (b) Arrhenius plot obtained from the data of Figure 6(b).

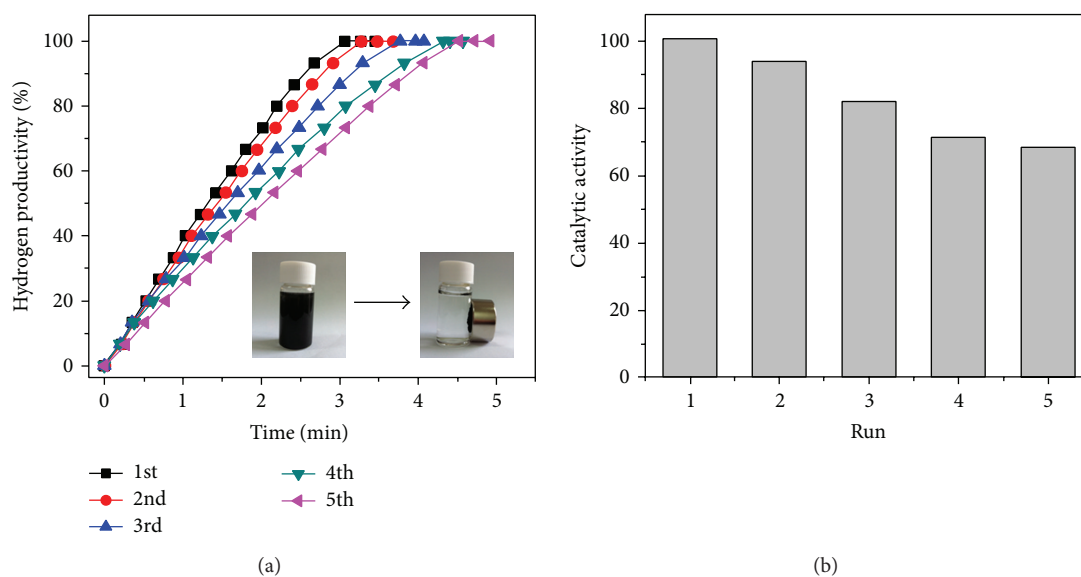


FIGURE 7: (a) Hydrogen generation from hydrolysis of ammonia borane (0.10 M, 10 mL) catalyzed by $\text{Co}_{0.5}\text{Ni}_{0.5}/\text{RGO}$ from the 1st to 5th cycle, $\text{CoNi}/\text{AB} = 0.05$, and (inset) photographs of the $\text{Co}_{0.5}\text{Ni}_{0.5}/\text{RGO}$ before (left) and after (right) the magnetic separation; (b) percentage of initial catalytic activity of $\text{Co}_{0.5}\text{Ni}_{0.5}/\text{RGO}$ in successive runs after the reuse for the hydrolysis of AB.

Conflict of Interests

The authors declare that there is no conflict of interests regarding the publication of this paper.

Acknowledgments

This work was financially supported by the National Natural Science Foundation of China (no. 21103074), the Natural Science Foundation of Jiangxi Province of China (nos. 20114BAB203010 and 20132BAB203014), Jiangxi Provincial Department of Science and Technology (no. 20111BDH80023), and the Scientific Research Foundation

of Graduate School of Jiangxi Province (YC2013-S105). Zhang-Hui Lu was supported by the Sponsored Program for Cultivating Youths of Outstanding Ability in Jiangxi Normal University, the Young Scientist Foundation of Jiangxi Province (20133BCB23011), and “Gan-po talent 555” Project of Jiangxi Province.

References

- [1] L. Schlapbach and A. Züttel, “Hydrogen-storage materials for mobile applications,” *Nature*, vol. 414, no. 6861, pp. 353–358, 2001.

- [2] J. S. Zhang, Y. Zhao, D. L. Akins, and J. W. Lee, "Calorimetric and microscopic studies on the noncatalytic hydrothermolysis of ammonia borane," *Industrial & Engineering Chemistry Research*, vol. 50, pp. 10407–10413, 2011.
- [3] U. Eberle, M. Felderhoff, and F. Schüth, "Chemical and physical solutions for hydrogen storage," *Angewandte Chemie International Edition*, vol. 48, pp. 6608–6632, 2009.
- [4] J. Yang, A. Sudik, C. Wolverton, and D. J. Siegel, "High capacity hydrogen storage materials: attributes for automotive applications and techniques for materials discovery," *Chemical Society Reviews*, vol. 39, no. 2, pp. 656–675, 2010.
- [5] U. B. Demirci and P. Miele, "Chemical hydrogen storage: "Material" gravimetric capacity versus "system" gravimetric capacity," *Energy and Environmental Science*, vol. 4, no. 9, pp. 3334–3341, 2011.
- [6] Z. H. Lu, Q. L. Yao, Z. J. Zhang, Y. W. Yang, and X. S. Chen, "Nanocatalysts for hydrogen generation from ammonia borane and hydrazine borane," *Journal of Nanomaterials*, vol. 2014, Article ID 729029, 2014.
- [7] Z. H. Lu and Q. Xu, "Recent progress in boron- and nitrogen-based chemical hydrogen storage," *Functional Materials Letters*, vol. 5, Article ID 1230001, 9 pages, 2012.
- [8] C. W. Hamilton, R. T. Baker, A. Staubitz, and I. Manners, "B-N compounds for chemical hydrogen storage," *Chemical Society Reviews*, vol. 38, no. 1, pp. 279–293, 2009.
- [9] M. Yadav and Q. Xu, "Liquid-phase chemical hydrogen storage materials," *Energy & Environmental Science*, vol. 5, pp. 9698–9725, 2012.
- [10] H. L. Jiang and Q. Xu, "Catalytic hydrolysis of ammonia borane for chemical hydrogen storage," *Catalysis Today*, vol. 170, no. 1, pp. 56–63, 2011.
- [11] U. B. Demirci and P. Miele, "Sodium borohydride versus ammonia borane, in hydrogen storage and direct fuel cell applications," *Energy and Environmental Science*, vol. 2, no. 6, pp. 627–637, 2009.
- [12] S. Akbayrak and S. Özkar, "Ruthenium(0) nanoparticles supported on multiwalled carbon nanotube as highly active catalyst for hydrogen generation from ammonia-borane," *ACS Applied Materials & Interfaces*, vol. 4, pp. 6302–6310, 2012.
- [13] J. Wang, Y. L. Qin, X. Liu, and X. B. Zhang, "In situ synthesis of magnetically recyclable graphene-supported Pd@Co core-shell nanoparticles as efficient catalysts for hydrolytic dehydrogenation of ammonia borane," *Journal of Materials Chemistry*, vol. 22, pp. 12468–12470, 2012.
- [14] J. M. Yan, Z. L. Wang, H. L. Wang, and Q. Jiang, "Rapid and energy-efficient synthesis of a graphene-CuCo hybrid as a high performance catalyst," *Journal of Materials Chemistry*, vol. 22, pp. 10990–10993, 2012.
- [15] L. Kesavan, R. Tiruvalam, M. H. A. Rahim et al., "Solvent-free oxidation of primary carbon-hydrogen bonds in toluene using Au-Pd alloy nanoparticles," *Science*, vol. 331, no. 6014, pp. 195–199, 2011.
- [16] R. Ghosh Chaudhuri and S. Paria, "Core/shell nanoparticles: classes, properties, synthesis mechanisms, characterization, and applications," *Chemical Reviews*, vol. 112, no. 4, pp. 2373–2433, 2012.
- [17] R. Ferrando, J. Jellinek, and R. L. Johnston, "Nanoalloys: from theory to applications of alloy clusters and nanoparticles," *Chemical Reviews*, vol. 108, no. 3, pp. 845–910, 2008.
- [18] R. C. Sekol, X. K. Li, P. Cohen, G. Doubek, M. Carmo, and A. D. Taylor, "Silver palladium core-shell electrocatalyst supported on MWNTs for ORR in alkaline media," *Applied Catalysis B: Environmental*, vol. 138–139, pp. 285–293, 2013.
- [19] Z. H. Lu, J. P. Li, A. L. Zhu et al., "Catalytic hydrolysis of ammonia borane via magnetically recyclable copper iron nanoparticles for chemical hydrogen storage," *International Journal of Hydrogen Energy*, vol. 38, pp. 5330–5337, 2013.
- [20] Q. Xu and M. Chandra, "Catalytic activities of non-noble metals for hydrogen generation from aqueous ammonia-borane at room temperature," *Journal of Power Sources*, vol. 163, no. 1, pp. 364–370, 2006.
- [21] Ö. Metin and S. Özkar, "Water soluble nickel(0) and cobalt(0) nanoclusters stabilized by poly(4-styrenesulfonic acid-co-maleic acid): highly active, durable and cost effective catalysts in hydrogen generation from the hydrolysis of ammonia borane," *International Journal of Hydrogen Energy*, vol. 36, pp. 1424–1432, 2011.
- [22] Y. S. Du, N. Cao, L. Yang, W. Luo, and G. Z. Cheng, "One-step synthesis of magnetically recyclable rGO supported Cu@Co core-shell nanoparticles: highly efficient catalysts for hydrolytic dehydrogenation of ammonia borane and methylamine borane," *New Journal of Chemistry*, vol. 37, pp. 3035–3042, 2013.
- [23] A. K. Figen, "Dehydrogenation characteristics of ammonia borane via boron-based catalysts (Co-B, Ni-B, Cu-B) under different hydrolysis conditions," *International Journal of Hydrogen Energy*, vol. 38, p. 9186, 2013.
- [24] Y. W. Yang, Z. H. Lu, Y. J. Hu et al., "Facile in situ synthesis of copper nanoparticles supported on reduced graphene oxide for hydrolytic dehydrogenation of ammonia borane," *RSC Advances*, vol. 4, pp. 13749–13752, 2014.
- [25] M. Chandra and Q. Xu, "Room temperature hydrogen generation from aqueous ammonia-borane using noble metal nanoclusters as highly active catalysts," *Journal of Power Sources*, vol. 168, no. 1, pp. 135–142, 2007.
- [26] M. Rakap, E. E. Kalu, and S. Özkar, "Polymer-immobilized palladium supported on TiO₂ (Pd-PVB-TiO₂) as highly active and reusable catalyst for hydrogen generation from the hydrolysis of unstirred ammonia-borane solution," *International Journal of Hydrogen Energy*, vol. 36, pp. 1448–1455, 2011.
- [27] G. P. Rachiero, U. B. Demirci, and P. Miele, "Facile synthesis by polyol method of a ruthenium catalyst supported on γ -Al₂O₃ for hydrolytic dehydrogenation of ammonia borane," *Catalysis Today*, vol. 170, no. 1, pp. 85–92, 2011.
- [28] P. X. Xi, F. J. Chen, G. Q. Xie et al., "Surfactant free RGO/Pd nanocomposites as highly active heterogeneous catalysts for the hydrolytic dehydrogenation of ammonia borane for chemical hydrogen storage," *Nanoscale*, vol. 4, pp. 5597–5601, 2012.
- [29] Q. L. Yao, W. M. Shi, G. Feng et al., "Ultrafine Ru nanoparticles embedded in SiO₂ nanospheres: highly efficient catalysts for hydrolytic dehydrogenation of ammonia borane," *Journal of Power Sources*, vol. 257, pp. 293–299, 2014.
- [30] J. M. Yan, X. B. Zhang, T. Akita, M. Haruta, and Q. Xu, "One-step seeding growth of magnetically recyclable Au@Co core-shell nanoparticles: highly efficient catalyst for hydrolytic dehydrogenation of ammonia borane," *Journal of the American Chemical Society*, vol. 132, pp. 5326–5327, 2010.
- [31] X. Yang, F. Cheng, Z. Tao, and J. Chen, "Hydrolytic dehydrogenation of ammonia borane catalyzed by carbon supported Co core-Pt shell nanoparticles," *Journal of Power Sources*, vol. 196, no. 5, pp. 2785–2789, 2011.
- [32] L. Yang, W. Luo, and G. E. Cheng, "Graphene-supported Ag-based core-shell nanoparticles for hydrogen generation in

- hydrolysis of ammonia borane and methylamine borane," *ACS Applied Materials & Interfaces*, vol. 5, pp. 8231–8240, 2013.
- [33] M. Wen, B. L. Sun, B. Zhou, Q. S. Wu, and J. Peng, "Controllable assembly of Ag/C/Ni magnetic nanocables and its low activation energy dehydrogenation catalysis," *Journal of Materials Chemistry*, vol. 22, pp. 11988–11993, 2012.
- [34] G. P. Rachiero, U. B. Demirci, and P. Miele, "Bimetallic RuCo and RuCu catalysts supported on γ -Al₂O₃. A comparative study of their activity in hydrolysis of ammonia-borane," *International Journal of Hydrogen Energy*, vol. 36, no. 12, pp. 7051–7065, 2011.
- [35] L. Yang, G. Cheng, J. Su, W. Luo, and X. Meng, "In situ synthesis of graphene supported Ag@CoNi core-shell nanoparticles as highly efficient catalysts for hydrogen generation from hydrolysis of ammonia borane and methylamine borane," *Journal of Materials Chemistry A*, vol. 1, pp. 10016–10023, 2013.
- [36] L. S. Ott and R. G. Finke, "Transition-metal nanocluster stabilization for catalysis: a critical review of ranking methods and putative stabilizers," *Coordination Chemistry Reviews*, vol. 251, pp. 1075–1100, 2007.
- [37] X. Huang, X. Y. Qi, F. Boey, and H. Zhang, "Graphene-based composites," *Chemical Society Reviews*, vol. 41, pp. 666–686, 2012.
- [38] S. Garaj, W. Hubbard, A. Reina, J. Kong, D. Branton, and J. A. Golovchenko, "Graphene as a subnanometre trans-electrode membrane," *Nature*, vol. 467, no. 7312, pp. 190–193, 2010.
- [39] Z.-H. Lu, H.-L. Jiang, M. Yadav, K. Aranishi, and Q. Xu, "Synergistic catalysis of Au-Co@SiO₂ nanospheres in hydrolytic dehydrogenation of ammonia borane for chemical hydrogen storage," *Journal of Materials Chemistry*, vol. 22, no. 11, pp. 5065–5071, 2012.
- [40] D. Q. Wu, F. Zhang, H. W. Liang, and X. L. Feng, "Nanocomposites and macroscopic materials: assembly of chemically modified graphene sheets," *Chemical Society Reviews*, vol. 41, pp. 6160–6177, 2012.
- [41] W. S. Hummers Jr. and R. E. Offeman, "Preparation of graphitic oxide," *Journal of the American Chemical Society*, vol. 80, no. 6, p. 1339, 1958.
- [42] N. I. Kovtyukhova, P. J. Ollivier, B. R. Martin et al., "Layer-by-layer assembly of ultrathin composite films from micron-sized graphite oxide sheets and polycations," *Chemistry of Materials*, vol. 11, pp. 771–778, 1999.
- [43] A. Roucoux, J. Schulz, and H. Patin, "Reduced transition metal colloids: a novel family of reusable catalysts?" *Chemical Reviews*, vol. 102, no. 10, pp. 3757–3778, 2002.
- [44] D. Astruc, F. Lu, and J. R. Aranzaes, "Nanoparticles as recyclable catalysts: the frontier between homogeneous and heterogeneous catalysis," *Angewandte Chemie International Edition*, vol. 44, no. 48, pp. 7852–7872, 2005.
- [45] P. Song, Y. Li, W. Li, B. He, J. Yang, and X. Li, "A highly efficient Co (0) catalyst derived from metal-organic framework for the hydrolysis of ammonia borane," *International Journal of Hydrogen Energy*, vol. 36, no. 17, pp. 10468–10473, 2011.
- [46] K. W. Park, J. H. Choi, B. K. Kwon, S. Lee, and A. Y. E. Sung, "Chemical and electronic effects of Ni in Pt/Ni and Pt/Ru/Ni alloy nanoparticles in methanol electrooxidation," *Journal of Physical Chemistry B*, vol. 106, pp. 1869–1877, 2002.

Review Article

Nanocatalysts for Hydrogen Generation from Ammonia Borane and Hydrazine Borane

Zhang-Hui Lu, Qilu Yao, Zhujun Zhang, Yuwen Yang, and Xiangshu Chen

College of Chemistry and Chemical Engineering, Jiangxi Normal University, Nanchang 330022, China

Correspondence should be addressed to Zhang-Hui Lu; luzh@jxnu.edu.cn and Xiangshu Chen; cxs66cn@jxnu.edu.cn

Received 15 February 2014; Accepted 26 February 2014; Published 14 April 2014

Academic Editor: Ming-Guo Ma

Copyright © 2014 Zhang-Hui Lu et al. This is an open access article distributed under the Creative Commons Attribution License, which permits unrestricted use, distribution, and reproduction in any medium, provided the original work is properly cited.

Ammonia borane (denoted as AB, NH_3BH_3) and hydrazine borane (denoted as HB, $\text{N}_2\text{H}_4\text{BH}_3$), having hydrogen content as high as 19.6 wt% and 15.4 wt%, respectively, have been considered as promising hydrogen storage materials. Particularly, the AB and HB hydrolytic dehydrogenation system can ideally release 7.8 wt% and 12.2 wt% hydrogen of the starting materials, respectively, showing their high potential for chemical hydrogen storage. A variety of nanocatalysts have been prepared for catalytic dehydrogenation from aqueous or methanolic solution of AB and HB. In this review, we survey the research progresses in nanocatalysts for hydrogen generation from the hydrolysis or methanolysis of NH_3BH_3 and $\text{N}_2\text{H}_4\text{BH}_3$.

1. Introduction

Hydrogen, as a globally accepted clean and source-independent energy carrier, has a high energy content per mass (120 MJ/kg) compared to petroleum (44 MJ/kg). It can serve as energy source for different end uses, such as hydrogen fuel cell vehicles and portable electronics [1], which will enable a secure and clean energy future. The use of hydrogen fuel cells in portable electronic devices or vehicles requires lightweight hydrogen storage or on-board hydrogen production. For vehicular applications, the US Department of Energy (DOE) has set storage targets; the gravimetric and volumetric system targets for near-ambient temperature and moderate pressure are 9.0 wt% and 81 g/L for 2015, respectively. In order to meet the targets set by the US DOE, various storage solutions have been developed and a large number of studies have been performed on the hydrogen storage materials [2–9], such as metal hydrides [2], organic hydrides [10], and metal organic frameworks [11]. However, big challenges still remain.

Chemical storage materials with low molecular weight and high gravimetric hydrogen density are highly promising as hydrogen sources [12–14]. Particularly, ammonia borane (AB, NH_3BH_3) and hydrazine borane (HB, $\text{N}_2\text{H}_4\text{BH}_3$) have attracted much attention. The simplest B-N compound of ammonia borane, which has a hydrogen capacity as high as

19.6 wt% and a low molecular weight (30.9 g/mol), exceeding that of gasoline and Li/NaBH_4 , has made itself an attractive candidate for chemical hydrogen storage applications [14]. The closely related compound hydrazine borane contains 15.4 wt% of hydrogen, which is greater than the 2015 target of US DOE, and needs to be considered as another B-N compound that can be used for the storage of hydrogen [15].

Ammonia borane and hydrazine borane can release their hydrogen through thermal dehydrogenation in solid state and solvolysis (hydrolysis and methanolysis) in solution [12]. Generally speaking, thermal dehydrogenation process requires high temperature and power consumption. In contrast, ammonia borane and hydrazine borane are able to release hydrogen via a room temperature solvolysis reaction in the presence of a suitable catalyst [5, 12, 15]. Various nanocatalysts have been tested for hydrogen generation from the solvolysis of AB and HB. This review is to serve as an up-to-date account of the recent progress in nanocatalysts for hydrogen generation from AB and HB.

2. Ammonia Borane

Ammonia borane is a colorless molecular crystal under ambient conditions with a density of 0.74 g cm^{-3} and soluble

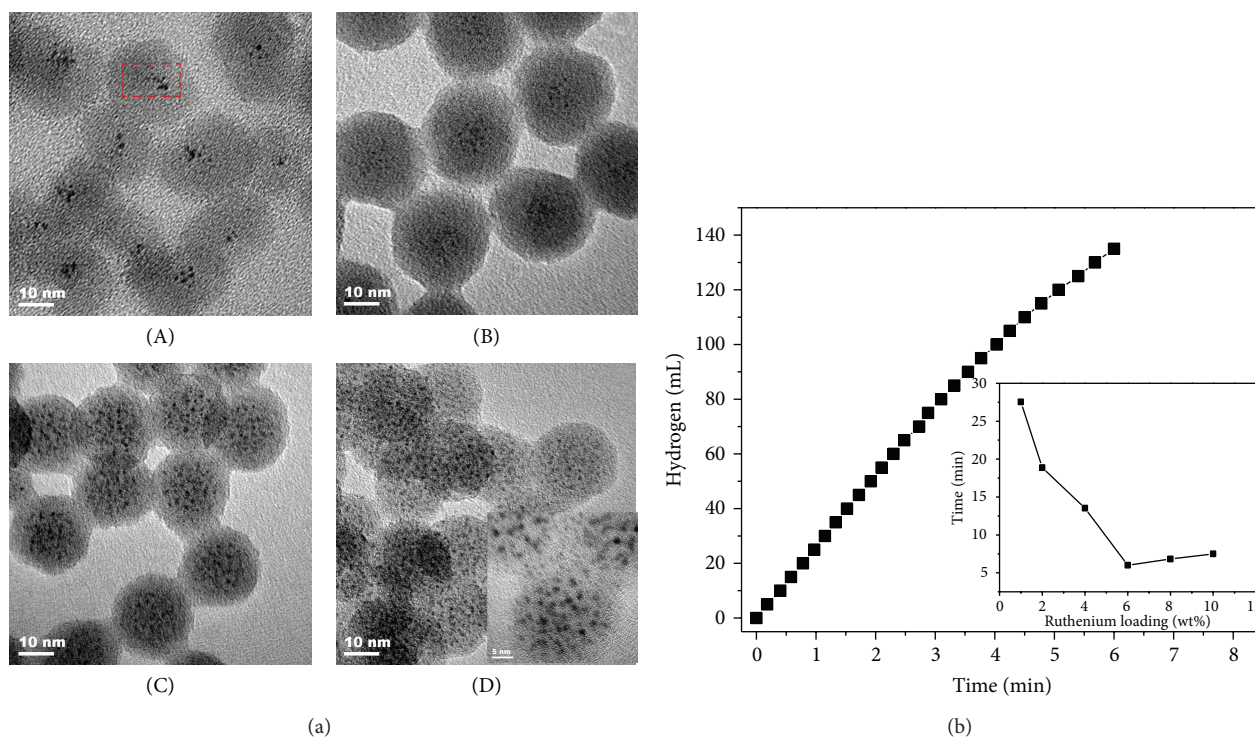


FIGURE 1: (a) Representative TEM images of the core-shell NPs Ru@SiO_2 with different Ru loadings: (A) 1 wt%, (B) 2 wt%, (C) 6 wt%, and (D) 10 wt%. (b) Hydrogen generation from hydrolysis of NH_3BH_3 (200 mM, 10 mL) by Ru@SiO_2 NPs (Ru loading = 6 wt% and $(\text{Ru}) = 0.5$ mM) at 298 K. The inset shows the reaction time versus the loading of ruthenium. Reprinted with the permission from [38]. Copyright: 2014 Elsevier.

in water and other relatively polar solvents. The hydrogen stored in AB can be released either by thermolysis in solid state and nonaqueous medium or metal catalyzed reactions in protic solvents (water and methanol) [14]. About 1 mol H_2 (i.e., 6.5 wt% H) per mol AB is released by thermal decomposition of AB under moderate conditions ($<100^\circ\text{C}$) [14]. However, to maximize the use of hydrogen in AB higher temperature is needed, which also results in the release of the side product borazine. To reduce the threshold temperature and volatile byproducts, a number of approaches have been achieved, including dehydrogenating AB on nanoscaffolding [16], catalytic modifications [17], dispersion in an ionic liquid [18], and the synthesis of derivatives (e.g., metal amidoboranes) [9].

Thermal decomposition of AB usually required high temperature and the reaction was relatively difficult to control. In contrast, the catalytic hydrolysis or methanolysis provides a more convenient strategy for hydrogen generation from AB [19–25]. In the presence of a suitable catalyst, hydrolysis of AB can release as much as 3 mol of hydrogen per mol of AB at room temperature via the following reaction:



In 2006, noble metal (Pt, Ru, and Pd) nanocatalysts were firstly found by Xu's group to have considerable activities toward hydrolytic dehydrogenation of AB [26]. The Al_2O_3 , C, and SiO_2 supported noble metals (Ru, Rh, Pd, Pt, and Au) nanoparticles were also investigated for hydrolysis of AB [27].

Among them, Pt-based nanocatalysts were found to be most active. Recently, ultrafine Pt NPs immobilized inside metal organic framework (MIL-101) were synthesized as highly efficient catalysts for hydrolytic dehydrogenation from AB [28]. Metin and coworkers found that the poly(4-styrenesulfonic acid-co-maleic acid) (PSSA-co-MA) stabilized Ru and Pd NPs having average particle size of 1.9 ± 0.5 and 3.5 ± 1.6 nm, respectively [29], were highly active catalysts for hydrolysis of AB. In addition, Ru, Rh, and Pd NPs stabilized by xonotlite [30], zeolite [31], hydroxyapatite [32], aluminum oxide [33], carbon black [34], carbon nanotubes [35], and graphene [36, 37] were also reported to have good catalytic activity in the hydrolytic dehydrogenation of AB. Particularly, the activation energy for the hydrolysis of AB in the presence of Ru/graphene was reported to be 11.7 kJ/mol [37], which is the lowest value ever reported for the same reaction. More recently, Ru NPs embedded in SiO_2 nanospheres (Ru@SiO_2 core-shell NPs) have been synthesized by us and used as catalysts for hydrolysis of AB [38], as shown in Figure 1. The characterized results show that ultrafine Ru nanoparticles (NPs) of around 2 nm are effectively embedded in the center of well-proportioned spherical and porous silica nanospheres (~ 25 nm in diameter). Interestingly, the number of Ru NPs increases inside the spherical particles of SiO_2 as the increase of Ru loading. The as-synthesized Ru@SiO_2 exhibited high catalytic activity and good durability for hydrogen generation from AB.

The noble metal-based catalysts provide significant catalytic activities in hydrogen generation from hydrolysis of

AB. For practical use, the development of low-cost and highly efficient catalysts is desired. Therefore, the development of efficient and economical nonnoble catalysts to further improve the kinetic properties is of great importance for the practical application of hydrogen generation/storage systems. The nonnoble metals (i.e., Fe, Co, Ni, and Cu) containing catalysts have been extensively investigated in the past several years [39–51], and among them, Co-based catalysts with similar structure or stabilizer were found to have the highest catalytic activity. The γ -Al₂O₃, SiO₂, and C supported nonoble metals (Co, Ni, and Cu) NPs were reported to be catalytically active, whereas supported Fe NPs were inactive for catalytic hydrolysis of AB [39]. Unexpectedly, amorphous Fe NPs synthesized by in situ reduction with AB and NaBH₄ exhibited the noble metal-like catalytic activity in the hydrolysis of AB (Fe/AB = 0.12) [40]. And then, the amorphous Co and Ni NPs were also found to have enhanced catalytic performance in comparison to their crystalline counterparts [41–43]. The high activity of the amorphous metal NPs could be attributed to the amorphous structure, which has a much greater structural distortion and therefore a much higher concentration of active sites for the reaction than its crystalline counterpart.

Unexpectedly, monodisperse 3.2 nm Ni NPs with a polycrystalline structure, supported on Ketjen carbon black [44], were shown to be a highly active catalyst for the hydrolysis of AB, with the total turnover frequency (TOF) reaching 8.8 mol⁻¹ H₂ mol⁻¹ Ni min⁻¹. But this Ni/C catalyst was not stable during the hydrolysis reaction due to the agglomeration of Ni NPs on the carbon support. 3.2 nm Ni NPs supported on SiO₂ were found by the same group to have the excellent activity and durability [45]. Recently, the Ni NPs (6.3 ± 1.7 nm) deposited into the nanoporous carbon (MSC-30) showed an excellent catalytic activity with a TOF value as high as 30.7 (mol⁻¹ H₂ mol⁻¹ Ni min⁻¹) [46], which is the highest one among all of the Ni nanocatalysts ever reported for this reaction at room temperature.

Compared to the Fe-, Co-, and Ni-based catalysts, the Cu-based catalysts were reported to have a lower catalytic activity [52–57]. Iron, cobalt, and nickel oxides formed from the corresponding metals under atmosphere condition were difficult to be reduced by weak reductants such as AB. Thus, before use to attain an effective catalyst, reductive pretreatment is necessary. However, copper oxides are easily reduced by a milder reductant (such as AB) and are exceptional catalysts working without reductive pretreatment in catalytic hydrolysis of AB. Nanostructured Cu, Cu₂O, and Cu@Cu₂O NPs synthesized by the solvated metal atom dispersion (SMAD) method were tested for the hydrolysis of AB [53]. Cu@Cu₂O showed better catalytic activity than Cu and Cu₂O. A series of Co₃O₄ NPs in which Cu was loaded on the surface were examined as catalysts in the hydrolysis of AB [54]. Their catalytic activity was dependent on the shape and size of nanosized Co₃O₄. Recently, capping of Cu₂O with organic reagents or inorganic materials was performed and tested in AB hydrolysis [55]. It was found that capping of Cu₂O with 50-facet Co₃O₄ NPs was the most active. Cu NPs supported on silica-coated cobalt(II) ferrite SiO₂/CoFe₂O₄

(CuNPs@SCF) were reported to have an initial TOF value of 2400 mol H₂ mol⁻¹ Cu h⁻¹ in air at room temperature [56]. They claimed that the TOF value was the highest one among the first row metal catalysts used in the hydrolysis of AB. It was noted that the CoFe₂O₄ of the support was not considered in the TOF test. Iron and cobalt oxides were difficult to be reduced by AB; however, they might be reduced by the Cu-H active species or H₂ generated in the hydrolysis reaction. In addition, zeolite and hydrogel networks-confined Cu NPs were synthesized and used as catalyst systems [48]. Graphene-supported Cu NPs were synthesized by us via a facile in situ procedure using AB as a reductant, which exert satisfied catalytic activity (3.61 mol H₂ mol catalyst⁻¹ min⁻¹) [57], appearing to be the best Cu nanocatalysts up to now.

Bimetallic catalysts usually show improved catalytic performance in comparison to their monometallic counterparts; due to that the metal-metal interactions in the bimetallic systems presumably account for the tuning of the bonding pattern of reactants and stabilization of reaction intermediates on the catalyst surface. A number of bimetallic catalysts [58–73], such as Au-Co [58, 59], Au-Ni [60, 61], Ru-Co [62], Ru-Ni [63, 64], Ru-Cu [62], Pt-Ni [65, 66], Pd-Co [67], Cu-Co [68, 69], Cu-Fe [70], Fe-Ni [71], Fe-Co [72], and Co-Ni [73], have been employed in the hydrolysis of AB. For example, small Au-Ni and Au-Co NPs (2–4 nm) embedded in SiO₂ nanospheres (about 15 nm) exhibited superior performance in the hydrolysis of AB [58, 61], in contrast to monometallic counterparts Au@SiO₂, Ni@SiO₂, and Co@SiO₂. After heat treatment in vacuum, multiple Au-Co NPs embedded in SiO₂ nanospheres merged into single Au-Co NPs within SiO₂, resulting in a size increase of the bimetallic core NPs [58], as shown in Figure 2. Unexpectedly, single Au-Co NPs within SiO₂ showed a better catalytic activity than multiple small bimetallic core NPs within SiO₂, which is due to the decrease in the content of basic ammine by the decomposition of metal ammine complexes (precursor) during the heat treatment.

Bimetallic NPs with core-shell architecture have attracted growing attention in recent years due to their unique and novel optical, electrical, and catalytic properties compared with their monometallic counterparts and alloys. Yan and coworkers prepared Au@Co core-shell NPs through the one-step seeding growth route with AB as the reductant [59]. By exposing a mixture of Au³⁺ and Co²⁺ precursors to the aqueous solution of AB at the same time, the core Au NPs can be formed first and then serve as the in situ seeds for successive catalytic reduction leading to the growth of outer shell Co NPs, which is to take advantage of the difference in reduction potentials of the two metal ions. A relative stronger reductant NaBH₄, instead of AB, causes the formation of Au-Co alloys. Therefore, a suitable reductant is essential in this one-step synthesis method. Compared to alloy and monometallic counterparts, the Au@Co NPs exhibited excellent catalytic activity and long-term stability in the hydrolysis of AB. A similar approach was used to synthesize bimetallic Cu@M [74], Pd@M [75], Ag@M [76], and Ru@M (M = Fe, Co, Ni) [77] and trimetallic Au@Co@Fe [78], Cu@FeNi [79], Cu@CoNi [80], Cu@FeCo [81], Cu@CoCr [82], Ag@CoFe

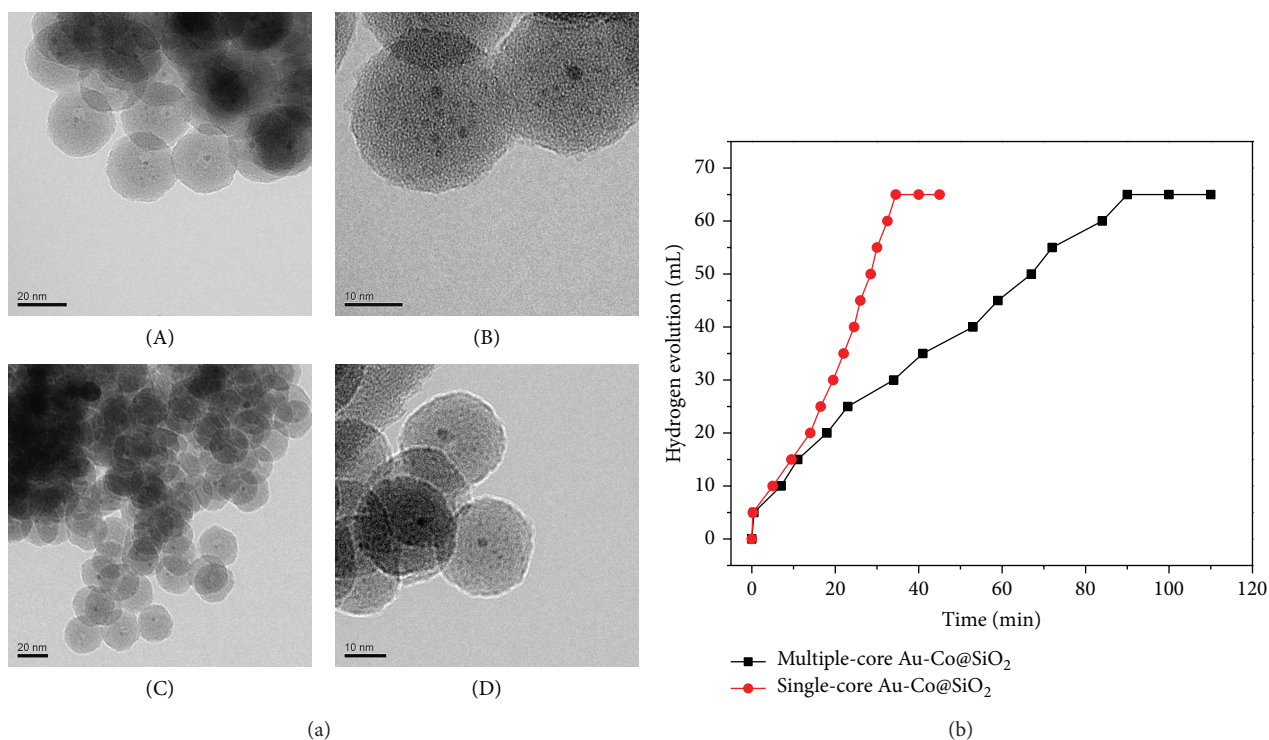


FIGURE 2: (a) Representative TEM images of the core-shell NPs Au-Cu@SiO₂ with multiple- (A-B) and single-core (C-D) NPs. (b) Hydrogen generation from hydrolysis of NH₃BH₃ (160 mM, 5 mL) by different catalysts at 298 K. Reprinted with the permission from [58]. Copyright: 2012 Royal Society of Chemistry.

[83], Ag@NiFe [83], Ag@CoNi [84], and Ag@Co@Ni [85] core shell NPs. It was found that all the obtained bimetallic or trimetallic core-shell NPs showed higher activities than the corresponding monometallic counterparts in the hydrolysis of AB. However, the Cu-Fe bimetallic nanoalloys synthesized by in situ reduction of Cu²⁺ and Fe²⁺ with AB and NaBH₄ as the reductant exhibited excellent catalytic activity, especially for Cu_{0.33}Fe_{0.67} alloy NPs outperforming the activity of monometallic counterparts and even of Cu_{0.33}@Fe_{0.67} core-shell NPs [70], as shown in Figure 3.

Besides the hydrolysis of AB, the methanolysis reaction has also taken place in the presence of suitable catalysts and has been developed to generate hydrogen. This catalytic methanolysis reaction can be expressed as follows:



The hydrogen capacity from this methanolysis reaction is estimated to be about 3.9 wt%, lower than that from the hydrolysis reaction (8.9 wt%). However, the hydrolytic system with high-concentration AB solution can lead to the release of small quantities of NH₃ along with H₂, whereas the methanolysis of AB can overcome this problem. What is more, the methanolysis product of NH₄B(OMe)₄ can be converted back to AB by treatment of lithium aluminium hydride with ammonium chloride. In 2007, RuCl₃, RhCl₃, PdCl₂, CoCl₂, NiCl₂, Pd/C, and Raney-Ni were firstly reported for the methanolysis of AB [86]. Since then, various catalysts have been examined in hydrogen generation from

the methanolysis of AB, such as PVP-stabilized Pd and Ru NPs [87, 88], Ru NPs immobilized in montmorillonite [89], Co-Co₂B, Ni-Ni₃B, Co-Ni-B [90], zeolite stabilized Rh NPs [91], and Cu@Cu₂O [53]. Recently, monodisperse 7 nm CoPd NPs with controlled compositions were synthesized and used for catalytic methanolysis of AB [92]. The CoPd NPs showed the composition-dependent methanolysis at room temperature, with Co₄₈Pd₅₂/C being the most active. More recently, various mesoporous Cu nanostructures with diverse morphologies have been synthesized by us via a facile and scalable wet-chemical method and applied as catalyst for hydrogen generation from the methanolysis of AB [93]. Among them, the flower-like mesoporous Cu showed the highest catalytic activity.

Catalytic hydrolysis or methanolysis reaction of AB proceeds with rapid kinetics in the presence of suitable metal nanocatalysts at ambient temperatures. A portable hydrogen generation system is expected to be established on the basis of the metal-catalyzed dehydrogenation of AB. A significant drawback of the hydrolysis system is that B-H bonds are converted to much stronger B-O bonds. These byproducts with B-O bonds generated during the hydrolysis reaction will be energetically costly to regenerate. Further experimental and theoretical researches toward the practical application, including the highly efficient catalyst with the low cost and long-time stability, and the regeneration of AB are highly desired. Notably, the convenience and reliability of performing AB hydrolysis reaction make it suitable for application. Like CO oxidation, the hydrolysis of AB has

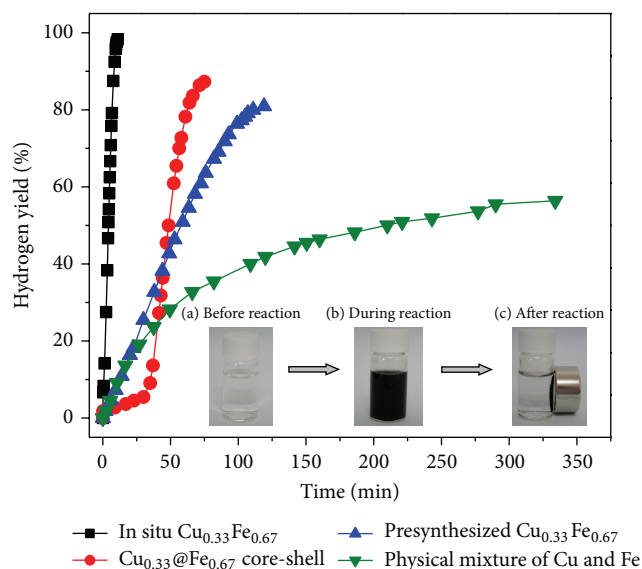


FIGURE 3: Hydrogen generation from the hydrolysis of AB in the presence of different metal nanocatalysts (metal/AB = 0.04). The insert shows photographs of the catalytic hydrolysis of AB via in situ synthesized $\text{Cu}_{0.33}\text{Fe}_{0.67}$ nanoalloy. Reprinted with the permission from [70]. Copyright: 2013 Elsevier.

already been widely used as a test (model) reaction for examining the catalytic activity of new nanomaterials.

3. Hydrazine Borane

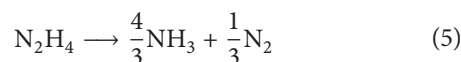
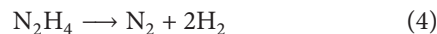
Hydrazine borane ($\text{N}_2\text{H}_4\text{BH}_3$, HB) is one of the hydrogen-dense derivatives of ammonia borane and has a gravimetric hydrogen capacity of 15.4 wt%, with 4 $\text{H}^{\delta+}$ and 3 $\text{H}^{\delta-}$. The first report concerning HB dates back to 1961 when Goubeau and Ricker published the synthesis HB by reaction of $(\text{N}_2\text{H}_5)_2\text{SO}_4$ with NaBH_4 in dioxane at room temperature [94]. Since then several studies were conducted [95–97], focusing on synthesis, decomposition, and hydrogen generating systems. Experimental spectroscopy and DFT calculation were performed to understand the structure of HB [98–100]. The release of hydrogen from HB can be obtained through either thermolysis or solvolysis. The thermal decomposition of solid HB was firstly studied by Goubeau and Ricker [94]. Hydrogen is released from HB in a controlled manner even at temperatures as high as 200°C. In the presence of LiH, 11 wt% H_2 can be released from HB at 150°C in less than an hour [15].

The hydrolysis of HB was firstly reported by Karahan and coworkers [4]. In the presence of RhCl_3 precatalyst, the aqueous solution of HB undergoes fast hydrolysis to release nearly 3.0 equivalent of H_2 with TOF = 1200 h^{-1} by hydrolysis of the BH_3 group. They also reported the preparation and characterization of the Rh NPs supported on hydroxylapatite ($\text{Ca}_{10}(\text{OH})_2(\text{PO}_4)_6$, HAP) and their catalytic hydrolysis of HB with a TOF value of 6700 h^{-1} at room temperature [101]. The poly(4-styrenesulfonic acid-co-maleic acid) (PSSMA) stabilized Ni NPs formed during the hydrolysis of HB were found to be highly active catalyst releasing 2.6–3.0 mol H_2

per mol HB with an initial TOF value of 3.05 min^{-1} [102]. However, only about 3/7 of its hydrogen was released by the hydrolysis of the BH_3 group of HB and the N_2H_4 group was not decomposed:



Like the BH_3 group of AB, the BH_3 group in HB is easy to hydrolyze in the presence of a suitable catalyst. However, unlike the NH_3 group of AB, the N_2H_4 group of HB can also be dehydrogenated in the presence of a selective catalyst (4), although this reaction is in competition with NH_3 release (5). Therefore, HB is of great interest in hydrolysis because the H atoms stored in the N_2H_4 moiety can be recovered as H_2 . The real grand challenge is to dehydrogenate the N_2H_4 group in HB under mild conditions. The key point is to find a suitable reactive and selective catalyst, active in dehydrogenating both BH_3 and N_2H_4 (6), while avoiding the occurrence of the side reaction producing NH_3 . Hence, HB could be ideally dehydrogenated into 5 mol H_2 per mol HB. Great efforts were devoted to synthesize a highly selective catalyst that can achieve the completely dehydrogenated HB [5, 104–107]. Different catalysts for catalytic dehydrogenation from HB are summarized in Table 1:



Singh and coworkers have studied the hydrogen evolution reaction from a mixture of N_2H_4 and NH_3BH_3 ($\text{N}_2\text{H}_4/\text{NH}_3\text{BH}_3 = 1:1$) in the presence of the $\text{Ni}_{0.99}\text{Pt}_{0.01}$ nanocatalysts at 25 and 50°C and proposed that the Ni-based bimetallic catalysts can be used to release five equivalents of H_2 and one equivalent of N_2 from an aqueous solution of HB [7]. Following researches confirmed this proposal [5, 104]. Hannauer and coworkers have investigated various transition metal chlorides as precursors of in situ forming catalysts by reduction in the presence of HB at 50°C [105]. They concluded that the dehydrogenation of HB is a two-step metal-catalyzed process, where first the hydrolysis of the BH_3 moiety occurs and second the decomposition of the N_2H_4 moiety takes place. The metals studied can be classified into 3 groups: (1) Fe- and Re-based catalysts, showing an incomplete conversion (<3 mol H_2) in the hydrolysis of the BH_3 group; (2) Co-, Ni-, Cu-, Pd-, Pt-, and Au-based catalysts, only active in the hydrolysis of BH_3 group (3 mol H_2 per mol BH_3 of HB); (3) Ru-, Rh-, and Ir-based catalysts, being also active in the decomposition of N_2H_4 group. With the in situ formed Rh(0) nanorods (10×4 nm), 4.1 mol ($\text{H}_2 + \text{N}_2$) per mol HB can be produced at 50°C [105]. It was found that most of the Ni-based bimetallic systems, with Pt, Ru, Rh, or Ir as the second metal, outperform the monometallic Ni, Pt, Ru, Rh, and Ir catalysts at 50°C [104]. The performance achieved is 5.1 ± 0.05 mol ($\text{N}_2 + \text{H}_2$) per mol (HB) with $\text{Ni}_{0.89}\text{Rh}_{0.11}$ (reductant: NaBH_4) and $\text{Ni}_{0.89}\text{Ir}_{0.11}$ (reductant: NH_3BH_3) nanocatalysts. Particularly, the hydrogen selectivity reaching $93 \pm 1\%$ and 5.79 ± 0.05 equiv. ($\text{H}_2 + \text{N}_2$) per

TABLE 1: Catalytic performance of metal nanocatalysts for hydrogen generation from hydrazine borane (HB).

Catalysts	Temperature ($^{\circ}\text{C}$)	$n(\text{H}_2 + \text{N}_2)/n\text{HB}$	Reference
RhCl ₃ precatalyst	25	2.93	[4]
RuCl ₃ precatalyst	25	~2.9	[4]
Rh NPs/Al ₂ O ₃	25	~2.6	[4]
Ru NPs/Al ₂ O ₃	25	~2.7	[4]
Rh NPs/hydroxyapatite	25	3	[101]
Ni NPs/PSSMA	25	2.6~3	[102]
NiCl ₂ precatalyst	25	3	[103]
Ni NPs/CTAB	50	~3.1	[5]
Pt NPs/CTAB	50	3	[5]
Ru NPs/CTAB	50	3.30 ± 0.05	[104]
Rh NPs/CTAB	50	3.30 ± 0.05	[104]
Ir NPs/CTAB	50	2.25 ± 0.05	[104]
Ni _{0.97} Pt _{0.03} NPs/CTAB	50	5.07 ± 0.05	[5]
Ni _{0.89} Pt _{0.11} NPs/CTAB	50	5.79 ± 0.05	[5]
Ni _{0.77} Pt _{0.23} NPs/CTAB	50	5.29 ± 0.05	[5]
Ni _{0.89} Rh _{0.11} NPs/CTAB	50	5.1 ± 0.05	[104]
Ni _{0.89} Ir _{0.11} NPs/CTAB	50	4 ± 0.05	[104]
Ni _{0.77} Ru _{0.23} NPs/CTAB	50	4 ± 0.05	[104]
RhCl ₃ precatalyst	50	4.1	[105]
RuCl ₃ precatalyst	50	3.3	[105]
IrCl ₃ precatalyst	50	4.4 ± 0.2	[106]
Ni NPs/CTAB	50	3.5 ± 0.1	[106]
Rh ₄ Ni NPs/CTAB	50	5.8 ± 0.2	[106]
Ni@(RhNi-alloy)/Al ₂ O ₃	50	5.74 ± 0.2	[107]
Ni ₁₅ Rh-alloy/Al ₂ O ₃	50	~4.15	[107]

HB could be released in the presence of Ni_{0.89}Pt_{0.11} NPs (reductant: NaBH₄), suggesting that 9.7 wt% of H₂ of the system HB-3H₂O is recovered [5]. More recently, Zhang and coworkers reported that the Rh₄Ni nanocatalyst exhibits high efficiency in dehydrogenation reaction of HB [106], as shown in Figure 4. The hydrogen selectivity reaches almost 100% at 50 $^{\circ}\text{C}$. Interestingly, the dehydrogenation of aqueous hydrazine borane catalyzed by the Rh₄Ni alloy cannot be simply divided into two steps. Moreover, well-dispersed core-shell Ni@(RhNi-alloy) NPs supported on Al₂O₃ exhibited high hydrogen production rate with complete hydrogen generation of HB, that is, 5.74 ± 0.2 equiv. (H₂ + N₂) per HB within 40 min at 50 $^{\circ}\text{C}$ [107].

In addition, the hydrogen of HB can be released through the catalytic methanolysis at room temperature (7). Karahan and coworkers firstly reported the metal-catalyzed methanolysis of HB using a NiCl₂ precatalyst at room temperature [103]. The methanolic solution of HB (HB/Ni ≥ 200) can release 3 equiv. of H₂ with a rate of 24 mol H₂ (mol Ni min)⁻¹ at room temperature. The catalytic methanolysis of HB can enable rapid and controllable hydrogen generation at ambient temperatures. The hydrogen capacity of this methanolysis reaction of HB is estimated to be only 3.5 wt%, lower than that of the hydrolysis reaction of HB or AB. This then makes this methanolysis reaction of HB less attractive than

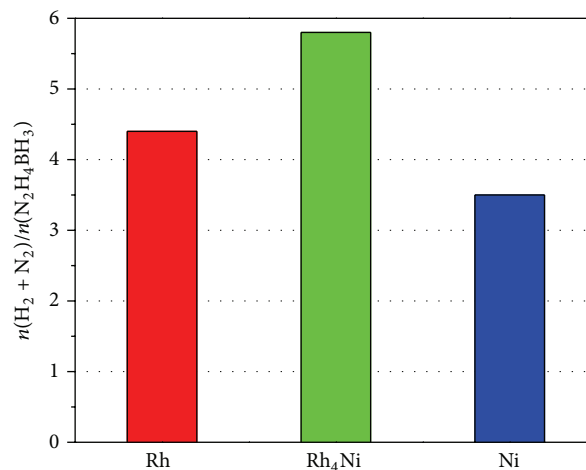
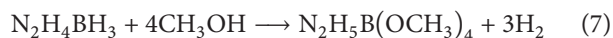


FIGURE 4: Evolution of the mol number of (H₂ + N₂) per mol of N₂H₄BH₃ in the presence of Rh, Rh₄Ni, and Ni nanocatalysts. The data are from [106].

the hydrolysis reaction. Very recently, Thoms and coworkers reported a study of the full dehydrogenation of HB to give H₂ and N₂ catalysed by a variety of group 4 metallocene alkyne complexes in THF at 25 and 50 $^{\circ}\text{C}$ [108]. It was observed

that the amount of hydrogen released is strongly dependent on both the metal and the cyclopentadienyl ligands. This work is the first example for a transition metal-catalysed homogenous process for the dehydrogenation of HB:



Hydrazine borane is a promising novel chemical hydrogen storage material because it stores 15.3 wt% (H) and can dehydrogenate in mild conditions. It can release 5 mol H₂ and 1 mol N₂ per mol HB via the hydrolysis of BH₃ moiety and the decomposition of N₂H₄ moiety in the presence of a suitable catalyst. The hydrolysis reaction system (HB-2H₂O) can ideally release 12.2 wt% H (excess GHSC) and the byproduct gas N₂ is inert towards fuel cells. Similar to AB hydrolysis, byproducts with strong B–O bonds are produced during the hydrolysis reaction, which are difficult to regenerate the B–O bonds to B–H bonds due to the stability of B–O bonds. Compared to AB, it has a higher potential owing to a superior excess gravimetric hydrogen storage capacity and the possibility to decompose the N₂H₄ moiety without liberation of NH₃. The current challenge is to find suitable reactive and selective catalysts to get a conversion of 100% while having selectivity in hydrogen of 100%.

4. Conclusion

Ammonia borane and hydrazine borane store 19.6 wt% and 15.3 wt% hydrogen, respectively, whose dehydrogenation can be approached by either pyrolysis or solvolysis. They have the potential to be used as hydrogen sources suitable for portable fuel cells. This review has summarized some recent progresses on the nanocatalysts for hydrogen generation from catalytic solvolysis of ammonia borane and hydrazine borane. Significant progresses have been obtained in the development of nanocatalysts with high efficiency and low cost, which makes AB and HB promising candidates for some specialized applications of power generation (e.g., emergency or portable power). However, big challenges still remain for practical application of nanocatalysts, such as catalyst cost, deactivation, and control of the reaction kinetics. We are looking forward to the further progress of nanocatalysts for catalytic dehydrogenation of AB and HB in the future.

Conflict of Interests

The authors declare that there is no conflict of interests regarding the publication of this paper.

Acknowledgments

Our work in this area has been supported by the National Natural Science Foundation of China (no. 21103074), the Natural Science Foundation of Jiangxi Province of China (nos. 20114BAB203010 and 20132BAB203014), Jiangxi Provincial Department of Science and Technology (no. 2011-BDH80023), and Scientific Research Foundation of Graduate School of Jiangxi Province (YC2013-S105). Zhang-Hui Lu was supported by the Sponsored Program for Cultivating Youths

of Outstanding Ability in Jiangxi Normal University, Young Scientist Foundation of Jiangxi Province (20133BCB23011), and “Ganpo Talent 555” Project of Jiangxi Province.

References

- [1] L. Schlapbach and A. Züttel, “Hydrogen-storage materials for mobile applications,” *Nature*, vol. 414, no. 6861, pp. 353–358, 2001.
- [2] P. Chen, Z. Xiong, J. Luo, J. Lin, and K. L. Tan, “Interaction of hydrogen with metal nitrides and imides,” *Nature*, vol. 420, no. 6913, pp. 302–304, 2002.
- [3] Z. Xiong, C. K. Yong, G. Wu et al., “High-capacity hydrogen storage in lithium and sodium amidoboranes,” *Nature Materials*, vol. 7, no. 2, pp. 138–141, 2008.
- [4] S. Karahan, M. Zahmakran, and S. Özkar, “Catalytic hydrolysis of hydrazine borane for chemical hydrogen storage: highly efficient and fast hydrogen generation system at room temperature,” *International Journal of Hydrogen Energy*, vol. 36, no. 8, pp. 4958–4966, 2011.
- [5] J. Hannauer, O. Akdim, U. B. Demirci et al., “High-extent dehydrogenation of hydrazine borane N₂H₄BH₃ by hydrolysis of BH₃ and decomposition of N₂H₄,” *Energy and Environmental Science*, vol. 4, no. 9, pp. 3355–3358, 2011.
- [6] K. S. Sanjay, X.-B. Zhang, and Q. Xu, “Room-temperature hydrogen generation from hydrous hydrazine for chemical hydrogen storage,” *Journal of the American Chemical Society*, vol. 131, no. 29, pp. 9894–9895, 2009.
- [7] S. K. Singh, Z.-H. Lu, and Q. Xu, “Temperature-induced enhancement of catalytic performance in selective hydrogen generation from hydrous hydrazine with Ni-based nanocatalysts for chemical hydrogen storage,” *European Journal of Inorganic Chemistry*, no. 14, pp. 2232–2237, 2011.
- [8] U. B. Demirci and P. Miele, “Cobalt in NaBH₄ hydrolysis,” *Physical Chemistry Chemical Physics*, vol. 12, no. 44, pp. 14651–14665, 2010.
- [9] Y. S. Chua, P. Chen, G. Wu, and Z. Xiong, “Development of amidoboranes for hydrogen storage,” *Chemical Communications*, vol. 47, no. 18, pp. 5116–5129, 2011.
- [10] X. Gu, Z.-H. Lu, H.-L. Jiang, T. Akita, and Q. Xu, “Synergistic catalysis of metal-organic framework-immobilized au-pd nanoparticles in dehydrogenation of formic acid for chemical hydrogen storage,” *Journal of the American Chemical Society*, vol. 133, no. 31, pp. 11822–11825, 2011.
- [11] X. Gu, Z.-H. Lu, and Q. Xu, “High-connected mesoporous metal-organic framework,” *Chemical Communications*, vol. 46, no. 39, pp. 7400–7402, 2010.
- [12] Z. H. Lu and Q. Xu, “Recent progress in boron- and nitrogen-based chemical hydrogen storage,” *Functional Materials Letters*, vol. 5, Article ID 1230001, 2012.
- [13] C. W. Hamilton, R. T. Baker, A. Staubitz, and I. Manners, “B–N compounds for chemical hydrogen storage,” *Chemical Society Reviews*, vol. 38, no. 1, pp. 279–293, 2009.
- [14] A. Staubitz, A. P. M. Robertson, and I. Manners, “Ammonia-Borane and related compounds as dihydrogen sources,” *Chemical Reviews*, vol. 110, no. 7, pp. 4079–4124, 2010.
- [15] T. Hugel, M. F. Kuhnel, and D. Lent, “Hydrazine borane: a promising hydrogen storage material,” *Journal of the American Chemical Society*, vol. 131, pp. 7444–7446, 2009.
- [16] Z. Li, G. Zhu, G. Lu, S. Qiu, and X. Yao, “Ammonia borane confined by a metal-organic framework for chemical hydrogen

- storage: enhancing kinetics and eliminating ammonia,” *Journal of the American Chemical Society*, vol. 132, no. 5, pp. 1490–1491, 2010.
- [17] C. A. Jaska, K. Temple, A. J. Lough, and I. Manners, “Transition metal-catalyzed formation of boron-nitrogen bonds: catalytic dehydrocoupling of amine-borane adducts to form aminoboranes and borazines,” *Journal of the American Chemical Society*, vol. 125, no. 31, pp. 9424–9434, 2003.
- [18] M. E. Bluhm, M. G. Bradley, R. Butterick III, U. Kusari, and L. G. Sneddon, “Amineborane-based chemical hydrogen storage: enhanced ammonia borane dehydrogenation in ionic liquids,” *Journal of the American Chemical Society*, vol. 128, no. 24, pp. 7748–7749, 2006.
- [19] U. B. Demirci and P. Miele, “Sodium borohydride versus ammonia borane, in hydrogen storage and direct fuel cell applications,” *Energy and Environmental Science*, vol. 2, no. 6, pp. 627–637, 2009.
- [20] U. Sanyal, U. B. Demirci, B. R. Jagirdar, and P. Miele, “Hydrolysis of ammonia borane as a hydrogen source: fundamental issues and potential solutions towards implementation,” *ChemSusChem*, vol. 4, no. 12, pp. 1731–1739, 2011.
- [21] B. Peng and J. Chen, “Ammonia borane as an efficient and lightweight hydrogen storage medium,” *Energy and Environmental Science*, vol. 1, no. 4, pp. 479–483, 2008.
- [22] M. Yadav and Q. Xu, “Liquid-phase chemical hydrogen storage materials,” *Energy & Environmental Science*, vol. 5, pp. 9698–9725, 2012.
- [23] H.-L. Jiang, S. K. Singh, J.-M. Yan, X.-B. Zhang, and Q. Xu, “Liquid-Phase chemical hydrogen storage: catalytic hydrogen generation under ambient conditions,” *ChemSusChem*, vol. 3, no. 5, pp. 541–549, 2010.
- [24] H.-L. Jiang and Q. Xu, “Catalytic hydrolysis of ammonia borane for chemical hydrogen storage,” *Catalysis Today*, vol. 170, no. 1, pp. 56–63, 2011.
- [25] Q. Xu and M. Chandra, “A portable hydrogen generation system: catalytic hydrolysis of ammonia-borane,” *Journal of Alloys and Compounds*, vol. 446–447, pp. 729–732, 2007.
- [26] M. Chandra and Q. Xu, “A high-performance hydrogen generation system: transition metal-catalyzed dissociation and hydrolysis of ammonia-borane,” *Journal of Power Sources*, vol. 156, no. 2, pp. 190–194, 2006.
- [27] M. Chandra and Q. Xu, “Room temperature hydrogen generation from aqueous ammonia-borane using noble metal nanoclusters as highly active catalysts,” *Journal of Power Sources*, vol. 168, no. 1, pp. 135–142, 2007.
- [28] A. Aijaz, A. Karkamkar, Y. J. Choi et al., “Immobilizing highly catalytically active Pt nanoparticles inside the pores of metal-organic framework: a double solvents approach,” *Journal of the American Chemical Society*, vol. 134, pp. 13926–13929, 2012.
- [29] Ö. Metin, Ş. Şahin, and S. Özkar, “Water-soluble poly(4-styrenesulfonic acid-co-maleic acid) stabilized ruthenium(0) and palladium(0) nanoclusters as highly active catalysts in hydrogen generation from the hydrolysis of ammonia-borane,” *International Journal of Hydrogen Energy*, vol. 34, no. 15, pp. 6304–6313, 2009.
- [30] S. Akabyrak and S. Özkar, “Ruthenium(0) nanoparticles supported on xonotlite nanowire: a long-lived catalyst for hydrolytic dehydrogenation of ammonia-borane,” *Dalton Transactions*, vol. 43, pp. 1797–1805, 2014.
- [31] M. Rakap and S. Özkar, “Zeolite confined palladium(0) nanoclusters as effective and reusable catalyst for hydrogen generation from the hydrolysis of ammonia-borane,” *International Journal of Hydrogen Energy*, vol. 35, no. 3, pp. 1305–1312, 2010.
- [32] S. Akbayrak, P. Erdek, and S. Özkar, “Hydroxyapatite supported ruthenium(0) nanoparticles catalyst in hydrolytic dehydrogenation of ammonia borane: insight to the nanoparticles formation and hydrogen evolution kinetics,” *Applied Catalysis B*, vol. 142, pp. 187–195, 2013.
- [33] G. P. Rachiero, U. B. Demirci, and P. Miele, “Facile synthesis by polyol method of a ruthenium catalyst supported on γ - Al_2O_3 for hydrolytic dehydrogenation of ammonia borane,” *Catalysis Today*, vol. 170, no. 1, pp. 85–92, 2011.
- [34] H. Y. Liang, G. Z. Chen, S. Desinan, R. Rosei, F. Rosei, and D. L. Ma, “In situ facile synthesis of ruthenium nanocluster catalyst supported on carbon black for hydrogen generation from the hydrolysis of ammonia-borane,” *International Journal of Hydrogen Energy*, vol. 37, pp. 17921–17927, 2012.
- [35] S. Akbayrak and S. Özkar, “Ruthenium(0) nanoparticles supported on multiwalled carbon nanotube as highly active catalyst for hydrogen generation from ammonia-borane,” *ACS Applied Materials & Interfaces*, vol. 4, pp. 6302–6310, 2012.
- [36] P. X. Xi, F. J. Chen, G. Q. Xie et al., “Surfactant free RGO/Pd nanocomposites as highly active heterogeneous catalysts for the hydrolytic dehydrogenation of ammonia borane for chemical hydrogen storage,” *Nanoscale*, vol. 4, pp. 5597–5601, 2012.
- [37] N. Cao, W. Luo, and G. Z. Cheng, “One-step synthesis of graphene supported Ru nanoparticles as efficient catalysts for hydrolytic dehydrogenation of ammonia borane,” *International Journal of Hydrogen Energy*, vol. 38, pp. 11964–11972, 2013.
- [38] Q. L. Yao, W. M. Shi, G. Feng et al., “Ultrafine Ru nanoparticles embedded in SiO_2 nanospheres: highly efficient catalysts for hydrolytic dehydrogenation of ammonia borane,” *Journal of Power Sources*, vol. 257, pp. 293–299, 2014.
- [39] Q. Xu and M. Chandra, “Catalytic activities of non-noble metals for hydrogen generation from aqueous ammonia-borane at room temperature,” *Journal of Power Sources*, vol. 163, no. 1, pp. 364–370, 2006.
- [40] J.-M. Yan, X.-B. Zhang, S. Han, H. Shioyama, and Q. Xu, “Iron-nanoparticle-catalyzed hydrolytic dehydrogenation of ammonia borane for chemical hydrogen storage,” *Angewandte Chemie—International Edition*, vol. 47, no. 12, pp. 2287–2289, 2008.
- [41] J.-M. Yan, X.-B. Zhang, H. Shioyama, and Q. Xu, “Room temperature hydrolytic dehydrogenation of ammonia borane catalyzed by Co nanoparticles,” *Journal of Power Sources*, vol. 195, no. 4, pp. 1091–1094, 2010.
- [42] T. Umegaki, J.-M. Yan, X.-B. Zhang, H. Shioyama, N. Kuriyama, and Q. Xu, “Preparation and catalysis of poly(N-vinyl-2-pyrrolidone) (PVP) stabilized nickel catalyst for hydrolytic dehydrogenation of ammonia borane,” *International Journal of Hydrogen Energy*, vol. 34, no. 9, pp. 3816–3822, 2009.
- [43] A. K. Figen, M. B. Piskin, B. Coskuner, and V. Imamoglu, “Synthesis, structural characterization, and hydrolysis of Ammonia Borane (NH_3BH_3) as a hydrogen storage carrier,” *International Journal of Hydrogen Energy*, vol. 38, pp. 16215–16228, 2013.
- [44] Ö. Metin, V. Mazumder, S. Özkar, and S. Sun, “Monodisperse nickel nanoparticles and their catalysis in hydrolytic dehydrogenation of ammonia borane,” *Journal of the American Chemical Society*, vol. 132, no. 5, pp. 1468–1469, 2010.

- [45] Ö. Metin, S. Özkar, and S. Sun, "Monodisperse nickel nanoparticles supported on SiO₂ as an effective catalyst for the hydrolysis of ammonia-borane," *Nano Research*, vol. 3, no. 9, pp. 676–684, 2010.
- [46] P. Z. Li, A. Aijaz, and Q. Xu, "Highly dispersed surfactant-free nickel nanoparticles and their remarkable catalytic activity in hydrolysis of ammonia borane for hydrogen generation," *Angewandte Chemie International Edition*, vol. 51, pp. 6753–6756, 2012.
- [47] T. Umegaki, Q. Xu, and Y. Kojima, "Effect of L-arginine on the catalytic activity and stability of nickel nanoparticles for hydrolytic dehydrogenation of ammonia borane," *Journal of Power Sources*, vol. 216, pp. 363–367, 2012.
- [48] M. Zahmkiran and S. Özkar, "Transition metal nanoparticles in catalysis for the hydrogen generation from the hydrolysis of ammonia-borane," *Topics in Catalysis*, vol. 56, pp. 1171–1183, 2013.
- [49] J. Du, F. Y. Cheng, M. Si, J. Liang, Z. L. Tao, and J. Chen, "Nanoporous Ni-based catalysts for hydrogen generation from hydrolysis of ammonia borane," *International Journal of Hydrogen Energy*, vol. 38, pp. 5768–5774, 2013.
- [50] N. Patel, R. Fernandes, S. Gupta, R. Edla, D. C. Kothari, and A. Mitoello, "Co-B catalyst supported over mesoporous silica for hydrogen production by catalytic hydrolysis of ammonia borane: a study on influence of pore structure," *Applied Catalysis B*, vol. 140, pp. 125–132, 2013.
- [51] Y. C. Luo, Y. H. Liu, Y. Hung, X. Y. Liu, and C. Y. Mou, "Mesoporous silica supported cobalt catalysts for hydrogen generation in hydrolysis of ammonia borane," *International Journal of Hydrogen Energy*, vol. 38, pp. 7280–7290, 2013.
- [52] S. B. Kalidindi, M. Indirani, and B. R. Jagirdar, "First row transition metal ion-assisted ammonia-borane hydrolysis for hydrogen generation," *Inorganic Chemistry*, vol. 47, no. 16, pp. 7424–7429, 2008.
- [53] S. B. Kalidindi, U. Sanyal, and B. R. Jagirdar, "Nanostructured Cu and Cu@Cu₂O core shell catalysts for hydrogen generation from ammonia-borane," *Physical Chemistry Chemical Physics*, vol. 10, no. 38, pp. 5870–5874, 2008.
- [54] Y. Yamada, K. Yano, Q. Xu, and S. Fukuzumi, "Cu/Co₃O₄ nanoparticles as catalysts for hydrogen evolution from ammonia borane by hydrolysis," *Journal of Physical Chemistry C*, vol. 114, no. 39, pp. 16456–16462, 2010.
- [55] Y. Yamada, K. Yano, and S. Fukuzumi, "Catalytic application of shape-controlled Cu₂O particles protected by Co₃O₄ nanoparticles for hydrogen evolution from ammonia borane," *Energy and Environmental Science*, vol. 5, no. 1, pp. 5356–5363, 2012.
- [56] M. Kaya, M. Zahmkiran, S. Özkar, and M. Volkan, "Copper(0) nanoparticles supported on silica-coated cobalt ferrite magnetic particles: cost effective catalyst in the hydrolysis of ammonia-borane with an exceptional reusability performance," *ACS Applied Materials & Interfaces*, vol. 4, pp. 3866–3873, 2012.
- [57] Y. W. Yang, Z. H. Lu, Y. J. Hu, Z. J. Zhang, W. M. Shi, and X. S. Chen, "Facile in situ synthesis of copper nanoparticles supported on graphene for hydrolytic dehydrogenation of ammonia borane," *RSC Advances*, vol. 4, pp. 13749–13752, 2014.
- [58] Z.-H. Lu, H.-L. Jiang, M. Yadav, K. Aranishi, and Q. Xu, "Synergistic catalysis of Au-Co@SiO₂ nanospheres in hydrolytic dehydrogenation of ammonia borane for chemical hydrogen storage," *Journal of Materials Chemistry*, vol. 22, no. 11, pp. 5065–5071, 2012.
- [59] J.-M. Yan, X.-B. Zhang, T. Akita, M. Haruta, and Q. Xu, "One-step seeding growth of magnetically recyclable AU@Co core-shell nanoparticles: Highly efficient catalyst for hydrolytic dehydrogenation of ammonia borane," *Journal of the American Chemical Society*, vol. 132, no. 15, pp. 5326–5327, 2010.
- [60] Q. L. Zhu, J. Li, and Q. Xu, "Immobilizing metal nanoparticles to metal-organic frameworks with size and location control for optimizing catalytic performance," *Journal of the American Chemical Society*, vol. 135, pp. 10210–10213, 2013.
- [61] H.-L. Jiang, T. Umegaki, T. Akita, X.-B. Zhang, M. Haruta, and Q. Xu, "Bimetallic Au-Ni nanoparticles embedded in SiO₂ nanospheres: synergetic catalysis in hydrolytic dehydrogenation of ammonia borane," *Chemistry*, vol. 16, no. 10, pp. 3132–3137, 2010.
- [62] G. P. Rachiero, U. B. Demirci, and P. Miele, "Bimetallic RuCo and RuCu catalysts supported on γ -Al₂O₃. A comparative study of their activity in hydrolysis of ammonia-borane," *International Journal of Hydrogen Energy*, vol. 36, no. 12, pp. 7051–7065, 2011.
- [63] G. Z. Chen, S. Desinan, R. Rosei, F. Rosei, and D. L. Ma, "Synthesis of Ni-Ru alloy nanoparticles and their high catalytic activity in dehydrogenation of ammonia borane," *Chemistry*, vol. 18, pp. 7925–7930, 2012.
- [64] G. Chen, S. Desinan, R. Nechache, R. Rosei, F. Rosei, and D. Ma, "Bifunctional catalytic/magnetic Ni@Ru core-shell nanoparticles," *Chemical Communications*, vol. 47, no. 22, pp. 6308–6310, 2011.
- [65] C. F. Yao, L. Zhuang, Y. L. Cao, X. P. Ai, and H. X. Yang, "Hydrogen release from hydrolysis of borazane on Pt- and Ni-based alloy catalysts," *International Journal of Hydrogen Energy*, vol. 33, no. 10, pp. 2462–2467, 2008.
- [66] F. Cheng, H. Ma, Y. Li, and J. Chen, "Ni_{1-x}Pt_x (x = 0–0.12) hollow spheres as catalysts for hydrogen generation from ammonia borane," *Inorganic Chemistry*, vol. 46, no. 3, pp. 788–794, 2007.
- [67] D. Sun, V. Mazumder, Ö. Metin, and S. Sun, "Catalytic hydrolysis of ammonia borane via cobalt palladium nanoparticles," *ACS Nano*, vol. 5, no. 8, pp. 6458–6464, 2011.
- [68] C. M. Li, J. Y. Zhou, W. Gao et al., "Binary Cu-Co catalysts derived from hydrotalcites with excellent activity and recyclability towards NH₃BH₃ dehydrogenation," *Journal of Materials Chemistry A*, vol. 1, pp. 5370–5376, 2013.
- [69] J. M. Yan, Z. L. Wang, H. L. Wang, and Q. Jiang, "Rapid and energy-efficient synthesis of a graphene-CuCo hybrid as a high performance catalyst," *Journal of Materials Chemistry A*, vol. 22, pp. 10990–10993, 2012.
- [70] Z. H. Lu, J. P. Li, A. L. Zhu et al., "Catalytic hydrolysis of ammonia borane via magnetically recyclable copper iron nanoparticles for chemical hydrogen storage," *International Journal of Hydrogen Energy*, vol. 38, pp. 5330–5337, 2013.
- [71] J.-M. Yan, X.-B. Zhang, S. Han, H. Shioyama, and Q. Xu, "Magnetically recyclable Fe-Ni alloy catalyzed dehydrogenation of ammonia borane in aqueous solution under ambient atmosphere," *Journal of Power Sources*, vol. 194, no. 1, pp. 478–481, 2009.
- [72] F. Y. Qiu, Y. J. Wang, Y. P. Wang et al., "Dehydrogenation of ammonia borane catalyzed by in situ synthesized Fe-Co nanoalloy in aqueous solution," *Catalysis Today*, vol. 170, no. 1, pp. 64–68, 2011.
- [73] W. Q. Feng, L. Yang, N. Cao et al., "In situ facile synthesis of bimetallic CoNi catalyst supported on graphene for hydrolytic dehydrogenation of amine borane," *International Journal of Hydrogen Energy*, vol. 39, pp. 3371–3380, 2014.
- [74] H.-L. Jiang, T. Akita, and Q. Xu, "A one-pot protocol for synthesis of non-noble metal-based core-shell nanoparticles under

- ambient conditions: toward highly active and cost-effective catalysts for hydrolytic dehydrogenation of NH_3BH_3 ,” *Chemical Communications*, vol. 47, no. 39, pp. 10999–11001, 2011.
- [75] J. Wang, Y. L. Qin, X. Liu, and X. B. Zhang, “In situ synthesis of magnetically recyclable graphene-supported Pd@Co core-shell nanoparticles as efficient catalysts for hydrolytic dehydrogenation of ammonia borane,” *Journal of Materials Chemistry*, vol. 22, pp. 12468–12470, 2012.
- [76] L. Yang, W. Luo, and G. Z. Cheng, “Graphene-supported Ag-based core-shell nanoparticles for hydrogen generation in hydrolysis of ammonia borane and methylamine borane,” *ACS Applied Materials & Interfaces*, vol. 5, pp. 8231–8240, 2013.
- [77] N. Cao, J. Su, W. Luo, and G. Z. Cheng, “Hydrolytic dehydrogenation of ammonia borane and methylamine borane catalyzed by graphene supported Ru@Ni core-shell nanoparticles,” *International Journal of Hydrogen Energy*, vol. 39, pp. 426–435, 2014.
- [78] K. Aranishi, H.-L. Jiang, T. Akita, M. Haruta, and Q. Xu, “One-step synthesis of magnetically recyclable Au/Co/Fe triple-layered core-shell nanoparticles as highly efficient catalysts for the hydrolytic dehydrogenation of ammonia borane,” *Nano Research*, vol. 4, no. 12, pp. 1233–1241, 2011.
- [79] H.-L. Wang, J.-M. Yan, Z.-L. Wang, and Q. Jiang, “One-step synthesis of Cu@FeNi core-shell nanoparticles: highly active catalyst for hydrolytic dehydrogenation of ammonia borane,” *International Journal of Hydrogen Energy*, vol. 37, pp. 10229–1035, 2012.
- [80] X. Y. Meng, L. Yang, N. Cao et al., “Graphenesupported trimetallic core-shell Cu@CoNi nanoparticles for catalytic hydrolysis of ammonia borane,” *ChemPlusChem*, vol. 79, pp. 325–332, 2014.
- [81] F. Y. Qiu, Y. L. Dai, L. Li et al., “Synthesis of Cu@FeCo core-shell nanoparticles for the catalytic hydrolysis of ammonia borane,” *International Journal of Hydrogen Energy*, vol. 39, pp. 436–441, 2014.
- [82] X. C. Shen, M. Dai, M. Gao, Z. B. Wang, B. Zhao, and W. P. Ding, “Core-shell structured Cu@CoCr catalyst: synthesis and catalytic performance for hydrolysis of ammonia borane aqueous solution,” *Chinese Journal of Inorganic Chemistry*, vol. 29, pp. 999–1006, 2013.
- [83] L. Yang, J. Su, W. Luo, and G. Z. Cheng, “Strategic synthesis of graphene supported trimetallic Ag-based core-shell nanoparticles toward hydrolytic dehydrogenation of amine boranes,” *International Journal of Hydrogen Energy*, vol. 39, pp. 3360–3370, 2014.
- [84] L. Yang, J. Su, X. Y. Meng, W. Luo, and G. Z. Cheng, “In situ synthesis of graphene supported Ag@CoNi core-shell nanoparticles as highly efficient catalysts for hydrogen generation from hydrolysis of ammonia borane and methylamine borane,” *Journal of Materials Chemistry A*, vol. 1, pp. 10016–10023, 2013.
- [85] F. Y. Qiu, G. Liu, L. Li et al., “Synthesis of triple-layered Ag@Co@Ni core-shell nanoparticles for the catalytic dehydrogenation of ammonia borane,” *Chemistry*, vol. 20, pp. 505–509, 2014.
- [86] P. V. Ramachandran and P. D. Gagare, “Preparation of ammonia borane in high yield and purity, methanolysis, and regeneration,” *Inorganic Chemistry*, vol. 46, no. 19, pp. 7810–7817, 2007.
- [87] H. Erdoğan, Ö. Metin, and S. Özkar, “In situ-generated PVP-stabilized palladium(0) nanocluster catalyst in hydrogen generation from the methanolysis of ammonia-borane,” *Physical Chemistry Chemical Physics*, vol. 11, no. 44, pp. 10519–10525, 2009.
- [88] H. Erdoan, Ö. Metin, and S. Özkar, “Hydrogen generation from the methanolysis of ammonia borane catalyzed by in situ generated, polymer stabilized ruthenium(0) nanoclusters,” *Catalysis Today*, vol. 170, no. 1, pp. 93–98, 2011.
- [89] H.-B. Dai, X.-D. Kang, and P. Wang, “Ruthenium nanoparticles immobilized in montmorillonite used as catalyst for methanolysis of ammonia borane,” *International Journal of Hydrogen Energy*, vol. 35, no. 19, pp. 10317–10323, 2010.
- [90] S. B. Kalidindi, A. A. Vernekar, and B. R. Jagirdar, “Co-Co₂B, Ni-Ni₃B and Co-Ni-B nanocomposites catalyzed ammonia-borane methanolysis for hydrogen generation,” *Physical Chemistry Chemical Physics*, vol. 11, no. 5, pp. 770–775, 2009.
- [91] S. Çalışkan, M. Zahmakiran, and S. Özkar, “Zeolite confined rhodium(0) nanoclusters as highly active, reusable, and long-lived catalyst in the methanolysis of ammonia-borane,” *Applied Catalysis B: Environmental*, vol. 93, no. 3–4, pp. 387–394, 2010.
- [92] D. H. Sun, V. Mazumder, O. Metin, and S. H. Sun, “Methanolysis of ammonia borane by CoPd nanoparticles,” *ACS Catalysis*, vol. 2, pp. 1290–1295, 2012.
- [93] Q. L. Yao, M. Huang, Z. H. Lu et al., “Methanolysis of ammonia borane by shape-controlled mesoporous copper nanostructures for hydrogen generation,” submitted to *Nano Energy*.
- [94] V. J. Goubeau and E. Ricker, “Borinhydrazine und seine pyrolyseprodukte,” *Zeitschrift für Anorganische und Allgemeine Chemie*, vol. 310, pp. 123–142, 1961.
- [95] C. Cakanyildirim, E. Petit, U. B. Demirci et al., “Gaining insight into the catalytic dehydrogenation of hydrazine borane in water,” *International Journal of Hydrogen Energy*, vol. 37, pp. 15983–15991, 2012.
- [96] V. S. Nguyen, S. Swinnen, J. Leszczynski, and M. T. Nguyen, “Formation and hydrogen release of hydrazine bisborane: transfer vs. attachment of a borane,” *Physical Chemistry Chemical Physics*, vol. 13, no. 14, pp. 6649–6656, 2011.
- [97] R. Moury, G. Moussa, U. B. Demirci et al., “Hydrazine borane: synthesis, characterization, and application prospects in chemical hydrogen storage,” *Physical Chemistry Chemical Physics*, vol. 14, no. 5, pp. 1768–1777, 2012.
- [98] Z. Qian, B. Pathak, and R. Ahuja, “Energetic and structural analysis of $\text{N}_2\text{H}_4\text{BH}_3$ inorganic solid and its modified material for hydrogen storage,” *International Journal of Hydrogen Energy*, vol. 38, pp. 6718–6725, 2013.
- [99] N. Vinh-Son, S. Swinnen, M. H. Matus, M. T. Nguyen, and D. A. Dixon, “The effect of the NH_2 substituent on NH_3 : hydrazine as an alternative for ammonia in hydrogen release in the presence of boranes and alanes,” *Physical Chemistry Chemical Physics*, vol. 11, no. 30, pp. 6339–6344, 2009.
- [100] G. Rasul, G. K. S. Prakash, and G. A. Olah, “B–H bond protonation in mono- and diprotonated borane complexes H_3BX ($\text{X} = \text{N}_2\text{H}_4, \text{NH}_2\text{OH}, \text{and H}_2\text{O}_2$) involving hypercoordinate boron,” *Inorganic Chemistry*, vol. 38, pp. 5876–5878, 1999.
- [101] D. Elik, S. Karahan, M. Zahmakran, and S. Özkar, “Hydrogen generation from the hydrolysis of hydrazine-borane catalyzed by rhodium(0) nanoparticles supported on hydroxyapatite,” *International Journal of Hydrogen Energy*, vol. 37, no. 6, pp. 5143–5151, 2012.
- [102] S. Sencanli, S. Karahan, and S. Ozkar, “Poly(4-styrenesulfonic acid-co-maleic acid) stabilized nickel(0) nanoparticles: highly active and cost effective catalyst in hydrogen generation from the hydrolysis of hydrazine borane,” *International Journal of Hydrogen Energy*, vol. 38, pp. 14693–14703, 2013.

- [103] S. Karahan, M. Zahmakiran, and S. Özkar, "Catalytic methanolysis of hydrazine borane: a new and efficient hydrogen generation system under mild conditions," *Dalton Transactions*, vol. 41, no. 16, pp. 4912–4918, 2012.
- [104] Ç. Çakanyildirim, U. B. Demirci, T. Şener, Q. Xu, and P. Miele, "Nickel-based bimetallic nanocatalysts in high-extent dehydrogenation of hydrazine borane," *International Journal of Hydrogen Energy*, vol. 37, pp. 9722–9729, 2012.
- [105] J. Hannauer, O. Akdim, U. B. Demirci et al., "High-extent dehydrogenation of hydrazine borane $N_2H_4BH_3$ by hydrolysis of BH_3 and decomposition of N_2H_4 ," *Energy and Environmental Science*, vol. 4, no. 9, pp. 3355–3358, 2011.
- [106] D. C. Zhang, K. Aranishi, A. K. Singh, U. B. Demirci, and Q. Xu, "The synergistic effect of Rh-Ni catalysts on the highly-efficient dehydrogenation of aqueous hydrazine borane for chemical hydrogen storage," *Chemical Communications*, vol. 48, pp. 11945–11947, 2012.
- [107] C. M. Li, Y. B. Dou, J. Liu et al., "Synthesis of supported Ni@ (RhNi-alloy) nanocomposites as an efficient catalyst towards hydrogen generation from $N_2H_4BH_3$," *Chemical Communications*, vol. 49, pp. 9992–9994, 2013.
- [108] J. Thoms, M. Klahn, A. Spannenberg, and T. Beweries, "Group 4 metallocene catalysed full dehydrogenation of hydrazine borane," *Dalton Transactions*, vol. 42, pp. 14668–14672, 2013.

Research Article

Formulation of Synthesized Zinc Oxide Nanopowder into Hybrid Beads for Dye Separation

H. Shokry Hassan,¹ M. F. Elkady,^{2,3} A. H. El-Shazly,² and Hisham S. Bamufleh⁴

¹ Electronic Materials Researches Department, Advanced Technology and New Materials Researches Institute, City of Scientific Researches and Technological Applications, New Borg El-Arab City, Alexandria 21934, Egypt

² Chemical and Petrochemical Engineering Department, Egypt-Japan University of Science and Technology, New Borg El-Arab City, Alexandria 21934, Egypt

³ Fabrication Technology Department, Advanced Technology and New Materials Research Institute (ATNMRI), City of Scientific Research and Technology Applications, Alexandria 21934, Egypt

⁴ Department of Chemical & Materials Engineering, Faculty of Engineering, King Abdulaziz University, P.O. Box 80204, Jeddah 21589, Saudi Arabia

Correspondence should be addressed to M. F. Elkady; maroelkady@yahoo.com

Received 11 December 2013; Revised 11 February 2014; Accepted 28 February 2014; Published 9 April 2014

Academic Editor: Shao-Wen Cao

Copyright © 2014 H. Shokry Hassan et al. This is an open access article distributed under the Creative Commons Attribution License, which permits unrestricted use, distribution, and reproduction in any medium, provided the original work is properly cited.

The sol-gel prepared zinc oxide nanopowder was immobilized onto alginate-polyvinyl alcohol polymer blend to fabricate novel biocomposite beads. Various physicochemical characterization techniques have been utilized to identify the crystalline, morphological, and chemical structures of both the fabricated zinc oxide hybrid beads and their corresponding zinc oxide nanopowder. The thermal stability investigations demonstrate that ZnO nanopowder stability dramatically decreased with its immobilization into the polymeric alginate and PVA matrix. The formulated beads had very strong mechanical strength and they are difficult to be broken up to 1500 rpm. Moreover, these hybrid beads are chemically stable at the acidic media (pH < 7) especially within the pH range of 2–7. Finally, the applicability of the formulated ZnO hybrid beads for C.I. basic blue 41 (BB41) decolorization from aqueous solution was examined.

1. Introduction

The huge increment in pollution level urges scientific community to research with more and more dedication in environmental remediation. One of the important classes of the pollutants is dyes; dyes have been extensively used in industries, such as textile, paper, printing, cosmetics, plastics, and rubber, for the coloration of products [1, 2]. They usually have a synthetic origin and are based on complex aromatic structures which make them stable and difficult to be biodegraded [1]. A small quantity of dyes can color large water bodies, which not only affects aesthetic merit but also reduces light penetration and photosynthesis. Moreover, many dyes are toxic in nature with suspected carcinogenic

and mutagenic effects that affect aquatic biota and also human beings [3, 4]. Therefore, the decolorization of dye-containing effluents is considered compulsory prior to discharge by the environmental regulations in most of the countries [5, 6]. In this respect, C.I. basic blue 41 (BB41) is a mono-azo-basic dye of bright blue hue; it is particularly suitable for dyeing acrylic substrates and can also be applied to some polyamide and polyester types, viscose, cotton, and wool. It is also effective as strainer for the identification of avian leukocytes and blood and bone-marrow cells [7]. This basic dye may be considered as one of the most toxic substances. It can cause eye burns which may be responsible for permanent injury to the eyes of human and animals. On inhalation, it can give rise to short periods of rapid or difficult breathing while ingestion through

the mouth produces a burning sensation and may cause nausea, vomiting, profuse sweating, mental confusion, and methemoglobinemia [8, 9]. Consequently, BB41 is selected as one of the simulated dye pollutants to assess its sorption behavior to be eliminated from polluted wastewaters.

Different techniques have been reported by various investigations for the removal of dyes from water and wastewater, including biological processes, combined chemical and biochemical processes, chemical oxidation, adsorption, coagulation, and membrane treatments; each of these has specific advantages and disadvantages. Among these several conventional chemical and physical methods, the adsorption process is one of the effective techniques that have been successfully employed for dye removal from wastewater. Adsorption is a classical technique which involves a variety of highly porous adsorbents to ensure adequate surface area for adsorption [10]. Accordingly, many porous adsorbent materials have been tested on the possibility for dye removal such as activated carbon [11], peat, chitin, and silica [12]. However, intraparticle diffusion associated with porous adsorbents may reduce the adsorption rate and capacity [13]. Consequently, there is a need to develop alternative novel adsorbents with both large surface area and small diffusion resistance characteristics. Recent advances in the field of nanotechnology offer a class of promising adsorbents that are ultrafine and characterized by their large surface area. Nanosized metal oxide nanoparticles have received considerable attention due to the simple procedure involved in synthesis with low capital cost compared to commercially available activated carbon. Diverse inorganic metal oxides may serve as good adsorbents, due to their relatively high surface area and thermal and chemical stabilities. Among these metal oxide nanopowders, Zinc oxide was distinguished by its significant sorption properties toward the polluted harmful ions presence in wastewater [14].

A wide number of methods have been used to prepare ZnO nanopowders, including homogeneous precipitation in aqueous solution of Zn^{2+} cations, hydrothermal synthesis, microwave synthesis, solution combustion, pulsed laser deposition, emulsion precipitation, ultrasonic atomization, spray pyrolysis, freeze-drying, and sol-gel processes [15–17]. Regarding the various stated preparation techniques, sol-gel represents one of the fastest growing fields of contemporary chemistry. Accordingly, this preparation technique was utilized for synthesis of ZnO nanoparticles. This is due to the fact that this preparation technique offers several advantages such as being easy, fast, and able to deform materials into complex geometries in a gel state with high purity [18]. Consequently, zinc oxide nanoparticles can be easily prepared using sol-gel technique. In spite of the prepared zinc oxide nanopowder having good adsorbent for dyes, however it is difficult to be handled in the adsorption techniques due to its small size and hydrophobic nature. In order to overcome this limitation of zinc oxide nanopowder, incorporation of a polymer material with the inorganic metal oxide provides an innovative class of hybrid materials [19]. Many investigators have introduced organic-inorganic hybrid changers consisting of inorganic sorbent materials and organic binding matrices [20, 21].

These materials have conjugated the mechanical properties of the organic polymers with the intrinsic properties of the inorganic compound creating a new class of hybrid organic-inorganic materials with improvement in mechanical properties, chemical inertness, high temperature and radiation stability, reproducibility, and high selectivity for harmful ions. Consequently, inorganic zinc oxide sorbent material may be encapsulated into porous polymeric matrices through the immobilization technique. The porous structure of polymer matrices allows the harmful ions to diffuse into the internal pores and be adsorbed into the internal sorbent materials. So, the major focus was to select a suitable polymeric material for the immobilization of the synthesized ZnO nanopowder. Various polymer matrices have been employed as immobilized matrix such as alginate, agar, polyacrylamide, chitosan, carrageenan, cellulose acetate, and polyvinyl alcohol (PVA) [22]. PVA may be considered as the largest synthetic water soluble polymer produced in the world and its application as an immobilized polymer matrix was initiated about 20 years ago [23, 24]. PVA is a polymer of great interest because of its desirable characteristics specifically for various pharmaceutical and biomedical applications [23]. PVA offers various advantages over the conventional alginate hydrogels including lower cost, higher durability, and chemical stability and its nontoxicity to viable cells [25]. However, the agglomeration problem that is associated with PVA gel beads is still the main drawback for utilizing PVA as immobilizing polymer matrix. Nevertheless, it is still used by many researchers through adding sodium alginate; thus the agglomeration of PVA gel beads can be reduced [26]. The combination of sodium alginate and PVA has already been reported in PVA-boric acid method, but usually the concentration of sodium alginate was below 0.4%. Generally, sodium alginate used at such low concentration would prevent the agglomeration of PVA gel beads [27]. In the present investigation, we are concerned with formulation of the synthesized zinc oxide nanopowder into innovative biocomposite beads, through the incorporation of ZnO into polymer blend of alginate and PVA. According to our best knowledge, this is the first report that deals with ZnO nanoparticles immobilized into mixed polymer matrices composed of alginate and PVA. So, the main focus of this study is to investigate the physicochemical properties of the fabricated zinc oxide biocomposite beads and their corresponding zinc oxide nanopowder. The feasibility of the formulated hybrid beads towards dye decolorization will be assigned. The variation in the operational parameters that affect behavior of the fabricated biocomposite beads will be examined.

2. Materials and Methods

2.1. Materials. The selected polluted dye model is the azo dye C.I. basic blue 41 (BB41) that was provided by Ciba Specialty Chemicals Inc. and was utilized without further purification; its characteristics and molecular structure are investigated in Table 1. A stock solution of 1000 mg/L was prepared by dissolving 1 g of dye powder in distilled water to prevent and

TABLE I: Chemical properties of C.I. basic blue 41 dye.

Molecular structure	Molecular formula	C.I. number	Chemical class	Molecular weight (g/mol)
	C ₂₀ H ₂₆ N ₄ O ₆ S ₂	11105	azo	482.57

minimize possible interferences and then used for further studies by diluting as required. Zinc chloride, sodium alginate, polyvinyl alcohol, hydrochloric acid, sodium hydroxide, ethanol, and other reagents used in this work were all A.R. grade reagents.

2.2. Synthesis of ZnO Nanopowder Using Sol-Gel Precipitation Technique. An ammonium hydroxide solution (1M) was added dropwise into a solution of 0.2 M zinc chloride in the presence of polyvinylpyrrolidone (PVP) with constant stirring till the solution pH is adjusted at 10. The reaction temperature of the solution mixture was maintained at 70°C under constant stirring overnight. The formed fine powder was separated and washed several times with distilled water and ethanol. The washed precipitate was then dried by gentle heating at 50°C. Then the product is ground into fine powder to be immobilized into the polymer matrix.

2.3. Fabrication of ZnO Hybrid Beads (ZOHB). 25 g of PVA has been dissolved in 250 mL of distilled water in the presence of known weight of sodium alginate until attaining clean aqueous solution. After complete dissolution of polymer matrix, 20 g from the synthesized zinc oxide nanopowder has been dispersed into the previous solution. The suspended ZnO slurry was stirred continuously using the homogenizer to ensure the complete nano-zinc oxide dispersion into the polymeric solution mixture. The resultant ZnO polymeric slurry was pumped into the cross-linker solution mixture composed of 3% CaCl₂ and 5% boric acid to be formulated into microbeads. The formed spherical beads were maintained under gentle stirring overnight to complete their gelation. The formulated beads were separated from the cross-linker solution and washed several times with distilled water and then dried at 40°C.

2.4. Characteristic Features of Fabricated ZnO Hybrid Beads and Their Corresponding Nano-Zinc Oxide. Various physicochemical characterization techniques have been utilized to identify the crystalline, morphological, and chemical structures for both the fabricated zinc oxide hybrid beads and their corresponding zinc oxide nanopowder.

In order to identify the main functional groups responsible for the dye sorption process, FT-IR spectra (Shimadzu

FTIR-8400 S) of synthesized zinc oxide before and after its fabrication into hybrid beads were examined using KBr disc technique over the wide wavelength range 500–4000 cm⁻¹.

The morphological structures of the synthesized nano-zinc oxide and its polymeric hybrid beads were detectable using JEOL JSM 6360LA scanning electron microscope (SEM). Chemical elemental analyses of these two samples were performed using the energy-dispersive X-ray spectroscopy (EDX) unit that combined with SEM equipment.

The crystal structures of both zinc oxide nanopowder and its polymeric hybrid were determined using X-ray diffractometry (Shimadzu-7000 diffractometer) with Cu K α radiation beam ($\lambda = 0.154060$ nm).

The thermal properties of both zinc oxide nanopowder and its polymeric hybrid were investigated over temperature range from ambient condition up to 800°C with a heating rate of 20°C/min in flowing N₂ using Thermal Gravimetric Analysis (Shimadzu TGA-50).

The BET surface area of nano-zinc oxide and its polymeric hybrid was calculated from the nitrogen gas adsorption using the Chemisorption-Physisorption analyzer (Beckman Coulter AS3100, USA).

The chemical stability of the prepared zinc oxide polymeric hybrid toward the hydrogen ion concentration was determined. Different acidic solutions in pH range 1–5 were prepared using hydrochloric acid. On the other hand, different alkaline solutions in pH range 8–12 were prepared using sodium hydroxide. The synthesized hybrid beads were immersed into these different acidic and alkaline solutions for 48 h. After this period the wetted beads were separated and then rinsed with distilled water and dried at 60°C until reaching constant weight [28].

The mechanical stability of the prepared zinc oxide polymeric hybrid beads was assigned using mechanical strength test. This test was performed using homemade designed plexiglass beaker divided into 4 equal segments through baffles (1 cm width). The cylindrical dimension of the beaker was 11 cm in diameter and 13 cm in height. One gram from zinc oxide hybrid beads was added to the beaker followed by 200 mL distilled water. The hybrid beads were agitated in the beaker for 72 h at different controlled mixing speed that varied from 500 rpm to 3000 rpm. The turbidity measurements were detected after the mixing period for each mixing speed. The remaining beads after mixing were

counted and then dried in a desiccator until no further change in weight was detected. Each run was performed in triplicate and the average measurements were recorded.

2.5. Evaluation of the Decolourization Behaviour of Fabricated ZnO Hybrid Beads. The decolourization availability of BB41 dye onto the fabricated ZOHB was evaluated through the batch adsorption technique using shaking incubator. Stock solution of BB41 dye (100 mg/L) was prepared. In a typical experiment, a known amount of dry ZnO hybrid beads was mixed with 25 mL of dye solution with specific concentration at conical flask and kept under constant agitation of 400 rpm for 60 minutes in the shaker incubator at different temperatures. After finishing the mixing period, the residual dye concentration was determined calorimetrically through measuring the absorbance of the dye solution at 610 nm using a UV-vis double beam spectrophotometer (Labomed model). The corresponding dye concentration in the supernatant solution was obtained using a previously constructed calibration graph. All the experiments measurements were carried out in duplicate and mean values are presented. The percentage decolourization efficiencies were then obtained using the following equation:

$$\% \text{ dye decolourization} = \left(\frac{C_0 - C}{C} \right) * 100, \quad (1)$$

where C_0 is the initial dye concentration (mg/L) and C is the final dye concentration in aqueous solution after phase separation (mg/L).

The ZOHB adsorption capacities were evaluated using the following mass balance equation:

$$Q \text{ (mg/g)} = \frac{V(C_0 - C)}{M}, \quad (2)$$

where Q is the stain uptake capacity (mg/g), C_0 and C are the initial and final dye concentrations (mg/L), V is the volume of dye solution (mL), and M is the ZOHB mass (g).

The equilibrium behavior of the basic dye adsorption process onto the fabricated beads was established using Langmuir and Freundlich equilibrium isotherm models. Moreover the kinetic of dye adsorption process was tested using the pseudo-first- and pseudo-second-order kinetic models.

3. Result and Discussion

3.1. Characteristic Features of Fabricated ZnO Hybrid Beads and Their Corresponding Nano-Zinc Oxide. Comparable investigation was established between the fabricated zinc oxide polymeric hybrid and its corresponding zinc oxide nanopowder to declare their characteristic properties.

3.1.1. Crystalline Structure Identification Using XRD. The XRD patterns of pure zinc oxide nanopowder (Figure 1(A)) clearly demonstrated that all the diffraction peaks of the formed ZnO nanoparticles can be indexed to the hexagonal wurtzite structure with high degree of crystallinity [29],

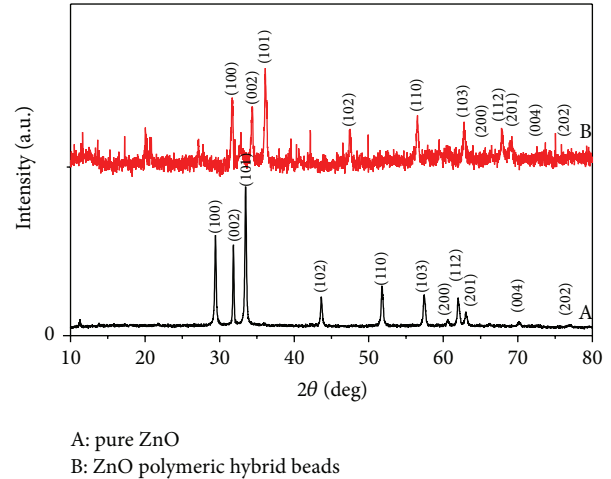


FIGURE 1: XRD spectrums of synthesized pure zinc oxide and its corresponding polymeric hybrid.

which is in good agreement with the value obtained by JCPDS (card number 01-089-1397). Comparing this spectrum with the ZnO reference card, no impurity phase was detected in the XRD pattern of the synthesized ZnO. The main ZnO characteristic diffraction peaks and their orientation planes for the prepared ZnO and its polymeric hybrid were indexed in Figure 1.

However, after immobilizing the prepared nano-zinc oxide onto the polymeric matrix composed of alginate and PVA blend to fabricate the hybrid beads, a new broad peak at $2\theta = 19.6^\circ$ has appeared (Figure 1(B)) beside the previous identified ZnO peaks. The broadening of this peak illustrates the amorphous nature of alginate/PVA polymer blend. This amorphous behaviour may be due to any weak interaction that happened between the two polymers on blending [30]. In fact, PVA structure is collapsed during the complex formation generating the small crystallites and hence an increase in interconnection between two phases leads to the broadening of the peak. This characteristic peak confirms alginate and PVA blending, where if the two polymers have not blended properly, all the respective peaks of both the polymers would have been seen separately which is not present at this case study [31]. Noticeable peak intensities decayed at the fabricated hybrid beads for all ZnO characteristic peaks compared with that presented at the pure zinc oxide nanopowder. This reduction in peaks intensities for the fabricated ZnO hybrid beads was associated with XRD spectrum distortions. This may be attributed to the introduction of the amorphous polymer blend shell matrix that immobilized the nanopowder zinc oxide [32].

3.1.2. Chemical Structure Identification Using FTIR. FTIR analysis technique is utilized to recognize the materials chemical bonding. It is used to identify the elemental constituents of a material. The characteristic peaks exhibited by

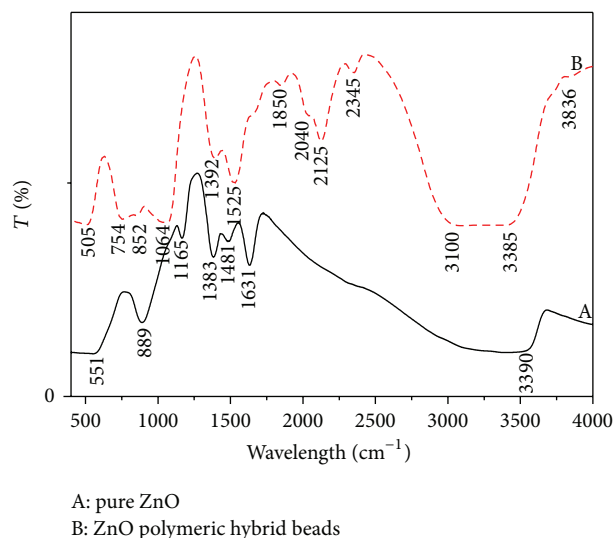


FIGURE 2: FTIR analysis of synthesized pure zinc oxide and its corresponding polymeric hybrid.

FTIR spectrums of both zinc oxide hybrid beads and their corresponding nano-zinc oxide were investigated in Figure 2.

All zinc oxide characteristic peaks appeared at the ZnO polymeric hybrid with slight peaks shifting due to presence of the polymer blend matrix that confirm ZnO immobilization onto the polymeric matrix. Where the two FTIR spectrums of ZnO nanoparticles and their polymeric hybrid showed identical characteristic peaks at about 551 cm^{-1} in case of pure ZnO which corresponds to the Zn–O bond stretching vibration that shifted to about 505 cm^{-1} for the polymeric hybrid [33]. Moreover the medium to weak bands at 889 cm^{-1} for pure ZnO and 852 cm^{-1} at ZnO polymeric hybrid are assigned to the vibrational frequencies due to the change in the microstructural features into Zn–O lattice [34]. The weak peaks sited at 1165 cm^{-1} and 1383 cm^{-1} for pure ZnO that shifted to 1064 cm^{-1} and 1392 cm^{-1} for polymeric hybrid were regarding presence of C–O and C–H vibration modes of PVP, which acts as a capping agent for synthesis of nano-zinc oxide [35]. The remaining ZnO characteristic peaks around 1600 cm^{-1} and 3400 cm^{-1} are due to normal polymeric O–H stretching vibration of the H_2O small amount inside the ZnO nanocrystals [36]. Considering the difference between the two spectrums of ZnO and its polymeric hybrid, two new peaks appear at 3100 cm^{-1} and 1850 cm^{-1} for the ZnO polymeric hybrid that assigned the interaction between alginate and PVA in its polymer blend matrix [31]. It is worth mentioning that the bands appearing in the region of 3100 cm^{-1} belong to all types of hydrogen bonded OH groups at the polymer blend and the bands appearing at 1850 cm^{-1} belong to all carboxylate groups present at the polymer matrix [37]. This FTIR analysis strongly supports the idea that hydrogen bonding could be formed between the hydroxyl groups of PVA and that group of alginate that composes the immobilized polymer matrix [37].

TABLE 2: EDX elemental analysis of formulated zinc oxide hybrid beads.

Elements	% atomic
C	29.75
O	51.4
Zn	13.86
Na	2.51
Ca	1.38
B	1.1

3.1.3. Morphological Structure Identification Using SEM. SEM imaging is one of the promising techniques for the topography study of the prepared samples, where it gives important information regarding the shape and size of the synthesized particles. The surface morphology of the prepared zinc oxide and its corresponding polymeric hybrid beads is illustrated in Figures 3(a)–3(c). The first entire SEM picture (Figure 3(a)) clearly showed that the as-prepared zinc oxide produced from the sol-gel technique composed of agglomerated nanoparticles with spherical shapes.

The average size of these sphere particles is of nanometer size order with average diameter equivalent to 40 nm. The incorporation of these ZnO nanoparticles onto the polymeric hybrid matrix beads was explored in the beads cross-section image (Figure 3(b)). The small lighted spots presence in the bead cross-section area is repressive for ZnO nanoparticles that immobilized onto alginate and PVA polymeric matrix. The homogeneity and uniform distribution of ZnO nanoparticles onto the polymeric matrix were observed from this image. Also, this image investigated clearly the porous structure of the formulated ZnO polymeric hybrid beads. The macroporous structures of the formulated ZnO hybrid beads were obviously clear from Figure 3(c). This micrograph investigates the open pores and cavities that are present inside the hybrid polymeric chains, which serve as host places for dye molecules entrapment during the dye sorption process onto the ZnO hybrid beads. In order to confirm the main constituents of the prepared hybrid beads, quantitative elemental of these beads were performed using EDX analysis. Table 2 investigates the atomic percentages of the hybrid beads elemental composition. It was indicated from this table that the beads are composed mainly of C, O, and Zn and traces from Ca, Na, and B ions. This is confirming that the main components of the hybrid beads are the host mixed polymer matrix of alginate and PVA and the immobilized ZnO nanoparticles.

3.1.4. Surface Area Identification Using BET. The nitrogen adsorption-desorption isotherms of zinc oxide nanopowder and its corresponding hybrid beads distinguish that both prepared materials are characterized by their high surface area. However, the calculated specific surface area of the formulated ZnO beads that is equal to $22.8\text{ m}^2/\text{g}$ is comparatively less than that of the free ZnO nanopowder that is equivalent to $64.9\text{ m}^2/\text{g}$. Also, the calculated pore volume of $0.132\text{ cm}^3/\text{g}$ value for the free powdered ZnO is much higher

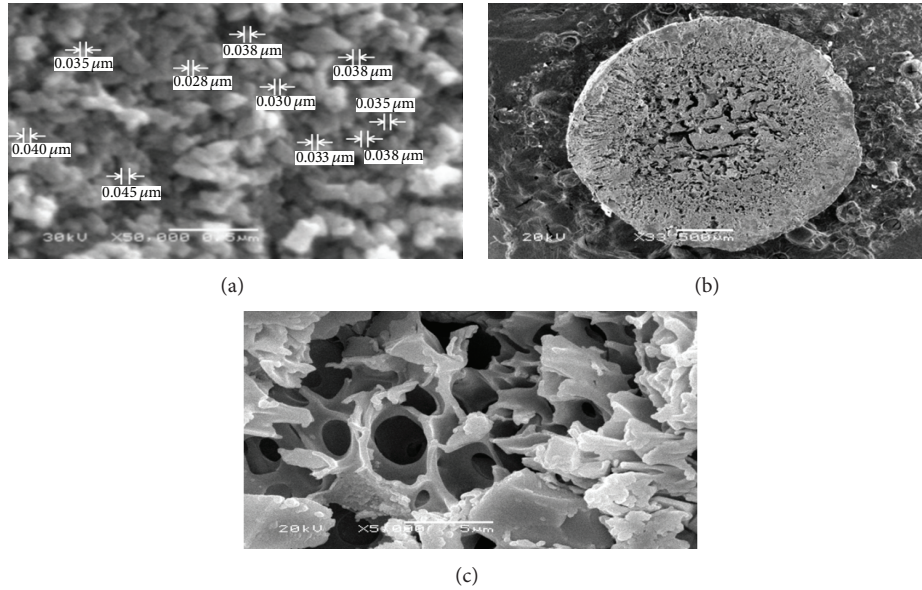


FIGURE 3: The SEM micrographs of (a) pure ZnO nanopowder, (b) cross-section of ZnO polymeric hybrid bead, and (c) internal structure ZnO polymeric hybrid beads.

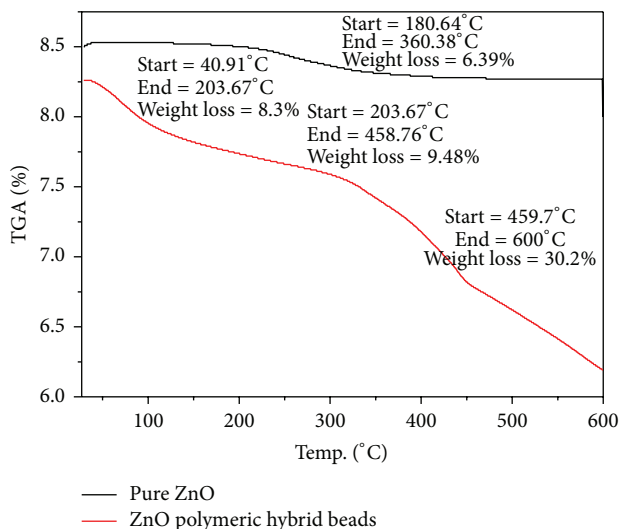


FIGURE 4: Thermal profiles of synthesized pure zinc oxide and its corresponding polymeric hybrid.

than that of its corresponding hybrid beads that record $4.64 \times 10^{-2} \text{ cm}^3/\text{g}$. These results may be respective to the conversion of ZnO nanopowder from nanoscale particles into microscale polymeric beads.

3.1.5. Thermal Profile Identification Using TGA. The thermal profiles of both as-prepared ZnO nanopowder and its corresponding polymeric hybrid beads were explored in Figure 4. It was evident from this figure that the thermal stability of ZnO nanopowder was decreased with its immobilization into the polymeric alginate and PVA matrix.

Zinc oxide nanopowder thermal profile shows one degradation step that begins at 180°C and finishes at 360°C that represent the surface adsorbed water molecules and the decomposition of traces remaining PVP polymeric matrix that utilized as stabilizing agent during its synthesizing process. After this temperature range ZnO showed high thermal stabilities up to 600°C , which is the characteristic property of all metal oxides. However, the thermal stability of ZnO polymeric beads is comparatively less than its parent ZnO nanopowder, where its thermal profile showed three main degradation steps. The first degradation step at $40\text{--}200^\circ\text{C}$ represented the physical water adsorbed onto the polymeric beads. The second degradation step at $200\text{--}460^\circ\text{C}$ is due to the thermal degradation of the immobilized polymer matrix that is composed of PVA and alginate [31]. The final degradation step may be corresponding to the byproduct formation of PVA during the TGA thermal degradation process. According to Holland and Hay's observations [38], thermal degradation could lead to the production of aldehyde and alkene end groups in the molten state, which could lead to the formation of vinyl ester by the rearrangement [37]. This result obvious that the ZnO hybrid beads were less thermally stable compared with their parent ZnO nanopowder, which is the leak property of the polymeric materials compared with inorganic compounds.

3.1.6. Chemical and Mechanical Stabilities of ZnO Hybrid Beads. The hybrid beads chemical stability at the acidic media ($\text{pH} < 7$) especially within the pH range of $2\text{--}7$ indicated that the number of beads remains constant throughout the period of experiment that is confirmed from Figure 5, where this figure investigated that there are no significant weight losses for the hybrid beads at the acidic pH range. This suggested the higher cross-linking inside the hybrid beads.

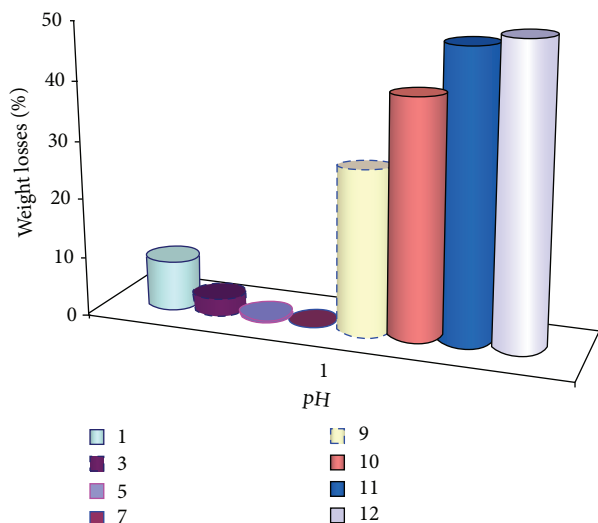


FIGURE 5: Chemical stability of prepared ZnO polymeric hybrid beads at various pH values.

Moreover, their physical appearance remains constant except that their diameter varied due to the water swelling for the porous polymeric hybrid. Accordingly, the hybrid beads were very stable within the acidic pH range. In contrast, regarding the alkaline media ($\text{pH} > 7$), Figure 5 showed notable weight losses for the hybrid beads after drying. These results decided that the excess OH^- ions that are present in the solution media may act as a chelating agent leading to the decross-linking of the hybrid beads and leaching their immobilized zinc oxide nanopowder that declines their weight. These results are in accordance with the other researchers' founding [39].

The mechanical properties of the prepared ZnO hybrid beads were elucidated to determine their availability for the column operations. Figure 6 shows evidence that the formulated beads had very strong mechanical strength and they are difficult to be broken, where slight decline in weight losses was noticeable as the mixing speed improved above 1500 rpm. This is due to the rubber-like elastic properties of ZnO hybrid beads, where PVA contributed strength and durability to the beads while alginate improved the surface properties that reduced the tendency to agglomerate [40]. These good mechanical properties were confirmed from the turbidity measurements after the stirring period. Slight observed turbidity was noticed as the agitation speed incremented above 2000 rpm (Figure 6). Accordingly, these hybrids beads are suitable to be packed into the treatment column to be utilized for continuous treatment operation.

3.2. Dye Decolorization Properties of Zinc Oxide Polymeric Hybrid Beads. The feasibility of the formulated ZnO polymeric hybrid beads for C.I. basic blue 41 dye decolorization from synthetic waste streams was examined. The applicability of the synthesized microbeads for dye removal was tested as a function of the different factors that affect the dye sorption process including the variation in contact time (0–120 min), initial dye concentration (1–100 ppm), dosage of ZnO hybrid

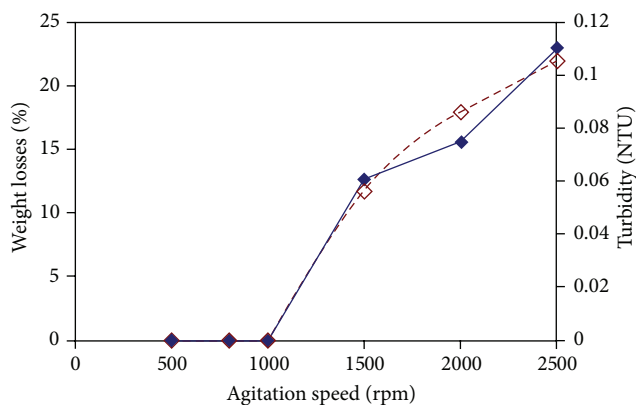


FIGURE 6: Mechanical stability of prepared ZnO polymeric hybrid beads at various mixing speeds.

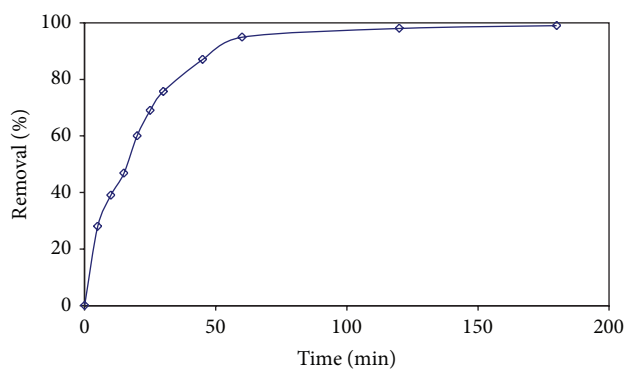


FIGURE 7: Effect of contact time on dye sorption process ($\text{pH} = 6$, initial dye concentration = 10 ppm, agitation speed = 400 rpm, ZOHB dosage = 5 g/L, and temperature = 22°C).

beads (1–10 g/L), dye solution pH (1–9), and dye solution temperature ($25\text{--}80^\circ\text{C}$).

3.2.1. Effect of Contact Time on the Dye Sorption Process onto ZnO Hybrid Beads. The effect of contact time on the adsorption of the basic blue dye onto zinc oxide hybrid beads was investigated over 120 minutes of time intervals. It can be noticed from Figure 7 that the removal of dye by adsorption onto ZOHB was found to be rapid at the initial period of contact time and then to slow down with time until reaching a constant value where no more dye was removed from the solution. At this point, the amount of dye being adsorbed onto the adsorbent was in a state of dynamic equilibrium with the amount of dye desorbed from the adsorbent. The time required to attain this state of equilibrium was termed the equilibrium time and the amount of dye adsorbed at the equilibrium time reflected the maximum dye adsorption capacity of the adsorbent under these particular conditions [41]. Figure 7 investigates that the equilibrium time of dye sorption onto ZOHB was recorded within 60 minutes.

3.2.2. Effect of ZnO Hybrid Beads on the Dye Sorption Process. The effect of ZOHB dosage on both the percentage dye

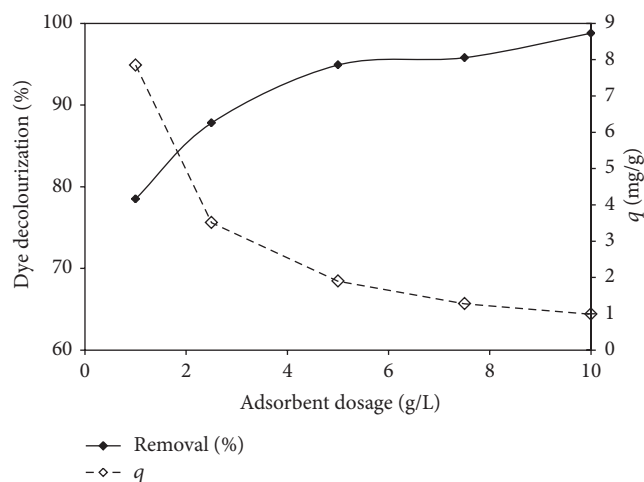


FIGURE 8: Effect of ZnO hybrid beads dosage on both the percentage of dye decolourization and dye uptake capacity (pH = 6, initial dye concentration = 10 ppm, agitation speed = 400 rpm, contact time = 60 min, and temperature = 22°C).

removal and the beads sorption capacity was examined after 60 minutes. Figure 8 indicated that the percentage of dye decolorization was enhanced from 78.5 to 98.8% as ZOHB improved from 1 to 10 g/L as well as an emphasized decrease being noticeable for the beads sorption capacity with increasing their concentrations. The decrease in unit adsorption with increasing beads concentration is basically due to adsorption sites remaining unsaturated during the adsorption reaction [41, 42]. Meanwhile, the improvement in the ZOHB dosage increases the adsorbent surface and the availability of more adsorption sites for dye removal. The optimum ZnO hybrid beads dosage that achieved the optimum dye decolourization percentage of 94.9% has been recorded from Figure 8 to be equal to 5 g/L.

3.2.3. Effect of Initial pH on Dye Adsorption Process. The pH of the dye solution plays an important role in the whole adsorption process. The dye adsorption process is highly pH dependent especially for the cationic dye adsorption [43]. The adsorption of these positively charged dye groups onto the adsorbent surface is primarily influenced by the surface charge of the adsorbent which in turn is affected by the pH of solution. Many oxide surfaces create a surface charge (positive or negative) [44]. Zinc oxide as most of metal oxide materials has an amphoteric character in aqueous medium; that is, it has hydroxyl groups only in acidic solutions (pH 4 and 6) and is converted into an anion-exchanger as the solution pH improved above 6 [45]. In this regard, the initial pH of the dye solution was studied within pH range from 1 to 9 and all other parameters were kept constant. Figure 9 investigates that, at the high acidic dye solution (low pH value), the percentage dye sorption removal was increased but with low limitations from 18% to 45.5% as the dye pH value increased from 1 to 3. Thereafter, the decolorization process increases rapidly and reaches a maximum level of 94.9% at the pH of 6. As the dye solution

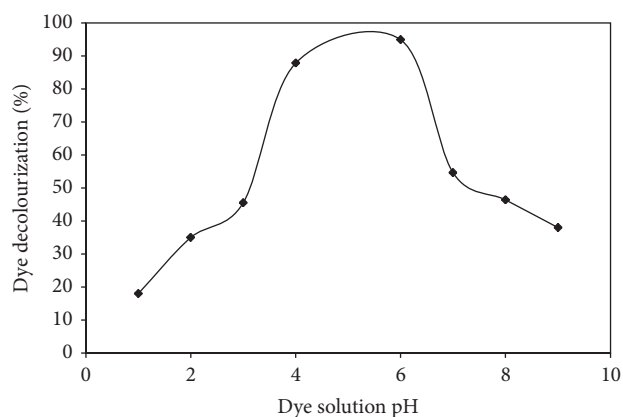


FIGURE 9: Effect of dye solution pH on the percentage of dye decolourization (initial dye concentration = 10 ppm, ZOHB dosage = 5 g/L, agitation speed = 400 rpm, contact time = 60 min, and temperature = 22°C).

pH incremented above value 6, the dye sorption removal dramatically decreased. These three different dye sorption behaviours may be explained as, at low pH value, the lower dye sorption onto ZOHB may be due to the presence of excess H^+ ions competing with the positive groups on the dye for the beads adsorption sites. As the solution pH increased (above 3), the active surface sites of the immobilized ZnO onto the hybrid beads are deprotonated and the competition between H^+ and dye cationic for the adsorption sites lessens, which increase the dye adsorption amount. So, the higher dye uptake values obtained at higher pH (above 3) values are due to the electrostatic attractions between the positively charged dye anions and the immobilized negatively charged ZnO [46]. As the solution pH incremented above 6, the immobilized ZnO nanospecies were positively charged and converted into an anionic-exchanger; accordingly, electrostatic repulsion forces between the ZOHB and the dye anions will be induced that decrease the dye uptake onto the hybrid beads.

3.2.4. Effect of Initial Dye Concentration Process. The effect of initial dye concentration on the equilibrium adsorption capacity (q_e) was carried out in the range of 1–100 mg/L at pH 6 using 5 g/L from the ZOHB for 1 h. The effect of initial dye concentration on the basic dye equilibrium adsorption capacity (q_e) and removal efficiency were illustrated in Figure 10. This figure explores that there is linear enhancement in the dye sorption capacity as the initial concentration of the dye is increased from 1 to 100 mg/L, which is in accordance with the previous studied researches [47]. The improvement in the dye sorption capacity as the initial dye concentration incremented was accompanied with a lower removal efficiency of the basic blue dye. This may be due to the saturation of the adsorption sites on the ZnO beads as the concentration of the dye increases. According to these results, the formulated zinc oxide hybrid beads are effectively capable of removing the C.I. basic blue 41 dye in solutions of a wide region of dye concentration completely.

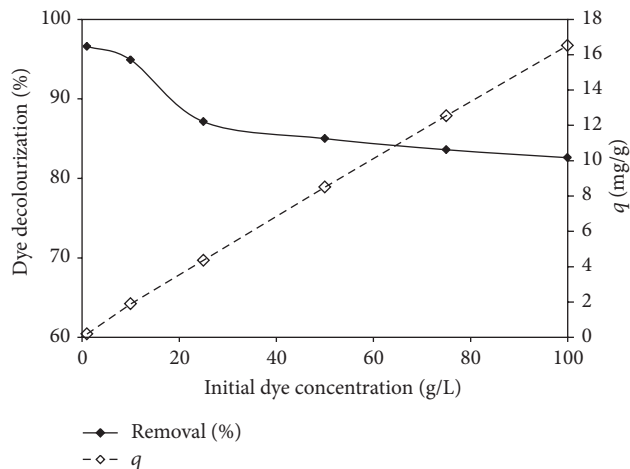


FIGURE 10: Effect of initial dye concentration on both the percentage of dye decolourization and dye uptake capacity (pH = 6, ZOHB dosage = 5 g/L, agitation speed = 400 rpm, contact time = 60 min, and temperature = 22°C).

3.2.5. Effect of Solution Temperature on Dye Adsorption Process. Temperature is well known to play an important role during the adsorption processes. It can affect several aspects of adsorption, for example, dye solubility, the swelling capacity of the sorbent, and the equilibrium position in relation to the endo- or exothermicity of the adsorption phenomenon [48]. So, the effect of temperature on the equilibrium basic blue dye adsorption onto the synthesized ZOHB was investigated in the temperature range of 25–80°C. The increment in the dye solution temperature has a negative effect on the dye adsorption process onto the prepared material as predicted from Figure 11. This indicated that the adsorption of the basic blue dye onto the synthesized ZOHB is an exothermic process. The decrease in the rate of adsorption with the increase in temperature may be attributed to the tendency of dye molecules to escape from the solid phase to bulk phase with the improvement in solution temperature [49]. Accordingly, it was reliable that the dye sorption process onto the fabricated composite beads is not favorable at the elevated dye solution temperature (above 25°C). This result may be explained by the deactivation of the zinc oxide polymeric beads surface or the destruction of some polymeric active sites on the adsorbent surface due to bond rupture [50].

Temperature dependence of the dye adsorption process onto ZOHB is associated with various thermodynamic parameters. To study the thermodynamics of the adsorption process, the standard Gibbs free energy of the process was evaluated by [51]

$$\Delta G^\circ = RT \ln k_c. \quad (3)$$

The equilibrium constant k_c was evaluated at each temperature using the relationship

$$k_c = \frac{C_{Be}}{C_{Ae}}, \quad (4)$$

where C_{Be} and C_{Ae} represent the equilibrium concentrations of dye on the ZOHB adsorbent and solution, respectively.

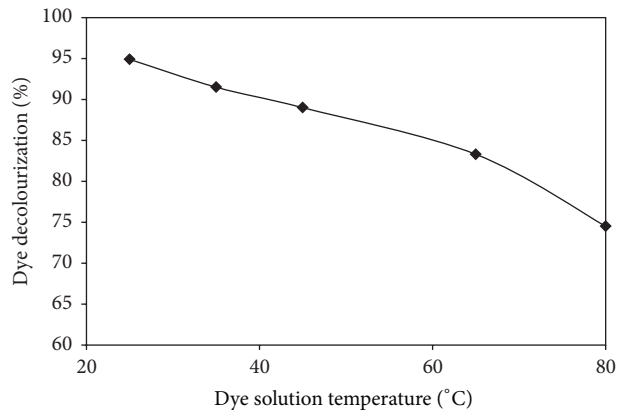


FIGURE 11: Effect of dye solution temperature on the percentage of dye decolourization (initial dye concentration = 10 ppm, ZOHB dosage = 5 g/L, agitation speed = 400 rpm, contact time = 60 min, and pH = 6).

TABLE 3: Thermodynamic parameters for dye adsorption onto ZOHB.

T (K)	ΔG° (kJ mol ⁻¹)	ΔH° (kJ mol ⁻¹)	ΔS° (J mol ⁻¹ K ⁻¹)
298	-7.24		
308	-6.08		
318	-5.53	-2.07	-4.199
338	-4.62		
353	-3.15		

Standard enthalpy (ΔH°) and entropy (ΔS°) were determined from the Van't Hoff equation:

$$\ln k_c = \frac{\Delta S^\circ}{R} - \frac{\Delta H^\circ}{RT}, \quad (5)$$

where ΔH° and ΔS° were obtained from the slope and intercept of the plot of $\ln k_c$ versus $1/T$ as shown in Figure 12 and listed in Table 3. Values of free energy changes ΔG° are negative, confirming that the dye adsorption process onto ZOHB is spontaneous and thermodynamically favorable. The decline in the negative values of ΔG° with the improvement in temperature decreases the driving force at the adsorption process. Accordingly, the improvement in temperature has negative impact on the dye sorption process. The value of ΔH° is negative, indicating that the adsorption process is exothermic in nature, while the negative value of entropy change (ΔS°) shows a decreased disorder at the solid/liquid interface during dye sorption. As the temperature increases, the mobility of dye ions increases causing the ions to escape from the solid phase to the liquid phase. Therefore, the amount of dyes that may be adsorbed will be decreased [51].

3.3. Equilibrium Isotherm Analysis of Dye Adsorption Process. Equilibrium data, commonly known as adsorption isotherms, are basic requirements for the design of adsorption systems [52]. In this regard, the equilibrium data for BB41 on the fabricated hybrid beads were modeled using the well-known isotherm models of Langmuir and Freundlich models.

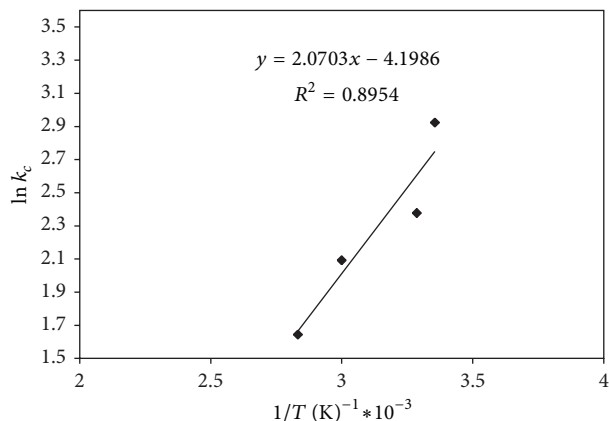


FIGURE 12: Arrhenius plot for dye sorption onto ZOHB at different solution temperatures (initial dye concentration = 10 ppm, ZOHB dosage = 5 g/L, agitation speed = 400 rpm, contact time = 60 min, and pH = 6).

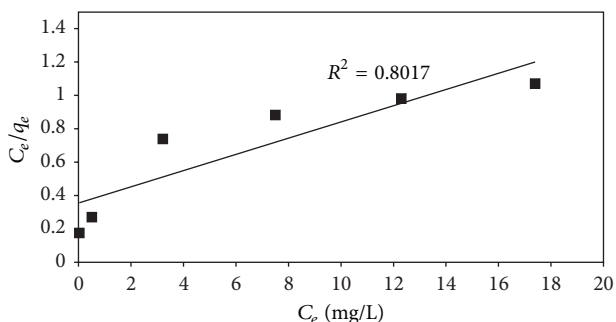


FIGURE 13: Langmuir isotherm for BB41 dye adsorption onto ZOHB.

The plot of C_e/q_e versus C_e (Figure 13) indicates a straight line with low value of the correlation coefficient ($R^2 = 0.8017$) for the linearized plot of the equation that is represented as [53]

$$\frac{C_e}{q_e} = \frac{1}{q_m K} + \frac{C_e}{q_m}, \quad (6)$$

where q_e is the amount adsorbed (mg/g), C_e is the equilibrium concentration of the adsorbate ions (mg/L), and q_m and K are Langmuir constants related to maximum adsorption capacity (monolayer capacity) (mg/g) and energy of adsorption (L/mg), respectively. Accordingly, the Langmuir isotherm model may be not adequate to describe the dye sorption process onto the fabricated zinc oxide hybrid beads.

Consider that Langmuir isotherm model assumes a monolayer coverage and uniform activity distribution on the adsorbent surface, which represent unexpected behavior for the decolorization of studied case onto the fabricated beads. However, the adsorption of basic blue dye onto ZOHHB beads suggested being a quite complex process, probably through forming multilayers and even closing some of the available pores at the bead surfaces [54]. Also, a variation of sorption activity is expected with surface coverage. So it can be expected that the Freundlich isotherm model was more suitable to describe the experimental data compared

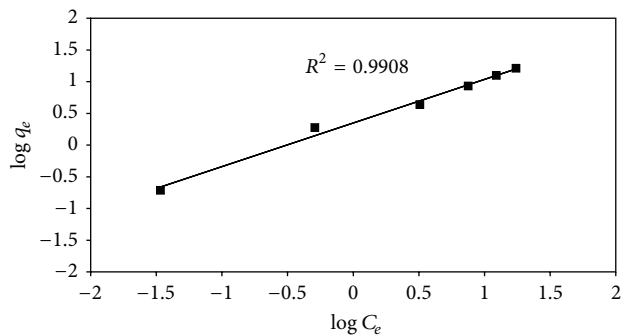


FIGURE 14: Freundlich isotherm for BB41 dye adsorption onto ZOHB.

with Langmuir model. The linearized form of the Freundlich equation may be expressed as [41]

$$\ln q_e = \ln K_F + \frac{1}{n_f} \ln C_e, \quad (7)$$

where K_F and n_f are Freundlich constants related to adsorption capacity and adsorption intensity, respectively. The Freundlich constants are related to the surface heterogeneity. Figure 14 investigates the Freundlich linear fit for the dye sorption process onto the fabricated hybrid beads. It is obvious that the correlation coefficient value ($R^2 = 0.991$) obtained through Freundlich isotherm is higher than that of the Langmuir fitting. So, Freundlich model was more appropriate for the prediction of the isothermal profiles for the basic dye sorption process onto the zinc oxide polymeric hybrid beads. This observation suggested that the sorption process is heterogeneous in nature and accomplished with a nonuniform distribution of heat of adsorption. The calculated n_f value that is equal to 1.45 was greater than unity and indicated that the dye sorption process onto ZOHB was favorable.

3.4. Kinetic Model of Dye Adsorption Process. The rate at which dissolved dye is removed from the aqueous solution by solid sorbents is essential to evaluate the adsorption kinetics using theoretical models in order to design and control the sorption process units. So, the applicability of the pseudo-first-order and pseudo-second-order models was tested for the adsorption of BB41 onto ZOHB. The best-fit model was selected based on the linear regression correlation coefficient, R^2 , values. The Lagergren first-order equation is given as [55]

$$\ln(q_e - q_t) = \ln q_e - k_1 t, \quad (8)$$

where q_e and q_t are amounts of dye ions sorbed (mg/g) at equilibrium and at time t (min), respectively. k_1 (min^{-1}) is the first-order reaction rate constant. If the pseudo-first-order kinetics is applicable to the experimental data, a plot of $\ln(q_e - q_t)$ versus t should present a linear relationship, as investigated in Figure 15; the calculated values of k_1 and q_e can be determined from the slope and intercept of the plot, respectively. The values of R^2 for the sorption of different

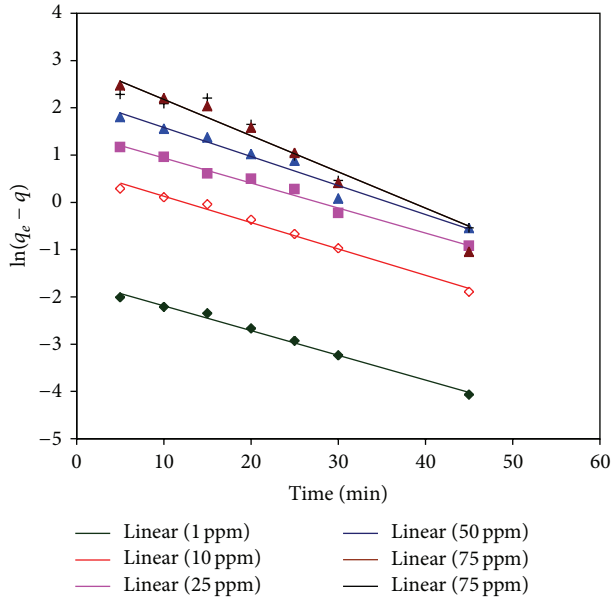


FIGURE 15: Pseudo-first-order kinetic model for BB41 dye adsorption onto ZOHB.

initial concentrations of basic blue dye ions onto ZOHB are tabulated in Table 4.

On the basis of linear regression values from this table (R^2), it may be predicted that the kinetics of dye sorption onto ZOHB be described well by the first-order kinetic model. Comparing the values of q_e calculated from the reaction kinetic curves (Table 4) with the experimental data, it is noticeable that the calculated q_e values that were obtained from the first-order kinetic model were compatible with the experimental q_e values. Thus, the first-order rate expression fits the data most satisfactorily. This gives prediction that the dye sorption process may take place basically through the physical sorption [56].

Moreover, the experimental kinetic data were further analyzed using the pseudo-second-order kinetic model that may be expressed in the following form [54]:

$$\frac{t}{q_t} = \left(\frac{1}{k_2 q_e} \right) + \frac{t}{q_e}, \quad (9)$$

where k_2 is the second-order reaction rate equilibrium constant (g/mg min). The plotting of t/q_t against t for different initial BB41 concentrations (Figure 16) investigated straight lines with low values of correlation coefficients compared with the first-order rate model (Table 4) for the different studied dye concentrations especially for the high dye concentrations. Also, the estimated values of q_e calculated from the equation differed from the experimental values. Accordingly, the first-order rate model is more appropriate to describe the dye sorption process onto the zinc oxide hybrid polymer compared with the second-order rate model.

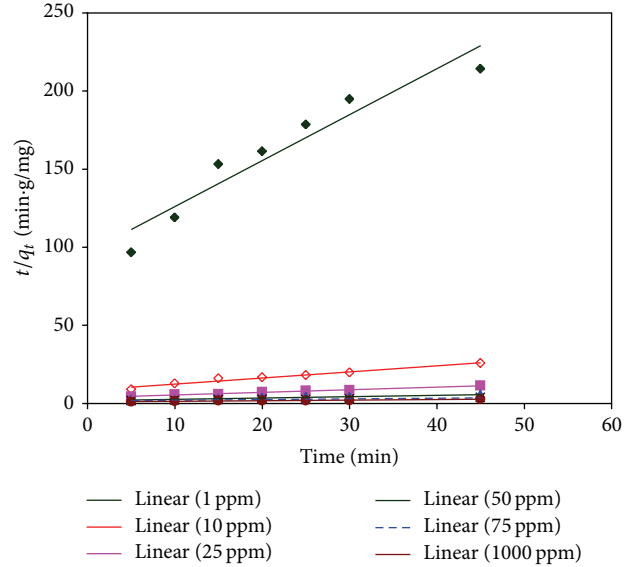


FIGURE 16: Pseudo-second-order kinetic model for BB41 dye adsorption onto ZOHB.

4. Conclusion

A novel fabricated microbead was successfully prepared from immobilization of the sol-gel synthesized zinc oxide nanopowder onto the PVA and alginate polymer matrix. The XRD and SEM results strongly support the physical interactions between zinc oxide nanoparticles and the polymer blend matrix. Furthermore, SEM examination and EDX analysis of the formulated hybrid beads confirm the incorporation of ZnO nanoparticles onto the polymeric hybrid matrix. Incorporation of polymeric matrix at the prepared zinc oxide hybrid beads decreases its thermal stability relatively compared with its immobilized pure zinc oxide. However, this polymer matrix has not any significant effect in the chemical and mechanical stabilities of the zinc oxide hybrid beads, where it is characterized by its good chemical and mechanical properties. The formulated hybrid beads have high dye adsorption performance for the C.I. 41 basic blue dye. The maximum dye sorption capacity was recorded as 16.5 mg/g using 100 ppm initial dye concentration. The improvement in the beads dosage has positive impact on the percentage dye removal. Meanwhile, the increment in both initial dye concentrations and dye solution temperature has negative impact on the dye sorption process onto the fabricated beads. The experimental results and Van't Hoff equation plot confirm that the dye adsorption process is exothermic. The equilibrium isotherm data of the dye sorption process was described well using the Freundlich isotherm model. However, the kinetics of basic dye sorption process onto the fabricated hybrid beads obeys the pseudo-first-order kinetic model, indicating that the dye sorption process may take place basically through the physical sorption.

TABLE 4: Kinetic parameters of dye adsorption onto ZOHB at different dye concentrations.

Kinetic model Dye concentration (mg/L)	$(q_e)_{\text{exp}}$ (mg/g)	Pseudo-first order			Pseudo-second order		
		$(q_e)_{\text{cal}}$ (mg/g)	K_1 (min^{-1})	R^2	$(q_e)_{\text{cal}}$ (mg/g)	K_2 (g/mg min)	R^2
1	0.193	0.19	-0.052	0.99	0.34	0.089	0.958
10	1.89	1.88	-0.0053	0.98	2.56	0.018	0.967
25	4.35	4.3	-0.0053	0.98	5.87	0.0079	0.985
50	8.5	8.9	-0.006	0.966	11.67	0.0041	0.975
75	12.54	18.9	-0.076	0.94	22.98	0.00114	0.917
100	16.25	19.1	0.078	0.94	25.2	0.0012	0.93

Conflict of Interests

The authors declare that there is no conflict of interests regarding the publication of this paper.

Acknowledgment

This work was funded by the Deanship of Scientific Research (DSR), King Abdulaziz University, Jeddah, under grant No. (135-021-D1434). The authors, therefore, acknowledge with thanks DSR technical and financial support.

References

- [1] I. Kiran, T. Akar, A. S. Ozcan, A. Ozcan, and S. Tunalı, "Biosorption kinetics and isotherm studies of Acid Red 57 by dried *Cephalosporium aphidicola* cells from aqueous solutions," *Biochemical Engineering Journal*, vol. 31, no. 3, pp. 197–203, 2006.
- [2] K. Vijayaraghavan and Y.-S. Yun, "Biosorption of C.I. Reactive Black 5 from aqueous solution using acid-treated biomass of brown seaweed *Laminaria* sp," *Dyes and Pigments*, vol. 76, no. 3, pp. 726–732, 2008.
- [3] T. O'Mahony, E. Guibal, and J. M. Tobin, "Reactive dye biosorption by *Rhizopus arrhizus* biomass," *Enzyme and Microbial Technology*, vol. 31, no. 4, pp. 456–463, 2002.
- [4] A. S. Özcan and A. Özcan, "Adsorption of acid dyes from aqueous solutions onto acid-activated bentonite," *Journal of Colloid and Interface Science*, vol. 276, no. 1, pp. 39–46, 2004.
- [5] M. C. Ncibi, B. Mahjoub, and M. Seffen, "Kinetic and equilibrium studies of methylene blue biosorption by *Posidonia oceanica* (L.) fibres," *Journal of Hazardous Materials*, vol. 139, no. 2, pp. 280–285, 2007.
- [6] T. Robinson, B. Chandran, and P. Nigam, "Removal of dyes from a synthetic textile dye effluent by biosorption on apple pomace and wheat straw," *Water Research*, vol. 36, no. 11, pp. 2824–2830, 2002.
- [7] M. Roulia and A. A. Vassiliadis, "Interactions between C.I. Basic Blue 41 and aluminosilicate sorbents," *Journal of Colloid and Interface Science*, vol. 291, no. 1, pp. 37–44, 2005.
- [8] I. A. W. Tan, B. H. Hameed, and A. L. Ahmad, "Equilibrium and kinetic studies on basic dye adsorption by oil palm fibre activated carbon," *Chemical Engineering Journal*, vol. 127, no. 1–3, pp. 111–119, 2007.
- [9] H. C. Chu and K. M. Chen, "Reuse of activated sludge biomass: I. Removal of basic dyes from wastewater by biomass," *Process Biochemistry*, vol. 37, no. 6, pp. 595–600, 2002.
- [10] B. S. Inbaraj, J. S. Wang, J. F. Lu, F. Y. Siao, and B. H. Chen, "Adsorption of toxic mercury(II) by an extracellular biopolymer poly(γ -glutamic acid)," *Bioresource Technology*, vol. 100, no. 1, pp. 200–207, 2009.
- [11] G. McKay, "The adsorption of dyestuffs from aqueous solution using activated carbon: analytical solution for batch adsorption based on external mass transfer and," *The Chemical Engineering Journal*, vol. 27, no. 3, pp. 187–196, 1983.
- [12] G. McKay, "Analytical solution using a pore diffusion model for a pseudo irreversible isotherm for the adsorption of basic dye on silica," *AIChE Journal*, vol. 30, pp. 692–697, 1984.
- [13] S.-Y. Mak and D.-H. Chen, "Fast adsorption of methylene blue on polyacrylic acid-bound iron oxide magnetic nanoparticles," *Dyes and Pigments*, vol. 61, no. 1, pp. 93–98, 2004.
- [14] R. Salehi, M. Arami, N. M. Mahmoodi, H. Bahrami, and S. Khorramfar, "Novel biocompatible composite (Chitosan-zinc oxide nanoparticle): preparation, characterization and dye adsorption properties," *Colloids and Surfaces B: Biointerfaces*, vol. 80, no. 1, pp. 86–93, 2010.
- [15] S. Park, J. C. Lee, D. W. Lee, and J. H. Lee, "Photocatalytic ZnO nanopowders prepared by solution combustion method for noble metal recovery," *Journal of Materials Science*, vol. 38, no. 22, pp. 4493–4497, 2003.
- [16] Z. V. Marinković, O. Milošević, M. V. Nikolić et al., "Evolution of the microstructure of disperse ZnO powders obtained by the freeze-drying method," *Materials Science and Engineering A*, vol. 375–377, no. 1–2, pp. 620–624, 2004.
- [17] H. Li, J. Wang, H. Liu, H. Zhang, and X. Li, "Zinc oxide films prepared by sol-gel method," *Journal of Crystal Growth*, vol. 275, no. 1–2, pp. e943–e946, 2005.
- [18] R. Kaur, A. Singh, K. Sehrawat, N. Mehra, and R. Mehra, "Sol-gel derived yttrium doped ZnO nanostructures," *Journal of Non-Crystalline Solids*, vol. 352, no. 23–25, pp. 2565–2568, 2006.
- [19] M. M. Abd El-Latif and M. F. El-Kady, "Developing & characterization of a new zirconium vanadate ion exchanger and its novel organic–inorganic hybrid," *Journal of Applied Sciences Research*, vol. 4, pp. 1–13, 2008.
- [20] K. G. Varshney and A. H. Pandith, "Synthesis and ion exchange behavior of acrylonitrile-based zirconium phosphate—a new hybrid cation exchanger," *Journal of the Indian Chemical Society*, vol. 78, no. 5, pp. 250–253, 2001.
- [21] A. A. Khan, A. Khan, and I. Inamuddin, "Preparation and characterization of a new organic-inorganic nano-composite poly-o-toluidine Th(IV) phosphate: its analytical applications as cation-exchanger and in making ion-selective electrode," *Talanta*, vol. 72, no. 2, pp. 699–710, 2007.
- [22] A. Nilchi, H. Atashi, A. H. Javid, and R. Saberi, "Preparations of PAN-based adsorbents for separation of cesium and cobalt from

- radioactive wastes," *Applied Radiation and Isotopes*, vol. 65, no. 5, pp. 482–487, 2007.
- [23] C. M. Hassan and N. A. Peppas, "Cellular PVA hydrogels produced by freeze/thawing," *Journal of Applied Polymer Science*, vol. 76, no. 14, pp. 2075–2079, 2000.
- [24] B. Ramaraj, "Crosslinked poly(vinyl alcohol) and starch composite films. II. Physicochemical, thermal properties and swelling studies," *Journal of Applied Polymer Science*, vol. 103, no. 2, pp. 909–916, 2007.
- [25] B. Cruz-Ortiz, L. Ríos-González, Y. García, J. Rodríguez de la Garza, and J. Rodríguez-Martínez, "Immobilization of thermomyces lanuginosus lipase in PVA-alginate beads," *Journal of Mexico Chemical Society*, vol. 55, pp. 176–180, 2011.
- [26] Z.-E. Long, Y. Huang, Z. Cai, W. Cong, and F. Ouyang, "Immobilization of acidithiobacillus ferrooxidans by a PVA-boric acid method for ferrous sulphate oxidation," *Process Biochemistry*, vol. 39, no. 12, pp. 2129–2133, 2004.
- [27] W. Yujian, Y. Xiaojuan, L. Hongyu, and T. Wei, "Immobilization of Acidithiobacillus ferrooxidans with complex of PVA and sodium alginate," *Polymer Degradation and Stability*, vol. 91, no. 10, pp. 2408–2414, 2006.
- [28] K.-M. Khoo and Y.-P. Ting, "Biosorption of gold by immobilized fungal biomass," *Biochemical Engineering Journal*, vol. 8, no. 1, pp. 51–59, 2001.
- [29] H. Shokry Hassan, A. B. Kashyout, H. M. A. Soliman, M. A. Uosif, and N. Afify, "Effect of reaction time and Sb doping ratios on the architecturing of ZnO nanomaterials for gas sensor applications," *Applied Surface Science*, vol. 277, pp. 73–82, 2013.
- [30] A. Mahmooda, S. Bano, S. GyunKim, and K. HoLee, "Water-methanol separation characteristics of annealed SA/PVA complex membranes," *Journal of Membrane Science*, vol. 415–416, pp. 360–367, 2012.
- [31] K. T. Shalumon, K. H. Anulekha, S. V. Nair, S. V. Nair, K. P. Chennazhi, and R. Jayakumar, "Sodium alginate/poly(vinyl alcohol)/nano ZnO composite nanofibers for antibacterial wound dressings," *International Journal of Biological Macromolecules*, vol. 49, no. 3, pp. 247–254, 2011.
- [32] F. F. Fang, J. H. Kim, and H. J. Choi, "Synthesis of core-shell structured PS/Fe₃O₄ microbeads and their magnetorheology," *Polymer*, vol. 50, no. 10, pp. 2290–2293, 2009.
- [33] J. Wang and L. Gao, "Synthesis and characterization of ZnO nanoparticles assembled in one-dimensional order," *Inorganic Chemistry Communications*, vol. 6, no. 7, pp. 877–881, 2003.
- [34] S. Muthukumar and R. Gopalakrishnan, "Structural, optical and photoluminescence studies of heavily Mn-doped ZnO nanoparticles annealed under Ar atmosphere," *Journal of Materials Science: Materials in Electronics*, vol. 34, pp. 1946–1953, 2012.
- [35] S. Amrut, J. Satish, S. Raghmani, J. Ahn, and B. Ramchandra, "Low temperature dielectric studies of zinc oxide (ZnO) nanoparticles prepared by precipitation method," *Advanced Powder Technology*, vol. 24, pp. 331–335, 2013.
- [36] K. Nakamoto, *Infrared and Raman Spectra of Inorganic and Coordination Compounds*, Parts A and B, John Wiley & Sons, New York, NY, USA, 1997.
- [37] M. S. Islam and M. R. Karim, "Fabrication and characterization of poly(vinyl alcohol)/alginate blend nanofibers by electrospinning method," *Colloids and Surfaces A: Physicochemical and Engineering Aspects*, vol. 366, no. 1-3, pp. 135–140, 2010.
- [38] B. J. Holland and J. N. Hay, "The thermal degradation of poly(vinyl alcohol)," *Polymer*, vol. 42, no. 16, pp. 6775–6783, 2001.
- [39] V. I. Lozinsky and F. M. Plieva, "Poly(vinyl alcohol) cryogels employed as matrices for cell immobilization. 3. Overview of recent research and developments," *Enzyme and Microbial Technology*, vol. 23, no. 3-4, pp. 227–242, 1998.
- [40] M. Abd El-Latif, M. El-Kady, M. Ibrahim, and M. E. Ossman, "Alginate/polyvinyl alcohol—kaolin composite for removal of methylene blue from aqueous solution in a batch stirred tank reactor," *Journal of American Science*, vol. 6, pp. 280–292, 2010.
- [41] M. F. Elkady, A. M. Ibrahim, and M. M. A. El-Latif, "Assessment of the adsorption kinetics, equilibrium and thermodynamic for the potential removal of reactive red dye using eggshell biocomposite beads," *Desalination*, vol. 278, no. 1-3, pp. 412–423, 2011.
- [42] Y. Al-Degs, M. A. M. Khraisheh, S. J. Allen, and M. N. Ahmad, "Effect of carbon surface chemistry on the removal of reactive dyes from textile effluent," *Water Research*, vol. 34, no. 3, pp. 927–935, 2000.
- [43] X. S. Wang, Y. Zhou, Y. Jiang, and C. Sun, "The removal of basic dyes from aqueous solutions using agricultural by-products," *Journal of Hazardous Materials*, vol. 157, no. 2-3, pp. 374–385, 2008.
- [44] Y. Al-Degs, M. A. M. Khraisheh, S. J. Allen, and M. N. Ahmad, "Effect of carbon surface chemistry on the removal of reactive dyes from textile effluent," *Water Research*, vol. 34, no. 3, pp. 927–935, 2000.
- [45] A. Demirci, E. Alver, K. Ada, and M. Ozcimder, "Liquid chromatographic column performance of α -alumina prepared by the reaction between aluminium sulphate and urea in boiling aqueous solution and an application to the separation of some common anions," *Bulletin of Pure and Applied Science C*, vol. 23, pp. 21–37, 2004.
- [46] V. Belessi, G. Romanos, N. Boukos, D. Lambropoulou, and C. Trapalis, "Removal of Reactive Red 195 from aqueous solutions by adsorption on the surface of TiO₂ nanoparticles," *Journal of Hazardous Materials*, vol. 170, no. 2-3, pp. 836–844, 2009.
- [47] Z. Aksu and G. Dönmez, "A comparative study on the biosorption characteristics of some yeasts for Remazol Blue reactive dye," *Chemosphere*, vol. 50, no. 8, pp. 1075–1083, 2003.
- [48] M. Wawrzkiwicz, "Removal of C.I. Basic Blue 3 dye by sorption onto cation exchange resin, functionalized and non-functionalized polymeric sorbents from aqueous solutions and wastewaters," *Chemical Engineering Journal*, vol. 217, pp. 414–425, 2013.
- [49] T. G. Venkatesha, R. Viswanatha, Y. Arthoba Nayaka, and B. K. Chethana, "Kinetics and thermodynamics of reactive and vat dyes adsorption on MgO nanoparticles," *Chemical Engineering Journal*, vol. 198–199, pp. 1–10, 2012.
- [50] H. D. Ozsoy, H. Kumbur, B. Saha, and J. H. van Leeuwen, "Use of Rhizopus oligosporus produced from food processing wastewater as a biosorbent for Cu(II) ions removal from the aqueous solutions," *Bioresource Technology*, vol. 99, no. 11, pp. 4943–4948, 2008.
- [51] W. S. Wan Ngah and M. A. K. M. Hanafiah, "Adsorption of copper on rubber (Hevea brasiliensis) leaf powder: kinetic, equilibrium and thermodynamic studies," *Biochemical Engineering Journal*, vol. 39, no. 3, pp. 521–530, 2008.
- [52] A. Özer and G. Dursun, "Removal of methylene blue from aqueous solution by dehydrated wheat bran carbon," *Journal of Hazardous Materials*, vol. 146, no. 1-2, pp. 262–269, 2007.
- [53] M. M. Abd El-Latif and M. F. Elkady, "Equilibrium isotherms for harmful ions sorption using nano zirconium vanadate ion exchanger," *Desalination*, vol. 255, no. 1-3, pp. 21–43, 2010.

- [54] M. Abd El-Latif, M. Ibrahim, and M. El-Kady, "Adsorption Equilibrium, kinetics and thermodynamics of methylene blue from aqueous solutions using biopolymer oak sawdust composite," *Journal of American Science*, vol. 6, pp. 267–283, 2010.
- [55] S. Lagergren, "About the theory of so-called adsorption of soluble substances," *Kungliga Svenska Vetenskapsakademiens Handlingar*, vol. 24, no. 4, pp. 1–39, 1898.
- [56] M. M. Abd El-Latif and M. F. Elkady, "Kinetics study and thermodynamic behavior for removing cesium, cobalt and nickel ions from aqueous solution using nano-zirconium vanadate ion exchanger," *Desalination*, vol. 271, no. 1–3, pp. 41–54, 2011.

Research Article

Development and Evaluation of Solbrax-Water Nanoemulsions for Removal of Oil from Sand

Priscila F. Oliveira, Thiago M. Oliveira, Luciana S. Spinelli, and Claudia R. E. Mansur

Institute of Macromolecules, Federal University of Rio de Janeiro, Avenue Horácio Macedo, 2030, Ilha do Fundão, 21941-598 Rio de Janeiro, RJ, Brazil

Correspondence should be addressed to Luciana S. Spinelli; spinelli@ima.ufrj.br

Received 8 January 2014; Accepted 26 February 2014; Published 30 March 2014

Academic Editor: Jie-Fang Zhu

Copyright © 2014 Priscila F. Oliveira et al. This is an open access article distributed under the Creative Commons Attribution License, which permits unrestricted use, distribution, and reproduction in any medium, provided the original work is properly cited.

In recent years, surfactants have been used to clean up soils and aquifers contaminated by petroleum and petroleum derivatives. The purpose of this study was to develop and evaluate nanoemulsions for remediation of soil contaminated by petroleum, by using a commercial solvent Solbrax. The nanoemulsions were prepared by the phase inversion temperature (PIT) method, using oil phase Solbrax (a solvent extracted from naphtha with low aromatics content) and a nonionic ethoxylated lauryl ether surfactant. The surfactant concentrations were varied from 10 to 12 wt% and the oil phase was varied from 5 to 20 wt%. A 2^3 factorial experimental design with center point run was used to evaluate the soil washing process, varying time, temperature, and shear rate of the system. The results show that the most efficient system (with 90% efficiency) was that using the nanoemulsion containing 5 wt% of Solbrax and 12 wt% of surfactant after four hours of washing, on 240 rotation·min⁻¹ of shear rate and at a temperature of 318 K.

1. Introduction

Contamination of the soil, water, and air has increased greatly in recent years. One of the main contributors is the petroleum industry, which causes contamination through release of various organic compounds along its productive chain. Among the contamination sources are fuel leaks during transport and spills caused by traffic accidents [1, 2].

Various chemical and physical treatment processes have been developed and tested to remove hydrocarbons from the soil. The processes used to contain spills on land vary according to the quantity and type of oil or derivative and soil. For example, the less viscous the oil is and the more porous the soil is, the faster the spill will spread [3–5].

Under natural conditions, Kuyukina et al. have shown that oil's penetration in the soil is a complex process that involves many chemical, physical, and biological factors. Crude oil is highly hydrophobic, as most of its components, with very low solubility in water [6]. According to the oil's origin, its chemical composition and physical properties can vary greatly, affecting the methods of treating contaminated areas. Physical characteristics of the oil such as density, temperature and surface/interfacial tension all affect the

mechanisms that can be used to remove oil from soil without causing chemical destruction or modification [7].

Chemical products such as surfactants have been used to remediate soils and aquifers contaminated with petroleum derivatives. Surfactants are compounds that have affinity for both water and oil, because their molecules (called amphiphilic molecules) have two functional groups: one that is hydrophilic and one that is lipophilic. This structural arrangement creates a monolayer at the water-oil interface, reducing the interfacial tension and the mobility of the contaminant [3, 7].

Since most organic contaminants are hydrophobic, the objective of using surfactants is to reduce the interfacial tension organic contaminant/water to increase its separation from the soil, both from the surface and pores of the grains. Under certain circumstances, electrolytes can also be used in aqueous surfactant solutions, with the aim of increasing the surfactant's efficiency in removing the oil [6, 8].

Although the use of surfactants to remediate soil contaminated by hydrocarbons has excellent potential, one of the drawbacks of this technique is the formation of macroemulsions, which are thermodynamically unstable and can break

down and form two immiscible phases consisting of oil and water. Besides this, due to the relatively large size of the droplets in the macroemulsion (between 100 and 1000 nm in diameter), these droplets tend to obstruct the pores during their transport in the soil, hindering the clean-up process [3, 9].

Oliveira and Maldonado [9] show that the use of microemulsions as an alternative to clean up areas contaminated by heavy oil fractions has been shown to have great potential. Among the advantages are these molecules' high capacities to dissolve the oil phase in aqueous systems and their good efficiency in remediation at ambient temperature. Vegetable oils and vegetable oils based nanoemulsions have shown one sustainable alternative for removal of oil of contaminated systems [10, 11].

Microemulsions and nanoemulsions are similar systems composed of a phase containing droplets of nanometric size (10 to 200 nm) dispersed in a continuous liquid medium. The main differences between these two systems, when both are prepared using surfactants, are related to the concentration of the surfactants used (nanoemulsions are prepared in the presence of lower surfactant concentrations in comparison with microemulsion), to the presence of cosurfactants (nanoemulsions do not require the presence of cosurfactants) and the methods used to prepare them [12–17].

Nanoemulsions can be prepared with high- and low-energy emulsification. In low-energy emulsification, nanoemulsions are prepared by altering the physical-chemical properties of the system. This method uses the energy stored within the molecular aggregates formed by the surfactant molecules present in the emulsion [18]. Among the low-energy emulsification methods is induced transitional phase inversion, also known as the phase inversion temperature (PIT) method, which uses a particular characteristic of emulsions stabilized by ethoxylated nonionic surfactants. In a fixed composition of the emulsion, the relative affinity of the surfactant for the different phases is altered and controlled by the temperature [19]. This phenomenon is due to the specific solubility of nonionic surfactants in function of temperature, reflected in the behavior of the phases of an emulsion [20].

In this work we prepared oil/water nanoemulsions using Solbrax Eco 225/255 and nonionic ethoxylated lauryl ether surfactant, applying the PIT method and characterizing them regarding their stability and particle size. We then evaluated these systems, according to the efficiency in removing the oil on sand contaminated with petroleum, by the variation of temperature, time, and shear rate washing with nanoemulsion flushing.

2. Experimental Procedure

2.1. Determination of the Cloud Point of the Nonionic Surfactants. For using low energy emulsification, it is necessary to identify the surfactants solubilization properties that change. We used the nonionic ethoxylated lauryl ether surfactant Ultrol L70, obtained from Oxiteno, Brazil (Ultrol L line), with seven ethylene oxide (EO) units in its chains. As the aqueous phase, we used distilled deionized water.

The cloud points of the aqueous surfactant solutions are the main measure to view this properties alteration. They were measured visually, using a test tube containing the surfactant solution immersed in a beaker with water heated over a hotplate. The temperature range analyzed was from 293 to 343 K, measured by a thermometer placed in the solution. The cloud point was determined by the average between the temperature at which the first visual indication of clouding occurred and the temperature at which it disappeared. In these analyses, aqueous solutions of Ultrol L70 were used at concentrations of 10, 11, and 12 wt%.

2.2. Measurement of the Oil/Water Interfacial Tension. The interfacial tension of the oil phase with the aqueous surfactant solution (Ultrol L70) was measured to observe the behavior of the surfactant at the water-oil interface. 40 g of aqueous surfactant solutions was prepared, at the same above concentrations. They were then left at rest for 24 hours to allow the system to dissolve completely. The interfacial tension measurements were performed with a Krüss K10 digital tensiometer, which uses the du Noüy ring method.

As the oil phase of the oil/water emulsion we used Solbrax Eco 225/255. This is a commercial solvent produced by Petrobras and was donated by its distribution subsidiary, BR Distribuidora. It is extracted from petroleum naphtha and composed mainly of aliphatic and naphthenic hydrocarbons with a distillation range between 498 and 528 K. The solvent was characterized by carbon nuclear magnetic resonance (NMR-13C), by which Costa et al. [21] observed signals characteristic of linear or branched hydrocarbons and monocyclic alkanes. The presence of other compounds, such as alkenes, aromatics, or heteroatoms, was not observed.

2.3. Determination of the Phase Inversion Temperature (PIT) of the Systems. The PIT of the systems was determined with a Haake RS600 rheometer with a DG41 double-gap accessory, at a constant shear rate ($\dot{\gamma}$) of 30 s^{-1} and temperature range of 293–353 K. The results were plotted on graphs of the logarithm of the viscosity (η) in function of the temperature (T). The dispersions were obtained by first adding the surfactant in the aqueous phase. Then after 24 hours the oil phase was added in the aqueous solution.

2.4. Preparation and Characterization of the Oil/Water Nanoemulsions by the PIT Method. According to Souza et al. [22], the process of preparing oil/water nanoemulsions by the PIT method consists of heating the system to temperatures near the PIT followed by rapid cooling, and the condition for nanoemulsion formation is the complete solubilization of the surfactant in the oil.

The Solbrax/water nanoemulsion was prepared by stirring the oil phase containing the surfactant (by a mechanical stirrer operating at 100 rpm) and then heating this phase and the aqueous phase separately to a temperature of 288 K above the corresponding PIT for each system. The purpose of the stirring and heating of the oil phase was to promote the complete solubilization of the surfactant.

When the desired temperature was reached, the two phases were mixed, under stirring, and the mixture was immersed in bain-marie and cooled slowly until reaching 275 to 279 K below the predetermined PIT; at this point the system was cooled further to room temperature (298 K) in an ice bath.

2.5. Analysis of Size and Size Distribution of the Droplets of Prepared Emulsions. The emulsion so formed was then left under light stirring for 5 min and the size and size distribution of the droplets formed were analyzed in a Zetasizer Nano ZS particle size analyzer (Malvern) that works on the typical principal of dynamic light scattering. By the photon correlation spectroscopy method and the refraction index and viscosity values, we obtained quantitative results in the form of graphs of scattered light volume as a function of the particle size of each emulsion produced.

2.6. Use of the Nanoemulsions to Wash Sand Contaminated with Oil. The tests to study the removal of oil from the sand were performed in four steps: contamination of the sand, mixture of the contaminated sand with the nanoemulsion, extraction of the oil from the sand, and quantification of the oil removed from the sand. The sand was contaminated by adding 2 g of oil in 10 g of sand. After 24 hours, this mixture was agitated in a shaker bath at a moderate speed of 60 cycles·min⁻¹ for 3 hours, at a temperature of 298 K. Then the mixture was left to rest for 24 hours. (The crude oil used came from a Brazilian well and was donated by the Petrobras Research Center. It had the following characteristics: °API = 21.2; saturates content = 40.7%; aromatics content = 34.1%; resins content = 22.9%; and asphaltenes content = 2.4%. And the sand came from Mineração Jundu, with the following characteristics: grain size from 150 to 500 mesh, surface area = 0.2284 m²/g, and pore diameter = 77.8430 Å.)

The cleaning was done by adding 30 mL of the nanoemulsion to this system and placing it in the shaker bath again. Another two flasks were filled with 30 mL of the nanoemulsion. One of these was left to rest at room temperature and the other was submitted to the same conditions as the flask containing the contaminated sand. The aim of this procedure was to observe the stability of the nanoemulsions submitted to the washing conditions.

To determine the best conditions to wash the contaminated sand, the time, temperature, and shaking speed in the shaker bath were varied. After the preestablished time, the flasks were removed from the shaker and left at rest for 24 hours, and then the nanoemulsion was separated out by centrifugation for characterization of the size of the dispersed droplets.

The process of extracting the oil from the sand was initially performed by adding two 30 mL aliquots of extractor solvent (Solbrax Eco 255/255 and toluene). This system was placed in the shaker bath at 298 K and agitated at 150 rpm for 1 hour. Then the system was left at rest for approximately 1 hour and placed in a centrifuge at 3000 rpm for 30 min to separate the sand from the solvent containing the oil. To guarantee that all of the oil was removed from the sand, the

same procedure was repeated with another 30 mL aliquot of the extractor solvent.

The chemical makeup of the oil removed from the sand was evaluated in a Varian Cary 50 series ultraviolet-visible spectrophotometer, using quartz cuvettes with a 2 mm optical pathway. The absorption intensity (*A*) readings of the electromagnetic radiation at the wavelength utilized for the extraction solutions were obtained directly from the device, and the oil content was calculated with the help of its respective response curve plotted from solutions in the extractor solvent of known concentrations. The wavelength chosen for the measurements was 750 nm, since at shorter wavelengths the absorption intensity values were off the device's scale or presented deviations from Lambert-Beer's Law [23].

3. Results and Discussion

3.1. Determination of the Cloud Point of the Nonionic Surfactants. The cloud point of aqueous solutions of nonionic surfactants is observed by increasing the temperature to the point where the ethylene oxide molecules become dehydrated and the surfactant separates out of the aqueous solution. The cloud point temperatures at concentrations of 10, 11, and 12 wt% are shown in Table 1.

It can be seen that an increasing surfactant concentration did not cause a significant variation in the cloud point values, which were within the measurement error range. The values presented in Table 1 are related to the first indication of clouding of the aqueous solutions of Ultrol L70. The clouding of the solution became more evident at higher temperatures (above 323 K), and the complete separation was observed at temperatures near 333 K.

3.2. Measurement of the Oil/Water Interfacial Tension. To produce stable nanoemulsions it is necessary for the oil/water interfacial tension to be minimized [24]. Therefore, analyses of this tension are very important, because they supply information about the surfactant concentrations at which sufficiently low interfacial tension values can be attained.

The interfacial tension of the water/Solbrax system was 19.5 mN·m⁻¹. Analysis of the oil/water interfacial tension values in Table 1 shows that the surfactant at the concentrations utilized reduced the tension values to very low levels.

3.3. Determination of the PIT of the Systems by Rheometry. The PIT values of the oil/water dispersions were determined by measuring the viscosity of the surfactant/water/Solbrax system at varied concentrations: 5 wt% Solbrax and 10 and 12 wt% surfactant (Figure 1) and 20 wt% Solbrax and 10 and 12 wt% surfactant (Figure 2).

The PITs of all the systems were above 338 K, because Solbrax is mainly composed of aliphatic solvents, so the solubility inversion of the nonionic surfactant with increasing temperature is hindered, requiring higher temperatures. The lowest oil phase content (5 wt%) also retarded the phase inversion of the system [14]. In the obtained graphs this

TABLE 1: Cloud point of aqueous solutions of Ultrol L70 surfactant.

Surfactant	Concentrations (wt.%)	Cloud point (K)	W/O interfacial tension (mN·m ⁻¹)
Ultrol L70	10	306 ± 1	0.9 ± 0.1
	11	307 ± 1	0.5 ± 0.1
	12	308 ± 1	0.5 ± 0.1

The analyses were made in triplicate and the results were presented as average of each measure with its standard deviation.

TABLE 2: Experimental matrix for each combination of levels of the washing process of the contaminated sand and their respective efficiencies.

Systems	Time (h)	Speed (cycles·min ⁻¹)	Temperature (K)	X ₁ ^a	X ₂ ^a	X ₃ ^a	E ^b (%)
1	1	120	298	-1	-1	-1	17.33
2	1	120	318	-1	-1	1	39.13
3	1	240	298	-1	1	-1	26.65
4	1	240	318	-1	1	1	68.03
5	4	120	298	1	-1	-1	21.19
6	4	120	318	1	-1	1	83.29
7	4	240	298	1	1	-1	33.99
8	4	240	318	1	1	1	95.78
9	2.5	180	308	0	0	0	21.63
10	2.5	180	308	0	0	0	22.20
11	2.5	180	308	0	0	0	19.95
12	2.5	180	308	0	0	0	19.44
13	2.5	180	308	0	0	0	21.64

^aRepresentation of minimum, maximum and center points run. ^bEfficiency calculated by the ratio of initial and final oil concentrations.

TABLE 3: Efficiency of the nanoemulsion of the washing process of the sand.

Factors	Efficiency (%)		
	Effect	Standard error	P
Average/interaction	48.17	1.17	0.000
(1) Time (L)	20.78	2.35	0.001
(2) Speed (L)	15.88	2.35	0.001
(3) Temperature (L)	46.77	2.35	0.001
1 by 2	-3.23	2.35	0.227
1 by 3	15.18	2.35	0.001
2 by 3	4.82	2.35	0.096

transition was not well observed because the PIT is near the upper limit of the analysis.

3.4. Preparation and Characterization of the Nanoemulsions.

The nanoemulsions obtained were characterized in the particle size analyzer. All the tests were run in triplicate. The graphs in Figures 3 and 4 show the average particle size distribution, accompanied by the respective error bars. The size of the droplets dispersed in the nanoemulsions was measured just after preparation (time 0) and at other time intervals until phase separation was observed.

It can be seen that as the concentration of the oil phase increased the size of the particles dispersed in the continuous phase increased as well. Also, the most stable nanoemulsion was that prepared with the lowest oil phase and the highest

surfactant levels (5 wt% and 12 wt%, resp., Figure 3(b)). This nanoemulsion was the only one still stable after four months.

3.5. Performance of the Nanoemulsions in Washing Sand Contaminated with Oil.

There is growing interest in finding better strategies to clean up contaminated soil. In this study, we evaluated the use of nanoemulsions to remove crude oil from sand.

When sand particles are contaminated, the oil is retained both on the surface and in the pores of the grains. The physical-chemical process to clean the sand with emulsions entails dissolving the oil in the droplets dispersed in these systems. The main advantage of using nanoemulsions is that the droplets' small size allows them not only to dissolve the oil on the surface of the grains, but also to penetrate into the pores to remove the oil retained there as well.

We tested the nanoemulsion prepared with 12 wt% of the Ultrol L70 surfactant and 5 wt% of Solbrax. We chose this nanoemulsion, because it had the smallest particle size and the best stability among those tested previously.

3.6. Influence of Time, Shear Rate, and Temperature on the Efficiency of the Nanoemulsions to Wash Sand.

We used a 2³ factorial experimental setup with center point run to analyze the performance of the nanoemulsion chosen in washing sand contaminated with oil. The parameters varied were temperature, shaking speed, and time in the shaker bath. The most stable nanoemulsion was formed by Solbrax as the oil phase was at surfactant concentrations of 5 wt% and 12 wt%.

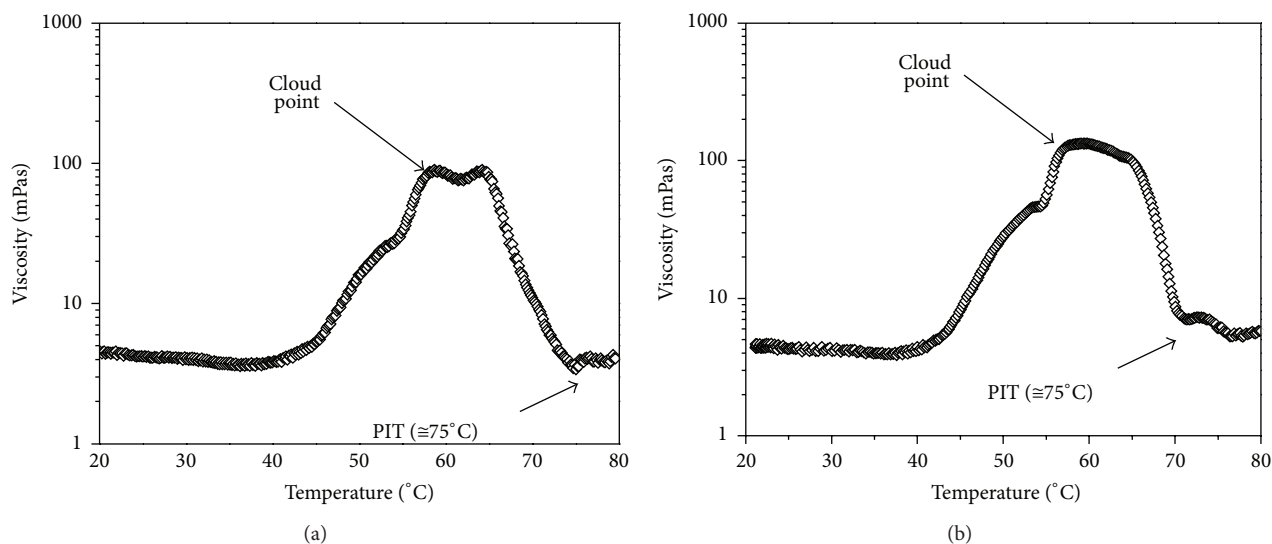


FIGURE 1: PIT for the systems of 5 wt% Solbrax and different concentrations of surfactant: (a) 10 wt% and (b) 12 wt%.

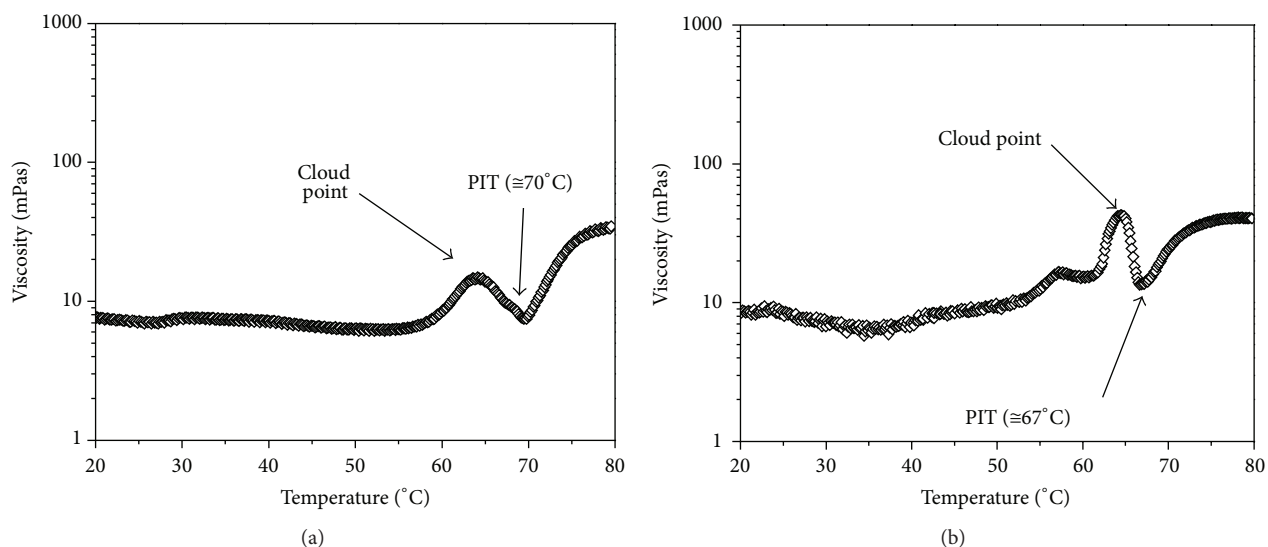


FIGURE 2: PIT for the systems of 20 wt% Solbrax and different concentrations of surfactant: (a) 10 wt% and (b) 12 wt%.

From the results of the previous experiments, we set a level for each variable to determine the interval that would be analyzed. The starting point was a temperature of 308 K, shear rate of $180 \text{ cycles} \cdot \text{min}^{-1}$, and washing time of 2.5 hours (called the center point run: 0). The intervals used were $\pm 10^\circ\text{C}$, $\pm 60 \text{ cycles/min}$, and $\pm 1.5 \text{ h}$. This design consists of 2 levels and 3 factors, requiring $2 \times 2 \times 2 = 8$ different tests. All told, we conducted 13 tests; 5 of them are repetitions at the center point run. Table 2 shows the experimental matrix and the efficiencies observed for each combination of levels.

We used the Statistica program to obtain the values of the effects of each parameter (time, speed, and temperature), as shown in Table 3, on the efficiency of the systems. In all cases, the results were considered significant when $P < 0.05$.

As can be seen in Table 2, the nanoemulsion's efficiency in washing the oil-contaminated sand was significantly affected

by the time and shear rate: the higher the factors, the more efficient the nanoemulsion. Regarding the interaction of one factor with the other, only the synergy between time and temperature was statistically significant. Figure 5 shows that the model proposed is able to represent the experimental data very well ($r^2 \cong 1$).

The results obtained show that the most efficient washing was attained at the highest temperature studied (318 K). The higher temperature probably facilitates the desorption process. Besides this, the washing time is more significant than the shear rate.

The predominance of these factors (temperature and time) can be explained by the low concentration of the oil phase in this emulsion (Solbrax Eco—5 wt%). However, the system's good efficiency shows its potential application even at low Solbrax Eco levels.

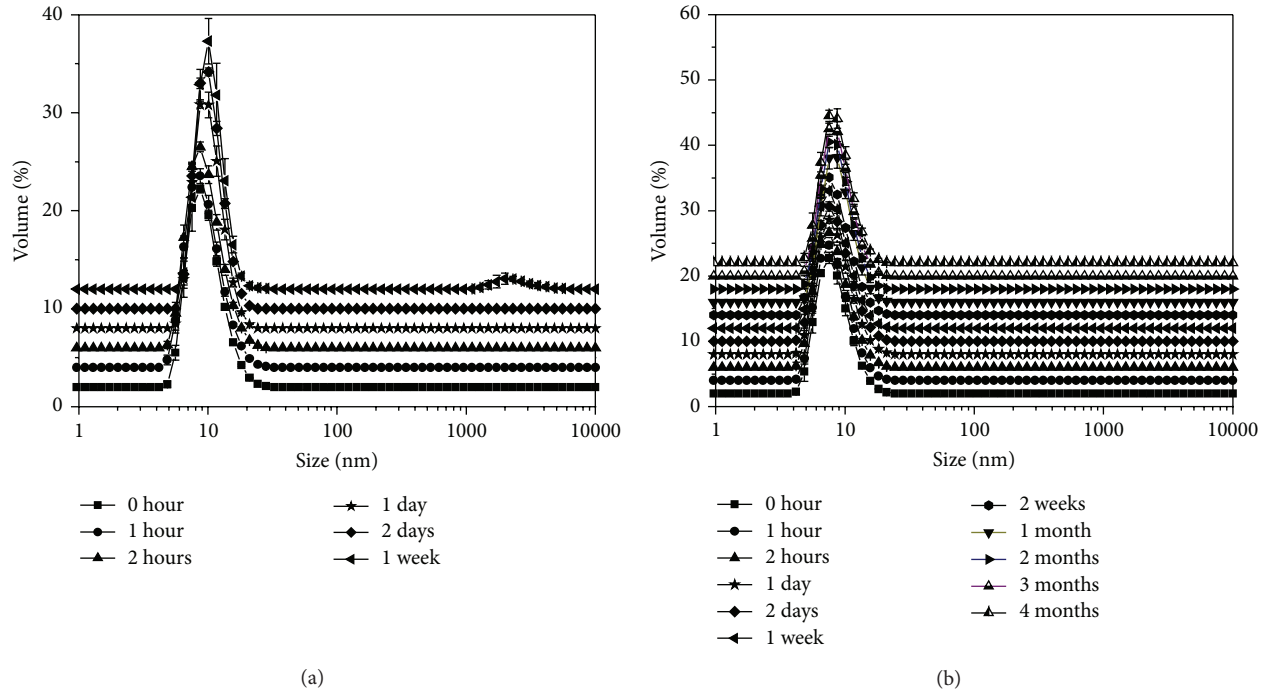


FIGURE 3: Particle size distribution of emulsions as a function of preparation time, using a 5 wt% Solbrax and different concentrations of surfactant: (a) 10 wt% and (b) 12 wt%.

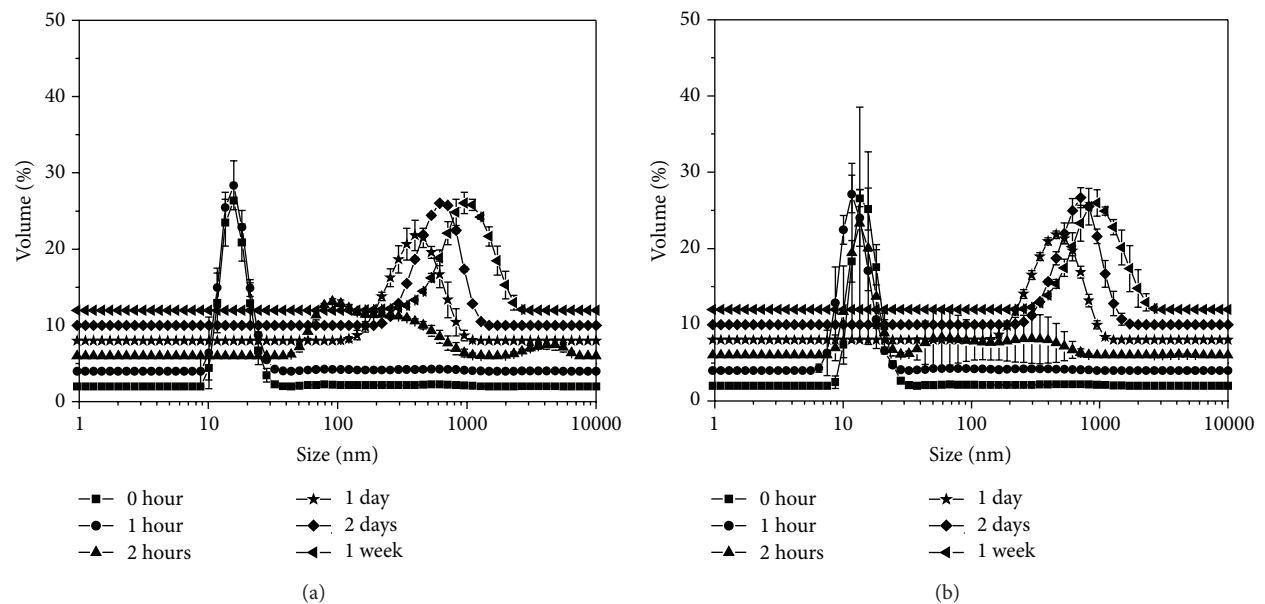


FIGURE 4: Particle size distribution of emulsions as a function of preparation time, using a 20 wt% Solbrax and different concentrations of surfactant: (a) 10 wt% and (b) 12 wt%.

Finally, the nanoemulsions remained stable during the entire cleaning process, for extraction of the quantity of oil used in this work (66,666 mg/L). The nanoemulsion evaluated was stable with droplet sizes within the same range presented in Figure 3(b), even under the varied time and shear rate conditions to which it was submitted.

This behavior is desirable to ensure the nanoemulsion's efficiency in removing the contaminant in the oil phase. As the temperature was varied from 298 to 318 K, there was a slight increase in the droplet size, which can be attributed to the lower solubility of the surfactant in the aqueous solution.

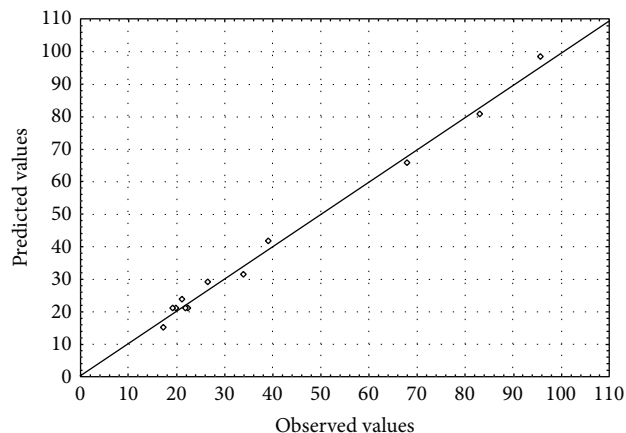


FIGURE 5: Observed versus predicted values of efficiency.

4. Conclusions

The phase inversion process caused by the variation in temperature (PIT), a known method to produce stable nanoemulsions, proved to be an effective method to produce stable nanoemulsions from Solbrax/water, in the presence of the nonionic ethoxylated lauryl ether surfactant (Ultrol L70), containing seven ethylene oxide units.

Efficiencies of around 90% were achieved in removing oil from contaminated sand using the most stable nanoemulsion (containing 5 wt% oil phase and 12 wt% Ultrol L70 surfactant).

The nanoemulsion utilized to wash the sand contaminated with crude oil remained stable, even when submitted to the conditions employed in this process (time, temperature, and shear rate).

Conflict of Interests

The authors declare that there is no conflict of interests regarding the publication of this paper.

Acknowledgments

The authors thank Oxiteno do Brasil for donating the polyoxide samples and the Petrobras Research Center (CEN-PES), the Coordinating Office for Improvement of University Researchers (CAPES), the National Council for Scientific and Technological Research (CNPq), the Office to Finance Studies and Projects (FINEP), and the National Petroleum Agency (ANP) for financial support.

References

- [1] K. Urum, S. Grigson, T. Pekdemir, and S. McMenemy, "A comparison of the efficiency of different surfactants for removal of crude oil from contaminated soils," *Chemosphere*, vol. 62, no. 9, pp. 1403–1410, 2006.
- [2] Q. Zhou, F. Sun, and R. Liu, "Joint chemical flushing of soils contaminated with petroleum hydrocarbons," *Environment International*, vol. 31, no. 6, pp. 835–839, 2005.
- [3] L. L. Schramm, *Surfactants: Fundamentals and Applications in the Petroleum Industry*, Cambridge University Press, New York, NY, USA, 1st edition, 2000.
- [4] D. H. Lee, R. D. Cody, D. J. Kim, and S. Choi, "Effect of soil texture on surfactant-based remediation of hydrophobic organic-contaminated soil," *Environment International*, vol. 27, no. 8, pp. 681–688, 2002.
- [5] A. M. Al-Sabagh, N. S. Ahmed, A. M. Nassar, and M. M. Gabr, "Synthesis and evaluation of some polymeric surfactants for treating crude oil emulsions. Part I. Treatment of sandy soil polluted with crude oil by monomeric and polymeric surfactants," *Colloids and Surfaces A: Physicochemical and Engineering Aspects*, vol. 216, no. 1–3, pp. 9–19, 2003.
- [6] M. S. Kuyukina, I. B. Ivshina, S. O. Makarov, L. V. Litvinenko, C. J. Cunningham, and J. C. Philp, "Effect of biosurfactants on crude oil desorption and mobilization in a soil system," *Environment International*, vol. 31, no. 2, pp. 155–161, 2005.
- [7] K. Urum, T. Pekdemir, and M. Gopur, "Optimum conditions for washing of crude oil-contaminated soil with biosurfactant solutions," *Process Safety and Environmental Protection*, vol. 81, no. 3, pp. 203–209, 2003.
- [8] K. Urum, T. Pekdemir, D. Ross, and S. Grigson, "Crude oil contaminated soil washing in air sparging assisted stirred tank reactor using biosurfactants," *Chemosphere*, vol. 60, no. 3, pp. 334–343, 2005.
- [9] M. C. K. Oliveira and G. G. Maldonado, PI 0605007-7. Composição para remediação de solos e resíduos sólidos contaminados por hidrocarbonetos de alto peso molecular, 2006.
- [10] C. L. Yap, S. Gan, and H. K. Ng, "Application of vegetable oils in the treatment of polycyclic aromatic hydrocarbons-contaminated soils," *Journal of Hazardous Materials*, vol. 177, no. 1–3, pp. 28–41, 2010.
- [11] P. F. Oliveira, L. S. Spinelli, and C. R. E. Mansur, "The application of nanoemulsions with different orange oil concentrations to remediate petroleum-contaminated soil," *Journal of Nanoscience and Nanotechnology*, vol. 12, no. 5, pp. 4081–4087, 2012.
- [12] T. Tadros, P. Izquierdo, J. Esquena, and C. Solans, "Formation and stability of nano-emulsions," *Advances in Colloid and Interface Science*, vol. 108–109, pp. 303–318, 2004.
- [13] K. Ouzineb, C. Lord, N. Lesauze, C. Graillat, P. A. Tanguy, and T. McKenna, "Homogenisation devices for the production of miniemulsions," *Chemical Engineering Science*, vol. 61, no. 9, pp. 2994–3000, 2006.
- [14] V. B. Souza, L. S. Spinelli, G. Gonzalez, and C. R. E. Mansur, "Determination of the phase inversion temperature of orange oil/water emulsions by rheology and microcalorimetry," *Analytical Letters*, vol. 42, no. 17, pp. 2864–2878, 2009.
- [15] L. S. Spinelli, C. R. E. Mansur, G. González, and E. F. Lucas, "Evaluation of process conditions and characterization of particle size and stability of oil-in-water nanoemulsions," *Colloid Journal*, vol. 72, no. 1, pp. 56–65, 2010.
- [16] L. R. Kourniatis, L. S. Spinelli, G. González, and C. R. E. Mansur, "Nanoemulsões óleo de laranja/água preparadas em homogeneizador de alta pressão," *Química Nova*, vol. 33, pp. 295–300, 2010.
- [17] L. R. Kourniatis, L. S. Spinelli, C. R. Piombini, and C. R. E. Mansur, "Formation of orange oil-in-water nanoemulsions using nonionic surfactant mixtures by high pressure homogenizer," *Colloid Journal*, vol. 72, no. 3, pp. 396–402, 2010.

- [18] D. J. Miller, T. Henning, and W. Grünbein, "Phase inversion of W/O emulsions by adding hydrophilic surfactant—a technique for making cosmetics products," *Colloids and Surfaces A: Physicochemical and Engineering Aspects*, vol. 183-185, pp. 681–688, 2001.
- [19] E. W. Duck, "Emulsion polymerization," in *Encyclopedia of Polymer Science and Technology*, H. F. Mark, N. G. Gaylord, and N. M. Bikales, Eds., vol. 5, pp. 801–859, Wiley-Interscience, New York, NY, USA, 1966.
- [20] N. Anton, P. Gayet, J.-P. Benoit, and P. Saulnier, "Nanoemulsions and nanocapsules by the PIT method: an investigation on the role of the temperature cycling on the emulsion phase inversion," *International Journal of Pharmaceutics*, vol. 344, no. 1-2, pp. 44–52, 2007.
- [21] J. A. Costa, E. F. Lucas, Y. G. C. Queirós, and C. R. E. Mansur, "Evaluation of nanoemulsions in the cleaning of polymeric resins," *Colloids and Surfaces A: Physicochemical and Engineering Aspects*, vol. 415, pp. 112–118, 2012.
- [22] V. B. Souza, S. M. Almeida, L. S. Spinelli, and C. R. E. Mansur, "Stability of orange oil/water nanoemulsions prepared by the PIT method," *Journal of Nanoscience and Nanotechnology*, vol. 11, no. 3, pp. 2237–2243, 2011.
- [23] J. A. McDonald and A. R. Rennie, "A structural study of mixed micelles containing C16TAB and C12E6 surfactants," *Langmuir*, vol. 11, no. 5, pp. 1493–1499, 1995.
- [24] D. J. Shaw, *Introdução à Química dos Colóides e de Superfícies*, Edgard Blücher Ltda, São Paulo, Brazil, 1975.

Research Article

Preparation of Polyvinyl Alcohol/Xylan Blending Films with 1,2,3,4-Butane Tetracarboxylic Acid as a New Plasticizer

Cun-dian Gao,¹ Jun-li Ren,¹ Shuai-yang Wang,¹ Run-cang Sun,^{1,2} and Li-hong Zhao¹

¹ State Key Laboratory of Pulp and Paper Engineering, South China University of Technology, Guangzhou, Guangdong 510641, China

² Institute of Biomass Chemistry and Technology, College of Materials Science and Technology, Beijing Forestry University, Beijing 100083, China

Correspondence should be addressed to Jun-li Ren; renjunli@scut.edu.cn and Li-hong Zhao; zhaohlh@scut.edu.cn

Received 24 January 2014; Accepted 17 February 2014; Published 27 March 2014

Academic Editor: Ming-Guo Ma

Copyright © 2014 Cun-dian Gao et al. This is an open access article distributed under the Creative Commons Attribution License, which permits unrestricted use, distribution, and reproduction in any medium, provided the original work is properly cited.

Miscible, biodegradable polyvinyl alcohol (PVA)/xylan blending films were firstly prepared in the range of the PVA/xylan weight ratio from 1:2 to 3:1 by casting method using 1,2,3,4-butane tetracarboxylic acid (BTCA) as a new plasticizer. The properties of blending films as functions of PVA/xylan weight ratio and BTCA amount were discussed. XRD and FT-IR were applied to characterize the blending films. Experimental results indicated that tensile strength (TS) and elongation at break (EAB) of blending films decreased along with the decrease of the PVA/xylan weight ratio. Both of TS and EAB firstly increased and then decreased as the amount of BTCA was increased. More importantly, blending films were biodegraded almost by 41% with an addition of 10% BTCA in blending films within 30 days in soil. For all hydroxyl functionalized polymers (xylan and PVA), their molecular interactions and miscibility with BTCA endowed blending films with the biocompatibility and biodegradability. Therefore, these blending films are environmentally friendly materials which could be applied as biodegradable plastics for food packaging and agricultural applications.

1. Introduction

In recent years, to meet the requirements for environmental protection, multifunctional utilization of natural resources, and increased pressure from related strict laws, efforts have been made to develop biodegradable composite plastic products by incorporating biocompatible polymers as an alternative to conventional synthetic plastic materials derived from petroleum [1, 2]. Moreover, there is an increasingly important trend to explore natural renewable raw materials for the food industries and nonfood industries owing to their sustainable and biodegradable features.

Xylan is derived from hemicellulose which is one of the three primary components of the plant cell wall [3] and many researchers paid extensive attention to the exploration of xylan because of its abundance and biodegradability. Hemicelluloses (mainly xylans and mannans) were used as sustainable packaging materials and more hydrophobic films with the low water vapor and oxygen permeability

could be obtained [4, 5]. Xylan films modified by long-chain anhydride were prepared [6]. Modified xylan had better film-forming performance and the tensile strength had increased and moisture-sensitive properties had been lessened due to long carbon chains modification. Xylan has poor film-forming ability and pure xylan films were brittle due to the hydroxyl groups present in each of their repeating units [7]. To solve this problem, different types of plasticizers such as oligosaccharides, polyols, some organic acids, lipids, and ether were added in order to improve mechanical performance of biopolymers films [8–11]. It was found that mechanical properties of xylan-based films were strengthened by blending with nanosized particles [5]. More hydrophobic butylated xylan films were prepared by Peresin et al. [11]. The water sensitivity and wetting behaviour of the xylan derivatives were altered during etherification. Mikkonen et al. [12] studied arabinoxylan films plasticized with glycerol and sorbitol; they found that an increase in the total plasticizer content resulted in more permeable films.

Polyvinyl alcohol (PVA) is excellently fit for blending with natural polymers as it is highly polar and controllable in water solutions [13]. Additionally, it is a biocompatible synthetic crystalline polymer with high tensile strength and flexibility [14]. Several investigations have been carried out on blending PVA with other biopolymers, such as PVA/chitosan [15], PVA/starch [16, 17], and PVA/gelatin [18]. Modification and biocompatibility of PVA/chitosan films were investigated by Zhuang et al. [15]. It was observed that the addition of PVA could improve the film's flexibility and wettability. All prepared PVA/chitosan films were biocompatible. Moreover, the tensile strength (TS) of the PVA/starch films increased about 60% without additives, while EAB decreased about 420.5% [17]. And the films were degraded by about 45–65% after 165 days in soil. Thus, the blending of PVA and natural polymers could improve the properties of natural polymers films for widening the application of films. However, few researchers have made attempts to study biomaterial films by blending PVA with xylan.

1,2,3,4-Butane tetracarboxylic acid (BTCA) is one of polycarboxylic acids (PCAs). BTCA as a crosslinking agent was used to produce a cotton fabric, and the treated fabric showed a reasonable hydrophobicity [19]. Water-resistant hemicelluloses (HC) films were prepared with about 10–11% of BTCA [20]. The water vapor permeability of HC films with a modification of BTCA reduced about twice the untreated films. The effects of BTCA on hydrophobic cellulose fabric by scanning electron microscopy were investigated and the better durable fabric was obtained [21]. So the addition of BTCA could have important effects on the properties of films and fabrics.

In view of the issue mentioned above, the objective of our study was to prepare miscible and biodegradable PVA/xylan blending films by casting method with the addition of BTCA as a plasticizer for improving the properties of blending films. The influences of the PVA/xylan weight ratio and BTCA amounts on the blending films properties were discussed. The mechanical properties, water vapor permeability, the degree of solubility, thermal stability, and degradability were evaluated for PVA/xylan blending films.

2. Experimental

2.1. Materials. Beech wood xylan ($M_w \sim 130,000$ g/mol) and PVA (M_w of 146,000–186,000 g/mol) were purchased from Sigma Aldrich (Germany) and used without further purification. BTCA was supplied by Aladdin Reagent Company Limited (Shanghai, China). Anhydrous calcium chloride (CaCl_2) and sodium chloride (NaCl) were of analytical-reagent grade and obtained from Guangzhou Chemical Reagent Factory (Guangzhou, China). Deionized water was used in the preparation of the blending films.

2.2. Blending Films Preparation. The PVA/xylan blending films were prepared by solution casting method. A predetermined amount of PVA was added to ultrapure water. The mixture was stirred for 0.5 h at room temperature and then heated at 95°C for 1.5 h. After PVA was dissolved completely,

TABLE 1: Detailed composition and abbreviations of PVA/xylan blending films.

Samples	PVA : xylan	BTCA (%)
P3X1	3 : 1	20
P2X1	2 : 1	20
P1X1	1 : 1	20
P1X2	1 : 2	20
PX0	3 : 1	0
PX5	3 : 1	5
PX10	3 : 1	10
PX15	3 : 1	15
PX25	3 : 1	25
PX30	3 : 1	30

xylan was added. After 30 minutes, BTCA as a new plasticizer was added in the mixture solution. The resulting solution reacted at 75°C for 4 h and then poured onto a 110 × 110 × 7 mm teflon mould. Water was dried slowly in a ventilated oven at 40°C overnight. All films were obtained with a uniform thickness and were stored at 23°C with 50% RH at least 48 h prior to all measurements. The blending films with different PVA/xylan weight ratio and BTCA amounts were shown in Table 1.

2.3. Method of Characterization

2.3.1. Tensile Strength (TS) and Elongation at Break (EAB). TS and EAB of films were evaluated using a tensile testing machine (Instron Universal Test Machine Model 5565, USA) fitted with a 100 N load cell. Five samples (110 mm length, 150 mm width) of each film were cut by a paper cutter (FQ-QZD15, Sichuan, China). The crosshead speeds of 30 mm and 20 mm/min were used for testing the mechanical properties. The maximum load and the final extension at break were used for calculation of TS and EAB, respectively.

2.3.2. Water Vapor Permeability (WVP). The WVP assessment was determined according to a gravimetric method and performed as described by Kayserilioğlu et al. [22] with minor modification. Film specimens were clamped on the top of polyethylene bottles containing 3 g anhydrous CaCl_2 to maintain 0% RH inside the bottle, followed by sealing the film over the edge of bottle with vaseline. And then the bottles were located in a dryer at 23°C and 75% RH. The RH was maintained by placing 500 mL of saturated NaCl solution in the bottom of the dryer. The bottle was weighed every 24 h, and WVP value was calculated by

$$\text{WVP} = \frac{\Delta w \times L}{(\Delta t \times A)}, \quad (1)$$

where WVP was water vapor permeability ($\text{g} \cdot \mu\text{m} \cdot \text{cm}^{-2} \cdot \text{h}^{-1}$). $\Delta w/\Delta t$ was the gain rate of bottle (g/h). A was exposed area of the film (cm^2). L was the mean thickness of the film (μm).

2.3.3. The Water Absorption (WA), Solubility (S), and Water Content (WC). A certain quality (m_0) of oven-dried

PVA/xylan blending films was cut into $2 \times 2 \text{ cm}^2$ and dipped in 20 mL ultrapure water for 24 h at room temperature. Then we wiped off the excess moisture in the surface of the swollen samples and weighed the weight (m_1). Afterward, the soaked films were dried again at 105°C to the constant weight (m_2). The water absorption (WA) and solubility (S) are calculated with

$$\text{WA} = \frac{(m_1 - m_2)}{m_0}, \quad (2)$$

$$S(\%) = \frac{(m_0 - m_2)}{m_2} \times 100.$$

Water content was determined at 23°C and 50% RH for two days when the weight of the films was regarded as m . Then the samples were dried at 105°C to reach constant weight (m_3). Water content (WC) was calculated as follows:

$$\text{WC}(\%) = \frac{(m - m_3)}{m_3} \times 100\%. \quad (3)$$

2.3.4. Thermogravimetric Analysis (TGA). A simultaneous thermal analyzer (TGA Q500, TA Instruments, New Castle, USA) was used for the thermogravimetric analysis of blending films. Film samples of approximately 9–11 mg were cut into pieces and heated at a rate of $10^\circ\text{C}/\text{min}$ from room temperature to 600°C under a nitrogen atmosphere (a flow rate about 20 mL/min). All films were conditioned at $23^\circ\text{C}/50\%$ RH for one week before TGA.

2.3.5. FTIR Spectra. Film samples were cut into pieces ($10 \text{ mm} \times 10 \text{ mm}$) and dried in the infrared drying oven. FTIR spectra were measured on a Fourier transform spectrophotometer (Nicolet 750, Florida, USA). The absorbance spectrum ($4000\text{--}400 \text{ cm}^{-1}$) was acquired at 4 cm^{-1} resolution and recorded for a total of 32 scans, using Attenuated Total Reflectance technique (see Figure 5).

2.3.6. X-Ray Diffraction. X-ray patterns of PVA, xylan, and PVA/xylan blending film were analyzed using an X-ray diffractometer (Bruker, model D8 advance) with $\text{Cu K}\alpha$ radiation at a voltage of 40 kV and 40 mA. The measurements were made with scattering angles of $3\text{--}40^\circ$ and a scanning speed of $2^\circ/\text{min}$. The samples were dried and stored in a desiccator before testing.

2.3.7. The Degradability of Blending Films in Soil. The degradability of blending films was determined by soil burial degradation. $3 \times 3 \text{ cm}$ squares were cut from the cast film and buried in the soil at the depth of 10 cm in a gardening pot. The pot was exposed to atmospheric conditions for 30 days. The time required for blending films to disintegrate was recorded. To determine the weight loss in specimens, films were first dry-cleaned with a brush and the weight was recorded. A specimen of each sample was quickly cleaned and then the sample was dried in an oven at 70°C to constant weight and

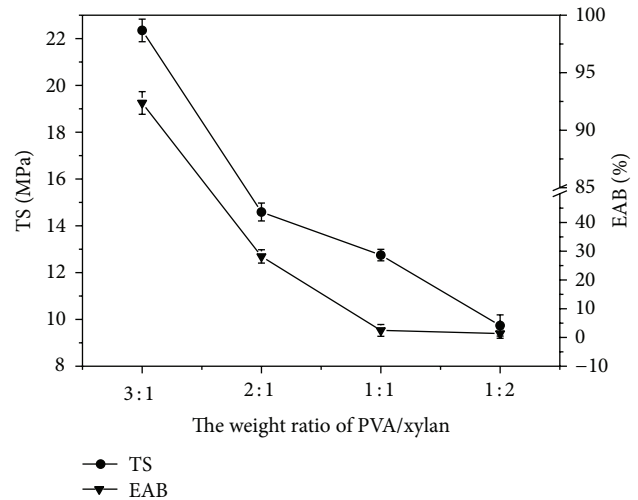


FIGURE 1: The effect of the weight ratio of PVA/xylan on TS and EAB of blending films with 20% BTCA.

allowed to equilibrate in desiccators prior to weighing. The degradation degree (the weight loss) was determined by

$$\text{Weight loss}(\%) = \frac{m_{\text{ini}} - m_{\text{dry}}}{m_{\text{ini}}} \times 100\%, \quad (4)$$

where m_{ini} is the initial weight of the film sample before burial and m_{dry} is the dry weight of the sample after burial for known days.

3. Results and Discussion

3.1. Mechanical Properties. The thickness of blending films which has a significant influence on mechanical properties of the PVA/xylan blending films was measured by Lorentzen & Wettre thickness gauge (Sweden) for precise specimens ($55\text{--}60 \mu\text{m}$). The effect of the weight ratio of PVA/xylan on TS and EAB of the blending films with the addition of 20% BTCA is shown in Figure 1. The results indicated that TS and EAB of the blending composite films decreased obviously along with the decrease of the weight ratio of PVA and xylan from 3:1 to 1:2. The reason explained was that PVA has high tensile strength with hydrogen bonds and xylan is brittle and amorphous with its acetyl and feruloyl groups, as well as $\alpha\text{-D-glucopyranosyl uronic acid}$ or 4-O-methyl ether [4, 10, 23]. The values of TS and EAB reached to 22.4 MPa and 92.4%, respectively, as the weight ratio of PVA and xylan was 3:1.

Figure 2 shows the effect of BTCA content on TS and EAB of blending films at the PVA/xylan weight ratio of 3:1. When BTCA content was 0%, the lowest value of EAB was obtained while relatively high TS value was present. With increasing BTCA content to 5%, a decrease in TS and an increase in EAB were observed. With a further increment of BTCA amount from 5% to 30%, both TS values and EAB increased first and then decreased in the range of 16.4–22.4 MPa and 45.5%–92.4%, respectively. It could be explained that polymer-polymer interactions strengthen intermolecular forces at the

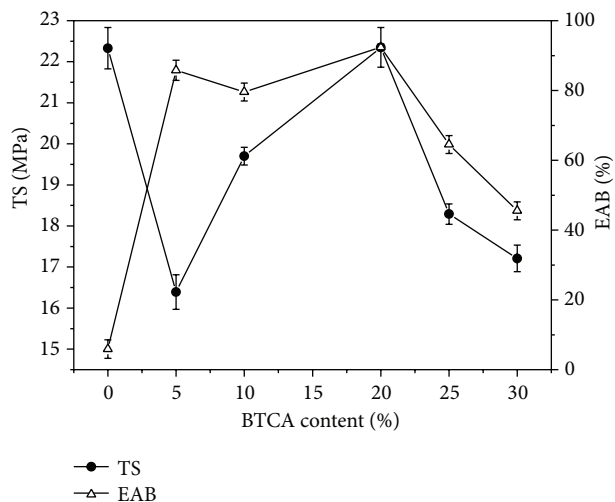


FIGURE 2: The effect of the BTCA content on TS and EAB of the blending films.

beginning of adding BTCA. Subsequently, the formation of polymer-plasticizer interactions among the macromolecules restrained intermolecular mobility and revealed the decrease of TS and EAB [24]. When BTCA amount reached 20%, TS and EAB obtained their maximum values simultaneously which were higher than the PVA/polysaccharides (angico gum and/or cashew gum) blended films investigated by Silva et al. [25]. Moreover, the addition of BTCA provided the hydroxyl-rich chemicals with carboxyl functional groups. Yoon et al. [26] verified that additives of the films with hydroxyl and carboxyl groups were stronger and more flexible than those with only hydroxyl groups. Thus BTCA had the important impact on mechanical properties of PVA/xylan blending films.

3.2. WVP Measurement. WVP is an important parameter of film for potential applications such as food packaging. Figure 3 illustrates the effect of the weight ratio of PVA/xylan and the BTCA content on WVP. Clearly, WVP was decreased slightly and then increased sharply with the weight ratio of PVA/xylan changing from 3:1 to 1:2 at the 20% BTCA content. The lowest value was achieved to $0.017 \text{ g}\cdot\mu\text{m}\cdot\text{cm}^{-2}\cdot\text{h}^{-1}$ when the PVA/xylan weight ratio was 2:1 (P2X1), and the highest value was $0.054 \text{ g}\cdot\mu\text{m}\cdot\text{cm}^{-2}\cdot\text{h}^{-1}$ at the PVA/xylan weight ratio of 1:2 (P1X2). These results could be attributed to the changes in the functionality properties of the blending films prepared in the different PVA/xylan weight ratio. Clearly, BTCA had a remarkable influence on WVP. When the BTCA content was 5%, WVP of PVA/xylan blending films had the lowest values for $0.015 \text{ g}\cdot\mu\text{m}\cdot\text{cm}^{-2}\cdot\text{h}^{-1}$ at the PVA/xylan weight ratio of 3:1. This meant that WVP decreased with addition of a little amount of BTCA. This result might be attributed to the water-resistant nature of BTCA. Nevertheless, the WVP increase was directly proportional to the BTCA content in the range of 10%–25% and then incremented sharply up to the highest values of $0.0274 \text{ g}\cdot\mu\text{m}\cdot\text{cm}^{-2}\cdot\text{h}^{-1}$ at the content of 30% BTCA. The

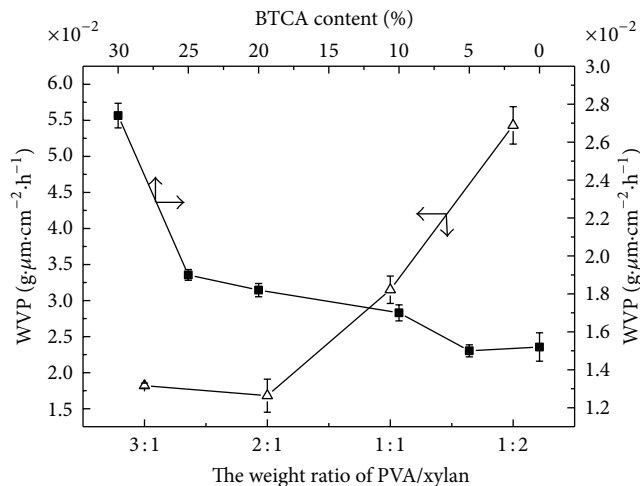


FIGURE 3: The effect of the weight ratio of PVA/xylan and the BTCA content on WVP.

TABLE 2: The WA, S, and WC of all the PVA/xylan blending films.

Samples	WA	S (%)	WC (%)
P3X1	0.45	19.16	8.53
P2X1	0.62	22.35	10.53
P1X1	0.84	26.38	11.65
P1X2	0.93	30.15	12.31
PX0	1.30	37.29	7.44
PX5	1.18	26.74	11.62
PX10	1.07	26.76	16.59
PX25	0.34	25.51	9.12
PX30	0.31	31.22	9.27

higher plasticizer content resulted in more permeable films [27]. Mikkonen et al. [12] gained the same conclusions. This may be due to the formation of intermolecular interactions of BTCA and polyhydroxylic compounds with the increase of BTCA content.

As reported in the literature, García et al. [28] speculated many factors such as polymeric chain mobility and specific interaction between the functional groups of the polymers had effects on WVP. The decrease of WVP may be due to the formation of new interchain interaction. Ghasemlou et al. [29] decreased WVP and improved barrier properties of starch films up to 50% relative to the control sample by adding *Zataria multiflora* Boiss (ZEO) or *Mentha pulegium* (MEO). They thought that the hydrogen and covalent interactions between the starch network and these polyphenolic compounds might limit the availability of hydrogen groups to form hydrophilic bonds with water.

3.3. The WA, S, and WC Determination. The WA, S, and WC of all the PVA/xylan blending films are shown in Table 2. These data were used to further analyze barrier properties of blending films according to the experimental design previously presented (Table 1). When the BTCA content

maintained 20%, the WA increased gradually with the weight ratio of PVA and xylan from 3 : 1 to 1 : 2. Comparatively, the highest WA value reached to 1.30 for the blending films in the PVA/xylan weight ratio of 3 : 1 without the addition of BTCA. When the weight ratio of PVA and xylan was 3 : 1, WA values were decreased along with BTCA amount increasing from 5% to 30%. So the addition of BTCA could efficiently reduce WA of blending films. It was due to increasing moisture barrier properties with addition of BTCA. The solubility of blending films is a crucial influencing factor for potential application such as food packaging. In most cases, water solubility should be lower in order to improve the water resistance and integrity of films, especially for packaging foods [30]. As we can see from Table 2, water solubility increased steadily from 19.16% (P3X1) to 30.15% (PIX2) with 20% BTCA. The increase of the solubility can be explained by the increase of content of hydroxyl groups with the increase of xylan in the blending films. The weight ratio of PVA and xylan was chosen for 3 : 1 which was superior to others as the solubility decreased up to 19.16%, lower than results of 20% solubility studied by Alves et al. [18]. Then *S* decreased with increasing BTCA content from 0% to 25%. However, when BTCA content reached 30%, the water solubility had a sudden increase which might be due to increment of hydrophilicity of blending films with high concentration of BTCA. Additionally, water content increased gradually with increasing weight ratio of PVA and xylan. For plasticized films, the addition of 20% BTCA to blending films (P3X1) was able to obtain relatively lower water content for 8.53%. This is interpreted as a result of interactions between BTCA and the PVA/xylan composite film matrix, which reduces in the film's affinity for water and limits the accessibility of water molecules in the films [31]. With a further increase of BTCA concentration, the film matrix exposed more hydroxyl groups and increased water uptake. Unplasticized samples had lower water uptake (7.44%).

3.4. Thermogravimetric Analysis (TGA). Thermogravimetric analysis is a standard technique to determine the composition or thermal stability of materials. The results of TGA and DTG curves of PVA/xylan blending films with different BTCA contents and PVA/xylan weight ratios are illustrated in Figure 4. The pure PVA/xylan films (PX0) exhibited apparently two-step degradation. With the degradation of PVA and xylan chains, the first step region occurred at around 250–330°C, and then carbonization of polymer matrix at the high temperature around 390–470°C formed the second degradation region. In contrast, the BTCA-plasticized films (P3X1, PIX1, and PX10) had three-step degradation process without obvious demarcation line. Four degradations peaks for PX0, P3X1, PX10, and PIX1 were observed at 316, 441, 361, and 433°C, respectively. The sudden drop in weight with increasing temperature occurred between 250 and 400°C. The decrease of hydrogen bonds may lead to the decreasing thermal stability of films, because the rupture of hydrogen bonds requires more energy during thermal degradation [6]. As expected, the total weight loss of the plasticized PVA/xylan films was lower than that of pure composite film (PX0).

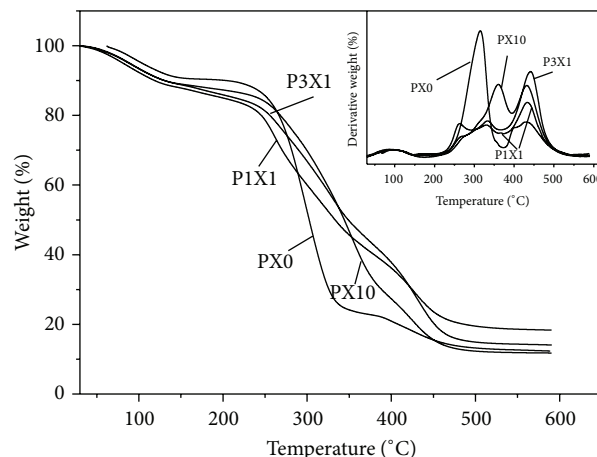


FIGURE 4: TGA and DTGA curves of PVA/xylan blending films.

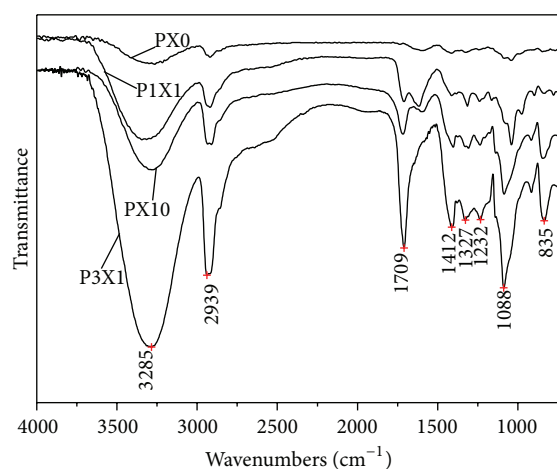


FIGURE 5: FTIR spectra of PVA/xylan blending films.

This might be due to the incorporation of the BTCA which stabilized the composites at high temperature.

3.5. FTIR Spectroscopy. FTIR spectroscopy was used to examine the interactions between PVA/xylan and BTCA. The broad band at 3285 cm^{-1} originates from the stretching of -OH groups; this peak was larger than the film PX0 due to overlapping stretching of hydrogen bonds, O-H stretching of the composite films [32], which shifts 22 cm^{-1} compared with that of unplasticized PVA/xylan (3263 cm^{-1}). It indicated that BTCA interacted with PVA/xylan films matrix, and the hydroxyl groups between PVA and xylan were partially destructed [33]. And the peak at 2939 cm^{-1} is assigned to CH- stretching. A sharp band at 1709 cm^{-1} is the C=O bond and suggested the presence of a carbonyl group mainly from BTCA in the film matrix and the C=O bond stretching was stronger with the increase of BTCA which had similar trend with -OH stretching. The absorption bands at 1412 cm^{-1} in P3X1 can be attributed to O-H , C-H bending from PVA structure and the absorption bands at 1327 cm^{-1} , 1232 cm^{-1}

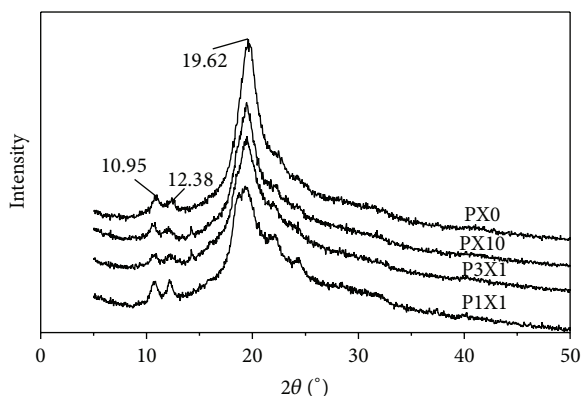


FIGURE 6: X-ray diffraction of PVA/xylan blending films.

to δ (OH) with C–H wagging, respectively. The bands from 835 to 1088 cm^{-1} corresponded to the C–O bond stretching.

3.6. X-Ray Diffraction. X-ray diffractograms of PVA/xylan blending films are shown in Figure 6. As observed, three main diffraction peaks (2θ about 10.95°, 12.38°, and 19.62°) were seen in the X-ray diffraction pattern. The unplasticized films had the highest intensity values corresponding to different regions. When the BTCA content increased from 10% to 20%, the intensity of crystalline peaks decreased a little and the diffraction patterns were quite similar and showed no significant differences with the presence of plasticizer (BTCA). However, the peak became wider and amorphous when the weight ratio of PVA and xylan reduced to 1:1. Furthermore, under this condition, two new peaks appeared at 2θ between 20° and 25°. These changes demonstrated an interaction between the components. The interaction restricted the mobility of the polymer chains and may lead to a considerable slowing of the recrystallization of the matrix during the drying process. This changes the crystalline structure of the composite films. Crystallinity analysis indicated that the xylan in the samples was semicrystalline [34]. Peng et al. [35] also found that the xylan films were semicrystalline.

3.7. Film Deterioration in Soil. The current study focused on increasing biocompatibility and degradability of blending films by adding biodegradable biopolymers. All the films had the same size and shape to prevent the external effects on biodegradation of films [36]. The dependence of degradation of PVA/xylan blending films with different BTCA contents as a function of time is presented in Figure 7. The test was carried out for 30 days of burial in soil under prevailing environmental conditions. For unplasticized films (PX0), the biggest characteristic of their decomposition rate was faster than plasticized films (PX10, PX30) in a beginning dozen days and then the weight loss gradually fell behind those that were plasticized by BTCA. After deterioration in soil about 12 days, blending films with 10% BTCA had higher weight loss ratio and showed a clear advantage. When the films were deteriorated for half a month, weight loss of PX10 reached 31.7%, while PX0 and PX30 were 28.5%, 26.6%,

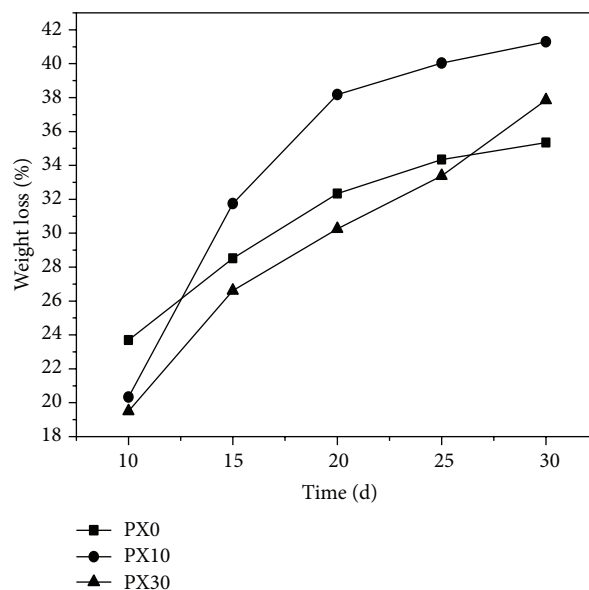


FIGURE 7: The effect of the different BTCA contents on the degradation of PVA/xylan blending films.

respectively. The weight loss of the PX30 films increased by 13.4% during the last 5 days in a month and rapidly surpassed the PX0 films. Eventually, the PX10 films were biodegraded by 41.29% within 30 days and the degree of disintegration was considerable. Chai et al. [16] investigated effects of the content of modified starch on the biodegradation of the PVA/modified starch blending films and the optimal degree of degradation was obviously below 40% within 30 days. The films with 30% BTCA also achieved 37.8%, while the weight loss of untreated films (PX0) was 35.3%, inferior to the plasticized films. Therefore, the addition of BTCA had a positive influence on degradation of PVA/xylan blending films. Imam et al. [37] explained that the addition of a plasticizer in formulations lowered the overall extent of degradation in composites. Also, biopolymers themselves like xylan have stronger biocompatibility and stimulate PVA degradation in soil.

4. Conclusions

PVA/xylan blending films by casting method were successfully synthesized by using BTCA as a new plasticizer. It was found that TS and EAB values reduced with the weight ratio of PVA/xylan from 3:1 to 1:2. Additionally, under the condition of optimal weight ratio of PVA/xylan for 3:1, both TS and EAB increased firstly and then decreased along with the increasing BTCA content. WVP was decreased first and then increased sharply with the decreasing weight ratio of PVA/xylan. The effect of BTCA content on WVP had similar tendency. The WA values were decreased along with increasing BTCA amount due to moisture barrier properties with addition of BTCA. The thermal stability of the plasticized blending films had improved. FTIR and XRD indicated the presence of interactions and structural changes between

BTCA and PVA/xylan matrix. During deterioration in soil for 30 days, PVA/xylan blending films achieved 41.3% weight loss. In summary, the PVA/xylan blending films performed desired mechanical properties and excellent biocompatibility and biodegradation, which indicate that PVA/xylan blending films have promising applications for food packaging and agricultural mulch owing to their sustainable and ecofriendly features.

Conflict of Interests

The authors declare that there is no conflict of interests regarding the publication of this paper.

Acknowledgments

This work was supported by Grants from National Natural Science Foundation of China (no. 31070530), the Author of National Excellent Doctoral Dissertation of China (201169), Guangdong Natural Science Funds for Distinguished Young Scholar (S20120011250), Science and Technology Project of Guangdong Province (2011B050400015), and the Fundamental Research Funds for the Central Universities (2014ZG0003), SCUT (South China University of Technology).

References

- [1] M. Jawaid and H. P. S. Abdul Khalil, "Cellulosic/synthetic fibre reinforced polymer hybrid composites: a review," *Carbohydrate Polymers*, vol. 86, no. 1, pp. 1–18, 2011.
- [2] Y. X. Xu, K. M. Kim, M. A. Hanna, and D. Nag, "Chitosan-starch composite film: preparation and characterization," *Industrial Crops and Products*, vol. 21, no. 2, pp. 185–192, 2005.
- [3] Z. Merali, J. D. Ho, S. R. A. Collins et al., "Characterization of cell wall components of wheat straw following hydrothermal pretreatment and fractionation," *Bioresource Technology*, vol. 131, pp. 226–234, 2013.
- [4] N. M. L. Hansen and D. Plackett, "Sustainable films and coatings from hemicelluloses: a review," *Biomacromolecules*, vol. 9, no. 6, pp. 1493–1505, 2008.
- [5] K. S. Mikkonen and M. Tenkanen, "Sustainable food-packaging materials based on future biorefinery products: xylan and mannans," *Trends in Food Science & Technology*, vol. 28, no. 2, pp. 90–102, 2012.
- [6] L. X. Zhong, X. W. Peng, D. Yang, X. F. Cao, and R. C. Sun, "Long-chain anhydride modification: a new strategy for preparing xylan films," *Journal of Agricultural and Food Chemistry*, vol. 61, no. 3, pp. 655–661, 2013.
- [7] Z. A. N. Hannai, J. McNamara, Y. H. Roos, and J. P. Kerry, "Effect of plasticizer content on the functional properties of extruded gelatin-based composite films," *Food Hydrocolloids*, vol. 31, no. 2, pp. 2642–2669, 2013.
- [8] N. Cao, X. Yang, and Y. Fu, "Effects of various plasticizers on mechanical and water vapor barrier properties of gelatin films," *Food Hydrocolloids*, vol. 23, no. 3, pp. 729–735, 2009.
- [9] J. Piermaria, A. Bosch, A. Pinotti, O. Yantorno, M. A. Garcia, and A. G. Abraham, "Kefiran films plasticized with sugars and polyols: water vapor barrier and mechanical properties in relation to their microstructure analyzed by ATR/FT-IR spectroscopy," *Food Hydrocolloids*, vol. 25, no. 5, pp. 1261–1269, 2011.
- [10] M. J. Fabra, P. Talens, R. Gavara, and A. Chiralt, "Barrier properties of sodium caseinate films as affected by lipid composition and moisture content," *Journal of Food Engineering*, vol. 109, no. 3, pp. 372–379, 2012.
- [11] M. S. Peresin, K. Kammiovirta, H. Setälä, and T. Temmelin, "Structural features and water interactions of etherified xylan thin films," *Journal of Polymers and the Environment*, vol. 20, no. 4, pp. 895–904, 2012.
- [12] K. S. Mikkonen, S. Heikkinen, A. Soovre et al., "Films from oat spelt arabinoxylan plasticized with glycerol and sorbitol," *Journal of Applied Polymer Science*, vol. 114, no. 1, pp. 457–466, 2009.
- [13] E. Chiellini, P. Cinelli, E. G. Fernandes, E.-R. S. Kenawy, and A. Lazzeri, "Gelatin-based blends and composites. Morphological and thermal mechanical characterization," *Biomacromolecules*, vol. 2, no. 3, pp. 806–811, 2001.
- [14] C.-C. Yang, "Synthesis and characterization of the cross-linked PVA/TiO₂ composite polymer membrane for alkaline DMFC," *Journal of Membrane Science*, vol. 288, no. 1–2, pp. 51–60, 2007.
- [15] P.-Y. Zhuang, Y.-L. Li, L. Fan, J. Lin, and Q.-L. Hu, "Modification of chitosan membrane with poly(vinyl alcohol) and biocompatibility evaluation," *International Journal of Biological Macromolecules*, vol. 50, no. 3, pp. 658–663, 2012.
- [16] W.-L. Chai, J.-D. Chow, and C.-C. Chen, "Effects of modified starch and different molecular weight polyvinyl alcohols on biodegradable characteristics of polyvinyl alcohol/starch blends," *Journal of Polymers & the Environment*, vol. 20, no. 2, pp. 550–564, 2012.
- [17] S.-D. Yoon, M.-H. Park, and H.-S. Byun, "Mechanical and water barrier properties of starch/PVA composite films by adding nano-sized poly(methyl methacrylate-co-acrylamide) particles," *Carbohydrate Polymers*, vol. 87, no. 1, pp. 676–686, 2012.
- [18] P. M. A. Alves, R. A. Carvalho, I. C. F. Moraes, C. G. Luciano, A. M. Q. B. Bittante, and P. J. A. Sobral, "Development of films based on blends of gelatin and poly(vinyl alcohol) cross linked with glutaraldehyde," *Food Hydrocolloids*, vol. 25, no. 7, pp. 1751–1757, 2011.
- [19] M. Montazer, P. Golshani, and M. B. Moghadam, "Hydrophobic, cross-linked and photoactive cotton fabric using nano TiO₂ and BTCA—statistically optimized by RSM," *Indian Journal of Fibre & Textile Research*, vol. 38, pp. 35–43, 2013.
- [20] J. Zoldners and T. Kiseleva, "Modification of Hemicellulose with polycarboxylic acids," *Holzforschung*, vol. 67, no. 5, pp. 567–571, 2013.
- [21] W. Huang, Y. Song, Y. Xing, and J. Dai, "Durable hydrophobic cellulose fabric prepared with polycarboxylic acid catalyzed silica sol," *Industrial and Engineering Chemistry Research*, vol. 49, no. 19, pp. 9135–9142, 2010.
- [22] B. S. Kayserilioğlu, W. M. Stevels, W. J. Mulder, and N. Akkas, "Mechanical and biochemical characterization of wheat gluten films as a function of pH and co-solvent," *Starch/Stärke*, vol. 53, no. 8, pp. 381–386, 2001.
- [23] A. Ebringerová and T. Heinze, "Xylan and xylan derivatives—biopolymers with valuable properties," *Macromolecular Rapid Communications*, vol. 21, no. 9, pp. 542–556, 2000.
- [24] M. Mohsin, A. Hossin, and Y. Haik, "Thermomechanical properties of poly(vinyl alcohol) plasticized with varying ratios of sorbitol," *Materials Science and Engineering A*, vol. 528, no. 3, pp. 925–930, 2011.

- [25] F. E. F. Silva, M. C. B. Di-Medeiros, K. A. Batista, and K. F. Fernandes, "PVA/polysaccharides blended films: mechanical properties," *Journal of Materials*, vol. 2013, Article ID 413578, 6 pages, 2013.
- [26] S.-D. Yoon, S.-H. Chough, and H.-R. Park, "Effects of additives with different functional groups on the physical properties of starch/PVA blend film," *Journal of Applied Polymer Science*, vol. 100, no. 5, pp. 3733–3740, 2006.
- [27] I. S. Arvanitoyannis, A. Nakayama, and S.-I. Aiba, "Chitosan and gelatin based edible films: state diagrams, mechanical and permeation properties," *Carbohydrate Polymers*, vol. 37, no. 4, pp. 371–382, 1998.
- [28] M. A. García, M. N. Martino, and N. E. Zaritzky, "Lipid addition to improve barrier properties of edible starch-based films and coatings," *Journal of Food Science*, vol. 65, no. 6, pp. 941–944, 2000.
- [29] M. Ghasemlou, N. Aliheidari, R. Fahmid et al., "Physical, mechanical and barrier properties of corn starch films incorporated with plant essential oils," *Carbohydrate Polymers*, vol. 98, no. 1, pp. 1117–1126, 2013.
- [30] S. F. Hosseini, M. Rezaei, M. Zandi, and F. F. Ghavi, "Preparation and functional properties of fish gelatin-chitosan blend edible films," *Food Chemistry*, vol. 136, no. 3-4, pp. 1490–1495, 2013.
- [31] L. Higuera, G. Lopez-Carballo, J. P. Cerisuelo, R. Gavara, and P. Hernandez-Munoz, "Preparation and characterization of chitosan/HP- β -cyclodextrins composites with high sorption capacity for carvacrol," *Carbohydrate Polymers*, vol. 97, no. 2, pp. 262–268, 2013.
- [32] K. S. V. K. Rao, B. Vijaya Kumar Naidu, M. C. S. Subha, M. Sairam, and T. M. Aminabhavi, "Novel chitosan-based pH-sensitive interpenetrating network microgels for the controlled release of cefadroxil," *Carbohydrate Polymers*, vol. 66, no. 3, pp. 333–344, 2006.
- [33] D. Huang, B. Mu, and A. Wang, "Preparation and properties of chitosan/poly (vinyl alcohol) nanocomposite films reinforced with rod-like sepiolite," *Materials Letters*, vol. 86, pp. 69–72, 2012.
- [34] S. L. Heikkinen, K. S. Mikkonen, K. Pirkkalainen, R. Serimaa, C. Joly, and M. Tenkanen, "Specific enzymatic tailoring of wheat arabinoxylan reveals the role of substitution on xylan film properties," *Carbohydrate Polymers*, vol. 92, no. 1, pp. 733–740, 2013.
- [35] X.-W. Peng, J.-L. Ren, L.-X. Zhong, and R.-C. Sun, "Nanocomposite films based on xylan-rich hemicelluloses and cellulose nanofibers with enhanced mechanical properties," *Biomacromolecules*, vol. 12, no. 9, pp. 3321–3329, 2011.
- [36] H.-S. Yang, J.-S. Yoon, and M.-N. Kim, "Dependence of biodegradability of plastics in compost on the shape of specimens," *Polymer Degradation and Stability*, vol. 87, no. 1, pp. 131–135, 2005.
- [37] S. H. Imam, P. Cinelli, S. H. Gordon, and E. Chiellini, "Characterization of biodegradable composite films prepared from blends of poly(vinyl alcohol), cornstarch, and lignocellulosic fiber," *Journal of Polymers and the Environment*, vol. 13, no. 1, pp. 47–55, 2005.

Research Article

Synthesis and Characterization of Different Crystalline Calcium Silicate Hydrate: Application for the Removal of Aflatoxin B1 from Aqueous Solution

Lu Zeng, Ligang Yang, Shuping Wang, and Kai Yang

College of Materials Science and Engineering, Chongqing University, Chongqing 400044, China

Correspondence should be addressed to Lu Zeng; zool@foxmail.com

Received 31 December 2013; Accepted 17 February 2014; Published 17 March 2014

Academic Editor: Ming-Guo Ma

Copyright © 2014 Lu Zeng et al. This is an open access article distributed under the Creative Commons Attribution License, which permits unrestricted use, distribution, and reproduction in any medium, provided the original work is properly cited.

Different crystalline calcium silicate hydrates (CSH) were synthesized under specific hydrothermal conditions and several methods were used to analyze samples. Amorphous calcium silicate hydrates (ACSH) mainly consists of disordered calcium silicate hydrate gel (C-S-H gel) and crystalline calcium silicate hydrates (CCSH) consists of crystallized tobermorite. The adsorption of carcinogenic aflatoxin B1 (AFB1) onto ACSH and CCSH was investigated. The adsorption kinetics was studied using pseudo-first-order and pseudo-second-order kinetic models and intraparticle diffusion model. The pseudo-second-order model provided the best correlation and the intraparticle diffusion controlled the adsorption process of AFB1 onto CCSH. Adsorption isotherm parameters were obtained from Langmuir and Freundlich and the adsorption data fitted to Freundlich much better. Based on the results of N_2 adsorption/desorption, adsorption kinetics, and adsorption isotherms, the adsorption mechanism of AFB1 onto CCSH was developed. All results indicate that CCSH has a great potential to be a safe, easy-made, and cost-effective material for the control of AFB1 contamination.

1. Introduction

The synthesis of calcium silicate hydrate (CSH) under the hydrothermal condition has been extensively studied to manufacture some functional materials. Under different hydrothermal conditions, varieties of CSH with different structures can be prepared, such as amorphous calcium silicate hydrate (ACSH) and crystalline calcium silicate hydrate (CCSH). ACSH, for example, calcium silicate hydration gel (C-S-H gel), consists of monomer silicate anions with silanol groups [1]. CCSH, for example, tobermorite and xonotlite, is built up of layers of Ca polyhedra and condensed by wollastonite-type silicate chains on both sides [2, 3]. CSH is used as functional Materials generally, especially as an adsorbent due to its high specific surface area and a large number of structural sites. In the study of Maeda and Ishida [4], slurries consisting of diatomaceous earth and slaked lime were hydrothermally reacted to synthesize composite C-S-H gel, which has superior dye-adsorption ability. A synthetic adsorbent of CCSH has been found highly effective for

endotoxin removal from aqueous solutions [5]. Katsumata et al. [6] removed natural organic polyelectrolyte (humic and fulvic acids) and their metal complexes by adsorption onto xonotlite. Siauciunas et al. [7] evaluated the effects of CO_2 chemisorptions on synthetic tobermorite. Novel technique for phosphorus recovery from aqueous solutions using ACSH was reported recently [8], and also CCSH with a low Ca/Si molar ratio of 0.8–1.0, such as tobermorite [9] and xonotlite [10], has been used for phosphorus recovery. Both of them are beneficial materials for phosphorus recovery and recycling. Moreover, CSH plays an essential role in fixing heavy metals by ways of ion-exchange, adsorption, and chemical restraint. Heavy metals of Nd(III), Zn(II), Cd(II), Cr(IV), and Sr(II) uptake by CSH have been reported in the literature [11–15].

Mycotoxins are secondary metabolites of filamentous fungi and naturally occur in food. They represent a large group of different substances produced by different mycotoxicogenic species. Aflatoxins are the most common mycotoxins and aflatoxin B1 (AFB1) has been demonstrated to be carcinogenic to animals and humans [16]. At present, the

TABLE 1: Hydrothermal synthesis conditions.

Samples	Ca/Si	w/s	Incubating time (h)	Temperature ($^{\circ}$ C)
ACSH	1.0	5	8	120
CCSH	1.0	10	12	185

most probable approach for controlling AFB1 contamination is the addition of nonnutritive adsorbent materials to the diet. Minerals such as montmorillonite, sepiolite, zeolite, and kaolinite are the main materials which have been used as the adsorbents of AFB1 [17]. However, these materials are nonrenewable and may be insecure as the natural substance could suffer some contamination (e.g., heavy metals); the US Food and Drug Administration (FDA) stated that “The use of sodium aluminosilicate and hydrated calcium sodium aluminosilicate as binders for mycotoxins is not considered to be generally recognized as safe” [18], so their application is limited in practice. To control AFB1 contamination, it is essential to develop a simple, safe, and cost-effective adsorbent.

Till now, CSH has not been used to bind AFB1 and the structures of CSH which can impact the adsorption capacity have not been studied too. In this study, different crystalline CSH were prepared under specific hydrothermal conditions and samples were characterized by several methods. The adsorption capacities of CSH for the removal of AFB1 from aqueous solutions were investigated and the adsorption mechanism of AFB1 on CCSH was explained.

2. Materials and Methods

2.1. Synthesis and Characterization of CSH. CSH was synthesized in an autoclave (Weihai Chemical Machinery Co. Ltd.). For preparation of CSH, the calcium oxide (99.99% CaO, Aladdin Co. Ltd.) and silicon oxide (99.99% SiO₂, Aladdin Co. Ltd) were mixed according to a certain proportion by molar (Ca/Si). The mixture was added to the water with a certain ratio of water-to-solid by mass (w/s), and then incubated at the set temperatures for several hours to manufacture ACSH and CCSH; the hydrothermal synthesis conditions are shown in Table 1 [19]. Samples of each synthesis were dried to constant mass in an oven at 80 $^{\circ}$ C and then milled to less than 45 μ m for the adsorption experiments.

ACSH and CCSH were characterized by different methods, including X-ray powder diffraction (XRD), scanning electron microscope (SEM), and N₂ adsorption/desorption. XRD was performed on a Rigaku D/max-1200 diffractometer with Cu K α radiation, in the range of 5 $^{\circ}$ –70 $^{\circ}$ 2 θ and at a step size of 0.02 $^{\circ}$. SEM micrographs were performed using a TESCAN VEGA II scanning electron microscope, operating at the accelerating voltage of 20 kV and taking images at different magnifications. Brunauer-Emmet-Teller (BET) specific surface area (S_{BET}), total pore volumes (V_{total}), and average pore diameter (D_p) of the samples before and after adsorption of AFB1 were measured from N₂ adsorption/desorption isotherms at 77 K, using an automatic specific surface area measuring equipment (ASAP, 2020, Micromeritics, USA) after a degassing under vacuum for 8 h at 110 $^{\circ}$ C.

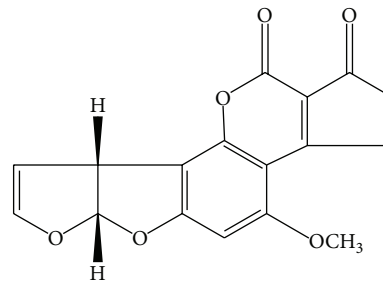


FIGURE 1: Structure of AFB1.

2.2. Adsorption Experiments. The method of enzyme linked immunosorbent assay (ELISA) was used to measure the amount of AFB1. AFB1 was purchased from Sigma-Aldrich Co and ELISA kits were purchased from R-Biopharm Co. The chemical structure of AFB1 is presented in Figure 1 [20]. Firstly, an AFB1 stock solution (2 μ g mL⁻¹) was prepared, and then 20 mg CSH was added to a tube that was filled with 10 mL AFB1 solution, adjusting the solution pH to 8 by adding 0.1M phosphate buffer as required. After 2 h at 28 $^{\circ}$ C in a temperature controlled shaking water bath pot at a shaking rate of 120 rpm, the tube was centrifuged for 10 min at 5000 rpm and then the amount of AFB1 remaining in the supernatant layer of dispersion by the method of ELISA was analyzed. The adsorbance of AFB1 was calculated from the difference between initial and equilibrium concentrations of AFB1. In addition, some experiments were performed at solution temperatures of 301, 306, and 311 K to determine the kinetic parameters with different time intervals. In order to determine adsorption isotherms parameters, experiments were carried out at solution temperatures of 301 K with different initial concentration which varied from 0.5 to 3 μ g mL⁻¹.

3. Results and Discussion

3.1. Characterization

3.1.1. XRD Characterization. The XRD patterns of ACSH and CCSH reveal the microstructure variety and comparative XRD patterns of them are presented in Figure 2. As can be seen, the ACSH consists of disordered calcium silicate hydrate (C-S-H) gels with peaks at 3.05, 2.81, and 1.81 \AA (corresponding to 29.1, 32.2, and 49.9 $^{\circ}$ 2 θ , resp.) and unreactive SiO₂ from quartz as well due to the short incubating period. The peak of C-S-H gel at 3.05 \AA is strong and broad, but the peaks at 2.81 and 1.81 \AA are weak, indicating a low-crystallinity structure [21]. On the contrary, the main composites of CCSH are crystallized tobermorite. The peaks at 11.30, 3.07, 2.97, 2.80, 1.84, and 1.67 \AA correspond to the main tobermorite component, especially at 11.30 \AA (corresponding to 8 $^{\circ}$ 2 θ) which is strong and sharp, reflecting an ordered and high-crystallinity structure [22]. Moreover, the peaks of quartz disappear, indicating more SiO₂ was dissolved in the liquid, which can be attributed to the higher reaction temperature and longer reaction time [19].

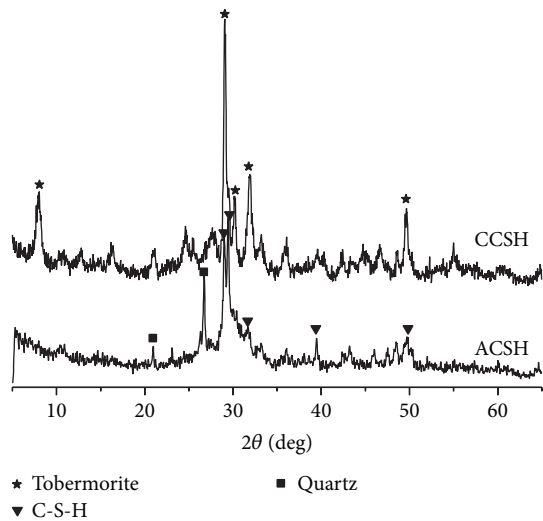


FIGURE 2: XRD patterns of ACSH and CCSH.

3.1.2. SEM Characterization. The SEM micrographs of ACSH and CCSH are shown in Figure 3. The microappearance is different from each other. The ACSH is agglomerated with some irregular flake and fibril. As a certain amount of water is wrapped in the floc, the particle of ACSH is made up of solids and solutions and its appearance is consistent with the typical characteristics of C-S-H gels [23]. Meanwhile, it can be seen that the CCSH consists of the crystals of a plate form which correspond to the microappearance of tobermorite. It is known that Ca^{2+} and H_2O insertions exist among tobermorite plates and space among tobermorite plates and insertions are referred to as tubular pores [24]. In addition, a small amount of floccules are observed in the micrograph of CCSH due to the residual C-S-H gels, which did not turn into tobermorite.

3.1.3. N_2 Adsorption/Desorption. The S_{BET} , V_{total} , and D_p of the samples before and after adsorption of AFB1 were measured. Meanwhile, the adsorbance of AFB1 on ACSH and CCSH (A_{AFB1}) was measured. All of the data were summarized in Table 2. The N_2 adsorption/desorption isotherms for samples of original (ACSH and CCSH) and after adsorption of AFB1 (ACSH-AFB1 and CCSH-AFB1) are shown in Figure 4. As can be seen from Figure 4(a), isotherms exhibit Type II behaviors according to the IUPAC classification [25], characteristics of major mesoporous, and a few macroporous adsorbents. Seen from the formed hysteresis loop, the N_2 adsorbance in the area of high relative pressure is higher, which fits to the third type of hysteresis loop (H3), indicating slit pores heaped up with flake particles. Meanwhile, compared with ACSH, the N_2 adsorbance of CCSH in the area of high relative pressure is much lower, which may be attributed to pores that formed from layer structure [25]. From Table 2, the S_{BET} of ACSH is larger than that of CCSH, because disordered ACSH has a structure of three-dimensional networks, while CCSH mainly has two-dimensional layer structure [26]. Moreover, it is shown in

TABLE 2: The structure characteristics of samples and adsorbance of AFB1.

Sample	S_{BET} ($\text{m}^2\cdot\text{g}^{-1}$)	V_{total} ($\text{cm}^3\cdot\text{g}^{-1}$)	D_p (nm)	A_{AFB1} ($\mu\text{g}/\text{g}$)
ACSH	89.636	0.469	20.372	274.355
CCSH	57.343	0.247	18.924	949.261
ACSH-AFB1	80.525	0.412	19.861	—
CCSH-AFB1	37.479	0.146	18.121	—

Figure 4(a) that, in the area of low relative pressure, there is a slight difference between the N_2 adsorbance of ACSH and that of CCSH. As the relative pressure increased, within the mesohigh relative pressure range and particularly within the high relative pressure range, the N_2 adsorbance of ACSH is significantly larger than CCSH, indicating a different pore structure, which is the main reason why the V_{total} and D_p of ACSH are larger than that of CCSH.

Figure 4(b) presents the N_2 adsorption/desorption isotherms of ACSH-AFB1 and CCSH-AFB1. Compared with the original sample, the S_{BET} , V_{total} , and D_p of ACSH-AFB1 slightly decrease and the N_2 adsorbance in the area of low relative pressure reduce, approaching closer to the x -axis, which can be attributed to micropore filling by the adsorbed AFB1. However, in the area of mesohigh relative pressure, the N_2 adsorbance does not show any obvious changes, indicating that the mesoporous does not fill with AFB1. As a mesoporous material, it was concluded that the main way of the adsorption of AFB1 onto ACSH is surface adsorption. On the contrary, the S_{BET} , V_{total} , and D_p of CCSH-AFB1 all are reduced significantly compared with the original sample and the curve approaches more closer to the x -axis in various relative pressure ranges. Furthermore, the adsorbance of AFB1 onto CCSH is much higher than that of ACSH. Such a difference is associated with the existing forms of AFB1 molecules in the layer structure of CCSH. There are two reactive mechanisms between CCSH and organic components [27]: one is the surface adsorption and the other is the interlayer adsorption as organic molecules insert into layers. The adsorbance of interlayer adsorption to the organics is much higher than the surface adsorption. As can be seen from Figure 1, AFB1 belongs to micromolecular organics, after being adsorbed by CCSH; the S_{BET} of CCSH-AFB1 is much smaller than that of the original sample. According to the effect of “pore blockage” when organic molecules fill pores result in the decrease of S_{BET} [28], it indicates that the interlayer adsorption is the dominant adsorption for the changes of CCSH isotherms before and after adsorption of AFB1. Besides, the hysteresis loop of CCSH-AFB1 fits to the second type of hysteresis loop (H2), indicating that “pore blockage” effect changes the pore structure, which forms ink-bottle pore (pores with narrow necks and wide bodies) [25]. Therefore, the interlayer adsorption is the main way for CCSH adsorbing AFB1.

3.2. Adsorption Kinetics. In order to quantify the changes in adsorption with time (Figure 5) and to evaluate kinetic parameters, three models were assessed, including the pseudo-first-order kinetic model, the pseudo-second-order

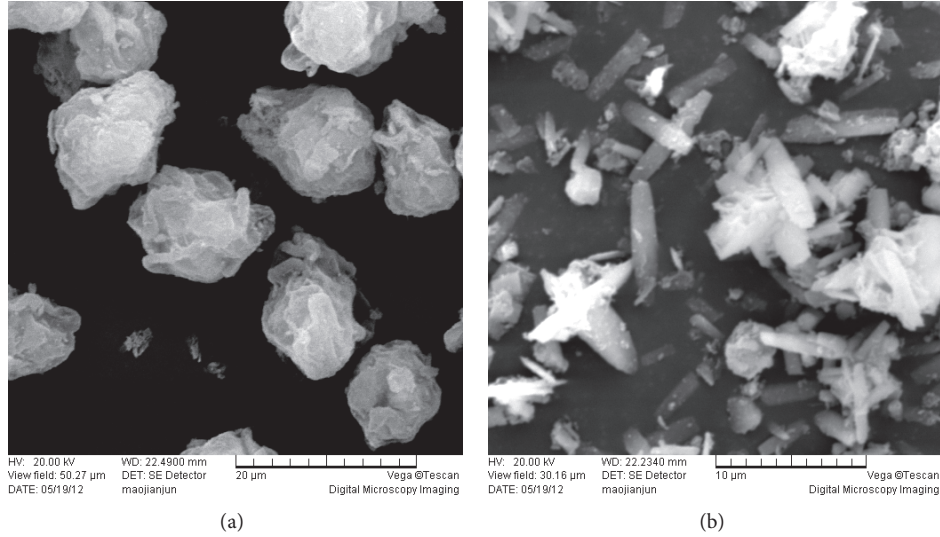


FIGURE 3: SEM micrographs of ACSH (a) and CCSH (b).

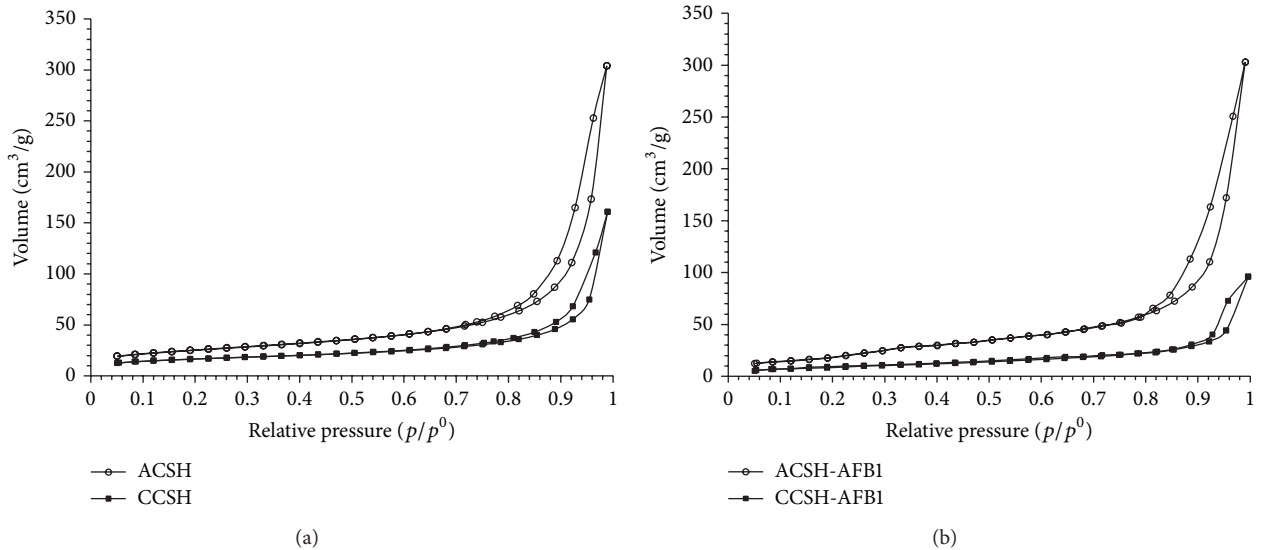


FIGURE 4: (a) The N_2 adsorption-desorption isotherms for ACSH and CCSH. (b) The N_2 adsorption-desorption isotherms for ACSH-AFB1 and CCSH-AFB1.

kinetic model, and the intraparticle diffusion model. The pseudo-first-order kinetic model [29] can be expressed as follows:

$$\lg(q_e - q_t) = \lg q_e - \frac{k_1}{2.303} t, \quad (1)$$

where q_e and q_t are the amounts of AFB1 adsorbed on CSH ($\mu\text{g g}^{-1}$) at equilibrium and at different time t (min) and k_1 (min^{-1}) is a rate constant for the adsorption process. Kinetic parameters (q_e and k_1) were calculated from the intercept and the slope of the pseudo-first-order straight line.

The pseudo-second-order rate expression [30] can be used to describe adsorption processes in which the reaction

rate is proportional to the square of the number of available adsorption sites:

$$\frac{t}{q_t} = \frac{1}{k_2(q_e)^2} + \frac{1}{q_e} t, \quad (2)$$

where k_2 ($\text{g mg}^{-1} \text{min}^{-1}$) is the rate constant and the values of q_e and k_2 were derived from the intercept and slope of a linear plot of t/q_t versus t .

An intraparticle diffusion model of Weber and Morris [31] is shown as

$$q_t = k_3 t^{1/2} + b, \quad (3)$$

where b represents the intercept and the values of intercept give an idea of the boundary layer thickness which is associated with the boundary layer effect. k_3 is the intraparticle

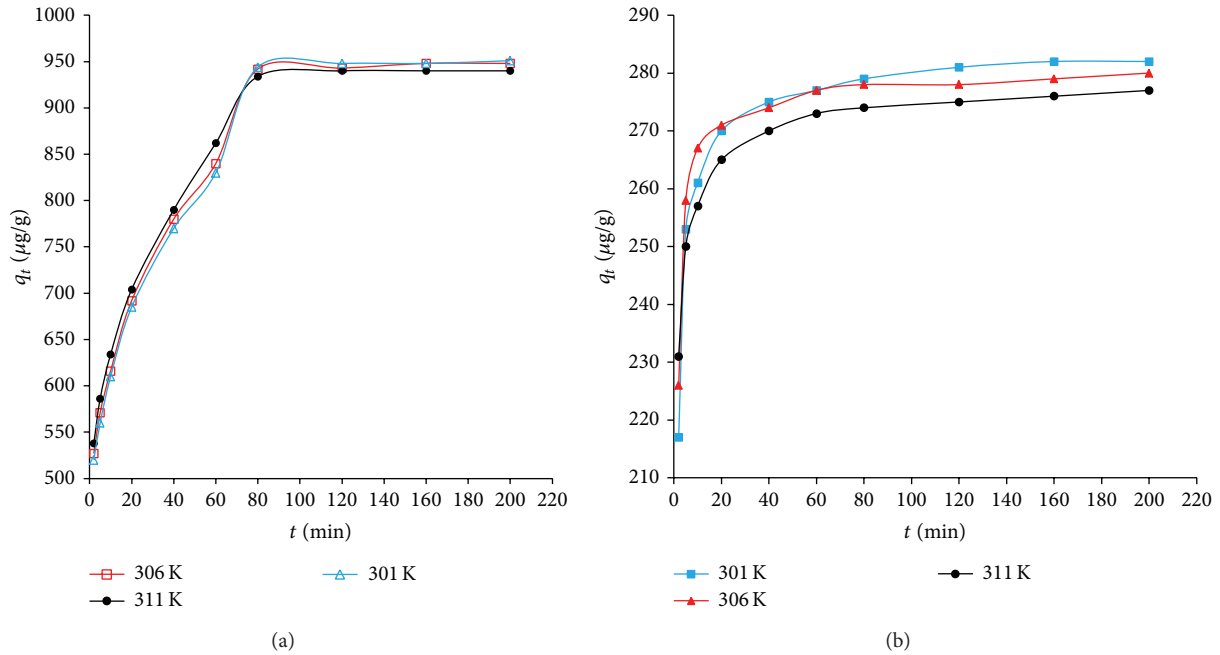


FIGURE 5: Adsorption kinetics for AFBI onto CCSH (a) and ACSH (b) at 301, 306, and 311 K.

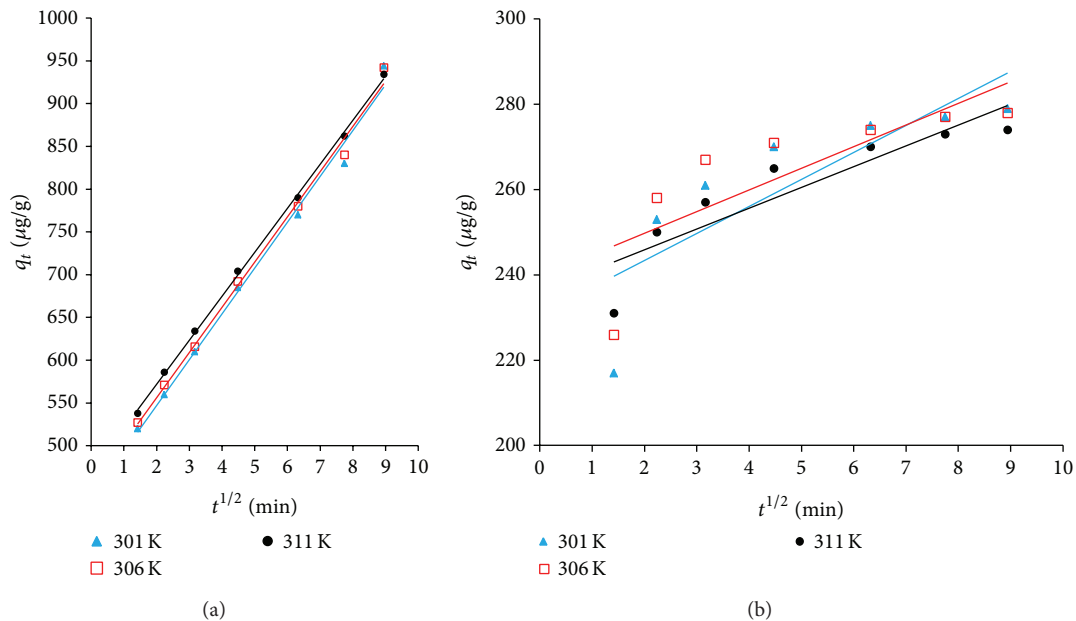


FIGURE 6: Intraparticle diffusion plot for AFBI onto CCSH (a) and ACSH (b) at 301, 306, and 311 K.

diffusion constant ($\text{mg g}^{-1} \text{min}^{-1/2}$) and the values of k_3 and b were obtained from the slope and intercept of a linear plot of q_t versus $t^{1/2}$ (Figure 6).

All parameters and correlation coefficients (R^2) are summarized in Table 3. It can be found that the correlation coefficients of the first-order kinetic model are lower than 0.9, which are less than the second-order kinetic model. Therefore, the adsorption processes was considered to be explained better by the second-order kinetic model. The values of q_e

are close to constant with an increase in temperature for adsorption of AFBI onto ACSH and CCSH. It implies that the temperature does not favor AFBI adsorption onto ACSH and CCSH and the type of adsorption can be considered as physisorption. The adsorption rate is an important indicator reflecting the properties of adsorbent that is described by the Weber-Morris equation. Generally, the adsorption processes include three stages. The first is considered as a diffusion of adsorbate through the solution to the external surface of

TABLE 3: Kinetic parameters for AFB1 adsorption onto ACSH and CCSH at different temperatures.

Kinetic models	T (K)	ACSH			CCSH		
		k_1 (min^{-1})	q_e ($\mu\text{g g}^{-1}$)	R^2	k_1 (min^{-1})	q_e ($\mu\text{g g}^{-1}$)	R^2
Pseudo-first-order	301	0.034	35.719	0.886	0.037	492.947	0.899
	306	0.035	27.283	0.879	0.041	541.502	0.890
	311	0.025	26.528	0.893	0.046	549.035	0.866
Pseudo-second-order		k_2 ($\text{g } \mu\text{g}^{-1} \text{ min}^{-1}$)	q_e ($\mu\text{g g}^{-1}$)	R^2	k_2 ($\text{g } \mu\text{g}^{-1} \text{ min}^{-1}$)	q_e ($\mu\text{g g}^{-1}$)	R^2
	301	0.0038	285.714	0.999	0.00017	981.448	0.998
	306	0.0056	277.778	0.999	0.00018	977.279	0.998
	311	0.0043	277.767	0.999	0.00021	966.428	0.998
Intraparticle diffusion		k_3 ($\mu\text{g g}^{-1} \text{ min}^{-1/2}$)	b	R^2	k_3 ($\mu\text{g g}^{-1} \text{ min}^{-1/2}$)	b	R^2
	301	6.317	230.76	0.684	53.534	440.40	0.991
	306	5.070	239.59	0.628	52.870	450.65	0.994
	311	4.877	236.10	0.808	51.435	469.11	0.999

adsorbent or faster adsorption stage. The second describes the gradual layer adsorption stage, where intraparticle diffusion is rate-controlled. The third stage is the final equilibrium stage [32]. It is important to note that the correlation coefficients are lower than 0.81 for ACSH at different temperatures, which suggest a nonlinear relationship. Hence, the adsorption process of AFB1 onto ACSH is not intraparticle diffusion predominantly and three possible adsorption processes may occur. In contrast, the correlation coefficients are higher than 0.99 for CCSH at different temperatures, indicating that the intraparticle diffusion controls the adsorption process, but the intraparticle diffusion curves do not pass through the origin; it indicates that besides intraparticle diffusion, other process may influence the adsorption rate. Moreover, the values of intercept b give an idea about the boundary layer thickness; the larger the intercept, the greater the boundary layer effect [33]. From Table 3, values of b of CCSH are greater than that of ACSH. This means that the greater boundary layer effect is in favor of AFB1 adsorption onto CCSH.

3.3. Adsorption Isotherms. Adsorption isotherm reflects the relationship between adsorption capacity and the concentration of solution at a fixed temperature. Analysis of the isotherm data is important to examine the adsorption mode of AFB1 onto ACSH and CCSH, and the results can be used for the design of more efficient materials to bind AFB1. Therefore, two main models of adsorption isotherm were analyzed, one is Langmuir isotherm [34] and the other is Freundlich isotherm [35], which is widely applied in liquid-solid adsorption system.

The Langmuir isotherm theory assumes monolayer coverage of adsorbate over a homogenous adsorbent surface. In a modified form it can also describe a bilayer deposition. Firstly, the adsorption data were fitted to the linear form of Langmuir adsorption model (see (4)) and obtained the Langmuir isotherm by plotting the particular adsorption (C_e/C) against the equilibrium concentration of AFB1 (C_e). C_e is the equilibrium concentration of AFB1 which means the final concentration ($\mu\text{g/L}$) of AFB1 in the solution after adsorption, C_m is the maximum adsorbance ($\mu\text{g/g}$), C is the amount of AFB1 being adsorbed by the sorbent at equilibrium

TABLE 4: Isotherm parameters for AFB1 adsorption onto ACSH and CCSH.

Sample	Langmuir			Freundlich		
	C_m (mg g^{-1})	K (L mg^{-1})	R^2	K_f ($\mu\text{g g}^{-1}$)	n_f	R^2
ACSH	-0.333	-0.284	0.807	0.005	1.483	0.996
CCSH	2.0	10.020	0.882	64.358	0.583	0.992

($\mu\text{g/g}$), and K is a constant related to the adsorption energy. The essential characteristics of the Langmuir isotherm can be expressed in terms of a dimensionless constant separation factor R_0 which is given by (5). C_0 is the initial AFB1 concentration ($\mu\text{g/mL}$). When R_0 is between 0 and 1, it indicates a favorable AFB1 adsorption, when R_0 is higher than 1, it indicates an unfavorable AFB1 adsorption.

Consider

$$\frac{C_e}{C} = \frac{1}{C_m K} + \frac{C_e}{C_m}, \quad (4)$$

$$R_0 = \frac{1}{KC_0 + 1}. \quad (5)$$

The adsorption data were also fitted to the linear form of Freundlich adsorption model which is shown as

$$\lg C = \lg K_f + n_f \lg C_e, \quad (6)$$

where K_f is Freundlich constant related to adsorption intensity and n_f is constant as well related to adsorption intensity, C ($\mu\text{g/g}$) and C_e ($\mu\text{g/L}$) denote adsorbance of AFB1 and equilibrium concentration of AFB1, respectively. Freundlich equation is an exponential variation in site energies and assumes that the adsorbent has a heterogeneous energy distribution of active sites. Theoretically, the Freundlich model is suitable for use with heterogeneous surfaces and with this expression, an infinite amount of adsorption can occur [36].

The adsorption isotherm curves of AFB1 onto CCSH and ACSH are shown in Figure 7, and all isotherm values are summarized in Table 4. For Langmuir isotherm shown

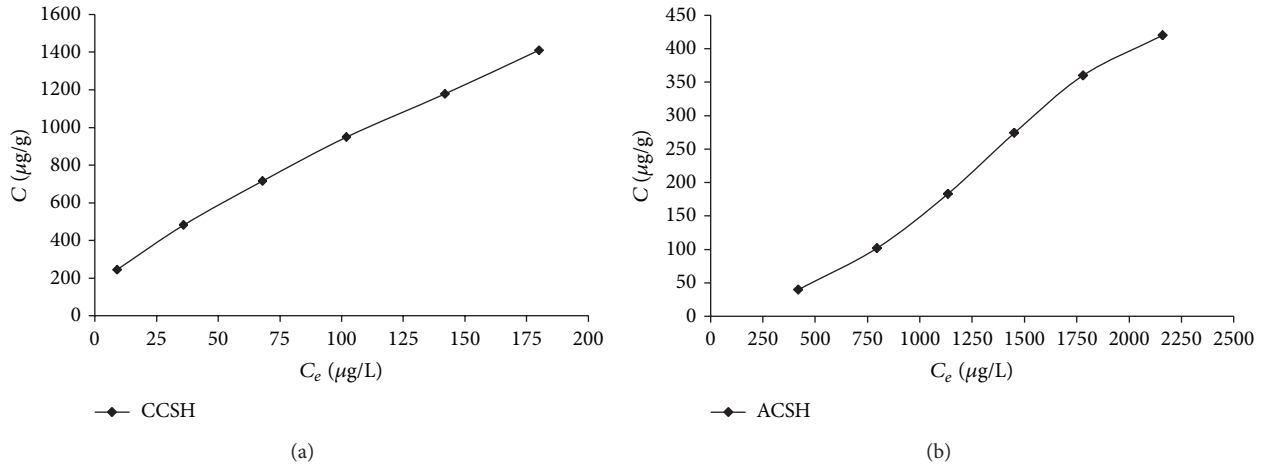


FIGURE 7: Adsorption isotherms for AFB1 onto CCSH (a) and ACSH (b) at 301 K.

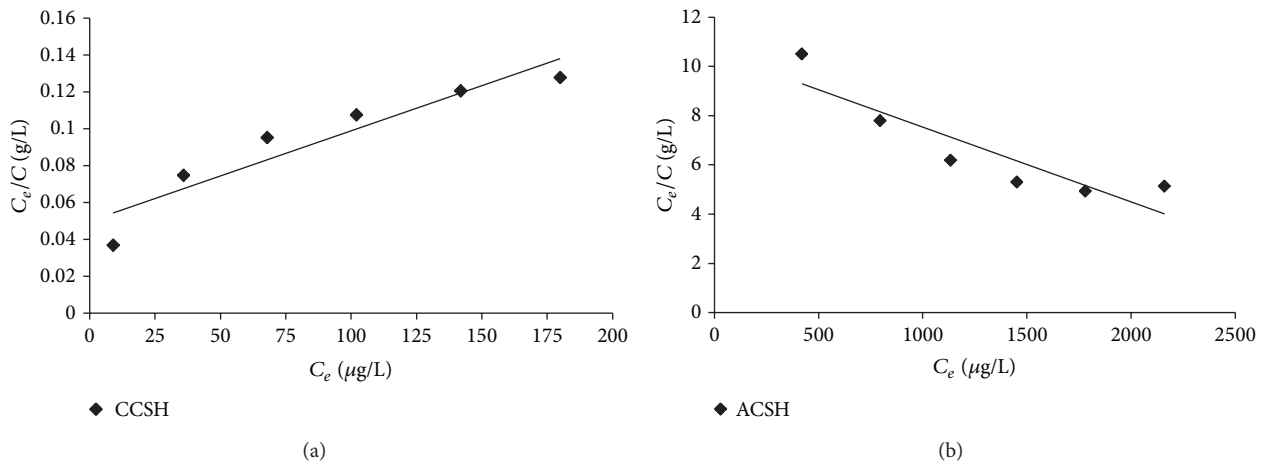


FIGURE 8: Langmuir isotherm for AFB1 onto CCSH (a) and ACSH (b) at 301 K.

in Figure 8, R_0 of CCSH is between 0.166 and 0.032, which indicates a favorable adsorption of AFB1 onto CCSH. R_0 of ACSH is higher than 1, indicating an unfavorable adsorption. Meanwhile, for Freundlich isotherm shown in Figure 9, n_f of ACSH at equilibrium is bigger than 1, as n_f is related to adsorption intensity or surface heterogeneity, which ranges between 0 and 1 when a favorable adsorption occurs. This result indicates that ACSH has a poor adsorption capacity of AFB1 in the solution. Meanwhile, n_f of CCSH is smaller than 1, so this adsorbent is favorable for adsorbing AFB1. Comparing the values of R^2 , it is noted that the Freundlich model yielded a much better fit than the Langmuir model for both of ACSH and CCSH. It can be deduced that the adsorptions of AFB1 on the surface of adsorbents are uneven.

3.4. Adsorption Mechanism. All results above indicate that CCSH is a suitable adsorbent for the adsorption of AFB1. In order to study it further, the adsorption mechanism of AFB1 onto CCSH was deduced in the following steps and the description is shown in Figure 10.

Firstly, when CSSH and AFB1 were mixed together in solution, the AFB1 molecules transfer from the bulk solution to the CCSH external surface by diffusing through the boundary layer. At this moment, the adsorption of AFB1 onto CCSH was surface adsorption. The main component of CCSH is tobermorite and an important feature of the structure of tobermorite is the cavity between two adjacent building layers, the “interlayer space,” which contain water and Ca^{2+} ions [26]. When Ca^{2+} ions diffuse into the solution, CCSH is electronegative. For AFB1 molecule, the center of positive charges and that of negative charges does not coincide, which belongs to polar molecule (Figure 1). Through the mode of charge adsorption, polar molecules of AFB1 are adsorbed onto CCSH with negative charges, while the Si-OH on the surface of CCSH can also bind AFB1 through the hydrogen bonding interaction [37]. This adsorption process has little influence on the adsorption rate.

The second reactive stage is the gradual layer adsorption stage. With the continuous adsorption reaction, the AFB1 molecules diffuse from the external surface into the interlayer of CCSH. While more and more AFB1 molecules diffuse into

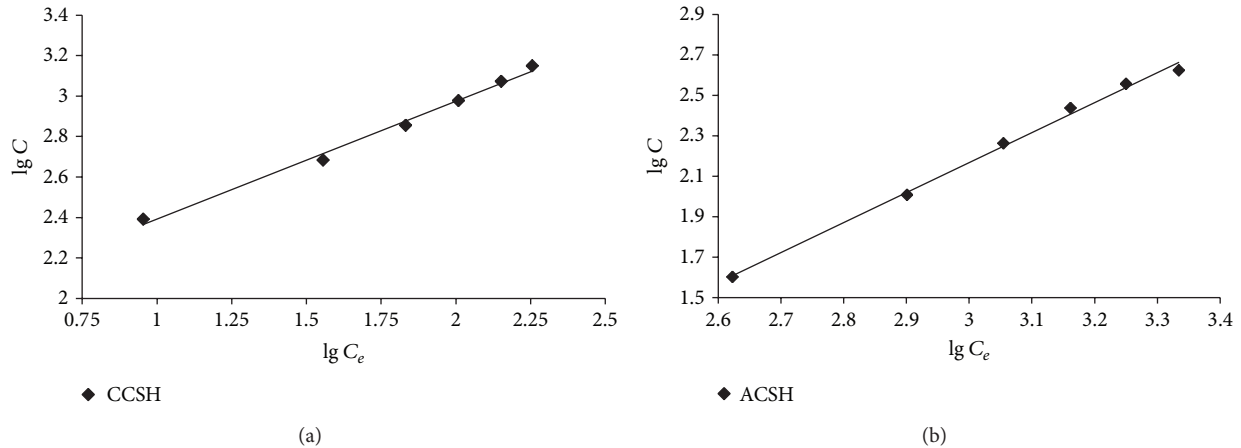


FIGURE 9: Freundlich isotherm for AFB1 onto CCSH (a) and ACSH (b) at 301 K.

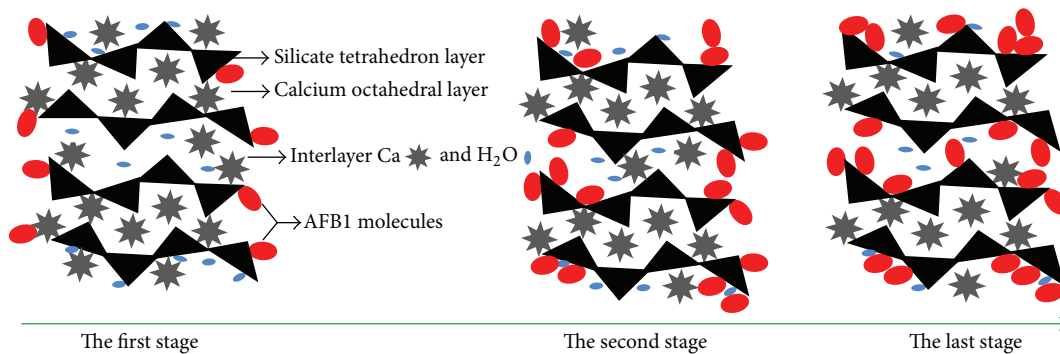


FIGURE 10: Adsorption description of AFB1 onto CCSH.

the interlayer, the “pore blockage” effect occurs which results in the decrease of S_{BET} and V_{total} . As the adsorption of AFB1 in the interlayer is uneven, several adsorption modes can occur (Fit to Freundlich). It means monolayer adsorption of AFB1 may occur in some locations of interlayer and multilayer adsorption of AFB1 may occur too in some other locations, and in the same way even zero adsorption may exist somewhere. Due to such special adsorption mode, the pore structure is changed and ink-bottle pores are formed. As the adsorption process of AFB1 onto CCSH is mainly controlled by intraparticle diffusion, most AFB1 are adsorbed at this stage with the longest reaction time, which controls the adsorption rate (Fit to intraparticle diffusion model). Meanwhile, it is seen that the concentrations of AFB1 and CCSH can also affect the adsorption rate (fit to the pseudo-second-order kinetic model).

The last stage is the final equilibrium stage. The diffusion of every substance in the system achieves a state of dynamic equilibrium, such as Ca^{2+} ions, AFB1 molecules, particles of adsorbent, and water molecules. At this stage, the adsorption reaction tends to be stable and the adsorbance of AFB1 on CCSH reaches the maximum value.

4. Conclusions

The results present in this paper demonstrate the characteristics of CSH and their performance in the adsorption of AFB1

from aqueous solution. It shows that both ACSH and CCSH can adsorb AFB1, but CCSH is more effective in the adsorption of AFB1. The CSH was characterized by several methods; from the analysis of results, it indicates that a regular layered structure is beneficial for the adsorption of AFB1. CCSH consisting of crystallized tobermorite mainly adsorbs AFB1 into its interlayer, resulting in a higher adsorption of AFB1 and the decrease of S_{BET} remarkably; it is also the reason for the change of pore structure. For CSH, kinetic studies indicates that the adsorption follows the pseudo-second-order kinetic model ($R^2 > 0.99$) and the adsorbance of AFB1 is near constant with an increase in temperature. The adsorption process of AFB1 onto CCSH is intraparticle diffusion ($R^2 > 0.99$) predominantly but not for ACSH ($R^2 < 0.81$). The data of equilibrium adsorption were fitted to Langmuir and Freundlich equations; Freundlich isotherm model correlates the experimental data better than Langmuir, which implies that adsorptions of AFB1 on the surface of CSH are uneven. Summary analysis of all results, the adsorption mechanism of AFB1 onto CCSH was deduced by dividing into three stages. As a result, it can be concluded that CCSH has a great potential to be used as an adsorbent for the removal of AFB1 from aqueous solutions, which is safe, easy-made, and cost effective.

Conflict of Interests

The authors declare no conflict of interests.

Acknowledgment

The study was supported by the Fundamental Research Funds for the Central Universities (CDJZR12130052).

References

- [1] Z. H. Wang, L. M. Sun, Y. F. Hou, and E. Z. Tang, "In situ monitoring of C-S-H gel processing by magnetic susceptibility and turbidity measurements," *Journal of the American Ceramic Society*, vol. 88, no. 7, pp. 1799–1802, 2005.
- [2] C. Hejny and T. Armbruster, "Polytypism in xonotlite $\text{Ca}_6\text{Si}_6\text{O}_{17}(\text{OH})_2$," *Zeitschrift für Kristallographie*, vol. 216, no. 7, pp. 396–408, 2001.
- [3] S. Merlino, E. Bonaccorsi, and T. Armbruster, "The real structure of tobermorite 11 Å: normal and anomalous forms, OD character and polytypic modifications," *European Journal of Mineralogy*, vol. 13, no. 3, pp. 577–590, 2001.
- [4] H. Maeda and E. H. Ishida, "Hydrothermal preparation of diatomaceous earth combined with calcium silicate hydrate gels," *Journal of Hazardous Materials*, vol. 185, no. 2-3, pp. 858–861, 2011.
- [5] Q. Wang, J. P. Zhang, T. R. Smith, W. E. Hurst, and T. Sulpizio, "An electrokinetic study on a synthetic adsorbent of crystalline calcium silicate hydrate and its mechanism of endotoxin removal," *Colloids and Surfaces B: Biointerfaces*, vol. 44, no. 2-3, pp. 110–116, 2005.
- [6] H. Katsumata, S. Kaneco, R. Matsuno et al., "Removal of organic polyelectrolytes and their metal complexes by adsorption onto xonotlite," *Chemosphere*, vol. 52, no. 5, pp. 909–915, 2003.
- [7] R. Siauciuonas, E. Rupsyte, S. Kitrys, and V. Galeckas, "Influence of tobermorite texture and specific surface area on CO_2 chemisorption," *Colloids and Surfaces A: Physicochemical and Engineering Aspects*, vol. 244, no. 1-3, pp. 197–204, 2004.
- [8] K. Okano, M. Uemoto, J. Kagami et al., "Novel technique for phosphorus recovery from aqueous solutions using amorphous calcium silicate hydrates (A-CSHs)," *Water Research*, vol. 47, no. 7, pp. 2251–2259, 2013.
- [9] W. Guan, F. Y. Ji, Q. K. Chen, P. Yan, and L. Pei, "Synthesis and enhanced phosphate recovery property of porous calcium silicate hydrate using polyethyleneglycol as pore-generation agent," *Materials*, vol. 6, no. 7, pp. 2846–2861, 2013.
- [10] X. Chen, H. Kong, D. Wu, X. Wang, and Y. Lin, "Phosphate removal and recovery through crystallization of hydroxyapatite using xonotlite as seed crystal," *Journal of Environmental Sciences*, vol. 21, no. 5, pp. 575–580, 2009.
- [11] P. Mandaliev, R. Dähn, J. Tits, B. Wehrli, and E. Wieland, "EXAFS study of Nd(III) uptake by amorphous calcium silicate hydrates (C-S-H)," *Journal of Colloid and Interface Science*, vol. 342, no. 1, pp. 1–7, 2010.
- [12] Q. Y. Chen, C. D. Hills, M. Tyrer, I. Slipper, H. G. Shen, and A. Brough, "Characterisation of products of tricalcium silicate hydration in the presence of heavy metals," *Journal of Hazardous Materials*, vol. 147, no. 3, pp. 817–825, 2007.
- [13] O. P. Shrivastava and T. Verma, " Sr^{2+} Sorption and leach rate studies on synthetic calcium silicate hydroxy hydrate," *Advanced Cement Based Materials*, vol. 2, no. 3, pp. 119–124, 1995.
- [14] M.-P. Pomiès, N. Lequeux, and P. Boch, "Speciation of cadmium in cement—part I. Cd^{2+} uptake by C-S-H," *Cement and Concrete Research*, vol. 31, no. 4, pp. 563–569, 2001.
- [15] C.-K. Lin, J.-N. Chen, and C.-C. Lin, "An NMR, XRD and EDS study of solidification/stabilization of chromium with portland cement and C_3S ," *Journal of Hazardous Materials*, vol. 56, no. 1-2, pp. 21–34, 1997.
- [16] A. Yiannikouris and J.-P. Jouany, "Mycotoxins in feeds and their fate in animals: a review," *Animal Research*, vol. 51, no. 2, pp. 81–99, 2002.
- [17] E. Afriyie-Gyawu, Z. Wang, N.-A. Ankrah et al., "NovaSil clay does not affect the concentrations of vitamins A and E and nutrient minerals in serum samples from Ghanaians at high risk for aflatoxicosis," *Food Additives and Contaminants A: Chemistry, Analysis, Control, Exposure and Risk Assessment*, vol. 25, no. 7, pp. 872–884, 2008.
- [18] M. Mézes, K. Balogh, and K. Tóth, "Preventive and therapeutic methods against the toxic effects of mycotoxins: a review," *Acta Veterinaria Hungarica*, vol. 58, no. 1, pp. 1–17, 2010.
- [19] S. Shaw, S. M. Clark, and C. M. B. Henderson, "Hydrothermal formation of the calcium silicate hydrates, tobermorite ($\text{Ca}_5\text{Si}_6\text{O}_{16}(\text{OH})_2 \cdot 4\text{H}_2\text{O}$) and xonotlite ($\text{Ca}_6\text{Si}_6\text{O}_{17}(\text{OH})_2$): an in situ synchrotron study," *Chemical Geology*, vol. 167, no. 1-2, pp. 129–140, 2000.
- [20] R. D. Hartley, B. F. Nesbitt, and J. O'Kelly, "Toxic metabolites of *Aspergillus flavus*," *Nature*, vol. 198, no. 4885, pp. 1056–1058, 1963.
- [21] A. Stumm, K. Garbev, G. Beuchle, L. Black, P. Stemmermann, and R. Nüesch, "Incorporation of zinc into calcium silicate hydrates, part I: formation of C-S-H(I) with C/S = 2/3 and its isochemical counterpart gyrolite," *Cement and Concrete Research*, vol. 35, no. 9, pp. 1665–1675, 2005.
- [22] K. Matsui, J. Kikuma, M. Tsunashima et al., "In situ time-resolved X-ray diffraction of tobermorite formation in autoclaved aerated concrete: influence of silica source reactivity and Al addition," *Cement and Concrete Research*, vol. 41, no. 5, pp. 510–519, 2011.
- [23] W. Nocuò-Wczelik, "Effect of Na and Al on the phase composition and morphology of autoclaved calcium silicate hydrates," *Cement and Concrete Research*, vol. 29, no. 11, pp. 1759–1767, 1999.
- [24] H. Youssef, D. Ibrahim, S. Komarneni, and K. J. D. Mackenzie, "Synthesis of 11 Å Al-substituted tobermorite from trachyte rock by hydrothermal treatment," *Ceramics International*, vol. 36, no. 1, pp. 203–209, 2010.
- [25] K. S. W. Sing, "Reporting physisorption data for gas/solid systems with special reference to the determination of surface area and porosity (Recommendations 1984)," *Pure and Applied Chemistry*, vol. 57, no. 4, pp. 603–619, 1985.
- [26] P. Mandaliev, R. Dähn, J. Tits, B. Wehrli, and E. Wieland, "EXAFS study of Nd(III) uptake by amorphous calcium silicate hydrates (C-S-H)," *Journal of Colloid and Interface Science*, vol. 342, no. 1, pp. 1–7, 2010.
- [27] A. Popova, G. Geoffroy, M.-F. Renou-Gonnord, P. Faucon, and E. Gartner, "Interactions between polymeric dispersants and calcium silicate hydrates," *Journal of the American Ceramic Society*, vol. 83, no. 10, pp. 2556–2560, 2000.
- [28] W. Zhang, J. Ye, Y. Wang, H. Wang, Y. Wang, and Y. Li, "Pore structure and surface fractal characteristics of calcium silicate hydrates contained organic macromolecule," *Journal of the Chinese Ceramic Society*, vol. 34, no. 12, pp. 1497–1502, 2006.
- [29] S. Lagergren, "Zur theorie der sogenannten adsorption gelöster stoffe," *Kungliga Svenska Vetenskapsakademiens Handlingar*, vol. 24, no. 4, pp. 1–39, 1898.

- [30] Y. S. Ho and G. McKay, "Pseudo-second order model for sorption processes," *Process Biochemistry*, vol. 34, no. 5, pp. 451–465, 1999.
- [31] W. J. Weber and J. C. Morris, "Kinetics of adsorption on carbon from solutions," *Journal of the Sanitary Engineering Division*, vol. 89, no. 2, pp. 31–60, 1963.
- [32] N. Rauf, S. S. Tahir, J. H. Kang, and Y. S. Chang, "Equilibrium, thermodynamics and kinetics studies for the removal of alpha and beta endosulfan by adsorption onto bentonite clay," *Chemical Engineering Journal*, vol. 192, pp. 369–376, 2012.
- [33] L. Zeng, S. P. Wang, X. Q. Peng, J. Q. Geng, C. Y. Chen, and M. Li, "Al-Fe PILC preparation, characterization and its potential adsorption capacity for aflatoxin B1," *Applied Clay Science*, vol. 83–84, pp. 231–237, 2013.
- [34] I. Langmuir, "The constitution and fundamental properties of solids and liquids. Part I. Solids," *The Journal of the American Chemical Society*, vol. 38, no. 11, pp. 2221–2295, 1916.
- [35] H. M. F. Freundlich, "Über die adsorption in lösungen," *Zeitschrift für Physikalische Chemie*, vol. 57, pp. 385–470, 1906.
- [36] B. Ismail, S. T. Hussain, and S. Akram, "Adsorption of methylene blue onto spinel magnesium aluminate nanoparticles: adsorption isotherms, kinetic and thermodynamic studies," *Chemical Engineering Journal*, vol. 219, pp. 395–402, 2013.
- [37] J. J. Beaudoin, B. Patarachao, L. Raki, and R. Alizadeh, "Adsorption of methylene blue as a descriptor of C-S-H nanostructure," *Cement and Concrete Composites*, vol. 33, no. 2, pp. 246–250, 2011.

Research Article

In Situ Formation of Carbon Nanomaterials on Bulk Metallic Materials

J. Y. Xu, X. C. Lei, R. Yang, and Z. Z. Fan

College of Materials Science and Engineering, Chongqing University, Chongqing 400030, China

Correspondence should be addressed to J. Y. Xu; junyaoxu@cqu.edu.cn

Received 25 December 2013; Accepted 6 February 2014; Published 11 March 2014

Academic Editor: Ming-Guo Ma

Copyright © 2014 J. Y. Xu et al. This is an open access article distributed under the Creative Commons Attribution License, which permits unrestricted use, distribution, and reproduction in any medium, provided the original work is properly cited.

Carbon nanomaterials were synthesized in situ on bulk 316L stainless steel, pure cobalt, and pure nickel by hybrid surface mechanical attrition treatment (SMAT). The microstructures of the treated samples and the resulted carbon nanomaterials were investigated by SEM and TEM characterizations. Different substrates resulted in different morphologies of products. The diameter of carbon nanomaterials is related to the size of the nanograins on the surface layer of substrates. The possible growth mechanism was discussed. Effects of the main parameters of the synthesis, including the carbon source and gas reactant composition, hydrogen, and the reaction temperature, were studied. Using hybrid SMAT is proved to be an effective way to synthesize carbon nanomaterials in situ on surfaces of metallic materials.

1. Introduction

Carbon nanofibers (CNFs) and nanotubes (CNTs) have attracted extensive attention in the scientific field because of their remarkable properties [1]. They are being investigated for a wide range of applications, especially for the promising applications in nanoelectronics and field emission devices [2–5]. To meet the requirements of the applications, it is anticipated to produce CNFs/CNTs directly on many substrates.

Up to now, several methods have been studied to synthesize CNFs/CNTs on various substrates. In many cases, the hydrocarbons decomposed on dispersed catalytic metal particles on a support [6, 7]. Also the possibility to use the developed CVD methods to synthesize carbon nanomaterials directly on the transition metal surface that is catalytically active exists [8–11]. However, difficulties persist in making effective carbon nanomaterials directly on bulk metal surface using a simple technique with low cost.

Surface mechanical attrition treatment (SMAT) has been proved to be an effective way to achieve surface nanocrystallization on various metallic materials [12–16] and can be used to accelerate the chemical reaction of a material surface. Great progress has been achieved in nitriding, chromizing, and synthesizing functional nanoproducs via SMAT [17–23]. Hence, we consider modifying the surface of the metallic materials by

SMAT and taking it as the catalyst as well as the substrate for the fabrication of CNFs/CNTs. Carbon nanomaterials were successfully synthesized in situ on bulk titanium by hybrid SMAT process [24]. In this study, the traditional catalytic transition metallic materials (Fe in its alloy forms stainless steel, cobalt, and nickel) were subjected to hybrid SMAT process to synthesize carbon nanomaterials. The morphologies and structures of the obtained carbon nanomaterials were investigated. The possible growth mechanism was discussed. Effects of the main parameters of the synthesis were studied. Hybrid SMAT is proved to be an effective and low-cost way to synthesize carbon nanomaterials in situ on surfaces of metallic materials. It is anticipated to get large-scale carbon nanomaterials/metallic materials composites by using this method to meet the application requirements.

2. Materials and Methods

Samples were stainless steel (AISI 316L), pure cobalt (purity 99.9%), and pure nickel (purity 99.9%) plates. The plates were 20 mm in diameter and 1 mm in thickness and were firstly subjected to the SMAT process. Details of SMAT can be found in the previous work [15, 16]. After SMAT, a nanocrystalline surface layer was achieved. During SMAT

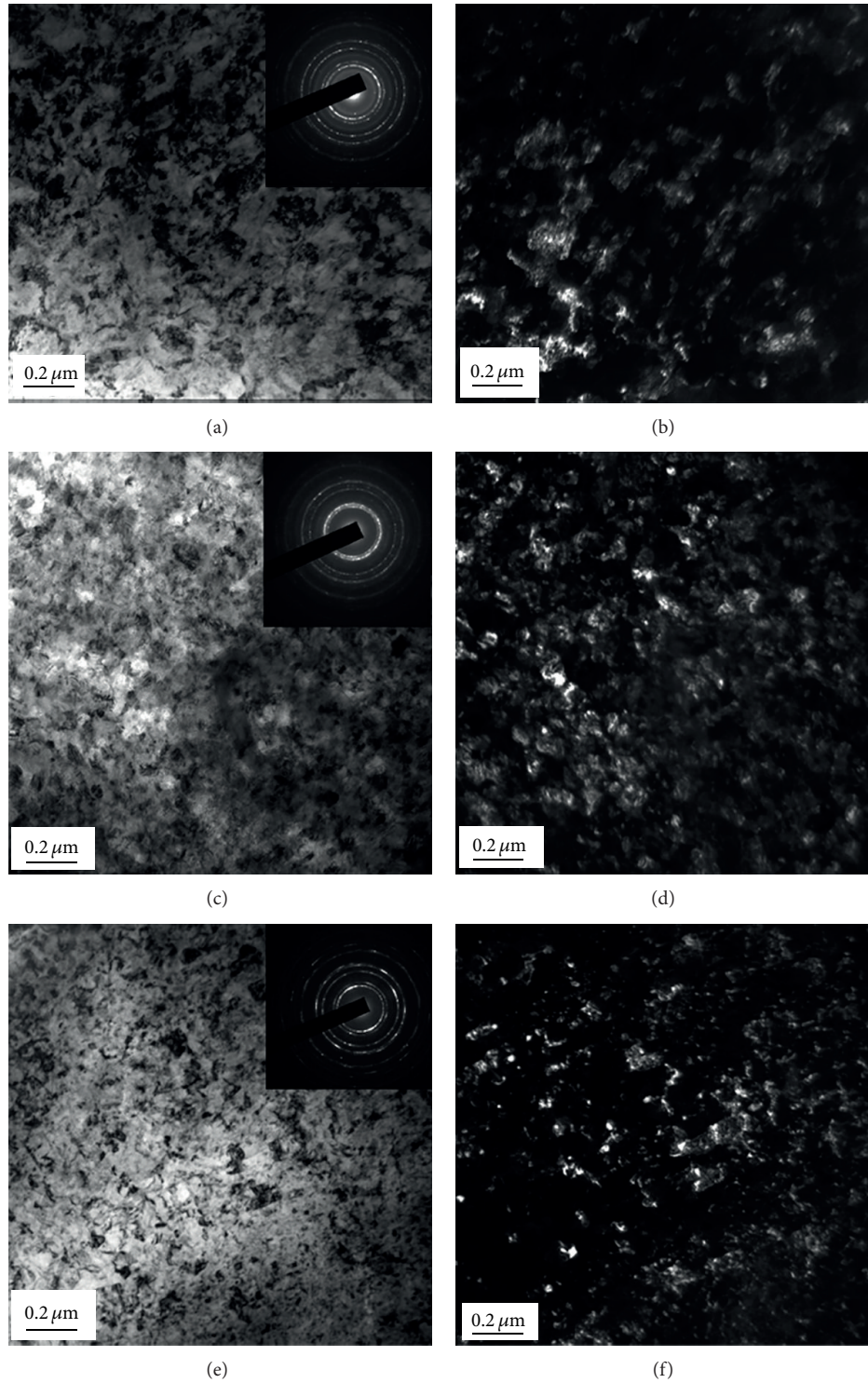


FIGURE 1: Bright-field (a, c, e) and dark-field (b, d, f) TEM images showing typical microstructures of the top surface layer in (a, b) SMAT 316L stainless steel; (c, d) SMAT Co; and (e, f) SMAT Ni. The insets are the corresponding SAED patterns.

process, a great amount of repeated and multidirectional impacts induce a severe plastic deformation (SPD) on the sample surface. Accordingly, grains of the surface layer were successfully refined from micrometer into nanometer. In the present work, the SMAT process was performed with a

vibration frequency of 20 kHz for 30 min, using the shot with a diameter of 2 mm.

Samples treated by SMAT (SMAT samples) were then subjected to a CVD process using a furnace with a quartz tube. The typical parameters were as follows. The reaction

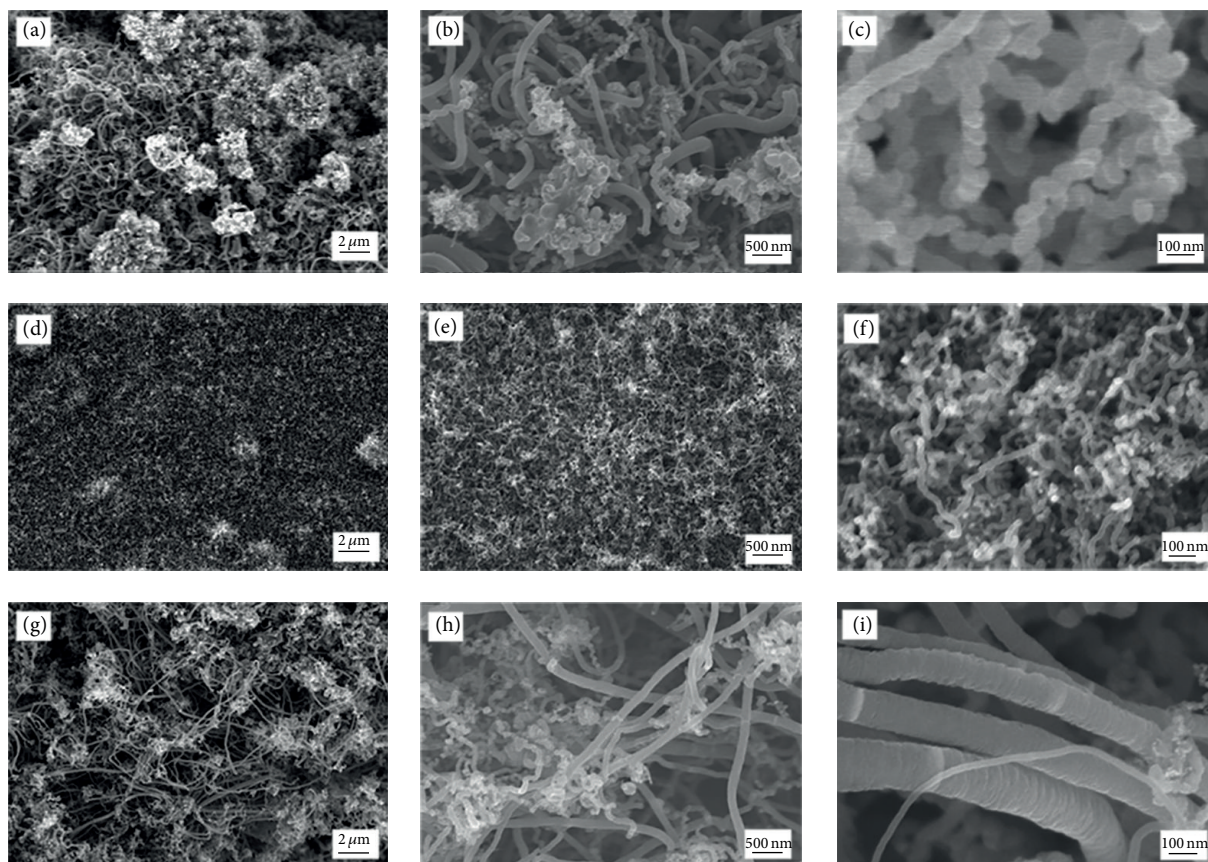


FIGURE 2: Comparison of the morphology of carbon products synthesized on different SMAT metals: (a) on SMAT 316L, $\times 5$ K; (b) on 316L, $\times 20$ K; (c) on 316L, $\times 90$ K; (d) on SMAT Co, $\times 5$ K; (e) on SMAT Co, $\times 20$ K; (f) on SMAT Co, $\times 90$ K; (g) on SMAT Ni, $\times 5$ K; (h) on SMAT Ni, $\times 20$ K; and (i) on SMAT Ni, $\times 90$ K.

was maintained in 550°C for 30 min. The reactant gas composition is $\text{C}_2\text{H}_2 : \text{H}_2 = 50 \text{ SCCM (mL/min)} : 100 \text{ SCCM}$ in a N_2 carrier of 300 SCCM. The main parameters of CVD, including carbon source, gas reactant composition, and temperature, were studied.

Transmission electron microscopy (TEM) observations were performed to characterize SMAT samples and the resulted carbon products using a Philips CM30 microscope working under 300 kV accelerated voltage.

Scanning electron microscopy (SEM) was also used to investigate the microstructures of the carbon products, using a Sirion, FEI working at 3 kV accelerated voltage.

3. Results and Discussion

TEM characterizations indicate the microstructural features of the very top surface of SMAT transition metallic materials, as can be seen in Figure 1.

Although the mechanisms of the nanocrystallization of three metallic materials are not the same [16], there is no evident difference from the surface layer except for the grain size. After SMAT under the same parameters, cobalt exhibits the smallest average grain size (about 30 nm), followed in

order by 316L stainless steel (about 70 nm) and nickel (about 110 nm) according to the TEM images. In spite of the grain size, the nanocrystalline surface layers of the SMAT metals exhibit similar appearance. On the very top surface, there are equiaxed nanograins with random crystallographic orientations, as shown by the inserted SAED patterns. Between this layer and the matrix, a transition layer with grain sizes increasing gradually is presented.

After CVD process, thin black films were fabricated on SMAT 316L stainless steel and SMAT Co, while soft black products with a certain thickness were synthesized on SMAT Ni. No product was found in the untreated zone of samples. The carbon deposit yields were measured experimentally. SMAT Ni has the largest carbon deposit yield, up to 62.29 mg/cm^2 , followed in order by SMAT Co (16.4 mg/cm^2) and SMAT 316L stainless steel (9.26 mg/cm^2).

We compared the morphologies of the carbon nanomaterials synthesized on different SMAT metals. Figure 2 shows SEM images of carbon nanomaterials in connection with various substrates at different magnifications. The lower magnification pictures are used to convey the relative density and uniformity of nanofiber growth. The higher magnification pictures convey the relative morphology of the CNFs.

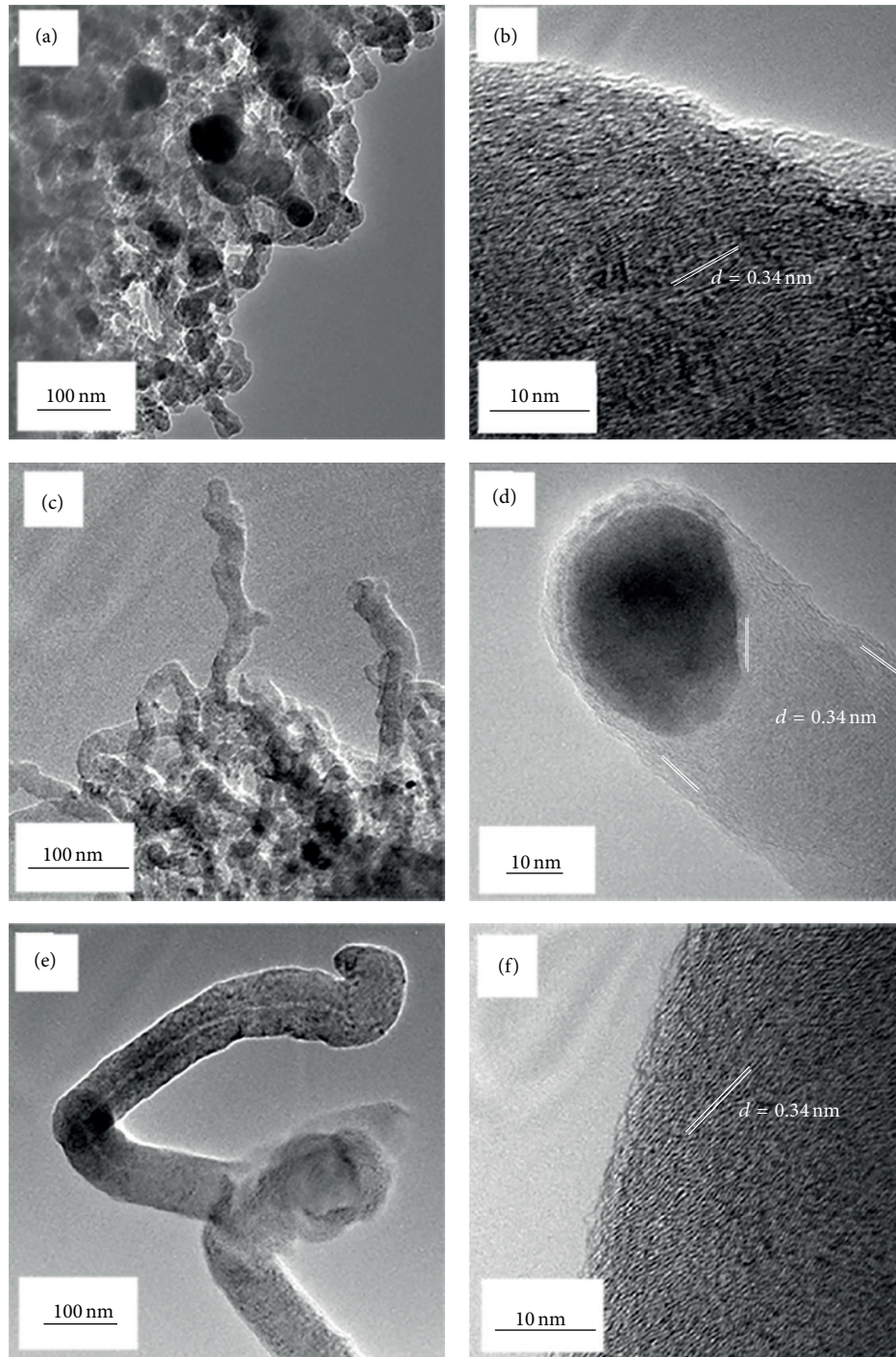


FIGURE 3: TEM images of the CNFs synthesized on different SMAT metals (a) on SMAT 316L stainless steel; (c) on SMAT Co; (e) on SMAT Ni and the related HREM images of the CNFs synthesized (b) on SMAT 316L stainless steel; (d) on SMAT Co; (f) on SMAT Ni.

It can be clearly seen that the morphologies and structures of the substrate-synthesized carbon nanostructures significantly depend on the type of substrate. CNFs synthesized on SMAT Co possess a fairly uniform size distribution of about 25 nm. In contrast to this, SMAT 316L stainless steel and SMAT Ni result in large diameter CNFs (more than 100 nm).

Besides the dimension, the morphologies are totally different. CNFs synthesized on SMAT 316L stainless steel are neither uniform nor dense, distributed among the metal clusters, with a broad diameter distribution ranging from tens of nanometers to several micrometers. Some of them appear to undergo a further partial and simultaneous change

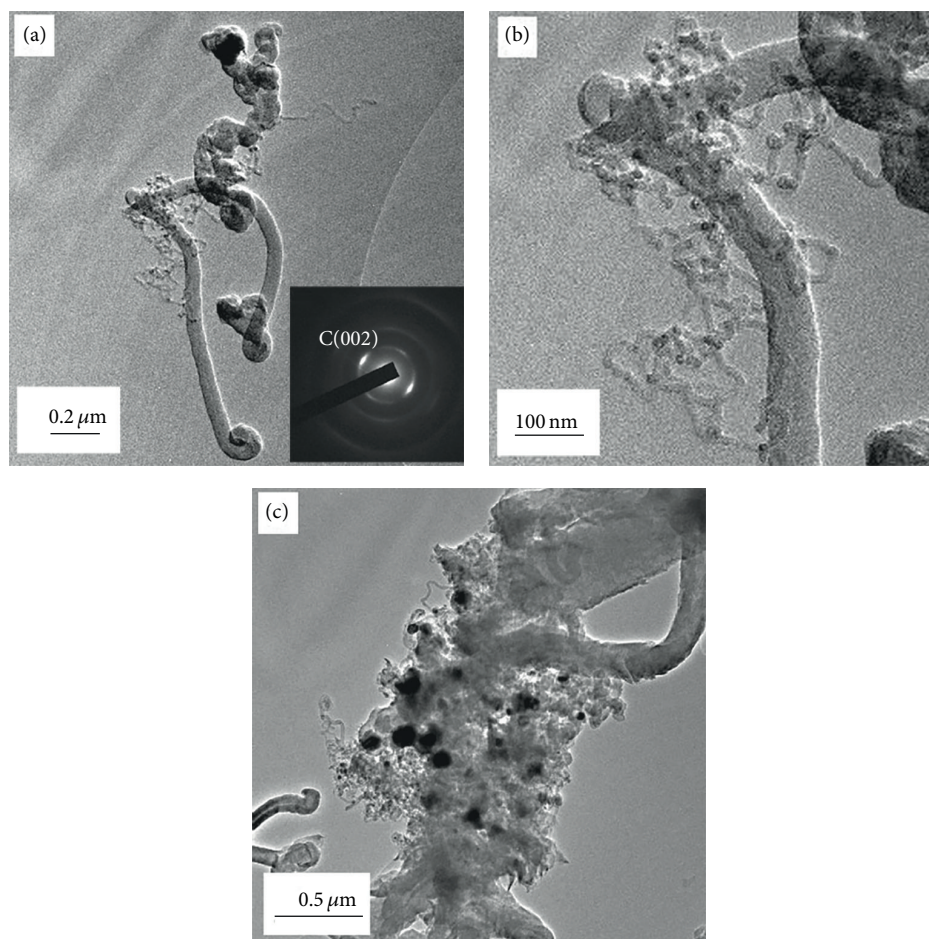


FIGURE 4: TEM images of carbon products synthesized on SMAT Ni (a) image at low magnification showing CNTs as well as CNFs; (b) image at high magnification showing details of CNTs; and (c) image showing the presence of the catalyst particles as well as CNFs.

in shape, rotating on an axis perpendicular to the direction of fiber growth, and thus forcing the filament to a helical form (Figure 2(c)). CNFs synthesized on SMAT Ni are straighter, longer, and even thicker than those grown on SMAT 316L stainless steel, tangled with microspheres (Figure 2(g)). The medium magnification (Figure 2(h)) reveals that the microspheres are composed of thin curly entangled fibers, twisted among the thick fibers. High magnification image revealed that the thick fibers synthesized on SMAT Ni are comprised of stacked graphene segments (Figure 2(i)). Unlike SMAT 316L stainless steel or SMAT Ni, SMAT Co results in quite uniform CNFs that entangle with each other, giving the appearance like dense grass in low magnification (Figure 2(d)). Twists are characteristic of the CNFs and no straight regions are observed (Figures 2(e) and 2(f)). In contrast to SMAT 316L stainless steel, occurrences of inactive metal articles appearing as isolated particles or clusters are rarely observed on SMAT Co and SMAT Ni.

TEM characterizations were performed to establish the nature of the fibers observed in SEM. Figure 3 shows the TEM images, which represent typical examples of the products synthesized on SMAT 316L stainless steel, SMAT Co, and SMAT Ni.

As shown in Figure 3(a), on the SMAT 316L stainless steel, a mixture of amorphous carbon and encapsulated particles is observed. Nanofibers are found stretched out from the mixture. Many metallic particles are still inactive toward nanofiber catalysis, becoming embedded. The catalysts are quasi-spherical metal particles with an average diameter of 60~70 nm, which is in accord with the results obtained by the TEM of the substrates (Figure 1(a)). As for SMAT Co, a significantly wide distribution in diameter and a greater variation in morphology are observed (Figure 3(c)). The fiber-like products are thin CNFs with an average diameter of about 25 nm. These CNFs are much thinner and more uniform than those synthesized on SMAT 316L stainless steel. Figure 2(d) also shows that the metal particles locate at the top ends of the nanofibers. Most of the pyrolysis products are thick CNFs showing either curved or straight shapes. Figure 3(e) shows the TEM views of typical CNFs synthesized on SMAT Ni, indicating thick CNFs of over 100 nm in diameter. The HREM image (Figure 3(f)) reveals that the nanofibers have a “herringbone” structure that consists of graphite sheet oriented at a specific angle to the fiber axis with an interlayer space of 0.34 nm. In addition to thick CNFs, thin CNTs are also observed in the products synthesized on

SMAT Ni. It can be clearly seen from Figure 4(a) that thick fiber is twisted by uniform thin fibers, which is similar to the products reported by Ding et al., and so forth. using a Ni-Ni₃P as a catalyst [25].

The curly fibers are entangled with each other. The inset image is the corresponding SAED pattern. The higher magnification (Figure 4(b)) revealed that those thin fibers are thin MWNTs with a diameter of about 10 nm and without any catalyst particle embedded at the tip. Thin CNTs are also observed stretched out from catalyst clusters, as can be seen from Figure 4(c). The observed metal particles are much bigger than the size of the carbon nanotubes. Therefore, it can be deduced that those thin CNTs are catalyzed by the thick CNFs rather than the Ni nanoparticles. Hollow thick CNFs are also found (Figure 3(e)).

Corresponding to the grain size distributions of SMAT transition metals, the diameter distributions of CNFs are illustrated in Figure 5. It is noted that the variation tendency of the CNFs sizes is similar to the variation of grain size of SMAT transition metals. However, in the cases of SMAT 316L stainless steel and SMAT Ni, the CNFs sizes are larger than the nanocrystalline grains.

Here we discuss a possible mechanism of the CNFs growth on the surface of SMAT metallic materials. The catalyst particles wrapped with graphite (Figure 3(a)) and encapsulated in a CNF (Figure 3(d)) have been found through TEM observations. The experimental observations lead to the proposal that the CNFs growth follows the mechanism presented by Baker et al. [26]. It is supposed that when the hydrocarbon meets the front-exposed metal particle surface, it decomposes and releases active hydrogen and carbon atoms. The carbon atoms dissolve and diffuse through the metal particles and precipitate on the rear face to form the carbon filament. The catalytic ability of the transition metallic materials to form carbon nanomaterials is related to a combination of factors that include the catalytic activity for the decomposition of unstable carbon compounds such as hydrocarbon, the formation of metastable carbides, and the diffusion of carbon through the metal particles [27]. It is known that a large number of grain boundaries and other defects in nanocrystalline materials may serve as fast atomic diffusion channels for the diffusion. In the previous work [17–23], it was found that the high chemical reactivity of the nanocrystalline that attributes to numerous grain boundaries and a large excess energy in the form of nonequilibrium defects such as dislocations and subgrain boundaries that are induced by plastic deformation arouse a considerable driving force which is stored on the surface of SMAT metallic materials. At the same time, the high concentration of the nonequilibrium defects may decrease the activation energy of diffusion. Experiments have also proved that when the grain size is reduced to nanoscale and defects are induced by SPD, the chemical reaction kinetics will be enhanced severely during mechanical attrition of metals [28, 29]. As a result, the atomic diffusivities were greatly enhanced after SMAT. When carbon atoms diffuse into the surface layer of SMAT metallic materials, the nanocrystalline grains act as catalyst particles, providing nuclei for the carbon nanomaterials.

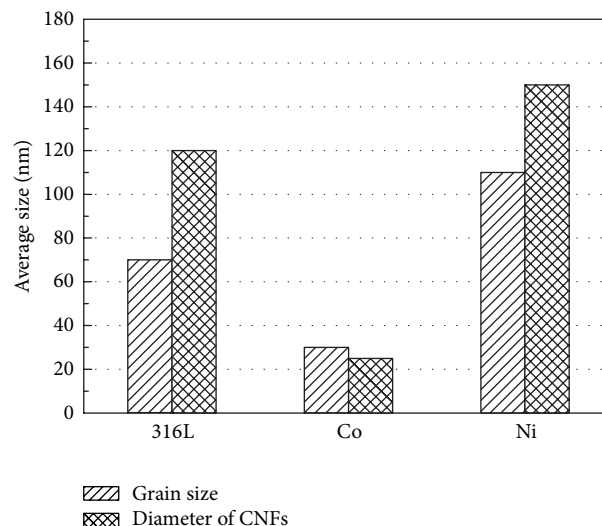


FIGURE 5: Average grain size of different SMAT metals and the average diameters of corresponding CNFs.

Using hybrid SMAT is proved to be an effective way to synthesize carbon nanomaterials in situ on surfaces of metallic materials. However, the whole process and mechanism are rather complicated. Further studies are needed for understanding the principles so that we could control the diameter and the morphology of the CNFs by changing the parameters of hybrid SMAT process.

Effects of the main parameters of the synthesis, including the carbon source, gas reactant composition, hydrogen, and the reaction temperature, were studied using SMAT Co. Similar phenomena were found in SMAT Ni and SMAT 316L stainless steel.

Carbon source is considered to contribute to the special structure and the yield. A series of experiments has been done on SMAT Co using CH₄ and C₂H₂ as carbon source.

When using CH₄ as carbon source, no evidence for the formation of filamentous carbon was observed upon SMAT Co in the temperature range 550–900°C, regardless of the CH₄/H₂/N₂ ratio. This phenomenon can be explained; that is, CH₄ is a most kinetically stable hydrocarbon and is hard to pyrolyze. CH₄ does not decompose at lower temperature (e.g., 550°C), while at higher temperature (e.g., 900°C), the nanocrystalline grains on the SMAT metal surface grow up and exhibit no catalytic activity. On the other hand, C₂H₂ is much easier to decompose at lower temperature and therefore can be regarded as good carbon source in this work.

Synthesis of carbon nanostructures is dependent on the reactant gas composition. The effect of the reactant composition on the carbon product is listed in Table 1. Best results were obtained with flow rates of C₂H₂ and H₂ of 50 SCCM and 100 SCCM, respectively, in a N₂ carrier of 300 SCCM. The relative yield and purity of these nanofibers are highly dependent upon the relative C₂H₂ to H₂ ratio and absolute C₂H₂ concentration. Gas mixture with lower C₂H₂ concentration is less active towards CNFs synthesis. Higher C₂H₂ results in higher yield of nanofibers, yet further

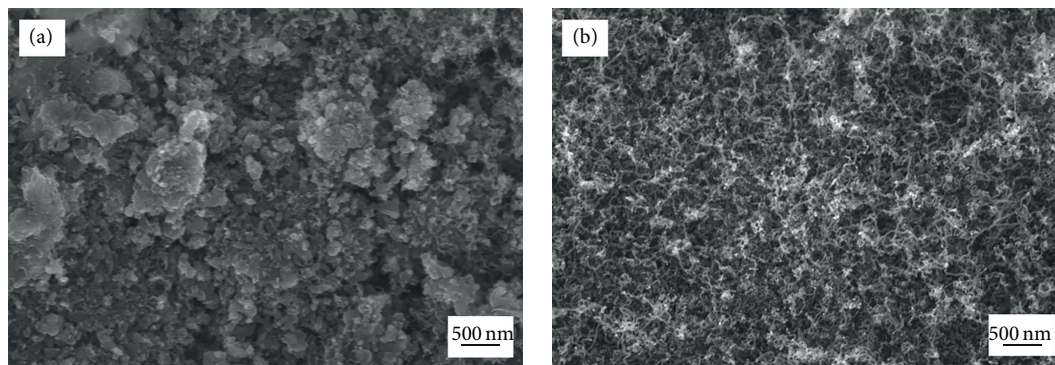


FIGURE 6: SEM images of the carbon products synthesized on SMAT Co after CVD process (a) without hydrogen and (b) with hydrogen.

TABLE 1: Carbon products related to different gas composition.

Gas composition ($C_2H_2 : H_2 : N_2$, SCCM)	Related products
30 : 100 : 300	Medium yield of CNFs
50 : 100 : 300	Abundant CNFs
50 : 50 : 300	CNFs with amorphous carbon
100 : 100 : 300	CNFs with encapsulated metal particles
300 : 300 : 300	Encapsulated metal particles with few CNFs

increasing in the C_2H_2 concentration, led to deactivation of the catalyst nanoparticles.

Hydrogen is also proved to be critical in creating CNFs/CNTs. The influence of absence of H_2 is evident. Without H_2 , the growth becomes sparse and irregular structures are prominent. However, extra H_2 is proved similarly detrimental towards CNFs/CNTs growth. Figure 6 shows the SEM images of SMAT Co after CVD process with and without hydrogen. It is clearly shown that the presence of hydrogen obviously affects CNFs growth. There were sintered metal clusters when using 50 SCCM C_2H_2 and 300 SCCM N_2 without any hydrogen but lots of uniform CNFs when 50 SCCM C_2H_2 , 100 SCCM H_2 and 300 SCCM N_2 were supplied.

As indicated in the literature [30], hydrogen serves several purposes within this growth process. Firstly, hydrogen can be regarded as the promoter of the catalyst. It not only forms sufficient concentrations of hydrocarbons, but also satisfies unfilled carbon valencies at the precipitating rear facets of the metal catalyst. Thus, hydrogen can act to etch or remove surface-adsorbed carbon from the catalyst particle rather than accelerating soot formation [31]. Without this surface cleaning process, the catalyst tended to be easily covered by amorphous carbon and would be poisoned and lead to catalyst deactivation. It is particularly important where the rate of carbon deposition exceeds that of solvation. With hydrogen being supplied, the catalyst keeps active so that the decomposition, diffusion, and precipitation of carbon atoms

work smoothly. Secondly, hydrogen has been postulated to be necessary to terminate dangling bonds located on edge-plane carbon atoms.

The reaction temperature is proved to be a crucial parameter for the synthesis of CNFs/CNTs by CVD method. Since the temperature affects the activity of the catalytic metallic materials and the decomposition of the carbon source gases, the microstructure and the yield of CNFs/CNTs vary with the growth temperature [32]. A series of experiments has been done at temperature from $300^\circ C$ to $900^\circ C$ in order to examine the influences of reaction temperature. It is observed that the optimum conditions for reaction are realized at $550^\circ C$. The carbon yield at $550^\circ C$ is 16.4 mg/cm^2 . If the temperature changes either above or below this point, this is a dramatically drop in the yield of the product. No product has been observed below $350^\circ C$ or over $850^\circ C$. The reason is that C_2H_2 does not decompose at the temperature below $350^\circ C$, while high temperature results in the growth of the nanograins on the surface layer, leading to catalytic deactivation.

4. Conclusions

Carbon nanomaterials have been successfully synthesized in situ on various bulk metallic materials by hybrid SMAT. CNFs were formed on SMAT 316L stainless steel and SMAT Co while CNFs and CNTs were formed on SMAT Ni. SMAT Ni is the most active one compared with SMAT Co and SMAT 316L stainless steel and has the largest carbon deposit yield. Different SMAT metals resulted in different morphologies of products. The diameter of CNFs is related to the size of the nanograins on the surface layer of SMAT metals. The possible growth mechanism was discussed. The atomic diffusivities were greatly enhanced after SMAT and the nanocrystalline grains act as catalyst particles, being nuclei for the carbon nanomaterials. Effects of the main parameters including the carbon sources, gas reactant compositions, hydrogen, and reactant temperature were also investigated. The optimized gas reactant composition is $C_2H_2 : H_2 : N_2 = 50 \text{ SCCM} : 100 \text{ SCCM} : 300 \text{ SCCM}$. The appropriate reaction temperature is $550^\circ C$.

Conflict of Interests

The authors declare that there is no conflict of interests regarding the publication of this paper.

Acknowledgments

The work was supported by National Natural Science Foundation of China (Grant no. 51201190), Natural Science Foundation of Chongqing, China (CSTC. 2011BB4080), and Fundamental Research Funds for the Central Universities (no. CDJZR12130043). The authors also gratefully acknowledge sharing fund of Chongqing University's large-scale equipment (no. 2012121519).

References

- [1] Y. Saito, *Carbon Nanotube and Related Field Emitters: Fundamentals and Applications*, Wiley-VCH, 2010.
- [2] H. C. Chang, C. C. Li, S. F. Jen et al., "All-Carbon field emission device by direct synthesis of graphene and Carbon nanotube," *Diamond and Related Materials*, vol. 31, pp. 42–46, 2012.
- [3] B. Li, X. Cao, H. G. Ong et al., "All-Carbon electronic devices fabricated by directly grown single-walled Carbon nanotubes on reduced graphene oxide electrodes," *Advanced Materials*, vol. 22, no. 28, pp. 3058–3061, 2010.
- [4] S. Claramunt, O. Monereo, M. Boix et al., "Flexible gas sensor array with an embedded heater based on metal decorated Carbon nanofibres," *Sensors and Actuators B*, vol. 187, pp. 401–406, 2013.
- [5] P.-C. Chen, G. Shen, Y. Shi, H. Chen, and C. Zhou, "Preparation and characterization of flexible asymmetric supercapacitors based on transition-metal-oxide nanowire/single-walled Carbon nanotube hybrid thin-film electrodes," *ACS Nano*, vol. 4, no. 8, pp. 4403–4411, 2010.
- [6] Y. Chen, Z. L. Wang, J. S. Yin, D. J. Johnson, and R. H. Prince, "Well-aligned graphitic nanofibers synthesized by plasma-assisted chemical vapor deposition," *Chemical Physics Letters*, vol. 272, no. 3-4, pp. 178–182, 1997.
- [7] Z.-H. Yuan, H. Huang, L. Liu, and S.-S. Fan, "Controlled growth of Carbon nanotubes in diameter and shape using template-synthesis method," *Chemical Physics Letters*, vol. 345, no. 1-2, pp. 39–43, 2001.
- [8] R. L. Vander Wal and L. J. Hall, "Carbon nanotube synthesis upon stainless steel meshes," *Carbon*, vol. 41, no. 4, pp. 659–672, 2003.
- [9] S. J. Chae, F. Güneş, K. K. Kim et al., "Synthesis of large-area graphene layers on poly-Nickel substrate by chemical vapor deposition: wrinkle formation," *Advanced Materials*, vol. 21, no. 22, pp. 2328–2333, 2009.
- [10] G. Atthipalli, R. Epur, P. N. Kumta, M. Yang, J.-K. Lee, and J. L. Gray, "Nickel catalyst-assisted vertical growth of dense Carbon nanotube forests on bulk Copper," *Journal of Physical Chemistry C*, vol. 115, no. 9, pp. 3534–3538, 2011.
- [11] E. Kukovitsky and S. Lvov, "Increased Carbon chemical vapor deposition and Carbon nanotube growth on metal substrates in confined spaces," *ECS Journal of Solid State Science and Technology*, vol. 2, no. 1, pp. M1–M8, 2013.
- [12] H. Q. Sun, Y. N. Shi, and M.-X. Zhang, "Sliding wear-induced microstructure evolution of nanocrystalline and coarse-grained AZ91D Mg alloy," *Wear*, vol. 266, no. 7-8, pp. 666–670, 2009.
- [13] S. Lu, Z. Wang, and K. Lu, "Strain-induced microstructure refinement in a tool steel subjected to surface mechanical attrition treatment," *Journal of Materials Science and Technology*, vol. 26, no. 3, pp. 258–263, 2010.
- [14] L. M. Wang, Z. B. Wang, and K. Lu, "Grain size effects on the austenitization process in a nanostructured ferritic steel," *Acta Materialia*, vol. 59, no. 9, pp. 3710–3719, 2011.
- [15] K. Lu and J. Lu, "Surface nanocrystallization (SNC) of metallic materials-presentation of the concept behind a new approach," *Journal of Materials Science and Technology*, vol. 15, no. 3, pp. 193–197, 1999.
- [16] K. Lu and J. Lu, "Nanostructured surface layer on metallic materials induced by surface mechanical attrition treatment," *Materials Science and Engineering A*, vol. 375–377, pp. 38–45, 2004.
- [17] W. P. Tong, N. R. Tao, Z. B. Wang, J. Lu, and K. Lu, "Nitriding iron at lower temperatures," *Science*, vol. 299, no. 5607, pp. 686–688, 2003.
- [18] Z. B. Wang, K. Lu, G. Wilde, and S. V. Divinski, "Interfacial diffusion in Cu with a gradient nanostructured surface layer," *Acta Materialia*, vol. 58, no. 7, pp. 2376–2386, 2010.
- [19] X. Si, B. N. Lu, and Z. B. Wang, "Aluminizing low Carbon steel at lower temperatures," *Journal of Materials Science and Technology*, vol. 25, no. 4, pp. 433–436, 2009.
- [20] S. D. Lu, Z. B. Wang, and K. Lu, "Enhanced chromizing kinetics of tool steel by means of surface mechanical attrition treatment," *Materials Science and Engineering A*, vol. 527, no. 4-5, pp. 995–1002, 2010.
- [21] J. Sun, W. P. Tong, H. Zhang, L. Zuo, and Z. B. Wang, "Evaluation of surface-modified 20CrMo by plasma nitriding coupled with ion sputtering and SMAT," *Surface and Coatings Technology*, vol. 213, pp. 247–252, 2012.
- [22] H. W. Chang, P. M. Kelly, Y. N. Shi, and M. X. Zhang, "Thermal stability of nanocrystallized surface produced by surface mechanical attrition treatment in aluminum alloys," *Surface and Coatings Technology*, vol. 206, pp. 3970–3980, 2012.
- [23] H. L. Wang, Z. B. Wang, and K. Lu, "Enhanced reactive diffusion of Zn in a nanostructured Fe produced by means of surface mechanical attrition treatment," *Acta Materialia*, vol. 60, no. 4, pp. 1762–1770, 2012.
- [24] X. F. Yang and J. Lu, "A new way to synthesize Carbon nanofiber film on bulk titanium via hybrid surface mechanical attrition treatment," *Applied Surface Science*, vol. 264, pp. 191–196, 2013.
- [25] D. Y. Ding, J. N. Wang, Z. L. Cao, J. H. Dai, and F. Yu, "Ni-Ni₃P alloy catalyst for Carbon nanostructures," *Chemical Physics Letters*, vol. 371, no. 3-4, pp. 333–336, 2003.
- [26] R. T. K. Baker, M. A. Barber, P. S. Harris, F. S. Feates, and R. J. Waite, "Nucleation and growth of Carbon deposits from the Nickel catalyzed decomposition of acetylene," *Journal of Catalysis*, vol. 26, no. 1, pp. 51–62, 1972.
- [27] S. B. Sinnott, R. Andrews, D. Qian et al., "Model of Carbon nanotube growth through chemical vapor deposition," *Chemical Physics Letters*, vol. 315, no. 1-2, pp. 25–30, 1999.
- [28] C. C. Koch, "The synthesis and structure of nanocrystalline materials produced by mechanical attrition: a review," *Nanosstructured Materials*, vol. 2, pp. 109–129, 1993.
- [29] C. Suryanarayana, "Mechanical alloying and milling," *Progress in Materials Science*, vol. 46, pp. 1–184, 2001.
- [30] F. Xu, X. Liu, and S. D. Tse, "Synthesis of Carbon nanotubes on metal alloy substrates with voltage bias in methane inverse diffusion flames," *Carbon*, vol. 44, no. 3, pp. 570–577, 2006.

- [31] R. T. K. Baker, C. R. F. Lund, and J. J. Chludzinski Jr., "Catalytic gasification of graphite by barium in steam, Carbon dioxide, Oxygen, and Hydrogen," *Journal of Catalysis*, vol. 87, no. 1, pp. 255–264, 1984.
- [32] P. Navarro López, I. Rodríguez Ramos, and A. Guerrero Ruiz, "A study of Carbon nanotube formation by C_2H_2 decomposition on an iron based catalyst using a pulsed method," *Carbon*, vol. 41, pp. 2509–2517, 2003.

Research Article

Influence of Sn Doping on Phase Transformation and Crystallite Growth of TiO₂ Nanocrystals

Guozhu Fu,¹ Yanqiu Yang,² Gang Wei,¹ Xin Shu,¹ Ning Qiao,¹ and Li Deng^{2,3}

¹ State Key Laboratory of Chemical Resource Engineering, Beijing University of Chemical Technology, Beijing 100029, China

² Beijing Bioprocess Key Laboratory, Beijing University of Chemical Technology, Beijing 100029, China

³ Amoy-BUCT Industrial of Biotechnovation Institute, Amoy 361026, China

Correspondence should be addressed to Li Deng; dengli@mail.buct.edu.cn

Received 16 January 2014; Accepted 2 February 2014; Published 10 March 2014

Academic Editor: Shao-Wen Cao

Copyright © 2014 Guozhu Fu et al. This is an open access article distributed under the Creative Commons Attribution License, which permits unrestricted use, distribution, and reproduction in any medium, provided the original work is properly cited.

Sn doped TiO₂ nanocrystals were synthesized via a single-step hydrothermal method and the influences of Sn doping on TiO₂ have been investigated. It is found that Sn doping not only facilitates the crystal transfer from anatase to rutile but also facilitates the morphology change from sphere to rod. The states of Sn were studied by XPS and the creation of oxygen vacancies by Sn doping is confirmed. Moreover, the HRTEM results suggest that Sn facilitates preferential growth of resulting nanocrystals along (110) axis, which results in the formation of rod-like rutile nanocrystals.

1. Introduction

In recent years, the applications of semiconductors in photocatalysis and other fields have attracted much interest [1, 2], and many semiconductor nanomaterials and their heterogeneous structures have been developed for their application in energy and environmental applications [3–5], for example, the investigations of TiO₂ on various organic pollutants photodegradation [6] due to its excellent photocatalytic activity, physical and chemical stability, and nontoxicity [7]. Because most of the solar energy is focused on the visible light, it is important to develop the visible-light-driven photocatalysts. However, TiO₂ is only sensitive to UV light because of its large band gap (3.2 eV). In order to efficiently use solar energy, many methods have been studied. An effective way is to introduce foreign ions into TiO₂, including rare earth element doping [8], metals doping [9], and nonmetals doping [10, 11].

The property of TiO₂ can also be affected by foreign metal ions doping. It has been shown that the photocatalytic activity of the modified TiO₂ improves to different extents depending on different ion doping, such as Mn²⁺ [12], Zr⁴⁺ [13], and Fe³⁺ [14]. Moreover, the phase transformation behavior and structure of TiO₂ are also affected by foreign metal ions. For

example, Ag⁺ [15], Mn²⁺ [16], and Cr³⁺ [17] are proved to promote phase transformation from anatase to rutile, while silicon ion doping strongly restrains the phase transformation [18] and lowers the phase transition temperature [19]. But, so far, no detailed study has been reported on the influence of Sn⁴⁺ doping on the phase transformation and structure of hydrothermal synthesis TiO₂.

In our work, Sn doped TiO₂ nanocrystals were prepared by hydrothermal method. The existing states of Sn and its role in phase transformation as well as the morphology evolution were investigated. Sn facilitates the phase conversion from anatase to rutile and prefers the morphology evolution from spherical shape to nanorods.

2. Experimental Section

Sn doped TiO₂ nanoparticles were prepared by hydrothermal method. 2.9 mL acetic acid was added to 17 mL tetrabutyl titanate and stirred for 15 min. The mixture was then poured into 73 mL of water and vigorously stirred for 1 hour. After adding 1 mL concentrated nitric acid, the mixture was heated to 80°C and peptized for 75 min. Then the volume was adjusted with water to 80 mL. The mixture was kept in a

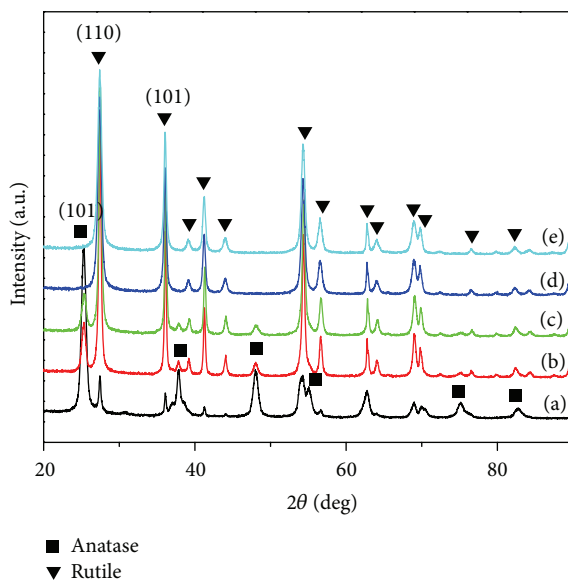


FIGURE 1: XRD patterns of TiO_2 samples prepared with different Sn doping ratios: (a) 0%, (b) 0.25%, (c) 0.50%, (d) 0.75%, and (e) 1.00%.

100 mL autoclave and heated at 200°C for 12 h. For Sn doped samples, appropriate volume of tin tetrachloride was added to distilled water in advance (the feed molar ratios of Sn/Ti were modulated as 0.25/100, 0.5/100, 0.75/100, and 1.0/100, resp.).

The powder XRD experiments were performed on Bruker D8 Advance X-ray diffractometer using monochromic $\text{Cu K}\alpha$ radiation ($\lambda = 0.15418\text{ nm}$). The scanning electron microscopy (SEM) images were recorded using S4700 Hitachi Ltd. The transmission electron microscopy (TEM) was performed with a Tecnai G2 20 transmission electron microscope of HongKong Co., Ltd. The X-ray photoelectron spectroscopy (XPS) experiments were carried out on Thermo ESCALAB 250 and the binding energies are calibrated by $\text{Cl}1s$ photoelectron peak (284.6 eV).

3. Results and Discussion

The X-ray diffraction patterns of TiO_2 samples with different Sn doping ratios are shown in Figure 1. It can be seen that the undoped TiO_2 is mainly composed of anatase and weak diffraction peaks of rutile TiO_2 can also be found in the XRD pattern. With the addition of Sn, the samples undergo “reutilization” to give rutile as the predominant polymorph, and the conversion from anatase to rutile is completed on 0.75% and 1.0% Sn doped samples, which suggests that the doped Sn ions can promote the formation of rutile.

The TEM results in Figure 2 show that the particle shape changed from sphere (diameter of 10–20 nm) to rod (width of $\sim 20\text{ nm}$ and length of 100–200 nm) by Sn doping, which are consistent with SEM results (not shown here). The space between the lattice planes of Sn-free TiO_2 (Figure 2(a)) is 0.35 nm, which corresponds well to the d value of (101) plane for anatase. The lattice space of 0.33 nm displayed in Sn- TiO_2 samples (Figures 2(b)–2(e)) is equal to the d value of

(110) plane for rutile. Therefore, it is reasonable to conclude that the Sn-free TiO_2 spherical nanocrystals are mainly anatase structure and the Sn doped TiO_2 rod-like particles are rutile. As for our samples, with an increasing of Sn doping amount in TiO_2 , the content of the spherical anatase decreases and the rod-like rutile increases, illustrating that Sn doping facilitates the phase conversion from anatase to rutile, which is consistent with XRD. Furthermore, the HRTEM images reveal rod-like building units and nanocrystal growth along the [110] axis, indicating that the formation of the rod-like TiO_2 is the result of the preferential growth (PG) in crystallographic orientation favored by Sn incorporation. Since Ti (IV) and Sn (IV) ions have the similar ionic radii, it is reasonable to deduce that Sn ions substitute lattice Ti, which is confirmed by our subsequent experiment. The EDX spectrum in Figure 2(e) also confirms the existence of Sn in TiO_2 nanocrystals.

Figure 3 shows the XPS spectra of Sn doped TiO_2 sample with Sn/Ti atomic ratio of 1%. As for Ti $2p_{3/2}$ spectrum in Figure 3(a), the two peaks at 458.1 eV and 458.7 eV could be assigned to O–Ti–O and Ti–O–Sn, respectively. Due to the electronegativity of Sn (1.96) which is larger than Ti (1.54) [20], the substitution of Sn for Ti in the lattice leads to the shift of binding energy to a higher value.

As for O1s spectrum in Figure 3(b), the peak at 532.2 eV is attributed to surface hydroxyl oxygen atoms. The peak at 529.3 eV is the binding energy of O1s in Ti–O–Ti, while the occurrence of the peak at 530 eV is the result of Sn substitute for Ti leading to the positive shift. These observations all confirm the formation of Ti–O–Sn structure in the Sn doped TiO_2 , owing to the substitution of Ti by Sn.

As shown in Figure 4, both anatase and rutile phase coexist at short treatment time, and the ratio of rutile/anatase increases with treatment time prolonging. A similar finding was reported by Zhang and Gao [21] who stated that

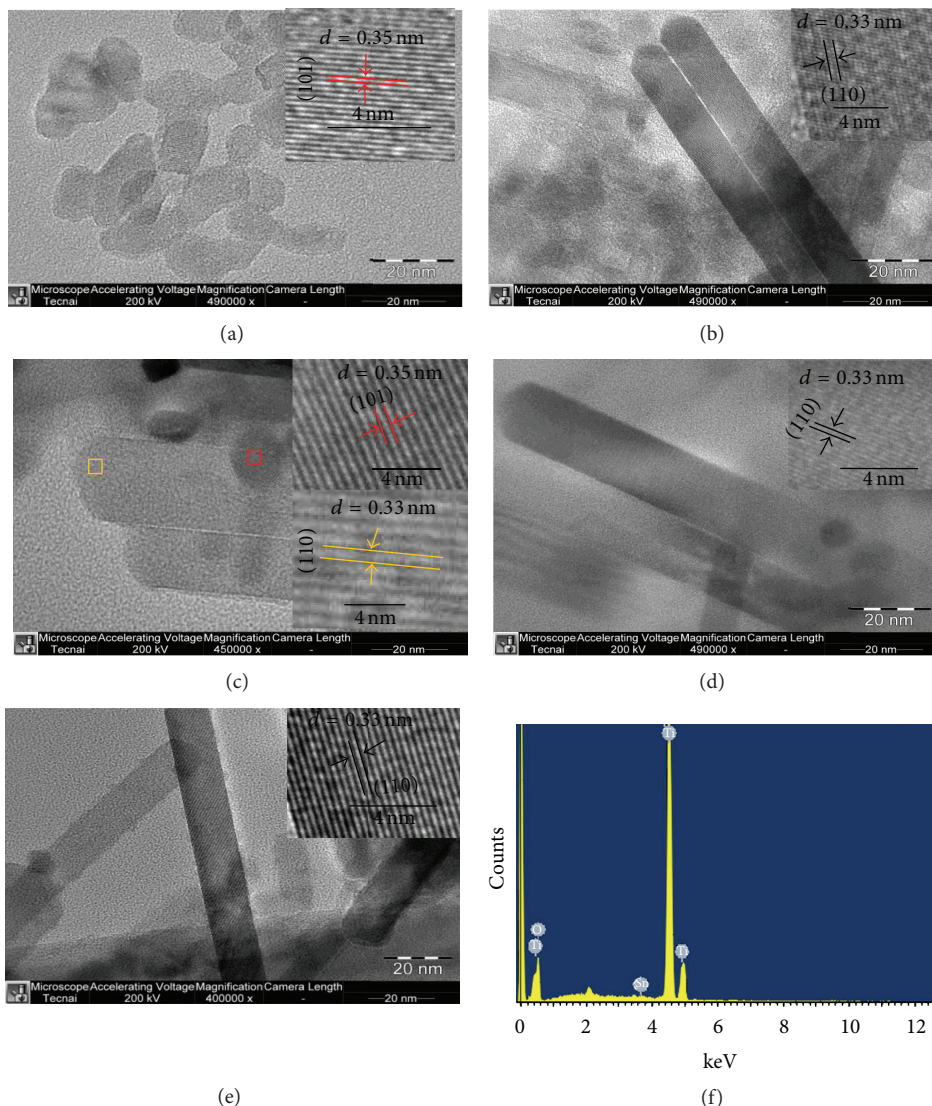


FIGURE 2: TEM images of TiO₂ samples prepared with different Sn doping ratios: (a) 0%, (b) 0.25%, (c) 0.50%, (d) 0.75%, (e) 1.00%, and (f) EDX spectrum of 1% Sn doped TiO₂ nanocrystals.

phase transformation occurred simultaneously with particle growth.

It has been shown that the oxygen vacancies of TiO₂ increase if foreign cations replace Ti⁴⁺ ions [22]. Vemury and Pratsinis [23] found that the formation of rutile phase was enhanced either by introducing dopant oxides with the same crystal structure as rutile or by creating oxygen vacancies by doping cations. It has been reported that the rutile fraction increases at a higher Eu³⁺ addition owing to the creation of oxygen vacancies by replacing the Ti⁴⁺ sites with subvalent Eu³⁺ ions in the TiO₂ [24]. In our samples, the creation of oxygen vacancies is by replacing the Ti⁴⁺ sites with Sn⁴⁺ ions in TiO₂ and therefore the rutile formation can be enhanced. Moreover, it was supposed that there is a relationship between the phase transformation and the

nanocrystal growth process [25] and the preferential growth process aids phase transformation. The minimization of the area of high-energy surface faces promoted by the preferential growth process may be an extra driving force for the phase transformation from anatase to rutile phase.

4. Conclusions

In summary, the promoting roles of Sn⁴⁺ in both TiO₂ phase transformation and morphology change have been confirmed in our study. The result demonstrated that morphology transition was related to the preferential growth process and the phase transformation was related to the creation of oxygen vacancies caused by Sn. Our observations of preferential growth coupled with phase transformation

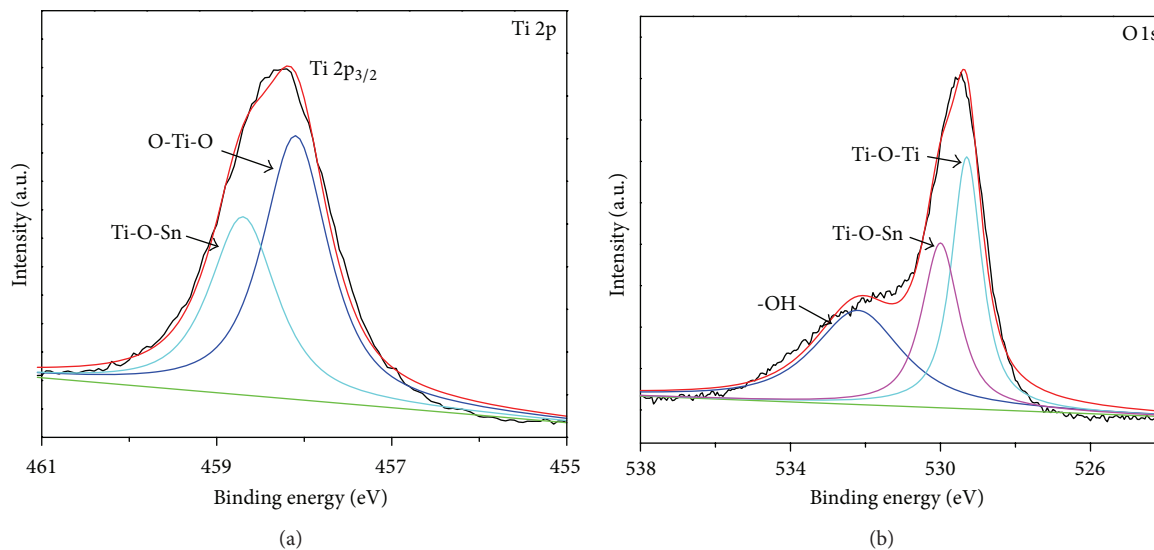


FIGURE 3: XPS spectra of the 1% Sn doped TiO_2 nanocrystals.

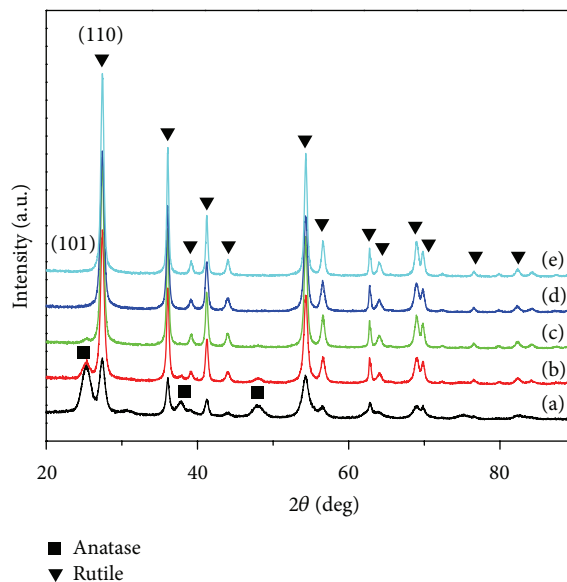


FIGURE 4: XRD patterns of the 1% Sn doped samples with different times: (a) 3 h, (b) 6 h, (c) 9 h, (d) 12 h, and (e) 15 h.

process led us to understand the preferential growth process aided phase transformation.

Conflict of Interests

The authors declare that there is no conflict of interests regarding the publication of this paper.

Acknowledgments

This work was supported by Beijing Key Laboratory of Bioprocess, State Key Laboratory of Chemical Resource Engineering, China 863 Project (nos. 2009AA03Z802 and

2009AA03Z803), and Amoy Major Scientific and Technological Innovation Project (2012S0305).

References

- [1] S. W. Cao, X. F. Liu, Y. P. Yuan et al., "Artificial photosynthetic hydrogen evolution over g- C_3N_4 nanosheets coupled with cobaloxime," *Physical Chemistry Chemical Physics*, vol. 15, no. 42, pp. 18363–18366, 2013.
- [2] P. Hu, S. S. Pramana, S. W. Cao et al., "Ion-induced synthesis of uniform single-crystalline sulphide-based quaternary-alloy hexagonal nanorings for highly efficient photocatalytic Hydrogen evolution," *Advanced Materials*, vol. 25, no. 18, pp. 2567–2572, 2013.

- [3] S. W. Cao, Y. P. Yuan, J. Fang et al., "In-situ growth of CdS quantum dots on g-C₃N₄ nanosheets for highly efficient photocatalytic hydrogen generation under visible light irradiation," *International Journal of Hydrogen Energy*, vol. 38, pp. 1258–1266, 2013.
- [4] M. S. Yao, P. Hu, Y. B. Cao, W. C. Xiang, X. Zhang, and F. L. Yuan, "Morphology-controlled ZnO spherical nanobelt-flower arrays and their sensing properties," *Sensors and Actuators B: Chemical*, vol. 177, pp. 562–569, 2013.
- [5] S. W. Cao, J. Fang, M. M. Shahjamali et al., "In situ growth of Au nanoparticles on Fe₂O₃ nanocrystals for catalytic applications," *CrystEngComm*, vol. 14, pp. 7229–7235, 2012.
- [6] A. Fujishima, T. N. Rao, and D. A. Tryk, "Titanium dioxide photocatalysis," *Journal of Photochemistry and Photobiology C: Photochemistry Reviews*, vol. 1, no. 1, pp. 1–21, 2000.
- [7] W. X. Dai, X. Chen, X. P. Zheng et al., "Photocatalytic oxidation of CO on TiO₂: chemisorption of O₂, CO, and H₂," *ChemPhysChem*, vol. 10, no. 2, pp. 411–419, 2009.
- [8] M. S. Hassan, T. Amna, O. B. Yang, H. C. Kim, and M. S. Khil, "TiO₂ nanofibers doped with rare earth elements and their photocatalytic activity," *Ceramics International*, vol. 38, pp. 5925–5930, 2012.
- [9] Y. X. Li, S. Q. Peng, F. Y. Jiang, G. X. Lu, and S. B. Li, "Effect of doping TiO₂ with alkaline-earth metal ions on its photocatalytic activity," *Journal of the Serbian Chemical Society*, vol. 72, no. 4, pp. 393–402, 2007.
- [10] P. Z. Si, W. Jiang, H. X. Wang et al., "Large scale synthesis of nitrogen doped TiO₂ nanoparticles by reactive plasma," *Materials Letters*, vol. 68, pp. 161–163, 2012.
- [11] G. S. Wu, J. L. Wen, J. P. Wang, D. F. Thomas, and A. C. Chen, "A facile approach to synthesize N and B co-doped TiO₂ nanomaterials with superior visible-light response," *Materials Letters*, vol. 64, pp. 1728–1731, 2010.
- [12] V. D. Binas, K. Sambani, T. Maggos, A. Katsanaki, and G. Kiriakidis, "Synthesis and photocatalytic activity of Mn-doped TiO₂ nanostructured powders under UV and visible light," *Applied Catalysis B: Environmental*, vol. 113–114, pp. 79–86, 2012.
- [13] H. J. Liu, G. G. Liu, and Q. X. Zhou, "Preparation and characterization of Zr doped TiO₂ nanotube arrays on the titanium sheet and their enhanced photocatalytic activity," *Journal of Solid State Chemistry*, vol. 182, no. 12, pp. 3238–3242, 2009.
- [14] L. Sikong, B. Kongreong, D. Kantachote, and W. Sutthisripok, "Photocatalytic activity and antibacterial behavior of Fe³⁺-doped TiO₂/SnO₂ nanoparticles," *Energy Research Journal*, vol. 1, no. 2, pp. 120–125, 2010.
- [15] J.-Y. Park, J.-J. Yun, C.-H. Hwang, and I.-H. Lee, "Influence of silver doping on the phase transformation and crystallite growth of electrospun TiO₂ nanofibers," *Materials Letters*, vol. 64, no. 24, pp. 2692–2695, 2010.
- [16] J. P. Xu, Y. B. Lin, Z. H. Lu et al., "Enhanced ferromagnetism in Mn-doped TiO₂ films during the structural phase transition," *Solid State Communications*, vol. 140, no. 11–12, pp. 514–518, 2006.
- [17] T. H. Jun and K. S. Lee, "Cr-doped TiO₂ thin films deposited by RF-sputtering," *Materials Letters*, vol. 64, no. 21, pp. 2287–2289, 2010.
- [18] Y.-H. Zhang and A. Reller, "Phase transformation and grain growth of doped nanosized titania," *Materials Science and Engineering C*, vol. 19, no. 1–2, pp. 323–326, 2002.
- [19] Y. Q. Cao, T. He, L. S. Zhao, E. J. Wang, W. S. Yang, and Y. A. Cao, "Structure and phase transition behavior of Sn⁴⁺-doped TiO₂ nanoparticles," *Journal of Physical Chemistry C*, vol. 113, no. 42, pp. 18121–18124, 2009.
- [20] J. Li and C. Z. Hua, "Hollowing Sn-doped TiO₂ nanospheres via Ostwald ripening," *Journal of the American Chemical Society*, vol. 129, no. 51, pp. 15839–15847, 2007.
- [21] Q. Zhang and L. Gao, "Preparation of oxide nanocrystals with tunable morphologies by the moderate hydrothermal method: insights from rutile TiO₂," *Langmuir*, vol. 19, no. 3, pp. 967–971, 2003.
- [22] R. Arroyo, G. Córroyo, J. Padilla, and V. H. Lara, "Influence of manganese ions on the anatase–rutile phase transition of TiO₂ prepared by the sol–gel process," *Materials Letters*, vol. 54, pp. 397–402, 2002.
- [23] S. Vemury and S. E. Pratsinis, "Dopants in flame synthesis of titania," *Journal of the American Ceramic Society*, vol. 78, no. 11, pp. 2984–2992, 1995.
- [24] J. G. Li, X. H. Wang, K. J. Watanabe, and T. M. Ishigaki, "Phase structure and luminescence properties of Eu³⁺-doped TiO₂ nanocrystals synthesized by Ar/O₂ radio frequency thermal plasma oxidation of liquid precursor mists," *The Journal of Physical Chemistry B*, vol. 110, no. 3, pp. 1121–1127, 2006.
- [25] C. Ribeiro, C. Vila, D. B. Stroppa et al., "Anisotropic growth of oxide nanocrystals: insights into the rutile TiO₂ phase," *Journal of Physical Chemistry C*, vol. 111, no. 16, pp. 5871–5875, 2007.

Research Article

A First Principle Comparative Study on Chemisorption of H_2 on C_{60} , C_{80} , and $Sc_3N@C_{80}$ in Gas Phase and Chemisorption of H_2 on Solid Phase C_{60}

Hongtao Wang,^{1,2} Lijuan Chen,² Yongkang Lv,² Jianwen Liu,³ and Gang Feng⁴

¹ College of Environmental Science and Engineering, Taiyuan University of Technology, Taiyuan, Shanxi 030024, China

² Key Laboratory of Coal Science and Technology of Shanxi Province and Ministry of Education, Taiyuan University of Technology, Taiyuan, Shanxi 030024, China

³ National Supercomputing Center in Shenzhen, Shenzhen 518055, China

⁴ Shanghai Research Institute of Petrochemical Technology SINOPEC, Shanghai 201208, China

Correspondence should be addressed to Yongkang Lv; lykang@tyut.edu.cn and Jianwen Liu; liujw@nscsz.gov.cn

Received 11 December 2013; Accepted 13 January 2014; Published 10 March 2014

Academic Editor: Wen Zeng

Copyright © 2014 Hongtao Wang et al. This is an open access article distributed under the Creative Commons Attribution License, which permits unrestricted use, distribution, and reproduction in any medium, provided the original work is properly cited.

The chemisorptions of H_2 on fullerenes C_{60} and C_{80} , endofullerene $Sc_3C@C_{80}$ and solid C_{60} were comparatively studied. A chain reaction mechanism for dissociative adsorption of H_2 on solid C_{60} is proposed under high pressure. The breaking of H–H bond is concerted with the formation of two C–H bonds on two adjacent C_{60} in solid phase. The adsorption process is facilitated by the application of high pressure. The initial H_2 adsorption on two adjacent C_{60} gives a much lower barrier 1.36 eV in comparison with the barrier of adsorption on a single C_{60} (about 3.0 eV). As the stereo conjugate aromaticity of C_{60} is destructed by the initial adsorption, some active sites are created. Hence the successive adsorption becomes easier with much low barriers (0.6 eV). In addition, further adsorption can create new active sites for the next adsorption. Thus, a chain reaction path is formed with the initial adsorption dominating the whole adsorption process.

1. Introduction

From the beginning of the “fullerene area,” hydrogenated fullerenes have attracted wide-spread attention due to their potential application. It may not only be interesting for hydrogen storage [1–5], but also be used as an additive for lithium ion cells to significantly prolong the lifetime of these cells [6].

Experimentally, studies on the interaction between hydrogen and fullerenes have been focused on the chemical process of hydrogenation, with the products $C_{60}H_x$ and $C_{70}H_x$ being of fundamental interest as a model for other fullerene derivatives [7, 8]. A variety of chemical procedures have been devised to produce hydrogen radicals that could adsorb readily on these carbon atoms, using either reducing reagents [1, 9, 10], or catalysts [11]. In addition, direct hydrogenation of C_{60} and C_{70} has also been achieved without the

usage of a catalyst by exposing solid-phase fullerenes to high-pressure hydrogen gas (0.5–30 kBar) at elevated temperature (500–600 K) [4].

Theoretically, hydrogen storage based on fullerene materials has attracted many attentions. Using first principle calculations based on density functional theory, Sun and coworkers reported that each $B_{36}C_{36}$ cage can store at most 18 hydrogen molecules at zero temperature [12]. They also find that an isolated $Li_{12}C_{60}$ cluster where Li atoms are capped onto the pentagonal faces of the fullerene not only is very stable but also can store up to 120 hydrogen atoms in molecular form with a binding energy of 0.075 eV/ H_2 [13]. Zhao and coworkers report that a particular Scandium organometallic buckyballs can bind as many as 11 hydrogen atoms per transition metal, which gives the maximum retrievable H_2 storage density 9 wt% [14]. Kang and coworkers reports that Ni-dispersed fullerenes are considered to be capable of

storing 6.8 wt% H_2 , with H_2 desorption activation barrier of 11.8 kcal/mol, which is ideal for many practical hydrogen storage [15].

However, the mechanism for direct reactions between H_2 and these fullerenes remains unexplained to the best of our knowledge. Chan et al. proposed the mechanism of H_2 molecule dissociative chemisorption on the close cousin of fullerenes, carbon nanotubes, in solid phase under high pressure [16]. The breaking of the H–H bond is concerted with the formation of two C–H bonds on two adjacent carbon nanotubes in solid phase, facilitated by the application of high pressure which shortens the interstitial distance between nanotubes. The adsorption behavior gives some hints on H_2 adsorption on fullerenes.

In this work, we proposed a chain reaction mechanism for H_2 molecules dissociative adsorption on solid C_{60} under high pressure. In comparison, we also studied H_2 adsorption on the most stable fullerenes C_{60} and C_{80} in gas phase as well as endofullerene $Sc_3N@C_{80}$.

2. Computational Method

The first principles total energy and electronic structure calculations were carried out within the framework of DFT [17] with a plane wave basis set and pseudopotentials for the atomic cores, as implemented in the Vienna ab initio simulation package (VASP) [18, 19]. The PW91 gradient correction was added to the local density exchange-correlation functional and projector augmented wave (PAW) pseudopotentials [20, 21] were employed, with an energy cutoff of 400 eV for the plane-wave expansion as these approaches have successfully applied to similar systems [16]. The supercell is sampled with a $1 \times 1 \times 1$ k -points mesh, generated by the Monkhorst-Pack algorithm. The convergence criteria were 1.0×10^{-4} eV for the SCF energy, 1×10^{-3} eV for total energy, and 0.05 eV/Å for atomic force, respectively.

A climbing image nudged elastic band method was used to locate the transition states [22–24]. The vibrational frequencies and normal modes were calculated by diagonalization of the mass-weighted force constant matrix, which was obtained using the method of finite differences of forces as implemented in VASP. The ions are displaced in the $+/-$ directions of each Cartesian coordinate by 0.02 Å. There is only one imaginary frequency for all these structures, indicating that they are indeed the transition states in the potential energy surface.

The adsorption energies (E_{ads}) for the adsorption of H_2 on fullerenes were calculated by

$$E_{ads} = E(\text{fullerene} + H_2) - [E(\text{fullerene}) + E(H_2)], \quad (1)$$

where $E(\text{fullerene} + H_2)$, $E(\text{fullerene})$, and $E(H_2)$ are the total energies of H_2 adsorbed fullerene, total energies of fullerene (fullerene = C_{60} , C_{80} , $Sc_3N@C_{80}$), and the total energies of H_2 , respectively. The larger adsorption energy indicates the stronger adsorption.

TABLE 1: Energy barriers and reaction energies (ΔE) for H_2 adsorption on C_{60} , C_{80} and $Sc_3N@C_{80}$ in gas phase. Energies are given in eV.

	Absorption site	Barrier (eV)	ΔE (eV)
C_{60}	6-6 parallel	3.68	−0.87
	6-6 perpendicular	3.57	−0.86
	5-6 parallel	3.04	−0.10
	5-6 perpendicular	3.05	−0.09
C_{80}	6-6 parallel	2.47	−0.50
	6-6 perpendicular	2.47	−0.50
	5-6 parallel	2.26	−1.10
	5-6 perpendicular	2.27	−1.10
$Sc_3N@C_{80}$	Sc non-bonded C	3.60	−0.14
	Sc bonded C	3.78	−0.04

3. Results and Discussion

3.1. H_2 Adsorption in Gas Phase. We firstly consider the H_2 adsorption on fullerenes C_{60} and C_{80} and endofullerene $Sc_3N@C_{80}$ to explore the possible adsorption media without any catalyst in gas phase. In the calculations, the interactions between H_2 molecule and fullerenes (or endofullerenes) were modeled in a supercell of size $16.0 \text{ \AA} \times 16.0 \text{ \AA} \times 16.0 \text{ \AA}$, with one k -point (gamma point). The energy barriers and reaction energies are listed in Table 1.

3.1.1. H_2 Adsorption on C_{60} in Gas Phase. The icosahedral C_{60} consists of 12 pentagons and 20 hexagons. Hence the bonds can be categorized as two types, pentagon-hexagon bonds (5-6 bond) and hexagon-hexagon bonds (6-6 bond). Addition on adjacent sites such as 5-6 bond and 6-6 bond engenders isomers. Furthermore, addition can take place on nonadjacent sites, which would produce many isomers. For $C_{60}H_2$, the simplest fullerene dihydride, there are 23 isomers. However, there is only one isomer that has been characterized. Among all kinds of $C_{60}H_2$ isomers, (1,2) addition products are considered as the most stable. To compare the adsorption difference, we investigated H_2 adsorption on both 5-6 and 6-6 bonds. In addition, two adsorption modes are considered. One case is that the H–H bond of incoming H_2 is to be considered to parallel the 6-6 bond (Structure A and Structure E in Figure 1). The other one is that the incoming H–H bond is to be considered to point perpendicularly to the C–C bond (Structure C and Structure G in Figure 1). Energetically, the total exothermic energy for the formation of the two C–H bonds in 6-6 bond addition production is 0.77 eV favorable than that for 5-6 bond addition (Table 1), indicating that 6-6 bond addition gives the most stable structure. The two adsorption modes result in two possible adsorption mechanisms. The parallel adsorption mode gives a concerted mechanism, in which two H atoms bonded to two C atoms (TS 1 in Figure 1), respectively. In contrast, the perpendicular adsorption mode gives a step mechanism (one H atom is adsorbed first, then the second one, TS 2 in Figure 1). The barriers for both concerted mechanism and step mechanism are so high that the reaction is very difficult

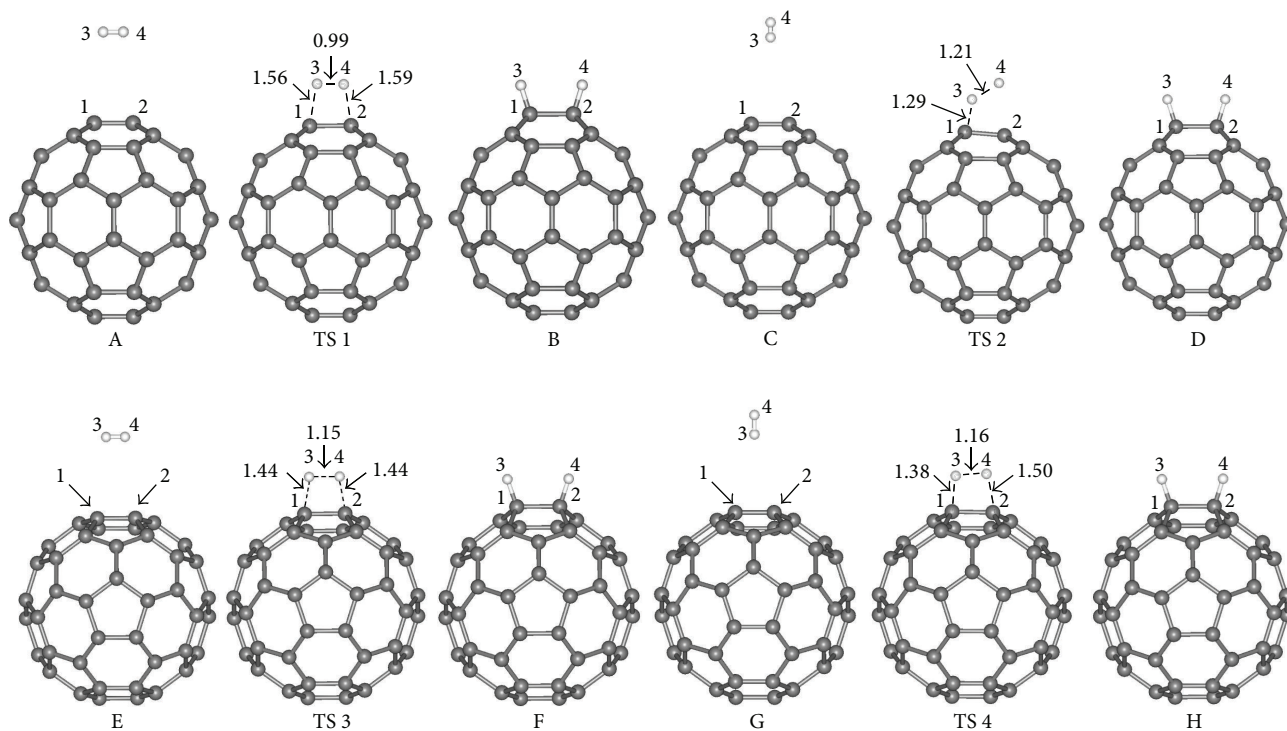


FIGURE 1: Structures and transition states structures for H_2 molecule adsorption on C_{60} in gas phase. Selective distances are given in Å.

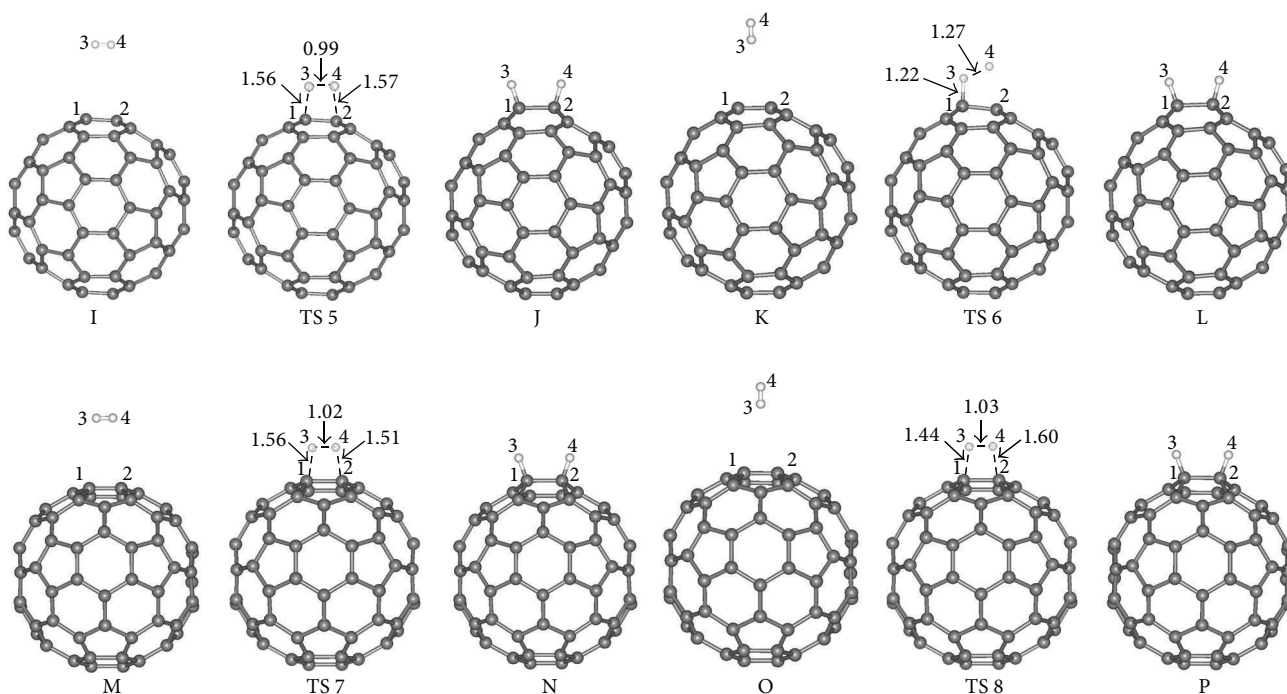


FIGURE 2: Optimized structures and transition states structures for H_2 molecule adsorption on C_{80} in gas phase. Selective distances are given in Å.

to take place, although the barrier for the step mechanism is 0.11 eV favorable than that for the concerted mechanism.

3.1.2. H_2 Adsorption on C_{80} in Gas Phase. C_{80} has the same I_h symmetry as C_{60} , so it can also be served as adsorption

media, although experimentally no hydride of C_{80} has been characterized. We carried out the same calculations as we did on C_{60} as shown in Figure 2. The 6-6 parallel and perpendicular adsorption modes have the same energy barrier of 2.47 eV whereas 5-6 parallel and perpendicular adsorption

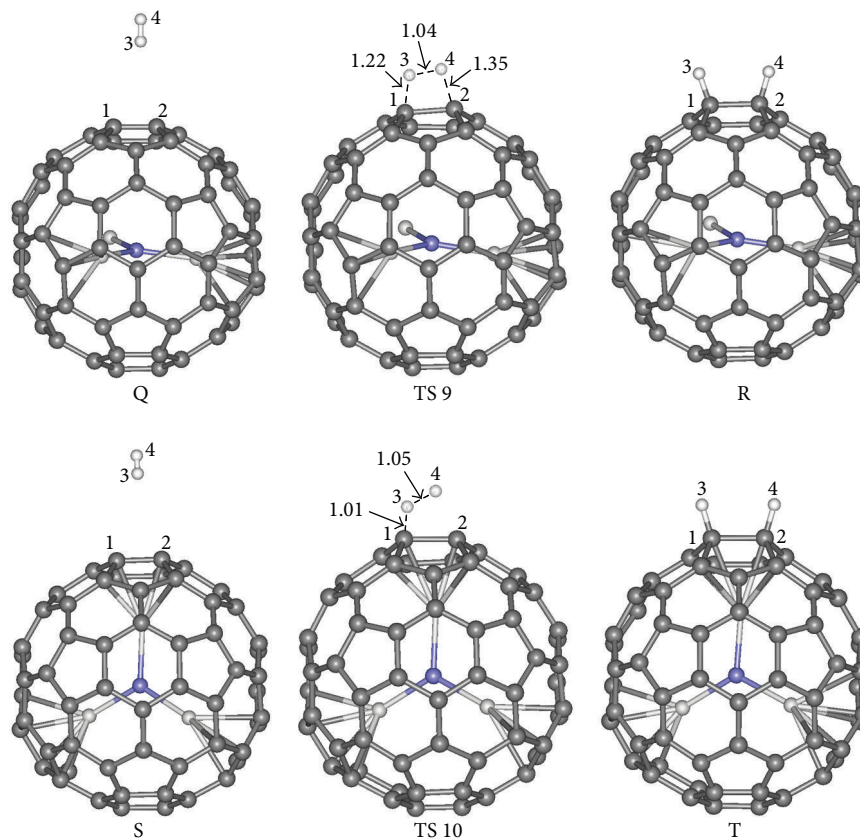


FIGURE 3: Optimized structures and transition states structures for H_2 molecule adsorption on $Sc_3N@C_{80}$ in gas phase. Selective distances are given in Å.

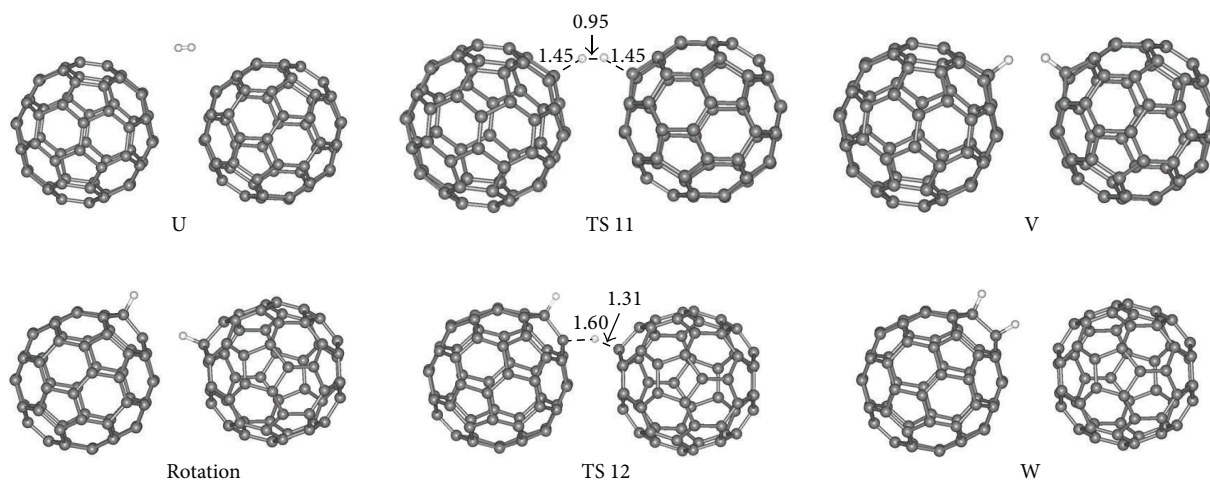


FIGURE 4: Optimized structures and transition state (TS) structures for the first H_2 dissociative chemisorption on solid C_{60} array. Selective distances are given in Å.

modes have the same barrier of 2.27 eV. Comparing to that of C_{60} , the calculated energy barrier is about 1 eV lower than that for C_{60} due to the less stability of C_{80} .

3.1.3. H_2 Adsorption on $Sc_3N@C_{80}$ in Gas Phase. As one of the most stable endofullerene, $Sc_3N@C_{80}$ has become

accessible in macroscopic quantities. Since the adsorption barrier for C_{80} has decreased more obviously than that for C_{60} , its stable derivative $Sc_3N@C_{80}$ is expected to be a promising hydrogenation material. As shown in Figure 3, we considered two different adsorption modes: either adsorption to Sc bonded C or Sc nonbonded C. However, whichever atom H bonds, the calculated energy barriers are more

TABLE 2: Reaction barriers and reaction energies (ΔE) for the second H_2 absorption on solid C_{60} with three different absorption modes.

Absorption site	Barrier (eV)	ΔE (eV)
(1,2)-(1,2)	0.76	-2.05
(1,2)-(1,4)	0.59	-1.82
(1,4)-(1,4)	0.52	-1.81
Former absorption	1.21	-1.77

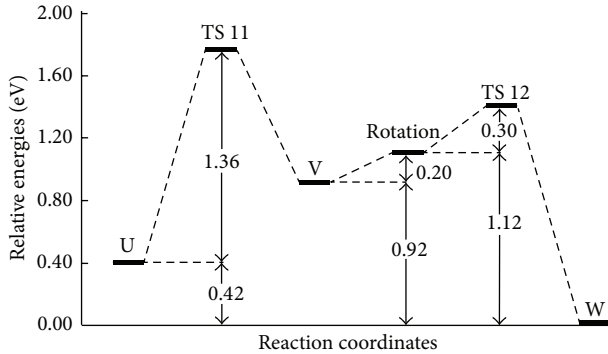


FIGURE 5: Reaction profile for the adsorption of the first H_2 on solid C_{60} array. Energies are given in eV.

than 3.5 eV, indicating that $Sc_3N@C_{80}$ can hardly react with H_2 . In addition, the overall exothermic energy is quite low at 0.1 eV, indicating that the reaction is not very favorable thermodynamically.

3.2. H_2 Adsorption in Solid Phase. In contrast, the solid phase, composed of bundles of C_{60} , provides a unique chemical environment dependent on the external pressure and makes it much easier for H_2 dissociative chemisorption on C_{60} bucky balls. In our calculations, the interactions between hydrogen molecule H_2 and C_{60} were modeled in a supercell of size $9.55 \text{ \AA} \times 9.55 \text{ \AA} \times 13.50 \text{ \AA}$, and an external pressure of $\sim 50 \text{ kBar}$ was introduced.

3.2.1. Adsorption of the First H_2 on Solid C_{60} . Under the pressure of $\sim 50 \text{ kBar}$, we explored the reactive trajectory of the first H_2 dissociative chemisorption on C_{60} as shown in Figure 4. There are three steps involved: first, the incoming H_2 dissociation and deposition on two adjacent C_{60} , from structure U to V, through transition structures (TS 11); second, the rotation of C_{60} ; and finally, hydrogen migration through TS 12 to structure W, a 1,2-addition product. Figure 5 gives the plot of the relative energies for the dissociative H_2 chemisorption on solid C_{60} . From this figure, we can see that the initial dissociative chemisorption step has a barrier of 1.36 eV, while the barrier for the subsequent H migration is much lower at 0.5 eV. Compared to adsorption barrier on single C_{60} in gas phase, the barrier for H_2 molecules adsorption on two adjacent C_{60} is quite low at 1.36 eV, which indicates that the reaction can easily take place

at room temperature [16]. The energy barrier differences are mainly due to the rotation. In high pressure, C_{60} does not stand in his own position quietly but rotates around the center of mass randomly. The rotation deforms the H-H bond to help break the H-H bond, which leads to lower reaction barrier.

In addition, we have made some comparison between the first H_2 chemisorption on solid C_{60} and solid (6,6) armchair carbon nanotube. The barrier difference for initial chemisorption is 0.14 eV. And the barrier difference for the H atom migration is 0.38 eV. Both the barrier differences are small. From this table, we can conclude that, energetically, there are no significant differences between the chemisorption on solid C_{60} and solid carbon nanotube under high pressure.

3.2.2. Adsorption of the Second H_2 on Solid C_{60} . To explore whether it is possible to chemisorb more H_2 on the solid C_{60} under high pressure, we investigate the reaction path for the addition of the second H_2 on C_{60} as shown in Figure 6. The reaction mechanism is quite similar to the addition of the first one. In this process, the second H_2 also dissociatively chemisorbs on two adjacent C_{60} in the initial step and then rotates slightly; one of the H atom migrates from one C_{60} to another and finally forms two 1,2-addition products. The relative energies for the chemisorption of second H_2 on solid C_{60} were shown in Figure 7. Compared to the first H_2 chemisorption, the calculated barrier for the second H_2 is 1.21 eV in the dissociation step, which is a little lower than that for the first H_2 adsorption. In addition, the overall process is also more exothermic, from 0.44 eV to 1.77 eV. This is mainly due to the fact that the first H_2 molecule adsorption has already partially disrupted the conjugated system, so further addition is much easier.

In the first H_2 adsorption process, we have mentioned that one of the H atoms will transfer from one C_{60} radical to another. There is another probability that H_2 molecules react with the intermediate radical directly. We also investigate this kind of adsorption modes. For the $C_{60}H$ intermediate, there are two active sites: site 2 and site 4. There are three probable adsorption modes: (1,2)-(1,2) adsorption, (1,4)-(1,4) adsorption, and (1,2)-(1,4) adsorption. For (1,2)-(1,2) adsorption, it means one H atom is adsorbed in site 2 and another H atom is also adsorbed in site 2 (Figure 8). The rules also apply for both (1,2)-(1,4) adsorption and (1,4)-(1,4) adsorption. The barriers of three category reactions are listed in Table 2. From this table, we can see that all the barriers are no more than 0.8 eV. They are much lower than the formerly calculated barrier 1.21 eV. The overall exothermic energies are also a little larger than the former calculated exothermic energy 1.77 eV. Based on these data, a conclusion can be drawn that the subsequent H_2 molecules will easily react with C_{60} intermediate radicals. Thus the reaction is a chain reaction: once the first H_2 is adsorbed, the H_2 will be adsorbed one by one. There is no extra energy needed because the overall exothermic energy will compensate the energy which is needed to overcome the barrier. Herein the first H_2 molecule adsorption has become the crucial step in the overall adsorption.

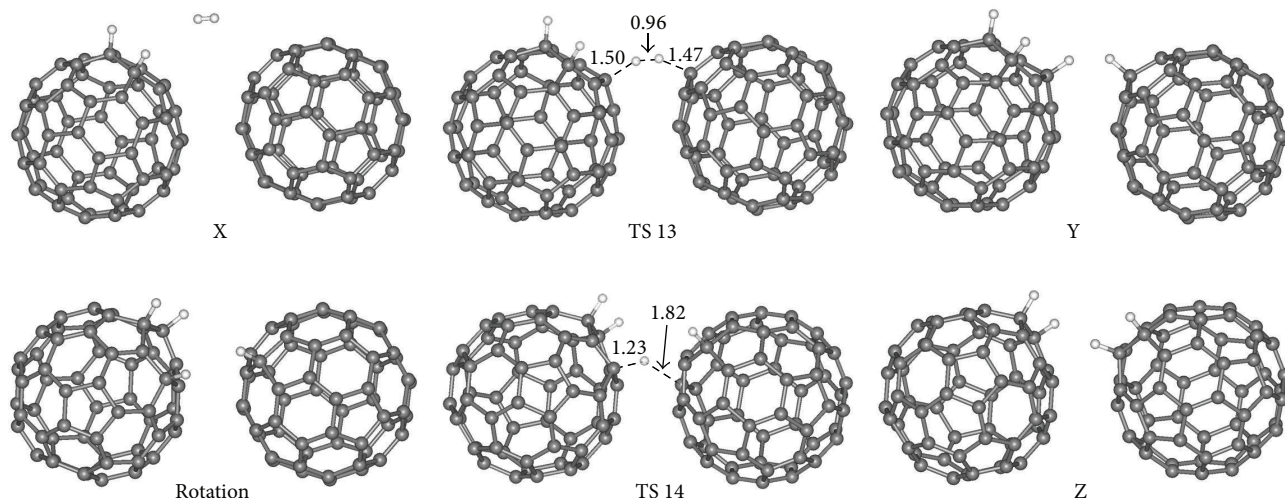


FIGURE 6: Optimized structures and transition state (TS) structures for the second H_2 dissociative chemisorption on C_{60} . Selective distances are given in Å.

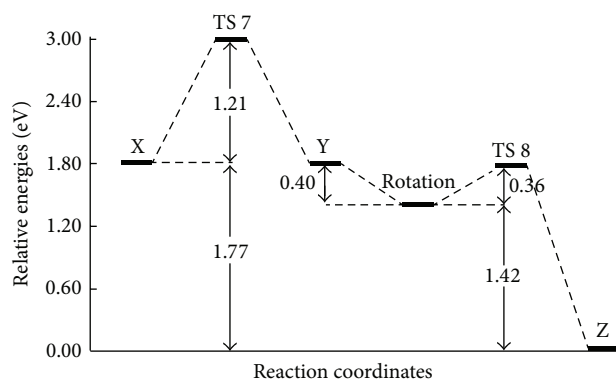


FIGURE 7: Reaction profile for the second H_2 , dissociative chemisorption on solid C_{60} . Energies are given in eV.

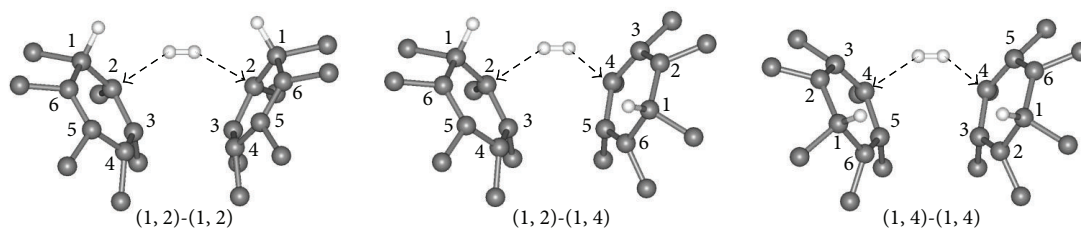


FIGURE 8: Adsorption modes for the second H_2 adsorption.

4. Conclusions

Based on the investigation of H_2 molecules chemisorption on fullerenes C_{60} and C_{80} and endofullerene $Sc_3C@C_{80}$, we proposed a mechanism for H_2 molecules adsorption on solid C_{60} under high pressure. Due to the rotation of C_{60} , the H_2 molecule will easily chemisorb on two adjacent C_{60} under high pressure, which is more favorable than the H_2 molecule adsorption on single C_{60} . The overall reaction is a chain reaction. The first H_2 molecules adsorption is the crucial step

in the overall H_2 molecules adsorption process. Once the first H_2 molecules is adsorbed on the C_{60} , the second and subsequent H_2 will easily be adsorbed on the C_{60} due to the lower reaction barrier.

Conflict of Interests

The authors declare that there is no conflict of interests regarding the publication of this paper.

Acknowledgments

This work is supported by the Shenzhen Strategic Emerging Industries Special Fund Program of China (Grant nos. GGJS20120619101655715 and JCY20120619101655719), the Program for International Cooperation Projects of Shanxi Province (Grant no. 2010081018), and National Natural Science Foundation of China (Grant no. 51078252).

References

- [1] C. C. Henderson and P. A. Cahill, " $C_{60}H_2$: synthesis of the simplest C_{60} hydrocarbon derivative," *Science*, vol. 259, no. 5103, pp. 1885–1887, 1993.
- [2] Y. Ye, C. C. Ahn, B. Fultz, J. J. Vajo, and Z. Zinck, "Hydrogen adsorption and phase transitions in fullerite," *Applied Physics Letters*, vol. 77, no. 14, pp. 2171–2173, 2000.
- [3] S. Ballenweg, R. Gleiter, and W. Kratschmer, "Hydrogenation of buckminsterfullerene C_{60} via hydrozirconation: a new way to organofullerenes," *Tetrahedron Letters*, vol. 34, no. 23, pp. 3737–3740, 1993.
- [4] C. Jin, R. Hettich, R. Compton, D. Joyce, J. Blencoe, and T. Burch, "Direct solid-phase hydrogenation of fullerenes," *Journal of Physical Chemistry*, vol. 98, no. 16, pp. 4215–4217, 1994.
- [5] A. A. Peera, L. B. Alemany, and W. E. Billups, "Hydrogen storage in hydrofullerides," *Applied Physics A: Materials Science and Processing*, vol. 78, no. 7, pp. 995–1000, 2004.
- [6] A. Hirsch and M. Brettreich, *Fullerenes: Chemistry and Reactions*, Wiley-VCH, New York, NY, USA, 2005.
- [7] P. A. Cahill and C. M. Rohlfing, "Theoretical studies of derivatized buckyballs and buckytubes," *Tetrahedron*, vol. 52, no. 14, pp. 5247–5256, 1996.
- [8] C. C. Henderson, C. McMichael Rohlfing, and P. A. Cahill, "Theoretical studies of selected $C_{60}H_2$ and $C_{70}H_2$ isomers," *Chemical Physics Letters*, vol. 213, no. 3-4, pp. 383–388, 1993.
- [9] R. E. Haufler, J. Conceicao, L. P. F. Chibante et al., "Efficient production of C_{60} (buckminsterfullerene), $C_{60}H_{36}$, and the solvated buckide ion," *Journal of Physical Chemistry*, vol. 94, no. 24, pp. 8634–8636, 1990.
- [10] C. C. Henderson, C. M. Rohlfing, K. T. Gillen, and P. A. Cahill, "Synthesis, isolation, and equilibration of 1,9- and 7,8- $C_{70}H_2$," *Science*, vol. 264, no. 5157, pp. 397–399, 1994.
- [11] L. Becker, T. P. Evans, and J. L. Bada, "Synthesis of $C_{60}H_2$ by rhodium-catalyzed hydrogenation of C_{60} ," *Journal of Organic Chemistry*, vol. 58, no. 27, pp. 7630–7631, 1993.
- [12] Q. Sun, Q. Wang, and P. Jena, "Storage of molecular hydrogen in B-N cage: energetics and thermal stability," *Nano Letters*, vol. 5, no. 7, pp. 1273–1277, 2005.
- [13] Q. Sun, P. Jena, Q. Wang, and M. Marquez, "First-principles study of hydrogen storage on $Li_{12}C_{60}$," *Journal of the American Chemical Society*, vol. 128, no. 30, pp. 9741–9745, 2006.
- [14] Y. Zhao, Y.-H. Kim, A. C. Dillon, M. J. Heben, and S. B. Zhang, "Hydrogen storage in novel organometallic buckyballs," *Physical Review Letters*, vol. 94, no. 15, Article ID 155504, 2005.
- [15] W. H. Shin, S. H. Yang, W. A. Goddard III, and J. K. Kang, "Ni-dispersed fullerenes: hydrogen storage and desorption properties," *Applied Physics Letters*, vol. 88, no. 5, Article ID 053111, pp. 1–3, 2006.
- [16] S.-P. Chan, G. Chen, X. G. Gong, and Z.-F. Liu, "Chemisorption of hydrogen molecules on carbon nanotubes under high pressure," *Physical Review Letters*, vol. 87, no. 20, Article ID 205502, 2001.
- [17] R. Car and M. Parrinello, "Unified approach for molecular dynamics and density-functional theory," *Physical Review Letters*, vol. 55, no. 22, pp. 2471–2474, 1985.
- [18] G. Kresse and J. Furthmüller, "Efficient iterative schemes for ab initio total-energy calculations using a plane-wave basis set," *Physical Review B*, vol. 54, no. 16, pp. 11169–11186, 1996.
- [19] G. Kresse and J. Furthmüller, "Efficiency of ab-initio total energy calculations for metals and semiconductors using a plane-wave basis set," *Computational Materials Science*, vol. 6, no. 1, pp. 15–50, 1996.
- [20] P. E. Blöchl, "Projector augmented-wave method," *Physical Review B*, vol. 50, no. 24, pp. 17953–17979, 1994.
- [21] G. Kresse and D. Joubert, "From ultrasoft pseudopotentials to the projector augmented-wave method," *Physical Review B*, vol. 59, no. 3, pp. 1758–1775, 1999.
- [22] G. Henkelman and H. Jónsson, "Improved tangent estimate in the nudged elastic band method for finding minimum energy paths and saddle points," *Journal of Chemical Physics*, vol. 113, no. 22, pp. 9978–9985, 2000.
- [23] G. Henkelman and H. Jónsson, "Improved tangent estimate in the nudged elastic band method for finding minimum energy paths and saddle points," *Journal of Chemical Physics*, vol. 113, no. 22, pp. 9978–9985, 2000.
- [24] G. Henkelman, B. P. Uberuaga, and H. Jónsson, "Climbing image nudged elastic band method for finding saddle points and minimum energy paths," *Journal of Chemical Physics*, vol. 113, no. 22, pp. 9901–9904, 2000.

Research Article

The Synthesis of a Novel Cellulose Physical Gel

Jiufang Duan,¹ Xiaojian Zhang,¹ Jianxin Jiang,¹ Chunrui Han,¹ Jun Yang,¹
Liujun Liu,¹ Hongyun Lan,² and Daozhan Huang²

¹Institute of Material Science and Technology, Beijing University of Forestry, Beijing 100083, China

²Guangxi Key Laboratory of Chemistry and Engineering of Forest Products, Guangxi University for Nationalities, Nanning 530006, China

Correspondence should be addressed to Jiufang Duan; duanjiu99@163.com

Received 25 November 2013; Revised 27 January 2014; Accepted 29 January 2014; Published 3 March 2014

Academic Editor: Wen Zeng

Copyright © 2014 Jiufang Duan et al. This is an open access article distributed under the Creative Commons Attribution License, which permits unrestricted use, distribution, and reproduction in any medium, provided the original work is properly cited.

Cellulose possessing β -cyclodextrin (β -CD) was used as a host molecule and cellulose possessing ferrocene (Fc) as a guest polymer. Infrared spectra, differential scanning calorimetry (DSC), ultraviolet spectroscopy (UV), and contact angle analysis were used to characterise the material structure and the inclusion behaviour. The results showed that the β -CD-cellulose and the Fc-cellulose can form inclusion complexes. Moreover, ferrocene oxidation, and reduction of state can be adjusted by sodium hypochlorite (NaClO) as an oxidant and glutathione (GSH) as a reductant. In this study, a physical gel based on β -CD-cellulose/Fc-cellulose was formed under mild conditions in which autonomous healing between cut surfaces occurred after 24 hours. The physical gel can be controlled in the sol-gel transition. The compressive strength of the Fc-cellulose/ β -CD-cellulose gel increased with increased cellulose concentration. The host-guest interaction between the side chains of cellulose could strengthen the gel. The cellulose physical gel may eventually be used as a stimulus-responsive, healing material in biomedical applications.

1. Introduction

In light of heightened environmental and energy concerns, cellulose based on nature biomass has been receiving increasing attention in recent years. Cellulose is the most abundant naturally occurring polymer of glucose, found as the main constituent of plants and natural fibres such as cotton and linen and is considered a renewable and sustainable resource of raw material to satisfy the increasing demand for environmentally friendly [1] and energy-generating products [2, 3]. Cellulose-based hydrogels are biocompatible and biodegradable materials which show promise for a number of industrial uses, especially in cases where environmental issues are important. Such natural polysaccharides have been widely used for the preparation of gels in various fields [4–7], for example: wastewater treatment, the food industry, cosmetics, biomedical, pharmaceutical, and tissue engineering applications, due to their unique properties such as high swelling capacity, biocompatibility, biodegradability, and biological functions.

Cellulose, the cellulose, the most abundant renewable polysaccharide on earth, is a strong candidate for the fabrication of gels and cellulose-based gels have been reported including cellulose-polymer composite gels and cellulose-inorganic hybrid gels. The design and use of cellulose-based hydrogels, which usually couple their biodegradability with a smart stimuli-sensitive behaviour, together with the large availability of cellulose in nature and the low cost of cellulose derivatives, make cellulose-based hydrogels particularly attractive.

Cellulose-based gels [8, 9] can be obtained by either physical or chemical stabilisation of aqueous solutions of cellulose derivatives [10–14]. Cellulose-based gels, either reversible or stable, can be formed by properly cross-linking aqueous solutions of cellulose ethers [12, 15, 16], such as methylcellulose, hydroxypropyl methylcellulose, ethyl cellulose (EC), hydroxyethyl cellulose (HEC), and sodium carboxymethylcellulose (NaCMC), which are among the most widely used cellulose derivatives. Depending on the cellulose derivative used, a number of cross-linking agents and catalysts can be used

to form gels. Epichlorohydrin, aldehydes, aldehyde-based reagents, urea derivatives, carbodiimides, and multifunctional carboxylic acids are the most widely used cross-linking agents for cellulose [17–21]. In light of material application concerns, cellulose gels have received increasing attention in recent years [22, 23]. Cellulose supramolecular materials linked by noncovalent bonds have attracted much more attention and have been widely studied [24]; their responsiveness to the external environment [25], such as temperature [26], pH [27], and medicine (drug release carriers) [28] have been of particular interest.

However, there are few reports on the application of cellulose gel used in healing. In this study, a novel cellulose physical gel was synthesised by β -CD-cellulose and Fc-cellulose. The host-guest interaction between the β -CD-cellulose and the Fc-cellulose, the sol-gel transition, and the redox stimuli properties of the supramolecular material were also studied.

2. Experimental

2.1. Material and Methods. Cellulose, β -cyclodextrin, epichlorohydrin, sodium hydroxide, lithium chloride, N,N-dimethyl acetamide, methylene chloride, ferrocene carboxylic acid, oxalyl chloride, sodium hypochlorite and glutathione were commercially available and used as received.

IR spectra were recorded by FTIR (Nicolet iN10 Thermo Fisher Scientific China) in the region of 400–4000 cm^{-1} . DSC measurements were carried out using a Diamond DSC apparatus (NETZSCH DSC 204). The dried samples were placed in pressure tight aluminum DSC cells from 20 to 150 °C with a heating rate of 10 °C min^{-1} . Surface contact angles were measured using a dynamic contact angle analyzer (HARKE-SPCA, error value of $\pm 0.1^\circ$, Beijing HARKE Experimental Instrument Factory). The cellulose powder samples were compressed using an infrared tablet. Surface contact angles were measured during liquid exposure to the test materials for 1 s in order to avoid material penetration factors as far as possible. The morphological characterization of gel was performed with scanning electron microscopy (S-3400N, HIACHI, Japan).

The gravimetric method was employed to measure the swelling ratios of the gels in distilled water at 25 °C. After immersion in distilled water for about 48 hr to reach swelling equilibrium, the gel samples were taken out and weighed after removing the excess water on the surfaces. Each data was measured three samples, and the average value of three measurements was taken. The equilibrium swelling ratio (SR) was calculated as $\text{SR} = W_s/W_d$, where W_s is the weight of the swollen gel and W_d is the weight of the gel at the dry state.

Reswelling ratios of the gels were measured as follows: the dry gel was placed in deionized water of 25 °C. At predetermined time, the gel samples were taken out from the aqueous solution and weighed the quality W_t , until it reached swelling equilibrium. Reswelling rate (r_{SR}): $r_{\text{SR}} = 100 * (W_t - W_d)/m_d$.

2.2. Preparation of Cellulose Inclusion Complexes

2.2.1. Preparation of Cellulose-CDs. Cellulose was dissolved in sodium hydroxide/urea. To this solution, cyclodextrin and epichlorohydrin were added. After stirring for 2 h, β -CD was added and the solution was stirred for another 12 h at room temperature. The polymer product was reprecipitated from distilled water and washed with distilled water. The degree of substitution is 0.32 wt%, which was detected by the phenolphthalein probe method [29].

In NaOH aqueous solution, cellulose and epichlorohydrin generate the epoxy cellulose, which connected hydroxy of β -cyclodextrin by the epoxy group as a cross-linking bridge.

2.2.2. Synthesis of Fc-COCl. Ferrocenecarboxylic acid was suspended in dichloromethane (DCM). Then oxalyl chloride was added dropwise, and the suspension was stirred for 3 h at room temperature. The orange suspension turned into a red solution. After evaporating the solvent, the solid product was collected.

2.2.3. Synthesis of Cellulose-Fc. Cellulose was dissolved in lithium chloride/dimethylacetamide (LiCl/DMAc). The ferrocenecarboxylic chloride solution was added dropwise. After stirring overnight at room temperature, the solution was washed with distilled water. The orange solid was washed with lithium chloride; the solid product was collected via a centrifuge and dried for 4 days at 50 °C to obtain cellulose-Fc as a yellow powder. The ferrocene grafting rate is 0.57~5.7 wt%, which was detected by weighing before and after the cellulose reaction.

2.2.4. Preparation of Redox Inclusion Complex. The oxidized state (or reduced state) products were prepared by shaking appropriate amounts of NaClO aq. (14 mM) (or GSH) and Fc-CD-cellulose inclusion complexes (or oxidized state products) at room temperature for 24 h. The solution was washed with distilled water and then the solid product was collected via a centrifuge and freeze-dried. A complex mixture was prepared by grinding powders for 20 min.

2.2.5. Synthesis of Cellulose Gel. The ferrocene-cellulose and cyclodextrin-cellulose were dissolved in N,N-Dimethylformamide (DMF) lithium chloride solution. We poured the solution into a glass mould in a humid box until the gel was stabilized.

3. Results and Discussion

3.1. Characterization. Figure 1 (curve (a)) and Figure 1 (curve (b)) show the infrared spectra of the cellulose and β -CD-cellulose. According to Figure 1 (curves (a) and (b)), absorption was observed at 3380 cm^{-1} (hydroxyl stretch influenced by hydrogen bonding), 1646 cm^{-1} and 1354 cm^{-1} (carbonyl stretch), 1043 cm^{-1} (carboxyl in ethers), and 2920 cm^{-1} (methylene), which were characteristic absorptions in cellulose and β -CD-cellulose structures. As seen from Figure 1

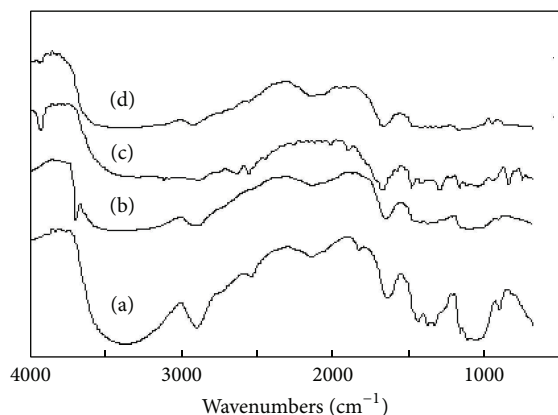


FIGURE 1: Infrared spectra of cellulose ((a) cellulose, (b) cellulose-CD, (c) cellulose-Fc, and (d) cellulose-CD-Fc inclusion).

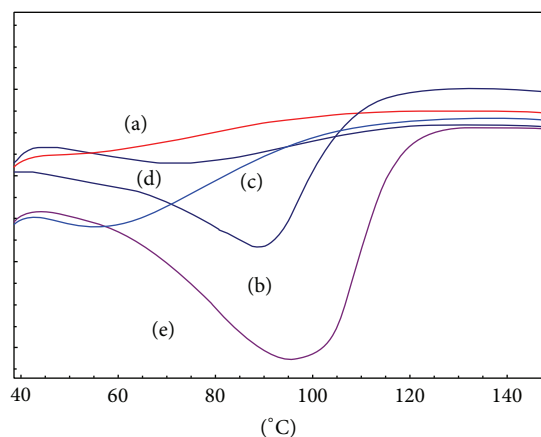


FIGURE 2: DSC curves of the series of cellulose ((a) cellulose, (b) cellulose-CD, (c) cellulose-ferrocene, (d) cellulose-CD-ferrocene inclusion, (e) simple mixing of cellulose-ferrocene, and cellulose-CD).

(curve (c)) the characteristic peaks of ferrocene-cellulose were 1402 cm^{-1} , 1100 cm^{-1} VC-C (cyclopentadienyl ring), and 816 cm^{-1} DC-H (cyclopentadienyl ring). The characteristic peaks of ferrocene disappeared from the infrared spectra of the envelope of the inclusion compound (curve (d)). This indicated that the ferrocene-cellulose and cyclodextrin cellulose have been formed in the inclusion complex. Similar findings were reported in the literature [30, 31].

3.2. Thermal Analysis. The thermal analysis curves of the cellulosic inclusion complexes are shown in Figure 2 where it can be seen that the curve (a) of cellulose is almost a straight line, but the curves (b) (CD-cellulose) and (e) (simple physical mixing of CD-cellulose and Fc-cellulose) had a strong exothermic peak (cyclodextrin dehydration absorption peaks [32] at 88.9°C and 95.9°C , resp.), corresponding to the loss of water from the CD cavity to atmosphere, indicating that CD was free from guest complexation in the physical mixture [32]. Otherwise, the curve (d) (the inclusion complex) showed a lack of endothermic peaks,

which suggested that a different molecule was present in the CD cavity, instead of the water molecules and a lack of pure CD in the complex sample. Similar results were reported in the literature for interactions between other drugs and CDs [30, 31, 33, 34].

3.3. The Redox Properties. The redox regulation process of inclusion complexes containing ferrocene has been studied extensively.

The host-guest interaction between the metal ferrocene with β -CD can also be a reversible regulation by oxidation and reduction of the ferrocene. More than 20 years ago, it was reported that the reduced ferrocene effectively forms an inclusion compound with the β -CD, while the oxidation of the ferrocene was impossible [35, 36]. The nature of ferrocene is hydrophobic in its reduced state and hydrophilic in its oxidized state. The reversible regulation of the inclusion complexes forming a binary complex can be achieved by changing the redox state of the ferrocene. Therefore, the cellulose materials were expected to have a redox response performance by grafting ferrocene onto the cellulose.

The host-guest interaction between the metal ferrocene with β -CD can also be a reversible regulation by oxidation and reduction of the ferrocene. More than 20 years ago, it was reported that the ferrocene reduced forms of the inclusion compound with the β -CD effectively, while the ferrocene oxidized is basically impossible [35, 36]. The nature of ferrocene is hydrophobic in the reduced state and hydrophilic in the oxidized state. The reversible regulation of the inclusion complexes form of binary complex can be achieved by changing the redox state of the ferrocene. Therefore, the cellulose materials are expected to have the redox response performance by grafting ferrocene on the cellulose.

The redox behaviour of ferrocene was studied by measuring the surface contact angle with water. The cyclodextrin-cellulose contact angle was 59.6° (Figure 3(a)) and the ferrocene-cellulose contact angle was 82.1° (Figure 3(b)). The contact angle changed from 82.1° to 61.2° (Figure 3(c)) when the ferrocene-cellulose and cyclodextrin-cellulose formed inclusion complexes. This demonstrated that the ferrocene was an inclusion in the cyclodextrin cavity.

Aqueous NaClO was chosen as an oxidant and GSH as a reductant. Adding aqueous NaClO to the cellulose- β CD/cellulose-Fc inclusion complexes increased the contact angle from 61.2° to 71.7° (Figure 3(d)). In contrast, continuous addition of GSH to the inclusion complexes recovered the Fc group, causing the contact angle to revert to its former value (Figure 3(e)). Cellulose- β -CD showed a high affinity for the reduced state of the Fc group due to its hydrophobic nature, whereas the oxidized state of the Fc group (Fc⁺) exhibited a low affinity for cellulose- β -CD due to the cationic Fc⁺ group [35–37]. Moreover, the cellulose inclusion complexes exhibited excellent lock and unlock properties controlled by the redox of ferrocene.

3.4. The Compressive Strength of Fc-Cellulose/ β -CD-Cellulose Gel. Gels are composed of a three-dimensional hydrophilic

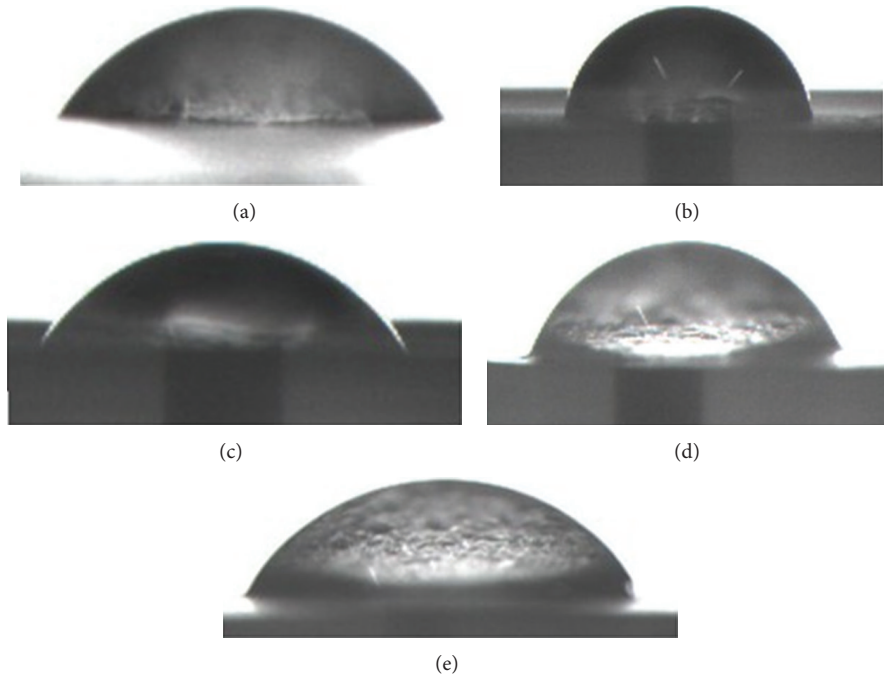


FIGURE 3: Contact angle images of the series of cellulose ((a) cellulose-CD, (b) cellulose-ferrocene, (c) cellulose-CD-ferrocene inclusion, (d) NaClO treated sample, and (e) GSH treated sample).

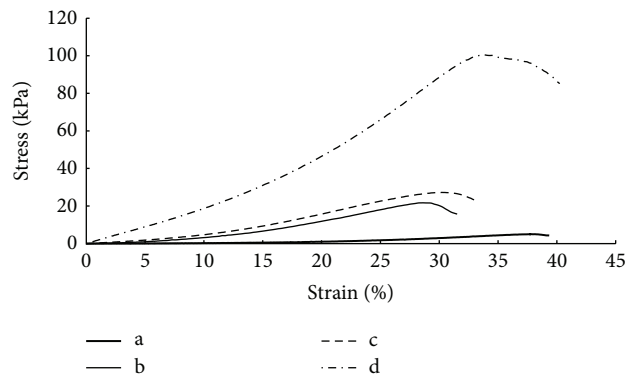


FIGURE 4: The compressive strength of different cellulose content ((a) 1 wt%, (b) 3 wt%, (c) 4 wt%, and (d) 5 wt%).

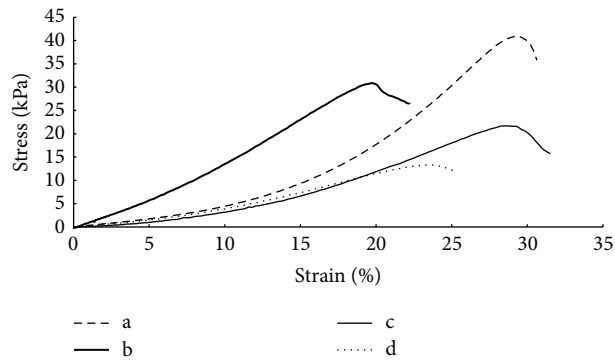


FIGURE 5: The compressive strength of different grafting ratio of ferrocene ((a) 5.66 wt%, (b) 2.83 wt%, (c) 1.41 wt%, (d) 0.57 wt%).

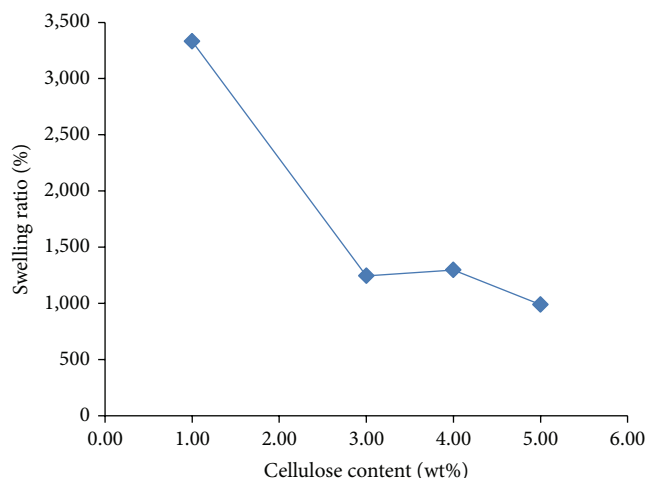


FIGURE 6: The swelling ratio of the Fc-cellulose/ β -CD-cellulose hydrogel.

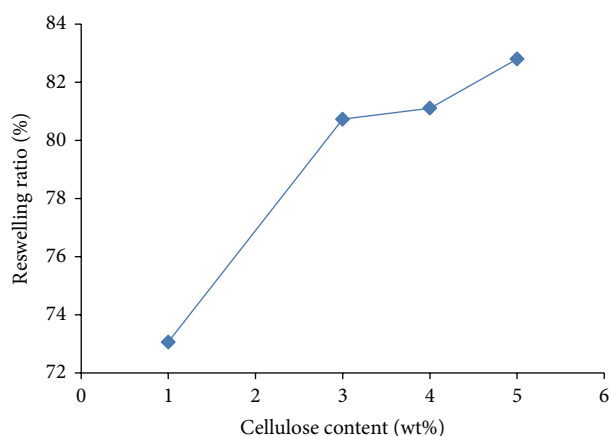


FIGURE 7: The reswelling ratio of the Fc-cellulose/ β -CD-cellulose hydrogel.

polymer network in which a large amount of water is interposed. The cross-linking ratio of the network is important to the mechanical properties. As the concentration of cellulose increased from 1% (w/w) to 5% (w/w) the gel strength increased from 5 kPa to 100.5 kPa (Figure 4). This was because the number of cross-linking sites *per* unit volume of the network increased with an increased number of functional groups on the molecular chain which was caused by the increased concentration of cellulose [38]. Similar improvements in the mechanical strength were also observed when increasing the cross-linking degree by changing the grafting ratio of Fc. The compressive strength of Fc-cellulose/ β -CD-cellulose gel changed from 13.32 kPa to 40.97 kPa as the grafting ratio of Fc changed from 0.57% (w/w) to 5.66% (w/w) (Figure 5), indicating that the host-guest interaction between the side chains of cellulose participated in the formation of the three-dimensional network structure of the gel and also affected its strength.

3.5. The Water Absorption of Fc-Cellulose/ β -CD-Cellulose Gel. The swelling ratio of the gel was the most important

variable to be evaluated for given environmental conditions, as it affected the diffusive, mechanical, optical, acoustic, and surface properties of the gel itself. The swelling ratio of the Fc-cellulose/ β -CD-cellulose gel decreased as the concentration of cellulose increased (Figure 6). This was because the amount of water retained by the mesh of the hydrogel network depended on the structure of the polymer network itself [39]. The Fc-cellulose/ β -CD-cellulose gel was formed by properly cross-linking the cellulose chains. The number of cross-linking sites *per* unit volume of the polymer network increased with increasing cellulose concentration. The larger degree of cross-linking was not conducive to the diffusion of water molecules.

The reswelling ratio of the Fc-cellulose/ β -CD-cellulose gel decreased from 3330% (w/w) (Figure 6) to 73.06% (w/w) (Figure 7), when the dry gel was placed in deionised water again. The pore sizes of the super-absorbent gel showed that it was the water retention capacity that engendered the efficiency of absorption. It can be observed that the larger number of pores can retain more water. Figure 8 shows the freeze-drying morphology of the cellulose gel and Fc-cellulose/ β -CD-cellulose gel; compared with the cellulose gel,

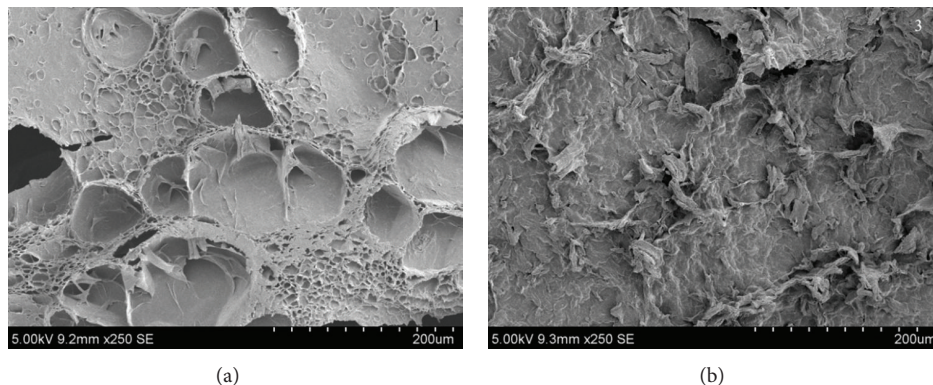


FIGURE 8: The SEM images of gel ((a) cellulose hydrogel and (b) Fc-cellulose/ β -CD-cellulose hydrogel).

the Fc-cellulose/ β -CD-cellulose gel had a more dense pore structure. After drying the gel, the dense pore structure was easily collapsed and confined; therefore, the reswelling ratio of the Fc-cellulose/ β -CD-cellulose gel was poor.

3.6. The Surface Morphology of the Gel. The surface morphology of the gel is also shown in Figure 8. Cellulose and Fc-cellulose/ β -CD-cellulose inclusion complexes gels were prepared by the same method. Cellulose gel (Figure 8(a)) had a relatively large, porous structure; as well as the Fc-cellulose/ β -CD-cellulose inclusion complexes, the gel had a relatively dense surface structure. This may have been caused by the different intermolecular forces arising from the alteration of the cellulose molecular chain structure.

4. Conclusions

Ferrocene and cyclodextrin were grafted onto the cellulose surface, respectively. The cellulose physical gel was prepared by Fc-cellulose and β -CD-cellulose at room temperature. The β -CD-cellulose and the Fc-cellulose can form inclusion complexes. Moreover, ferrocene oxidation and reduction of state can be adjusted by sodium hypochlorite (NaClO) as an oxidant and glutathione (GSH) as a reductant. The sol-gel transition can be controlled. The compressive strength of Fc-cellulose/ β -CD-cellulose gel increased with increasing cellulose concentration. The host-guest interaction between the side chains of cellulose can strengthen the gel. Thus, it was believed that these stimulus-responsive, healing properties may eventually be used in various biomedical applications.

Conflict of Interests

The authors declare that there is no conflict of interests regarding the publication of this paper.

Acknowledgments

This paper is supported by “the Fundamental Research Funds for the Central Universities” and “Guangxi Key Laboratory

of chemistry and Engineering of Forest Products Open Fund Project GXFC12-03.”

References

- [1] P. Béguin and J.-P. Aubert, “The biological degradation of cellulose,” *FEMS Microbiology Reviews*, vol. 13, no. 1, pp. 25–58, 1994.
- [2] M. Knauf and M. Moniruzzaman, “Lignocellulosic biomass processing: a perspective,” *International Sugar Journal*, vol. 106, no. 1263, pp. 147–150, 2004.
- [3] B. D. Solomon, J. R. Barnes, and K. E. Halvorsen, “Grain and cellulosic ethanol: history, economics, and energy policy,” *Biomass and Bioenergy*, vol. 31, no. 6, pp. 416–425, 2007.
- [4] K. M. Rao, B. Mallikarjuna, K. S. V. Krishna Rao, M. N. Prabhakar, K. C. Rao, and M. C. S. Subha, “Preparation and characterization of pH sensitive poly(vinyl alcohol)/sodium carboxymethyl cellulose IPN microspheres for in vitro release studies of an anti-cancer drug,” *Polymer Bulletin*, vol. 68, no. 7, pp. 1905–1919, 2012.
- [5] C. Yang, C. Gao, Y. Wan, T. Tang, S. Zhang, and K. Dai, “Preparation and characterization of three-dimensional nanostructured macroporous bacterial cellulose/agarose scaffold for tissue engineering,” *Journal of Porous Materials*, vol. 18, no. 5, pp. 545–552, 2011.
- [6] N. Isobe, D.-S. Lee, Y.-J. Kwon et al., “Immobilization of protein on cellulose hydrogel,” *Cellulose*, vol. 18, no. 5, pp. 1251–1256, 2011.
- [7] S. Yan, J. Yin, L. Tang, and X. Chen, “Novel physically cross-linked hydrogels of carboxymethyl chitosan and cellulose ethers: structure and controlled drug release behavior,” *Journal of Applied Polymer Science*, vol. 119, no. 4, pp. 2350–2358, 2011.
- [8] X. Y. Qiu and S. W. Hu, “Smart materials based on cellulose: a review of the preparations, properties, and applications,” *Materials*, vol. 6, no. 3, pp. 738–781, 2013.
- [9] L. H. Fan, C. Tan, L. W. Wang et al., “Preparation, characterization and the effect of carboxymethylated chitosan-cellulose derivatives hydrogels on wound healing,” *Journal of Applied Polymer Science*, vol. 128, no. 5, pp. 2789–2796, 2013.
- [10] C. Chang, L. Zhang, J. Zhou, L. Zhang, and J. F. Kennedy, “Structure and properties of hydrogels prepared from cellulose in NaOH/urea aqueous solutions,” *Carbohydrate Polymers*, vol. 82, no. 1, pp. 122–127, 2010.

- [11] Z. Wang, S. Liu, Y. Matsumoto, and S. Kuga, "Cellulose gel and aerogel from LiCl/DMSO solution," *Cellulose*, vol. 19, no. 2, pp. 393–399, 2012.
- [12] J. Zhang, J. Rong, W. Li, Z. Lin, and X. Zhang, "Preparation and characterization of bacterial cellulose/polyacrylamide hydrogel," *Acta Polymerica Sinica*, no. 6, pp. 602–607, 2011.
- [13] C. Zhou, Q. Wu, Y. Yue, and Q. Zhang, "Application of rod-shaped cellulose nanocrystals in polyacrylamide hydrogels," *Journal of Colloid and Interface Science*, vol. 353, no. 1, pp. 116–123, 2011.
- [14] A. L. Buyanov, I. V. Gofman, L. G. Revel'skaya, A. K. Khripunov, and A. A. Tkachenko, "Anisotropic swelling and mechanical behavior of composite bacterial cellulose-poly(acrylamide or acrylamide-sodium acrylate) hydrogels," *Journal of the Mechanical Behavior of Biomedical Materials*, vol. 3, no. 1, pp. 102–111, 2010.
- [15] M. S. M. Eldin, H. M. El-Sherif, E. A. Soliman, A. A. Elzatahry, and A. M. Omer, "Polyacrylamide-grafted carboxymethyl cellulose: smart pH-sensitive hydrogel for protein concentration," *Journal of Applied Polymer Science*, vol. 122, no. 1, pp. 469–479, 2011.
- [16] R. Das, A. B. Panda, and S. Pal, "Synthesis and characterization of a novel polymeric hydrogel based on hydroxypropyl methyl cellulose grafted with polyacrylamide," *Cellulose*, vol. 19, no. 3, pp. 933–945, 2012.
- [17] C. Chang, B. Duan, and L. Zhang, "Fabrication and characterization of novel macroporous cellulose-alginate hydrogels," *Polymer*, vol. 50, no. 23, pp. 5467–5473, 2009.
- [18] C. Demitri, R. Del Sole, F. Scalera et al., "Novel superabsorbent cellulose-based hydrogels crosslinked with citric acid," *Journal of Applied Polymer Science*, vol. 110, no. 4, pp. 2453–2460, 2008.
- [19] C. Chang, A. Lue, and L. Zhang, "Effects of crosslinking methods on structure and properties of cellulose/PVA hydrogels," *Macromolecular Chemistry and Physics*, vol. 209, no. 12, pp. 1266–1273, 2008.
- [20] M. C. I. Mohd Amin, N. Ahmad, N. Halib, and I. Ahmad, "Synthesis and characterization of thermo- and pH-responsive bacterial cellulose/acrylic acid hydrogels for drug delivery," *Carbohydrate Polymers*, vol. 88, no. 2, pp. 465–473, 2012.
- [21] W. D. Li, J. H. Rong, Z. D. Lin, and X. J. Zhang, "Preparation and characterization of bacterial cellulose reinforced PVA/PVP hydrogels," *Acta Polymerica Sinica*, no. 4, pp. 357–364, 2012.
- [22] R. Cha, Z. He, and Y. Ni, "Preparation and characterization of thermal/pH-sensitive hydrogel from carboxylated nanocrystalline cellulose," *Carbohydrate Polymers*, vol. 88, no. 2, pp. 713–718, 2012.
- [23] C. Chang, M. He, J. Zhou, and L. Zhang, "Swelling behaviors of pH- and salt-responsive cellulose-based hydrogels," *Macromolecules*, vol. 44, no. 6, pp. 1642–1648, 2011.
- [24] W. Liu, Y. Liu, X. Hao et al., "Backbone-collapsed intra- and inter-molecular self-assembly of cellulose-based dense graft copolymer," *Carbohydrate Polymers*, vol. 88, no. 1, pp. 290–298, 2012.
- [25] W. Yuan, J. Zhang, H. Zou, T. Shen, and J. Ren, "Amphiphilic ethyl cellulose brush polymers with mono and dual side chains: facile synthesis, self-assembly, and tunable temperature-pH responsivities," *Polymer*, vol. 53, no. 4, pp. 956–966, 2012.
- [26] H. T. T. Phan, K. Zhu, A.-L. Kjøniksen, and B. Nyström, "Temperature-responsive self-assembly of charged and uncharged hydroxyethylcellulose-graft-poly(N-isopropylacrylamide) copolymer in aqueous solution," *Colloid and Polymer Science*, vol. 289, no. 9, pp. 993–1003, 2011.
- [27] D. Wang, J. Tan, H. Kang et al., "Synthesis, self-assembly and drug release behaviors of pH-responsive copolymers ethyl cellulose-graft-PDEAEMA through ATRP," *Carbohydrate Polymers*, vol. 84, no. 1, pp. 195–202, 2011.
- [28] M. Bagheri and S. Shateri, "Thermosensitive nanosized micelles from cholesteryl-modified hydroxypropyl cellulose as a novel carrier of hydrophobic drugs," *Iranian Polymer Journal*, vol. 21, no. 6, pp. 365–373, 2012.
- [29] J. Wan, Z. Hu, W. Chen, H. Chen, and Z. Yu, "Synthesis and application on enrichment of metal ions of cellulose fibre grafted β -cyclodextrin," *Acta Polymerica Sinica*, no. 4, pp. 566–572, 2004.
- [30] E. Kosecka-Judin, M. Wesolowski, and D. Pauksza, "Pattern recognition methods as supplementary techniques for identification of salicylamide—cyclodextrins inclusion complexes," *Central European Journal of Chemistry*, vol. 10, no. 5, pp. 1534–1546, 2012.
- [31] C. Volobuef, C. M. Moraes, L. A. S. Nunes et al., "Sufentanil-2-hydroxypropyl- β -cyclodextrin inclusion complex for pain treatment: physicochemical, cytotoxicity, and pharmacological evaluation," *Journal of Pharmaceutical Sciences*, vol. 101, no. 10, pp. 3698–3707, 2012.
- [32] M. J. Arias-Blanco, J. R. Moyano, J. I. Perez-Martinez, and J. M. Gines, "Study of the inclusion of gliclazide in α -cyclodextrin," *Journal of Pharmaceutical and Biomedical Analysis*, vol. 18, no. 1-2, pp. 275–279, 1998.
- [33] F. Giordano, C. Novak, and J. R. Moyano, "Thermal analysis of cyclodextrins and their inclusion compounds," *Thermochimica Acta*, vol. 380, no. 2, pp. 123–151, 2001.
- [34] B. Szafran and J. Pawlaczyk, "Preparation and characterization of the β -cyclodextrin inclusion complex with sulfafurazole," *Journal of Inclusion Phenomena and Molecular Recognition in Chemistry*, vol. 23, no. 4, pp. 277–288, 1996.
- [35] A. Harada and S. Takahashi, "Preparation and properties of cyclodextrin-ferrocene inclusion complexes," *Journal of the Chemical Society, Chemical Communications*, no. 10, pp. 645–646, 1984.
- [36] T. Matsue, D. H. Evans, T. Osa, and N. Kobayashi, "Electron-transfer reactions associated with host-guest complexation: oxidation of ferrocenecarboxylic acid in the presence of β -cyclodextrin," *Journal of the American Chemical Society*, vol. 107, no. 12, pp. 3411–3417, 1985.
- [37] M. Nakahata, Y. Takashima, H. Yamaguchi, and A. Harada, "Redox-responsive self-healing materials formed from host-guest polymers," *Nature Communications*, vol. 2, no. 1, article 511, 2011.
- [38] A. Nakayama, A. Kakugo, J. P. Gong et al., "High mechanical strength double-network hydrogel with bacterial cellulose," *Advanced Functional Materials*, vol. 14, no. 11, pp. 1124–1128, 2004.
- [39] A. Sannino, C. Demitri, and M. Madaghiele, "Biodegradable cellulose-based hydrogels: design and applications," *Materials*, vol. 2, no. 2, pp. 353–373, 2009.

Research Article

Effects of Emulsifiers on Preparing Spherical Urea-Formaldehyde Paraffin Capsules Modified by β -Cyclodextrin for Energy Storage

Xin Yu,¹ Zhanhua Huang,^{1,2} and Kaixuan Yu¹

¹ Key laboratory of Bio-based Material Science and Technology of Ministry of Education, Northeast Forestry University, Harbin 150040, China

² School of Renewable Natural Resources, Louisiana State University Agricultural Center, Baton Rouge, LA 70803, USA

Correspondence should be addressed to Zhanhua Huang; huangzh1975@163.com

Received 22 November 2013; Revised 12 January 2014; Accepted 12 January 2014; Published 24 February 2014

Academic Editor: Ming-Guo Ma

Copyright © 2014 Xin Yu et al. This is an open access article distributed under the Creative Commons Attribution License, which permits unrestricted use, distribution, and reproduction in any medium, provided the original work is properly cited.

Urea-formaldehyde (UF) paraffin capsules (B-UPCS) modified by β -cyclodextrin (β -CD) were successfully prepared with excellent energy storage capacity using different emulsifiers. B-UPCS were characterized by FT-IR, DSC SEM, optical microscopy, and laser particle size distribution analyzer. The effects of different emulsifiers and the stirring rate of emulsion on the microstructure, average particle diameter, and the content of paraffin were discussed in details. The results show that OP-10 for use with PCMs as emulsifier has a better emulsifying capacity, thermal stability, and mechanical stirring stability than SDBS for use with PCMs as emulsifier. As a result, the optimum dosage of OP-10 was 3% to 7%, and the suitable stirring rate of emulsion was 7500 to 12500 rpm. At this time, the spherical particle diameter of B-UPCS was about 1.0 μm , the paraffin content was 78%, and the enthalpy of B-UPCS can reach 161.0 J/g.

1. Introduction

Phase change materials (PCMs) have been gradually attracting attention of people as new types of energy storage media. PCMs can store or release energy during the physical phase change process. For solid-liquid PCMs and liquid-liquid PCMs, they require a package to control and regulate energy during the phase change process. Encapsulation technology for use with PCMs is one kind of effective ways for preparing the core-shell capsule energy storage materials. The capsule shell acts like a container for PCMs encapsulation to achieve different sizes package for PCMs [1]. PCMs can improve the energy efficiency and expand the diversification of energy in intelligent ways. As a result, it has become the focus of research on PCMs in recent decades.

There are various methods for preparing PCMs, such as in situ polymerization [2], interfacial polymerization [3], sol-gel method [4], and spray drying [5]. The shell materials of PCMs are mainly melamine resin [6–9] and urea-formaldehyde

resin [10–12]. But these kinds of shell materials in the preparation process require a large amount of formaldehyde, which is known as teratogenic substance and easy to cause environmental problems and public safety issues. Therefore, it makes great senses to use less formaldehyde or formaldehyde-free materials for preparing PCMs. At the same time, it is necessary to improve the crosslinked degree of melamine resin and urea-formaldehyde resin as shell materials.

At present, emulsifiers used for the preparation of PCMs contain anionic surfactants, cationic surfactants, and non-ionic surfactants, such as SMA [13, 14], SDBS [15], OP-10 [16], imidazoline [17], and the compound emulsifier [18]. These emulsifiers can reduce Gibbs free energy produced by the mechanical agitation process of emulsion. And the thermal stability and mechanical stability of the emulsion are very important for the core material emulsion in avoiding phase separation phenomenon in the preparation of PCMs [19, 20]. And emulsifiers have a great influence on the morphology and encapsulation effects of the phase change capsules. Few

studies about the effects of the different types of emulsifiers on the preparing B-UPCS have been reported. In this study, B-UPCS were synthesized by microencapsulation technology using different types of emulsifiers. In this paper, effects of OP-10 and sodium dodecyl benzene sulfonate (SDBS) in preparation of B-UPCS were discussed in detail. It also offered some useful data for finding a suitable emulsifier or compound emulsifier to get novel PCMs in the future research work.

2. Experimental

2.1. Materials. Urea (Yongda Chemical Reagent Co., Ltd., Tianjin, China) and formaldehyde (37%, Tianli Chemical Reagent Co., Ltd. Tianjin, China) were used to synthesise UF resin. β -CD (Baishi Chemical Co., Ltd., Tianjin, China) was used as modifier. OP-10 (Guangfu Fine Chemical Research Institute, Tianjin, China) and SDBS (Bodi Chemical Co., Ltd., Tianjin, China) were used as emulsifiers. Resorcin (Kermel Chemical Reagents Co., Ltd., Tianjin, China) and ammonium chloride (Yongda Chemical Reagent Co., Ltd., Tianjin, China) were used as curing agent. Triethanolamine (Hongyan Chemical Reagent Co., Ltd., Tianjin, China) and citric acid (Tianjin Ruijinte Chemical Reagent Co., Ltd., Tianjin, China) were used as pH regulators. Paraffin (Ruhr Energy Technology Co., Ltd., Hangzhou, China) was used as the core material.

2.2. Preparation of Spherical β -UPCS. Urea, formaldehyde aqueous solution (37 wt%), and distilled water were mixed and the pH was adjusted to 8-9 with triethanolamine, and then the mixture was stirred at 70°C with a stirring rate of 450 rpm for 60 min to prepare UF precursor solution. β -CD was added into the UF precursor solution and mixed in ice bath for 15 min to obtain the B-CD-UF mixture. The emulsifier, paraffin melt, water, and cyclohexane were dispersed at the high stirring speed for 15 min to form an oil-in-water dispersion. Afterwards, the B-CD-UF mixture, citric acid solution, ammonium chloride, and resorcin were added into the paraffin dispersion with a stirring rate of 500 rpm and kept to 75°C for 3 hours. After filtration, washing with distilled water, and drying for 48 h at room temperature, B-UPCS paraffin capsules were obtained.

2.3. Characterization. Fourier transform infrared spectroscopy (FTIR) spectra of B-UPCS were analyzed on a Thermo Fisher Nicolet 6700 FTIR spectrometer (USA) to determine the chemical structure of B-UPCS. The morphology (SEM) of B-UPCS was observed by an FEI QUANTA 200 scanning electronic microscope (USA). Optical micrographs of paraffin emulsions were obtained by a Nikon E200 optical microscope (Japan). Particle sizes of the products were studied by a Brookhaven ZetaPlus zeta potential analyzer (USA). The thermal property measurements were carried out on a TA Q20 differential scanning calorimeter (DSC) (USA) at a heating rate of 5°C/min in the range of 10 to 65°C under nitrogen atmosphere.

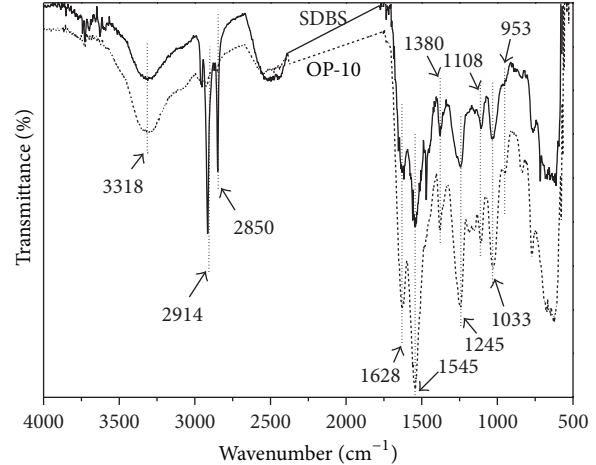


FIGURE 1: FT-IR spectra of B-UPCS with different types of emulsifiers.

2.4. Calculation of Paraffin Content in β -UPCS. The core material content of B-UPCS directly affects heat storage capacity. The content of the core material can be obtained in different ways. In this study, the paraffin content of β -UPCS was calculated as follows:

$$Ca (\%) = \frac{\Delta H_{\text{microPCM}}}{\Delta H_{\text{PCM}}} \times 100\%, \quad (1)$$

where $\Delta H_{\text{microPCM}}$ is enthalpy of β -UPCS, ΔH_{PCM} is enthalpy of paraffin itself [20, 21].

3. Results and Discussion

3.1. FTIR Spectra of B-UPCS with Different Types of Emulsifiers. FTIR spectra of B-UPCS with different types of emulsifiers are shown in Figure 1. As seen from Figure 1. The peak at 3318 cm^{-1} corresponded to stretching vibrations of N-H and O-H [22]. Bands of 2914 cm^{-1} and 2850 cm^{-1} can be attributed to $-\text{CH}_2$ stretching vibration asymmetric and symmetric adsorption. The peaks around 1628 cm^{-1} , 1545 cm^{-1} were attributed to stretching vibration of C=O and deformation vibration of CN, N-H [23, 24]. The absorption peak at 1380 cm^{-1} can be attributed to C-H bending vibration and the band at 1245 cm^{-1} was assigned to C-OH in-plane stretching vibration. The band 1033 cm^{-1} corresponded to asymmetric stretching vibration of C-O-C [25]. Thus, in view of the above, it is established that B-UPCS have been synthesized successfully both with OP-10 and SDBS as emulsifier. Comparing the FTIR spectra of B-UPCS with OP-10 and SDBS as emulsifier, the emulsifiers had emulsification effects on forming homogeneous paraffin emulsion and there were no significant impacts on the chemical structures of B-UPCS.

3.2. Effects of the Dosage of Emulsifiers on the Average Diameter of B-UPCS. The relationships among OP-10 dosage, the average particle diameter of B-UPCS, and the particle size of paraffin emulsion are shown in Figure 2. As seen

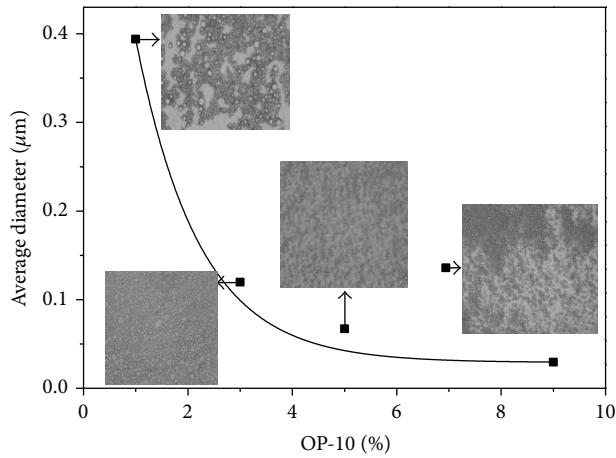


FIGURE 2: Effect of the dosage of OP-10 on average particle diameter of B-UPCS and the optical micrographs of paraffin emulsion.

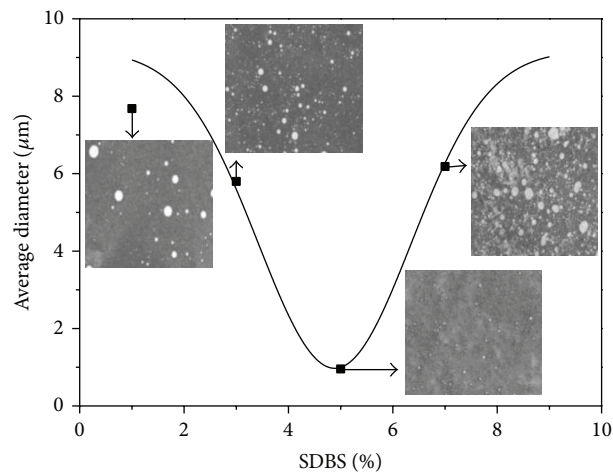


FIGURE 3: Effects of the dosage of SDBS on average particle diameter of B-UPCS and the optical micrographs of paraffin emulsion.

from Figure 2, the particle sizes of B-UPCS and paraffin emulsion were decreased rapidly with the increase of the OP-10 dosage. When the dosage of OP-10 reached 3% to 7%, the particle sizes of B-UPCS were approximately $0.1 \mu\text{m}$. The result indicates that OP-10 adhered to the droplets surface and brought a balance state between the prepolymers and the curing resin. When the dosage of OP-10 reached 7% to 9%, the average diameter of B-UPCS remained unchanged with the increase of OP-10. At this condition, the effects of OP-10 on the average particle size of B-UPCS and paraffin emulsion were not remarkable. The drastic self-polymerization reaction between methylolureas and β -CD did not occur in the end due to the fact that the main composition of OP-10 is polyoxyethylene alkylphenol with a high Hydrophile-lipophile balance number (HLB) value of 14.5. OP-10 had a strong emulsifying ability for paraffin to form a uniform, stable, and well-dispersed emulsion solution because of the nonpolar groups in OP-10 [26]. Thus, the dosage of emulsifier is a key factor for the droplet size of paraffin-water emulsion

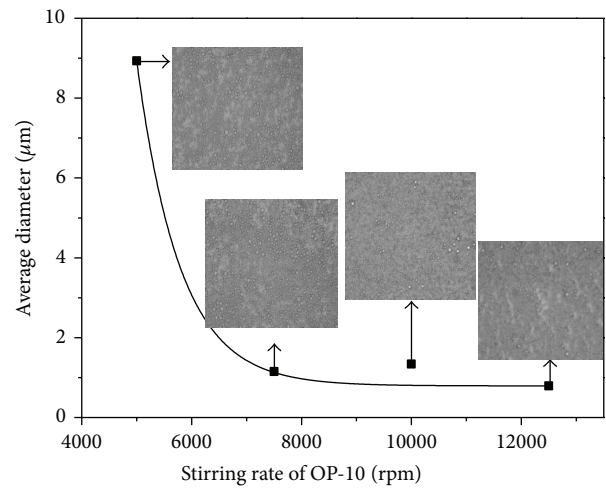


FIGURE 4: Effects of stirring rate of OP-10 on average particle diameter of B-UPCS and the optical micrographs of paraffin emulsion.

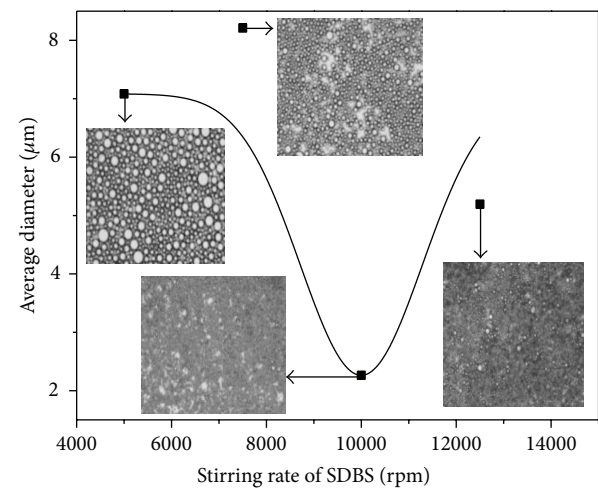


FIGURE 5: Effects of stirring rate of SDBS on average particle diameter of B-UPCS and the optical micrographs of paraffin emulsion.

and the uniformity of the core material. Based on the above results, the optimum dosage of OP-10 was 3% to 7%.

The relationships among SDBS dosage, the average particle diameter of B-UPCS, and the particle size of paraffin emulsion are shown in Figure 3. With the increase of SDBS dosage, the average particle diameter of B-UPCS presented sudden decrease firstly and later increase trend. When the dosage of SDBS was 1% to 5%, the average particle diameter of B-UPCS decreased rapidly because the surface charges of SDBS reduced oil-water interfacial tension and Gibbs free energy of paraffin emulsion solution. With the increase of the dosage of SDBS, a homogeneous paraffin emulsion solution was gradually formed with a good resistance to temperature and the mechanical agitation. When the amount of SDBS reached more than 7%, the particle diameter of B-UPCS increased rapidly, and the probable reason for this phenomenon was the violent curing reaction or the sensitivity of SDBS for temperature or mechanical agitation

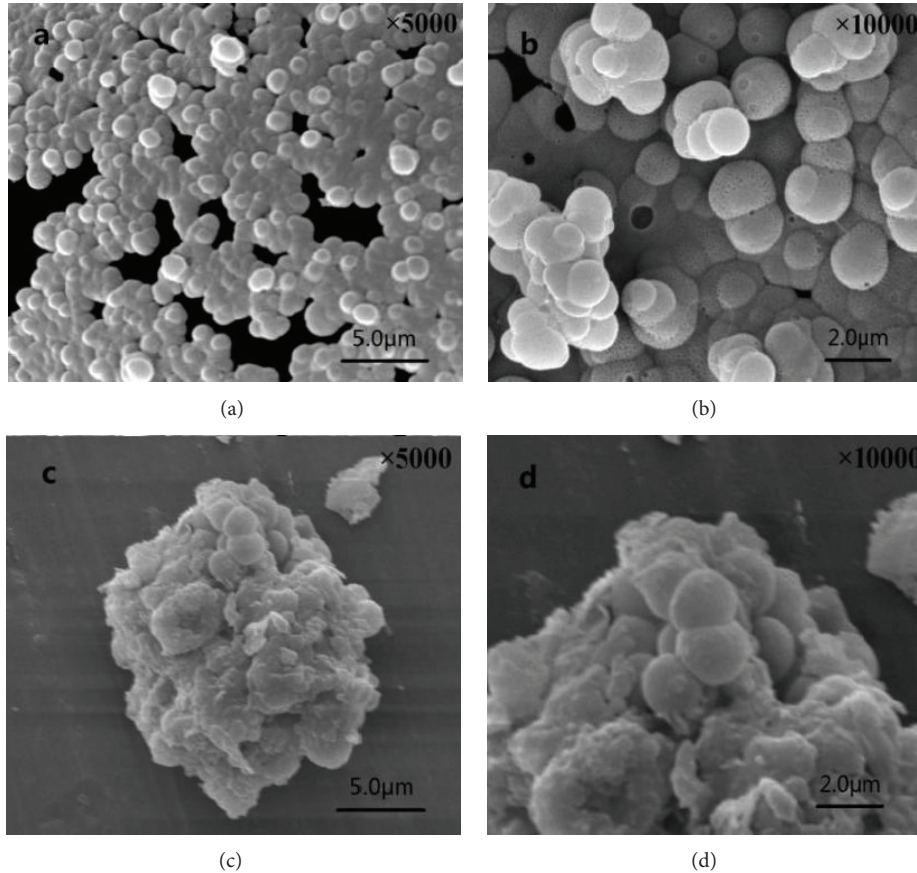


FIGURE 6: SEM images of B-UPCS prepared with different emulsifiers. The dosage of emulsifiers was 0.3 g, and the stirring rate of paraffin was 10000 rpm.

to result in phase separation phenomenon, thereby generating a large block of B-UPCS [27]. Thus, the optimum dosage of SDBS was 4% to 6%.

3.3. Effects of the Stirring Rate of Emulsifiers on Average Diameter of B-UPCS. The dosage of emulsifier is a key factor on dispersing the core material of B-UPCS. It had great influences on the preparing PCMs with uniform particle size. Effects of stirring rate of OP-10 on average particle diameter of B-UPCS are shown in Figure 4. With the stirring rate of OP-10 increasing, the average particle diameter of B-UPCS and the size of paraffin droplets decreased rapidly (Figure 4). When the stirring rate reached 10000 rpm, the core material began to form uniform and stable emulsion solution, and the average particle diameter of B-UPCS remained unchanged. And this trend is in accordance with the literature [28]. Thus, OP-10 had a strong stability of temperature and the mechanical agitation and the phase separation phenomenon was difficult to occur. As a result, OP-10 can be used as an emulsifier with a broader range of the stirring rate. In this study, the optimum stirring rate of OP-10 was 7500~12500 rpm with desired emulsion effects.

Effects of stirring rate of SDBS on average particle diameter of B-UPCS are shown in Figure 5. As seen from Figure 5, the optimum stirring rate of SDBS as emulsifier was

10000 rpm. Phase separation phenomenon occurred when the stirring speed increased to 12500 rpm, resulting in a sharp increase of the particle diameter. The results were consistent with the ones of the optical microscope. Therefore, the stirring rate of SDBS was 10000 rpm.

3.4. Effects of Different Types of Emulsifiers on Microstructure of B-UPCS. SEM images of B-UPCS with OP-10 (Figures 6(a) and 6(b)) and SDBS (Figures 6(c) and 6(d)) as emulsifier are shown in Figure 6. It can be seen from Figures 6(a) and 6(b) that B-UPCS prepared by in situ polymerization were spherical. The capsule particles were composed of many small particles depositing on the surface of B-UPCS, only a few collapse and breakage phenomenon in B-UPCS. B-UPCS had uniform particle. This result indicated that OP-10 had good emulsion effects on the dispersion of the core material, and the result was consistent with the results above.

As seen from Figures 6(c) and 6(d), a large area of adhesion and accumulation existed on the surfaces of B-UPCS. The probable reason is that the prepolymer attached to the surface of the paraffin droplets and cured violently. Besides, it is obvious that B-UPCS consist of many small spherical capsules with tightness surface, which is more suitable for providing good encapsulation effects and almost no leakages for the core material.

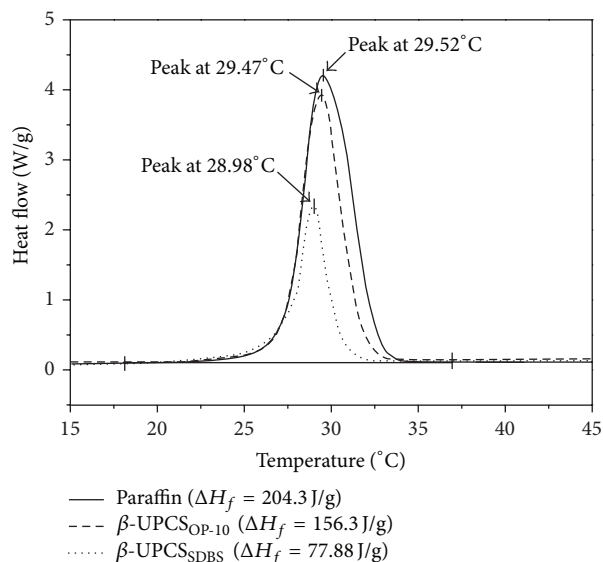


FIGURE 7: DSC curves of B-UPCS and paraffin.

3.5. DSC Curves of B-UPCS. The DSC curves of B-UPCS with OP-10 and SDBS as emulsifier are shown in Figure 7. The phase change enthalpy of B-UPCS with OP-10 as emulsifier was higher than the one with SDBD as emulsifier. Most of B-UPCS prepared with OP-10 as emulsifier were spherical with good barrier properties and most paraffin was wrapped into B-UPCS. For SDBS as emulsifier, too violent curing reaction resulted in only part of paraffin wrapped in B-UPCS. The main reason is that the poor dispersion capacity of SDBS led to the self-polymerization reaction of monomer. As a result, the enthalpy of B-UPCS with SDBS as emulsifier was low. This result was consisted with SEM. As seen from Figure 7, the phase transition temperatures of B-UPCS were different from pure paraffin, probably due to the interactions between the core and shell material in B-UPCS [21]. The results were the same as our previous literatures [29–31].

3.6. Effects of Different Types of Emulsifiers on the Paraffin Content. Effects of the dosage of OP-10 and SDBS as emulsifiers on the content of paraffin in B-UPCS are shown in Figure 8. And in this paper, the paraffin content of β -UPCS was calculated according to (1). With the dosage of OP-10 increasing, the content of paraffin in B-UPCS increased at first and then decreased slightly. When the dosage of OP-10 reached 3% to 7%, the content of paraffin was about 78%. When the dosage of OP-10 reaches 9%, the content of paraffin in B-UPCS tended to decrease. When the dosage of OP-10 was low, it helped to reduce Gibbs free energy, caused by temperature and mechanical stirring, and promoted to help the monomer adhere to the droplets surface of paraffin emulsion and formed the core-shell structure capsules [31]. However, when the dosage of OP-10 continued to increase, the paraffin-water phase was separated and the polycondensation reaction occurred among the monomers of the shell material. As a result, the paraffin in B-UPCS declined. And, with SDBS as emulsifier, the content of paraffin in β -UPCS was increased

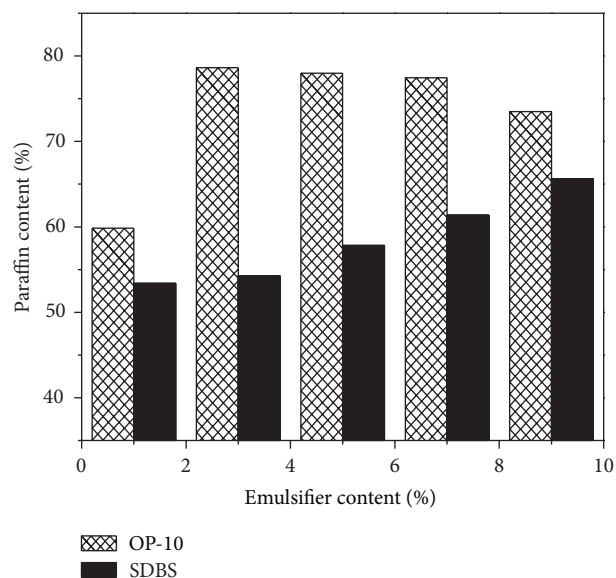


FIGURE 8: Effects of the emulsifier dosage on the content of paraffin in B-UPCS.

slowly with the increase of SDBS dosage. This was perhaps because SDBS was ionic surfactant and it has little influences on wrapping paraffin in water-oil phase. However, at the same dosage of OP-10 as emulsifier, the paraffin content in B-UPCS was significantly higher because OP-10 has better emulsion effect than SDBS on dispersing the core material. Hence, it could continuously promote prepolymers to curing on the droplet surface of paraffin emulsion by crosslinked reaction and formed well-encapsulated B-UPCS.

4. Conclusion

In this study, the effects of two types of emulsifiers (OP-10, SDBS) on paraffin content average particle size and microstructure of B-UPCS were discussed by changing the stirring rate and the dosage of emulsifiers. The experimental results showed that when the dosage of OP-10 reached 4% to 7% and the stirring rate was 7500~12500 rpm, the spherical particle diameter of B-UPCS was uniform and the paraffin content was 78%, and the enthalpy of B-UPCS can reach 161.0 J/g. When the dosage of SDBS reached more than 7% or the stirring rate increased to 12500 rpm, demulsification phenomenon of paraffin emulsion occurred, led to a rapid curing reaction. Comparing with SDBS as emulsifier, OP-10 had good emulsion results with a high content of paraffin, uniform particle size, and good dispersion effects. However, there were some individual damaged capsules with OP-10 as emulsifier. In the following study, we will explore different types of compound surfactants for the preparation of the core-shell energy storage materials.

Conflict of Interests

The authors declare that there is no conflict of interests regarding the publication of this paper.

Acknowledgments

This work was supported financially by the National Natural Science Foundation of China (no. 31000277) and the Central University Basic Scientific Research Project of China (no. 2572014DB01).

References

- [1] V. A. A. Raj and R. Velraj, "Review on free cooling of buildings using phase change materials," *Renewable and Sustainable Energy Reviews*, vol. 14, no. 9, pp. 2819–2829, 2010.
- [2] X. Hu, Z. Huang, and Y. Zhang, "Preparation of CMC-modified melamine resin spherical nano-phase change energy storage materials," *Carbohydrate Polymers*, vol. 101, pp. 83–88, 2014.
- [3] A. Malfliet, G. Deferme, L. Stappers, and J. Fransaeer, "Synthesis and characterization of composite coatings for thermal actuation," *Journal of the Electrochemical Society*, vol. 154, no. 1, pp. D50–D56, 2007.
- [4] H. Zhang, X. Wang, and D. Wu, "Silica encapsulation of n-octadecane via sol-gel process: a novel microencapsulated phase-change material with enhanced thermal conductivity and performance," *Journal of Colloid and Interface Science*, vol. 343, no. 1, pp. 246–255, 2010.
- [5] M. N. A. Hawlader, M. S. Uddin, and M. M. Khin, "Microencapsulated PCM thermal-energy storage system," *Applied Energy*, vol. 74, no. 1-2, pp. 195–202, 2003.
- [6] J.-F. Su, x.-Y. Wang, and H. Dong, "Influence of temperature on the deformation behaviors of melamine-formaldehyde microcapsules containing phase change material," *Materials Letters*, vol. 84, pp. 158–161, 2012.
- [7] H. Zhang and X. Wang, "Fabrication and performances of microencapsulated phase change materials based on n-octadecane core and resorcinol-modified melamine-formaldehyde shell," *Colloids and Surfaces A*, vol. 332, no. 2-3, pp. 129–138, 2009.
- [8] Z. Xue and J. Li, "Preparation and characterization of microencapsulated phase change liquid paraffin," *The Chinese Journal of Process Engineering*, vol. 12, no. 2, pp. 293–301, 2012.
- [9] K. Sun, B. Zhang, F. Yan, G. Yin, and Y. Cui, "Preparation and characterization of microcapsule with paraffin phase change materials for energy storage," *Chemical Industry and Engineering Progress*, vol. 30, no. 12, pp. 2676–2678, 2011.
- [10] Z. Jin, Y. Wang, J. Liu, and Z. Yang, "Synthesis and properties of paraffin capsules as phase change materials," *Polymer*, vol. 49, no. 12, pp. 2903–2910, 2008.
- [11] M. Delgado, A. Lázaro, J. Mazo, and B. Zalba, "Review on phase change material emulsions and microencapsulated phase change material slurries: materials, heat transfer studies and applications," *Renewable and Sustainable Energy Reviews*, vol. 16, no. 1, pp. 253–273, 2012.
- [12] C. Fan and X. Zhou, "Influence of operating conditions on the surface morphology of microcapsules prepared by in situ polymerization," *Colloids and Surfaces A*, vol. 363, no. 1–3, pp. 49–55, 2010.
- [13] X.-L. Ren, L.-X. Wang, L. Ren, and J.-F. Su, "Preparation of phase change materials microcapsules by in-situ polymerization," *Journal of Functional Materials*, vol. 36, no. 11, pp. 1722–1727, 2005.
- [14] W. Li, X.-X. Zhang, X.-C. Wang, and J.-J. Niu, "Preparation and characterization of microencapsulated phase change material with low remnant formaldehyde content," *Materials Chemistry and Physics*, vol. 106, no. 2-3, pp. 437–442, 2007.
- [15] L. Yuan, G.-Z. Liang, J.-Q. Xie, J. Guo, and L. Li, "Thermal stability of microencapsulated epoxy resins with poly(urea-formaldehyde)," *Polymer Degradation and Stability*, vol. 91, no. 10, pp. 2300–2306, 2006.
- [16] Q. Lin, D. Zhu, J. Li, F. Luo, and W. Zhou, "Preparation and phase change properties of paraffin microcapsules," *Fine Chemicals*, vol. 28, no. 1, pp. 10–13, 2011.
- [17] X. Liu, S. Wang, and H. Liu, "Preparation and characteristics of paraffin microencapsulated in melamine-urea-formaldehyde by in-situ polymerization," *Journal of Chemical Industry and Engineering*, vol. 57, no. 12, pp. 2991–2996, 2006.
- [18] Y. Yan, H. Zhang, and J. Liu, "Preparation and characteristics of microencapsulated phase change materials," *Materials Review*, vol. 23, no. 2, pp. 49–51, 2009.
- [19] F. Tiarks, K. Landfester, and M. Antonietti, "Preparation of polymeric nanocapsules by miniemulsion polymerization," *Langmuir*, vol. 17, no. 3, pp. 908–918, 2001.
- [20] A. Sari, C. Alkan, and A. Karaipekli, "Preparation, characterization and thermal properties of PMMA/n-heptadecane microcapsules as novel solid-liquid microPCM for thermal energy storage," *Applied Energy*, vol. 87, no. 5, pp. 1529–1534, 2010.
- [21] L. Pan, Q. Tao, S. Zhang et al., "Preparation, characterization and thermal properties of micro-encapsulated phase change materials," *Solar Energy Materials and Solar Cells*, vol. 98, pp. 66–70, 2012.
- [22] G. Fang, H. Li, F. Yang, X. Liu, and S. Wu, "Preparation and characterization of nano-encapsulated n-tetradecane as phase change material for thermal energy storage," *Chemical Engineering Journal*, vol. 153, no. 1-3, pp. 217–221, 2009.
- [23] H. Li, *Research on surface modification of PUF microcapsules and self-healing performance for epoxy [Ph.D. thesis]*, Harbin Institute of Technology, Harbin, China, 2010.
- [24] J.-Q. Xie, F.-M. Feng, W. Hu, H.-J. Mao, H. Yan, and C. Li, "Preparation of a microcapsule containing the paraffin as the core material by in-situ polymerization method without prepolymerization and capability of the microcapsule," *Journal of Functional Materials*, vol. 39, no. 2, pp. 293–296, 2008.
- [25] L. Yuan, G. Liang, J. Xie, L. Li, and J. Guo, "Preparation and characterization of poly(urea-formaldehyde) microcapsules filled with epoxy resins," *Polymer*, vol. 47, no. 15, pp. 5338–5349, 2006.
- [26] X. Hu, Z. Huang, X. Yu, and B. Li, "Preparation and thermal energy storage of carboxymethyl cellulose-modified nanocapsules," *BioEnergy Research*, vol. 6, no. 4, pp. 1135–1141, 2013.
- [27] M. Alcoutlabi and G. B. McKenna, "Effects of confinement on material behaviour at the nanometre size scale," *Journal of Physics Condensed Matter*, vol. 17, no. 15, pp. R461–R524, 2005.
- [28] Z.-H. Chen, F. Yu, X.-R. Zeng, and Z.-G. Zhang, "Preparation, characterization and thermal properties of nanocapsules containing phase change material n-dodecanol by miniemulsion polymerization with polymerizable emulsifier," *Applied Energy*, vol. 91, no. 1, pp. 7–12, 2012.
- [29] C. Alkan, A. Sari, and A. Karaipekli, "Preparation, thermal properties and thermal reliability of microencapsulated n-eicosane as novel phase change material for thermal energy storage," *Energy Conversion and Management*, vol. 52, no. 1, pp. 687–692, 2011.
- [30] G. Fang, Z. Chen, and H. Li, "Synthesis and properties of microencapsulated paraffin composites with SiO₂ shell as thermal energy storage materials," *Chemical Engineering Journal*, vol. 163, no. 1-2, pp. 154–159, 2010.

- [31] X. L. Shan, J. P. Wang, X. X. Zhang, and X. C. Wang, "Formaldehyde-free and thermal resistant microcapsules containing n-octadecane," *Thermochimica Acta*, vol. 494, no. 1-2, pp. 104–109, 2009.

Research Article

Organic/Inorganic Superabsorbent Hydrogels Based on Xylan and Montmorillonite

Shuang Zhang,¹ Ying Guan,¹ Gen-Que Fu,¹ Bo-Yang Chen,¹
Feng Peng,¹ Chun-Li Yao,¹ and Run-Cang Sun^{1,2}

¹ Institute of Biomass Chemistry and Technology, College of Materials Science and Technology,
Beijing Forestry University, Beijing 100083, China

² State Key Laboratory of Pulp and Paper Engineering, South China University of Technology, Guangzhou 510640, China

Correspondence should be addressed to Feng Peng; fengpeng@bjfu.edu.cn and Chun-Li Yao; chunliyao2006@163.com

Received 10 December 2013; Accepted 2 January 2014; Published 12 February 2014

Academic Editor: Ming-Guo Ma

Copyright © 2014 Shuang Zhang et al. This is an open access article distributed under the Creative Commons Attribution License, which permits unrestricted use, distribution, and reproduction in any medium, provided the original work is properly cited.

The unique organic/inorganic superabsorbent hydrogels based on xylan and inorganic clay montmorillonite (MMT) were prepared via grafting copolymerization of acrylic acid (AA) and 2-acrylamido-2-methylpropanesulfonic acid (AMPS) with *N,N*-methylenebisacrylamide (MBA) as a cross-linking agent and potassium persulfate (KPS) as an initiator. The effect of variables on the swelling capacity of the hydrogels, such as the weight ratios of MMT/xylan, MBA/xylan, and AMPS/AA, was systematically optimized. The results indicated that the superabsorbent hydrogels comprised a porous cross-linking structure of MMT and xylan with side chains that carry carboxylate, carboxamide, and sulfate. The hydrogels exhibit the high compressive modulus (E), about 35–55 KPa, and the compression strength of the hydrogels increased with an increment of the MMT content. The effect of various cationic salt solutions (LiCl, CaCl₂, and FeCl₃) on the swelling has the following order: Li⁺ > Ca²⁺ > Fe³⁺. Furthermore, the influence of pH values on swelling behaviors showed that the superabsorbent composites retained around 1000 g g⁻¹ over a wide pH range of 6.0–10.0. The xylan-based hydrogels with the high mechanical and swelling properties are promising for the applications in the biomaterials area.

1. Introduction

Superabsorbent hydrogels are slightly cross-linked hydrophilic polymers with a three-dimensional network structure. They can absorb water in the amount from 10% up to thousands of times based on their dry weight and retain large amounts of aqueous fluids even under some pressure. Due to the special characteristics, these materials have been widely applied in various fields, such as agriculture [1, 2], biomedical area [3, 4], waste-water treatment [5, 6], biosensors [7], and tissue engineering [8, 9].

Polysaccharide-based hydrogels are currently attracting much interest for their unique properties, that is, biocompatibility, biodegradability, renewability, and nontoxicity. Various polysaccharides, such as chitosan [10], starch [11], cellulose [12], alginate [13], carrageenan [14], and gellan gum [15], have been investigated on hydrogel formulations. Typically, hemicelluloses are the second most abundant polysaccharides

in biomass, which are commonly defined as cell wall heterogeneous polysaccharides. Compared with other polysaccharides, hemicelluloses have been somewhat neglected in research and are normally disposed as organic waste from the forest industry side streams. While recent research has shown that hemicelluloses have significant potential as a material resource for hydrogel preparation. A series of hemicelluloses-based hydrogels were synthesized from galactoglucomannans, via introducing functional monomers with unsaturated bonds to the backbone of hemicelluloses and chemically cross-linking the modified hemicelluloses [16–20]. The hydrogels, presenting good biodegradability, nontoxicity, and controllable swelling capacity, were fully developed for drug delivery systems. In addition, xylan-based hydrogels have also shown potential applications as pH-sensitive controlled drug delivery vehicles by blending aspen hemicelluloses and chitosan in acidic conditions [21]. Furthermore, xylan-rich hemicelluloses-based hydrogels were prepared and used

as a novel porous bioabsorbent by graft copolymerization of acrylic acid and hemicelluloses for absorption of heavy metal ions from aqueous solutions [22, 23]. Therefore, the applications of hemicelluloses in hydrogels field are gradually expanding.

Arabinoxylans (AXs) are the main hemicelluloses of Gramineae, which have been generally present in a variety of tissue of the main cereals of commerce: wheat, rye, barley, oat, rice, corn, and sorghum, as well as other plants: pangola grass, bamboo shoot, and ray grass [24]. Gramineae is similar to hardwood xylan, but the amount of L-arabinose is higher. Hydrogels have been prepared from AXs extracted from wheat bran as controlled release matrices, which were synthesized via the oxidative cross-linking using either chemical (ferulic chloride and ammonium persulphate) or enzymatic (laccase/O₂ and peroxidase/H₂O₂) free radical-generating agents [25–27]. The gels present interesting properties like neutral taste and odor, high water absorption capability (up to 100 g of water per gram of dry polymer), and absence of pH, electrolyte, and temperature susceptibility [28]. However, the water absorption capacity and mechanical strength of the AXs hydrogels are much lower than those of petroleum-based hydrogels such as poly(acrylic acid) and poly(acrylamide) hydrogels. Furthermore, the absence of multistimulus response properties severely restricts their applications. Therefore, more research attention should be paid to develop new approaches for modifying and cross-linking AXs to improve the properties of the hydrogels, such as absorption capacity, mechanical strength, and stimuli-responsive physical properties (normally temperature-, pH-, salt-, or osmosis-controlled changes).

Recently, much attention has been focused on inorganic materials for preparation of superabsorbent composites, such as attapulgite [29], kaolin [30], and sodium silicate [31]. The introduction of inorganic clay into polysaccharides not only reduces production costs but also improves the properties (e.g., swelling ability, gel strength, and mechanical and thermal stability) of hydrogels and accelerates the generation of new materials for special application [32]. Among the clays, montmorillonite (MMT), a layered aluminum silicate with exchangeable cations and reactive –OH groups on the surface, has been widely used to improve the properties of hydrogels, due to its good absorption, extensive swelling in water and cation exchange capacity [33]. Yet, to the best of our knowledge, there has been no report on the preparation of superabsorbent hydrogels based on xylan and inorganic clays.

Acrylic acid (AA) and 2-acrylamido-2-methylpropanesulfonic acid (AMPS) are important monomers that are widely used for the preparation of functional hydrogels. AMPS is hydrophilic monomer containing nonionic and anionic groups; meanwhile, AA is anionic monomer. The incorporation of ionic groups in the superabsorbent is known to increase their swelling capacity, while the nonionic groups can improve their salt tolerance. In this paper, a unique organic/inorganic hydrogel was prepared by grafting copolymerization of AA and AMPS monomers along the chains of AXs in the presence of MMT. The intermolecular interaction and morphological change of the hydrogels

were characterized by FT-IR spectra and scanning electron microscope (SEM). Moreover, the swelling properties and behaviors under different pH and salt concentrations were investigated.

2. Experimental

2.1. Materials. Xylan was isolated from bamboo (*Phyllostachys pubescens*) holocellulose obtained by using 3% NaOH at 75°C for 3 h with a solid to liquid ratio of 1:25 (g·mL⁻¹). The holocellulose was obtained by delignification of the extractive-free bamboo (40–60 mesh) with 6% sodium chlorite in acidic solution (pH 3.6–3.8, adjusted by 10% acetic acid) at 75°C for 2 h. The composition of neutral sugars and uronic acids and the molecular weights of the hemicellulosic samples were determined according to the literature [34]. The sugar composition of the xylan (83.5% xylose, 5.1% arabinose, 4.2% glucose, 0.4% galactose, and 6.8% glucuronic acid (relatively molar percent)) was tested by high performance anion exchange chromatography (HPAEC). The molecular weights obtained by gel permeation chromatography (GPC) showed that the native xylan had a weight average molecular weight (M_w) of 13,420 g·mol⁻¹ and a polydispersity of 4.1, corresponding to a degree of polymerization of 88. 2-Acrylamido-2-methyl-1-propanesulfonic acid (AMPS) and montmorillonite (MMT) were purchased from A Johnson Matthey Company. *N,N*-Methylenebisacrylamide (MBA) and potassium persulfate (KPS) were purchased from Tianjin Jinke Refined Chemical Engineering Research Institute, China. All of these chemicals were used without any further purification. AA (Beijing Yili Fine Chemical Co., Ltd., China) was purified by distillation under reduced pressure to remove the inhibitor hydroquinone before use. All other reagents used were analytical grade, and all solutions were prepared with distilled water.

2.2. Preparation of Hydrogels. Xylan (1.0 g) was dissolved in 35.0 mL of distilled water in a three-neck reactor equipped with a mechanical stirrer, a reflux condenser, and a nitrogen line at 85°C until a homogeneous solution was obtained. Then appropriate amounts (0.00–0.12 g) of MMT were added to this solution with stirring to form a uniform sticky solution under nitrogen. After cooling the reactant to 70°C, 0.08 g of KPS were added, stirred, and kept for 10 min to generate radicals. Subsequently, the mixture of AA (1.43–2.86 g, neutralization degree of 70% with sodium hydroxide solution), AMPS (1.14–2.57 g), and MBA (0.05–0.25 g) was added to the flask. All the reactions were carried out under nitrogen, and the reaction mixture was continuously stirred for 4 h. At the end of the propagation reaction, the gel product was poured into excess ethanol (200 mL) and remained for 48 h to dewater. Then, the dewatered product was dried to constant mass at 70°C, grounded, and passed through 100-mesh sieve. Finally, the powdered products were stored away from moisture, heat, and light. The feed compositions of all samples are listed in Table 1.

TABLE 1: The reaction conditions for xylan-*g*-poly(AA-AMPS)/MMT hydrogels.

Sample codes	MMT/xylan (g g ⁻¹)	AMPS (g)	MBA (g)	AA (g)
1	—	1.00	0.10	2.00
2	0.03	1.00	0.10	2.00
3	0.05	1.00	0.10	2.00
4	0.08	1.00	0.10	2.00
5	0.11	1.00	0.10	2.00
6	0.08	2.00	0.05	2.00
7	0.08	2.00	0.10	2.00
8	0.08	2.00	0.15	2.00
9	0.08	2.00	0.20	2.00
10	0.08	2.00	0.25	2.00
11	0.08	1.14	0.10	2.28
12	0.08	1.78	0.10	2.22
13	0.08	2.00	0.10	2.00
14	0.08	2.33	0.10	1.67
15	0.08	2.57	0.10	1.43

2.3. Method of Characterization

2.3.1. FT-IR Spectroscopy. FT-IR spectra of the MMT, xylan, xylan-*g*-poly(AA-AMPS), and xylan-*g*-poly(AA-AMPS)/MMT hydrogels were recorded using a Thermo Scientific Nicolet iN 10 FT-IR Microscopy (Thermo Nicolet Corporation, Madison, WI) equipped with a liquid nitrogen cooled MCT detector. Dried samples were grounded and palletized using BaF₂ and their spectra were recorded from 4000 to 650 cm⁻¹ at a resolution of 4 cm⁻¹ and 128 scans per sample.

2.3.2. Surface Morphology of the Hydrogels. The equilibrium-swollen samples of the hydrogels in deionized water at room temperature were quickly frozen and then freeze-dried for morphological analysis. Scanning electron microscopy (SEM) of the hydrogel samples was carried out with a Hitachi S-3400N II (Hitachi, Japan) instrument at 15 kV. Prior to taking pictures, the samples were sputter-coated with a thin layer of gold. Images were obtained at magnifications ranging from 200x to 5000x, which was dependent on the feature to be traced.

2.3.3. Swelling Measurements. The preweighted dry hydrogels were immersed into excessive distilled water to reach a state of equilibrium swelling. The swollen superabsorbent was filtered using 100-mesh sieve and drained for 20 min until no free water remained. After weighing the swollen hydrogels, the equilibrium water absorption was calculated by using the following equation:

$$Q_{eq} = \frac{W_2 - W_1}{W_1}, \quad (1)$$

where Q_{eq} is the equilibrium water absorption defined as grams of water per gram of sample; W_1 and W_2 are the mass of sample before and after swelling, respectively.

2.3.4. Mechanical Measurement. Dynamic mechanical analysis (DMA, TA Instruments Q800 Series) was used to determine the compressive modulus of the swollen hydrogel samples. To reach swelling equilibrium, hydrogels were incubated in distilled water for 24 h at room temperature before test. The disk-shaped samples were 1 cm × 0.5 cm (diameter × height) in dimension and were tested in compression mode at 25°C. Rheological measurements were carried out at 25°C on ARES-RFS III rheometer (TA Instruments, USA). The mixture of xylan (1.0 g), KPS (0.08 g), AA (1.0 or 2.0 g), MBA (0.05–0.25 g), and MMT (0.00–0.12 g) was stirred to form a homogeneous solution. This hybrid system was quickly transferred into rheometer for testing.

2.3.5. Swelling in Various Salt Solutions. The swelling capacity of the hydrogels was measured in different concentrations (0.5, 1.0, 1.5, 2.0, and 2.5 mol·L⁻¹) of LiCl, CaCl₂, and FeCl₃ salt solutions according to the above method described for swelling measurement in distilled water.

2.3.6. Swelling at Various pHs. Individual solutions with acidic and basic pHs were prepared by the dilution of NaOH (pH 12.0) and HCl (pH 2.0) solutions to achieve pH ≥ 6.0 and <6.0, respectively. The pH values were precisely checked by a pH meter (PB-10, Sartorius). Then, the preweighted dried hydrogels were used for the swelling measurements according to the above method described for swelling measurement in distilled water.

2.3.7. Water Retention Measurement. The water retention (WR) was determined by centrifuging the water-swollen hydrogels at 2000 rpm. The weight of the hydrogels was determined every 30 s. The WR of the hydrogels was calculated according to

$$WR (\%) = \frac{m_2}{m_1} \times 100\%, \quad (2)$$

where m_1 is the weight of the fully swollen hydrogel and m_2 is the weight of the hydrogel centrifuged for different times at 2000 rpm.

3. Results and Discussion

3.1. Synthesis and Spectral Characterization. The superabsorbent hydrogel was prepared by the graft copolymerization of acrylic acid (AA) and 2-acrylamido-2-methyl-1-propanesulfonic acid (AMPS) onto xylan in the presence of a cross-linking agent (MBA), powdery montmorillonite (MMT), and potassium persulfate (KPS) as an initiator. The persulfate initiator was decomposed under heating to produce sulfate anion radicals that abstract hydrogen atoms from the hydroxyl groups of the xylan backbones. Therefore, this redox system resulted in active centers capable of radically initiating the polymerization of AA and AMPS, leading to a graft copolymer. Since a cross-linking agent (MBA) was present in this system, the copolymer comprised a cross-linked structure. The MMT in the polymerization reaction can also be considered as a cross-linking agent [35]. The proposed mechanism for the grafting and chemically cross-linking reactions is outlined in Figure 1.

Infrared spectroscopy was carried out to confirm the chemical structure of the superabsorbent hydrogel. FT-IR spectra of MMT, xylan, xylan-g-poly(AA-AMPS), and xylan-g-poly(AA-AMPS)/MMT superabsorbent hydrogel are shown in Figure 2. In the spectrum (see Figure 2(c)) of xylan, the region between 3500 cm^{-1} and 1800 cm^{-1} presents two major peaks at about 3411 cm^{-1} (corresponding to the absorption of stretching of the hydroxyl groups) and at 2911 cm^{-1} (corresponding to the C-H stretching of the CH_2 groups). The absorption peak at 1600 cm^{-1} is related to the uronic acid carboxylate [36]. The bands at the range of 1452 and 1048 cm^{-1} are assigned to the C-H and C-O bond stretching frequencies. The low intensity of the peaks at 990 and 1166 cm^{-1} suggests the presence of arabinosyl units, which have been reported to be attached only at position 3 of the xylopyranosyl constituents [37]. A sharp band at 895 cm^{-1} is due to β -glycosidic linkages between the sugar units. On comparing the spectra of xylan and xylan-g-poly(AA-AMPS) (see Figure 2(d)), new characteristic absorption bands at 1651 , 1558 , and 1442 cm^{-1} are assigned to the stretching vibration of C=O, asymmetrical stretching vibration of COO^- , and symmetrical stretching vibration of COO^- , respectively [38]. Moreover, the characteristic absorption peaks of AMPS units are shown at 1400 , 1040 , and 627 cm^{-1} , which are attributed to C-N stretching vibration of the amide, S-O stretching vibration of $-\text{SO}_3\text{H}$, and C-S stretching vibration, respectively [39]. These bands indicated that AA and AMPS monomers were actually grafted onto the backbone of xylan.

In the spectrum (see Figure 2(a)) of MMT, the characteristic vibration bands are shown at 3400 and 3630 cm^{-1} , which correspond to $-\text{OH}$ stretching band for adsorbed interlayer water and $-\text{OH}$ stretching band for $\text{Al}-\text{OH}$, respectively. The absorption peaks at 1631 and 1423 cm^{-1} are attributed to the deformation vibration of the hydroxyl groups. The

characteristic peaks at 1150 and 1090 cm^{-1} are due to Si-O stretching (out-of plane) for MMT and Si-O stretching (in plane) vibration for layered silicates, respectively. The peaks at 915 , 845 , and 796 cm^{-1} are assigned to $\text{Al}-\text{Al}-\text{OH}$, $\text{Al}-\text{Mg}-\text{OH}$, and Si-O-Al bending vibrations, respectively [40-42]. As can be seen, compared to the spectrum of MMT (Figure 2(b)), the intensities of absorption bands at 3630 cm^{-1} ascribed to $-\text{OH}$ of MMT disappeared in the spectrum of xylan-g-poly(AA-AMPS)/MMT (Figure 2(a)). In addition, the intensity of the absorption peaks due to Si-O stretching also decreased. These results indicated that MMT participated in polymerization reaction through its active $-\text{OH}$ groups and chemically cross-linked with polymer chains. Therefore, it could be concluded that the superabsorbent hydrogel product comprised a cross-linking structure of xylan and MMT with side chains carrying carboxylate, carboxamide, and sulfate.

3.2. Morphological Analysis. The morphologies of the freeze-dried xylan-g-poly(AA-AMPS) and xylan-g-poly(AA-AMPS)/MMT composites are depicted in Figure 3, respectively. Obviously, the surface morphology of the xylan-g-poly(AA-AMPS)/MMT hydrogel is different from that of xylan-g-poly(AA-AMPS). It could be observed that the cross-linked xylan-g-poly(AA-AMPS) (Figure 3(a)) displayed a porous structure with many large pores. However, for hydrogel containing MMT (Figure 3(b)), the pore size became smaller and it showed a sheet-like structure with significant interconnection forming a three-dimensional network, which was beneficial for the diffusion of aqueous fluid into the superabsorbent polymer and increasing the water absorption rate [43, 44]. In addition, the degree of dispersion of clay micropowder in the polymer matrix is more important for an organic-inorganic composite [45, 46]. As can be seen from Figures 3(c) and 3(d), the microstructure of pure MMT clay was flaky (Figure 3(c)), while these clays were randomly dispersed in the polymer matrix and almost embedded within xylan-g-poly(AA-AMPS) in the composites (Figure 3(d)), and no flocculation of MMT particles could be observed. These SEM results confirmed that the MMT was finely dispersed in the composite to form a homogeneous composition.

3.3. Mechanical Properties of Hydrogels. The mechanical properties of the xylan-based hydrogels with different ratios of MMT to xylan have been determined. Figure 4(a) presents the typical compressive modulus-strain curves of xylan-based hydrogels at room temperature. Obviously, all the samples exhibited the high compressive modulus (E), about 35 – 55 KPa . This indicated that the hydrogels had excellent mechanical properties. As expected, the compressive modulus of the hydrogels increased with the increment of the MMT content in the hydrogels, in the order Gel 5 > Gel 4 > Gel 3 > Gel 2 > Gel 1. The results strongly demonstrated that MMT contributed to the enhancement of the mechanical properties of the hydrogels. On the other hand, the strains of hydrogels decrease from 92% to 66% , when the MMT content was increased in the hydrogel.

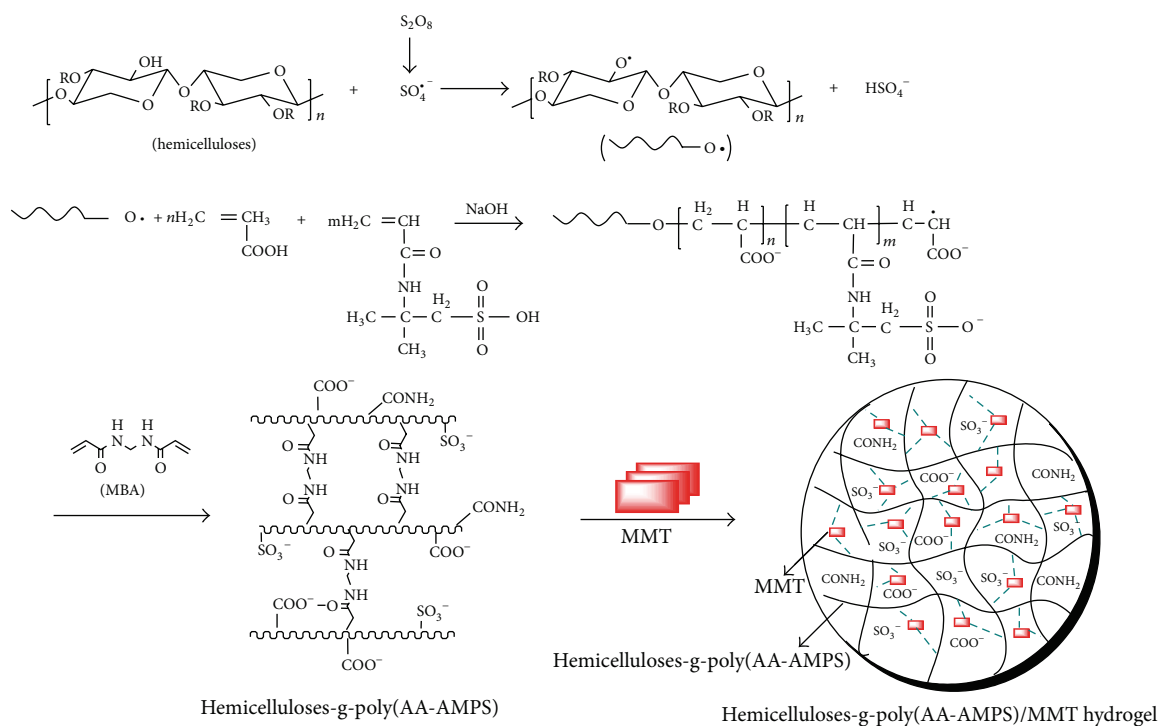


FIGURE 1: Proposed reaction mechanism for synthesis of xylan-g-poly(AA-AMPS)/MMT superabsorbent hydrogels.

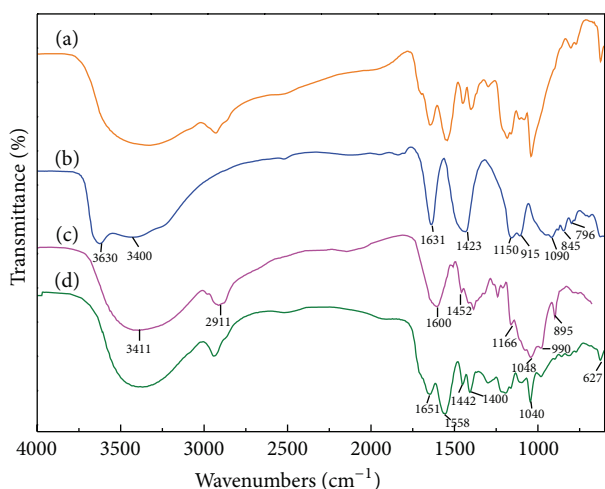


FIGURE 2: FT-IR of (a) xylan-g-poly(AA-AMPS)/MMT, (b) MMT, (c) xylan and (d) xylan-g-poly(AA-AMPS).

To monitor the gelation process, a time sweep measurement for viscoelastic properties of each sample was carried out at 25°C [47]. Figures 4(b) and 4(c) show the storage modulus (G') of hydrogels with different MMT concentrations and various MBA contents, respectively. Apparently, a significant increase of G' values at about 300 s in Figure 4(b) indicated that the rapid gelation process and phase separation occurred during the initial stage. Moreover, the maximum storage modulus of the hydrogels increased with the increase of the MMT/xylan weight ratios from 0.00 to 0.11. It was

further proved that the MMT played an important role in improving the strength of hydrogels. Meanwhile, Figure 4(c) shows the time dependence of the storage modulus of the hydrogels with different MBA contents. Cross-linking agent induced a stable network with the polymers by covalent bonds; thus, the increment of MBA content led to the regular increase of the maximum storage modulus of the hydrogels.

3.4. Effect of MMT Content on Swelling Capacity. The influence of MMT/xylan weight ratio on water absorbency of the superabsorbent hydrogels is shown in Figure 5. It is obvious that MMT content is an important factor influencing water absorbency of the hydrogels. Increasing MMT/xylan weight ratios from 0.00 to 0.08 caused an increment in water absorbency. The maximum water absorbency (1423 g g^{-1}) was obtained at weight ratio of MMT/xylan (0.08). This trend was attributed to the fact that the active $-OH$ groups of MMT could react with the $-OH$, $-SO_3H$, and $-COOH$ groups of the polymeric chains, as indicated by FT-IR spectra (Figure 2). Hence, it can relieve the entanglement of graft polymeric chains and weaken the hydrogen-bonding interaction among hydrophilic groups, which decreases the physical cross-linking degree and improves polymeric network. As a result, the water absorbency can be enhanced by introducing moderate amount of MMT. However, a further increase of MMT caused a decrease in water absorbency. This phenomenon may be attributed to the fact that the MMT can act as an additional cross-linking point in the polymeric network to decrease the elasticity of polymers. Additionally, the excess of MMT would also decrease the hydrophilicity as well as

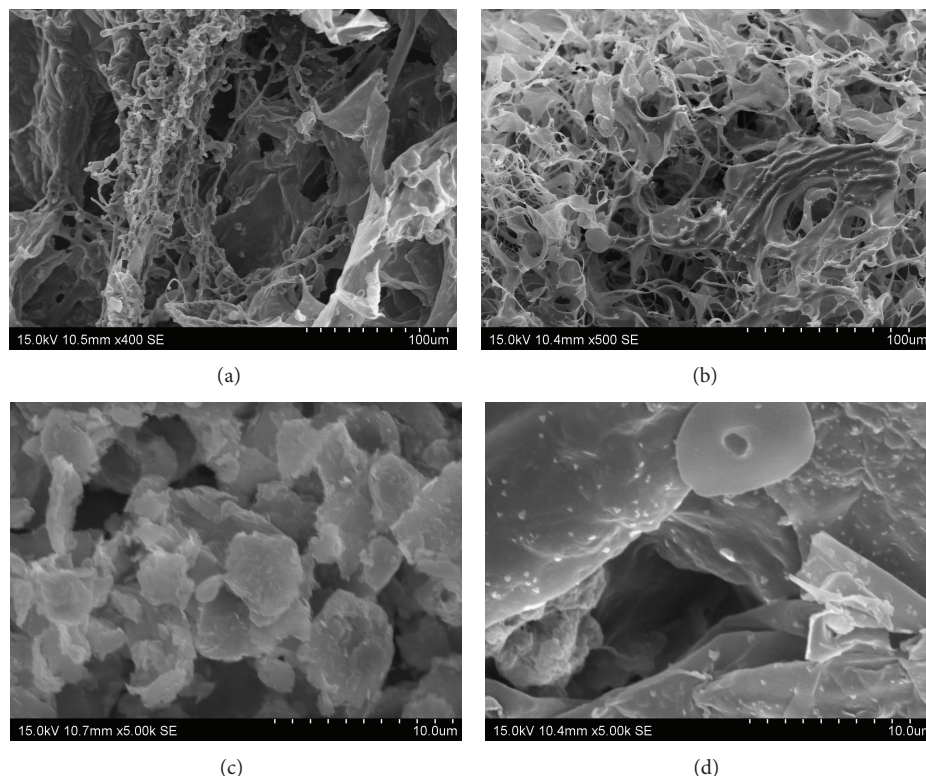


FIGURE 3: SEM images of (a) xylan-g-poly(AA-AMPS), (b) xylan-g-poly(AA-AMPS)/MMT at low magnification and (c) MMT, (d) xylan-g-poly(AA-AMPS)/MMT at high magnification.

the osmotic pressure difference, resulting in shrinkage of the composite [48].

3.5. Effect of MBA Content on Swelling Capacity. The amount of cross-linking agent determines the cross-linking density of the hydrogel network, which is an important swelling-control element. The effect of cross-linker (MBA) to xylan weight ratio on the swelling capacity of the superabsorbent hydrogels was investigated. As shown in Figure 6, the swelling ratio rose from 585 to 864 g g^{-1} when the MBA/xylan weight ratio increased from 0.05 to 0.2, while it decreased with a further increase in the weight ratio. The hydrophilic polymer chains would dissolve in an aqueous environment with just a few cross-linkers. Therefore, the network cannot be formed efficiently, and the water molecules cannot be held, which results in a decrease in the water absorbency. Contrarily, the excess cross-linking concentration causes the higher cross-linking density and decreases the space of polymer three-dimensional network, and consequently, it would not be beneficial to expand the structure and hold a large quantity of water.

3.6. Effect of Monomer Ratio on the Swelling Capacity. The swelling capacity of hydrogels prepared with various weight ratios of AMPS/AA is shown in Figure 7. As can be seen, increasing the AMPS concentration at monomer feed composition, the swelling capacity increased. Swelling and absorption properties are attributed to the presence of

hydrophilic groups, such as $-\text{OH}-$, $\text{CONH}-$, $-\text{CONH}_2-$, and $-\text{SO}_3\text{H}$ in the network. $-\text{SO}_3^-$ groups associated to AMPS present better affinity than $-\text{COO}^-$ group of AA. Moreover, the nonionic groups such as $\text{CONH}-$ can improve their salt tolerance.

3.7. Equilibrium Swelling at Various pH Values. The xylan-g-poly(AA-AMPS)/MMT, containing carboxylate, carboxamide, and sulfonate groups, are the majority of anionic-type hydrogels. Ionic superabsorbent hydrogels exhibit swelling changes for a wide range of pHs. Since the swelling capacity of all “ionic” hydrogels is strongly influenced by ionic strength, no buffer solutions are used. Hence, stock NaOH (pH 13.0) and HCl (pH 1.0) solutions were diluted with distilled water to reach desired basic and acidic pH values, respectively. These results are illustrated in Figure 8. The swelling ratios of the superabsorbent hydrogels were finely preserved around 1000 g g^{-1} in a wide range of pH (6.0–10.0). However, swelling capacity was significantly decreased at pH lower than 6.0 and higher than 10.0, which reached to 108 g g^{-1} at pH 2.0 and 148 g g^{-1} at pH 12.0, respectively. In acidic media, the carboxylate and sulfonate anions were protonated. Moreover, the hydrogen-bonding interactions among carboxylate and sulfonate groups were strengthened, which generated the additional physical cross-linking. At higher pH (6.0–10.0), nearly all of the $-\text{COOH}$ and $-\text{SO}_3\text{H}$ groups were converted to $-\text{COO}^-$ and $-\text{SO}_3^-$. Consequently, the hydrogen-bonding interaction was eliminated and the electrostatic repulsion

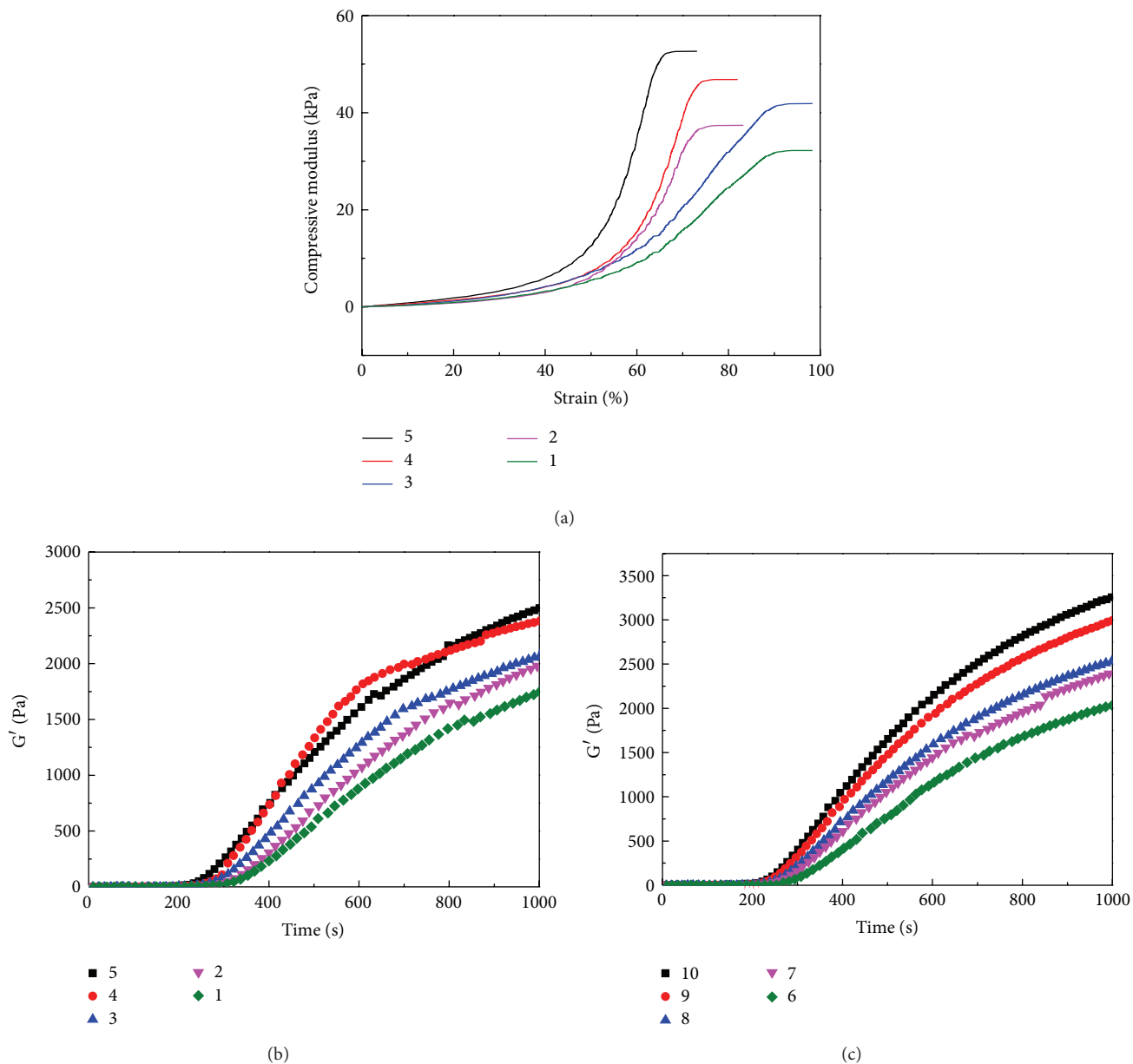


FIGURE 4: Compressive stress-strain curves for hydrogels with different MMT contents (a). The time dependence of storage modulus (G') for hydrogels with different MMT contents (b) and different MBA contents (c).

among the anionic groups increased. Therefore, the polymer network tended to swell more. At pHs greater than 10, the excess Na^+ cations from NaOH shielded the $-\text{COO}^-$ and $-\text{SO}_3^-$ groups, which prevented effective anion-anion repulsion.

3.8. Swelling in Salt Solutions. The characteristics of external solution such as salt concentration and charge valency greatly influence the swelling behavior of the superabsorbent hydrogels. The swelling ratios of hydrogels in aqueous solution of LiCl, CaCl_2 , and FeCl_3 with various concentrations are shown in Figure 9. Obviously, the swelling ratio decreased

with increasing the concentration of external salt solutions. This well-known undesired swelling loss is often attributed to a “charge screening effect” of the additional cations causing a nonperfect anion-anion electrostatic repulsion [49]. Therefore, the osmotic pressure generating from the mobile ion concentration difference between the gel and aqueous phases decreased and resulted in shrinkage of the network. In addition, as shown in Figure 9, the swelling ratio in multivalent cationic saline (CaCl_2 and FeCl_3) solution was almost close to zero at the concentration above 0.1 mol L^{-1} , while it reached 31 g g^{-1} (0.1 mol L^{-1}) and 21 g g^{-1} (0.25 mol L^{-1}) in monovalent cationic solution (LiCl), which are probably due to the complexation of the carboxylate and sulfonate groups

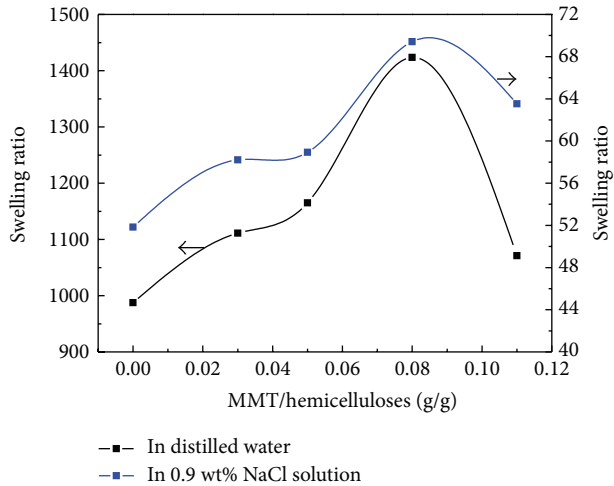


FIGURE 5: Effect of MMT contents on water absorbency of the hydrogels.

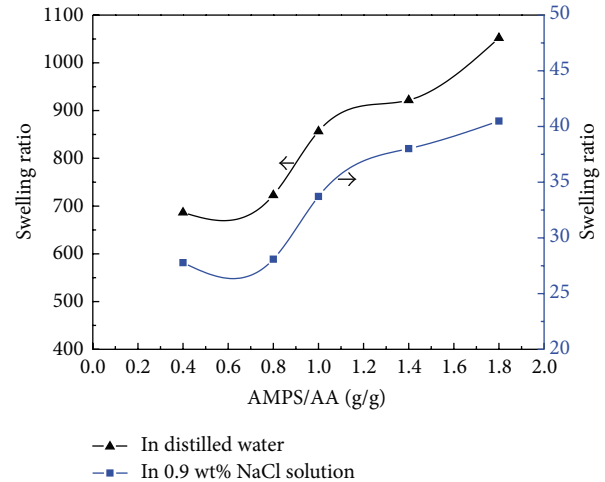


FIGURE 7: Effect of monomer ratios on water absorbency of the hydrogels.

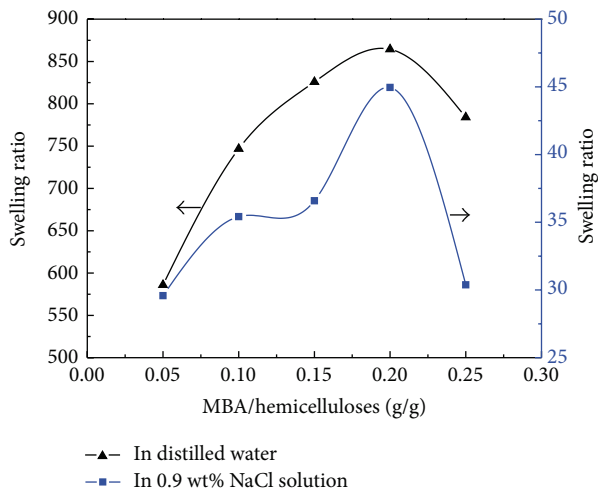


FIGURE 6: Effect of MBA contents on water absorbency of the hydrogels.

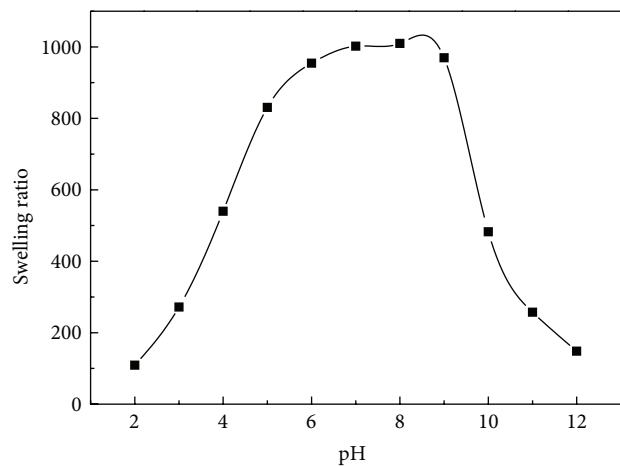


FIGURE 8: Effect of external pH on the water absorbency of the hydrogels.

with the multivalent cations inducing the formation of the additional cross-link points at the surface of particles. Hence, the network cross-link density was enhanced, resulting in the shrinkage of the network. As a result, the water absorbency was decreased considerably ($\text{LiCl} > \text{CaCl}_2 > \text{FeCl}_3$).

3.9. Effect of MMT Content on Water Retention. The water retention ability is an important parameter for hydrogels, especially used in dry and desert regions. The water retention abilities of the hydrogels with different MMT/xylan weight ratios are shown in Figure 10. From this figure, the water retention of the hydrogels was rapidly decreased within 30 s, while small changes in the water retention occurred with prolonging the time. This behavior may be explained as follows: absorbed water in the network of hydrogels can exist in three states: bound, half bond, and free water. Free water is the easiest to remove, compared with bound and half-bond

water. Additionally, the water retention of the hydrogels with various MMT/xylan weight ratios of 0.00, 0.03, 0.05, 0.08, and 0.11 was 65, 69, 74, 60, and 53%, respectively, centrifuged at 2000 rpm for 360 seconds. It can be concluded that the water retention can be enhanced with the moderate amount of MMT. This may be explained by the barrier effect of polymer/MMT hydrogels [50]. The nano-dispersed MMT in the composite, acted as an additional crosslinking point, impeded the diffusion of the water molecules, and made the diffuse path for water vapor longer. However, a further increase of MMT caused a decrease in water retention, which was probably due to that it was difficult to disperse MMT in the homogeneous network solution at higher MMT content, resulted in decreasing the water retention ability.

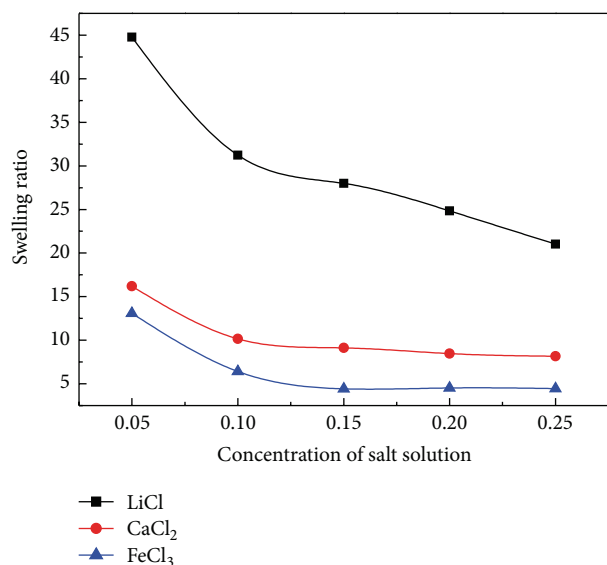


FIGURE 9: Effect of different salt solution on the water absorbency of the hydrogels.

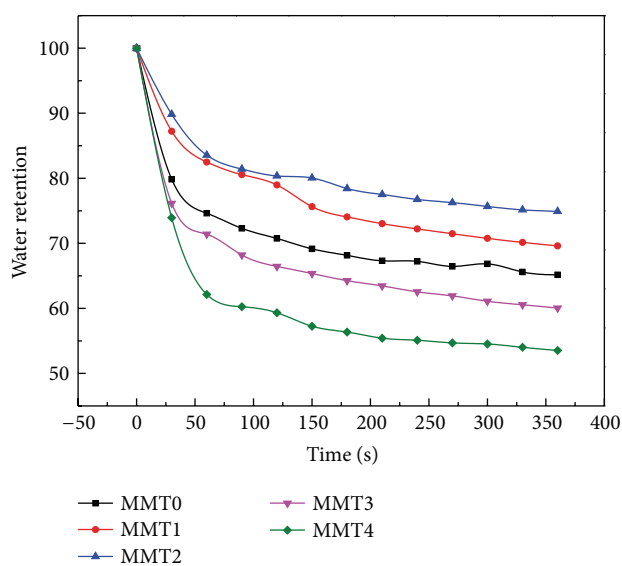


FIGURE 10: Effect of MMT contents on water retention of the hydrogels.

4. Conclusions

The superabsorbent hydrogels were prepared by the graft copolymerization of AA and AMPS onto xylan in the presence of a cross-linking agent (MBA), MMT, and KPS as an initiator. The results of FT-IR showed that the superabsorbent hydrogel products comprised cross-linking structures of xylan and MMT with side chains carrying carboxylate, carboxamide, and sulfate. SEM studies showed that a sheet-like structure with significant interconnection formed a three-dimensional network, where MMT was finely dispersed to form a homogeneous composition. All the samples exhibited the high compressive modulus (E), about 35–55 KPa. The

compressive modulus of the hydrogels increased with the increment of the MMT content in the hydrogels, in the order Gel 5 > Gel 4 > Gel 3 > Gel 2 > Gel 1. The maximum equilibrium swelling ratios of hydrogels in distilled water and 0.9 wt% sodium chloride solutions were up to 1423 g g⁻¹ and 69 g g⁻¹, respectively. The effect of various cationic salt solutions (LiCl, CaCl₂, and FeCl₃) on the swelling has the following order: Li⁺ > Ca²⁺ > Fe³⁺. As a result, these inorganic/organic hydrogels from xylan will have wide applications in the fields of agriculture, foods, tissue engineering, and drug delivery, due to their high swelling capacity and multistimulus response properties.

Conflict of Interests

The authors declare that there is no conflict of interests regarding the publication of this paper.

Acknowledgments

This work was supported by Grants from 2013 National Student Research Training Program (SRTP-201310022034), Excellent Youth Scholars of Ministry of Education of China (20110014120006), Ministries of Education (NCET-13-0670 and 113014A), Postdoctoral Science Foundation of China (2012M510328), and Ministry of Science and Technology (973 Project, 2010CB732204).

References

- [1] M. R. Guilherme, A. V. Reis, A. T. Paulino, T. A. Moia, L. H. C. Mattoso, and E. B. Tambourgi, "Pectin-based polymer hydrogel as a carrier for release of agricultural nutrients and removal of heavy metals from wastewater," *Journal of Applied Polymer Science*, vol. 117, no. 6, pp. 3146–3154, 2010.
- [2] F. Puoci, F. Iemma, U. G. Spizzirri, G. Cirillo, M. Curcio, and N. Picci, "Polymer in agriculture: a review," *American Journal of Agricultural and Biological Science*, vol. 3, no. 1, pp. 299–314, 2008.
- [3] T. Ooya, H. Mori, M. Terano, and N. Yui, "Synthesis of a biodegradable polymeric supramolecular assembly for drug delivery," *Macromolecular Rapid Communications*, vol. 16, no. 4, pp. 259–263, 1995.
- [4] P. S. K. Murthy, Y. Murali Mohan, K. Varaprasad, B. Sreedhar, and K. Mohana Raju, "First successful design of semi-IPN hydrogel-silver nanocomposites: a facile approach for antibacterial application," *Journal of Colloid and Interface Science*, vol. 318, no. 2, pp. 217–224, 2008.
- [5] W. Kangwansupamonkon, W. Jitbunpot, and S. Kiatkamjornwong, "Photocatalytic efficiency of TiO₂/poly[acrylamide-co-(acrylic acid)] composite for textile dye degradation," *Polymer Degradation and Stability*, vol. 95, no. 9, pp. 1894–1902, 2010.
- [6] H. Kaşgöz and A. Durmus, "Dye removal by a novel hydrogel-clay nanocomposite with enhanced swelling properties," *Polymers for Advanced Technologies*, vol. 19, no. 7, pp. 838–845, 2008.
- [7] L.-M. Zhang, G.-H. Wang, and Z. Xing, "Polysaccharide-assisted incorporation of multiwalled carbon nanotubes into sol-gel silica matrix for electrochemical sensing," *Journal of Materials Chemistry*, vol. 21, no. 12, pp. 4650–4656, 2011.

- [8] F. Brandl, F. Sommer, and A. Goepferich, "Rational design of hydrogels for tissue engineering: impact of physical factors on cell behavior," *Biomaterials*, vol. 28, no. 2, pp. 134–146, 2007.
- [9] K. Y. Lee and D. J. Mooney, "Hydrogels for tissue engineering," *Chemical Reviews*, vol. 101, no. 7, pp. 1869–1879, 2001.
- [10] X. Qu, A. Wirsen, and A.-C. Albertsson, "Novel pH-sensitive chitosan hydrogels: swelling behavior and states of water," *Polymer*, vol. 41, no. 12, pp. 4589–4598, 2000.
- [11] S.-Y. Yang and C.-Y. Huang, "Plasma treatment for enhancing mechanical and thermal properties of biodegradable PVA/starch blends," *Journal of Applied Polymer Science*, vol. 109, no. 4, pp. 2452–2459, 2008.
- [12] F. Lenzi, A. Sannino, A. Borriello, F. Porro, D. Capitani, and G. Mensitieri, "Probing the degree of crosslinking of a cellulose based superabsorbing hydrogel through traditional and NMR techniques," *Polymer*, vol. 44, no. 5, pp. 1577–1588, 2003.
- [13] S. Hua and A. Wang, "Synthesis, characterization and swelling behaviors of sodium alginate-g-poly(acrylic acid)/sodium humate superabsorbent," *Carbohydrate Polymers*, vol. 75, no. 1, pp. 79–84, 2009.
- [14] A. Pourjavadi and H. Ghasemzadeh, "Carrageenan-g-poly(acrylamide)/poly(vinylsulfonic acid, sodium salt) as a novel semi-IPN hydrogel: synthesis, characterization, and swelling behavior," *Polymer Engineering and Science*, vol. 47, no. 9, pp. 1388–1395, 2007.
- [15] Y. Gong, C. Wang, R. C. Lai, K. Su, F. Zhang, and D.-A. Wang, "An improved injectable polysaccharide hydrogel: modified gellan gum for long-term cartilage regeneration in vitro," *Journal of Materials Chemistry*, vol. 19, no. 14, pp. 1968–1977, 2009.
- [16] M. S. Lindblad, A.-C. Albertsson, E. Ranucci, M. Laus, and E. Giani, "Biodegradable polymers from renewable sources: rheological characterization of hemicellulose-based hydrogels," *Biomacromolecules*, vol. 6, no. 2, pp. 684–690, 2005.
- [17] A.-C. Albertsson, J. Voepel, U. Edlund, O. Dahlman, and M. Söderqvist-Lindblad, "Design of renewable hydrogel release systems from fiberboard mill wastewater," *Biomacromolecules*, vol. 11, no. 5, pp. 1406–1411, 2010.
- [18] A. A. Roos, U. Edlund, J. Sjöberg, A.-C. Albertsson, and H. Stalbrand, "Protein release from galactoglucomannan hydrogels: influence of substitutions and enzymatic hydrolysis by β -mannanase," *Biomacromolecules*, vol. 9, no. 8, pp. 2104–2110, 2008.
- [19] Y. Lu, L. Zhang, X. Zhang, and Y. Zhou, "Effects of secondary structure on miscibility and properties of semi-IPN from polyurethane and benzyl konjac glucomannan," *Polymer*, vol. 44, no. 21, pp. 6689–6696, 2003.
- [20] U. Edlund and A.-C. Albertsson, "A microspheric system: hemicellulose-based hydrogels," *Journal of Bioactive and Compatible Polymers*, vol. 23, no. 2, pp. 171–186, 2008.
- [21] A. M. Karaaslan, M. A. Tshabalala, and G. Buschle-Diller, "Wood hemicellulose/chitosan-based semi: interpenetrating network hydrogels: mechanical, swelling and controlled drug release properties," *BioResources*, vol. 5, no. 2, pp. 1036–1054, 2010.
- [22] X.-W. Peng, L.-X. Zhong, J.-L. Ren, and R.-C. Sun, "Highly effective adsorption of heavy metal ions from aqueous solutions by macroporous xylan-rich hemicelluloses-based hydrogel," *Journal of Agricultural and Food Chemistry*, vol. 60, no. 15, pp. 3909–3916, 2012.
- [23] X.-W. Peng, J.-L. Ren, L.-X. Zhong, F. Peng, and R.-C. Sun, "Xylan-rich hemicelluloses-graft-acrylic acid ionic hydrogels with rapid responses to pH, salt, and organic solvents," *Journal of Agricultural and Food Chemistry*, vol. 59, no. 15, pp. 8208–8215, 2011.
- [24] T. Ishii, "Acetylation at O-2 of arabinofuranose residues in feruloylated arabinoxylan from bamboo shoot cell-walls," *Phytochemistry*, vol. 30, no. 7, pp. 2317–2320, 1991.
- [25] M. C. Figueroa-Espinoza and X. Rouau, "Oxidative cross-linking of pentosans by a fungal laccase and horseradish peroxidase: mechanism of linkage between feruloylated arabinoxylans," *Cereal Chemistry*, vol. 75, no. 2, pp. 259–265, 1998.
- [26] A. Skendi, C. G. Biliaderis, M. S. Izydorczyk, M. Zervou, and P. Zoumpoulakis, "Structural variation and rheological properties of water-extractable arabinoxylans from six Greek wheat cultivars," *Food Chemistry*, vol. 126, no. 2, pp. 526–536, 2011.
- [27] E. Carvajal-Millan, S. Guilbert, M.-H. Morel, and V. Micard, "Impact of the structure of arabinoxylan gels on their rheological and protein transport properties," *Carbohydrate Polymers*, vol. 60, no. 4, pp. 431–438, 2005.
- [28] M. S. Izydorczyk and C. G. Biliaderis, "Cereal arabinoxylans: advances in structure and physicochemical properties," *Carbohydrate Polymers*, vol. 28, no. 1, pp. 33–48, 1995.
- [29] J. Zhang and A. Wang, "Study on superabsorbent composites. IX: synthesis, characterization and swelling behaviors of polyacrylamide/clay composites based on various clays," *Reactive and Functional Polymers*, vol. 67, no. 8, pp. 737–745, 2007.
- [30] X. Shi, S. Xu, J. Lin, S. Feng, and J. Wang, "Synthesis of SiO₂-polyacrylic acid hybrid hydrogel with high mechanical properties and salt tolerance using sodium silicate precursor through sol-gel process," *Materials Letters*, vol. 63, no. 5, pp. 527–529, 2009.
- [31] P. K. Sahoo and P. K. Rana, "Synthesis and biodegradability of starch-g-ethyl methacrylate/sodium acrylate/sodium silicate superabsorbent composite," *Journal of Materials Science*, vol. 41, no. 19, pp. 6470–6475, 2006.
- [32] D. Gao, R. B. Heimann, J. Lerchner, J. Seidel, and G. Wolf, "Development of a novel moisture sensor based on superabsorbent poly(acrylamide)-montmorillonite composite hydrogels," *Journal of Materials Science*, vol. 36, no. 18, pp. 4567–4571, 2001.
- [33] Y. Bao, J. Ma, and N. Li, "Synthesis and swelling behaviors of sodium carboxymethyl cellulose-g-poly(AA-co-AM-co-AMPS)/MMT superabsorbent hydrogel," *Carbohydrate Polymers*, vol. 84, no. 1, pp. 76–82, 2011.
- [34] F. Peng, J.-L. Ren, F. Xu, J. Bian, P. Peng, and R.-C. Sun, "Fractionation of alkali-solubilized hemicelluloses from delignified populus gansuensis: structure and properties," *Journal of Agricultural and Food Chemistry*, vol. 58, no. 9, pp. 5743–5750, 2010.
- [35] P. Uthirakumar, K. S. Nahm, Y. B. Hahn, and Y.-S. Lee, "Preparation of polystyrene/montmorillonite nanocomposites using a new radical initiator-montmorillonite hybrid via in situ intercalative polymerization," *European Polymer Journal*, vol. 40, no. 11, pp. 2437–2444, 2004.
- [36] M. Kačuráková, N. Wellner, A. Ebringerová, Z. Hromačková, R. H. Wilson, and P. S. Belton, "Characterisation of xylan-type polysaccharides and associated cell wall components by FT-IR and FT-Raman spectroscopies," *Food Hydrocolloids*, vol. 13, no. 1, pp. 35–41, 1999.
- [37] A. Ebringerová, Z. Hromádková, J. Alfoldi, and G. Berth, "Structural and solution properties of corn cob heteroxylans," *Carbohydrate Polymers*, vol. 19, no. 2, pp. 99–105, 1992.

- [38] W. Wang, Q. Wang, and A. Wang, "PH-responsive carboxymethylcellulose-g-poly(sodium acrylate)/polyvinylpyrrolidone semi-IPN hydrogels with enhanced responsive and swelling properties," *Macromolecular Research*, vol. 19, no. 1, pp. 57–65, 2011.
- [39] M. Dalaran, S. Emik, G. Güçlü, T. B. İyim, and S. Özgümüş, "Removal of acidic dye from aqueous solutions using poly(DMAEMA-AMPS-HEMA) terpolymer/MMT nanocomposite hydrogels," *Polymer Bulletin*, vol. 63, no. 2, pp. 159–171, 2009.
- [40] S. W. Xu, J. P. Zheng, L. Tong, and K. De Yao, "Interaction of functional groups of gelatin and montmorillonite in nanocomposite," *Journal of Applied Polymer Science*, vol. 101, no. 3, pp. 1556–1561, 2006.
- [41] H. A. Patel, R. S. Somani, H. C. Bajaj, and R. V. Jasra, "Synthesis and characterization of organic bentonite using Gujarat and Rajasthan clays," *Current Science*, vol. 92, no. 7, pp. 1004–1009, 2007.
- [42] M. Baek, J.-H. Choy, and S.-J. Choi, "Montmorillonite intercalated with glutathione for antioxidant delivery: synthesis, characterization, and bioavailability evaluation," *International Journal of Pharmaceutics*, vol. 425, no. 1-2, pp. 29–34, 2012.
- [43] D. R. Nisbet, K. E. Crompton, S. D. Hamilton et al., "Morphology and gelation of thermosensitive xyloglucan hydrogels," *Biophysical Chemistry*, vol. 121, no. 1, pp. 14–20, 2006.
- [44] J. Wang, W. Wang, and A. Wang, "Synthesis, characterization and swelling behaviors of hydroxyethyl cellulose-g-poly(acrylic acid)/attapulgit superabsorbent composite," *Polymer Engineering and Science*, vol. 50, no. 5, pp. 1019–1027, 2010.
- [45] F. Santiago, A. E. Mucientes, M. Osorio, and C. Rivera, "Preparation of composites and nanocomposites based on bentonite and poly(sodium acrylate). Effect of amount of bentonite on the swelling behaviour," *European Polymer Journal*, vol. 43, no. 1, pp. 1–9, 2007.
- [46] T. Gao, W. Wang, and A. Wang, "A pH-sensitive composite hydrogel based on sodium alginate and medical stone: synthesis, swelling, and heavy metal ions adsorption properties," *Macromolecular Research*, vol. 19, no. 7, pp. 739–748, 2011.
- [47] C. Chang, S. Chen, and L. Zhang, "Novel hydrogels prepared via direct dissolution of chitin at low temperature: structure and biocompatibility," *Journal of Materials Chemistry*, vol. 21, no. 11, pp. 3865–3871, 2011.
- [48] L. Wu and M. Liu, "Slow-release potassium silicate fertilizer with the function of superabsorbent and water retention," *Industrial and Engineering Chemistry Research*, vol. 46, no. 20, pp. 6494–6500, 2007.
- [49] M. Sadeghi and M. Yarahmadi, "Synthesis and characterization of superabsorbent hydrogel based on chitosan-g-poly (acrylic acid-coacrylonitrile)," *African Journal of Biotechnology*, vol. 10, no. 57, pp. 12265–12275, 2011.
- [50] H. Qiu and J. Yu, "Polyacrylate/(carboxymethylcellulose modified montmorillonite) superabsorbent nanocomposite: preparation and water absorbency," *Journal of Applied Polymer Science*, vol. 107, no. 1, pp. 118–123, 2008.

Research Article

Catalytic Properties of Pd Modified Cu/SAPO-34 for NO_x Removal from Diesel Engine

J. C. Wang,¹ H. Qiao,¹ L. N. Han,^{1,2} Y. Q. Zuo,¹ L. P. Chang,¹ W. R. Bao,¹ and G. Feng³

¹ Key Laboratory of Coal Science and Technology, Ministry of Education and Shanxi Province, Taiyuan University of Technology, Taiyuan, Shanxi 030024, China

² School of Materials Science and Engineering, Taiyuan University of Technology, Taiyuan, Shanxi 030024, China

³ Shanghai Research Institute of Petrochemical Technology SINOPEC, Shanghai 201208, China

Correspondence should be addressed to W. R. Bao; baoweiren@tyut.edu.cn and G. Feng; fengg.sshy@sinopec.com

Received 20 November 2013; Accepted 12 December 2013

Academic Editor: Wen Zeng

Copyright © 2013 J. C. Wang et al. This is an open access article distributed under the Creative Commons Attribution License, which permits unrestricted use, distribution, and reproduction in any medium, provided the original work is properly cited.

The Cu/SAPO-34 catalysts with different Cu contents were prepared by in situ hydrothermal synthesis. The selected Cu/SAPO-34 was modified by impregnating 1 wt% Pd(NO₃)₂. The morphology and structure of the samples were characterized via XRD and SEM techniques. The effects of Cu contents and the Pd modification on the de-NO_x activity of the samples were investigated through the selective catalytic reduction by C₃H₆ and NH₃. The Cu contents do not change the skeleton structure of the SAPO-34 crystalline and the Cu/SAPO-34 catalysts with Cu/Si ratios of 0.05, 0.1, and 0.2 have better de-NO_x activity than other catalysts. The addition of Pd can improve the de-NO_x activity of the Cu/SAPO-34 catalysts. The maximum of NO conversion of samples with Pd could reach 90%. Besides, the effect of aging treatment for Cu/SAPO-34 catalysts with and without Pd on the de-NO_x activity was also investigated. The results indicated that the Cu/SAPO-34 catalysts modified by Pd have better antiaging performance than raw samples.

1. Introduction

NO_x can react with hydrocarbons (HC) and produce photochemical smog, which is increasingly highlighted and to be concerned about [1–3]. Selective catalytic reduction (SCR) is an effective method for controlling the emission of NO_x, which has already been used in industry [4–6]. The development of high efficiency catalyst, as the key technology of SCR, has received more and more concerns [7]. Depending on high thermal and hydrothermal stability [8–11], metal-SAPO-34 has a broad application prospect. The proper pore structure makes it exhibit excellent properties in the region of diesel engine exhaust purification [12]. As is known to all, the dispersion of the active sites is closely related to the metal loading for the supported catalysts. When the loading amount of metal is much too high, it could aggregate easily during the calcination process. Therefore, there should be a suitable amount of active components, neither too much nor too little, loading on the support. Meunier et al. [13]

found that a maximum NO_x conversion could be available on Ag/Al₂O₃ when the Ag loading was 1%; however, the conversion decreased obviously when Ag loading was 2%. Horiuchi et al. [14] reported that the highest activity could be achieved over Co/Al₂O₃ when Co loading was 0.5%. These results indicate that the active metal content of the catalysts is very important for the catalytic activity.

As a kind of low-cost active constituent for the SCR of NO, Cu has drawn the attentions of many researchers [15, 16], but diesel exhaust is often at high temperatures (>650°C) and the antiaging capacity is required [17, 18]. Moreover, as one of the noble metals, Pd is a promising candidate for HC-SCR in excess oxygen [19–21]. In this paper, a series of Cu/SAPO-34 catalysts were prepared by hydrothermal synthesis. The effect of Cu content and Pd modifying on the de-NO_x activity were investigated. The morphology and structure of the samples were characterized using XRD and SEM. In addition, the influence of the aging treatment of the prepared catalysts was studied.

2. Experimental

2.1. Preparation of Catalysts. The Cu/SAPO-34 catalysts with different Cu contents were prepared by in situ hydrothermal synthesis, and the details were as follows: CuO, H₃PO₄, Al(OH)₃, and silica gel were used as the sources of Cu, P, Al, and Si, respectively. Morpholine (C₄H₉NO) was selected as the template. The crystallization gel was prepared according to the mole ratio of n CuO : 0.2 SiO₂ : 0.92 Al(OH)₃ : 0.9 H₃PO₄ : 1.25 C₄H₉NO : 50 H₂O : 0.01 HF ($n = 0, 0.005, 0.01, 0.02, 0.04, \text{ and } 0.08$). Firstly, H₃PO₄ was added to deionized water, followed by CuO at 80°C while stirring until dissolved completely. And then, Al(OH)₃, silica gel, morpholine, and HF were added. The initial gel was loaded into the stainless reaction kettles equipped with a polytetrafluorethylene liner of 200 mL and crystallized for 72 h at 190°C. The product was washed and then calcined. Finally, the Cu/SAPO-34 catalysts were obtained. And the preparation method had been described in our previous paper [22].

The Pd modified Cu/SAPO-34 catalysts were prepared with pore volume impregnation. The details were as follows: the Cu/SAPO-34 catalysts were impregnated by Pd(NO₃)₂ solution (1 mol/L) overnight to give a 0.5% Pd loading, and then dried at 120°C and calcined at 600°C for 3 h.

2.2. Characterization. The XRD patterns of powder samples were obtained on a Japanese Rigaku D/MAX2500 diffractometer at 45 kV and 100 mA with CuK α radiation ($\lambda = 0.154$ nm). The scanning rate and range were 8°/min and 5°–85°, respectively.

The SEM images were obtained by a Japanese Jeol Jsm-6700 F at 10 kV. The samples were covered with a thin gold layer before scanning.

The Cu content was measured using an atomic absorption spectroscopy (AAS; Varian AA240FS, USA) with a 324.7 nm Cu testing wavelength, operating at 3.0 mA lamp current and a fuel gas of C₂H₂ (1700 mL/min).

2.3. Activity and Antiaging Capacity Test. The activities of the Cu/SAPO-34 catalysts for the selective catalytic reduction (SCR) of NO_x by C₃H₆ or NH₃ at atmospheric pressure were determined using a fixed-bed flow microreactor. The devices were composed of a gas-way equipped with a flow controller, fixed-bed quartz reactor ($\Phi = 8.5$ mm), a temperature controller, and a detection system. A total flow rate of 100 mL/min was used for the catalytic activity runs. The feed gas consisted of 0.6% NO, 0.6% C₃H₆ or 0.6% NH₃, and 5% O₂ with He as the balance gas. The catalyst powder (40–60 mesh) was placed into the center of the quartz reactor.

Firstly, He gas flow of 100 mL/min was used to sweep off for 2 h in order to eliminate the N₂ residue in the reactor and then switched to the simulated exhaust. The reactor was heated up to 50°C, holden for 0.5 h, and then risen to 600°C at a rate of 7°C/min. NO, NO₂, O₂, and C₃H₆ in the gases before and after the catalytic reaction were analyzed simultaneously online by gas chromatograph (GC-9890A, Shanghai Linghua Instrument Company Limited) equipped with column Porapak Q for separating N₂O and CO₂ and column molecular sieve 5A for separating N₂, O₂ and CO.

The aging treatment is also carried out using the above-mentioned fixed-bed flow microreactor. Catalyst samples were exposed to a stream of gases containing 0.03% SO₂ and 10% vapor balanced with Ar with the total rate of 400 mL/min at the temperature of 720°C for 10 h. Then, the same way as described above was used to test the aged catalyst activity.

NO conversion was calculated using the following equation:

$$X = \frac{(c_1 - c_0)}{c_1} \times 100\%, \quad (1)$$

where X is the conversion of NO and c_1 and c_0 are the concentrations of NO_x (NO, NO₂, and N₂O) before and after the reaction, respectively.

3. Results and Discussion

3.1. Effect of Cu Content on NO Conversion. The NO conversions over the Cu/SAPO-34 catalysts with different Cu contents were investigated using C₃H₆ and NH₃ as the reductant. The Cu content can be represented by the Cu/Si atom ratio of the crystallization gel. In this paper, the Cu/Si atom ratios included 0 (without Cu), 0.025, 0.05, 0.1, 0.2, and 0.4.

The NO conversions of the Cu/SAPO-34 catalysts with different Cu/Si atom ratios are shown in Figure 1 ((a): C₃H₆-SCR and (b): NH₃-SCR). When the reductant was C₃H₆, the NO conversions of all catalysts were below 70% in the temperature range of 100–600°C; Particular, that of the catalyst without Cu was below 20%. It can be also seen that the NO conversions of the catalysts with Cu/Si atom ratios 0.05, 0.1 and 0.2 were higher than these with Cu/Si atom ratios of 0.025 and 0.4. The NO conversions of all Cu/SAPO-34 catalysts increased as the temperature increases from 100°C to 600°C. Moreover, the NO conversions of all Cu/SAPO-34 catalysts increased sharply at low temperature, while it increased slowly at high temperature.

When the reductant was NH₃, the NO conversions of all catalysts were much higher than using C₃H₆ as the reductant in the temperature range of 100–600°C. Particular, at 600°C, the NO conversions of the Cu/SAPO-34 catalysts can reach to about 96% using NH₃ as the reductant, while it only reached 65% using C₃H₆ as the reductant. In addition, like C₃H₆, the NO conversions of the catalysts with Cu/Si atom ratios from 0.05 to 0.2 were higher than these with Cu/Si atom ratios of 0.025 and 0.4.

On the basis of the above results, it can be concluded that as the Cu/Si atom ratios of the crystallization gel were in the range of 0.05–0.2, the de-NO_x activity of the Cu/SAPO-34 catalysts was better than others.

The XRD patterns of the Cu/SAPO-34 catalysts with different Cu contents are shown in Figure 2. It can be obviously found that all samples have SAPO-34 characteristic peaks around $2\theta = 9.45^\circ \sim 9.65^\circ, 16.0^\circ \sim 16.2^\circ, 17.85^\circ \sim 18.15^\circ, 20.55^\circ \sim 20.9^\circ, 24.95^\circ \sim 25.4^\circ, \text{ and } 30.5^\circ \sim 30.7^\circ$, indicating that SAPO-34 was successfully formed using in-situ hydrothermal synthesis. As the Cu content increases, the peaks position of all the samples do not change. It indicates that the amount of

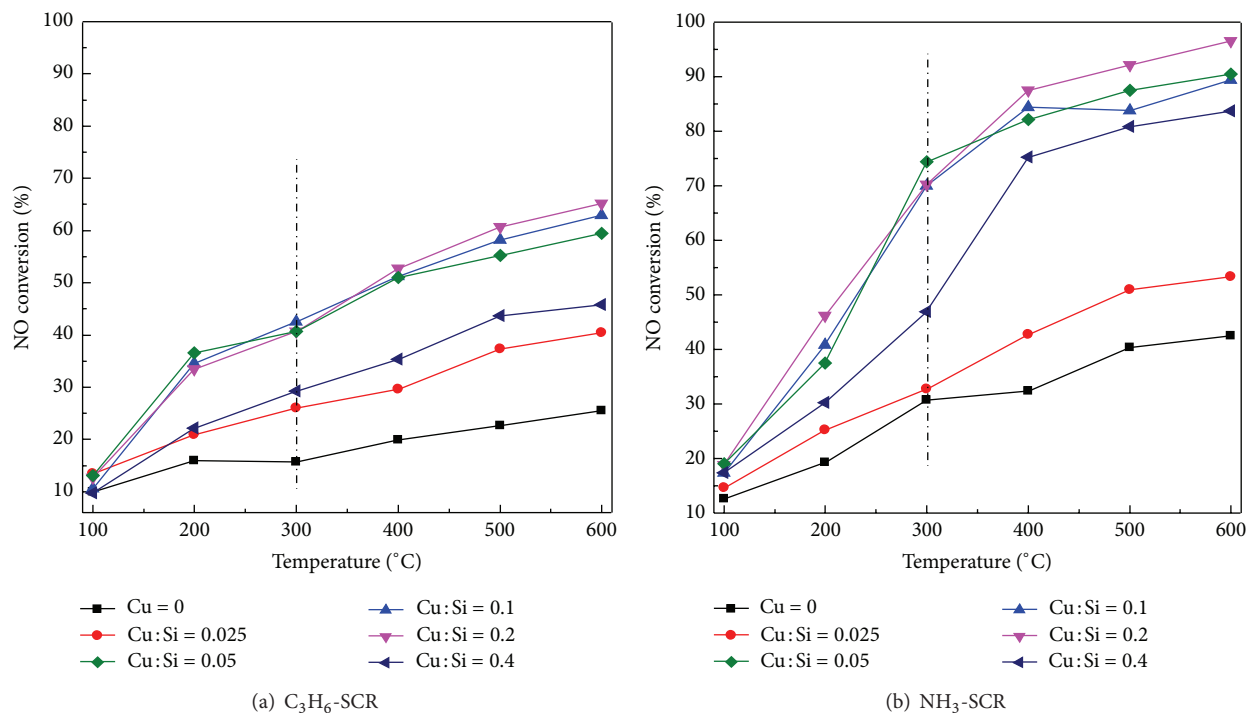


FIGURE 1: Effect of the Cu contents of crystallization gel of Cu/SAPO-34 on NO conversion (GHSV: $10,000\text{ h}^{-1}$).

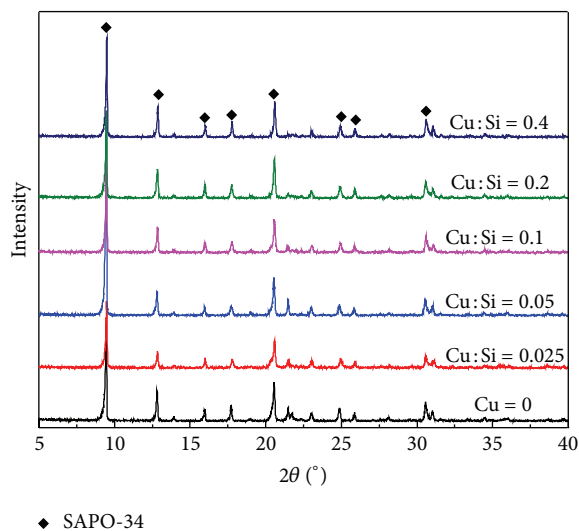


FIGURE 2: XRD patterns of SAPO-34 catalysts with different Cu contents in the crystallization gel.

Cu content has no effect on the CHA structure of SAPO-34. Besides, it should be noted that the peaks became higher and sharper as the SAPO-34 was modified by Cu because the introduction of Cu into the framework could reduce the crystal defects and increase the crystallinity [23–26]. It is also found that no peaks related to CuO and Cu_2O species appeared in the XRD spectrum of catalyst, indicating that the Cu loadings were low or the Cu species were not big enough to be detected [27, 28].

The SEM images of the Cu/SAPO-34 catalysts with different Cu contents are displayed in Figure 3. The morphology features of the Cu/SAPO-34 catalysts with different

Cu contents were compared with those without Cu. It can be found that all the samples were cubic crystals with similar averaged sizes ($0.6\text{--}2\text{ }\mu\text{m}$), which suggested that the addition of Cu did not change the CHA structure and crystal morphology of SAPO-34. It is consistent with the XRD results. When the Cu/Si atom ratios were 0 and 0.025, there was no random-shaped material around the cubic crystals. Some random-shaped materials appeared as the Cu content in Cu/SAPO-34 catalysts increased. When the Cu/Si atom ratio was 0.2, the surface of the crystals was nearly covered with the random-shaped material. When the Cu/Si atom ratio was 0.4, big cubic SAPO-34 crystals were formed with the random-shaped material. It should be noted that the relative crystallinity of all the samples was above 92% (Table 1). It means that the random-shaped material was not copper oxide and they could be SAPO-34 crystals with different crystal morphologies. Thus, it can be deduced that the high Cu content could change the morphology of SAPO-34 crystal.

For clarifying the effect of different Cu contents in Cu/SAPO-34 explicitly, the physical properties of samples are summarized in Table 1. It is notable that the Cu/Si atom ratios of Cu/SAPO-34 catalysts were quite different from those of precursor solution, but the trend was inconsistent. It indicated that only a part of Cu could enter into the pore and the skeleton of SAPO-34. In addition, it can be seen from Table 1 that the range of grain sizes of the Cu/SAPO-34 catalysts became smaller as the Cu/Si ratio increases from 0 to 0.2. The smaller grain sizes may be beneficial to the catalytic activity. The sample *e* (Cu/Si = 0.2) has the highest crystallinity and the smallest grain sizes among the six samples, which is consistent with its high de- NO_x activity.

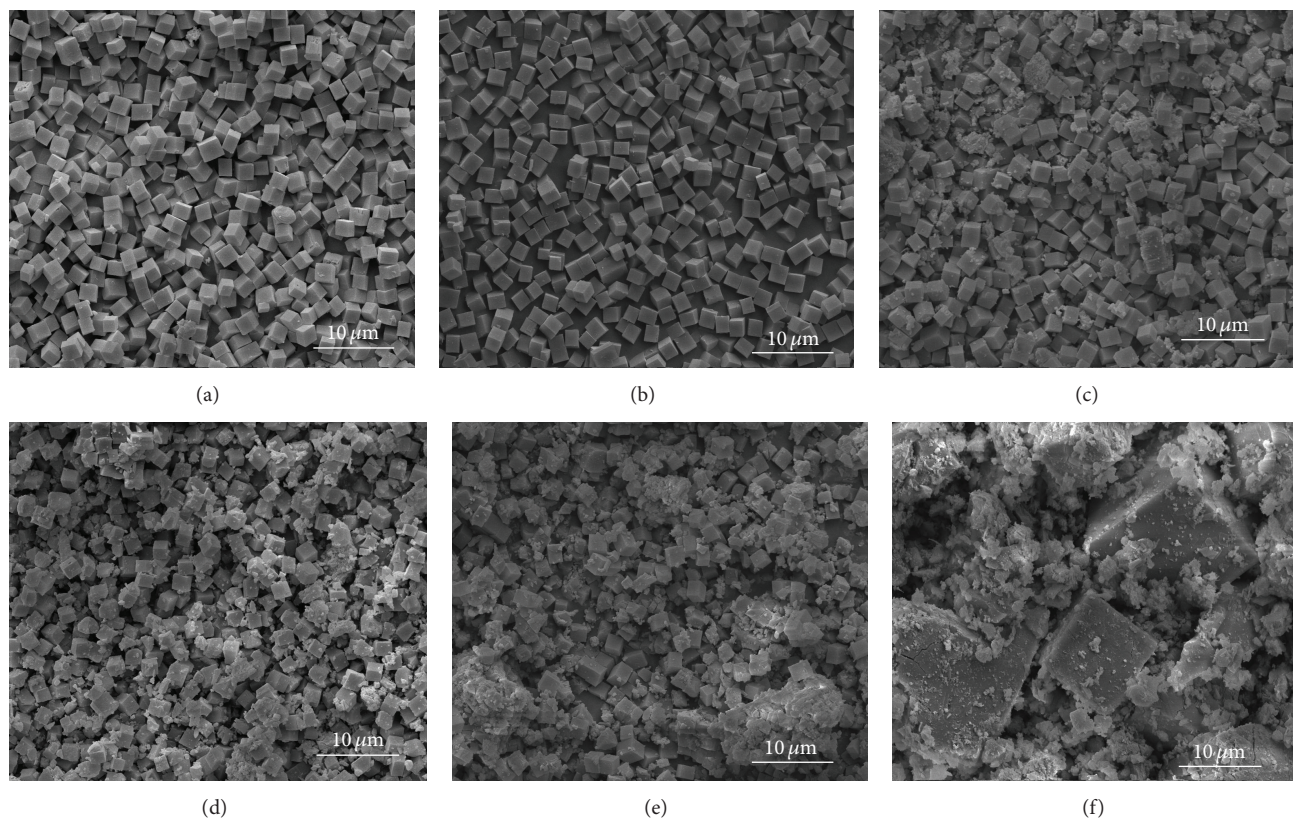


FIGURE 3: SEM images of Cu/SAPO-34 catalysts with different Cu contents ((a): Cu/Si = 0, (b): Cu/Si = 0.025, (c): Cu/Si = 0.05, (d): Cu/Si = 0.1, (e): Cu/Si = 0.2, and (f): Cu/Si = 0.4).

TABLE 1: Physical properties of the Cu/SAPO-34 catalysts with different Cu contents.

Physical properties	Samples					
	a	b	c	d	e	f
Cu/Si atom ratio of initial gel	0	0.025	0.05	0.1	0.2	0.4
Cu/Si atom ratio of Cu/SAPO-34	0	0.023	0.038	0.065	0.120	0.171
Relative crystallinity %	98.36	94.21	93.81	94.83	99.65	92.18
Grain size/ μm	0.6–2.0	1.5–2.0	1.2–2.0	0.8–2.0	1.0–1.5	0.6–18

3.2. Activity Test of Pd Modified Cu/SAPO-34. For further improving the de- NO_x activity of the Cu/SAPO-34 catalysts, the noble metal Pd was introduced into the Cu/SAPO-34 catalysts with Cu/Si = 0.05 and 0.2 by impregnated using $\text{Pd}(\text{NO}_3)_2$ as precursor. The Pd loading on catalyst was 0.5% (denoted as PdCu/SAPO-34). Figure 4 illustrates the NO conversions of the PdCu/SAPO-34 catalysts. The experimental GHSV is $40,000 \text{ h}^{-1}$, which is close to the real diesel engine exhaust.

When C_3H_6 was used as reducing agent and the temperature was below 300°C , the NO conversions of the PdCu/SAPO-34 catalysts were similar to the samples without Pd. However, when the temperature rises from 300°C to 600°C , the advantage of Pd became significant. The NO conversions of PdCu/SAPO-34 catalysts were much higher than these of Cu/SAPO-34 catalysts and it can reach to around 70%. It is also found that the de- NO_x activities of the PdCu/SAPO-34 catalysts with Cu/Si = 0.2 were superior to these of Cu/Si = 0.05, especially, at the higher temperature.

When NH_3 was used as reducing agent, the NO conversions of the PdCu/SAPO-34 catalysts were similar to those of the Cu/SAPO-34 catalysts, especially, at the low temperature. The de- NO_x activities of the PdCu/SAPO-34 catalysts with Cu/Si = 0.2 were higher than these with Cu/Si = 0.05, and the maximum of the NO conversion can reach to 90%. That is because the reaction between NH_3 and NO with low activation energy is quite easy [29]. According to the previous reports [30], the ammonium ion would react with the NO-Pd^{2+} species to give N_2 . Similarly, the activity of the Pd modified Cu/SAPO-34 samples was superior to those without Pd, especially, at the high temperature.

3.3. Antiaging Performance of Catalysts

3.3.1. Cu/SAPO-34 Catalysts. The effects of aging on the de- NO_x activity of the Cu/SAPO-34 catalysts with Cu/Si = 0.2 and Cu/Si = 0.05 were shown in Figures 4(a) and 4(c). The NO conversion of the two kinds of the Cu/SAPO-34 catalysts

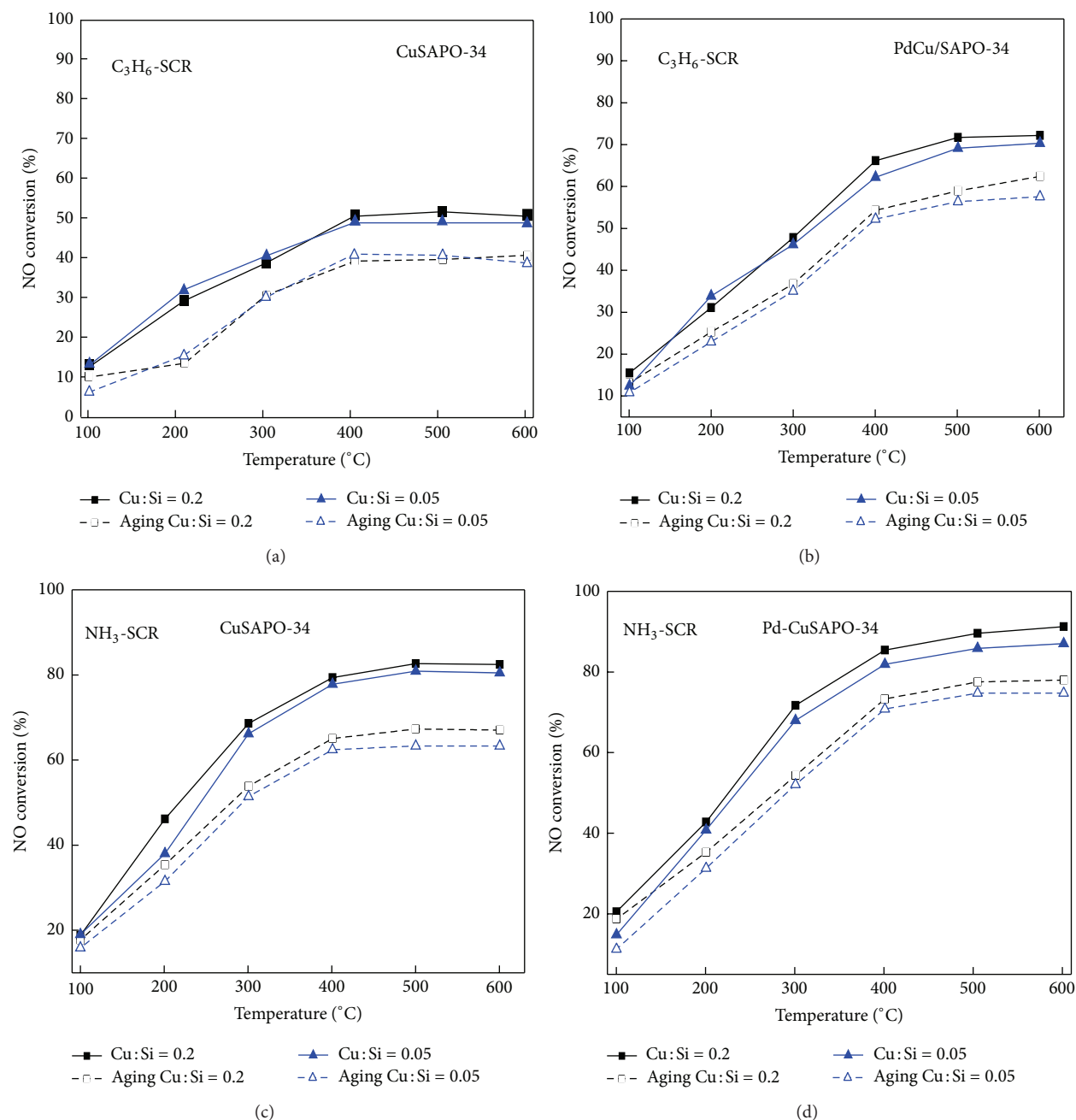


FIGURE 4: NO conversion of PdCu/SAPO-34 and Cu/SAPO-34 catalysts (GHSV: 40,000 h⁻¹).

decreased sharply after aging for C₃H₆-SCR, especially, when the temperature is in the range of 200–600°C. For NH₃-SCR, the NO conversions of the two kinds of Cu/SAPO-34 catalysts decreased slightly at low temperature, but it decreased significantly as the temperature was above 200°C, particularly, for the sample with Cu/Si = 0.05.

Figure 5 illustrates the XRD patterns of the Cu/SAPO-34 catalysts before and after aging. The intensities of the characteristic peaks weakened after aging compared with the fresh samples, which indicated that the aging process had a negative effect on the crystallinity. It may be the reason for the decrease of the de-NO_x activity.

In order to investigate the effect of aging on the morphology and structure of the Cu/SAPO-34 catalysts, the samples before and after aging were characterized by SEM and the results are shown in Figure 6. Comparing with the fresh samples, more random-shaped materials were found around the crystal particles; the smooth and regular crystal grains were partly destroyed, which leads to the decrease of the NO conversion of the Cu/SAPO-34 catalysts.

3.3.2. PdCu/SAPO-34 Catalysts. The activity test of the PdCu/SAPO-34 catalysts before and after aging in C₃H₆ and NH₃ is also shown in Figures 4(b) and 4(d). The NO

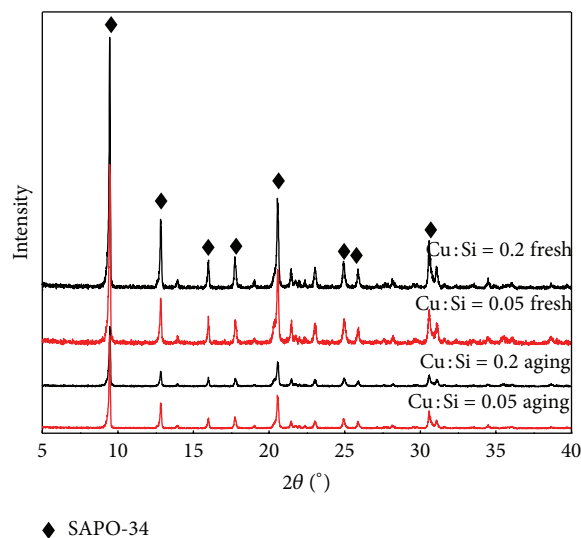


FIGURE 5: XRD patterns of Cu/SAPO-34 samples before and after aging.

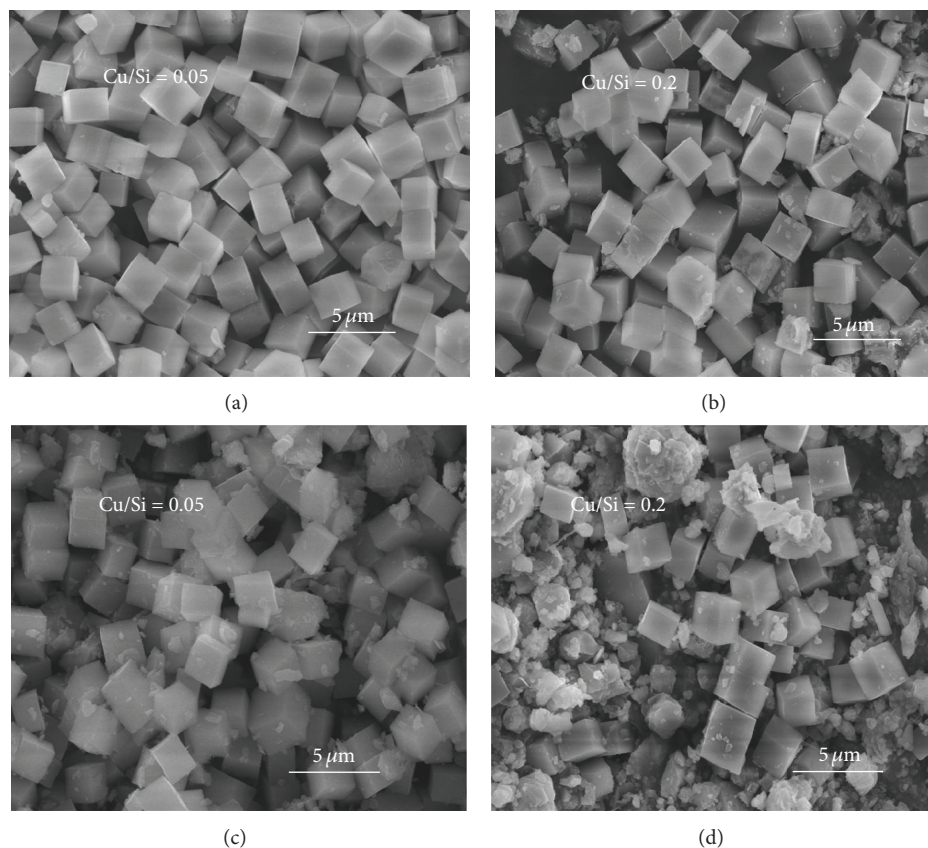


FIGURE 6: SEM images of Cu/SAPO-34 before ((a) and (b)) and after aging ((c) and (d)).

conversion of the two PdCu/SAPO-34 samples decreased less than the samples without Pd after aging. Besides, the de-NO_x activities of the aged PdCu/SAPO-34 catalysts were superior to that of the aged Cu/SAPO-34 catalysts. It indicated that the addition of Pd can improve the antiaging performance of the Cu/SAPO-34 catalysts.

The XRD patterns of the PdCu/SAPO-34 catalysts are shown in Figure 7. Compared with Figure 1, it can be found

that the peaks positions are not remarkably changed by the addition of Pd. No characteristic peak for Pd was visible, which should be related to the low Pd addition amount. The crystal type was still mainly occupied by the SAPO-34 catalyst. The XRD patterns of the PdCu/SAPO-34 samples after aging treatment are also displayed in Figure 7. The crystalline types of samples before and after aging treatment had no obvious changes and also mainly composed of the SAPO-34

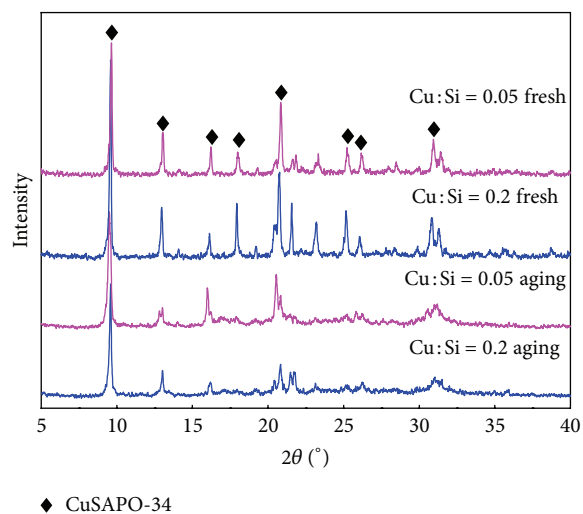


FIGURE 7: XRD patterns of PdCu/SAPO-34 before and after aging treatment.

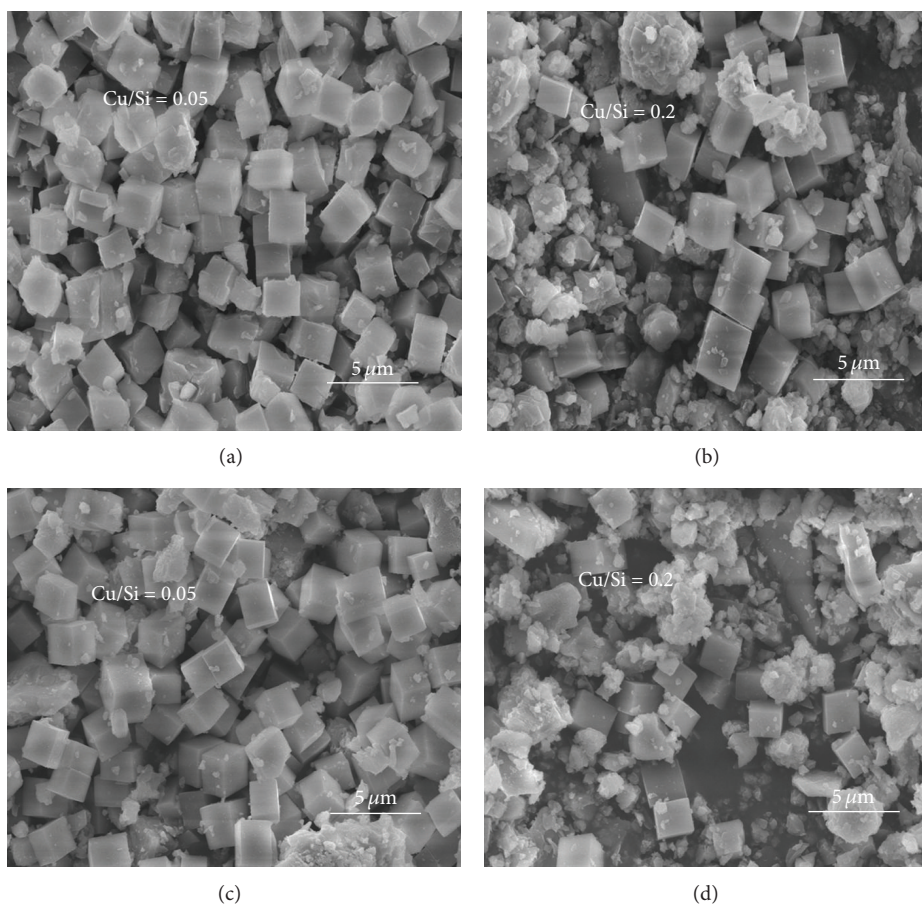


FIGURE 8: SEM images of PdCu/SAPO-34 before ((a) and (b)) and after aging ((c) and (d)).

catalyst. However, the peaks intensity of the SAPO-34 catalyst corresponding to $2\theta = 16.0^\circ\sim 16.2^\circ$, $17.85^\circ\sim 18.15^\circ$, $20.55^\circ\sim 20.9^\circ$, $24.95^\circ\sim 25.4^\circ$, and $30.5^\circ\sim 30.7^\circ$ was weakened obviously, indicating that the aging treatment partially destroyed the regularity and crystallinity of SAPO-34.

The SEM images of the PdCu/SAPO-34 catalyst with Cu/Si = 0.05 and 0.2 are given in Figure 8. All of the samples were mainly composed of the cubic crystal grains, which were the SAPO-34 crystals surrounded by some random-shaped materials. Comparing with the fresh samples, the

aged samples had more random-shaped materials which were the fragment of SAPO-34 crystals. It suggested that more SAPO-34 crystals had been broken after aging treatment, which resulted in the decrease of the NO conversion of the PdCu/SAPO-34 catalysts.

It can be concluded that the de-NO_x activity of the Cu/SAPO-34 and PdCu/SAPO-34 catalysts had a decrease due to the rupture of SAPO-34 crystals resulted by the aging treatment. But the antiaging performance of PdCu/SAPO-34 catalysts was better than Cu/SAPO-34 catalysts.

4. Conclusions

The Cu/SAPO-34 catalysts were successfully prepared by in-situ hydrothermal synthesis. The results of XRD and SEM analysis indicated that the addition of Cu does not change the CHA structure of SAPO-34 crystal and the prepared Cu/SAPO-34 catalysts were cubic crystals with similar averaged sizes (0.6–2 μm). But the high Cu content could change the morphology of the SAPO-34 crystals. The Cu/SAPO-34 catalysts with Cu/Si = 0.05, 0.1, and 0.2 had better de-NO_x activities than other Cu/SAPO-34 and SAPO-34 catalysts.

The antiaging performance of the Cu/SAPO-34 and PdCu/SAPO-34 catalysts was studied and the experiment results suggested that the de-NO_x activity of the Cu/SAPO-34 and PdCu/SAPO-34 catalysts had a decrease due to the rupture of SAPO-34 crystals resulted by the aging treatment. However, the addition of Pd could improve the de-NO_x activity and antiaging performance of the catalysts.

Acknowledgments

The authors gratefully thank NSFC (20906067), CPSF (2011M500543), and the Program for the Top Young Academic Leaders of Higher Learning Institutions of Shanxi for their financial support.

References

- [1] J. N. Armor, "Environmental catalysis," *Applied Catalysis B*, vol. 1, no. 4, pp. 221–256, 1992.
- [2] Y. Kondo, T. Kitada, M. Koike, S. Kawakami, and Y. Makino, "Nitric oxide and ozone in the free troposphere over the western Pacific Ocean," *Journal of Geophysical Research*, vol. 98, no. 11, pp. 20527–20535, 1993.
- [3] R. Impens, "Automotive traffic risks for the environment," in *Studies in Surface Science and Catalysis*, A. Crucq and A. Frennet, Eds., pp. 11–29, New York, NY, USA, 1987.
- [4] H. Bosch, F. J. G. Janssen, F. M. G. van den Kerkhof, J. Oldenziel, J. G. van Ommen, and J. R. H. Ross, "The activity of supported vanadium oxide catalysts for the selective reduction of NO with ammonia," *Applied Catalysis*, vol. 25, pp. 239–248, 1986.
- [5] L. Wang, J. R. Gaudet, W. Li, and D. Weng, "Migration of Cu species in Cu/SAPO-34 during hydrothermal aging," *Journal of Catalysis*, vol. 306, pp. 68–77, 2013.
- [6] J. J. Xue, X. Q. Wang, G. S. Qi, J. Wang, M. Q. Shen, and W. Li, "Characterization of copper species over Cu/SAPO-34 in selective catalytic reduction of NO_x with ammonia: relationships between active Cu sites and de-NO_x performance at low temperature," *Journal of Catalysis*, vol. 297, pp. 56–64, 2013.
- [7] L. Wang, W. Li, G. Qi, and D. Weng, "Location and nature of Cu species in Cu/SAPO-34 for selective catalytic reduction of NO with NH₃," *Journal of Catalysis*, vol. 289, pp. 21–29, 2012.
- [8] H.-X. Liu, Z.-K. Xie, C.-F. Zhang, and Q.-L. Chen, "Synthesis of SAPO-34 molecular sieve using hydrogen fluoride and triethylamine as composite template," *Chinese Journal of Catalysis*, vol. 16, no. 6, pp. 521–527, 2003.
- [9] Z. M. Liu, X. Y. Huang, C. Q. He, Y. Yang, L. X. Yang, and G. Y. Cai, "Thermal and hydrothermal stability of SAPO-34 molecular sieve," *Chinese Journal of Catalysis*, vol. 17, no. 6, pp. 540–543, 1996.
- [10] M. Goepper, F. Goth, L. Delmotte, J. L. Guth, and H. Kessler, "Effect of template removal AMD rehydration on the structure of AlPO₄ and AlPO₄-based microporous crystalline solids," *Studies in Surface Science and Catalysis*, vol. 49, pp. 857–866, 1989.
- [11] J. C. Wang, Z. Q. Liu, G. Feng, L. P. Chang, and W. R. Bao, "In situ synthesis of CuSAPO-34/cordierite and its selective catalytic reduction of nitrogen oxides in vehicle exhaust: the effect of HF," *Fuel*, vol. 109, pp. 101–109, 2013.
- [12] T. Ishihara, M. Kagawa, F. Hadama, and Y. Takita, "Copper ion-exchanged SAPO-34 as a thermostable catalyst for selective reduction of NO with C₃H₆," *Journal of Catalysis*, vol. 169, no. 1, pp. 93–102, 1997.
- [13] F. C. Meunier, R. Ukrepec, C. Stapleton, and J. R. H. Ross, "Effect of the silver loading and some other experimental parameters on the selective reduction of NO with C₃H₆ over Al₂O₃ and ZrO₂-based catalysts," *Applied Catalysis B*, vol. 30, no. 1-2, pp. 163–172, 2001.
- [14] T. Horiuchi, T. Fujiwara, L. Chen, K. Suzuki, and T. Mori, "Selective catalytic reduction of NO by C₃H₆ over Co/Al₂O₃ catalyst with extremely low cobalt loading," *Catalysis Letters*, vol. 78, no. 1-4, pp. 319–323, 2002.
- [15] M. Kantcheva, "FT-IR spectroscopic investigation of the reactivity of NO_x species adsorbed on Cu²⁺/ZrO₂ and CuSO₄/ZrO₂ catalysts toward decane," *Applied Catalysis B*, vol. 42, no. 1, pp. 89–109, 2003.
- [16] D. Pietrogioacomi, D. Sannino, A. Magliano, P. Ciambelli, S. Tuti, and V. Indovina, "The catalytic activity of CuSO₄/ZrO₂ for the selective catalytic reduction of NO_x with NH₃ in the presence of excess O₂," *Applied Catalysis B*, vol. 36, no. 3, pp. 217–230, 2002.
- [17] L. Ma, Y. S. Cheng, G. Cavataio, R. W. McCabe, L. X. Fu, and J. H. Li, "Characterization of commercial Cu-SSZ-13 and Cu-SAPO-34 catalysts with hydrothermal treatment for NH₃-SCR of NO_x in diesel exhaust," *Chemical Engineering Journal*, vol. 225, pp. 323–330, 2013.
- [18] J. H. Kwak, D. Tran, S. D. Burton, J. Szanyi, J. H. Lee, and C. H. F. Peden, "Effects of hydrothermal aging on NH₃-SCR reaction over Cu/zeolites," *Journal of Catalysis*, vol. 287, pp. 203–209, 2012.
- [19] F. Diehl, J. Barbier Jr., D. Duprez, I. Guibard, and G. Mabilon, "Catalytic oxidation of heavy hydrocarbons over Pt/Al₂O₃. Influence of the structure of the molecule on its reactivity," *Applied Catalysis B*, vol. 95, no. 3-4, pp. 217–227, 2010.
- [20] L. F. Liotta, "Catalytic oxidation of volatile organic compounds on supported noble metals," *Applied Catalysis B*, vol. 100, no. 3-4, pp. 403–412, 2010.
- [21] R. J. Farrauto and K. E. Voss, "Monolithic diesel oxidation catalysts," *Applied Catalysis B*, vol. 10, no. 1-3, pp. 29–51, 1996.

- [22] Y. Q. Zuo, L. N. Han, W. R. Bao, L. P. Chang, and J. C. Wang, "Effect of CuSAPO-34 catalyst preparation method on NO_x removal from diesel vehicle exhausts," *Chinese Journal of Catalysis*, vol. 34, no. 6, pp. 1112–1122, 2013.
- [23] Z. Sarbak and M. Lewandowski, "Catalytic elimination of nitrogen organic compounds from the coal-liquid and structural properties of NiMo catalysts supported on NaX and NaY zeolites modified with transition metal cations," *Applied Catalysis A*, vol. 208, no. 1-2, pp. 317–321, 2001.
- [24] T. Armaroli, L. J. Simon, M. Digne et al., "Effects of crystal size and Si/Al ratio on the surface properties of H-ZSM-5 zeolites," *Applied Catalysis A*, vol. 306, pp. 78–84, 2006.
- [25] F. Benaliouche, Y. Boucheffa, P. Ayrault, S. Mignard, and P. Magnox, " NH_3 -TPD and FTIR spectroscopy of pyridine adsorption studies for characterization of Ag- and Cu-exchanged X zeolites," *Microporous and Mesoporous Materials*, vol. 111, no. 1-3, pp. 80–88, 2008.
- [26] Y. X. Wei, D. Z. Zhang, L. Xu et al., "Synthesis, characterization and catalytic performance of metal-incorporated SAPO-34 for chloromethane transformation to light olefins," *Catalysis Today*, vol. 131, no. 1-4, pp. 262–269, 2008.
- [27] L. Huang, F. Peng, H. Wang, H. Yu, and Z. Li, "Preparation and characterization of $\text{Cu}_2\text{O}/\text{TiO}_2$ nano-nano heterostructure photocatalysts," *Catalysis Communications*, vol. 10, no. 14, pp. 1839–1843, 2009.
- [28] Z. Liu, L. Tang, L. Chang, J. Wang, and W. Bao, "In situ synthesis of Cu-SAPO-34/cordierite for the catalytic removal of NO_x from diesel vehicles by C_3H_8 ," *Chinese Journal of Catalysis*, vol. 32, no. 4, pp. 546–554, 2011.
- [29] I. Mejía-Centeno, S. Castillo, R. Camposeco, and G. A. Fuentes, "SCR of NO_x by NH_3 over model catalysts: the kinetic data-linear free energy relation," *Catalysis Communications*, vol. 31, pp. 11–15, 2013.
- [30] K.-I. Shimizu, F. Okada, Y. Nakamura, A. Satsuma, and T. Hattori, "Mechanism of NO reduction by CH_4 in the presence of O_2 over Pd-H-mordenite," *Journal of Catalysis*, vol. 195, no. 1, pp. 151–160, 2000.